DTIC FILE COPY

AD-A208 837

GC-TR-89-1683

LASER MELT/PARTICLE INJECTION PROCESSING; CHARACTERIZATION AND PERFORMANCE OF MATERIALS



GEO-CENTERS, INC.

89 6 08 069

①

GC-TR-89-1683

LASER MELT/PARTICLE INJECTION PROCESSING; CHARACTERIZATION AND PERFORMANCE OF MATERIALS

Prepared For
Naval Research Laboratory
4555 Overlook Drive, S.W.
Washington, D.C. 20375-5000
Under Contract No. N00014-86-C-2265

DTIC ELECTE JUN 03 1989 S D

Prepared By
GEO-CENTERS, INC.
7 Wells Avenue
Newton Centre, MA 02159

May 1989

This document has been approved for public release and sale; its distribution is unlimited.

GEO-CENTERS, INC.

REPORT DOCUMENTATION PAGE

ADA208837

1a. REPORT SECURITY CLASSIFICATION UNCLASSIFIED	1b. RESTRICTIVE MARKINGS
2a. SECURITY CLASSIFICATION AUTHORITY	3. DISTRIBUTION/AVAILABILITY OF REPORT Approved for public release; distribution unlimited
2b. DECLASSIFICATION/DOWNGRADING SCHEDULE	
4. PERFORMING ORGANIZATION REPORT NUMBER(S) GC-TR-89-1683	5. MONITORING ORGANIZATION REPORT NUMBER(S)
6a. NAME OF PERFORMING ORGANIZATION GEO-CENTERS, INC. 6b. OFFICE SYMBOL (If applicable)	7a. NAME OF MONITORING ORGANIZATION
6c. ADDRESS (City, State, and ZIP Code) 7 Wells Avenue Newton Centre, MA 02159	7b. ADDRESS (City, State, and ZIP Code)
8a. NAME OF FUNDING/SPONSORING ORGANIZATION Naval Research Laboratory 8b. OFFICE SYMBOL (If applicable) Code 6301	9. PROCUREMENT INSTRUMENT IDENTIFICATION NUMBER Contract Number N00014-86-C-2265
8c. ADDRESS (City, State, and ZIP Code) 4555 Overlook Avenue, S.W. Washington, DC 20375-5000	10. SOURCE OF FUNDING NUMBERS PROGRAM ELEMENT NO. / PROJECT NO. / TASK NO. / WORK UNIT ACCESSION NO

11. TITLE (Include Security Classification)
Laser Melt/Particle Injection Processing; Characterization and Performance of Materials (U)

12. PERSONAL AUTHOR(S)
Drs. K. Cooper, M.S. Duesbery, N.P. Louat, and H.Y. Yu

13a. TYPE OF REPORT	13b. TIME COVERED	14. DATE OF REPORT (Year, Month, Day)	15. PAGE COUNT
Final	FROM 8/86 TO 3/89	May 1989	574

16. SUPPLEMENTARY NOTATION

17. COSATI CODES			18. SUBJECT TERMS (Continue on reverse if necessary and identify by block number)
FIELD	GROUP	SUB-GROUP	Laser Processing, Powder Metallurgy, Ceramics, Composite Materials, Fracture Mechanics

19. ABSTRACT (Continue on reverse if necessary and identify by block number)

This report summarizes work accomplished in the following task areas for the duration of this contract: a) The development of the Laser Melt/Particle Injection Process as a means to form sound, wear-resistant surfaces on soft metallic substrates; b) The research and development of powder metallurgy processes to further the understanding of particle atomization and to evaluate novel material production; and c) The characterization and testing of high performance metallic, ceramics and composite materials.

20. DISTRIBUTION/AVAILABILITY OF ABSTRACT ☒ UNCLASSIFIED/UNLIMITED ☐ SAME AS RPT. ☐ DTIC USERS	21. ABSTRACT SECURITY CLASSIFICATION UNCLASSIFIED
22a. NAME OF RESPONSIBLE INDIVIDUAL Mr. Ralph Judy, Jr.	22b. TELEPHONE (Include Area Code) 202-767-2345 22c. OFFICE SYMBOL Code 6301

DISCLAIMER NOTICE

THIS DOCUMENT IS BEST QUALITY PRACTICABLE. THE COPY FURNISHED TO DTIC CONTAINED A SIGNIFICANT NUMBER OF PAGES WHICH DO NOT REPRODUCE LEGIBLY.

OR are
Blank pgs
that have
Been Removed

BEST
AVAILABLE COPY

TABLE OF CONTENTS

Section		Page
1.0	EXECUTIVE SUMMARY	1
2.0	LASER MELT/PARTICLE INJECTION PROCESSING	3
3.0	POWDER METALLURGY	9
4.0	CHARACTERIZATION AND TESTING OF MATERIALS	14
	Ceramic and Composite Materials	14
	Dispersion Hardening in Metals	17
5.0	MECHANICS OF MATERIALS	21
	Directional Instability of Dynamic Cracks in Materials	21
	Non-Linear Constitutive Behavior of Composites	22
	High Damping Materials with Nanometer Voids	25
	Compact Micromechanics Tester	26
	Compositionally Modulated Thin Films	27
	Three Dimensional Stresses in a Half-Space Due to Axisymmetrical Ellipsoidal Inclusions	27
	Elastic Constraints of Films Determined by the Indentation Test-Theoretical Considerations	28
	Phase Trans. and Strength of Materials	29
	High Temperature Materials	31
	Applied Ceramics and Composites	31

1.0 EXECUTIVE SUMMARY

The following final technical report is a compilation of a three year research and development effort undertaken to investigate several technical issues of interest to the Navy.

This research program represented a multi-task, multidisciplinary effort consisting of sixteen separate work elements which could be grouped into three technological areas:

1) Laser Melt-Particle Injection Processing

2) Development of High Performance Ceramic Materials and Ultrafine Metal Powders

3) Mechanical Testing of Naval Materials

The laser melt-particle injection process is a technique which has been developed as a method to produce wear resistant surfaces on metallic substrates. The modified surface layer is an injected carbide/metal matrix composite which is particularly useful for tribological applications. Under the current effort, GEO-CENTERS' scientists have developed techniques to form injected layers wider than 1.0 cm, eliminated closure problems associated with making circular melt passes for the shaft seal test samples, have identified the crystal structure and nature of the resolidification products and the solidification reactions, and have determined the processing conditions that produce crack-free injected layers. The primary substrate material was Inconel 625, a nickel-based corrosion resistant superalloy, with additional materials including Tribaloy 400, and Ti-6Al-4V alloy. The injected materials consisted of tungsten and titanium carbides.

In developing ultrafine metal powders, GEO-CENTERS has investigated several techniques which depend upon the rapid solidification of liquid metal which is subdivided into droplets of ultra-fine size distributions. Rapid solidification of these materials results in non-equilibrium microstructures which are known to impart superior properties which are highly desirable in the manufacture of components that are slated to operate under adverse environmental conditions (such as high temperature or corrosive environments). The primary rapid solidification technique consisted of high pressure gas atomization, but also included investigations of counter rotating fluid atomization, and rapidly spinning cup atomization as alternatives.

The failure criteria for Naval structures are based upon the analysis of failure mechanisms which are determined after subjecting the materials to anticipated service conditions. By examining the experimental data specifying the strength, fracture toughness, fatigue, crack growth, etc., theoretical and numerical approaches to continuum mechanics may subsequently be used to predict the structural behavior of a particular material. In so doing, predictions as to the material's response to mechanical, thermal, and environmental loading may be made, as well as providing valuable insights into the optimization of metallurgical and processing variables used during component fabrication. These techniques have been applied by GEO-CENTERS' scientists to study metals, ceramics, and composite materials.

The majority of this report is a compilation of the technical documents written for publication in refereed journals, or for presentation at national meetings in each field. These documents summarize the results of our research and development efforts under this contract.

Accession For	
NTIS GRA&I	X
DTIC TAB	☐
Unannounced	☐
Justification	
By	
Distribution/	
Availability Codes	
Dist	Avail and/or Special
A-1	



2.0 LASER MELT/PARTICLE INJECTION PROCESSING

Introduction

In a previous report on laser melt/particle injection processing (Ref. 1), the development of a technique to form wear resistant surfaces on metallic substrates was described. The modified surface layer was an injected carbide/metal matrix composite which was found to be hard and wear resistant, especially under tribological conditions. The technique allowed for the processing of injected layers of desired dimensions and geometry. In that study, the effects of processing parameters on the microstructure, carbide volume fraction and dimensional stability were determined. The rate of particle injection was found to be a critical parameter. The basic microstructure was uniformly dispersed carbide particulate in a metal matrix. In addition, the metal matrix consisted of resolidified carbides and eutectic carbides which were formed as the injected carbide dissolution products and which had a strong influence on the microhardness. Having established the optimum processing conditions, test samples in the form of a shaft seal ring were fabricated and successfully tested.

The subsequent research and development tasks undertaken for this contract effort included: a) developing techniques to form injected layers wider than 1.0 cm; b) the elimination of closure problems associated with making circular melt passes for the shaft seal test samples; c) identifying the crystal structure and the nature of the resolidification products and the solidification reactions; and d) the determination of processing conditions that would produce crack-free injected layers.

Approach

The approach to the problems identified above was two-fold. One was to modify the engineering of the laser melt/particle injection process to solve problems such as forming wider injected layers, eliminating closure problems and minimizing cracking within the layers. The second was to do a detailed analysis of the microstructures using SEM and TEM and to determine microstructural influence on properties such as microhardness and wear. Most of this work involved carbides of tungsten and titanium and, because of its obvious interest to the Navy, the substrate material investigated was Inconel 625, a nickel-based, corrosion resistant superalloy. Additional work involved laser cladding with Tribaloy-400, a cobalt-based hardfacing alloy, and Ti-6Al-4V alloy substrate for comparative analysis.

Process Development and Discussion

Details of the development work on laser melt/particle injection processing are given in the attached publications (Ref. 2 to 7). Inconel 625 alloy coupons injected with WC and TiC particles were evaluated for microhardness and wear resistance (Ref. 2). It was found that the metal matrix in the WC injected samples was much harder than that in the TiC injected samples. Correspondingly, the friction wear behavior of the WC injected samples was more satisfactory than that of the TiC injected samples. Although the coefficient of friction, μ_k, progressively increased with the number of cycles, it never approached the value of the untreated sample. In the case of WC, this increase in μ_k was mainly due to slider wear, while in the case of TiC, this increase was due to a combination of matrix and slider wear. The advantage of injecting with finer sized particles was mainly to reduce slider-matrix contact and improve friction wear behavior.

Process modifications and technical considerations to form wider injected layers with single melt passes are discussed in Ref. 3. Previously, larger surface areas were treated by overlapping several narrow melt passes. But this practice caused segregation and severe cracking within the overlapped regions. In addition, making several melt passes was a time consuming and expensive process. Selected areas having desired dimensions were produced by oscillating the laser beam over the substrate and forming a wide melt pool. Into the wide melt pool carbide particles were fed via a specially designed injection nozzle. This nozzle had a slotted opening that formed a rectangular particle spray. By controlling the oscillation amplitude, injected layer widths from 0.4 to 2.2 cm were obtained. An electromagnetically driven oscillating mirror was used to form a line energy source on the sample surface. Feeding the powder from the receding edge of the melt pool was necessary to form uniformly thick layers and a continuous overlap upon closure of a circular injected pass. Furthermore, porosity and other defects in the closure overlap were minimized by reducing the beam-off shutter speed.

When a modified surface layer is hard and brittle, it can crack under the strain of residual stresses. A study was undertaken to determine the effect of various processing parameters on the cracking tendency in particle injected layers. The results of this discussion are summarized in Ref. 4. Several conclusions were made from this investigation. Due to their composite nature and modified matrix microstructure, particle injected layers were subjected to complex residual stresses. It was found that cracks initiated within the hard injected carbide phase. With medium and coarse WC, the crack density decreased with increasing powder feed rate. Samples injected with TiC exhibited more cracking than samples injected with WC. Layers made with the fine WC showed more cracking than layers made with the coarse WC. The crack density

decreased with increasing melt width. In general, conditions that favored reductions in cooling rate and matrix embrittlement resulted in a lower cracking tendency. To eliminate cracking in the injected layers and to improve their fracture properties, samples were preheated before laser treatment. An investigation was made to determine the degree of preheat and the mechanism by which cracking could be eliminated. The results of this study are given in Ref. 7. It was found that preheat eliminated cracking purely by reducing the residual stresses as the sample cooled from the melt temperature. There were no microstructural modifications brought by preheating. In the narrower, 1 cm wide, injected layers, a preheat of about 300°C was sufficient to prevent cracking. While, in the 2 cm. wide injected layers, a preheat of about 450°C was needed to eliminate cracking. These preheat temperatures were much lower than those reported in laser cladding studies.

Detailed microstructural analysis and microstructural influence on microhardness and wear are summarized in Refs. 5 and 6. As the injected carbide particles mixed with the molten pool, dissolution occurred, the extent to which depended upon the type of carbide and substrate, and the volume and size of the carbide. The initial solidification products were the resolidified carbides which appear as blocky, separate dendrites as in the case of WC, or as a network of dendrites as in the case of TiC. Resolidified carbides were heavily alloyed by elements from the substrate and had a crystal structure of the type MC, similar to the injected carbides. Next, the inter-particulate melt solidified in a dendritic or cellular mode. And as the solute was rejected, inter-dendritic eutectic carbides appeared as the final solidification products. TEM analysis revealed that the eutectic carbides were of the MC, M_2C and M_6C types having lamellar and script-type morphologies. SEM analysis showed preferential alloying of the

resolidified and eutectic carbides by selected elements from the substrate. Whether the alloying element depletion from the substrate was significant enough to adversely affect properties such as corrosion was not determined. While resolidified carbides hardened the matrix in both samples, the eutectic carbides in WC injected samples hardened the matrix to a greater extent than those in the TiC injected samples.

An integral part of the developmental work in this task area was to identify the major problems associated with transfer of this technology to an industrial setting. The laser melt/particle injection technology was explained to the Navy so that potential Navy clients could utilize the technology to fabricate large scale test samples for actual real time testing. In this regard, processing parameters such as laser power, sample speed, powder feed rate, preheat temperature, etc. were provided. In addition, possible modifications to the process were suggested to the sponsor.

References (Appendix I)

(1) K. P. Cooper, "Laser Melt/Particle Injection Processing", Corporate Report, GC-TR-86-1506, GEO-CENTERS, INC., Newton Centre, MA, (1986).

(2) K. P. Cooper, J. Vac. Sci. Technol. A, 4 (6), Nov/Dec (1966), 2857-2861.

(3) K. P. Cooper, R. Beigel and P. Slebodnick, in The Changing Frontiers of Laser Materials Processing, C. M. Banas and G. L. Whitney, eds., IFS(Publs) Ltd., U.K., (1987), 169-176.

(4) K. P. Cooper and J. D. Ayers, in Focus on Laser Materials Processing, S. L. Ream, ed., IFS Publ., U.K., (1988), 179-187.

(5) K. P. Cooper, in Laser Beam Surface Treating and Coating, SPIE vol. 957, Gerd Sepold, ed., SPIE, Bellingham, WA, (1988), 42-53.

(6) K. P. Cooper and J. D. Ayers, in Laser Surface Modification, AWS, Miami, FL, (1989), 115-131.

(7) K. P. Cooper and P. Slebodnick, to be published in the Proceedings of ICALEO '88, Laser Institute of America, Toledo, OH, (1989).

3.0 POWDER METALLURGY

Introduction

Solidification of liquid metal which is subdivided into droplets of ultra-fine size distributions, results in non-equilibrium microstructures. Depending upon the alloy system under consideration and the effective solidification rates, refined phase distributions, super-saturated solid solutions, metastable intermediate phases and amorphous phases are some of the microstructures observed in these materials. These microstructures are known to impart superior properties to the material which are highly desirable in the manufacture of components that are slated to operate under adverse environmental conditions such as high temperature or extreme corrosion. The rate of quenching or cooling of the volume of liquid is critical in the selection of one of these microstructures. Due to their high surface-to-volume ratio, small droplets are prone to cool and solidify more rapidly than large droplets. Rapid quenching brings the undercooled liquid into varying degrees of metastable states. The ensuing rapid solidification in the deep undercooled regime is essential in synthesizing novel microstructures. With this theoretical background in mind, it was important to develop a process that can form rapidly solidified powders having ultra-fine size distributions. High pressure gas atomization was one technique that was examined for producing ultra-fine metal powder.

Experimental Procedures

The high pressure gas atomization unit consisted of an atomizing die or nozzle and a bottom-pour furnace arranged in a vacuum chamber. The molten metal was poured through the die by lifting a stopper rod. High pressure gas jets leaving the atomizing die disrupted the melt stream into fine metal droplets

that convectively cooled and that solidified at a rapid rate further downstream. The powder was collected via a cyclone chamber in a container. The gasses left the chamber through a liquid scrubber. The entire operation was controlled by a programmable controller which was programmed to operate the stopper rod, the high pressure gas valve, the exit ball valve, etc. in a given time sequence. It was also programmed for fail-safe shut-down. The atomization runs were video-taped to observe and analyze the process in order to improve upon the processing conditions. Other parameters such as chamber pressure, run time, volume of gas used, pour temperature, etc. were also noted as a means for process characterization, diagnostics and trouble-shooting.

Prior to melting, the chamber was evacuated and backfilled with an inert gas such as argon. The atomizing gas was usually argon, helium or nitrogen, each gas having unique heat transfer and density properties. The use of inert gas atmospheres was essential in having a clean environment so that the formation of surface oxides were minimized. Surface oxides are harmful in that they catalyze the nucleation of solidification at an early stage in the undercooling behavior which is not desirable. Atomizing gas pressures of 1000 to 2000 psig were used, and at these pressures experiments have shown that a series of harmonic shock waves develop in the gas jets which when coupled with the free-falling melt stream effectively atomize it. Conventional gas atomization produces a size distribution of 30 to 300 microns with a mean size of about 100 microns. High pressure gas atomization produced a much finer and narrower size distribution, typically in the 1 to 100 micron size range, with the majority of them less than 30 microns. Besides the level of the atomizing gas pressure, which was needed to promote aspirating conditions within the pour tube,

the relative position of the pour tube with respect to the die cavity was important in arriving at optimized conditions for producing ultra-fine metal particles.

Copper and iron-based alloys were gas atomized. Copper-based alloys are useful in high thermal conductivity situations, aqueous corrosion conditions and high electrical conductivity applications. When alloyed with chromium or niobium, the high temperature strength of copper is improved. Iron-based alloys are useful in magnetic applications, especially when alloyed with cobalt and nickel. The melting and alloying of the base metal with some of the additional elements required a careful selection of crucible and stopper rod materials, thermocouples and furnace power requirements. For Cu-Cr-Ag alloys, a magnesia crucible surrounded by a graphite susceptor was used to melt the raw material charge. The stopper rod was actually an alumina tube into which was placed a Type B thermocouple which read the melt temperature. The melt was superheated to 200°C above the melting point. The pour tube was made of BN, while the stopper rod seat was made of MgO. The atomizing gas pressure was typically 1750 psig.

Analysis and Characterization

The gas atomized powder was characterized for particle size distribution, mean particle size, particle shape, appearance and color, surface structure and chemistry, crystal structure and microstructure and segregation. Standard sieve analysis was typically used to determine the size distribution. Appearance and color were gauged visually, while scanning electron microscopy was applied to determine the particle morphology. Optical and electron microscopies were used to determine the internal and surface microstructures and the microchemistry. While the optical microscope was suitable for coarser particles giving good phase contrast, the SEM was essential in determining the fine

microstructural variations in the ultra-fine particles. The SEM was also used to determine the microchemistry of the phase constituents which gave an idea of microsegregation and the degree of compositional homogeneity. X-ray crystallography was used to determine the crystal structure of the various phases in the powder. Powder diffraction data were used to arrive at structures which may not be equilibrium structures. These results were essential in determining the degree of structural modification in rapidly solidified powders and the amount of benefits thus derived. The feedback from the powder characterizations were used to optimize the processing conditions.

High pressure gas atomized Cu-Cr-Ag alloy powders contained a fine dispersion of Cr particles in a supersaturated Cu-rich matrix. Although the Cu-Cr phase diagram is a simple eutectic, in a slightly metastable state, a miscibility gap forms. We believe the Cr globules form initially as a result of a liquid phase separation reaction. As the liquid cools further, the Cu-rich matrix forms. The remarkable aspect about this microstructure is its high temperature stability. Rapidly solidified powders that were subsequently hot isostatic press processed showed little coarsening. In addition, the consolidated samples that were swaged and wire-drawn contained filaments of Cr that imparted strength without sacrificing conductivity.

Theoretical Considerations

In addition to gas atomization, techniques such as counter rotating fluid atomization and rapidly spinning cup atomization were also studied. By either method, a stream of melt was broken down by a rapidly rotating wall of liquid quenchant. The quenchant was typically an oil. The velocity and the pressure gradients in the oil acted to atomize the liquid stream. Besides the speed of the cup that held the quenchant, the velocity with which the melt

impinged upon the quenchant was also studied. Other variables that were investigated are atmospheric pressure, melt superheat and alloying elements. Besides finding conditions that produced the finest particles, these atomization techniques were also used to study the melt breakdown process. From this analysis, mechanisms could be proposed that would lead to a better understanding of the melt disintegration process, ultimately leading to the refinement and development of sophisticated atomization techniques. The goal was to produce a majority of particles in the sub-micron (<1 um) size range, because sub-micron particles have exciting, new properties.

The majority of this initial research and development effort was done on pure tin. Preliminary results of this work were published in Ref. 1 which is attached. Additional results were presented at international conferences. Results showed a dependency of particle shape on melt superheat and particle size distribution on outer cup speed. The inner cup speed had a marginal influence on particle size. Along with the spherical shape, long rods and thin flakes were also observed in the counter-rotating fluid atomized samples. We believe the non-spherical shapes are precursors of the final spherical form. For example, the edges of the thin flakes curl up and form the rods which break-down by Rayleigh instabilities into spheres. Under conditions of low superheat, these intermediate shapes were frozen-in.

Reference (Appendix II)

(1) J. D. Ayers and K. P. Cooper, in the Proceedings of the 2nd. Intl. Conf. on Rapidly Solidified Materials, ASM, Metals Park, OH, (1988), 199-206.

4.0 CHARACTERIZATION AND TESTING OF MATERIALS

CERAMIC AND COMPOSITE MATERIALS

Introduction

Porosity in ceramic materials can affect physical properties such as tensile strength, fracture behavior and piezoelectric response. It is believed that modifications induced by the pores, or voids, in the internal stress and electric field distributions are responsible. The effects can be enhanced by deliberate control of the size, shape and spatial distribution of the voids. In particular, it has been found experimentally that certain ordered arrangements of voids do not lead to the expected degradation of failure strength. In order to understand the reason for this behavior and hence to permit design optimization, a computer model of the system borrowing both from finite-element and molecular dynamic methods, was developed. Essentially, the composite material was modelled as a two-dimensional assembly of regularly spaced mass points interacting via parametric pair forces selected to match the elastic properties.

Work in the composites area involved materials and process development, theoretical modelling and experimental testing. The major thrust was the development of novel diagnostic methods for the study of the mechanical testing of small volume solid samples and thin films of composite materials, superalloys, superconductors and compositionally-modulated thin films.

Analysis and Characterization

Three distinct sources of internal stress modulation have been identified as follows. A uniaxial applied stress is assumed.

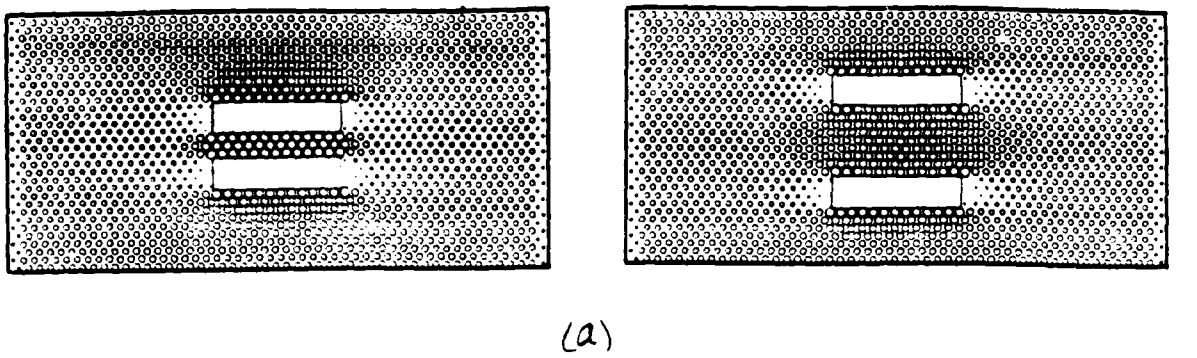
(a) Channelling Effect. This effect occurs because of the need to satisfy the equilibrium condition that the divergence of the stress must vanish. By analogy with magnetic flux lines, conservation of which is a consequence of an exactly similar constraint, it is possible to define lines of force which can end only at points of loading. The density of the force lines defines the stress. The lines of force must be deflected to pass through the intervoid channels, resulting in a higher 'flux' density and consequent higher stress in these regions. Examples are shown in Fig. 1(a), in which the tensile stresses in the direction of the applied stress are displayed as circles centered on the particle positions, with radius proportional to the magnitude of the stress. The stress concentrations in the intervoid channels are clearly visible.

(b) Shape Effect. The action of the external stress in deforming the void surfaces causes a stress concentration at the void surfaces parallel to the stress direction in the same way that the Griffith-Inglis mechanism causes a stress concentration at the tip of a crack. The stress concentration is always present, but is largest when the small dimension of the void is parallel to the stress direction and increases with increasing void aspect ratio. Extreme examples are shown for isolated voids in the diagrams of Fig. 1(b).

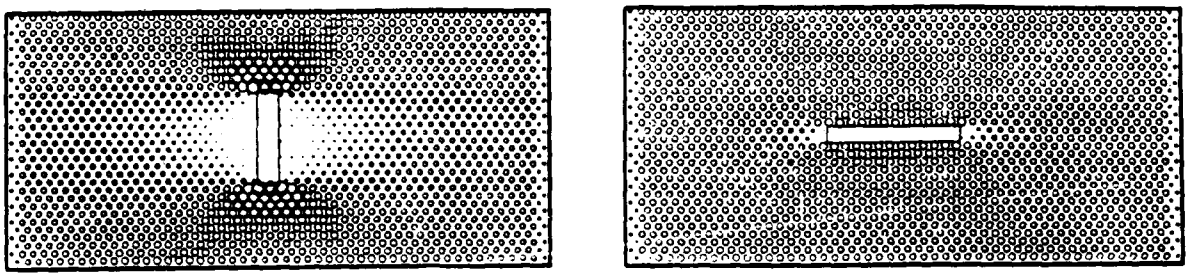
(c) Boundary Effect. The boundary conditions at internal voids require that there be no surface stress. For uniaxial stresses this means that there is a region of depleted stresses adjacent to the void surfaces normal to the applied tensile stress. Examples of the effect can be seen in Fig. 1(c).

For a closely-spaced array of voids, the intervoid spaces parallel to the stress direction can be nearly stress-free. This implies that there is no elastic energy stored in these regions; this is important for the fracture properties. The boundary effect (c) interacts strongly with the shape effect (b). The depletion

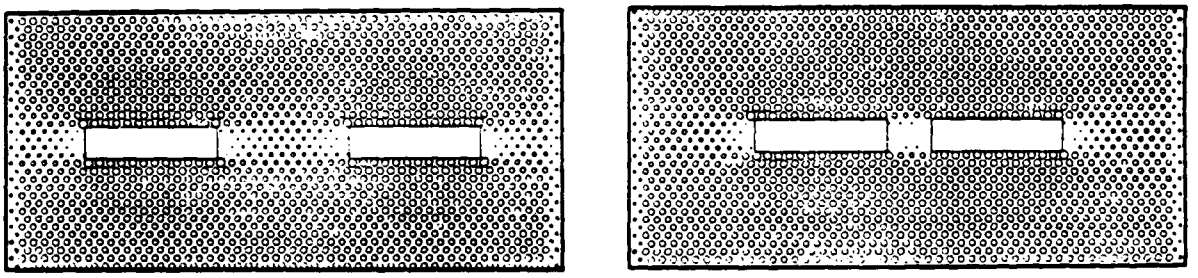
Figure 1.



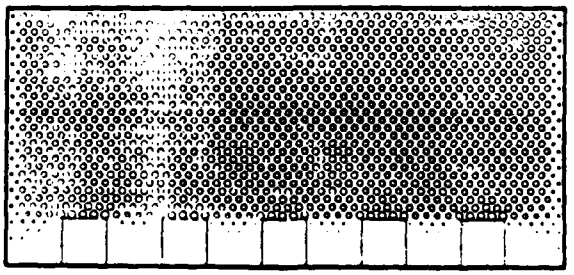
(a)



(b)



(c)



← all stresses →

(d)

GEO-CENTERS, INC.

of stress acts to relieve the tensile stress acting on each void; the stress concentrations at the void ends, which are proportional to these tensile stresses, are thereby also reduced.

Our overall conclusion was that while the internal stress enhancements can be minimized, it is not possible to construct a void array without some degree of stress concentration. Therefore, in general, void array composites are mechanically weaker than homogeneous ceramics. However, failure in ceramics is most frequently nucleated at a surface. For a composite containing void arrays there are both internal and external surfaces. The internal surfaces are thermally smoothed during the firing process; external surfaces, in contrast, are mechanically abraded at relatively low temperatures during component forming, and hence contain a higher density of microscopic flaws. If the voids are engineered to intersect the surface (Fig. 1(d)), the boundary effect unloads the surface, greatly reducing the probability of failure nucleation at the surface.

The reason for this low probability of surface failure is that crack propagation between voids is strongly inhibited by the low level of stored elastic energy in the inter-void regions. In order for the crack to propagate, a virtual movement of the crack tip must be capable of releasing enough energy to create new surfaces. In the energy-depleted areas between the voids (e.g. Fig. 1(d)), this condition cannot be satisfied and the crack cannot propagate. Hence the most likely crack path lies through the voids. This explanation has been confirmed by using different inter-particle potentials, each matching the same elastic properties, but with different surface energies. It has been found that in models with lower surface energy, cracks can more readily penetrate the low-stress intervoid regions. Details of the analysis are given in Refs. 1 and 2.

References (Appendix III)

(1) M. S. Duesbery and M. Kahn, "Computer Modelling of Ceramic-Air PZT Composites, Part I", submitted to the J Amer. Ceram.Soc.

(2) M. S. Duesbery and M. Kahn, "Computer Modelling of Ceramic-Air PZT Composites, Part II", submitted to the J Amer. Ceram. Soc.

DISPERSION HARDENING IN METALS

Introduction

The theoretical strength of a crystalline solid is of the order of one tenth of the shear modulus, a factor of up to 10^3 larger than the failure limits commonly observed in real materials. The source of the difference is rooted in the properties of crystal dislocations. Paradoxically, dislocation-based weakness in materials may result from exceptionally high or low dislocation mobility. For metals, high dislocation mobility and ease of multiplication combine to cause plastic failure at low applied stresses. In ceramics, on the other hand, it is the low mobility of dislocations which prevents stress relaxation at cracks and permits failure by brittle fracture at relatively low stress.

The problem, therefore, is to develop methods for reducing dislocation mobility in metals, and for increasing it in ceramics. The theoretical study of this requires the modelling of dislocation behavior on scales from an atomic to a macroscopic level. A specific example is the modelling of dispersion hardening in metals.

Analysis and Characterization

It has been known for many years that metals can be hardened significantly by precipitation of a second phase. Specific strengthening mechanisms have been identified and include:

(a) Coherency strengthening, caused by the stress field around a precipitate with a lattice constant different from that of the matrix.

(b) Modulus strengthening, caused by a difference in elastic moduli between precipitate and matrix.

(c) Order strengthening, caused by the need to create an antiphase domain boundary when a dislocation passes through an ordered precipitate.

(d) Stacking fault strengthening, due to a difference in stacking fault energy between precipitate and matrix.

(e) Surface strengthening, caused by the creation of new particle-matrix interfaces as the precipitate is sheared.

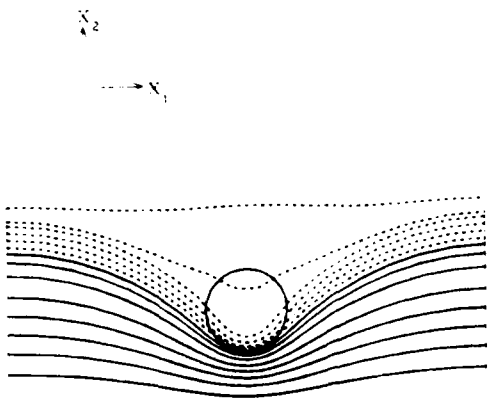
The principles underlying the hardening effect are understood at a qualitative level. The precipitates act as obstacles to the passage of dislocations, which must bypass the obstacles in order for plastic flow to proceed. Bypass can occur via any one of a number of processes, depending on the details of the second phase particles and the character of the dispersion. For example, soft precipitates may be easily intersected by dislocations. A harder second phase may require the dislocations to loop around the inclusions, leaving loops and debris which can contribute to the hardening effect; in this case the precipitates can sometimes fail unexpectedly, leading to avalanches of plastic flow and catastrophic failure of the material.

Quantitative understanding, in contrast, is poor, and the development of improved dispersion-hardened materials proceeds in large part by the slow and inefficient avenue of empiricism. This was understandable twenty-five years ago when the elastic theory of dislocations was insufficiently advanced to treat the self and interaction energies of arbitrarily shaped dislocations, and when the facilities for numerical modelling were severely limited. However, it is now possible to develop formally self-consistent Hamiltonians for the problem and to solve them numerically, making possible a cost-effective alternative to empirical experimentation.

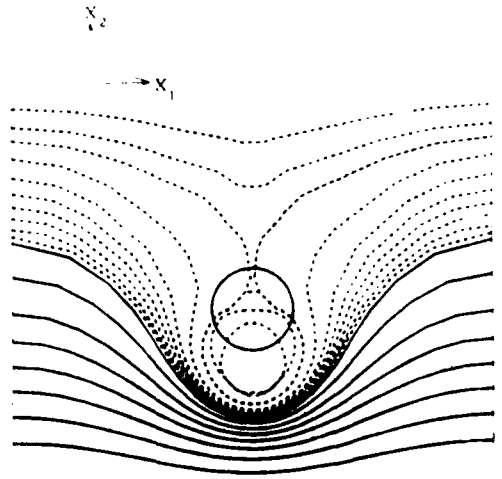
There are two levels to the problem. At the micromechanical level, it is necessary to understand the detailed interaction of dislocations with precipitates of different character, in order to categorize bypass mechanisms as a function of obstacle characteristics and determine the associated critical parameters. These results must then be used at a macroscopic level to model the statistical mechanics of dislocation motion through realistic distributions of dispersed obstacles.

We have considered the interaction of dislocations with one specific class of precipitate, elastically coherent spherical inclusions. The numerical method used was adapted from molecular dynamics techniques, treating the dislocation line as a set of discrete line segments, each moving according to Newtonian dynamics in the potential field of the remainder. The advantage of this approach is that finite temperatures and dynamic effects can be simulated. Examples of dislocation bypass of coherent obstacles by intersection and Orowan looping are shown in Fig. 2(a) and Fig. 2(b), respectively. Fig. 2(a) shows successive equilibrium positions of the dislocation for an obstacle-matrix lattice constant mismatch of 0.1% as the stress is increased in steps of

Figure 2.



(a)



(b)

GEO-CENTERS, INC.

$0.05\tau_o$, where τ_o is the line tension Orowan stress, from $0.15\tau_o$ to the bypass stress; non-equilibrium (dynamic) configurations for an applied stress $0.1\tau_o$ larger than critical are shown also (dashed lines) to illustrate the evolution of the bypass process. Bypass in this case occurs by intersection. A larger mismatch of 1% forces the dislocation to pass the obstacle array by the Orowan process, leaving behind a loop which lies partly inside the obstacle (Fig. 2(b)). The equilibrium configurations shown in Fig. 2(b) begin at a stress of $0.3\tau_o$ and advance in steps of $0.1\tau_o$ to bypass stress; subsequent non-equilibrium shapes (dashed lines) are the result of an additional stress increment of $0.1\tau_o$. A detailed analysis of this problem is given in Ref. 1.

Reference (Appendix IV)

(1) M. S. Duesbery, N. Louat and K. Sadananda, "The Interactions of Dislocations with Coherent Dislocations", submitted to the Phil. Mag.

5.0 MECHANICS OF MATERIALS

Introduction

Directional Instability of Dynamic Cracks in Materials

The instability associated with crack propagation occurs in the form of sudden curving or sudden bifurcation in two or more branches for no apparent reason. Answers to the questions why it is happening and when it is happening have been attempted by a host of investigators since the very early days of dynamic fracture. The common characteristic of all these approaches can be detected to be that they employ one physical quantity, which when exceeds a critical value directional instability occurs. A plethora of different quantities were introduced to be responsible (i.e. crack speed, dynamic stress intensity factor, energy release rate, strain energy density, dilatational strain energy density, etc.) without a clear specification of which conditions were including the simultaneous satisfaction of conditions related to the rest of them. No negative experiment was ever reported, such as refutation of the criticality or participation of a given parameter would be deducted. All theories were yield relatively accurate predictions for narrow classes of materials (i.e. very brittle isotropic and homogeneous materials and in some cases ductile materials), and they could only be judged on the basis of their prediction's accuracy when compared with the experimental observations. No assumptions related to the homogeneity of the material or the non-dissipative character of the propagation, or the stochasticity of the void-particle-crack interaction processes need to be made. Traditionally, introduction of this type of assumptions introduced undesirable redundancy. In our formalization, the actual behavior of the system will "inform" the system via its training process what actually happens.

Non-Linear Constitutive Behavior of Composites

Design needs for new structures, as well as survivability of existing ones, require a knowledge of the constitutive behavior of the composite materials used, under the influence of generalized loads, governed by mission requirements.

Furthermore, knowledge of the non-linear constitutive behavior of materials is important, not only because it accounts for the internal energy dissipative processes, but also because it results in a direct and detailed representation of the progress of damage in the material, and accordingly it can be used to assess the failure characteristics of the given material-structure combinations. Historically, the approaches taken to establish the failure behavior of composites falls into two radically different categories.

According to the first of the general methodologies, a model idealizing a real structure is built. Then the model is usually enhanced by extending techniques used for metals, such as Linear Elastic Fracture Mechanics and/or continuum theories. The purpose of this approach is to obtain a theoretical behavior of the model such that it will be similar to that of the actual physical structure described by the model.

Furthermore, because the physical problem usually solved by the model is a very generic one, such as a flat panel with an existing flaw, the lack of a procedure to extend the predictions of the model to real life structure and conditions is present. Thus, these approaches are limited. The approach followed can be described as an industrialized way of extracting data for the non-linear behavior of composites by observing, acquiring and processing data from the actual behavior of materials. The plethora of data and the requirements for a highly efficient

process requires the construction of an automated research plant meeting the above mentioned objectives. This plant is being consisted by two main components: The hardware (called the "in-plane loader system") recreates actual loading conditions on the materials and acquires the data; and the software, which is the methodology used to extract the non-linear behavior of composites from this data.

Theoretical Considerations

A model introduced the concept of the "equivalent crack particle", in order to describe both the deterministic aspects of the propagating crack in a perfect continuum, as well as the stochastic ones due to the micromechanical characteristics of the real materials. The Langevin equations of motion and the corresponding Fokker-Planck equation, were derived for the modelled and natural systems. A quantitative calibration of the model was proposed, such as consistent to the experimental data criteria, and the micromechanical descriptions of the dynamic fracture processes introduced by previous investigators, are simultaneously satisfied. As a result, a single criterion is proposed, which predicts simultaneously the location and the angle of the occurrence of the directional instability with both deterministic and stochastic properties being incorporated.

In addition, the propagating crack in a particulate composite, has been treated as a system to be identified, such as a model can be built to be used as a predictive tool. The identification process was applied in both the space of morphology of the bifurcated cracks as well as the space of the behavior parameters characterizing the cracks.

It was shown that a sample of topologically singular polynomial has all the properties needed to capture the morphology

of the crack after the critical point. The isomorphic relationship of this polynomial to the potential characterizing the equilibrium of an equivalent particle was also derived.

The model represented by this polynomial was trained to the actual experimental results gathered by several investigators in the form of a diffeomorphic tuning of the coefficients.

In order to extend the modelling of such as the stochastic character of the particle-matrix interaction was incorporated, and the Fokker-Planck equation has been used to replace the classical Langevin equations of motion. Thus, the probability density distribution function for the crack tip to be on an exact path was proposed to more efficiently capture the non-deterministic attributes of the crack propagation.

A completely phenomenological approach was incorporated to identify the non-linear behavior of composite materials. Failure characteristics of composite structures, were established by obtaining the energy dissipated by the material after exposing it on a representative sub-space of the loading space of all possible combinations. This was achieved by utilizing an automated procedure, mainly consisting of controlling and acquiring loading and displacement combinations applied by the "in-plane" loader. A theoretical procedure was developed to characterize the failure behavior of actual naval structures, by utilizing the constitutive behavior characteristics established by the "in-plane loader" system. Application of the process is demonstrated for different naval structures made of different materials.

Analysis and Characterization

It was shown that the crack curving and branching can be derived as intrinsic analytical properties of the equilibrium

dynamics of the crack system, provided that there are non-linear terms in the potential energy polynomial as a result of the dissipative forces. Details of this discussion appear in Refs. 1 and 2.

A methodology was developed to extract the constitutive behavior of composites such as it can be used in different naval structures for predicting the damage inflicted by various causes on structural components. Details of the results are given in Ref. 1.

References (Appendix V)

(1) J. G. Michopoulos, Theoretical and Applied Fracture Mechanics, 10, (1988), 177-189.

(2) J. G. Michopoulos, in COMP88 Intl. Symp. on Phase Interaction in Composite Materials, Patras, Greece, (1988).

Reference (Appendix VI)

(1) J. G. Michopoulos et al, "Failure Behavior of Composite Materials for Ship Applications", to be submitted for publication.

High Damping Materials with Nanometer Voids

Theoretical prediction of high damping due to voids and the fact that damping is independent of the size of the voids which can be used to design high damping materials with nanometer voids. It is proposed to mix nanometer sized particles of two metals; a structural metal such as iron or copper and a soft metal such as gallium or tin. The two metals must be insoluble with each other and the volume fraction of the soft metal should be small (1% or less). If the thermal expansion of the soft metal is larger than the strong metal, the mixture should be compact at some high

temperature and cooled down to room temperature. Otherwise, compact at a low temperature and warm up to room temperature. The presence of the soft metal will stabilize the voids and prevent them from disappearing by sintering. The soft metal should also provide a path for interface diffusion of atoms. If successful, the result should be a strong structure material with large damping With the application of these materials, noise and vibration reduction capacity can be incorporated into machinery designs. The material can also be used as a substitute or replacement material in machinery that has been poorly designed and subject to vibration. In this case, the vibrational energy would dissipate in the form of heat in the material.

Disclosure of invention follows in Reference (1).

Compact Micromechanics Tester

Under this contract, we have developed a simple, inexpensive method to design a compact micromechanics tester to study the mechanical properties, especially the Young's modulus of thin films, fibers and whiskers. This innovative tester has uses a passive loading mechanism which utilizes the thermal expansive properties of certain materials (as opposed to active loading mechanisms). The main technical advantages are: (a) there are no moving parts in this tester, therefore simplifying the design and reducing the cost, (b) with the exception of the elongation measuring device, no instrument is required to apply the load, thus the size dimensions of the system are reduced dramatically, and (c) it is easy to modify to different load ranges by simply changing the passive element.

Disclosure of invention follows in Reference (2).

Compositionally Modulated Thin Films

We have developed, modified and installed a data acquisition and control software for the dual ion beam physical vapor deposition system. The software was written in C-language for the AMIGA PC. The computer controlled deposition system is equipped with two broad beam ion guns, one for sputtering target materials and the other for substrate etching and ion-assisted deposition. The target indexing assembly permits the sequential deposition for different materials. The substrate stage can be rotated continuously and accommodates six one inch square substrates. The substrate stage can be heated up to 600°C and titled with respect to the target source. The base pressure inside the 14-inch diameter water-cooled deposition chamber is 2×10^{-7} Torr. The system is designed especially for the processing of compositionally-modulated thin films of few hundred layers and wavelength can be as small as few nanometers. Some superlattice compositionally modulated Cu-Ni, Fe-Ni films have been synthesized and confirmed by x-ray satellite peaks.

Three-Dimensional Stresses in a Half-Space Due to Axisymmetrical Ellipsoidal Inclusion

We have developed an innovative method for solving the axisymmetric elastic fields in the half-space with an isotropic ellipsoidal inclusion or an ellipsoidal inhomogeneity. The application of this method has significant implications in the study of the mechanical behavior of materials such as the fracture and fatigue of polycrystalline and composite materials. This new approach involves the application of the Hankel transformation method for prismatic dislocation loops and Eshelby's solution for ellipsoidal inclusions. Solutions for inclusions with pure dilatation misfit in a half-space are shown to be special cases of the present more general solution. Closed-form solutions of the elastic field for both the inclusion with nonshear eigenstrain and

the penny shape crack in half-space have been obtained. This new approach, which provides the solution of three-dimensional axisymmetric problems from a two-dimensional formulation, can also be used in other potential function related problems in the half-space.

The elastic solution for ellipsoidal inclusion with shear eigenstrain in the half-space are obtained by the combination of present innovative method and Mindlin's point force method.

A copy of the NRL Report 9134 for the penny shape inclusion and a copy of the paper for inclusion in general ellipsoidal shape with nonshear eigenstrain which had been accepted by the Journal of Applied Mechanics, and are incorporated herein.

Elastic Constants of Films Determined by the Indentation Test - Theoretical Considerations

The elastic solutions of axisymmetric mixed boundary value problems have been examined. It is assumed that an elastic film is either in smooth contact or perfectly bonded to a semi-infinite elastic half-space along its plane surface. The elastic field caused by indentation of the elastic layer by a rigid punch is solved for spherical, conical and flat-ended cylindrical punches. The results are obtained by solving a Fredholm integral equation of the second kind with a continuous symmetrical kernel which depends on the bonding conditions. Numerical results are given for different elastic moduli of both film and substrate, and layer thickness for each indenter shape. This provides a guideline for choosing the appropriate film thickness and substrate properties to determine the elastic constant of thin films by the indentation test. This elastic constant plays an important role in the study of the mechanical properties of composite materials. The solution of the elastic field at the film/substrate interface can also be

used to study the debonding behavior in composites. Additionally, these results are applicable to the design of columns on elastic foundations.

A copy of the NRL Report 9168 is attached. A condensed paper will be submitted to the Journal of Mechanics and Physics of Solids.

Reports and publications are given in References (3) to (5).

References (Appendix VII)

(1) H.-Y. Yu et al, "High Damping Materials with Nanometer Voids", Invention Disclosure, Dept. of Navy, (1988).

(2) H.-Y. Yu and S. C. Sanday, "Micro-mechanics Tester with Passive Loading Mechanism", Invention Disclosure, Dept. of Navy, (1989).

(3) H.-Y. Yu and S. C. Sanday, "Ellipsoidal Inclusion in a Half Space", to be published in the ASME J of Appl. Mech., (1989).

(4) H.-Y. Yu and S. C. Sanday, NRL Report 9134, Aug. 19, 1988.

(5) H.-Y. Yu, S. C. Sanday and B. B. Rath, NRL Report 9168, Jan. 12, 1989.

Phase Transformations and Strength of Materials

This portion of the research and development effort involved the utilization of mathematical models, which were used to predict the strength and toughness of materials. Accordingly, this research was concerned with questions regarding crystal morphology on the one hand and work hardening consequence on plastic deformation on the other hand. Specific questions elucidated were: the contributions to strength from the presence of interfaces as

compared and contrasted to those from other sources such as dispersed particles; the inhibition of grain growth (depletion of interfaces) by solute atoms and by precipitate particles; and work hardening as it relates to fracture. Apart from their general applicability to material properties the results of this research will in particular bear directly on the development of super strength alloys for use at high temperatures as in gas turbines. Details of the research work are given in Refs. 1 to 8. As the references indicate, the work has covered a considerable range of interest to the Navy's materials program.

References (Appendix VIII)

(1) N. P. Louat et al, Surface and Coatings Technol., 36, (1988), 61-74.

(2) N. P. Louat et al, in the Proceedings of the 2nd. Intl. Conf. on Surface Modification Technologies, TMS, Warrendale, PA, to be published.

(3) N. P. Louat and M. A. Imam, "On the Achievement of Strength at High Temperature in Binary Alloys", submitted to Scripta Met.

(4) N. P. Louat and K. Sadananda, "Some Consequences of the Elastic Interaction of Particles and Free Surfaces", submitted to Phil. Mag.

(5) N. P. Louat and K. Sadananda, "Peeling of Epitaxial Layers", to be submitted for publication.

(6) N. P. Louat and K. Sadananda, "On the DFZ and the Modification of G by Work Hardening", to be submitted for publication.

(7) N. P. Louat, "On the Interaction of Cracks with Cylindrical Microvoids", to be submitted for publication.

(8) N. P. Louat et al, "Computer Simulation of Dislocation Motion", to be submitted for publication.

High Temperature Materials

In the high temperature materials area, work was confined to the analysis and summary of high temperature testing data on several engineering alloys. Details of the fatigue and crack growth behavior of a couple of alloys are summarized in Refs. 1 and 2.

References (Appendix IX)

(1) P. Shahinian and K. Sadananda, "Fatigue and Creep Crack Growth Behavior of Inconel MA 6000", submitted to Materials Science and Engineering.

(2) P. Shahinian and K. Sadananda, "Fatigue and Creep Crack Growth in Oxide Dispersion Strengthened Inconel MA 754", Submitted to Met. Trans.

Applied Ceramics and Composites

This portion of the research effort concentrated on developing new high temperature superconductors and on developing new processes of forming high temperature superconductors. Fabrication of powder, coatings and thin films were some of the processes explored. Details of the research work are given in Refs. 1 to 3.

References (Appendix X)

(1) J. R. Spann, "Process of Making High Temperature $Ba_2YCu_3O_7$ Superconducting Powder", Invention Disclosure, Dept. of Navy, (1988).

(2) J. R. Spann et al, "Preparation and Characterization of BSCCO Films on Ceramic Substrates", presented at the Amer. Ceram. Soc. Meeting in Indianapolis, IN, (April 1989).

(3) J. R. Spann et al, "Preparation and Characterization of Orthorhombic BYCO Powder for Thick Film Coatings", presented at the Amer. Ceram. Soc. Meeting in Indianapolis, IN, (April 1989).

APPENDIX I

Proceedings of SPIE—The International Society for Optical Engineering

Volume 957

Laser Beam Surface Treating and Coating

Gerd Sepold
Chair/Editor

Cosponsored by
SPIE—The International Society for Optical Engineering
and
ESD—The Engineering Society

Cooperating Organizations
Applied Optics Laboratory/New Mexico State University
Center for Applied Optics/University of Alabama in Huntsville
Center for Electro-Optics/University of Dayton
College of Engineering/University of Michigan
Illuminating Engineering Society of North America
Industrial Technology Institute

29-30 June 1988
Dearborn, Michigan

Published by
SPIE—The International Society for Optical Engineering
P.O. Box 10, Bellingham, Washington 98227-0010 USA
Telephone 206/676-3290 (Pacific Time) • Telex 46-7053

SPIE (The Society of Photo-Optical Instrumentation Engineers) is a nonprofit society dedicated to advancing engineering and scientific applications of optical, electro-optical, and optoelectronic instrumentation, systems, and technology.

Invited Paper

Surface Treating by Laser Melt/Particle Injection

Khershed P. Cooper

Geo-Centers, Inc.
10903 Indian Head Highway, Suite 502, Fort Washington, MD, 20744

ABSTRACT

By the laser melt/particle injection process, an in situ composite surface layer of particulate material in a matrix made up of the parent metal is formed. The particles are usually metal carbides which makes the injected surface layer hard and wear resistant. In this paper, the processing technique and the microstructures obtained are described. In addition, the hardness and wear characteristics of the modified surface are discussed.

1. INTRODUCTION

Lasers are used extensively to modify metal surfaces to enhance resistance to wear, friction, corrosion and high temperature oxidation. Laser heat treatment, laser melting, laser alloying and laser cladding are the various established techniques available for surface modification. Their selection depends upon the material being treated and the specific application that one has in mind. For example, cast irons and some steels are easily laser heat treated for surface hardening and wear resistance[1]. Laser alloying of low carbon steels with chromium enhances corrosion resistance[2]. Laser cladding with Ni-Cr-WC improves the wear resistance of steels[3], while laser cladding with Ni-Fe-Cr-Al-Hf improves the high temperature oxidation behavior of nickel-base superalloys[4].

In laser cladding, since the clad layer is necessarily of a different material than the substrate, the properties of the modified surface will not reflect those of the substrate. For example, although a hardfacing alloy would improve the wear resistance of a nickel-base alloy, it may fail in a corrosive environment. The laser melt/particle injection process was developed to improve properties such as wear resistance while retaining substrate properties such as corrosion resistance[5]. It is also one of the few means available to improve the wear resistance of alloys that are difficult to harden by conventional means, for example, aluminum alloys[5]. In laser alloying, the material added to the substrate melt dissolves completely to form an alloyed surface. In laser cladding, the material added fuses against the substrate with the least amount of dissolution or dilution. In laser melt/particle injection, high melting particles such as carbides are forcibly entrained into the laser melt pool so that upon solidification, a particulate composite surface forms with a matrix that is of a composition similar to the base metal[5,6]. Neither fusion nor complete dissolution of the particles into the melt occurs. The presence of the carbide particles increases hardness and

wear resistance, while the matrix, which is structurally continuous with the substrate, retains much of the properties of the base metal. Such a surface would be suitable for applications involving a high wear and corrosive environment.

2. LASER MELT/PARTICLE INJECTION PROCESSING

A schematic diagram of the laser melt/particle injection process is given in Figure 1. A shallow melt pool was formed on a translating substrate by a high power CW, CO_2 laser beam. The slightly off-focus beam melted a 2 to 3 mm wide layer. Wider melt passes were made by oscillating the laser beam using a dithering mirror[7]. A copper nozzle with a slotted opening injected the carbide particles into the melt pool. Upon solidification, the carbide/melt mixture formed the injected layer. The width of the melt pass was controlled by varying the laser beam oscillation amplitude. By this means, injected layer widths from 4 to 20 mm were produced. Laser power levels of 8 to 10 kW were used and the sample translation velocities were varied from 0.25 to 1.5 cm sec^{-1} depending upon the width of the melt pass. Typically, the injected layers were 1.0 to 1.5 mm thick. The powder particles were carried by helium gas, which not only served to propel them but also to keep them from heating to fusion as they travelled through the laser beam. Particle size distributions of 45-75 um and 75-150 um were used. Finer particles overheated and dissolved excessively into the melt pool. Coarser tended to clog the delivery line and were difficult to drive into the melt pool.

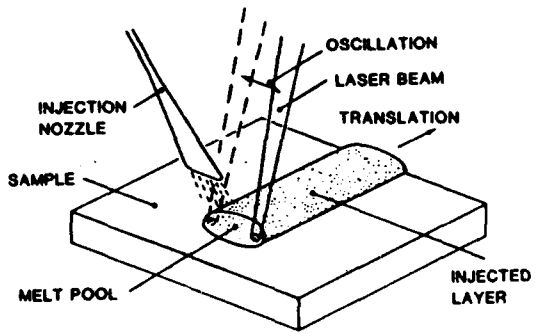


Figure 1. Schematic diagram of the laser melt/particle injection process.

A cross-section of the injected layer in a WC injected Inconel 625 alloy sample appears in Figure 2. The layer is a particulate composite in which the WC particles appear as light grains which are surrounded by the grey Inconel metal matrix. The carbide particles appear uniformly distributed throughout the injected layer occupying a volume fraction of about 0.5. Since a portion of the melt is displaced by the particles, the excess material appears as the mounding above the sample surface. The mounding and the penetration depth make up the layer thickness. These three dimensions and the carbide volume fraction can be controlled by carefully selecting processing parameters such as sample translation rate, laser power and powder feed rate. Composite surface layers can also be produced by adding particulate mixtures of carbide and metal using methods such as

plasma transferred arc[8] and laser cladding[3]. But there are problems associated with feeding mixtures of powder of varying density. Also, with laser cladding, the carbide volume fraction in the overlay is usually small[3], about 0.15 to 0.2.

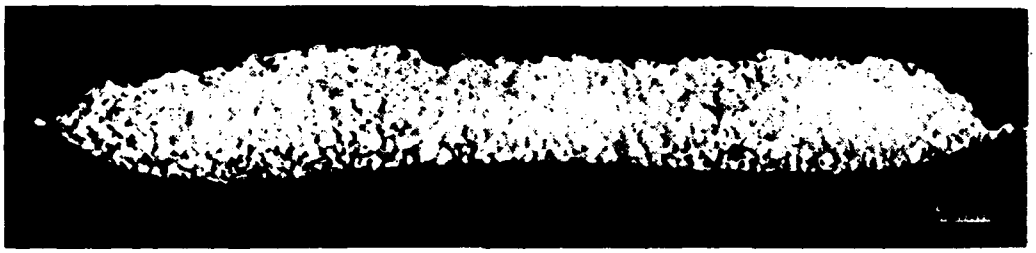


Figure 2. SEM micrograph of cross-section of WC injected Inconel 625.

The influence of processing parameters such as sample translation rate, laser power and powder feed rate on injected layer characteristics was investigated for TiC injected Ti-6Al-4V[9]. In this study, each parameter was varied keeping the other two constant. Increasing the sample translation rate decreased the injected layer dimensions. This happens because higher sample speeds reduce the laser energy density needed to melt the surface. The flowing particles assisted in coupling the laser beam to the sample surface, but when the sample translation rate was too rapid, this coupling did not occur and an injected layer could not be formed. While having no effect on the mounding, increasing the laser power increased the penetration depth and, hence, the thickness because a larger volume of the surface was melted. Since the same quantity of powder was fed into a progressively larger volume of melt, the carbide volume fraction decreased. Increasing the powder feed rate had no effect on penetration depth, but increased the mounding and, hence, the thickness because more and more particulate material displaced the fixed volume of melt. This also increased the carbide volume fraction, but to a limit of about 0.6. Beyond this limit, the melt just dissolved the excess carbide. Although the powder feed rate could be varied to obtain different volume fractions of the hard phase, typically feed rates of about 40-50 mm^3 sec^{-1} were employed to give a consistent volume fraction of about 0.5.

3. STRUCTURAL MODIFICATION

As shown in Figure 2, the major surface modification is in the form of a particulate composite. The matrix in the injected layer is structurally continuous with the substrate. This gives the process a couple of unique advantages. One is strong metallurgical bonding throughout the surface layer and the other continuity of properties at the layer/substrate interface. This helps in preventing delamination and in retaining substrate properties.

Ideally, the particle injected surface should consist of hard particles surrounded by a metal matrix having the same composition and microstructure as the base metal. Such a structure was obtained in aluminum alloys that were injected with TiC[10]. In high melting alloys

like those based on Fe, Ni and Ti, the melt temperatures are high and partial dissolution of the carbide particles into the melt occurs. As a result, several resolidification products form from the carbide enriched melt. In addition, depending upon the base metal and the solidification rates, other structural modifications occur. For example, transformation products such as martensite form in tool steels, fine grain structures in aluminum bronze, supersaturated solid solutions and precipitation reaction products in stainless steels[11].

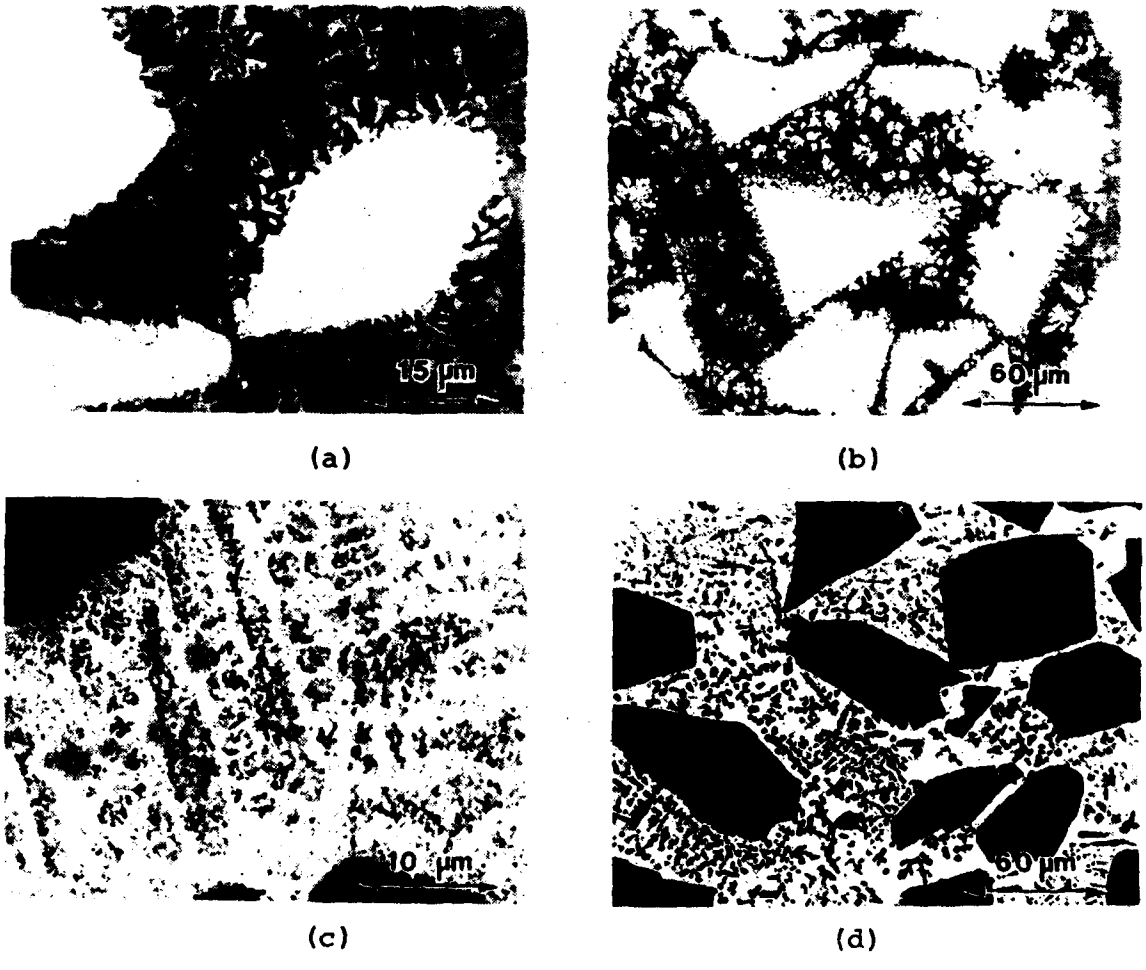


Figure 3. SEM micrographs of microstructures in particle injected Inconel 625. a) WC injected, eutectic carbides. b) WC injected, resolidified carbides. c) TiC injected, eutectic carbides. d) TiC injected, resolidified carbides.

The metal matrix is cellular, as in Ti-6Al-4V, or dendritic, as in Inconel 625[12]. Within the metal matrix are found eutectic phases and resolidified carbides, the products of carbide dissolution. Examples of microstructures obtained in WC and TiC injected Inconel 625 alloy samples appear in Figure 3. The eutectic phases occur in the inter-dendritic regions of the Ni-rich dendrites and have been identified to be complex carbides[13]. Eutectic carbides have an

APPENDIX I

Improving the wear resistance by forming hard metal matrix–ceramic composite surface layers

Khershed P. Cooper
Geo-Centers, Inc., Suitland, Maryland 20746

(Received 4 April 1986; accepted 9 May 1986)

Using an oscillating high energy laser beam, wide melt pools were formed on the surface of Inconel 625 alloy samples. Metal carbide particles, such as WC and TiC, were injected into the melt to form hard metal matrix–ceramic composite layers upon solidification. The injected layers were uniformly distributed in the carbide phase but exhibited variations in microstructure and microhardness. These variations were a result of carbide dissolution which depended upon the type of carbide and the thermal conditions within the melt pool. The wear behavior of the injected surface was characterized by coefficient of friction (μ_k) measurements. In contact with a hard 52100 steel ball, the μ_k values of the treated surface varied from 0.33 to 0.44 after a series of cycles. This compared with a value of 0.7 for the untreated surface. Observed wear modes included matrix abrasion and wear debris deposition, the extent and nature of which depended upon the matrix microhardness and the wear mechanism. The effects of carbide type and size on friction wear behavior of Inconel 625 are also discussed. Results show that Inconel 625 injected with 45–75 μm WC performs best under sliding friction conditions.

I. INTRODUCTION

A technique for enhancing the wear resistance of metals is to form hard composite surface layers. This is achieved by impregnating ceramic particles into the surface by the laser melt-particle injection process.[1,2] Besides hardening the surface,[3] particle injection was shown to improve abrasion and erosion wear.[4] A method for evaluating the tribological properties of a treated surface is to conduct coefficient of friction measurements. Extensively used to study ion implanted surfaces,[5] this laboratory scale test is sensitive to changes in the surface microstructure and properties, making it a suitable test to evaluate the relative merits of the various injected species.

II. EXPERIMENTAL PROCEDURES

A. Laser melt-particle injection processing

Inconel 625 alloy samples were injected with WC and TiC particles of 45–75 μm and 75–150 μm size ranges. Table I gives the material properties. A 10 kW, CW CO_2 laser beam, oscillating with a frequency of 110 Hz, was used to form 8–12 mm wide melt passes on a moving substrate. In order to get a thick (1–2 mm) injected layer, relatively slow sample scan rates, 0.5–0.75 cm s^{-1}, were selected. The powder, fed at rates of 0.35–0.5 cm^3 s^{-1}, was carried by helium gas flowing under a pressure of 35–85 kPa. Higher powder feed rates and lower gas pressures were necessary when injecting the lighter TiC particles. Two conical sprays, formed by a dual injection nozzle, uniformly distributed the powder over the melted region. Figure 1 shows a schematic representation of the process. Processing details appear elsewhere.[6]

B. Evaluation of the injected surface

Cross sections of the injected layers were examined for carbide distribution, and the extent of microstructural modification within the solidified melt pool. Furthermore, the structures were characterized for carbide volume fraction, superficial hardness, and Vickers (100 g) microhardness. A "stick-slip" machine, described by Singer *et al.*,[5] was used to measure the kinetic coefficient of friction between a 1.27 cm diam 52100 steel ball and the treated sample surface. The tests were performed dry at 298 K, employing a slider velocity of 0.01 cm s^{-1} and a slider pressure of 9.8 N. Up to 15 passes were made in the same track. Additionally, the damaged surface was evaluated for the type and extent of wear.

III. RESULTS

A. Injected layer characteristics

Cross-sectional views of the surfaces injected with the 45–75 μm size carbides are shown in Fig. 2. The structures show a uniform distribution of the carbide phase, occupying about 50% of the total volume. On the microscopic scale, a variety of microstructures were observed in the injected samples, examples of which appear in Fig. 3. In all cases the interparticle matrix consisted of (Ni)-rich dendrites with a complex interdendritic eutectic phase, Figs. 3(a) and 3(c). Additionally, dendritic resolidified carbides appeared in the matrix, Figs. 3(b) and 3(d). Matrix microhardness readings along the thickness of the injected layer are plotted in Fig. 4. Microhardness trends show an increase with thickness, the magnitude of which is a function of the type of carbide and the particle size.

TABLE I. Materials and properties.

Material	Density (g cm^{-1})	Thermal diffusivity (cm^2 s^{-1})	Free energy of formation* (cal g^{-1})	Hardness (HV)
WC	15.63	0.69	−43	1800
TiC	4.93	0.132	−660	3000
1625	8.44	0.029	...	300

*At 1773 K.

 0734-2101/86/062857-05$01.00 © 1986 American Vacuum Society

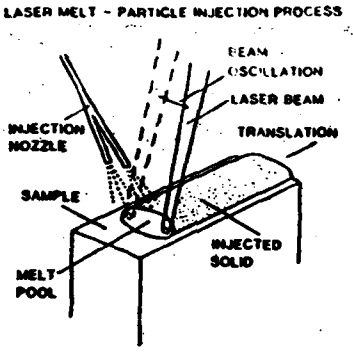


FIG. 1. Schematic representation of the laser melt-particle injection process.

B. Coefficient of friction measurements

Trends in the coefficient of friction (μ_k) as a function of the number of passes are graphically presented in Fig. 5. In most cases, μ_k increased to a constant value after a certain number of cycles. The increasing rate, defined in Table II as the pass number at which maximum μ_k is reached, depended upon the carbide type and the particle size. Table II summarizes the friction test results and also gives, for comparison, the surface hardness, matrix microhardness, and carbide volume fraction.

Examples of wear scars are given in Figs. 6 and 7. Matrix abrasion in the WC injected sample was mild, Fig. 6(a), compared to that in the TiC injected sample, Fig. 7(a). In WC injected samples, some of the carbides appeared to have fractured under the stress of the steel slider, Fig. 6(a). In some cases wear debris was observed along the cracks, indicated by arrows in Fig. 6(b). The debris appeared as thin films, not only on the carbide surface, but also on the matrix and along the carbide-matrix interface, Fig. 6(c). Selected area diffraction, Fig. 6(d), of the wear debris revealed the presence of iron. Besides matrix abrasion in the TiC injected sample, Fig. 7(a), an abundance of wear debris was found spread over the surface. Selected area diffraction of the debris revealed iron and Inconel 625 alloying elemental peaks, Fig. 7(b).

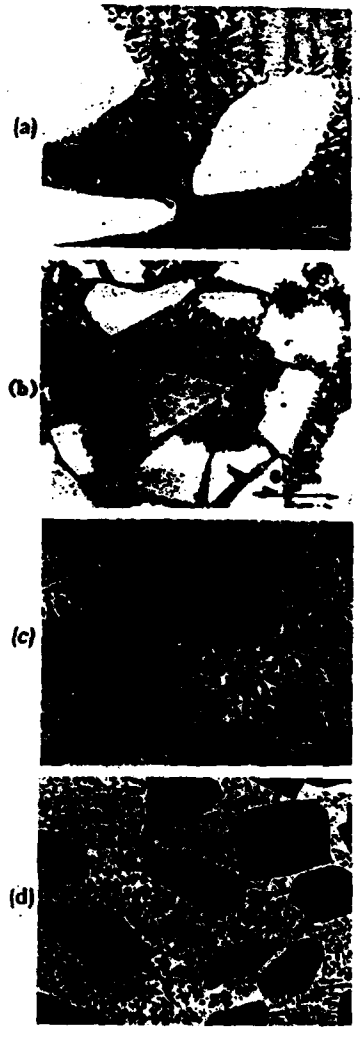


FIG. 3. SEM micrographs of injected samples. (a) WC—eutectic phase. (b) WC—resolidified carbides. (c) TiC—eutectic phase. (d) TiC—resolidified carbides.

IV. DISCUSSION

In spite of the vast density difference between WC, TiC, and Inconel 625 (see Table I), it is evident from the structures presented in Fig. 2 that, under the right processing conditions, the particles can be made to distribute uniformly throughout the cross section. But a variety of microstructures were observed in the injected samples due to the dissolution of the carbide phase into the melt. The dissolution rate depended upon the type of carbide, particle size, and the thermal conditions prevailing in the melt pool. Examining

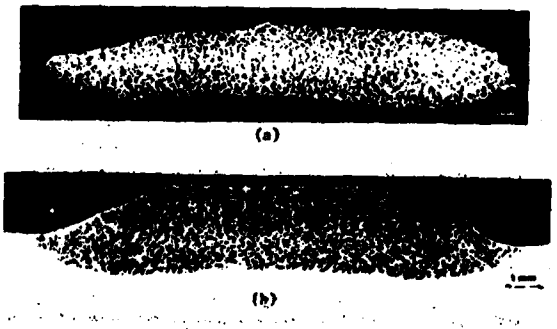


FIG. 2. Injected layer structures of samples treated with 45–75 μm size particles: (a) WC, (b) TiC.

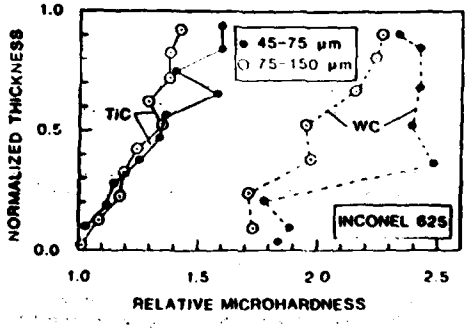


FIG. 4. Matrix microhardness relative to base metal as a function of the thickness of the injected layer. Base metal microhardness is 280–305 HV.

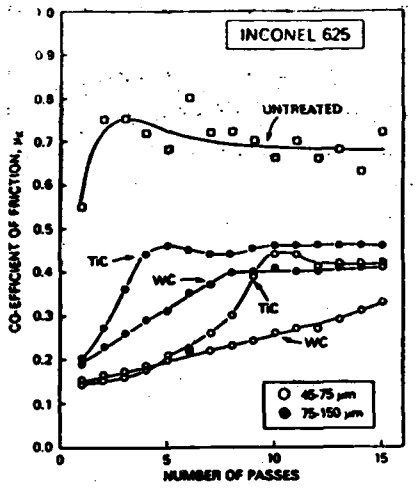


FIG. 5. Coefficient of friction as a function of the number of passes.

the carbide morphologies in Figs. 3(b) and 3(d), it is evident that a higher degree of melt interaction occurred with WC than with TiC. WC particles show growth perturbations, while the TiC particles are smooth and featureless. Higher thermal diffusivity and lower free energy of formation (Table I) favored WC dissolution over TiC dissolution.

That the dissolution process, however limited, occurs throughout the melt is evident from the modification of the matrix microstructure throughout the injected layer. In non-injected, laser remelted Inconel 625, the structure is essentially single phase dendritic (Fig. 8), with no evidence of interdendritic precipitation. In injected samples, secondary phases formed as interdendritic eutectic mixtures upon solidification. The eutectic morphology in WC treated samples appears irregular in the scanning electron microscope (SEM) micrograph, Fig. 3(a), but transmission electron microscopy (TEM) analysis revealed small lamellar eutectic colonies.[7] The interdendritic eutectic phase in TiC injected samples is also lamellar and is easily resolved in the optical micrograph of Fig. 9. In addition to the eutectic phase, resolidified carbides were found in the matrix, but mostly in the upper region of the injected layer. Being closer to the laser beam, the upper portion of the melt is the hottest and, hence, would experience the greatest amount of dissolution. Carbide dissolution occurs by a liquation process, which is usually promoted by alloying of the carbide surface.[7] The perturbed carbide surface shown in Fig. 3(b) supports this dissolution mechanism.

Examining the microhardness trends in Fig. 4, it is evident that WC dissolution has a much stronger influence (1.7–1.9×base metal) on matrix hardening than TiC dissolution (1.05–1.2×). The exact reason for this contrasting behavior is not known, but the composition, the size, and the spacing of the eutectic phase may determine the degree of hardening. The occurrence of resolidified carbides hardens the matrix even more, 1.2–1.3× in WC injected samples, and 1.33–1.4× in TiC injected samples. Finely dispersed throughout the matrix, resolidified carbides probably harden the matrix by a dispersion hardening mechanism. Greater matrix hardening occurs with the finer sized particles compared to that with the coarser ones, but mostly in the upper regions of the injected layer. Finer particles offer a larger surface area for melt-carbide reactions, thereby facilitating dissolution. The increase in hardness due to particle size is modest, 1.06× for WC and 1.11× for TiC, reflecting a particle size reduction from an average of 112–60 μm. It is important to determine the microstructure and microhardness trends along the thickness of the injected layer. Since a portion of the injected layer is removed to form a flat surface, the structure and hardness of the matrix at that level will determine properties such as wear and corrosion.

The reduction in μ_k and wear scar width (Table II) demonstrates the effectiveness of carbide injection in reducing friction wear. Since the surface hardness (HRC) and carbide content are nearly the same for all treated samples (see Table II), the response of the injected surface to the friction test will depend upon factors such as matrix microstructure and microhardness. The μ_k curves of Fig. 5 show increasing trends at different rates to a constant value. The rate of increase in μ_k appears to depend upon particle size and type of carbide. Since friction between carbide and steel is minimal the increase in μ_k is mostly due to friction between the ma-

TABLE II. Friction test results.

Carbide			Hardness		μ_k			
Type	Size (μm)	Vol. fract.	(HRC[a])	(HV[b])	1 pass	15 passes	Pass No.[c]	Scar width[d] (μm)
Untreated			20	292	0.55	0.72	1	300
WC	60	0.47	51	618	0.15	0.33	15	90
WC	112	0.51	54	605	0.19	0.41	8	100
TiC	60	0.50	49	516	0.15	0.41	10	80
TiC	112	0.48	43	406	0.17	0.44	4	150

[a] Of composite.
[b] Of matrix.
[c] When maximum μ_k is reached.
[d] After 15 passes.

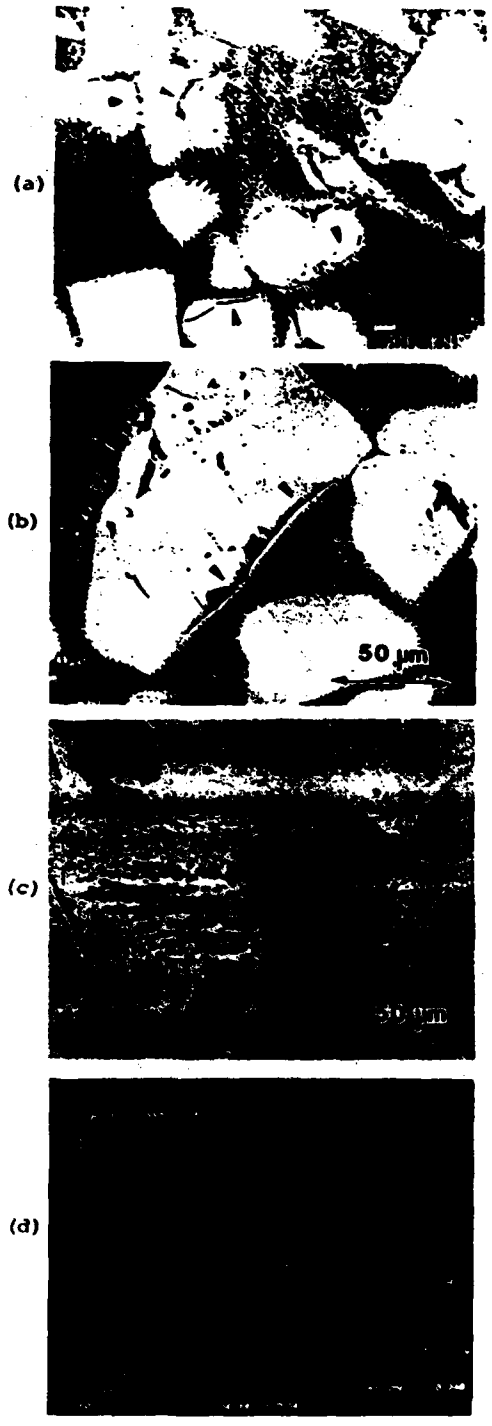


FIG. 6. Wear modes in WC injected samples. (a) Matrix wear and carbide cracking (arrows). (b) Debris (arrows) along cracks. (c) Wear debris. (d) x-ray energy dispersive spectra (EDS) of debris in (b), dark spectrum is of the unaffected carbide.

trix and the steel slider. Since the carbides occupy 50% of the total volume, the interparticle spacing is of the order of a particle dimension. Hence coarser particles allow more slider–matrix contact, thereby increasing the friction, while finer particles allow less contact, thereby reducing the friction. Within the same size distribution, μ_k rises less rapidly over the entire test in the case of the harder WC injected matrix than the softer TiC injected matrix. In fact, the harder (600 HV) WC injected matrix, Fig. 6(a), showed little damage, compared to the softer (500 HV) TiC injected matrix, Fig. 7(a). This was true in spite of the presence of resolidified carbides in the sample injected with the finer TiC. This means that even though resolidified carbides harden the matrix, they do not necessarily minimize wear.

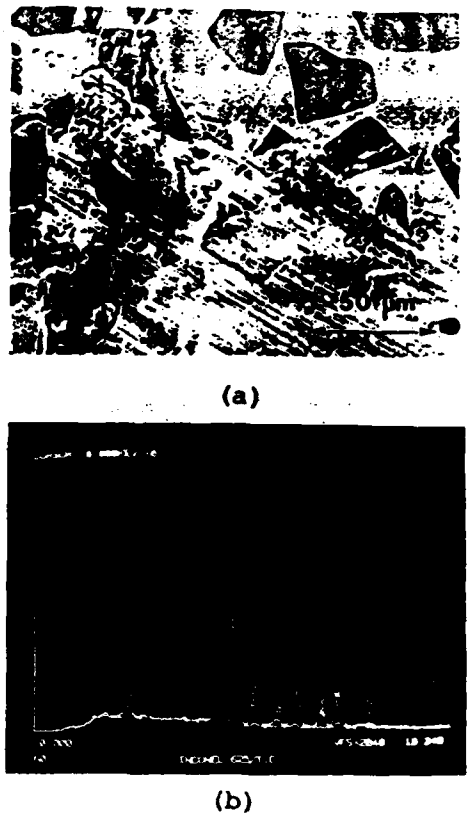


FIG. 7. Wear modes in TiC injected samples. (a) Matrix wear and wear debris. (b) EDS of debris at arrow in (a), dark spectrum is of the unaffected carbide.

The increasing μ_k trend is not solely due to matrix wear. Slider wear can also contribute to the increasing trend. With a hardness of 60 HRC or 700 HV, the steel slider is consider



FIG. 8. Optical micrograph of laser remelted Inconel 625

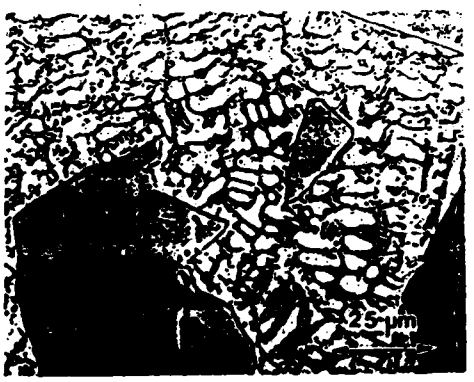


FIG. 9. Optical micrograph showing eutectic phase in a TiC injected sample.

ably softer than the hard carbides (Table I). Furthermore, slider wear is compounded by the presence of pre-existing cracks and cracks formed during testing. The occurrence of slider debris along cracks [Fig. 6(b)] and along carbide edges [Fig. 6(c)] supports this mechanism. While the wear debris in WC injected samples is composed mostly of slider material [Fig. 6(d)], the wear debris in TiC injected samples is a mixture of matrix and slider material [Fig. 7(b)]. Simultaneous wear of the slider and the matrix would certainly accelerate friction wear. That μ_k stabilizes around 0.4–0.44 is probably due to the prevention of further wear by the shielding action of the wear debris.

V. CONCLUSIONS

The injected structures are uniformly distributed in the carbide phase throughout the cross section, but a variety of microstructures formed, depending upon the carbide type and the thermal conditions within the melt pool. Due to the dissolution of the carbide phase, inter-dendritic eutectic phases formed in the matrix. In the hotter upper regions of the melt, resolidified carbides precipitated. The matrix in WC injected samples was much harder than that in TiC injected samples. In both cases, resolidified carbides hardened the matrix even more. The reduction in μ_k and wear scar width after a series of cycles does show that forming metal-carbide composite surfaces reduces the coefficient of friction of Inconel 625 alloy in contact with a steel slider. Being harder, the WC treated matrix wore less compared to the softer TiC treated matrix. In fact, the increasing μ_k trend in WC injected samples was due mostly to slider wear, while the same behavior in TiC injected samples was due to a combination of slider and matrix wear. The advantage of the finer particle size is mainly in reducing slider–matrix contact, thereby minimizing friction wear. Results show that the sample injected with the finer WC performed best under sliding friction with a steel slider.

ACKNOWLEDGMENTS

The author would like to thank Dr. J. D. Ayers and the Naval Research Laboratories in Washington, DC for providing the facilities to do the work.

[1] J. D. Ayers, R. J. Schaefer, and W. P. Robey, J. Met. 33, 19 (1981).
[2] J. D. Ayers, in *Lasers in Metallurgy*, edited by K. Mukherjee and J. Mazumder (The Metallurgical Society of AIME, Warrendale, PA, 1981), p. 115.
[3] K. P. Cooper and J. D. Ayers, Surf. Eng. 1, 263 (1985).
[4] J. D. Ayers, Wear 97, 249 (1984).
[5] I. L. Singer, C. A. Carosella, and J. R. Reed, Nucl. Instrum. Methods 182/183, 923 (1981).
[6] K. P. Cooper, presented at ASM's International Conference on Surface Modifications and Coatings, Toronto, Canada, 14–16 Oct. 1985.
[7] K. P. Cooper and A. Singh (to be published).

THE CHANGING FRONTIERS OF

LASER MATERIALS PROCESSING

Proceedings of the 5th International Congress on Applications of Lasers and Electro-optics ICALEO '86

Edited by C. M. Banas and G. L. Whitney

10-13 November 1986
Arlington, Virginia, USA

IFS (Publications) Ltd, UK
Springer-Verlag
Berlin · Heidelberg · New York
London · Paris · Tokyo

Surface processing of metals using an oscillating laser beam

K. P. Cooper
Geo-Centers Inc., USA
and
R. Beigel and P. Slabodnick
Naval Research Laboratory, USA

Abstract

The interest in surface processing with an oscillating laser beam is prompted by the need to process wider selected surface areas with a single melt pass. By mounting a flat mirror on a rapidly vibrating electromagnetic device, a high power CO_2 laser beam was made to oscillate over a moving sample surface. The resulting melt pool had a slight dog-bone shape, and, by controlling the current to the oscillating device, melt widths of 1.0-2.0 cm were attained. Since the objective of this work was to form hard, wear resistant surfaces on Inconel 625 alloy samples, the sample surfaces were treated with hardfacing alloys such as WC, TiC, SiC and Tribaloy. The WC and TiC particles were injected into the melt to form a metal matrix-carbide composite layer, SiC was laser consolidated as a thin fused layer, while Tribaloy was fed into the laser beam to form a cladding. Particle injection over the wider melted area was achieved through a slitted nozzle that formed a flat spray of the powder. Topographical and cross-sectional views of structures formed by the oscillating laser beam are described in this paper. Finally, the influence of the powder feed direction relative to the moving melt pool on factors such as the particle injection efficiency, the shape of the solidified melt pool and the nature of the overlap at the end of a circular pass is discussed.

Introduction

One advantage laser processing offers over other surface processing techniques is the ability to modify surfaces of selected geometry and dimensions without adversely affecting neighboring regions. Normally, the laser beam is held stationary while the sample is moved underneath it. This produces a narrow melt pass, usually 0.2-0.3 cm wide. Frequently, it is necessary to process surfaces wider than that. Wide strips can be melted by oscillating the laser beam to form a line energy source on the sample surface. This can be done by oscillating a flat mirror either by mechanical means such as a cam drive or by electromagnetic means. A wide range of oscillation frequencies are possible with a cam driven oscillating mirror, but, for a particular experimental set-up, the oscillation amplitude is fixed by the distance of the mirror from the sample surface. Electromagnetic drive systems rely upon the system resonance, allowing few options with the oscillation frequency. On the other hand, the oscillation amplitude, and hence the melt width, are easily changed by powering the device at different levels without changing the experimental set-up. It is for this reason that an electromagnetically driven oscillating mirror was employed to form wide melts during the course of this work. Part of the experimental investigation was to determine how the oscillating beam would influence the shape of the melt pool, not only for the simple case of surface remelting, but also for processes such as particle injection, coating consolidation and surface cladding.

Processing Technique

In order to improve the wear resistance of soft metals, the laser melt-particle injection process was developed[1,2]. By this means hard particles, such as carbides, were blown into a laser melted surface to form, upon solidification, a metal matrix-carbide composite layer. In this section, techniques for oscillating the laser beam and for feeding the powder will be described. Besides particle injection, surface modification processes such as laser consolidation and cladding are also described. Details of the laser apparatus and the experimental procedures are given elsewhere[3,4]. The improved friction wear resistance of particle injected surfaces was demonstrated by Cooper[5].

The Oscillating Beam

Extensive development work on laser melt-particle injection processing was done using a stationary laser beam to melt a narrow track and a small circular nozzle to feed the particles. In order to selectively process wider strips, an oscillating laser beam was used to melt a wide track[3]. To oscillate the laser beam, a flat mirror, placed about 2 m from the sample, was mounted on an electromagnetic shaker which was energized by a function generator via an audio amplifier. The set-up of the beam oscillation mechanism appears in figure 1. With this device, the mirror would only oscillate near the resonant frequency of the system. Resonance occurred at 45 and 110 Hz. The frequency of 110 Hz was selected because it was considered to be rapid enough to sustain a line energy source on the sample surface for a

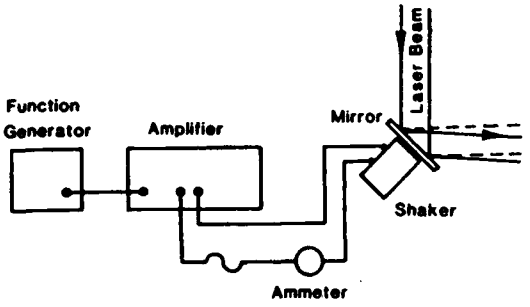


Figure 1. Technique for oscillating the laser beam.

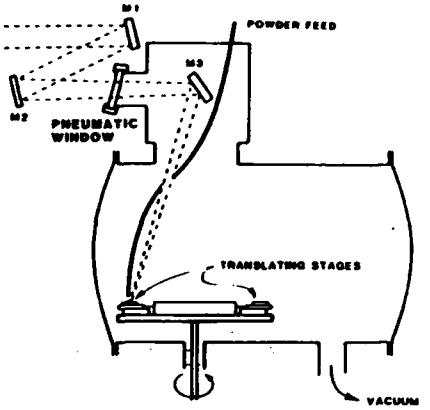


Figure 2. Laser processing apparatus showing the laser beam path.

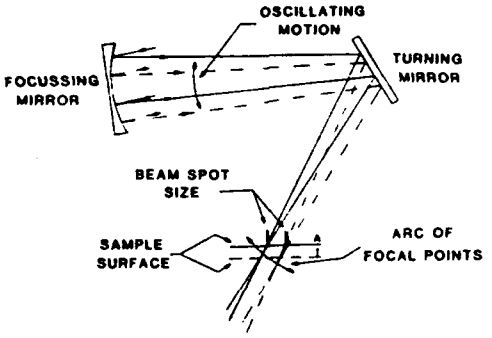


Figure 3. Diagram demonstrating the change in spot size as the beam oscillates.

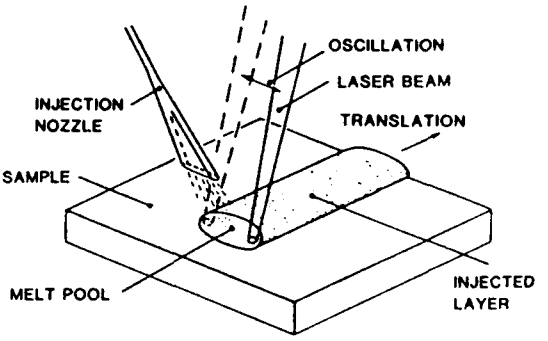


Figure 4. Schematic representation of the laser melt-particle injection process.

range of sample translation rates. The oscillation amplitude, and hence the melt width, was controlled by adjusting the current passing through the shaker. The oscillating mirror tends to remain longer at the extremities of the cycle. To reduce this dwell time, a signal of triangular waveform was used to drive the shaker. A high power CW CO_2 laser beam was used in the unstable resonator, or near Gaussian mode. After leaving the oscillating mirror, the laser beam follows a complicated path as shown in figure 2. The beam is reflected by mirror M1 onto a 1 m focal length mirror M2. It enters the vacuum chamber through a pneumatically operated window and is deflected by mirror M3 and brought to a near focus on the sample surface.

The sample is attached to a rotating table so that circular melt passes of different diameters are possible. Thus, the focussing beam falls on the sample at different angles depending upon the melt radius. As shown in figure 3, the oscillating beam describes an arc of focal points. As it intercepts the sample in position A, the beam spot size incident upon the sample changes. This changes the incident laser energy density from the inner to the outer radius of the melt pass. The difference in spot size would be accentuated at larger melt diameters. For sample position I, the sample intercepts the oscillating beam above and below the focal point and the beam spot sizes are equal. This would be the ideal sample position, but it requires extremely precise positioning which may not be practical. In addition, for a circular melt pass, since the translation velocity is slower at the inner radius, the laser energy density near the inner extremity would be higher than that near the outer extremity. The discrepancy in the energy density would diminish for larger diameter melt passes. Part of the investigation was to determine if the laser energy density asymmetries described above are significant enough to influence the level of symmetry across the melt pass.

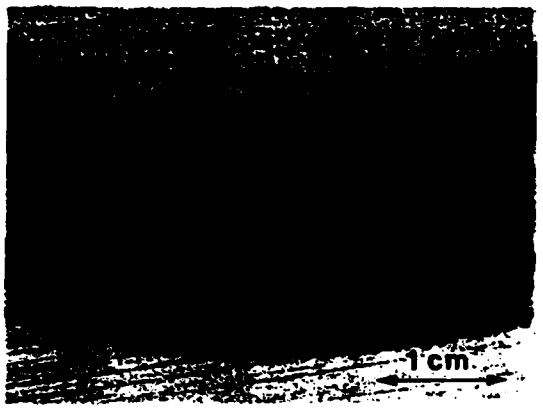
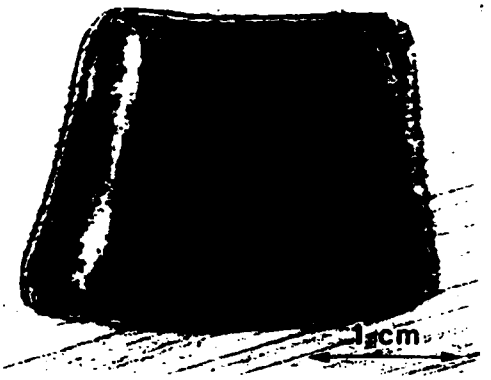


Figure 5. Melt track on a rapidly moving sample surface. No. 66-4.



(a)



(b)

Figure 6. Melt pass on a slowly moving sample surface. No. 66-3. a)Topographical view. b) Cross-sectional view.

The Injection Nozzle

In order to distribute the powder evenly over the wider melt, a dual injection nozzle with two circular openings was used. The spacing between the openings was adjusted so that the particles could be injected over a wide range of melt widths. This powder injection system served well for melts of up to a cm. For wider melts, a nozzle with a slot as an opening was employed. The slitted nozzle formed a flat, rectangular spray of the powder. It was designed so that the powder was delivered with sufficient velocity to penetrate the molten surface at a uniform rate across the entire melt width thereby forming a uniformly thick injected layer. A schematic representation of the laser melt-particle injection process using an oscillating beam and a slitted nozzle appears in figure 4. The nozzle is usually 1-2 cm from the sample surface and is inclined at an angle of 30° from the vertical. Although the diagram shows the powder being fed ahead of the moving melt pool, it could also be introduced from behind the melt pool. The merits and demerits of the powder feed direction relative to the melt pool will be discussed in a later section.

Types of Laser Surface Modification

Although the primary aim of laser melt-particle injection processing was to form composite layers of hard carbides in a metal matrix, the same technique can also be used for surface cladding. In addition, using the oscillating beam, coatings deposited on the sample surface were laser consolidated. With this in mind, various types of surfaces were generated on Inconel 625 alloy samples. The choice of Inconel 625 was dictated by its obvious interest to the Navy. Carbides of W, Ti and Si were used in powder form to produce injected surface composites. Deposited coatings of WC, SiC, and mixtures of WC and SiC with Inconel 625 powder were laser consolidated, while pneumatically delivered Tribaloy-400 powder was laser clad on the metal surface. The particles were fed using helium as a carrier gas. For laser consolidation, 1-2 mm thick coatings of a slurry of the powder in alcohol were applied to the sample surface. Before processing, the coated samples were thoroughly dried. Laser processing was conducted in a vacuum chamber, shown in figure 2, that was back-filled with helium. Since the laser beam entered the chamber through a pneumatically operated window, a positive pressure was maintained in the chamber.

Results and Discussion

Process analysis consisted of determining the nature of the oscillating beam and its influence on the shape and structure of the solidified melt pool. In this context, topographical and cross-sectional views of structures formed by the different surface modification processes were examined and analysed for morphology, dimensional uniformity and structural homogeneity. Based on these results, the feasibility of a particular process was determined. In the following discussion, each melt pass shown in the figures is identified by a sample

number. The processing conditions corresponding to each sample number are given in table I.

Table I Processing conditions for the various surface modification techniques

Sample No.	Process	Beam Width (cm)	Laser Power (kW)	Powder Feed Rate (cm^3/sec)	Sample Velocity (cm/sec)
66-4	Remelt	1.7	10	--	4.5
66-3	Remelt	1.5	10	--	0.38
4-1	WC(A) Injected	0.2*	10	0.3	2.0
6-2	WC(A) Injected	0.8	10	0.15	1.0
92-2	WC(B)# Injected	1.6	10	0.5	0.41
58-5	SiC(C) Consol.	1.5	8	--	0.37
59-6	SiC(C)@ Consol.	1.5	11	--	0.36
65-4	WC(A) Consol.	1.6	11	--	0.4
65-3	WC(A)@ Consol.	1.6	11	--	0.38
100-1	T400(D)# Cladding	1.6	10	0.15	0.4
61-5	WC(A) Injected	1.5	10	0.225	0.39
75-4/5	WC(A) Injected	1.7	10	0.3	0.39
80-2/3	WC(A)# Injected	1.6	10	0.3	0.27

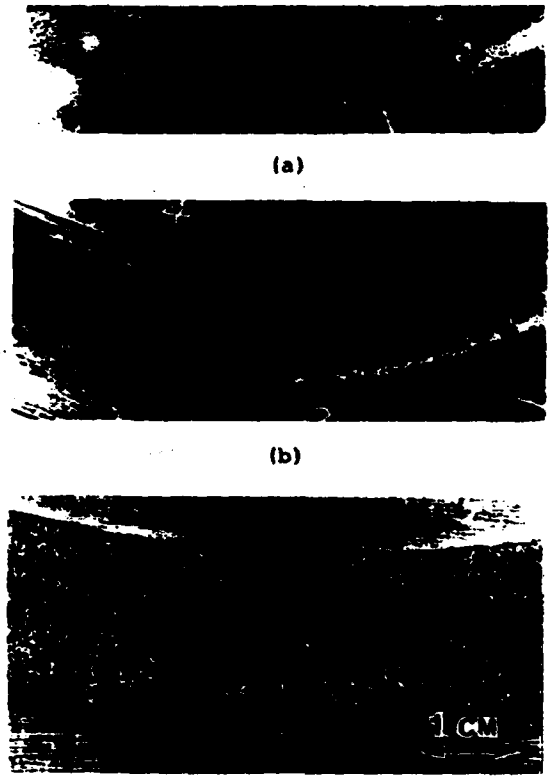
*Stationary beam. #Powder fed behind the melt pool. @Mixed with 45-75 um I625. Particle size (um) code: A=45-75, B=75-150, C=60, D=75.

The Nature of the Oscillating Beam

A melt pass formed by the oscillating laser beam on a rapidly moving Inconel 625 alloy sample is shown in figure 5. The melt trails are denser towards the extremities than in the middle of the track. This demonstrates that the beam dwells considerably longer at the cusps of the oscillation cycle than at the nodes. For high energy laser work, molybdenum mirrors were used, and, due to inertia, the heavy oscillating mirror tends to remain longer at the extreme positions of the cycle. The laser energy distribution generated by the oscillating beam, just described, would be higher near the extremities of the oscillation cycle than in the center. In fact, from the appearance of the melt track in figure 5, it would seem that a substantial amount, 2-3 times, of melting should occur near the edges of the melt pool than in the middle. In other words, the melt pool would be significantly dog-bone in shape and the melt depth, 2-3 times deeper near the edges.

Topographical and cross-sectional structures of a remelted surface made by the oscillating laser beam on a slowly moving substrate confirm the predicted variations in the shape of the melt pool. But the extent of the variations is much less than might be expected from figure 5. As shown in figure 6(a), the solidified melt pool at the end of the pass appears remarkably even except for a slight dog-bone shape. This is because diffusion of heat from the hotter extremities to the middle would tend to equilibriate the shape of the melt pool. In cross-section, as shown in figure 6(b), the melt depth is sinusoidal with deeper penetration occurring near the edges of the melt pool. But the melt depth varies little, from 0.8-1.2 mm, which is a variation of only 20%. The shape of the melt pool, figure 6(a), and the melt depth profile, figure 6(b), are reasonably symmetric about the middle. This means that neither the circular geometry of the melt pass, nor the change in the beam spot size, described in figure 3, had much bearing on the distribution of the incident laser energy density. The average radius of the melt pass in figure 6 is 6.35 cm and its width is 1.8 cm. For this geometry, the variation in the laser energy density from one edge of the melt pool to another is only 7%, not sufficient to cause an asymmetric melt pool. Also, since a laser beam with the smallest possible diameter was selected, the depth of focus was probably long enough to keep variations in the beam spot size to a minimum. The only factor that affected the symmetry of the melt pool was a beam that was not centered on the oscillating mirror. An off-centered beam formed a lop-sided or teardrop shaped melt pool. The melt pass in figure 6(a) shows surface ripples that parallel the moving melt pool. Whether these are caused by the oscillating motion of the laser beam or by convective motion in the "rectangular" melt pool has not been established.

Topographical views of layers formed by injecting WC particles into the melt pool are given in figure 7. The injected layer in figure 7(a) was formed by a 0.2 cm diameter stationary beam and a single circular nozzle. The injected strip in figure 7(b) was produced by a 0.8 cm wide oscillating beam and a dual circular nozzle. A 1.5 cm wide oscillating beam and a slitted nozzle were used to form the injected track shown in figure 7(c). In order to maintain a similar laser energy density over the wider area as that for the stationary beam, slower sample translation rates were used for the oscillating beam. These values appear in table I. The injected layers appear uniform with minor surface fluctuations. Figure 7 demonstrates the capability of producing single melt passes of desirable width using the particle injection process and an oscillating laser beam. With the set-up shown in figure 1, the amplitude of the oscillating beam incident upon the sample surface was limited to about 1.8 cm at the frequency of 110 Hz. But wider oscillation amplitudes were possible at the lower resonant frequency of 45 Hz. Thus, with proper nozzle design and laser energy density,



(a)

(b)

(c)

Figure 7. Topographical views of WC injected surfaces. a)Stationary beam. No. 4-1. b)0.8 cm wide oscillating beam. No. 6-2. c)1.5 cm wide oscillating beam. No. 92-2.



Figure 8. Cross-sectional view of WC injected layer. No. 92-2.

injected strips wider than 2.0 cm are feasible.

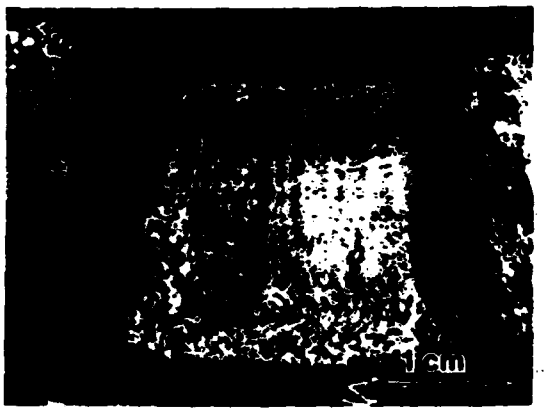
Surface Modification

As mentioned earlier, the main thrust of this work was to form hard metal matrix-carbide composite layers on Inconel 625 (I625) alloy substrates. Being heavier than I625, WC particles were easily impregnated into the surface and formed evenly shaped, thick injected layers. A cross-sectional view of a WC injected layer appears in figure 8. The layer has a fairly flat top and a slightly varied melt depth. In addition, the carbide phase is uniformly distributed throughout the cross-section. On the other hand, being lighter than I625, considerable effort was needed to drive the TiC particles into the melt and usually a thin dumbbell shaped injected layer resulted. The dumbbell shape was attributed to the deeper melting occuring on either side of the melt pool. Particle injection with SiC failed to form a composite layer because SiC dissociated in the intense heat of the laser beam. Being refractory in nature, SiC absorbs the laser energy more readily than the metallic WC and TiC, thereby heating up to a greater degree and accelerating the decomposition process.

An alternative means of incorporating SiC on the metal surface was to consolidate a coating of SiC powder. A topographical view of the surface layer appears in figure 9(a). Except at the edges of the layer, consolidation is complete throughout the melted region. A few cracks parallel to the melt pass direction demonstrate the brittle nature of the coating. Variations in the surface contrast are probably due to segregation or fluid flow patterns. In cross-section, figure 9(b), the consolidated layer has a flat top and a mildly sinusoidal melt depth. Unlike WC, the SiC particles were not retained as a separate phase and appear to have fused into a thin layer. Consolidation of a 50-50 mixture of SiC and I625 resulted in a uniform, crack-free surface layer as shown in figure 10, with the shape of the layer being nearly lenticular. The extent of alloying with the substrate, the microstructural details and the properties of the consolidated layers are subjects for a future study.

Laser consolidation of a WC coating resulted in an extremely uneven composite surface as shown in figure 11. Besides, on either side of the layer, considerable material overhang is observed. This material appears to have been ejected from the melt pool. The poor appearance of the WC consolidated layer makes a strong case for particle injection as a means to treat samples with carbides such as WC. Laser consolidation of a 50-50 mixture of WC and I625 (No. 65-3 in table I) was more successful, forming an even injected layer. But the heavier carbide phase tended to settle to the bottom of the melt pool. In all laser processing methods used for WC, the laser energy conditions were such that no fusing or melting of the carbide particles occurred.

Figure 12 (a) shows a topographical view of laser clad Tribaloy-400 powder. The cladding appears quite uniform with no surface ripples. Stray particles that adhered to the cladding after it had solidified are observed on the surface. In cross-section, the clad layer is uniformly thick as shown in figure 12(b). The nearly flat bottom of the cladding indicates that the laser oscillations had little influence on the shape of the melt pool.



(a)



(b)

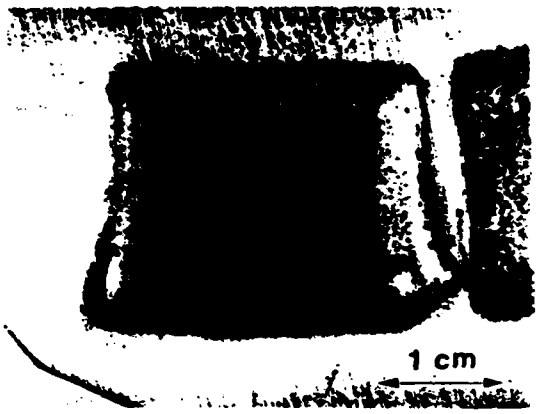
Figure 9. Consolidated layer of SiC coating. No. 58-5. a)Topographical view. b)Cross-sectional view.



Figure 10. Cross-section of consolidated layer of a mixture of SiC and I625. No. 59-6.



Figure 11. Cross-section of consolidated layer of WC coating. No. 65-4.



(a)



(b)

Figure 12. Surface cladding of Tribaloy-400. No. 100-1. a)Topographical view. a)Cross-sectional view.

Effect of Powder Feed Direction

The direction in which the powder is fed relative to the moving melt pool has been a subject for study by many. For greater efficiency, feeding ahead or in front of the melt pool is desirable. The effect of powder feed direction on the characteristics of the melt pool was studied only for particle injection with WC. A diagram illustrating this experiment is shown in figure 13. When fed ahead of the moving melt pool, the powder spray encounters a larger melt surface area making it a more efficient process compared to when the powder is fed behind the melt pool. The efficiency of particle injection was borne out by the fact that lower powder feed rates formed equally thick layers when the powder was fed in front of the melt pool than when fed behind the melt pool. For example, the cross-sectional structures shown in figures 8 and 14 have nearly the same thickness, about 1.5-2.0 mm. But the layer in figure 8 was formed by injecting behind the melt pool with a powder feed rate of 0.5 $cm^3 sec^{-1}$ while the layer in figure 14 was formed by injecting ahead of the melt pool with a lower powder feed rate of 0.225 $cm^3 sec^{-1}$. In spite of this advantage, it will be demonstrated below that feeding ahead of the melt pool can be undesirable.

A comparison of figures 8 and 14 show the profound influence of the powder feed direction on the shape of the melt pool. Feeding behind the melt pool resulted in an injected surface that was reasonably flat-bottomed and had a flat top surface as shown in figure 8. Feeding in front of the melt pool accentuated the sinusoidal shape of the melt depth and formed an uneven top surface that paralleled the depth contour as shown in figure

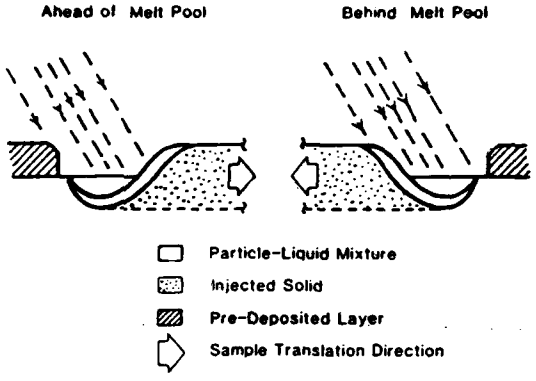


Figure 13. Schematic diagram showing the study of the powder feed direction.

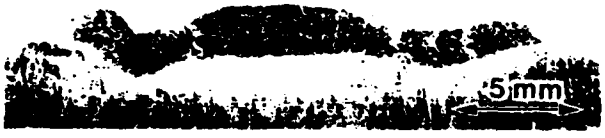
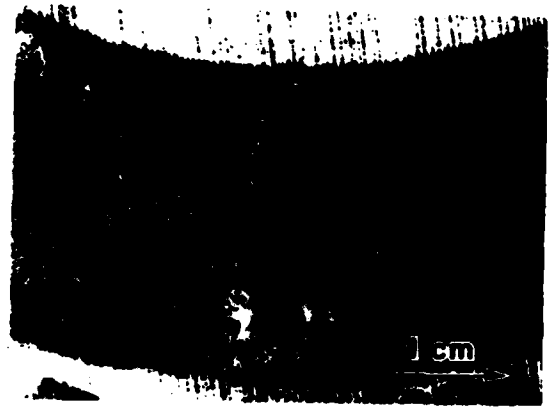
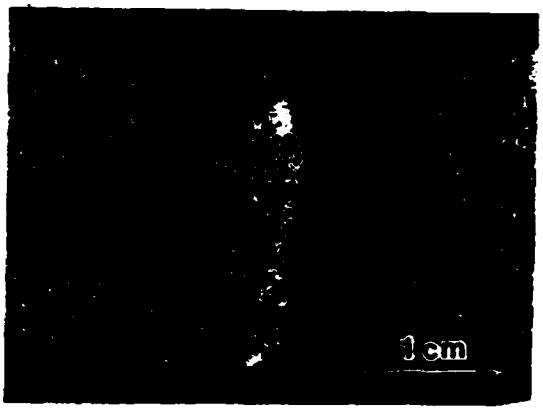


Figure 14. Cross-section of WC injected layer obtained by feeding the powder ahead of the melt pool. No. 61-5.

14. Since the injected layer is ground down to a flat before it can function as a wear resistant surface, an uneven layer such as the one shown in figure 14 is highly undesirable.



(a)



(b)

Figure 15. Effect of the powder feed direction on closure of a circular injected pass. a) Powder fed ahead of the melt pool. No. 75-4/5. b) Powder fed behind the melt pool. No. 80-2/3.

One of the stipulations of this work was to form an injected melt pass of circular geometry. This meant that at the end of the pass there would be a small overlap to complete the circle. When the particles were injected ahead of the melt pool, a discontinuous overlap resulted as shown in figure 15(a) while, as shown in figure 15(b), the overlap is continuous when the powder was injected behind the melt pool. To understand this we refer to figure 13. As the circular pass approaches closure, the initial pre-deposited layer blocks the powder spray when feeding ahead of the melt pool, thereby causing the discontinuity seen in figure 15(a). On the other hand, when feeding behind the melt pool, the pre-deposited layer does not hinder the particle spray and a continuous overlap ensues as shown in figure 15(b). The inability to form a continuous closure for a circular pass is another reason particle injection ahead of the melt pool is not desirable.

Summary

An electromagnetically driven oscillating mirror was successfully used to form a line laser energy source on the sample surface in order to melt strips of selected dimensions. With an oscillation frequency of 110 Hz, melt widths of upto 2 cm were easily obtained. Although the oscillating beam dwelled much longer near the extremities of the oscillation cycle, the variations in the melt pool shape and the melt depth profile were minimal. The solidified melt pool was symmetric about the middle and the top surface nearly flat. These characteristics of the melt pool were true for most of the surface modification processes attempted. Particle injected layers and laser clad surfaces of uniform thickness were obtained by employing a slitted nozzle to feed the powder. Finally, for particle injection, feeding the powder behind the melt pool was essential to form uniformly thick injected layers and continuous overlaps upon closure of a circular injected pass.

ACKNOWLEGEMENT: One of the authors, Dr. Cooper, would like to thank Dr. J. D. Ayers for his support and the Naval Research Laboratory for providing the facilities to do the work.

References

1. Ayers, J. D., R. J. Schaefer and W. P. Robey (1981). J METALS 33 (8) 19-23.
2. Ayers, J. D. (1981). THIN SOLID FILMS 84 323-331.
3. Cooper, K. P. and J. D. Ayers (1985). SURFACE ENGINEERING 1 (4) 263-272.
4. Cooper, K. P. (1986). Proc. Intl. Conf. on Surface Modifications and Coatings, Ed. R. D. Sisson, Jr. ASM, Metals Park, OH. 409-420.
5. Cooper, K. P. (Nov/Dec 1986). J VACUUM SCIENCE AND TECHNOLOGY in press.

Mr. Khershed Cooper is a Group Supervisor with Geo-Centers, Inc. His main function is to conduct contract research at the Naval Research Laboratory. He has a PhD in Metallurgical Engineering from the University of Wisconsin-Madison. His scientific interests include laser surface modification, surface coatings, metal casting and rapid solidification processing.

Mr. Robert Beigel is an Engineering Technician at the Naval Research Laboratory. He is in charge of operating the high power CO_2 laser facilities used for, among others, material processing such as surface modification and laser welding.

Mr. Paul Slebodnick is a Physical Science Engineer at the Naval Research Laboratory. He is in charge of the operation of the main Metallography Laboratory. His expertise is in Microscopy and unusual sample preparation techniques.

FOCUS ON

LASER MATERIALS PROCESSING

**Proceedings of the
6th International Congress on
*Applications of***
**Lasers and Electro-optics
ICALEO '87**

Edited by S. L. Ream

**8-12 November 1987
San Diego, California**

IFS Publications
Springer-Verlag
Berlin · Heidelberg · New York
London · Paris · Tokyo

The influence of processing parameters on the cracking tendency of laser processed composite surfaces

K P Cooper
Geo-Centers Inc., USA
and
J D Ayers
Naval Research Laboratory, USA

Abstract

In order to improve the wear resistance of engineering materials, hard composite surface layers, made up of carbide particles in a metal matrix, were formed on metals by the laser melt-particle injection process. Particle injection with carbides of tungsten and titanium increased the hardness of Inconel 625 alloy and reduced the coefficient of friction. However, the improvement in wear properties was offset by the presence of undesirable hairline cracks within the injected layer. In this study, the influence of melt pass width, carbide type and size, and carbide feed rate on the cracking tendency of the modified surface was evaluated. Fewer cracks occurred under conditions that favored a a reduction in the solidification and cooling rates. For example, the crack density was reduced as the melt width increased. At moderate to high carbide feed rates, an increased cracking tendency was found in layers injected with the fine WC and the medium TiC particles. In layers made with the medium and the coarse WC, the crack density reduced with increasing powder feed rate. Microstructural analysis showed that cracks form initially in the brittle carbide phase when the residual stress in the solidified composite are just sufficient to cause cracking. The cracks then propagate into the inter-particle matrix phase if the matrix is embrittled by carbide dissolution.

Introduction

Lasers have been used extensively to modify metal and alloy surfaces to improve their service life[1]. But a frequently encountered problem with laser surface processing is the occurrence of intermittent cracks in the modified surface. These cracks form when the modified region is unable to withstand the residual stresses that result from the thermal cycle of rapid surface melting and constrained cooling of the solidified melt. The cracking tendency depends upon the level of stress, the stress distribution, and the strength of the phases present.

Residual stresses can assume different forms depending upon the type of laser surface treatment. Li and Easterling[2] determined that the stresses from laser transformation hardening of steel were compressive as a result of the austenite to martensite phase change. Lamb, West and Steen[3] found that in laser melted single tracks, martensitic stainless steels developed compressive stresses, while austenitic stainless steels developed tensile stresses comparable to the yield stress of the material. Rawers et al[4] found that the residual stresses from laser glazing of steel caused surface cracks, and the cracking tendency increased with higher traverse speeds and with highly focussed beam conditions. Chabrol and Vannes[5] report that cladding of Co-and Ni-base powders on martensitic steels produced tensile stresses in the cladding and compressive stresses in the substrate. Similar observations were made by Weerasinghe, Steen and West[6] upon cladding stainless steel powder on mild steel. Furthermore, Weerasinghe and Steen[7] observed cracking in hard coatings such as iron/boron, but none in ductile coatings such as stainless steel or stellite when clad on mild steel. They found that cracking of the hard coatings was eliminated by preheating the sample to 700 °C.

Laser cladding by powder feeding involves minimum melting of the substrate and complete fusion of the powder. The laser melt-particle injection process involves melting of the substrate but not the powder. In some respects the process resembles laser alloying, except that processing conditions are normally chosen to minimize dissolution of the injected particles. Instead, the particles displace a portion of the melt and help to form a metal matrix composite. The metal matrix is altered only slightly in composition from that of the substrate. The processing technique and process optimization have been described elsewhere[8-10]. By this technique, the superficial hardness of Inconel 625 alloy samples injected with WC and TiC was increased from <20 to 50 HRC, an increase of nearly three-fold, and the coefficient of friction against a hard 52100 steel ball was reduced from 0.72 to 0.40[11]. In this study, an attempt is made to understand the nature of the stresses in the injected layer and to determine the influence of various processing parameters on its cracking behavior.

Experimental Procedure

Laser Processing

A CW CO_2 high power laser was used to melt the surface of 1.5 cm thick Inconel 625 alloy samples. The laser beam was oscillated above the sample with a frequency of about 110 Hz. to form melt passes of desired dimensions. Helium gas carried the carbide particles from a slotted nozzle into the molten pool as the sample was swept under the oscillating laser beam. The nozzle, inclined 30° from the surface normal, was positioned 1.0 to 1.25 cm from the melt pool and was directed such that the particles entered the melt pool from its receding edge rather than from its leading edge. The melt passes were 8-8.5 cm long arcs having a radius of 6.35 cm and the melt widths were varied from 0.4 to 2.0 cm. Details of the oscillating beam laser process were given in an earlier study[12].

Melt Width Variations

For these experiments, the laser power was held constant at 10 kW. To maintain a constant melt depth and, hence, injected layer thickness, the incident laser energy density or fluence was held constant by changing the beam oscillation width and the sample traverse speed. For simplicity, the oscillating beam was assumed to be a line source having a constant energy distribution and a width corresponding to the oscillation amplitude. Table I gives the beam width, the laser power density, the calculated traverse speed and the laser beam interaction time for the various beam conditions. For these calculations, a measured beam diameter of 0.2 cm was used. The calculated laser fluence in the oscillating beam was 16.67 kJ cm^{-2}. The calculated traverse speeds were used in the experiments except for sample 52-2 for which the traverse speed was 0.3 cm s^{-1}.

Table I: Laser Beam Conditions.

Sample I.D.	Beam Width (cm)	Power Density (kW cm^{-2})	Traverse Speed (cm s^{-1})	Interaction Time (s)
77-1	0.2*	318.5	3.82	0.05
49-2	0.4	125.0	1.50	0.13
49-1	0.8	62.5	0.75	0.27
52-1	1.2	41.67	0.50	0.40
52-2	1.6	31.25	0.375	0.53

*Stationary beam.

The carbide particles were directed towards the melt pool at a constant rate of 0.5 cm^3 s^{-1} under a carrier gas pressure of 110-124 kPa. For this study, WC particles of 45-75 μm size distribution were used. For comparison, injected layers using a stationary laser beam and a circular injection nozzle were also made. The beam conditions for this sample (77-1) are also given in Table I.

Carbide Feed Rate Variations

In addition to studying the effect of carbide feed rate on the cracking tendency of injected layers, this experiment was designed to include studies on the effect of carbide type (WC and TiC) and carbide size (<45 μm, 45-75 μm and 75-150 μm WC). For this study the melt width was kept nearly constant at 1.1-1.2 cm. Also held constant were laser power at 10 kW and the sample traverse speed at 0.75 cm s^{-1}. Depending upon the carbide density and size, the carrier gas pressure was varied from 80 to 140 kPa for effective particle injection.

The carbide feed rate was changed by controlling the rotational speed of the powder feeder auger which dispenses the powder into the carrier gas stream. The volume feed rate, which is independent of the type or size of the carbide, was varied from as little as 0.025 to as much as 0.65 cm^3 s^{-1}. Although, from experience, only about 10-15% of the carbide volume gets into the melt, a determination of the carbide incorporation rate was made by weighing the sample before and after particle injection.

Measurement of Crack Density

In order to reveal the cracks in the injected layer, a dye penetrant non-destructive test was used. In this test, defects in the sample fluoresce when viewed under a UV light source. The crack density was determined as the total crack length in the longitudinal and transverse directions divided by the injected layer surface area.

Results

Structural Characteristics

As shown in figure 1(a), the injected layer appears as a rough melt track on the sample surface. In cross-section, the injected layer appears "cigar-shaped" with a width of 2.0 cm and with the thickness varying from 0.18-0.2 cm as shown in figure 1(b). In general, the thickness of the WC injected Inconel 625 alloy layers varied little, but layers injected with TiC showed a larger variation in thickness. In figure 1(b), the dark, uniformly distributed grains are the WC particles and they occupy about 50% of the composite volume, the remaining space being the metal matrix.

The Effect of Melt Width

Figure 2(a) shows cracks in the injected layer as they appear under UV light. The melt passes were made with the stationary laser beam. The cracks here are mostly of the transverse kind, with a few longitudinal. Figures 2(b & c) demonstrate the effect of melt width on the degree of cracking in particle injected layers formed by the oscillating laser beam. With increasing melt width, a gradual decrease in the number of transverse cracks and the appearance of longitudinal cracks are observed. Also evident is the overall reduction in crack density with increase in melt width. This trend is graphically represented in figure 3. In melt passes made with the oscillating laser beam, the variation appears to be linear, the reduction in crack density dropping from 1.9 to 0.3 cm cm^{-2}. In the injected layer made with the stationary laser beam, the crack density was 3.75 cm cm^{-2}.

The Effect of Powder Feed Rate

The effect of powder feed rate or, more accurately, powder incorporation rate, on the crack density is graphically represented in figure 4 for the four carbide forms studied. In spite of some scatter in the data, certain trends are demonstrated. For the medium (45-75 μm) and the coarse (75-150 μm) WC, the crack density diminishes with increasing powder feed rate. This drop is from about 2.25 to 1.25 cm cm^{-2}. For the medium (45-75 μm) TiC, the crack density increases form a low value of 0.6 cm cm^{-2} at low powder feed rates to a high value of 2.75 cm cm^{-2} at medium powder feed rates followed by a light decline at higher powder feed rates. The trend for the fine (<45 μm) WC also shows an increase from a low value of 1.5 cm cm^{-2} at low powder feed rates, but no definite trend is observed at higher powder feed rates. At medium to high powder feed rates (20-50 mm^3 s^{-1}), a substantially larger degree of cracking occurs in layers treated with the fine WC and the medium TiC, compared to those treated with the medium and coarse WC. Also, in this powder feed rate regime, the degree of cracking in both the medium and coarse WC injected layers is about the same. As an example, in figure 5 the crack populations in samples injected with three different carbides are shown. For these melt passes, the powder feed rate was nearly the same, about 39 mm^3 s^{-1}. This figure compares WC of two different sizes as well as WC and TiC of the same size. Visually, the degree of cracking in the two WC injected sample appears substantially higher. In fact, in the 45-75 μm and the 75-150 μm WC the crack density was 1.4 and 1.37 cm cm^{-2}, respectively, while the crack density in the 45-75 μm TiC was 2.3 cm cm^{-2}.

Discussion

Since cracking in laser modified surfaces results from thermally induced stresses, it would be beneficial to understand the development of these stresses. Simple laser melting, if there are no phase transformations during cooling of the solidified melt, generates stresses which are tensile and whose magnitudes depend upon the properties and elastic constants of the work piece. When extraneous material is added to the melt, e.g. by particle injection, the nature of the stresses is considerably more complex. If particle injection results in alloying, e.g. the dissolution of Si particles in 5052 Al[13], then the composition of the melt is changed and a different set of elastic constants, corresponding to the new alloy, apply. If laser alloying produces additional phases, e.g. the formation of dendritic carbides upon alloying of Ti-6Al-4V with graphite[14], then the determination of residual stresses would involve consideration of the resolidification products as well. A similar situation prevails in the work reported here.

Microstructure and Stresses in a Composite Surface Layer

Laser melt-particle injection with WC and TiC forms a composite surface layer in which some alloying occurs as a result of carbide dissolution. This dissolution, which may be desirable or undesirable, can result in the formation of several resolidification products. In Inconel 625 alloy samples that were injected with WC and TiC particles, the resolidification products included resolidified dendritic carbides, solute-rich eutectic

colonies having novel crystal structures, and a solute depleted matrix phase[11,15]. As a result of these reactions the large undissolved carbides are contained within a metal matrix with a different microstructure and chemistry than the work-piece. Microstructural modification of the inter-particle matrix due to dissolution leads to an alloy with properties that may be quite different from those of the substrate. For example, precipitation of resolidified carbides has been known to harden the matrix[16]. This embrittlement is important because it can lessen the ability of the matrix to withstand the tensile residual stresses that develop with laser melting.

Any analysis of the stresses in an injected layer containing primary carbides, resolidified carbides and eutectic phases must consider the complex stresses and strains which operate. The solidified melt, which forms the metal matrix, is under a tensile stress due to thermal contraction. The primary carbide particles and the resolidifeid dendritic carbides have lower thermal expansion coefficients than the matrix, and thus should on average be subjected to less tensile stress than the metal matrix. Earlier observations on Ti-6Al-4V and Inconel 750 injected with WC and TiC[16] show that individual carbide particles often crack, even when there is insufficient thermally induced stress to fracture the matrix. This effect, which can also be seen in figure 6, demonstrates that despite the lower expansion coefficient of the carbides some of them at least must be subjected to tensile stresses greater than their fracture strength. Any numerical analysis of the fracture pfoblem would be very complicated because of the irregular geometry of the particles. This irregular geometry coupled with stress distributions resulting from plastic deformation of the matrix can obviously create high levels of tensile stress in the carbides. In ductile metal matrices it is sometimes observed that localized deformation can cause cracking of the carbide particles in a nearly planar array, but that the matrix accomodates the strain plastically. This phenomenon, observed in TiC injected Al bronze, is shown in figure 6, which is reproduced from reference 17. The discontinuity of the crack is clearly evident in figure 6(b). In this alloy carbide dissolution was negligible and the matrix remained ductile. Even when the matrix cracked, the crack width in the matrix was found to be narrow compared to that in the carbide phase. Figure 7 shows cracks in a sample from this study as they appear on the injected surface in the SEM. The cracks in the carbide phase are 2 to 5 times wider (see arrows) than those in the surrounding matrix.

The Influence of Powder Feed Rate

In an earlier study on Ti-6Al-4V samples injected with TiC particles[10], it was demonstrated that the carbide volume fraction in the melt can be increased by increasing the powder feed rate, but then the carbide volume fraction was limited to 0.5-0.6. In this study the powder feed rate was used as an estimate of the carbide volume fraction in the injected layer, it should be remembered that the relationship is not linear. In addition to increasing the carbide volume fraction, increasing the carbide feed rate was found to increase the carbide dissolution rate and the matrix microhardness. Increased carbide volume fraction and increased matrix hardness would tend to lower the ductility of the composite layer and increase its susceptibility to cracking.

That the carbide type and size influence the matrix properties in Inconel 625 is demonstrated in figure 8. Plotted as a function of the normalized thickness of the injected layer, this figure makes evident two important trends in the matrix microhardness relative to that of the substrate. First, WC injection hardens the matrix much more than TiC injection. Secondly, the coarser particle size distribution has a somewhat lesser influence on the matrix microhardness than the finer variety[11,15]. If microhardness is an accurate indicator of embrittlement, then WC would tend to harden and embrittle the matrix to a greater extent than TiC and finer sizes of the carbides would have a greater hardening effect than coarser ones.

If cracking was equated solely with embrittlement of the matrix, the likelihood of cracking in the injected layer, a) would increase with increasing carbide volume fraction, b) would increase with decreasing carbide particle size distribution, and c) would be greater with WC injection than with TiC injection. The results in figure 4 are contrary to most of the above premises. With the exception of the behavior at low powder feed rate of the fine WC and the medium TiC, the crack density actually declined with increasig carbide feed rate. This reduction in the crack density with increasing carbide feed rate may indicate that despite its higher hardness and lessened ductility, the composite may have higher fracture resistance with a high fraction of the carbide phase than it does with lower carbide contents. Another possible explanation is a reduction in the tensile residual stresses in the matrix in the presence of increasing quantities of the second phase. Gurland[18] reported that in the Co-WC system, at higher volume fractions of WC, the thermal residual stresses in the Co matrix became compressive. A third possible reason for the declining trend in the crack density is a reduction in the residual tensile stresses brought about by the decreasing solidification and cooling rates observed at

higher powder feed rates. Increasing the powder feed rate introduces additional heat into the melt pool by improving the laser beam-substrate coupling. The excess heat content of the melt would tend to lower the cooling rates.

In the mid to high powder feed rate range, cracking was more pronounced in layers injected with the medium and coarse WC, which was predicted from matrix hardening arguments. But the lack of particle size effect between the medium and the coarse WC may be due to a smaller than predicted influence of the dissolution products. Comparing surfaces containing WC and TiC particles of the same size, cracking in the TiC injected layers is consistently higher (1.5-1.7 times) than that in the WC injected layers, except at very low powder feed rates. This is contrary to expectations based on matrix hardening arguments alone. There is substantially less dissolution of TiC during processing than there is of WC and this is reflected in a lesser degree of hardening of the TiC injected matrix, as can be seen from figure 8. Additional factors which may affect the relative cracking frequency of surfaces injected with the two carbides are the mechanical properties of the carbides and geometric effects in the processed surfaces. The room temperature hardness of TiC is substantially higher than that of WC, 3200 HV versus 1800 HV, but at high temperatures WC is much harder than TiC. At 1000 °C, the hardness of WC is 900 HV and that of TiC is 260 HV[19]. Also WC has nearly twice the fracture strength and is twice as tough as TiC[20]. This greater fracture strength and hot hardness of WC would explain the high carbide feed rate results of figure 4, but not those at lower feed rates. At higher feed rates the greater degree of cracking may also be related to the uneven shape of the TiC injected layers. Brought about by a general difficulty in injecting the lighter TiC in the heavier Inconel 625 alloy melt, the uneven injected layer may produce sharp increases in residual stresses, exceeding those in evenly shaped injected layers. The unevenness was manifested as periodic thickness variations along the length of the injected melt pass. In fact, this explains the occurrence of periodic cracks seen in figure 5(c). Large thickness variations were not evident in WC injected layers. Below a certain powder feed rate the TiC injected layers were uniformly thick and, in these samples, the cracking tendency was dependent primarily upon the mechanical properties of the principle phases. We can offer no good explanation of why the TiC containing surface should, under these conditions, be less susceptible to cracking than those containing WC. One possible explanation is the greater ductility of the matrix in the TiC injected layer compared to that of the WC injected layer at low carbide volume fractions.

The Influence of Melt Width

One of the advantages of laser material processing is its ability to process selected areas without affecting the neighboring regions. Large areas can be processed by overlapping several adjacent melt passes. Another method is to process wider surface strips using a line energy source such as an oscillating beam. In figure 9, a likely distribution of the stresses after laser surface melting is shown. Adapted from Masubuchi's[21] treatment of the welding problem, this diagram gives a schematic representation of the longitudinal (σ_x) and the transverse (σ_y) stress distributions. Parallel to the melt pass, figure 9(b), the entire melt width and portions of the adjacent substrate are under tension. Further away from the melt pass, the substrate is under compression. As the melt width is increased, the maximum tensile stress increases and centerline cracks of the type shown in figure 2 begin to appear. The transverse stress, figure 9(c), is tensile in character near the middle of the melt pass and compressive near the beginning and the end of the melt pass. In practice, as the heat source moves along the length of the melt pass, periodic cycles of heating, cooling, stress build-up and cracking occur in longitudinal segments of the injected layer. Thus the transverse cracks occur in a periodic fashion as shown in figures 2 and 5.

Cracking occurs when the residual stresses are high due to differential cooling between the melt zone and the substrate, these differences arising from the rapid heating and cooling rates in the laser heated region. To make wider melt passes with the same laser energy density, slower traverse speeds were used. Reducing the traverse speed increase the beam interaction time (see Table I) which results in a reduction in the solidification and cooling rates in the injected layer. Also, the oscillating heat source promotes a more uniform temperature distribution, which results in lessened residual stresses and a lesser tendency towards cracking. A stationary heat source on a more rapidly moving sample causes steeper temperature gradients, sharper increases in residual stresses and a greater tendency towards cracking. These effects result in the reduction in the crack density with increasing melt width demonstrated in figures 2 & 3. Also, as the cooling rates are reduced, the period between the thermal cycles explained above increases and the spacing between the transverse cracks increases.

Conclusions

1. Unlike claddings, which may be considered as homogeneous surface layers, particle

injected layers are two-phase composites. Due to its composite nature and because of structural modification of the metal matrix, carbide injected layers are subjected to complex residual stresses. These stresses are a function of the carbide volume fraction and the elastic-plastic and thermal properties of the carbide and the modified matrix phases.

2. There is evidence that the cracks initiate in the carbide phase and then continue into the matrix phase.

3. In medium and coarse WC injected layers the crack density decreases with increasing powder feed rate. This was attributed to several factors including an increased fracture resistance at higher carbide volume fractions, and reductions in the tensile residual stresses at higher volume fractions and with lower cooling rates.

4. Under most processing conditions, samples injected with TiC exhibited more cracking than samples injected with WC. This difference results from differences in the mechanical properties of the carbides, and probably also from microstructural and injected layer shape effects resulting from processing.

5. Layers injected with the fine WC showed a greater degree of cracking than those made with the coarser WC. This was attributed to greater carbide dissolution and, hence, greater embrittlement of the matrix. The difference in cracking tendency betweent he medium and coarse WC was slight because, in these size ranges, the difference in the degree of matrix embrittlement was not significant.

6. The cracking tendency in WC injected Inconel 625 decreased with increasing melt width because of reductions in the cooling rate and the induced stresses. In addition, with increasing melt width, centerline cracks replaced transverse cracks as the dominant fracture mode as a result of higher longitudinal residual stresses.

Acknowledgement

The authors would like to thank Mr. R. Stegman and Mr. R. Beigel of the Laser Materials Processing Group for use of their facilities and for their technical assistance.

References

1. Gnanamuthu, D. S. (1979). Applications of Lasers in Materials Processing. ASM, Metals Park, OH. 177-211.

2. Li, W. D. and K. E. Easterling (1986). SURFACE ENGRG. 2 43-48.

3. Lamb, M., D. R. F. West and W. M. Steen (1986). MATS. SCI. & TECHNOL. 2 974-980.

4. Rawers, J. C., M. Vanderzanden, S. Duft and B. Nelson (1986). SCRIPTA MET. 20 167-172.

5. Chabrol, C. and A. B. Vannes (1986). Laser Surface Treatment of Metals, Martinus Nijhoff Publ., Dordrecht, The Netherlands. 435-450.

6. Weerasinghe, V. M., W. M. Steen and D. R. F. West (1987). SURFACE ENGRG. 3 147-153.

7. Weerasinghe, V. M. and W. M. Steen (1983). Lasers in Materials Processing, ASM, Metals Park, OH. 166-174.

8. Ayers, J. D., R. J. Schaefer and W. P. Robey (1981). J. METALS 33 19-23.

9. Cooper, K.P. and J. D. Ayers (1985). SURFACE ENGRG. 1 263-272.

10. Cooper, K. P. (1986). Surface Modifications and Coatings, ASM, Metals Park, OH. 409-420.

11. Cooper, K. P. (1986). J. VAC. SCI. TECHNOL. A 4 2857-2861.

12. Cooper, K. P., R. E. Beigel and P. Slebodnick (1987). Laser Materials Processing, ICALEO'86, LIA, Toledo, OH. 169-176.

13. Ayers, J. D. (1981). THIN SOLID FILMS 84 323-331.

14. Flower, H. M., A. Walker and D. R. F. West (1985). SCRIPTA MET. 19 923-926.

15. Cooper, K. P., J. D. Ayers and A. K. Singh, to be published.

16. Schaefer, R. J., T. R. Tucker and J. D. Ayers (1980). Laser and Electron Beam Processing of Materials, Academic Press, New York, N. Y. 754-759.

17. Ayers, J. D. (1981). Lasers in Metallurgy, TMS-AIME, Warrendale, PA. 115-125.

18. Gurland, J. (1958). TRANS. ASM 50 1063-1071.

19. Westbrook, J. H. and E. R. Stover (1967). High Temperature Materials and Technology, Wiley, New York, N. Y. 312-348.

20. Murray, M. J. and C. M. Perrott (1977). PHIL. MAG. 35 1675-1679.

21. Masubuchi, K. (1980). Analysis of Welded Structures, Pergamon Press, New York, N. Y. 192.

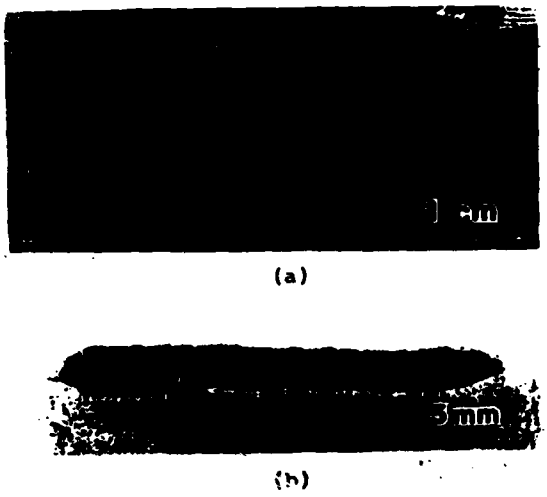


Fig. 1 Inconel 625 alloy injected with WC particles. Optical micrographs. a) Topographical view. b) Cross-sectional view.

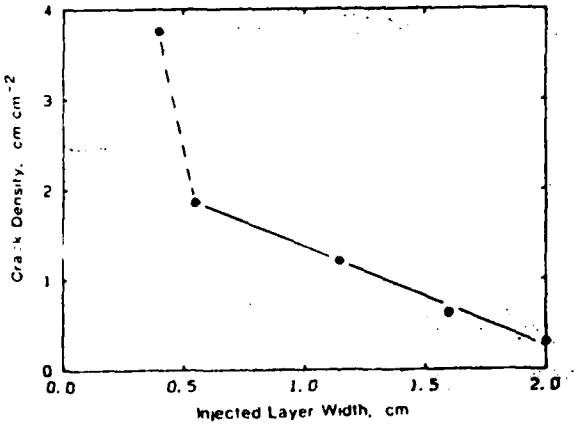


Fig. 3 Graphical representation of the effect of injected layer width on crack density.

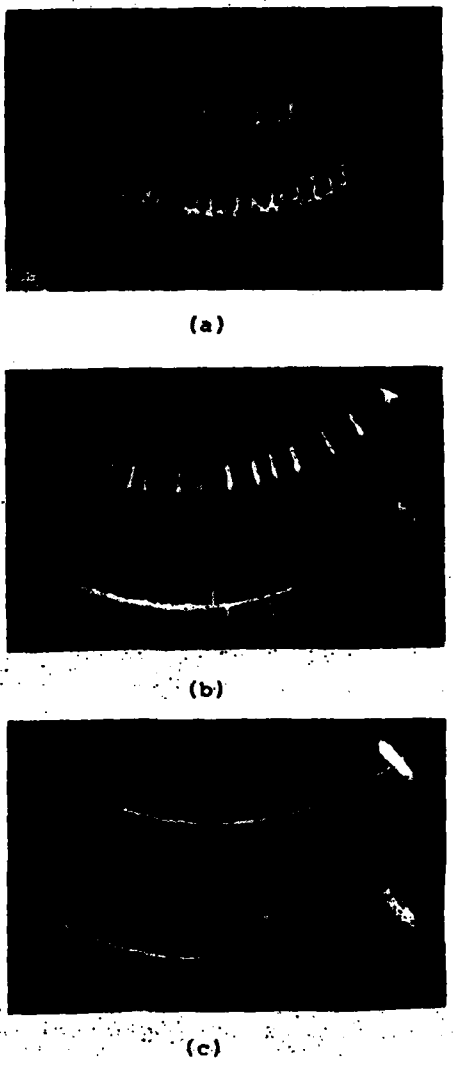


Fig. 2 Demonstration of the effect of melt width on cracking. Cracks revealed with dye penetrant and UV lighting. a) Sample melted with a stationary beam. b) Oscillating beam melt passes 0.55 and 1.15 cm wide. c) Oscillating beam melt passes 1.6 and 2.0 cm wide.

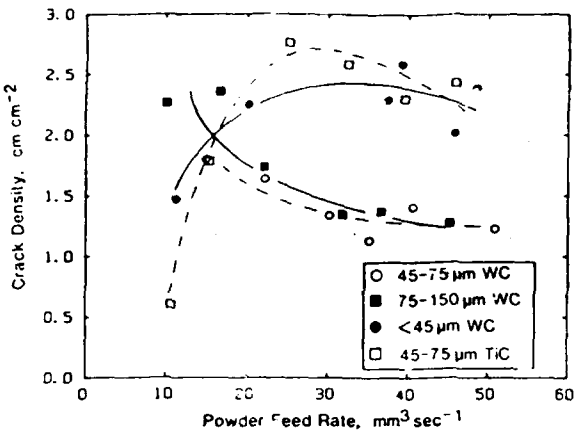


Fig. 4 Plots of the effect of powder feed rate on the crack density in layers injected with various carbides.

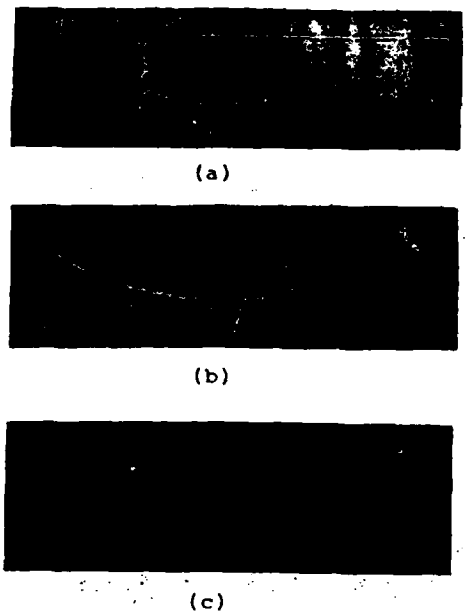


Fig. 5 Crack population in samples injected with various carbides at a constant rate of 39 mm^3 s^{-1}. Cracks revealed with dye penetrant and UV lighting. a) 75-150 μm WC. b) 45-75 μm WC. c) 45-75 μm TiC.

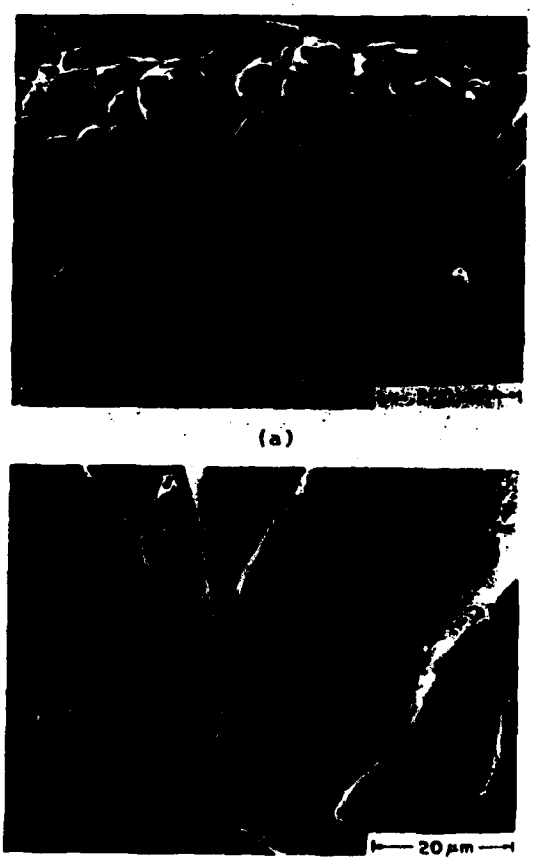


Fig. 6 Cracking in TiC injected Al bronze from Ref. 17. SEM micrographs. a) Crack in cross-section. b) High magnification.

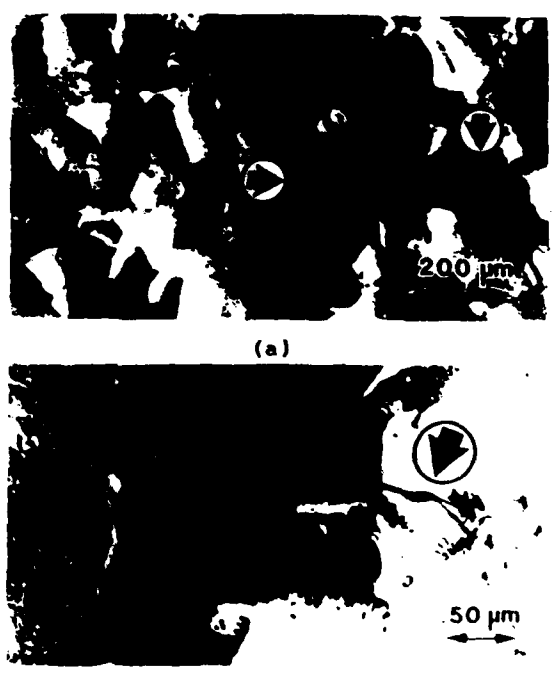


Fig. 7 Topographical views of cracks in WC injected Inconel 625. SEM micrographs. a) Cracks on injected surface. b) High magnification. Arrows show larger cracks in carbides.

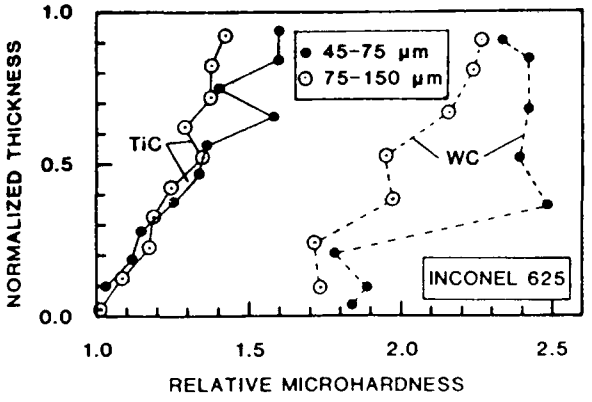
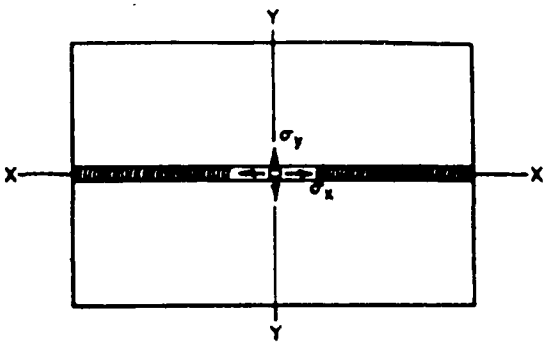


Fig. 8 Matrix microhardness relative to that of the substrate as a function of the normalized thickness of the injected layer from Ref. 11.

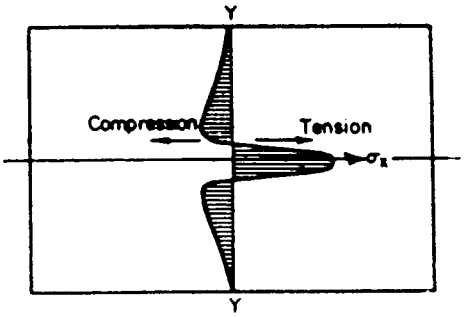
Meet the Authors

Khershed P. Cooper is a Group Supervisor with Geo-Centers, Inc. for whom he conducts contract research at the Naval Research Laboratory. He has a PhD in Metallurgical Engineering from the University of Wisconsin-Madison. His scientific interests include laser surface modification, surface coatings, metal casting, powder metallurgy and rapid solidification processing.

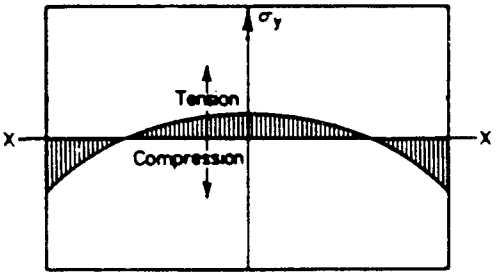
Jack D. Ayers is Head of the Alloy Development and Processing Section of the Physical Metallurgy Branch of the Naval Research Laboratory. He was awarded a PhD in Materials Science by Carnegie-Mellon University. He is also interested in diverse types of metals processing.



(a)



(b)



(c)

Fig. 9 Schematic representation of the stress distributions in laser melted surfaces after Masubuchi[21]. a) Laser melt pass. b) Longitudinal stress. c) Transverse stress.

Proceedings of SPIE—The International Society for Optical Engineering

Volume 957

Laser Beam Surface Treating and Coating

Gerd Sepold
Chair/Editor

Cosponsored by
SPIE—The International Society for Optical Engineering
and
ESD—The Engineering Society

Cooperating Organizations
Applied Optics Laboratory/New Mexico State University
Center for Applied Optics/University of Alabama in Huntsville
Center for Electro-Optics/University of Dayton
College of Engineering/University of Michigan
Illuminating Engineering Society of North America
Industrial Technology Institute

29-30 June 1988
Dearborn, Michigan

Published by
SPIE—The International Society for Optical Engineering
P.O. Box 10, Bellingham, Washington 98227-0010 USA
Telephone 206/676-3290 (Pacific Time) • Telex 46-7053

SPIE (The Society of Photo-Optical Instrumentation Engineers) is a nonprofit society dedicated to advancing engineering and scientific applications of optical, electro-optical, and optoelectronic instrumentation, systems, and technology.

Invited Paper

Surface Treating by Laser Melt/Particle Injection

Khershed P. Cooper

Geo-Centers, Inc.
10903 Indian Head Highway, Suite 502, Fort Washington, MD, 20744

ABSTRACT

By the laser melt/particle injection process, an in situ composite surface layer of particulate material in a matrix made up of the parent metal is formed. The particles are usually metal carbides which makes the injected surface layer hard and wear resistant. In this paper, the processing technique and the microstructures obtained are described. In addition, the hardness and wear characteristics of the modified surface are discussed.

1. INTRODUCTION

Lasers are used extensively to modify metal surfaces to enhance resistance to wear, friction, corrosion and high temperature oxidation. Laser heat treatment, laser melting, laser alloying and laser cladding are the various established techniques available for surface modification. Their selection depends upon the material being treated and the specific application that one has in mind. For example, cast irons and some steels are easily laser heat treated for surface hardening and wear resistance[1]. Laser alloying of low carbon steels with chromium enhances corrosion resistance[2]. Laser cladding with Ni-Cr-WC improves the wear resistance of steels[3], while laser cladding with Ni-Fe-Cr-Al-Hf improves the high temperature oxidation behavior of nickel-base superalloys[4].

In laser cladding, since the clad layer is necessarily of a different material than the substrate, the properties of the modified surface will not reflect those of the substrate. For example, although a hardfacing alloy would improve the wear resistance of a nickel-base alloy, it may fail in a corrosive environment. The laser melt/particle injection process was developed to improve properties such as wear resistance while retaining substrate properties such as corrosion resistance[5]. It is also one of the few means available to improve the wear resistance of alloys that are difficult to harden by conventional means, for example, aluminum alloys[5]. In laser alloying, the material added to the substrate melt dissolves completely to form an alloyed surface. In laser cladding, the material added fuses against the substrate with the least amount of dissolution or dilution. In laser melt/particle injection, high melting particles such as carbides are forcibly entrained into the laser melt pool so that upon solidification, a particulate composite surface forms with a matrix that is of a composition similar to the base metal[5,6]. Neither fusion nor complete dissolution of the particles into the melt occurs. The presence of the carbide particles increases hardness and

wear resistance, while the matrix, which is structurally continuous with the substrate, retains much of the properties of the base metal. Such a surface would be suitable for applications involving a high wear and corrosive environment.

2. LASER MELT/PARTICLE INJECTION PROCESSING

A schematic diagram of the laser melt/particle injection process is given in Figure 1. A shallow melt pool was formed on a translating substrate by a high power CW, CO_2 laser beam. The slightly off-focus beam melted a 2 to 3 mm wide layer. Wider melt passes were made by oscillating the laser beam using a dithering mirror[7]. A copper nozzle with a slotted opening injected the carbide particles into the melt pool. Upon solidification, the carbide/melt mixture formed the injected layer. The width of the melt pass was controlled by varying the laser beam oscillation amplitude. By this means, injected layer widths from 4 to 20 mm were produced. Laser power levels of 8 to 10 kW were used and the sample translation velocities were varied from 0.25 to 1.5 cm sec^{-1} depending upon the width of the melt pass. Typically, the injected layers were 1.0 to 1.5 mm thick. The powder particles were carried by helium gas, which not only served to propel them but also to keep them from heating to fusion as they travelled through the laser beam. Particle size distributions of 45-75 um and 75-150 um were used. Finer particles overheated and dissolved excessively into the melt pool. Coarser tended to clog the delivery line and were difficult to drive into the melt pool.

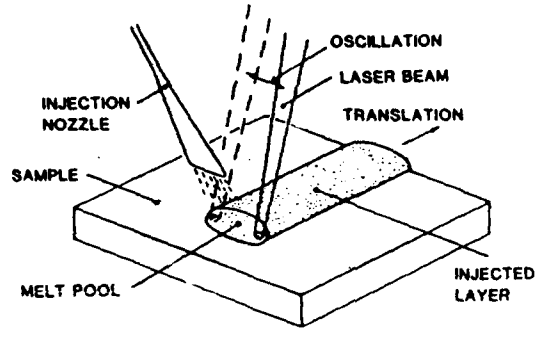


Figure 1. Schematic diagram of the laser melt/particle injection process.

A cross-section of the injected layer in a WC injected Inconel 625 alloy sample appears in Figure 2. The layer is a particulate composite in which the WC particles appear as light grains which are surrounded by the grey Inconel metal matrix. The carbide particles appear uniformly distributed throughout the injected layer occupying a volume fraction of about 0.5. Since a portion of the melt is displaced by the particles, the excess material appears as the mounding above the sample surface. The mounding and the penetration depth make up the layer thickness. These three dimensions and the carbide volume fraction can be controlled by carefully selecting processing parameters such as sample translation rate, laser power and powder feed rate. Composite surface layers can also be produced by adding particulate mixtures of carbide and metal using methods such as

plasma transferred arc[8] and laser cladding[3]. But there are problems associated with feeding mixtures of powder of varying density. Also, with laser cladding, the carbide volume fraction in the overlay is usually small[3], about 0.15 to 0.2.



Figure 2. SEM micrograph of cross-section of WC injected Inconel 625.

The influence of processing parameters such as sample translation rate, laser power and powder feed rate on injected layer characteristics was investigated for TiC injected Ti-6Al-4V[9]. In this study, each parameter was varied keeping the other two constant. Increasing the sample translation rate decreased the injected layer dimensions. This happens because higher sample speeds reduce the laser energy density needed to melt the surface. The flowing particles assisted in coupling the laser beam to the sample surface, but when the sample translation rate was too rapid, this coupling did not occur and an injected layer could not be formed. While having no effect on the mounding, increasing the laser power increased the penetration depth and, hence, the thickness because a larger volume of the surface was melted. Since the same quantity of powder was fed into a progressively larger volume of melt, the carbide volume fraction decreased. Increasing the powder feed rate had no effect on penetration depth, but increased the mounding and, hence, the thickness because more and more particulate material displaced the fixed volume of melt. This also increased the carbide volume fraction, but to a limit of about 0.6. Beyond this limit, the melt just dissolved the excess carbide. Although the powder feed rate could be varied to obtain different volume fractions of the hard phase, typically feed rates of about 40-50 mm^3 sec^{-1} were employed to give a consistent volume fraction of about 0.5.

3. STRUCTURAL MODIFICATION

As shown in Figure 2, the major surface modification is in the form of a particulate composite. The matrix in the injected layer is structurally continuous with the substrate. This gives the process a couple of unique advantages. One is strong metallurgical bonding throughout the surface layer and the other continuity of properties at the layer/substrate interface. This helps in preventing delamination and in retaining substrate properties.

Ideally, the particle injected surface should consist of hard particles surrounded by a metal matrix having the same composition and microstructure as the base metal. Such a structure was obtained in aluminum alloys that were injected with TiC[10]. In high melting alloys

like those based on Fe, Ni and Ti, the melt temperatures are high and partial dissolution of the carbide particles into the melt occurs. As a result, several resolidification products form from the carbide enriched melt. In addition, depending upon the base metal and the solidification rates, other structural modifications occur. For example, transformation products such as martensite form in tool steels, fine grain structures in aluminum bronze, supersaturated solid solutions and precipitation reaction products in stainless steels[11].

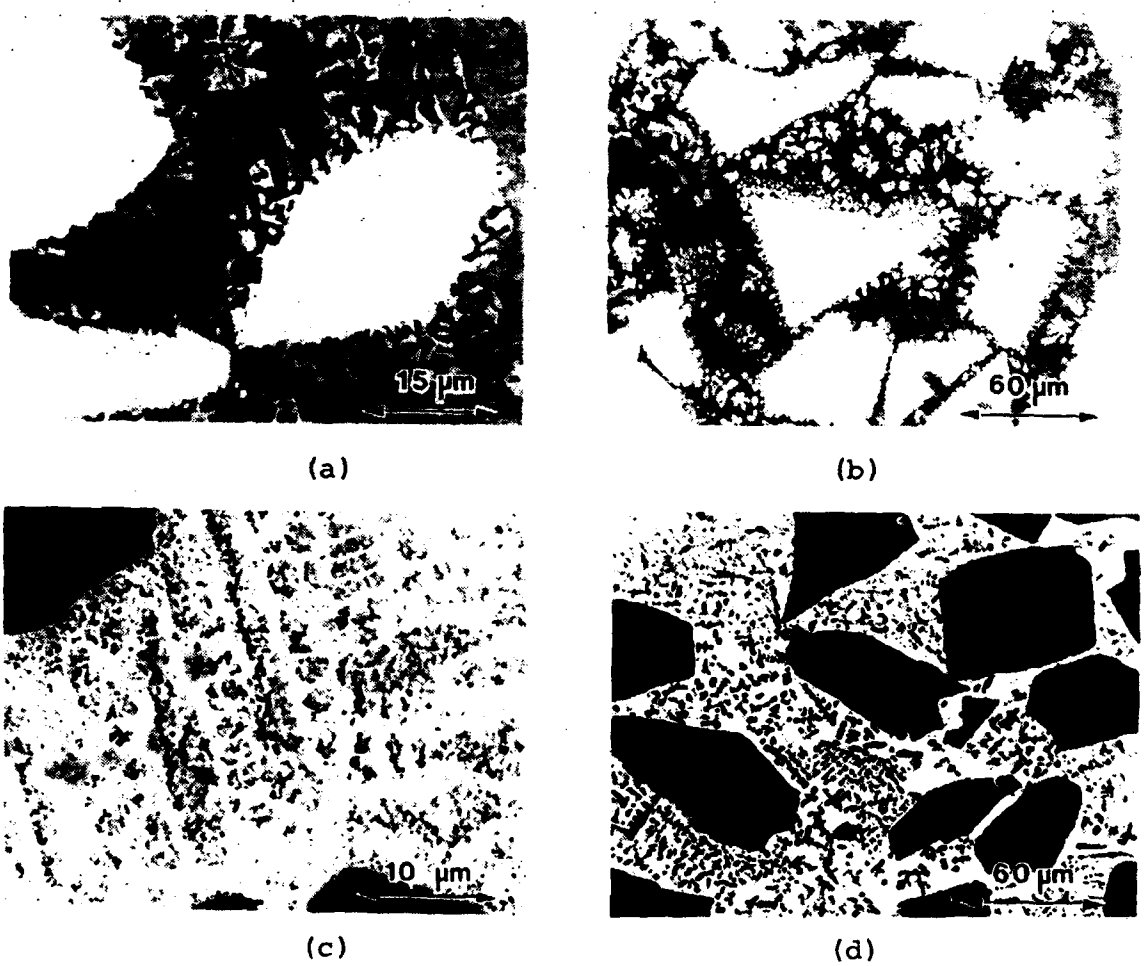


Figure 3. SEM micrographs of microstructures in particle injected Inconel 625. a) WC injected, eutectic carbides. b) WC injected, resolidified carbides. c) TiC injected, eutectic carbides. d) TiC injected, resolidified carbides.

The metal matrix is cellular, as in Ti-6Al-4V, or dendritic, as in Inconel 625[12]. Within the metal matrix are found eutectic phases and resolidified carbides, the products of carbide dissolution. Examples of microstructures obtained in WC and TiC injected Inconel 625 alloy samples appear in Figure 3. The eutectic phases occur in the inter-dendritic regions of the Ni-rich dendrites and have been identified to be complex carbides[13]. Eutectic carbides have an

irregular or script-type morphology as in the WC injected micrograph shown in Figure 3(a), or a lamellar morphology as in the TiC injected micrograph shown in Figure 3(b). A second eutectic carbide having a lamellar morphology was also identified in the WC injected sample[13]. Eutectic carbides predominate the microstructure where the dissolution kinetics are less severe. In the lower portion of the melt pool, the melt is conduction cooled rapidly allowing for modest dissolution. In the upper portion of the melt pool which is superheated, the dissolution rate is high and resolidified carbides predominate the microstructure. While the eutectic carbides are the final solidification products as the solute-enriched inter-dendritic liquid freezes, resolidified carbides are free dendrites that form from the melt before the melt begins to solidify. Resolidified carbides have no orientation relationship with the metal matrix. They grow with the preferred crystallographic orientation of the carbide from which they are derived. Hence, in the WC injected micrograph shown in Figure 3(c), the resolidified carbides appear as isolated, equiaxed dendrites demonstrating an apparent relationship to the hexagonal WC crystal. In the TiC injected micrograph shown in Figure 3(d), the resolidified carbides appear as a network of dendrites oriented in the <100> direction demonstrating an apparent relationship to the cubic TiC crystal.

In addition to the appearance of the dissolution products, modifications in the injected carbide morphology occur. Before they interact with the melt, the ball-milled carbide particles are angular and smooth. Where the dissolution rates are low, the WC particles appear smooth with only modest rounding and are decorated with the eutectic carbides as shown in Figures 3(a). The TiC surface is smooth and slightly rounded as shown in Figure 3(c). Where the dissolution rates are high, the WC particles appear perturbed or scalloped as shown in Figure 3(b). Perturbations were present to a very small degree in TiC as shown in Figure 3(d). Whether smooth or perturbed, that a strong metallurgical bond exists between the injected carbide particles and the metal matrix is evident from the micrographs in Figure 3. This is not surprising because both WC and TiC are wetted easily by most liquid metals. The strong metallurgical bond is important because it will determine the hardness and wearability of the particle injected surface. Both the eutectic and the resolidified carbides are heavily alloyed, but partition of the alloying elements from the base metal is selective. In Inconel 625, depending upon their nature, the resolidification products were selectively alloyed by Cr, Mo and Nb. The injected particle surface is also alloyed and has a composition similar to that of the resolidified carbides[9].

Eutectic and resolidified carbides were also observed in WC and TiC injected Ti-6Al-4V alloy samples[9,12]. With the exception of the resolidified carbides in Ti-6Al-4V/TiC, the morphologies of the dissolution products in Ti-6Al-4V were different from those in Inconel 625[12]. Comparing particle morphologies in Figures 3(b) and 3(d), it is evident that WC particles dissolve to a greater extent than TiC particles. This is because at high temperatures, TiC is thermodynamically more stable than WC[14].

The implications of these matrix microstructural modifications are several. Not only would they influence surface properties such as hardness, friction and wear, they would also affect inherent material properties such as corrosion and toughness. In practice, the processing conditions and particulate material are selected for maximum gain in tribological properties with minimum loss of base metal properties.

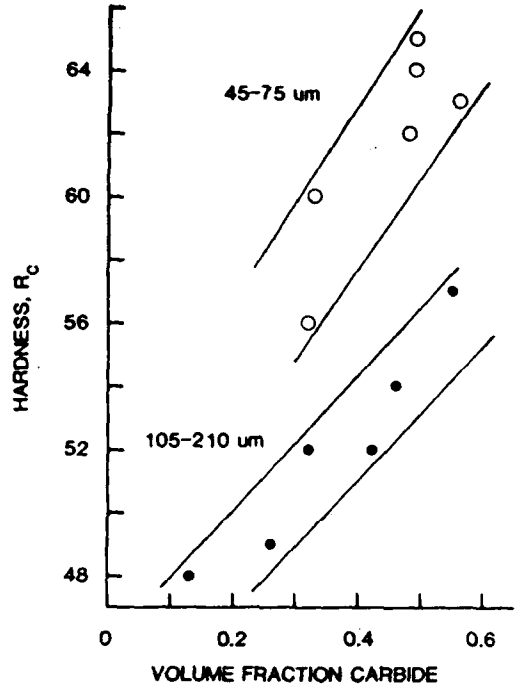


Figure 4. Relationship between surface hardness and carbide volume fraction for Ti-6Al-4V/TiC.

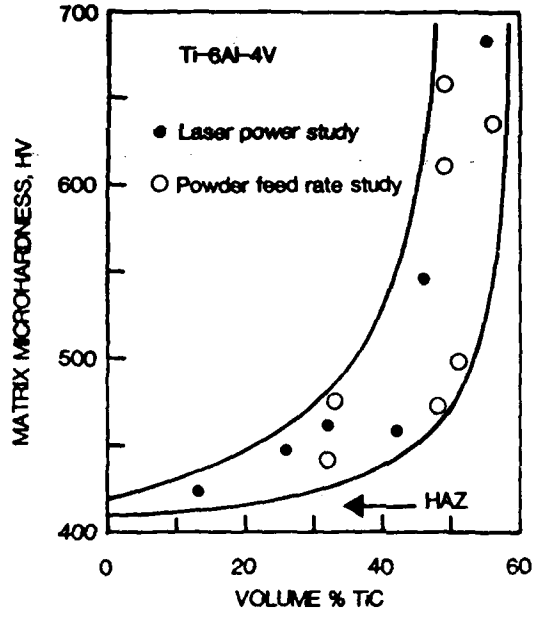


Figure 5. Relationship between matrix microhardness and volume % carbide for Ti-6Al-4V/TiC.

4. HARDENING BY PARTICLE INJECTION

One of the goals of laser melt/particle injection processing was to harden metals. To study the hardening of particulate composites, one of the variables investigated was the volume fraction of the carbide phase. It was found that carbide volume fraction influenced not only the hardness of the composite layer, but also that of the inter-particle matrix[9]. Surface hardness has an approximate linear dependence on the carbide volume fraction. This was demonstrated for TiC injected Ti-6Al-4V alloy samples as shown in Figure 4. For these studies, an indentation load of 15 N was used. Since the indentation intercepted only a few carbide particles, we see a scatter in the data as well as a particle size dependence. For the coarser particles, the inter-particle spacing is larger and fewer particles are intercepted by the indentor, effectively giving a lower value. To intercept more particles, a larger load would be required, but then the hardness

reading would be influenced erroneously by the substrate below the injected layer. In this alloy, the hardness of the base metal was 35 HRC which, with only 0.15-0.20 vol. fraction of carbide, was increased to 48 HRC. The maximum volume fraction of carbide injected into the alloy was 0.55% which gave a hardness of about 60 HRC. It appeared that with only modest volume fractions of the carbide phase, a significant increase in hardness can be achieved.

Increasing the carbide volume also increased the matrix microhardness. This trend was seen in TiC injected Ti-6Al-4V and is shown in Figure 5. The trend is a rapidly increasing one, especially in the high volume % range. The increase in matrix microhardness is due to the presence of increasing quantities of resolidification products. As larger volumes of carbide particles are injected into the melt, the carbide surface area in contact with a finite volume of melt increases, resulting in increased carbide dissolution. Also, at higher carbide volume feed rates, it was observed during processing that the melt temperatures were higher which would promote more dissolution. In fact, instead of increasing the carbide volume fraction continuously to higher values, increasing the powder feed rate only increased the dissolution rate and, thereby, the amount of resolidification products.

Table I. Hardness Values in Several Alloys as a Result of Particle Injection.

Alloy	Hardness (HR)			Microhardness (HV)			
	Base	Injected	Ratio*	Base	HAZ	Matrix	Ratio#
304 SS/TiC	B78	C37	2.4	152	196	219	1.4
4340 Tool/TiC	C27	C62	2.6	430	950	1061	2.5
5052 Al/TiC	B50	B61	1.2	78	70	71	0.9
Al bronze/TiC	C25	C27	1.1	225	239	287	1.3
Inconel 625/TiC	B93	C46	2.2	300	302	460	1.5
Inconel 625/WC	B93	C53	2.7	282	289	612	2.2
Ti-6Al-4V/TiC	C35	C64	2.3	348	414	626	1.8
Ti-6Al-4V/WC	C36	C42	1.2	360	405	430	1.2

*Injected to base after converting to DPH.
#Matrix to base.

For different alloy systems, the degree of hardening is different. The Rockwell hardness and the relative increase in hardness for several alloys are given in Table I. Also given in the table are the matrix microhardness values and their relative increase over that of the base metal. The microhardness was measured on the Vicker's scale using a 100 g load. Part of the data is taken from Ref. 11. In all cases the particle volume was about 40-50 % so the effect of carbide volume fraction on the hardness was minimized. Particle injection increased the surface hardness by as little as 1.1 times in Al bronze/TiC to as much as 2.7 times in Inconel 625/WC. The major hardening mechanism is the inhibition of plastic flow during

deformation by the injected phase. It was also discovered that deformation stresses in WC particles were relieved by the formation of deformation bands in the carbide phase[12]. In some alloys, other hardening mechanisms associated with microstructural changes also played a role. Depending upon the base metal, solid solution strengthening, precipitation hardening, transformation hardening and hardening due to microstructural refinement are some of these hardening mechanisms as explained below.

As shown in Table I, the increase in matrix microhardness over that of the base metal can be as little as 1.2 times in Ti-6Al-4V/WC to as much as 2.5 times in 4340 tool steel/TiC. In the case of 5052 Al/TiC, slight softening occurred both in the matrix and the HAZ probably due to the dissolution of precipitates which normally harden the alloy. In 304 stainless steel, 4340 tool steel, Inconel 625 and Ti-6Al-4V, the presence of carbide dissolution products such as resolidified carbides enhanced matrix microhardness probably by a dispersion hardening mechanism. In Al bronze, no dissolution products were found and structural refinement was the main reason for the increased matrix microhardness. Microstructural refinement and solid solution strengthening further contributed to the microhardening in Ti-6Al-4V, stainless steel and tool steel alloy samples. Additionally, in the tool steel sample, transformation hardening due to martensite resulted in a significantly harder matrix as well as HAZ. In most other alloys, the HAZ shows a slightly higher microhardness than the base metal and this is mostly due to structural refinement. In Inconel 625, the base metal and the HAZ have nearly the same microhardness. The effective absence of a HAZ in this alloy demonstrates the high temperature stability of the superalloy microstructure.

A comparison of hardening in Inconel 625 and Ti-6Al-4V alloys injected with TiC and WC revealed contrasting trends. When injected with WC, Inconel 625 is harder both on the macroscopic as well as on the microscopic scale than when injected with TiC. The opposite is true in Ti-6Al-4V. It seems that the dissolution products in Inconel 625/WC are more effective in hardening the matrix than those in Inconel 625/TiC. On the other hand, the dissolution products in Ti-6Al-4V/TiC appear to be more effective in hardening the matrix than those in Ti-6Al-4V/WC. The effect of carbide type on matrix microhardening is illustrated in Figure 6 for Inconel 625. In this figure, matrix microhardness relative to that of the substrate is plotted as a function of injected layer thickness. It is apparent that WC injection produces more hardening than TiC injection. There is also a particle size effect. Particles with a finer size distribution dissolve to a greater extent than particles with a coarser size distribution thereby hardening the matrix to a greater extent. Another trend in the microhardness is the increasing trend with layer thickness. This is because in the upper portions of the injected layer resolidified carbides predominate and harden the matrix to a greater degree than the eutectic carbides that predominate in the lower portions of the injected layer. These differences in the hardening trends will dictate the choice of the type and size distribution of the particulate material. Determining the degree of

hardening due to microstructural modification from the various solidification reactions is important because it will influence the friction and wear behavior of the surface composite.

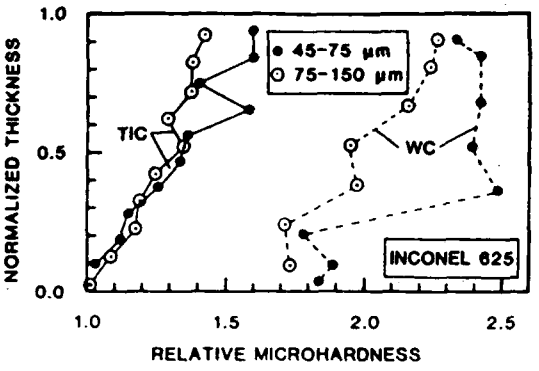


Figure 6. Matrix microhardness relative to base metal as a function of the thickness of the injected layer.

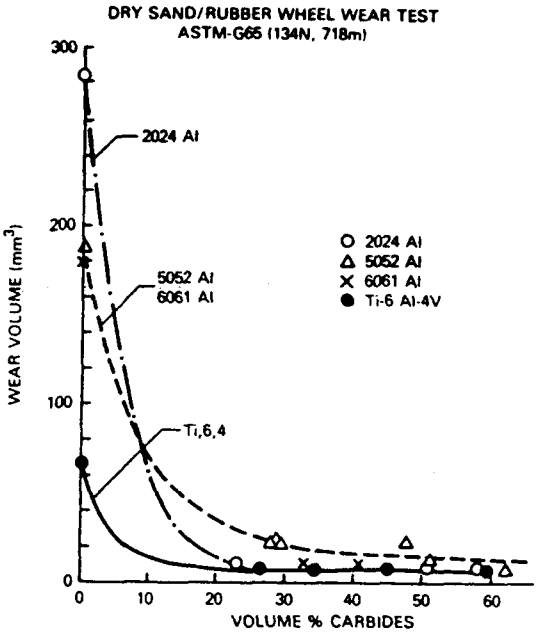


Figure 7. Wear volume as a function of volume % carbide after dry sand/rubber wheel testing[15].

5. FRICTION AND WEAR BEHAVIOR OF PARTICLE INJECTED SURFACES

To evaluate the response of particle injected surfaces to wear, standard dry sand/rubber wheel erosion wear tests were performed on Ti-6Al-4V and several Al alloys injected with TiC particles[15]. The samples were ground down to produce flat wear surfaces. Each test involved a sliding distance of 718 m and a contact load of 134 N. After each test the wear volume was measured. In Figure 7, the wear volume is plotted as a function of the vol. % carbide. With as little as 25 to 30 vol. % of carbide present, a significant reduction in wear volume occurred. The improvement in erosion wear resistance was as much as 38 times for 2024 Al with 58 vol. % TiC to 14 times for Ti-6Al-4V with 60 vol. % TiC. The wear rates were found to approach those of cast commercial wear resistant alloys tested under similar conditions[15].

An examination of the injected surface in the SEM after erosion wear testing revealed that the carbide particles had become rounded, but most of the erosion was confined to the inter-particle matrix. Also, matrix erosion was not sufficient to cause particle pullout, nor did the wear stress cause any particle fracture[15]. Similar results were reported when the same alloys were abrasive wear tested with fine diamond particles[16]. The abrasive wear resistance of Al alloys improved by as much as a factor of 30 in samples containing TiC, while for the Ti-6Al-4V containing TiC, the largest improvement was by a factor of about 4. The results were less dramatic with the Ti alloy

because even in the untreated form Ti exhibits a relatively high resistance to abrasive wear.

Another test of improved wear behavior is the dynamic coefficient of friction (u_k) test. Before the measurement, the sample surface was ground smooth and polished up to 3 um diamond. Both the sample surface and a 1.27 cm diameter 52100 steel slider were thoroughly cleaned. The tests were made in an unlubricated condition with a 9.8 N load and a slider velocity of 0.01 cm s^{-1}. For Ti-6Al-4V/TiC, after the first slide, u_k decreased from a value of 0.4 to 0.2 with only 20 vol. % of carbide present in the injected surface[15]. With 50 vol. % carbide, u_k reduced to 0.16. With repeated cycles in the same track, u_k remained 0.4 for the untreated sample, but increased to 0.3 for the 20 vol. % sample and to 0.23 for the 50 vol. % sample[15].

The low u_k value after the initial cycle is what one would expect for a steel ball in contact with only the carbide phase. This observation suggests that in the initial phase of the measurement there is very little contact between the slider and the metal matrix, especially since polishing leaves the carbide particles standing in relief above the metal matrix. In effect, the slider rides along the top of the protruding carbides making only intermittent contact with the matrix. This accounts for the low u_k value during the initial slides in all samples. In higher carbide content samples, the carbide particles are more densely packed and slider/matrix contact is further minimized, and a still lower u_k results. Some of the intermittent metal-to-metal contacts express themselves as an increase in u_k. As the number of slides increases, the probability of slider/matrix contact increases, thereby increasing u_k. In the untreated form, the wear scars produced by the slider were deeper and wider compared to those in the injected samples. In the injected sample, the wear scar was confined to the matrix, the carbides themselves showing little damage.

Frictional damage of the metal matrix and the u_k of the injected layer would depend upon the microstructural and microhardness characteristics of the matrix. This aspect was investigated for Inconel 625 alloy samples injected with WC and TiC[14]. Both the matrix microstructure and microhardness vary widely in this alloy depending upon the type of injected carbide. In this experiment, besides measuring u_k as a function of the number of passes, the wear scars were examined in the SEM and evaluated for the extent of wear and the nature and composition of the wear debris. In the untreated condition, u_k increased from 0.55 to 0.72 after 15 slider passes. After the same number of passes, u_k increased gradually from 0.15 to 0.33 for a WC injected sample and somewhat rapidly from 0.15 to 0.41 for a TiC injected sample. These increasing trends for u_k are similar to those found in Ti-6Al-4V injected with TiC discussed earlier.

The increase in u_k as a function of the number of slides was due to the progressive deposition of wear debris on the sample surface[14]. In the WC injected samples, SEM examination showed mild abrasion of the hard metal matrix, but, along the leading edges of the carbide particles, wear debris was found. Microprobe analysis showed that the

wear debris was made up of mostly slider material with only a trace of matrix material. In the TiC injected samples, SEM examination revealed a heavily damaged matrix and wear debris that was identified as a mixture of slider and matrix material. In this case, the slider appeared to have plowed through the soft metal even in the presence of trace amounts of resolidified carbides such as the ones shown in Figure 3(d). Having no orientation relationship with the metal matrix, the resolidified carbides were just pushed aside as the matrix abraded under the stress of the slider. Both the WC and the TiC injected sample microstructures contained eutectic carbides. But the irregular eutectic in the WC injected sample, shown in Figure 3(a), made the matrix harder than the lamellar eutectic in the TiC injected sample, shown in Figure 3(c). These microstructure-microhardness observations suggest that the presence of eutectic carbides and the resulting degree of hardening appear to be more important in determining frictional wear resistance than the presence of resolidified carbides.

6. CONCLUSIONS

1. In situ surface composites of particulate material in a matrix made up of the parent metal can be formed by the laser melt/particle injection process.

2. When the injected particles are metal carbides, the injected surface becomes hard and wear resistant. Since the metal matrix is of a composition similar to the substrate, the modified surface retains many of the properties of the base material such as corrosion resistance. Also, since the matrix is structurally continuous with the substrate, delamination and spalling do not occur.

3. Laser beam parameters and particle injection rates can be selected to achieve the desired injected layer dimensions such as penetration depth, mounding and thickness and the desired carbide volume fraction which is usually limited to about 0.6.

4. Although not desired, partial dissolution of the carbide phase into the laser melt does occur and the dissolution products appear as dendritic resolidified carbides and as eutectic carbides having various morphologies. The types of resolidification products depend upon the substrate material, the type and size distribution of the carbide and the location in the melt pool.

5. Injected layer surface hardness increases linearly with increasing carbide volume fraction. Resistance to plastic flow by the dispersed particles during indentation deformation is the principal mechanism for the increase in hardness. But additional hardening mechanisms such as dispersion hardening by the resolidification products and transformation hardening also play a role. When carbide dissolution products are present, the matrix microhardness shows a rapidly increasing trend with increasing carbide volume fraction.

6. Erosion and frictional wear decrease rapidly with increasing carbide volumes in the injected layer. Resistance to erosive and

abrasive wear by the hard carbide particles contributes largely to enhancing the wear resistance of particle injected samples. Most materials have a low coefficient of friction in sliding contact with carbides. This and the fact that the matrix can be hardened by dissolution reactions reduces friction wear in particle injected samples.

7. ACKNOWLEDGEMENT

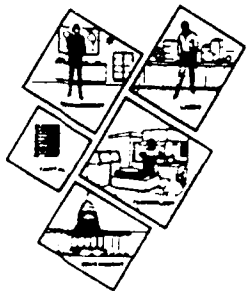
The author would like to thank Dr. Jack Ayers for his insights into laser-material processing and Mr. Dick Stegman and Mr. Bob Beigel for their assistance in doing the work.

8. REFERENCES

1. F.D. Seaman and D.S. Gnanamuthu, Metal Progress, 67-74 (Aug. 1975).
2. P.G. Moore, in Laser Applications in Materials Processing, J.F. Ready, ed., Proc. SPIE, 120-125 (1980).
3. R. Padmanabhan, in Laser Materials Processing, ICALEO'86, C.M. Banas and G.L. Whitney, eds., LIA, 185-192 (1987).
4. J. Singh and J. Mazumder, Acta. Metall., 35(8), 1995-2003 (1987).
5. J.D. Ayers, R.J. Schaefer and W.P. Robey, J Metals, 33(8), 19-23 (1981).
6. K.P. Cooper and J.D. Ayers, Surface Eng., 1(4), 263-272 (1985).
7. K.P. Cooper, R.E. Beigel and P. Slebodnick, in Laser Materials Processing, ICALEO'86, C.M. Banas and G.L. Whitney, eds., LIA, 169-176 (1987).
8. G.A. Saltzman, Metal Progress, 25-50 (Feb. 1986).
9. K.P. Cooper, in Surface Modifications and Coatings, R.D. Sisson, Jr., ed., ASM, 409-420 (1986).
10. J.D. Ayers, Thin Solid Films, 84, 323-331 (1981).
11. J.D. Ayers, in Lasers in Metallurgy, K. Mukherjee and J. Mazumder, eds., AIME, 115-125 (1981).
12. K.P. Cooper and J.D. Ayers, in the Proc. of the 1988 Conf. on Laser Surface Modification, AWS, in press.
13. K.P. Cooper and A. Singh, to be published.
14. K.P. Cooper, J. Vac. Sci. Technol.A, 4(6), 2857-2861 (1986).
15. J.D. Ayers, Wear, 97, 249-266 (1984).
16. J.D. Ayers and R.N. Bolster, Wear, 93, 193-205 (1984).

Proceedings from the
1988 Conference on

Laser Surface Modification



Cosponsored by the
American Welding Society
and
The Manufacturing Productivity Center

April 14-15, 1988
New Orleans, Louisiana

SURFACE MODIFICATION BY THE LASER MELT/PARTICLE INJECTION PROCESS

Khershed P. Cooper, Geo-Centers, Inc., 10903 Indian Head Highway, Suite 502, Fort Washington, MD 20744.

Jack D. Ayers, Naval Research Laboratory, Code 6320, Physical Metallurgy Branch, Washington, D.C. 20375.

ABSTRACT

Metal surfaces are hardened and made wear resistant by pneumatically injecting carbide particles into a melt pool formed by a high energy, oscillating CO_2 laser beam. The injected layer is a metal matrix/carbide particulate composite which is structurally continuous with the substrate. Because the metal matrix has a composition and properties similar to the substrate, particle injected layers, while acquiring superior tribological properties, retain much of the corrosion resistance and toughness of the original material. Laser parameters and powder feeding conditions can be chosen to achieve the desired carbide volume fraction (limited to about 0.6) and the selected injected layer dimensions. The major modification of surface properties is due to the presence of the carbide phase in the metal surface. Additional changes result from the partial dissolution of the carbide particles into the molten metal matrix. The nature of the starting materials and the processing and thermal conditions determine the extent of the dissolution process. Resolidified carbides and solute-rich eutectic regions are some of the microstructural modifications observed in the metal matrix. These microstructures promote microhardening which reduces the coefficient of sliding friction, and may, together with the undissolved injected carbide, affect the tribological behavior.

INTRODUCTION

Surface modification and coating of materials is done to enhance resistance to wear, friction, corrosion and high temperature oxidation. Of the various surface modification technologies available, laser surface modification is gaining recognition for its unique advantages and capabilities (1). Among other advantages the rapid heating and cooling rates brought on by the high energy density and short interaction time makes the laser stand apart from other modes of heat input such as flame spray and weld overlay. Rapid cooling rates in the melt formed by the laser beam can be of the order of 10^4-10^8 ^oC sec^{-1} depending upon the melt depth and the self-quenching ability of the substrate. Under these solidification conditions, novel and refined microstructures having useful properties can form in the melted layer.

If alloying additions are made into the melt pool, the surface chemistry of the material can be altered. For example, the addition of

chromium to low carbon steels can form a stainless steel type of a surface that is resistant to corrosion (2). Alternatively, the addition of carbide forming alloying elements, such as a Cr-Mn-C mixture, can form a surface having dispersed carbides which makes the material resistant to wear (3). Materials having totally different chemistry and properties from that of the substrate can also be fused as claddings on the sample surface. While complete alloying or dilution is sought with laser alloying, minimum dilution of the overlayer is sought with laser cladding. Minimum dilution is sought in order to preserve the desired properties of the clad material. To enhance wear resistance, hardfacing alloys are clad onto softer, less wear resistant metals. For example, cladding of a Ni-Cr-WC mixture was done to improve the wear resistance of steels (4). A problem with laser cladding is the possible loss of the original base material properties such as corrosion.

The laser melt/particle injection process was developed to improve properties such as wear resistance while retaining properties such as corrosion resistance (5). It provides a means to improve the wear resistance of alloys that are difficult to harden by conventional means, for example, aluminum and copper alloys. It also strives to harden alloys that cannot be easily hardfaced due to the formation of brittle intermetallics at the interface, for example, titanium alloys. Laser melt/particle injection is neither alloying or cladding. In this process hard particles such as carbides are impregnated into the metal surface to form a particulate/metal matrix composite surface layer (5,6). The wear resistance is derived from the hard constituent of the composite, normally a metal carbide, while the metal matrix, which is of a composition similar to the substrate and which is structurally continuous with the substrate, retains much of the properties of the parent metal such as corrosion resistance and toughness.

PROCEDURES

A shallow melt pass was made on the surface of a sample by translating it through a laser beam. High melting point particles were pneumatically injected into the melt pool to form the hardened surfaces. A high power continuous wave, CO_2 laser beam was used in the unstable resonator mode. The slightly defocussed laser beam would, if not oscillated, melt a shallow layer 2 to 3 mm in diameter. By oscillating one of the reflecting mirrors, the laser beam was shaped into a line energy source so that melt passes of different widths could be produced. In order to inject the particles over the wide melt area, a specially designed slotted nozzle was used. The nozzle was placed at a 45 to 60^{0} angle, 1 to 2 cm away from the sample surface. Powder particles were blown into the melt pool at a rate of 0.2 to 0.5 cm^3 sec^{-1} by helium carrier gas. A schematic diagram of the laser melt/particle injection process is shown in figure 1. The laser was used at power levels of 8 to 10 kW, and sample translation rates were varied from 0.25 to 1.5 cm sec^{-1} depending upon the width of the melt pass.

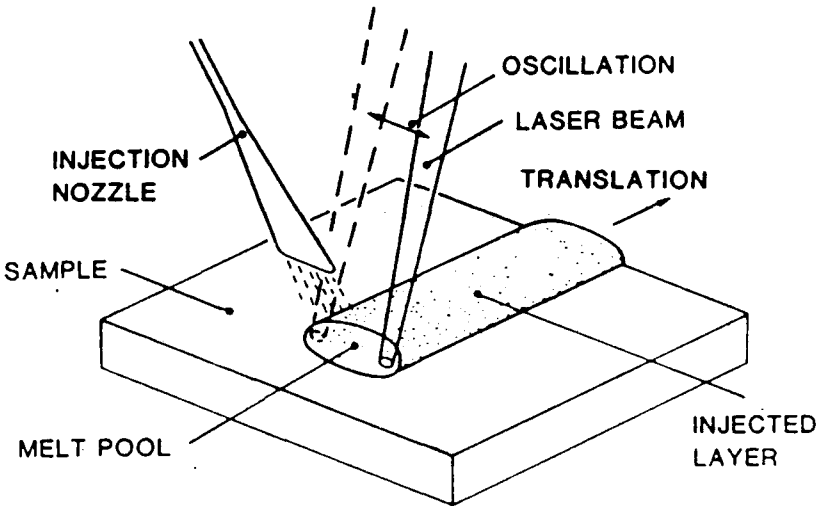


Figure 1. Schematic diagram of the laser melt/particle injection process.

Several alloys, especially low density/high strength aluminum and titanium alloys, have been processed by this technique and evaluated for wear behavior (7,8). Most of the work reported herein was done on Ti-6Al-4V and Inconel 625 alloy samples injected with WC or TiC. The titanium alloy has high strength, but poor galling resistance, while the nickel base superalloy has high corrosion resistance and toughness, and limited wear resistance. Carbide particle sizes varied from 45 to 150 microns. Both carbides are commonly used in hardfacing operations and are inert to corrosive environments.

The choice of the processing parameters depended upon the desired characteristics of the injected layer. Thickness, width and carbide volume fraction were some of the injected layer characteristics considered when choosing laser power, sample translation rate and powder feed rate. Material property differences also played a part in the choice of processing conditions. For example, density differences between the particulate material and the substrate melt governed particle injection conditions, lighter particles needing greater momentum than heavier particles. In an earlier study (9), the effects of processing parameters on the injected layer dimensions, the carbide volume and the hardness were investigated for Ti-6Al-4V alloy samples injected with TiC particles. That study showed, among other results, that the carbide volume fraction in the injected layer was limited to 0.6.

Particle injected samples were examined using optical microscopy and scanning electron microscopy. Injected samples were polished to one micron diamond and etched to reveal the microstructure. The various microconstituents were identified in the SEM, and electron

microprobe analysis was carried out to determine the compositional variations in the modified surface layer. Further analysis of the injected surface involved determining the macrohardness of the composite surface and the microhardness of the inter-particle matrix. The superficial macrohardness was measured with a Rockwell indentor using a 15 kg load, and the microhardness was measured on a Vickers tester with a 100 g load. Kinetic coefficient of friction measurements were made between a 1.27 cm diameter 52100 hard steel ball and the polished sample surface. The test is described elsewhere (10). The damaged surface was evaluated for the type and extent of wear using the SEM.

RESULTS AND DISCUSSION

Surface modification by the laser melt/particle injection process produces a unique surface structure. The structure is an in situ particulate/metal matrix composite. In between the particles there are varying degrees of microstructural modifications, each dependent upon the nature of the starting materials and upon the processing conditions. Accompanying these microstructural modifications are improvements in hardness and wear resistance, which are the main goals of the particle injection laser surface modification technique.

Microstructures of Particle Injected Surfaces.

The composite nature of a particle injected layer is evident from the SEM micrograph of figure 2. This micrograph is of an Inconel 625 alloy sample that was injected with WC particles. The WC particles appear as light grains surrounded by the greyish inconel metal matrix. The carbide particles appear uniformly distributed throughout the injected layer and occupy about 50% of the total volume. There is no volume fraction gradient between the top and bottom portions of the melt pool. The injected layer is dense showing very little porosity.

The melt interface has a slightly sinusoidal shape brought on by the oscillating motion of the laser beam. Since a portion of the melt is displaced by the injected particles, the excess material shows up as the mounding above the original sample surface. The mounded portion of the injected layer is nearly flat, but it is rough due to the presence of projecting carbide particles. Before the particle injected sample is used in a wear test, the roughness is removed by grinding. The injected layer appears uniformly thick and almost rectangular in cross-section. The layer thickness in figure 2 varies from 1.2 to 1.5 mm. The width of the injected layer is about 1 cm, but by suitably adjusting the oscillation amplitude of the laser beam, injected layer widths from 0.4 to 2.0 cm were achieved.

Similar cross-sectional structures were observed in TiC injected Inconel 625 alloy samples and in WC and TiC injected Ti-6Al-4V alloy samples. Regardless of the starting materials, the carbide particles were distributed uniformly throughout the cross-section. It was

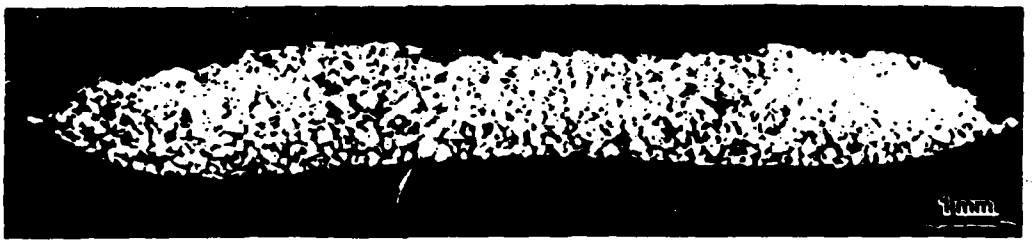


Figure 2. SEM micrograph showing the cross-sectional macrostructure of Inconel 625 injected with WC particles.

difficult to drive the low density TiC particles into the higher density inconel melt pool and form layers of uniform thickness. Precise processing conditions were necessary to achieve the desired results. For the Ti alloy, TiC injection appeared to be more suitable, because WC injection caused gas porosity near the melt interface. The porosity appeared to have resulted from reactions between the carbide and metal which produced a gaseous phase.

Ideally, particle injected surfaces should consist of the hard particles surrounded by a metal matrix having the same chemistry and microstructure as the base metal. A structure close to this ideal was obtained in aluminum alloys (11). In high melting point alloys such as those based on Fe, Ni and Ti, partial dissolution of the carbide particles into the melt occured. As a result, a series of resolidification products formed from the carbide enriched melt. In addition, the rapid quenching of the melt caused additional structural changes. Ayers (12) identified several solidification reactions when studying particle injection of tool steels, stainless steels, superalloys, and titanium, copper, and aluminum alloys. Fine grain structures, supersaturated solid solutions, phase transformation products, precipitates and dispersoids were some of the microstructural constituents identified in the various alloys.

A close-up view of the injected layer/substrate interface infigure 2 is given in the optical micrograph of figure 3. The equiaxed grain structure of the annealed Inconel 625 was unaffected outside the melt zone. Note the absence of any structural discontinuity at the melt interface due to a reaction product such as an intermetallic phase. Reaction products at the melt interface, when brittle, are known to render surface coatings unsuitable by making them prone to spalling and delamination. In between the WC particles, the melt solidified dendritically. The dendritic structure is fine-scaled, with a spacing of about 3 to 5 microns, demonstrating fairly rapid solidification rates as expected of self quenching processes.

It is in a sence fortuitous that the solidification rates at the laser melted interface are rapid for this allows minimal time for interaction between the carbide and the melt, and lessens the probability of compositional changes in the matrix. The matrix

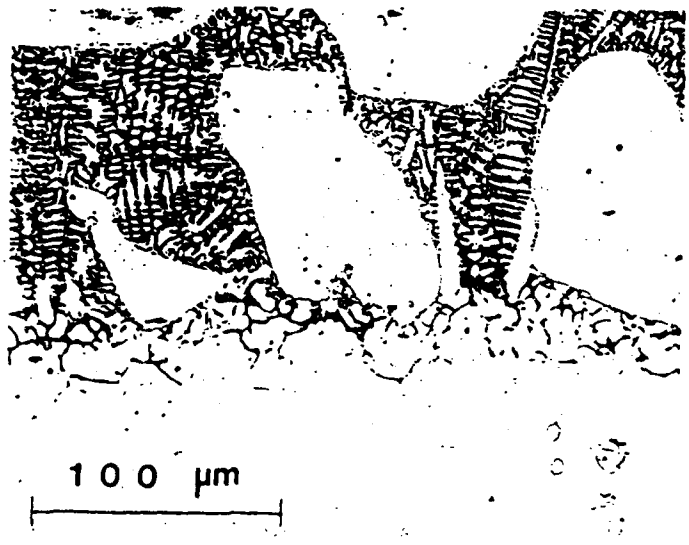


Figure 3. Optical micrograph showing the microstructural transition at the injected layer/substrate interface in a WC injected Inconel 625 alloy sample.

maintains its identity with the underlying substrate, both in chemistry and phase constituents. In the upper regions of the melt, the temperatures are high and the times at temperature are long, both of which promote more carbide dissolution and, with it, a significant deviation from the original composition and microstructure.

A variety of microstructures were observed in particle injected Inconel 625 and Ti-6Al-4V alloy samples, examples of which are given in figures 4-7. The microstructures were classified as those with solute-rich phases such as eutectics and those with resolidified carbides. When the degree of dissolution was modest, eutectic structures predominated in the matrix, and when the degree of dissolution was high, resolidified carbides predominated. While the solute-rich product phases occured throughout the injected layer, resolidified carbides occured mostly in the upper portions of the injected melt where the dissolution kinetics were rapid due to higher levels of superheating. Depending upon the base alloy and the type of carbide, the dissolution products assumed different morphologies and compositions. As shown in the SEM micrograph of figure 4(a), the eutectic phases in WC injected Inconel 625 appear as fine-scale lamellae surrounding the carbide particles and as irregular, script-type in other regions of the matrix. The WC surface is slightly perturbed and shows a reaction layer which formed during the resolidification process. The eutectic phase in TiC injected Inconel 625 is mostly lamellar and needle-like as shown in figure 5(a). Although lightly alloyed, the TiC surface appears smooth with no perturbations indicating a very low level of regrowth during solidification of the molten matrix, and hence a limited degree of particle dissolution.

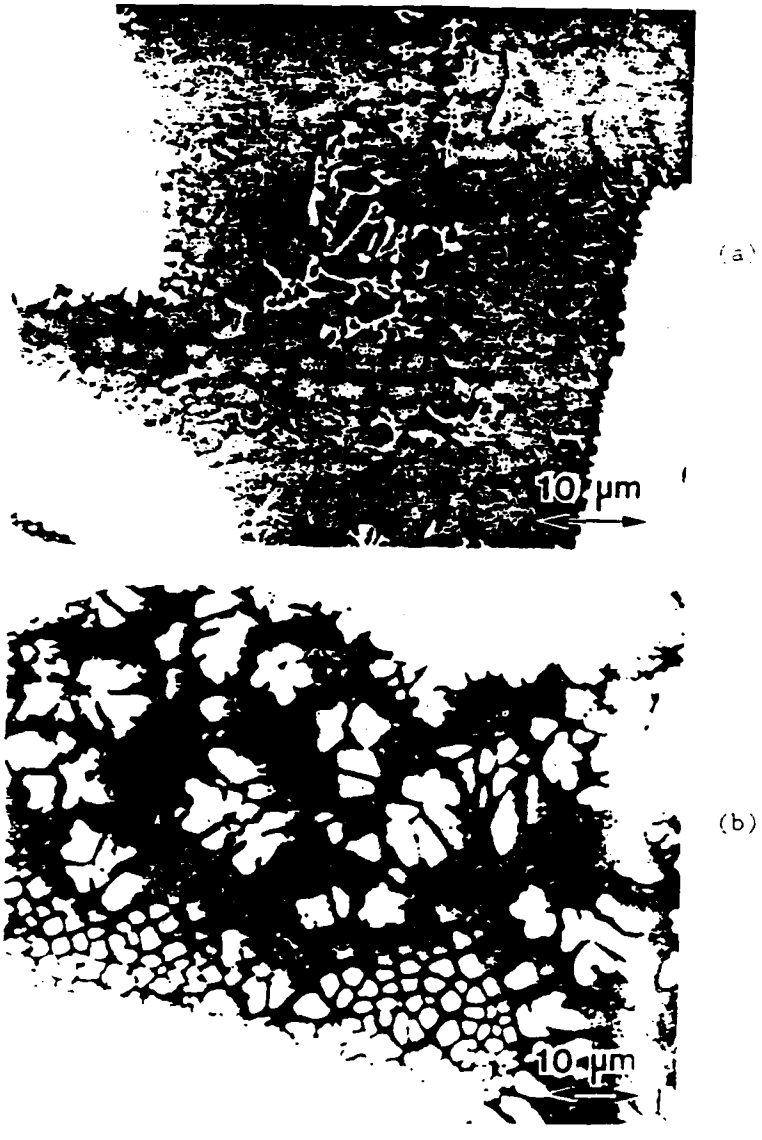
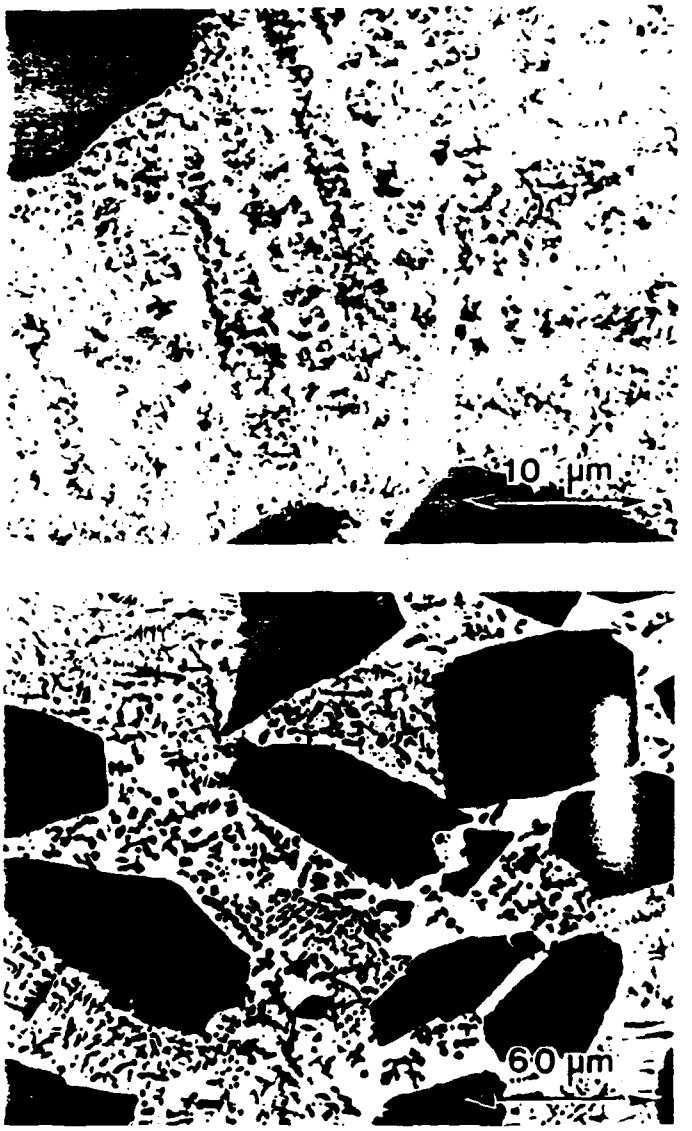


Figure 4. SEM micrographs showing dissolution products in a WC injected Inconel 625 sample. (a) Lamellar and script eutectic phases. (b) Equiaxed resolidified carbide dendrites.

The matrix assumes quite a different appearance when there is a greater degree of carbide dissolution. As shown in the SEM micrograph of figure 4(b), the resolidified carbides in WC injected Inconel 625 appear as "free-floating" equiaxed dendrites. These carbide dendrites are heavily alloyed, their metallic constituents being mostly Ni and Cr and have a composition similar to that of the surface of the injected carbide particles. The growth nuclei for these resolidified carbides probably originated from the partially dissolved injected particle.



(a)

(b)

Figure 5. SEM micrographs showing dissolution products in a TiC injected Inconel 625 sample. (a) Needle-like lamellar eutectic phase (b) Network of resolidified carbide dendrites.

surface. The highly perturbed fine-scale surface morphology and rounded shape of the injected WC particles demonstrate a high degree of dissolution into the melt. As shown in figure 5b, the resolidified carbides in TiC injected Inconel 625 appear as a network of dendrites. These carbides are also heavily alloyed, containing Ti and Ti among other elements. The injected carbide particle surface shows no perturbations, but is rounded thus revealing modest dissolution. It is possible that the origins of the resolidified carbides in TiC injected

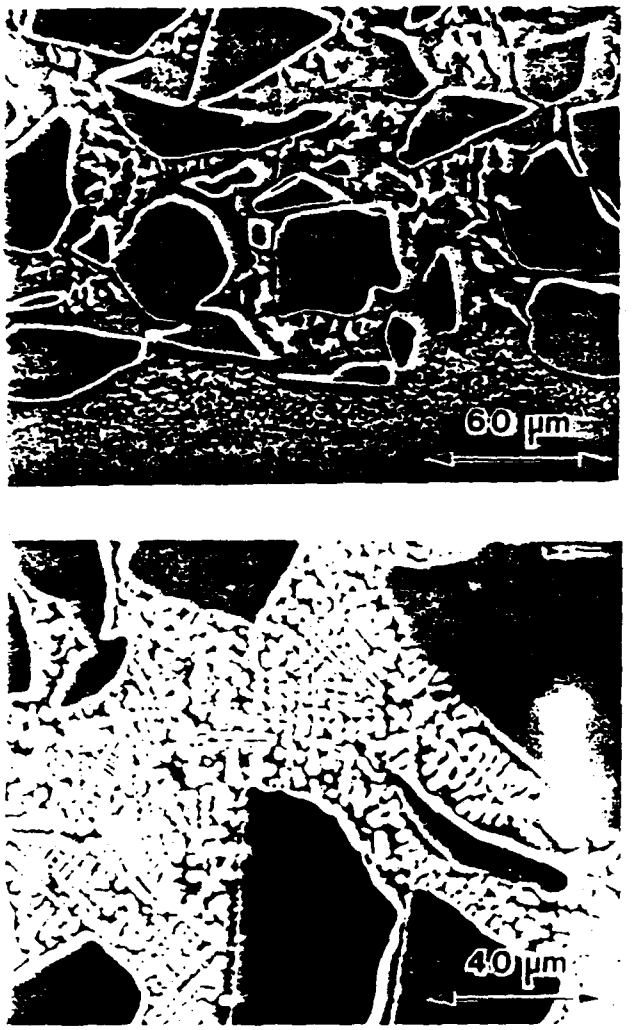


Figure 6. SEM micrographs showing dissolution products in a TiC injected Ti-6Al-4V sample. (a) Feathery inter-cellular solute-rich eutectic phase. (b) Dendritic network of resolidified carbides.

Inconel 625 were very fine injected particles that dissolved completely and provided growth nuclei for subsequent resolidification. This would explain the observation that [illegible] injected samples occurred only in segregated patches.

In particle injected Ti-6Al-4V, the solute-rich phase appears feathery as shown in the TiC injected sample of figure [illegible] granular as shown in the WC injected sample of figure [illegible]. These eutectic phases are most probably alloy carbides forming eutectics. Pure binary titanium easily forms a eutectic with carbon. The matrix in this alloy is made up of martensitic cells delineated by the solute-rich



Figure 7. SEM micrograph showing granular inter-cellular solute-rich eutectic phase in a WC injected Ti-6Al-4V sample.

phases. This martensitic structure is similar to that in the heat affected zone, except that it is on a finer scale. The TiC particles show few perturbations, but are somewhat rounded from modest dissolution. On the other hand, the WC particles appear severely rounded and show a highly alloyed and structurally complex reaction layer on the surface thus demonstrating a substantial level of dissolution. In TiC injected Ti-6Al-4V, the resolidified carbides appear as a network of dendrites as shown in the SEM micrograph of figure 6(b). A similarity with the dendritic morphology in figure 5(b) is apparent and a resolidification mechanism similar to that in the TiC injected Inconel 625 is possible. Resolidified carbides were not observed as separate "free-floating" products in the matrix of the WC injected sample even though the injected carbide morphology of figure 7 demonstrates that a high degree of dissolution had occured.

Resolidified carbides are the first solidification products, either nucleating on the injected carbide surface or independently in the carbide enriched liquid. These initial solidification reactions were identified by an examination of the microstructures which revealed that the resolidified carbides had no orientation relationship with the metal matrix. The next solidification reaction produces the bulk of the metal matrix. In Inconel 625, the metal matrix is predominantly nickel-rich dendrites or cells, while in Ti-6Al-4V, the solidified matrix structure is the precurser to the martensitic cells. Solute is rejected as this metallic phase grows and leads to the formation of the final solidification products, solute-rich eutectic phases that form in the inter-dendritic and inter-cellular regions of the matrix.

It should be noted that the micrographs of figures 4 to 7 are of samples that were injected with a nearly constant volume fraction of the carbide phase, about 0.5. This selection was made so that the

effect of carbide volume fraction on the dissolution kinetics could be neglected. Other factors do however affect the dissolution kinetics. From the microstructural evidence presented in figures 4 to 7, it is clear that WC dissolves to a greater extent than TiC. This is because WC is less stable thermodynamically than TiC. At 1500 ^{0}C, the free energy of formation of WC is -8.4 kcal mole^{-1} and that of TiC is -39.5 kcal mole^{-1}. Particle size and carbide volume fraction also play an important role in the dissolution kinetics. Finer carbide particles dissolve to a greater extent than coarser ones because they offer a greater surface area to volume ratio. Increasing the carbide volume fraction in the injected melt increases the dissolution rate because there is more net carbide surface area, the melt is at a higher temperature and the diffusional distances are effectively reduced. Thus a greater degree of microstructural modification ensues with the finer variety of carbides and with increasing carbide volume fraction.

The presence of solute enriched resolidification products implies that the metal matrix is depleted of essential alloying elements. For example, the resolidified carbides in Inconel 625 were found to be rich in chromium. Excessive partitioning of Cr from the Inconel 625 matrix may adversely affect its resistance to corrosion. It is therefore imperative that carbide dissolution be kept to a minimum. This can be achieved by lowering the carbide volume fraction or by using coarser particlesizes. These solutions are constrained by the requirements for achieving high hardness and improved wear resistance, requirements for which a large quantity of carbides are essential.

Hardening of Particle Injected Surfaces.

In Inconel 625 alloy samples injected with 50 volume % of carbides, the surface hardness was increased from <20 HRC to about 50 HRC regardless of the type and size of the carbide particles (9). The hard carbide particles present in the injected layer act as obstacles to plastic flow during deformation by a hardness indentor. The optical micrograph shown in figure 8 shows the deformation produced in a WC injected Inconel 625 alloy sample by a superficial hardness indentor. Metal matrix plastic flow inhibition by the carbide particles is evident in the micrograph. In fact, the plastic strain has produced deformation bands in the carbide phase. Some cracking of the carbide particles by the indentor occurred, but separation of the carbide particle from the metal matrix under the strain was minimal. The partially dissolved carbide surface ensured a strong metallurgical bond between the carbide particles and the metal matrix.

Plastic flow inhibition is the major mode of hardening in particle injected surfaces. Other factors also play a role. For example, in Ti-6Al-4V, transformation hardening by the martensitic reaction also contributed to the increased surface hardness. In this alloy the superficial hardness was increased from 33 HRC to as high as 64 HRC when injected with TiC (9). The hardness increase was linear in the carbide volume fraction range of 0.1 to 0.6. Even with only small fractions of the carbides, the hardness was already up to 48 HRC

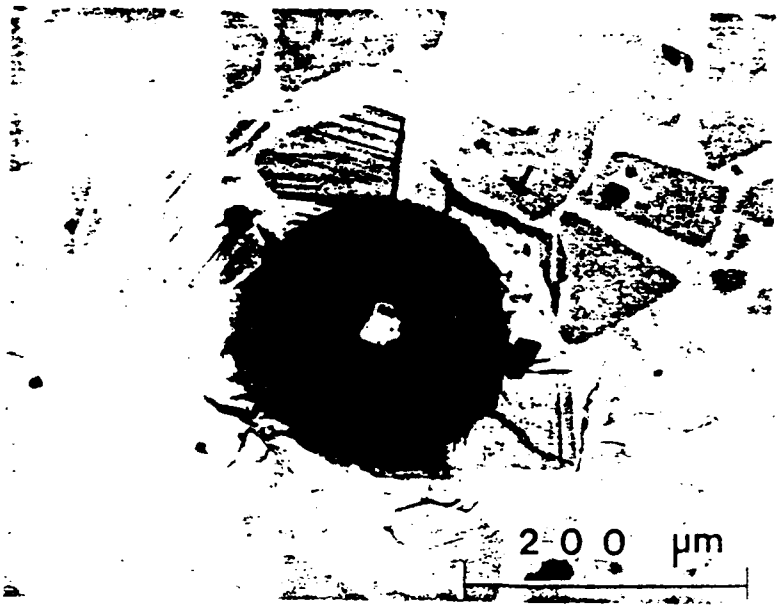


Figure 8. Optical micrograph showing deformation produced by the superficial hardness indentor on a polished WC injected Inconel 625 alloy sample surface.

evidently due to the presence of the martensitic phase.

Besides altering the microstructure and chemistry of the metal matrix, carbide dissolution also affects the matrix microhardness. As products of the dissolution process, the solute-rich eutectic phases and the resolidified carbides harden the metal matrix by dispersion hardening mechanisms. Some of the eutectics in the injected Inconel 625 alloy samples were identified as complex multi-component carbides (13). Depending upon the type of the resolidification product, microhardening occurred to various extents.

Figures 9 and 10 show the microhardness variations in the injected layer matrix as a function of depth in the injected surface. Figure 9 shows the influence of carbide type and size on the matrix microhardness relative to that of the substrate in particle injected Inconel 625 alloy samples. In all cases the microhardness appears to increase with decreasing depth. This increase is due to the progressively increasing fraction of resolidified carbides from the bottom to the top portions of the injected layer. In the lower portions of the injected layer, hardening of the matrix on a microscopic scale results only from the eutectic phases. An important effect evident from figure 9 is that of the hardness increase due to the injected carbide type. Matrix hardening from WC injection is much greater than with TiC injection. This distinction is easily seen in the lower third of the injected layer which is dominated by eutectics. The eutectic phase in the TiC injected sample had little influence on

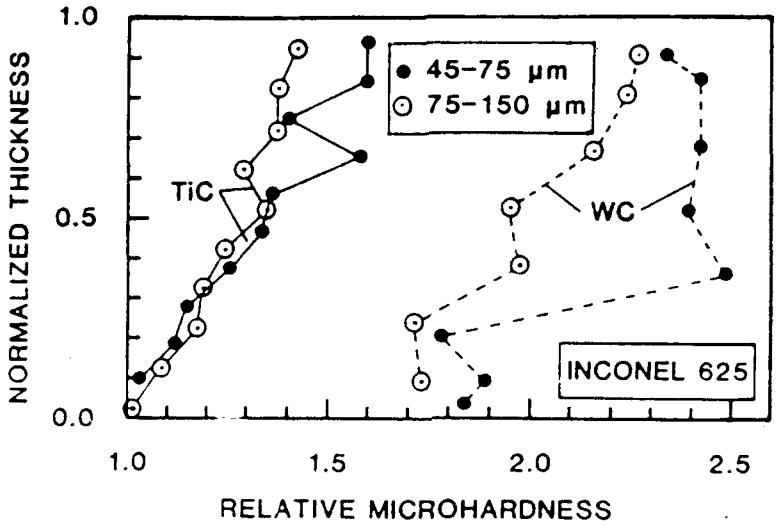


Figure 9. Matrix microhardness relative to the substrate as a function of injected layer thickness in particle injected Inconel 625. The microhardness of the substrate was about 300 HV.

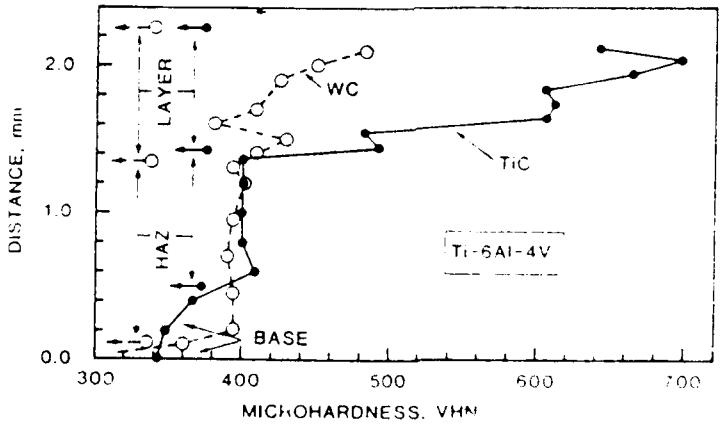


Figure 10. Microhardness as a function of distance below the surface of carbide injected Ti-6Al-4V.

hardening, probably because of its coarse spacing and needle-like appearance. In the WC injected sample the eutectic phases had a greater influence on hardening, produced probably because of their fine spacing and spheroidal morphology. The increase in microhardness because of the presence of the resolidified carbides was the same, about 50%, for both types of injected carbides. Another effect is that of the injected carbide size. Regardless of carbide type, finer

particles dissolved to a greater extent, thus hardening the matrix to a greater degree.

The influence of carbide type on the hardening in the Ti-6Al-4V alloy matrix is opposite to that in the Inconel 625 alloy matrix. In figure 10, the microhardness is plotted as a function of depth below the surface for the two types of carbides. As shown in figure 10, with reducing depth, the matrix microhardness increases very rapidly in the TiC injected sample, but only modestly in the WC injected sample. In most of the WC injected sample and in the lower portion of the TiC injected sample, the microhardness increase over that of the heat affected zone is from the presence of the finer martensitic cells and the inter-cellular eutectic phases. In the mid and upper portions of the TiC injected layer increasing fractions of resolidified carbides contributed to the rapid increase in microhardness. Although the microstructures show that WC dissolved to a greater degree than TiC, the dissolution products in the WC injected sample do not appear to increase the microhardness significantly.

Frictional Wear Characteristics of Injected Layers.

Hardening by particle injection improves the frictional wear behavior of particle injected surfaces. The kinetic coefficient of friction between the polished Inconel 625 alloy sample surface and a hard steel ball was reduced from 0.55 to between 0.15 and 0.2 after one slide (10). After 15 passes in the same track, the coefficient of friction for the untreated sample increased to 0.72 and that for the treated samples increased to between 0.33 and 0.44 depending upon the type and size of the carbide particles. For the untreated sample the scar width was 300 microns and for the treated samples the scar width varied from 80 to 150 microns. Figure 11 shows the wear scar appearance after 15 slides on a WC injected Inconel 625 alloy sample surface. Damage to the injected surface appears to be very slight. This is because in particle injected surfaces, the slider tends to mostly ride over the carbide particles, the carbides acting to protect the metal matrix from contact with the slider. A similar observation was made by Ayers et al (14) during their frictional wear studies on TiC injected Ti-6Al-4V alloy samples. The steel slider has a very low coefficient of friction against the carbide particles. Both the lower coefficient of friction and the smaller scar width demonstrate the improvement in sliding wear resistance brought about by particle injection.

The increase in the coefficient of friction with the number of slides was due to the formation of wear debris. The wear debris in the WC injected sample is shown in figure 12 and was composed mostly of slider material. Electron microprobe analysis revealed the debris to be mostly Fe, the major component of the steel slider (10). In addition, abrasive wear of the metal matrix was mild due to its high microhardness (about 620 HV). Thus most of the wear occured in the steel slider. The wear debris in the TiC injected sample is shown in figure 13 and was composed mainly of the metal matrix material.

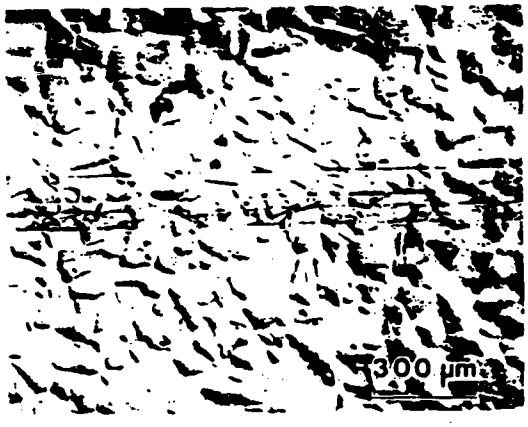


Figure 11. Optical micrograph showing the wear scar formed by a steel slider on a polished WC injected Inconel 625 alloy surface.



Figure 12. Optical micrograph showing detail of the wear scar and the wear debris in WC injected Inconel 625.

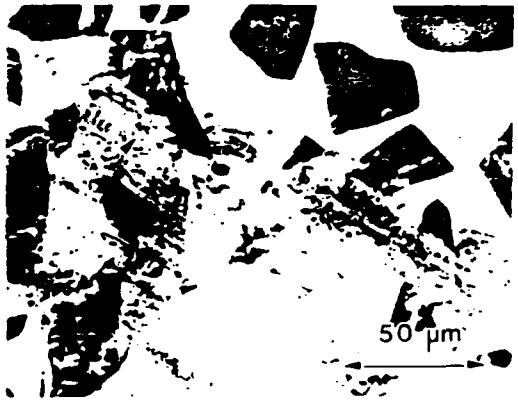


Figure 13. SEM micrograph showing the wear scar and the wear debris in TiC injected Inconel 625.

Electron microprobe analysis identified Ni, Cr and other alloying elements of Inconel 625 in the debris (10). Also present was a small quantity of Fe. Hence, in this case, the debris was a mixture of matrix and slider materials. Most of the abrasive wear occured in the metal matrix due to its low microhardness (about 400 HV). Although resolidified carbides increased the microhardness to about 500 HV, it did not diminish frictional wear. Since the matrix underlying the resolidified carbides was soft, the slider pushed aside the resolidified carbides as it ploughed through the metal matrix. It appears that in Inconel 625 alloy samples, particle injection with WC not only reduced the coefficient of friction but also the abrasive wear of the metal matrix. It is beneficial to harden the inter-particle metal matrix since it improves abrasive wear, but this should not be achieved at the expense of matrix embrittlement.

SUMMARY

Laser melt/particle injected surfaces are metal matrix/metal carbide composites which are hardened by the carbide phase and in which the matrix phase serves to maintain some of the original substrate properties. The hardening is due to the inhibition of plastic flow by the injected species and by finer carbide constituents which form during solidification. Near the injected layer/substrate interface, the matrix is structurally continuous with and chemically similar to the base metal so that a strong metallurgical bond is maintained.

Partial dissolution of the carbide particles into the melt produces a variety of microstructures whose form depend upon both the starting materials and the processing conditions. When the dissolution rates are low, only solute-rich, eutectic structures are observed in the matrix, while when the dissolution rates are high, resolidified carbides form as additional products. These microstructural changes are usually accompanied by undesirable compositional changes in the metal matrix. Depending upon their nature, the dissolution products also harden the metal matrix to various degrees. This microhardening is desirable because it reduces the coefficient of friction and lessens abrasive wear. The improved wear resistance is due to the low friction between the carbides and most metals and due to the shielding of the metal matrix from the slider by the carbides.

ACKNOWLEDGEMENT: The authors would like to thank Mr. R. Stegman and Mr. R. Beigel of the Laser Materials Processing Group at the Naval Research Laboratory for their technical assistance.

REFERENCES

1. G. M. Eboo and A. E. Lindemanis, in "Applications of High Power Lasers", Ed. R. R. Jacobs, SPIE, Bellingham, WA, (1985), 86-94.

2. P. G. Moore, in "Laser Applications in Materials Processing", Ed. J. F. Ready, SPIE, Bellingham, WA, (1980), 120-125.

3. J. Singh and J. Mazumder, Met. Trans A, 18A, (1987), 313-322.

4. R. Padmanabhan, in "Laser Materials Processing, ICALEO'86", Ed. C. M. Banas and G. L. Whitney, LIA, Toledo, OH, (1987), 185-192.

5. J. D. Ayers, R. J. Schaefer and W. P. Robey, J Metals, 33, (8), (1981), 19-23.

6. K. P. Cooper and J. D. Ayers, Surface Engineering, 1, (4), (1985), 263-272.

7. J. D. Ayers, T. R. Tucker and R. J. Schaefer, in "Rapid Solidification Processing - Principles and Technologies", Vol. II, Ed. M. Cohen, B. Kear and R. Mehrabian, Claitors Publishing Div., Baton Rouge, LA, (1980), 212-221.

8. J. D. Ayers, Wear, 97, (1984), 249-266.

9. K. P. Cooper, in "Surface Modifications and Coatings", Ed. R. D. Sisson, Jr., ASM, Metals Park, OH, (1986), 409-420.

10. K. P. Cooper, J Vac Sc Technol A, 4, (6), (1986), 2857-2861.

11. J. D. Ayers, Thin Solid Films, 84, (1981), 323-331.

12. J. D. Ayers, in "Lasers in Metallurgy", Ed. K. Mukherjee and J. Mazumder, AIME, Warrendale, PA, (1981), 115-125.

13. K. P. Cooper, A. K. Singh and J. D. Ayers, to be published.

14. J. D. Ayers, T. R. Tucker and R. C. Bowers, Scripta Met., 14, 549-550.

RECENT DEVELOPMENTS IN LASER MELT/PARTICLE INJECTION PROCESSING

K. P. Cooper, Geo-Centers, Inc., Fort Washington, MD 20744

and

P. Slebodnick, Naval Research Lab., Washington, D.C. 20375

To be published in the Proceedings of ICALEO '88, an International Conference sponsored by the Laser Institute of America and held in Santa Clara, CA on Oct. 30 - Nov. 4, 1988.

Recent Developments in Laser Melt/Particle Injection Processing

K. P. Cooper* and P. Slebodnick#
*Geo-Centers, Inc.
Fort Washington, Maryland.
#Naval Research Laboratory
Washington, D.C.

Abstract

Investigations into crack formation in particle injected surfaces and into microstructural evolution during cladding were some of the recent developments in laser melt/particle injection processing. Both surface modification techniques involved blowing powder particles into a melt pool formed by a laser beam. With metal carbide particles, composite surface layers were formed and the thermal stresses that developed during cooling of the injected layer resulted in the formation of microcracks. It was found that modest levels of preheating were sufficient to prevent cracking and that cracking was eliminated mainly by the reduction in thermal stresses and not by changes in microstructure. With low-melting alloy powders, clad overlays were formed. It was found that the limited mixing between the clad material and the substrate resulted in complex microstructures containing fluid-flow driven segregation bands. The degree of microstructural inhomogeneity depended upon the type of substrate material, and had a direct influence on the soundness of the cladding.

Introduction

One of the most common techniques of laser surface modification is the pneumatic feeding of powder particles into laser melt pools. If the powder particles are binderless metal carbides which are not melted by the laser beam, particle injected composite surface layers are formed[1,2]. These layers consist of discrete particles surrounded by a metal matrix which is structurally continuous and chemically similar to the substrate. Particle injected layers are hard and wear resistant[3,4]. If the powder is a hardfacing alloy that is easily melted by the laser beam, then its fusion with the substrate produces a clad layer[5]. Such a surface layer can also be hard and wear resistant.

Whether produced by heat treatment or by cladding, laser modified surfaces are subject to thermally induced residual stresses. When the modified surface is not able to withstand the thermal stress, it can crack. This is especially true of hardened surfaces which are usually brittle. The nature and magnitude of the thermal stresses and related cracking phenomena will be different for different laser surface modification techniques, and the understanding of these problems in laser processing is critical to the production of sound overlays that are not susceptible to delamination or spalling. In an earlier study[6], the influence of processing and material parameters on the cracking tendency of particle injected composite surfaces was discussed. In that study

WC and TiC particles of various size distributions were injected at different powder feed rates into laser melt pools of various dimensions that were formed on Inconel 625 alloy samples. Several observations were made from that investigation. For example, the crack density was reduced as the melt width was increased. In layers made with the medium and coarse WC, the crack density reduced with increasing powder feed rate. But with the fine WC and the medium-sized TiC, at low to moderate powder feed rates an increased cracking tendency was found. The degree of cracking in particle injected layers depended upon a balance between forces that promoted matrix embrittlement, such as excessive carbide dissolution, and forces that reduced the tensile residual stresses such as slower solidification and cooling rates. Cracks can be prevented by careful control of the processing conditions such as laser energy density[7], by composite cladding (forming an intermediate clad layer)[8] or by careful control of the microchemistry and microstructure of the modified surface. Details of these crack prevention techniques are not readily available because of the proprietary nature of the solutions. The most common method of crack prevention is by preheating. In this investigation, the role of preheating on cracking in particle injected layers was determined.

Laser cladding is a widely accepted surface modification technique for selected area laser processing. By this means, wear resistant[9], corrosion resistant[10] and high temperature oxidation resistant[11] coatings have been deposited on a variety of substrates. Ideal laser cladding conditions require that there be a minimum of dilution (< 5%) with the substrate. Excessive dilution can result in the loss of clad material properties[12]. Most of the developmental work has been aimed at determining conditions that result in minimum dilution and maximum metallurgical bonding[8]. But questions remain as to the nature of the clad layer, its microstructure and properties when some amount of mixing between the pneumatically delivered powder and the molten substrate does occur. In this paper, these aspects of cladding and their implications will be discussed for a couple of different alloy substrates.

Experimental Procedures

Laser Melt/Particle Injection Processing

Laser melt/particle injection processing involves simultaneous laser melting and powder feeding of a metal surface. A high power CW CO_2 laser was used to melt short arcs on 1 to 1.5 cm thick samples. Different melt widths were obtained by oscillating the laser beam with different amplitudes. The laser beam oscillation frequency was rapid enough to generate a line energy source. Powder particles were propelled into the laser melt pool by helium carrier gas via a copper nozzle positioned nearby. To inject into a wider melt area, an injection nozzle with a slotted opening that formed a rectangular spray was used. Details of the process have been given elsewhere[13,14].

Preheating Experiments

Preheat studies were done on Inconel 625 alloy samples that were injected with WC particles having a size distribution of 45-75 μm. A sketch of the preheating experimental set-up appears in figure 1. The sample was placed on a stage which was attached to a rotating table. A few layers of zirconia paper insulated the sample from the stage. Through a hole on the side of the sample, a Type K thermocouple read the temperature of the substrate. A resistance heater suspended above the sample heated it by radiative and convective means. By controlling the power to the heater using a variac, the preheat temperature was controlled. The entire assembly was placed in a vacuum chamber which was backfilled with argon. After the sample reached the desired temperature, it was soaked for a few minutes and then translated at a predetermined rate. Just before the sample passed below the laser beam, the automatic control sequence was initiated. A few seconds after the powder feeder started the laser beam was enabled. The interaction of the laser beam and the particle spray with the substrate formed the injected layer. For a particular melt width, the "beam on" duration was kept constant so that the particle injected surface area was the same from sample to sample. The crack density of the injected layer was measured as the total crack length in both the longitudinal and transverse directions averaged over the injected layer surface area. The cracks were revealed under UV light after the samples were treated in a dye penetrant bath. These studies were done on 1 and 2 cm wide melt passes, the processing conditions for which are given in table I. The powder feed rate, carrier gas pressure, nozzle distance and sample speed were adjusted to give the same carbide volume percent and thickness of the injected layer.

Table I Processing Conditions for Laser Melt/Particle Injection.

	Preheat Studies Melt Width, cm		Cladding Studies Substrate Alloy	
	1	2	In 625	Ti-6-4
Laser Power, kW	10	10	8-10	4-8
Beam Dia. or Width, cm	0.2	0.2	0.7-1.6	0.4
Powder Feed Rate, $cm^3\ s^{-1}$	0.5	0.45	.15-.225	0.15-0.5
Carrier Gas Pressure, kPa	110	124	70-85	70
Nozzle Distance, cm	1.25	1.10	2.2	1.9
Sample Speed, $cm\ s^{-1}$	0.75	0.3	.35-.75	1.0-1.5

Cladding Experiments

Inconel 625 and Ti-6Al-4V alloy sample coupons were laser clad with Tribaloy (T-400), a Co-based hardfacing alloy. The clad alloy powder had a mesh size of 75 μm. The powder particles were fed directly into a very shallow melt pool formed on the substrate by the laser beam. Typical processing conditions for the two substrate alloys are given in table I. The goal of these

experiments was to examine the complex path of microstructural evolution in each alloy. Processing conditions were selected to produce claddings that were smooth, uniformly shaped and fully dense.

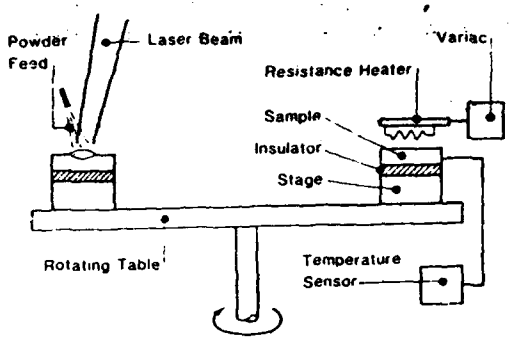
Characterization of the Laser Modified Surface

After carefully sectioning selected samples, metallographic specimens were prepared for microstructural evaluation. The carbide injected samples were etched with a peroxide etch which revealed the inter-particle matrix microstructure and the laser clad samples were etched with Marble's etch which revealed the microstructure of the Tribaloy phase. A Nikon Epiphot optical microscope was used to examine the macrostructure of the modified surface and to determine the nature and extent of the macrosegregation. High magnification microstructural and analytical studies were done with a Hitachi Model S-800 Field Emission Scanning Electron Microscope and associated Princeton Gamma-Tech Microanalysis system. The SEM was used in both the secondary electron imaging mode for high resolution microscopy and the back-scattered electron imaging mode for atomic number contrast studies. Microanalysis involved selected area diffraction and x-ray mapping. Furthermore, the metallography samples were evaluated for microhardness variations in the modified surface using a Buehler Micromet II Digital Microhardness Tester. Microhardness readings were taken using a Vickers indentor and a 100 g load.

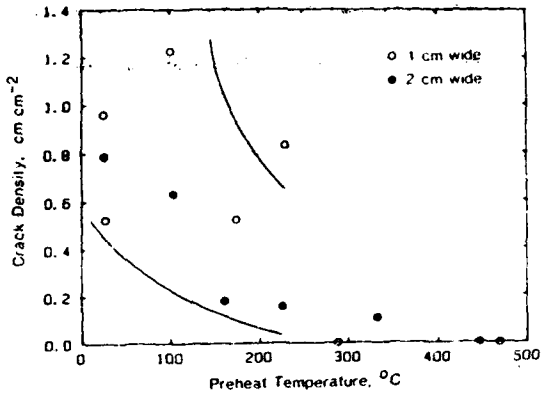
Results

Preheating Study

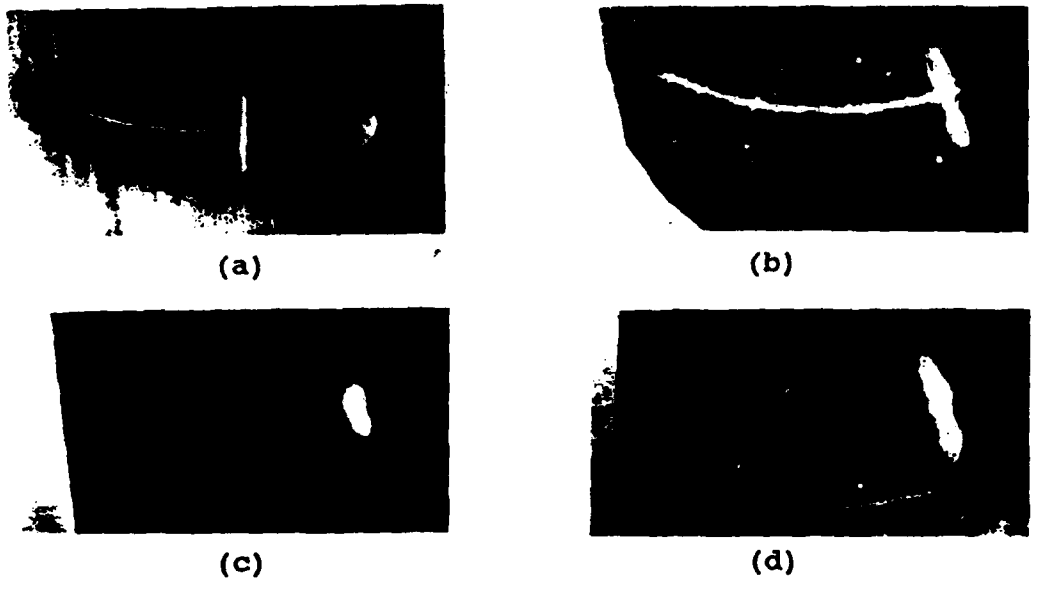
In figure 2, the crack density as a function of preheat temperature is plotted. Although there is some scatter in the data, a general reducing trend in the crack density with preheat temperature is observed. While cracks in the 1 cm wide injected layers were eliminated at preheat temperatures of about 300 °C and above, higher preheat temperatures of about 450 °C and above were necessary to eliminate cracks in the 2 cm wide injected layers. Figure 3 shows the appearance of the injected layers under UV light. Without preheat, a transverse and a longitudinal crack, making up a crack density of 1 cm cm^{-1}, formed in the narrower injected layer as shown in figure 3(a). With a preheat of 288 °C, a crack-free injected layer was formed as shown in figure 3(b). In the wider injected layer, without preheat a single longitudinal crack giving a crack density of 0.8 cm cm^{-1} formed as shown in figure 3(c). A crack-free injected layer was formed only with a preheat of 446 °C as shown in figure 3(d). The inter-particle matrix microhardness as a function of distance from the injected layer surface is plotted in figure 4. Data points within the injected layer region which is to the left of the arrows show a large amount of scatter, with the matrix microhardness varying from 450 to 600 HV. As the transition from the injected layer to the substrate is made, the microhardness drops to about 250 HV in the Inconel 625 alloy substrate.



1. Schematic diagram of preheating experimental set-up.



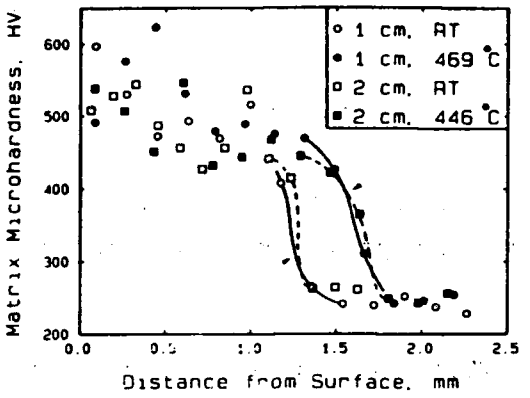
2. Crack density as a function of preheat temperature.



3. UV light photographs of injected layers showing the effect of preheating on cracking. a) No preheat, 1 cm wide. b) No preheat, 2 cm wide. c) 288 °C preheat, 1 cm wide. d) 446 °C preheat, 2 cm wide.

Cladding Studies

Macrostructures of Tribaloy-400 (T-400) clad Inconel 625 (I625) and Ti-6Al-4V (Ti-6-4) are shown in the optical micrographs of figures 5(a) and 6(a), respectively. The clad layers are 1 cm and 0.4 cm wide, respectively. The etching contrast shows the significant macrosegregation observed in the clad layer. X-ray dot mapping of the clad surface showed that the segregation bands are rich in alloying elements originating from the substrate. The x-ray map of Ni in figure 5(b) and that of Ti in figure 6(b) show the



4. Plot of microhardness in WC injected Inconel 625 as a function of distance from the surface. Arrows indicate melt-substrate boundary.



(a)



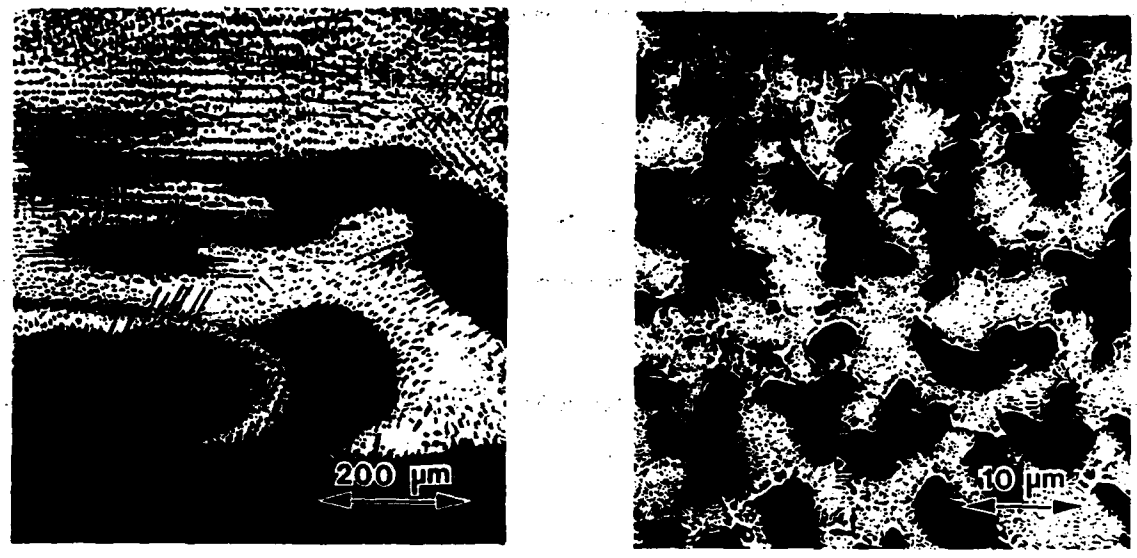
(b)

5. Cross-sections of Tribaloy-400 clad Inconel 625. a) Optical micrograph showing macrosegregation. b) SEM x-ray map of Ni.



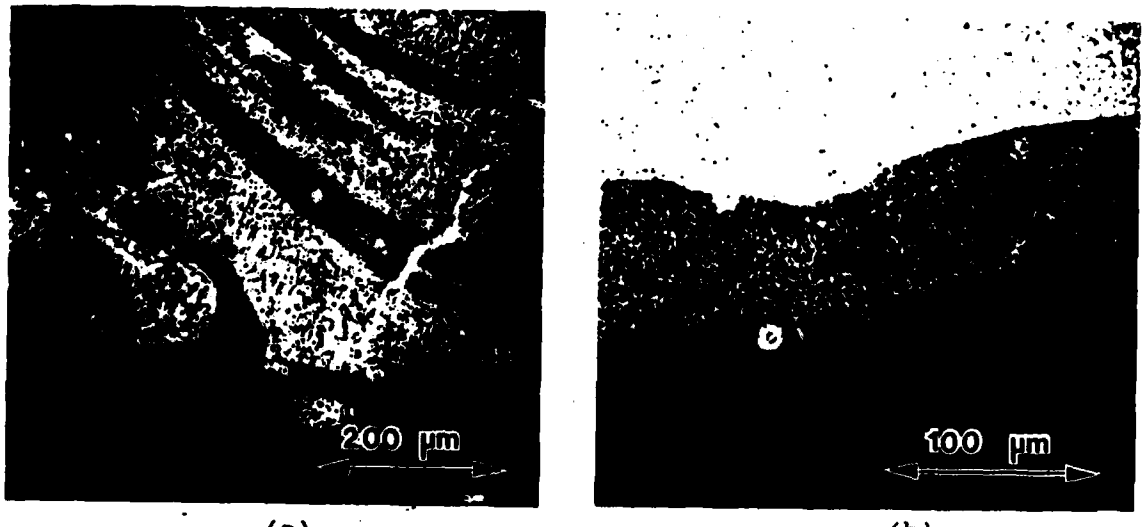
(a) (b)

6. Cross-sections of Tribaloy-400 clad Ti-6Al-4V. a) Optical micrograph showing macrosegregation. b) SEM x-ray map of Ti.



(a) (b)

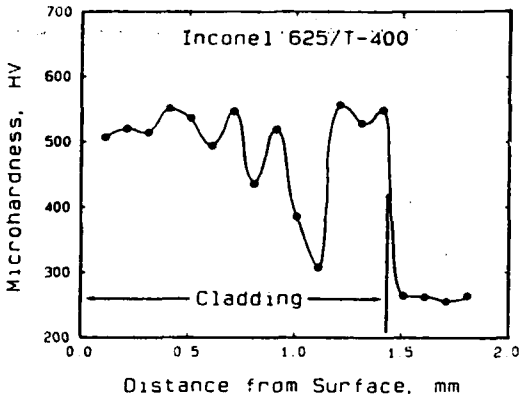
7. SEM micrographs of T-400/I625 cladding. a) Detail of clad-substrate interface. b) Laves dendrites and eutectic in cladding.



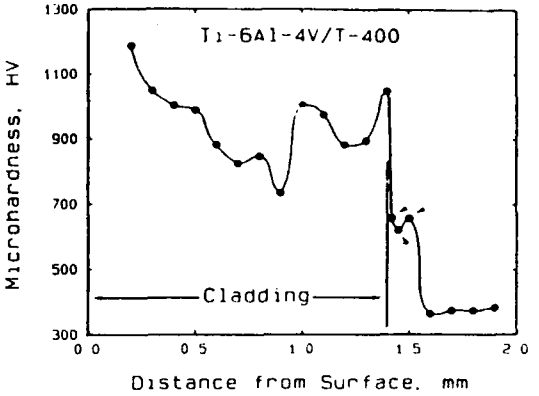
(a) (b)

8. SEM micrographs of T-400/Ti-6-4 cladding. a) Segregation bands in cladding. b) Detail of intermediate layer at interface.

concentration of these elements in regions corresponding to the segregation bands appearing in figures 5(a) and 6(a), respectively. Similar x-ray maps were obtained for the other major alloying elements such as chromium in I625. While the melt-substrate interface in the I625 sample appears discontinuous and wavy, that in the Ti-6-4 sample appears continuous and relatively smooth. Amplified views of the interfaces appear in the SEM micrographs of figures 7(a) and 8(a). The uneven melt depth in the T-400/I625



9. Microhardness variations as a function of distance from surface in T-400 clad I625.



10. Microhardness variations as a function of distance from surface in T-400 clad Ti-6-4.

sample is clearly evident in figure 7(a) and the cladding microstructure appears dendritic. As shown in figure 7(b), these dendrites, which are probably Laves phases, appear to be surrounded by a fine eutectic structure which is typical of T-400 alloy. In T-400/Ti-6-4, the melt-substrate interface appears to be fairly even as shown in figure 8(a). In addition, segregation bands are clearly evident in this material. A closer look at the interface revealed an intermediate layer between the cladding and the substrate as shown in figure 8(b). Microhardness variations as a function of distance from the cladding surface are plotted in figures 9 and 10 for T-400/I625 and T-400/Ti-6-4 claddings, respectively. In both cases, a wide variation in the microhardness within the clad layer is evident. In T-400/I625, the microhardness varied from 300 to 550 HV in the cladding and fell to about 250 HV in the I625 substrate. In T-400/Ti-6-4, the microhardness varied from 700 to 1200 HV in the cladding and fell to about 350 HV in the Ti-6-4 substrate. Additionally, the intermediate phase at the T-400/Ti-6-4 interface had a microhardness of about 600 to 650 HV (marked by arrows in figure 10).

Discussion

Preheat studies

From the results of the preheat experiments the following observations are made. In carbide particle injected samples, cracking is eliminated by preheating the samples to modest temperatures. For the wider injected layer sample, a higher preheat was needed to prevent cracking compared to the narrower injected layer. Preheating serves two purposes. It minimizes the formation of solidification reaction products that may embrittle the laser modified surface and make it susceptible to cracking, and it lowers the solidification and cooling rates thereby reducing the thermal stresses that can initiate thermal cracking. Due to limited dissolution of the carbide phase, the matrix in particle

injected surfaces showed a complex array of microstructures[15]. These consisted of resolidified carbides that are free floating dendrites and eutectic carbides that form within the (Ni)-rich dendrites or in the inter-rich dendritic regions of the (Ni)-rich dendrites. Lamellar and script-type eutectic carbides have been identified in WC injected Inconel 625 with examples given in figure 11. These carbides are MC, M_2C and M_6C type and they tend to harden the matrix to different degrees[15] and embrittle it. When the dissolution rate is excessive, such as when very fine carbide particles are injected into the melt, matrix embrittlement is acute and cracking easily occurs[6]. Microstructural examination of several samples revealed that the matrix microstructures were similar in nature regardless of the injected layer width and whether preheating treatment was given or not. The lack of microstructural change is not surprising since the preheat temperatures were not high enough to significantly influence the solidification reactions. The similarity in microstructure between the four samples is confirmed by the similarity in the microhardness results. As shown in figure 4, the matrix microhardness shows no dependence on injected layer width or on preheating. Only the thickness of the injected layer, which averaged at about 0.15 cm, appears to have been affected. As indicated by arrows, the thickness increased with preheating due to more efficient laser-metal interaction.

Since preheating had little influence on the microstructure, the only other effect it could have is to reduce the thermal stresses by reducing the cooling rates. Masubuchi has reported reductions in the cooling rates in the melt pools of bead-on-plate steel specimens as a result of preheating[16]. In its simplest form, the maximum residual tensile stress (σ_x) in a thick plate subjected to a gaussian temperature distribution on one face is given by[17],

$$\sigma_x = \frac{2E\alpha\ (T_1 - T_0)}{3 + \nu}$$

where T_1 is the maximum temperature, T_0 the initial sample temperature, E is the modulus of elasticity, α is the coefficient of thermal expansion and ν is the Poisson's ratio of the material. By preheating, T_0 is increased, thereby reducing the residual tensile stress σ_x.

To prevent crack formation in laser clad materials high preheat temperatures were necessary. A study by Weerasinghe and Steen[18] found that a preheat of 700 °C and above was needed to eliminate cracking in a hard iron/boron coating that was clad on mild steel. By comparison, this work has demonstrated that low preheat temperatures of 300 to 450 °C were enough to prevent cracks in particle injected layers. The injected layer is a composite of hard carbide particles in a softer metal matrix. As the composite material cools, the second phase particles impose a hydrostatic stress on the matrix. If the second phase particle distribution is assumed to be a close packed arrangement of spheres, the



11. SEM micrograph showing carbide dissolution products in the matrix of WC injected Inconel 625.

hydrostatic stress on the matrix (σ_m) is of the order of[19],

$$\sigma_m = - \sigma_p \left(\frac{6}{2^{0.5}\,\pi}\right) f$$

where σ_p is the hydrostatic stress on the particle and f is the particle volume fraction. The hydrostatic stress is a compressive stress. When superimposed on the tensile residual stress developed in the cooling composite, it would tend to reduce this tensile stress. It is because of this reduction in the residual tensile stress that modest preheat temperatures were adequate in preventing cracking in particle injected layers. Another demonstration of the presence of superimposed compressive stresses is that even when a crack does form in the injected layer, its width is small. Figure 12(a) shows a thermal crack in a WC injected Inconel 625 layer with an average crack width of about 5 μm. By comparison, the thermal crack in a laser clad layer made under comparable processing conditions is wide. Figure 12(b) shows a thermal crack in a Tribaloy-400 clad Inconel 625 sample with an average crack width of about 80 μm which is considerably wider than that in the WC injected surface.

Previous work on the effect of melt width on cracking showed that the crack density decreased with increasing melt width[6]. The reduction in the crack density was mainly a consequence of a reduction in the number of transverse cracks. To obtain the same melt depth in melts of increasing width, the incident laser energy density should be constant. This was achieved by decreasing the sample traverse speed (v) while keeping the laser power constant[6]. Reducing v increased the laser/melt interaction time (τ). Increasing τ reduced the solidification and cooling rates in the melt thereby reducing the residual stresses. The elimination of



(a) (b)

12. Nature of thermal cracks. a) SEM micrograph of WC injected Inconel 625. b) Optical micrograph of T-400 clad Inconel 625.

transverse cracks in wider injected layers is a consequence of this reduction in the residual stress. Preheating achieves the same results in narrower injected layers. In wider injected layers, while transverse cracks disappeared, a centerline crack began toappear. The dominant residual stress component shifted from being parallel to the melt pass to being perpendicular to the melt pass. The oscillating laser beam used to make wider melt passes tended to dwell at the extremities of the oscillation cycle, leaving the sides of the melt pass hotter than its center. As these regions shrink upon cooling, a strong tensile transverse stress component developed, causing the longitudinal or centerline crack. Because of this unusually strong tensile stress component, much higher preheat temperatures were needed to eliminate cracking in wider injected layers.

Cladding studies

Laser processing conditions were determined to form uniformly shaped, fully dense Tribaloy-400 claddings on Inconel 625 and on Ti-6Al-4V alloy substrates, but significant macrosegregation was observed in the clad layers as shown in figures 5(a) and 6(a). The nature of the macrosegregation indicates that it can only be brought about by fluid flow driven forces. A careful examination of the segregation pattern in figure 5(a) suggests that the fluid flow is from the bottom of the melt pool towards the center and then towards the top of the melt pool moving away from the center in a recirculatory motion. This motion appears to have formed eddy current loops on either side of the melt. As mentioned earlier, the oscillating beam, needed to make wider melt passes, keeps the sides of the melt pool hotter than the center. Such a temperature distribution would promote the fluid flow pattern described above. The structure in figure 6(a) indicates that only a single recirculatory flow exists in the narrower melt pass. Although an

oscillating laser beam was used, its amplitude was so small that the temperature distribution could be considered nearly gaussian leading to the fluid flow pattern just described. In this technique of laser cladding, both laser beam oscillations and particle injection velocity affect convection in the melt pool. A detailed analysis of these effects is beyond the scope of this investigation.

The fluid flow patterns described above can only form when limited mixing of the injected molten droplets and the shallow melt pool occurs. Thermally induced convection in the melt pool enhances clad material-substrate interaction leading to the transport of substrate material well into the clad layer. The presence of significant amounts of Ni and Ti in the segregation bands of the cladding was demonstrated in figures 5(b) and 6(b). From these figures, dilution was estimated at 30% for T-400/I625 and at 10% for T-400/Ti-6-4. Selected area diffraction estimated 13-15% Ni and increased Cr in the T-400/I625 clad layer and 15-18% Ti in the T-400/Ti-6-4 clad layer. The ease with which the Co-based Tribaloy-400 cladding was alloyed with Ni from the Inconel 625 substrate is explained by the fact that Co and Ni form a continuous series of solid solutions at all compositions[20]. Besides being alloyed with Ti, the possibility of the formation of intermetallic compounds in the T-400/Ti-6-4 cladding was investigated. The Co-Ti phase diagram[21] shows a series of intermetallic compounds at various compositions. The segregation bands within the cladding such as the ones shown in figure 8(a) were analyzed to be high in Ti, nearly 23-25% with a strong possibility of the segregation band containing complex intermetallic compounds. Another observation in Ti-6-4 was the occurrence of an intermediate phase at the interface between the cladding and the substrate. From its morphology, which is revealed in figure 8(b), the intermediate phase can only form by solid-state diffusion of elements such as Co and Mo from T-400 into Ti-6-4. In this phase, Co and Mo were detected and estimated at 20 and 10%, respectively, with Ti being about 60%. Whether this layer contains intermetallic compound or is a β-Ti solid solution could not be determined.

Besides affecting the macrostructure and the macrosegregation of the clad layer, the dilution process also affects the cladding properties. Cast Tribaloy-400 has a hardness of 51-58 HRC or 550-675 HV for optimum wear properties. The microhardness of the T-400/I625 cladding was 300-550 HV which is lower than that of the cast T-400. Alloying with small quantities of Ni and other I625 alloying elements softened the clad layer and reduced the wear resistance[22]. On the other hand, the microhardness of 700-1200 HV for the T-400/Ti-6-4 cladding is higher than that of the cast T-400. Alloying with small amounts of Ti appears to have improved the hardness and probably the wear resistance. Unfortunately, in some T-400/Ti-6-4 samples, small cracks were detected within the Ti-rich segregation bands and within the intermediate interface layer. If the segregation bands and the intermediate phase are brittle intermetallics, the formation of microcracks is not

surprising. In an extreme case involving a high powder feed rate, the cladding delaminated along the interface boundary and along the segregation contours. Dilution is undesirable because in T-400/I625 it resulted in a loss of cladding properties and in T-400/Ti-6-4 it promoted cracking.

Summary

The preheat studies demonstrated that modest levels of preheat were sufficient to prevent thermal cracking in WC injected Inconel 625 alloy samples. The preheat temperatures were much less than those required for cladding due, in part, to lower thermal stresses. Due to a higher transverse tensile stress component, wider injected layers required a higher preheat than narrower injected layers.

Injection of Tribaloy-400 powder into laser melt pools formed on Inconel 625 and T-6Al-4V alloy substrates resulted in fluid flow driven macrosegregation and macroalloying in the clad layer. Besides inhomogenious microstructures, the microhardness of the cladding varied considerably, with the average hardness of the T-400/I625 cladding being lower than that of cast T-400, and the average hardness of T-400/Ti-6-4 being higher than that of cast T-400. In the T-400/Ti-6-4 cladding, besides macroalloying, brittle intermetallics decorated the segregation contours and the cladding-substrate interface thereby affecting the soundness of the cladding.

Acknowledgement

The authors would like to thank Mr. R. Stegman and Mr. R. Beigel of the Laser Materials Procesing group for their technical assistance and for the use of their facilities.

References

1. Ayers, J.D., R.J. Schaefer and W.P. Robey (1981). J. METALS 33 19-23.

2. Cooper, K.P. and J.D. Ayers (1985). SURFACE ENGRG. 1 263-272.

3. Ayers, J.D. (1984). WEAR 97 249-266.

4. Cooper, K.P. (1986). J. VAC. SCI. TECHNOL. A 4 2857-2861.

5. Eboo, G.M. and A.E. Lindemanis (1985). Applications of High Power lasers, SPIE, Bellingham, WA. 86-94.

6. Cooper,K.P. and J.D. Ayers (1988). Laser Materials Processing, ICALEO'87, LIA, Toledo, OH. 179-187.

7. Steen, W.M. (1986). Laser Surface Treatment of Metals, Martinus Nijhoff Publ., Dordrecht, The Netherlands. 369-387.

8. Bruck, G.J. (1987). J. METALS 39 10-13.

9. Padmanabhan, R. (1987). Laser Materials Processing, ICALEO'86, LIA, Toledo, OH. 185-192.

10. Chande, T., A. Ghose and J. Mazumder (1987). SURFACE ENGRG. 3 53-58.

11. Singh, J. and J. Mazumder (1987). ACTA METALL. 35 1995-2003.

12. Bruck, G.J. (1987). Laser Materials Processing, ICALEO'86, LIA, Toledo, OH. 149-159.

13. Cooper, K.P. (1986). Surface Modifications and Coatings, ASM, Metals Park, OH. 409-420.

14. Cooper, K.P., R.E. Beigel and P. Slebodnick (1987). Laser Materials Processing, ICALEO'86, LIA, Toledo, OH. 169-176.

15. Cooper, K.P. and J.D. Ayers (1988). Proc. of the 1988 Conf. on Laser Surface Modification, AWS, Miami, FL. in press.

16. Masubuchi, K. (1980). Analysis of Welded Structures, Pergamon Press, New York, N.Y. 75-80.

17. Goodier, J.N. (1937), ASME J. APPL. MECH. 4 A33-A36.

18. Weerasinghe, V.M. and W.M. Steen (1983). Lasers in Materials Processing, ASM, Metals Park, OH. 166-174.

19. Ledbetter, H.M. and M.W. Austin (1987). MATERIALS SCI. & ENGRG. 89 53-61.

20. Hansen, M. and K. Anderko (1958). Constitution of Binary Alloys, McGraw-Hill, New York, N.Y. 485-487.

21. Elliott, R.P. (1965). Constitution of Binary Alloys, First Supplement, McGraw-Hill,New York, N.Y. 339-340.

22. Cooper, K.P. unpublished results.

Meet the Authors

Mr. Khershed P. Cooper is a Group Supervisor with Geo-Centers, Inc. for whom he conducts contract research at the Naval Research Laboratory. He has a PhD in Metallurgy from the University of Wisconsin-Madison. His scientific interests include laser materials processing, coatings, powder metallurgy and rapid solidification technology.

Mr. Paul Slebodnick is a Physical Science Engineer at the Naval Research Laboratory. He is in charge of the day-to-day operation of the Metallography Laboratory. His expertise is in Microscopy and Failure Analysis.

APPENDIX II

8802-011

COUNTER ROTATING FLUID ATOMIZATION OF TIN

J.D. Ayers
Naval Research Laboratory
Washington, DC 20375, USA

K.P. Cooper
Geo-Centers Inc.
Fort Washington, Maryland 20744, USA

2nd International Conference on Rapidly Solidified Materials, San Diego, CA, 7-9 March 1988; Proceedings published by ASM INTERNATIONAL™.

ABSTRACT

A new atomization process has been developed which combines features of the rapidly spinning cup process and of centrifugal atomization. In this process, molten metal is discharged into the inside of a shallow rapidly spinning cup equipped with a rim which prevents the melt from spilling over the top. The melt issues instead from small holes on the perimeter of the cup. The fine streams of molten metal are atomized as they enter a liquid quenchant contained within the rim of an outer cup which rotates in the opposite direction. Results are described from studies of the atomization of tin with different combinations of cup speeds.

MUCH OF THE INTEREST in rapid solidification processing in recent years has centered on powder metallurgy technology because of the many advantages it offers in the fabrication of useful shapes. Most of the research employing powder metallurgy techniques has employed gas atomized powder, even though the solidification rate is normally substantially lower than is possible with processes such as chill block melt spinning. It is widely appreciated that the finest size particles produced by gas atomization cool at very high rates, and there have been many attempts to reduce mean particle sizes, both because of interest in the properties of the fine particles and because there are some applications which require powders finer than those typical of gas atomization processes. Atomized powders generally have mean particle sizes of 30 μm or more, though mean sizes as small as 10 μm are possible (1,2). Applications which require or benefit from powder sizes smaller than 10 μm include injection molding (3,4), magnetic devices (5,6), and electronic devices (7,8).

Perhaps the only commercial means for producing powder in the 10 μm range of complex alloys is the water atomization process. This process produces very rapid cooling rates, but it is not well suited for use with reactive alloys because they tend to from irregularly shaped particles with oxide skins (9). The formation of oxidized surfaces could be prevented by using oils or other oxygen free liquids, but these fluids are generally too viscous to use effectively in a process like water atomization which depends upon squirting the atomizing fluid from nozzles at high velocities. An innovative new process which helps to overcome that limitation has been reported by Raman, Patel and Carbonara (10). This process consists of squirting a stream of molten metal from a nozzle into an atomization/quenching fluid contained within the perimeter of a rapidly spinning cup. They report very low oxygen, nitrogen, and hydrogen levels for a superalloy atomized in oil (10). These authors do not report detailed size analyses, but mean particle sizes near 10 μm have been achieved (11). The major limitation to further reduction in particle size by the rapidly spinning cup process derive from physical limitation on how rapidly a fluid containing cup can be made to spin (11). This consideration led to the design of the apparatus described below.

APPARATUS DESCRIPTION AND OPERATION

The counter rotating fluid atomization process consists of combining a centrifugal atomizer with a rapidly spinning cup device. Centrifugal atomizers are normally constructed to fling molten droplets from the rim of a rapidly spinning disc or cup, but in our current configuration the molten metal issues from fine holes on the perimeter of a shallow rimmed cup. As is illustrated schematically in Fig. 1, this atomizer is positioned within a rapidly spinning cup that rotates in the opposite direction. The fine streams of molten metal which issue from the inner cup strike the fluid contained within the outer cup and are atomized and quenched by it. The molten metal is fed into the previously

heated inner cup from a small furnace positioned above it. In a simple early configuration of the apparatus the two cups were mounted directly on the output shafts of air motors, as illustrated in Fig. 1. A more elaborate version of the apparatus was used for the work reported here. In it the the two cups are positioned within a vacuum vessel and are mounted on the shafts of water cooled rotary motion feedthroughs manufactured by Ferrofluidics. The inner cup, made of stainless steel, is heated by a helical resistance heater positioned just within its upper lip. While the inner cup is being heated, the outer cup, made of 6061 Al, is in contact with the bottom of the water cooled vacuum vessel and is conduction cooled by it. Just prior to the run the vacuum vessel is dropped out of contact, that motion being made possible by a metal bellows, and the cup thereafter is cooled only by conduction through the rotary motion feedthrough shaft, a less efficient process. During heating of the inner cup, the outer cup is stationary and empty. After the vacuum vessel is dropped, the outer cup is spun up to speed and then filled with oil through a fine tube that fits down between the two cups. This procedure minimizes heating of the oil prior to the experiment. When both cups are at speed, molten metal is discharged from a small furnace into the inner cup by means of a pushrod activated stopper. All experiments are conducted with the chamber evacuated by means of a mechanical pump.

The two cups run in close proximity to one another in order to minimize breakup of the melt streams before entry into the oil. The inner cup has an outer diameter of 147 mm and is penetrated by two holes 0.35 mm in diameter. The outer cup has an inner diameter of 152 mm and was filled with oil to its full depth of 9 mm. The speeds of the two cups, determined by the pressure of the air to the motors, cannot be accurately controlled but are accurately monitored by means of digital tachometers. The air motors are capable of driving the disks to rotational speeds well in excess of 10,000 rpm, but the speeds have been held much lower for safety reasons. During heating of the inner cup its temperature is monitored by means of a fine gage thermocouple inserted in a hole on its upper surface. This thermocouple is retracted before the cup is spun up to speed. There are no means for measuring the outer cup temperature when the system is evacuated. The temperature of the oil at the end of an atomization run can be measured by decreasing the cup speed, opening the system, and inserting a fine gage thermocouple directly into the oil. During the first minute or two the oil cools rather quickly, so its peak temperature may have been 30°C or more above that measured.

The experiments reported here employed mechanical vacuum pump oil as a quenchant. Samples of tin for atomization were cut from high purity rods. Each weighed approximately 1.5 grams.

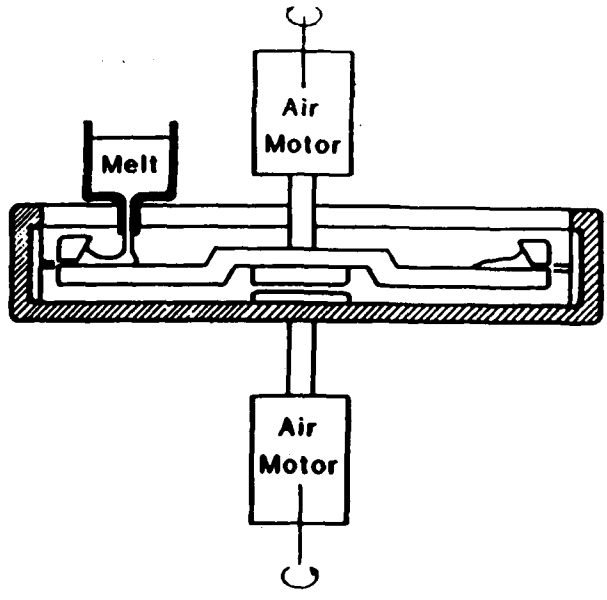


Fig. 1 Schematic representation of counter rotating fluid atomizer in cross section.

POWDER RECOVERY AND CHARACTERIZATION

Powder was recovered from the quench fluid by lowering the speed of the outer cup to about 200 rpm, raising the inner cup (which is attached via the feedthrough to the lid of the vacuum vessel), and carefully pipetting off most of the oil while leaving the remaining oil and the powder against the wall of the cup. The remaining oil and powder were then recovered by pipetting, the thin oil layer being replenished repeatedly with kerosene to assure full recovery of the powder. The powder was washed in kerosene, centrifuged, and most of the kerosene decanted off. The powder was then washed in acetone, centrifuged, and the bulk of the acetone decanted off. Samples were prepared for scanning electron microscopy (SEM) at this stage by transferring a small portion of the slurry to the surface of a specimen holder and simply allowing the acetone to evaporate. All SEM photographs were done in the secondary electron imaging mode with an accelerating voltage of 25kV.

Screening for particle size analysis was accomplished by placing the acetone/powder slurry successively in 120 mesh (125 μm opening), 230 mesh (63 μm opening) and 30 μm sieves and by squirting acetone onto and through the sieves thus recovering most of the fines which would otherwise adhere to larger particles and flakes. The different size fractions were centrifuged, decanted, and the residual acetone evaporated to yield clean, dry powder. The dry powder was then weighed for size analysis.

POWDER MORPHOLOGY

Pure tin was atomized under diverse operating conditions and the resultant product examined by SEM. Experimental powder lots examined in this study and the conditions used to produce them are listed in Table I. Under most of the operating conditions listed in Table I, a major portion of the melt was reduced to fine, nearly spherical particles. Figure 2 shows a representative view of powder from Run 9 whose conditions produced relatively fine particles. One can see that the particle sizes range from 50 μm or so down to 2 μm or less, and higher magnification views of this sample showed some particles smaller than 1 μm in diameter. While the product of all experiments contained a large proportion of spherical or nearly spherical powder particles, many other particulate morphologies were also generated. Some of these are shown in Fig. 3, which shows two views from Run 10. The low magnification view, Fig. 3a, shows some large nonspherical particles as well as several of a fibrous nature. It is not easy to visualize what processes might have influenced the shape of some of the larger irregularly shaped particles, but the flat bottomed one in the lower portion of the photo shows clear evidence of having contacted the perimeter of the quenching cup while it was still molten. Flat bottomed particles of this type were seen only infrequently, and invariably they were of large size. This indicates that nearly all of the particles were solidified before they penetrated the 9 mm quenchant depth.

The fibrous particles evident in Fig. 3a and at higher magnification in Fig. 3b demonstrate that the atomization process produced some melt filaments a few micrometers in diameter and as much as 100 μm long. It is likely that many of the finer particles were produced by capillary

Table I - Processing Conditions

Run No.	Melt Temp. (°C)	Inner Cup Temp. (°C)	Oil Temp. (°C)	Inner Cup Speed (ms^{-1})	Outer Cup Speed (ms^{-1})
1	393	403	104	16.4	28.3
2	278	268	41	17.6	30.0
3	296	306	68	19.3	33.6
4	371	350	90	23.1	32.0
5	353	315	73	14.6	33.6
6	364	379	79	19.6	35.6
7	367	362	73	16.6	7.44
8	377	358	76	22.1	25.4
9	363	356	70	17.5	30.8
10	360	328	58	16.8	40.1
11	386	373	71	16.8	9.35
12	384	348	86	15.9	16.8
13	395	350	89	17.6	25.4
14	312	346	84	9.05	31.3
15	391	359	90	22.9	32.3
16	328	375	87	30.4	32.4

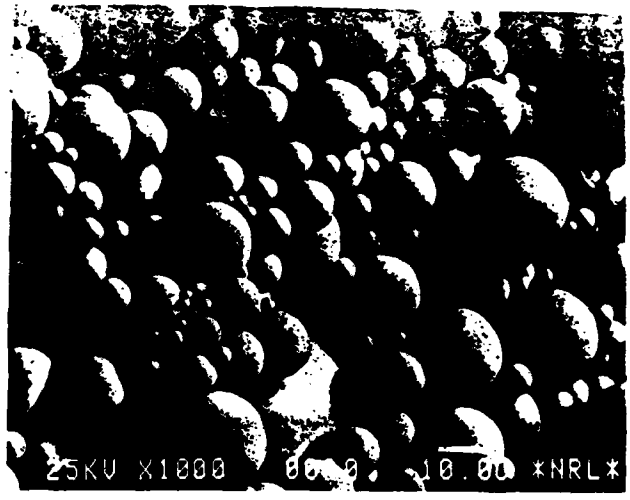
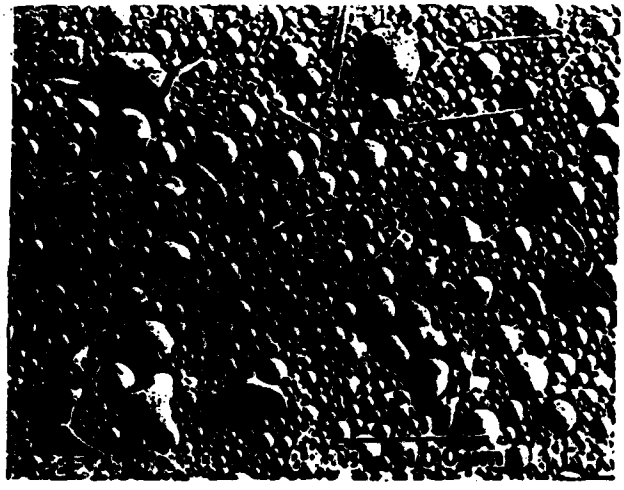
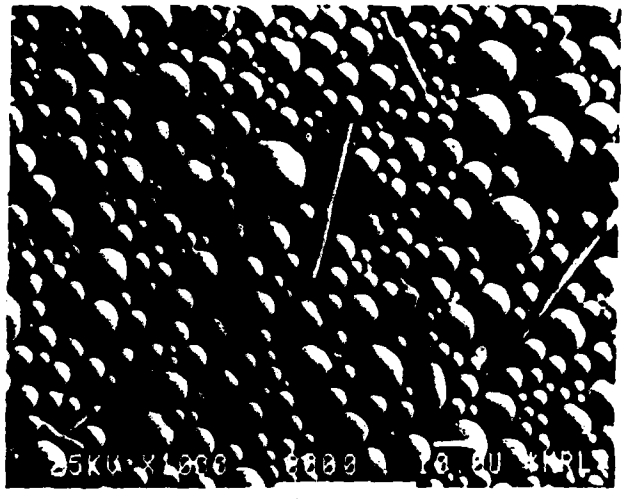


Fig. 2 Tin powder produced with an inner cup speed, V_i, of 17.5 ms^{-1} and an outer cup speed, V_o, of 30.8 ms^{-1}.

driven breakdown of even finer filaments, a process which is expected to occur on a submicrosecond time scale (12). The fibrous particles observed in this study often exhibited evidence of the Rayleigh instabilities which lead to this breakdown. In some fibers, such as the one near the top of Fig. 3b, the instabilities had proceeded to a marked degree before the fibe solidified. The fact that some of these fine fibers survived suggests that the rate of solidification was very high. The proportion of fibers in the melt was dependent on the melt superheat prior to atomization, with fewer fibers being generated at greater superheats, presumably because the additional superheat permitted time for their spheration before solidification. Conversely, melts atomized with low superheats exhibited a diverse range of particle shapes which could only have been produced with very high rates of cooling. The most striking product morphology under these conditions is thin flake of the type shown in Figs. 4 and 5. The flake Fig. 4 shows very clearly that the thin sheet of liquid tin solidified in a dendritic mode. The flake contains several dendrites which grew competitively. Across the upper edge of the flake it appears as if the sheet of liquid roll up before it solidified. In some areas this flake and others are extremely thin, a point which is demonstrated by Fig. 5. Figure 5a shows the major portion of a flake in which the crystallite morphology is less regular than in Fig. 4, but which is still recognizably dendritic in nature. Portions of this flake give the impression of being translucent, particularly that area shown in Fig. 5b. In this figure one can see fine spheres and fibers right through the flake. The difference in appearance of the particles above and below the flake leave no doubt that it is thin enough to be transparent to the 25kV electrons used to form the image. This means that in these areas the flakes are no more



(a)



(b)

Fig. 3 Tin powder produced with V_i = 16.8 ms^{-1} and V_o = 40.1 ms^{-1}. (a) Low magnification view. (b) Fibers showing Rayleigh instabilities.

than a few tens of nanometers thick. Such thin films must have solidified very rapidly to have avoided breaking down by Rayleigh instabilities, though at present we have no way to assess the rate of cooling or the solidification rate.

Despite the possibility of very high cooling rates evidenced by these thin flakes, much of the melt was converted to powder. The atomization process is very complex, but the nonspherical products generated with low superheats provide some insights into the complexities. For example, the rounded upper edge on the flake pictured in Fig. 4 suggests that at least some of the fibers form by the breakdown of sheets of liquid. This formation of fibers from sheets has been considered earlier (13) in terms of Rayleigh instabilities, but Fig. 6 demonstrates that the process may be more complex than was previously



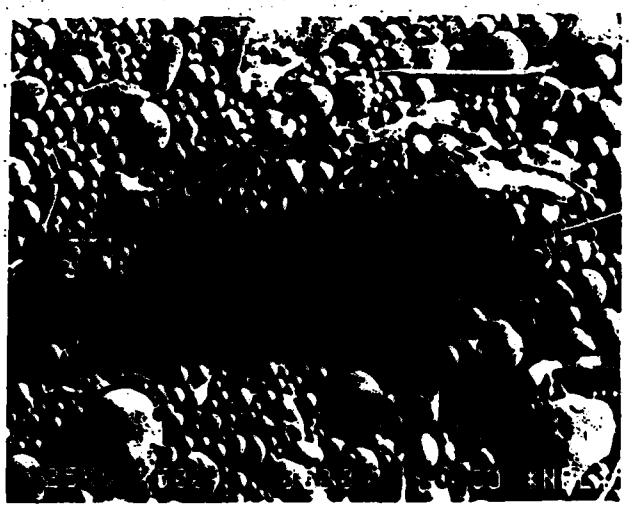
Fig. 4 Flake produced when melt had a low level of superheat. Processing conditions shown in Run 2 data of Table I.

visualized. This photo shows the formation of a fiber by the rolling up of a film fragment. This photo also shows how the fiber can incorporate fine particles which are adjacent to it as it forms, for the fiber has a series of bumps that must have been produced in such a way.

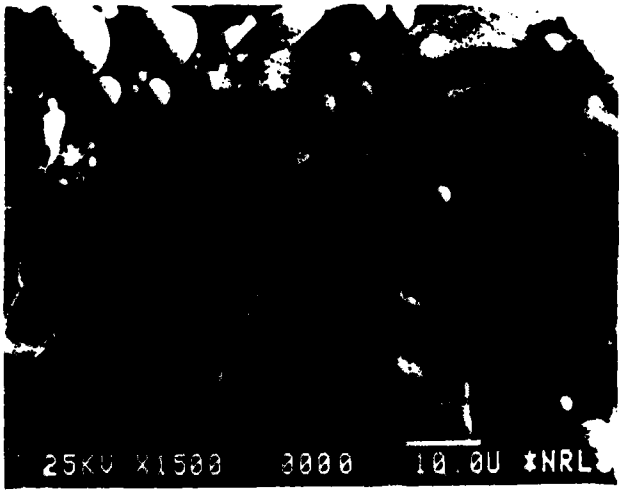
Figure 3b and earlier work (13) demonstrate how spherical particles can form from fibers, but Figs. 7 and 8 demonstrate that other routes are possible. Figure 7 shows a film fragment of complex shape which was rolling up around much of its perimeter when it solidified. Note that it has also incorporated small particles as it collapsed. Figure 8 shows a particle which probably formed in a similar fashion, but which incorporated even more small particles. Under slower cooling conditions these particles might well have formed spheres. These particles suggest that many of the large spherical particles observed in the work reported here may have resulted from a very complex chain of events. Particles of intermediate size would be expected to have experienced fewer interactions, a supposition which is supported to a limited degree by Fig. 9. This photo shows a film fragment which, with a little more superheat, would have formed a sphere of perhaps 10 μm diameter. The finest particles probably formed from breakup of small portions of the very thin film fragments, though the breakup process itself could be quite complex.

CUP SPEED EFFECTS

The experimental test conditions listed in Table I cover a range of operating speeds for both the inner and outer cups. The effect of these cup speeds on particle size has been examined by both TEM and by particle size analysis conducted by screening and weighing.



(a)



(b)

Fig. 5 Another flake from Run 2. High magnification view in (b) shows that flake is electron transparent.

The SEM examination is somewhat judgmental because the areas selected for photographs are subject to operator prejudice. Also, the number of particles sampled is limited and sampling errors can be significant. Despite these sampling problems, the SEM photos give a good visual impression of the size differences resulting from the process variations. The most apparent variation in particle size distribution was caused by varying the speed of the outer cup. Comparison of Fig. 3a and Fig. 10 gives a good indication of this effect. The runs from which these samples were taken both employed an inner cup rim speed, V_i, of 16.8 ms^{-1}, but the surface velocity of the oil in the outer cup, V_o, was 40.1 ms^{-1} for Fig. 3a and 9.35 ms^{-1} for Fig. 10. The photos were taken at the same magnification (300x), so one can readily see that the higher



Fig. 6 Partially formed fiber from Run 2.

outer cup speed produced substantially finer powder. The real difference in size is probably even greater than one would guess from looking at the two photos because Fig. 3a shows a greater number of large particles than was typical of the sample.

The effect of inner cup speed on particle size is demonstrated to some extent by Figs. 11 and 12. These photos are from runs which were done with nearly equal V_o's (31.3 ms^{-1} for Fig. 11 and 32.4 ms^{-1} for Fig. 12), but their V_i's varied substantially (9.05 ms^{-1} for Fig. 11 and 30.4 ms^{-1} for Fig. 12). Again, the photos are at the same magnification (300x), and the area shown in the photo with finer powder was deliberately selected to show a high proportion of coarse powder particles. The difference in size between the powder particles shown in these two photographs is not as great as that between [illegible].



Fig. 7 Irregularly shaped particle which solidified before spheration was complete. From Run 2.



Fig. 8 Irregularly shaped particle which incorporated many small particles. From Run 2.

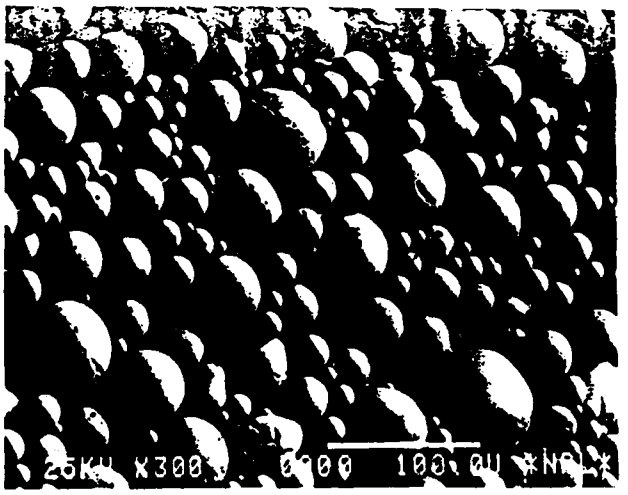


Fig. 10 Powder produced with V_i = 16.8 ms^{-1} and V_o = 9.35 ms^{-1}. Compare to Fig. 3a, which shows powder made with higher V_o.

3a and 10, but there is no doubt that the experiment done with a higher inner cup speed generated a finer powder.

The size effects which are illustrated by the SEM photographs just discussed were examined in a quantitative fashion for eight of the runs by screening the powders as described in the Powder Recovery and Characterization section. This analysis produced the data given in Table II. In this table, the five experimental runs with numbers 9 through 13 were conducted with inner cup speeds near 17 ms^{-1} and with varying outer cup speeds, while runs 9 and 14-16 were done with outer cup speeds near 32 ms^{-1} and varying inner cup speeds. Run 6 does not fit into either series, but the data from it complements the other in a way which will be discussed later. The data from runs 9-13,



Fig. 9 Small flake frozen before it could consolidate into a sphere. From Run 2.

plotted in Fig. 13, demonstrate the effect of increasing outer cup speed on particle size. The particle size analysis yielded only four data points, so the curves of Fig. 13 are somewhat schematic, but they clearly demonstrate that increasing the outer cup speed refines the mean particle size. At the lowest outer cup speed, for example, there is a peak in particle size in the size range 63 to 125 μm, and the peak shifts to progressively finer sizes at higher speeds. The peaks for the two runs with the fastest outer cup speeds both fall in the -30 μm range so the screening analysis could not determine the peak position.

The data for runs with a nearly constant outer cup speed are plotted in Fig. 14. The curves are again somewhat schematic, but they are calculated to interpolate between the data points. The differences between the curves are small, no doubt because the relatively high outer cup speed tends to mask the effects of varying the inner cup speed, the data shows that the slowest inner cup speed produced the coarsest powder, but that the finest powder was produced with an inter-

Table II - Particle Size Distribution Data

Run No.	V_i (ms^{-1})	V_o (ms^{-1})	Weight in Size Range -30 μm	+30 μm -63 μm	+63 μm -125 μm	+125 μm
6	19.6	35.6	77.9	21.2	0.9	0.0
9	17.5	30.8	70.5	24.3	4.6	0.6
10	16.8	40.1	74.1	17.7	4.7	3.5
11	16.8	9.35	4.1	39.2	41.2	15.5
12	15.9	16.8	17.5	50.8	27.5	4.2
13	17.6	25.4	44.3	43.2	11.4	1.1
14	9.05	31.3	50.8	37.1	8.5	3.4
15	22.9	32.3	61.9	32.0	5.5	0.6
16	30.4	32.4	64.0	31.5	3.9	0.5



Fig. 11 Powder produced with V_i = 9.05 ms^{-1} and V_o = 31.3 ms^{-1}.

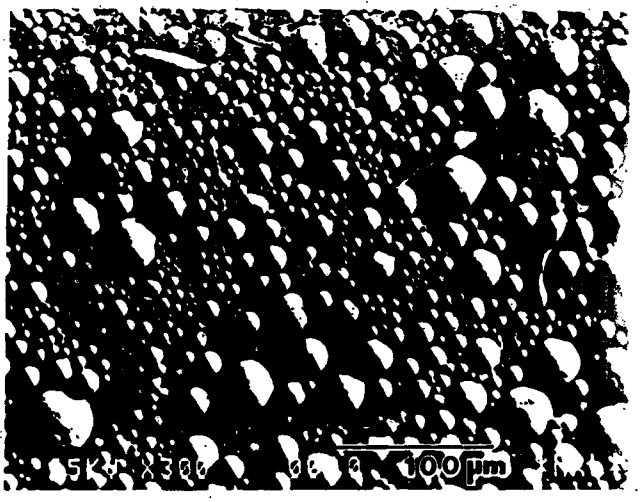


Fig. 12 Powder produced with V_i = 30.4 ms^{-1} a V_o = 32.4 ms^{-1}.

mediate inner cup speed (i.e. 17.5 ms^{-1}). This observation clearly suggests that if one's goal is to produce the finest powder, then the outer cup should be run at the highest practical speed, and the optimum speed for the inner cup should be experimentally determined. This hypothesis has not yet been rigorously tested, but the data for run 6 in Table II seem to confirm it. This run, done before the hypothesis was constructed, had a relatively high outer cup speed and an intermediate inner cup speed, and it produced the finest powder of all the runs conducted.

SUMMARY

These experiments demonstrate that the counter rotating fluid stomization process is capable of generating fine powder from molten metal, and that when the superheat is sufficiently high (100-125°C for tin) nearly all of the powder particles are spherical. With lower superheats much of the melt solidified before it had an opportunity to spherate, and the widely diverse nonspherical forms were examined to learn details of the atomization process. Neither cooling rates nor solidification rates have been determined, but the morphologies of the many nonspherical shapes derived from a low superheat melt suggest that they are very high. Mean particle sizes below 30 μm have been achieved, and there is good reason to believe that with higher cup speeds considerably smaller sizes could be produced.

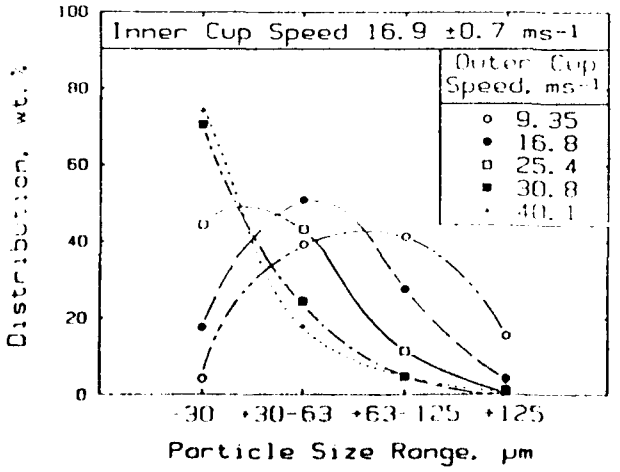


Fig. 13 Variation of particle size with outer cup speed when inner cup speed is nearly constant.

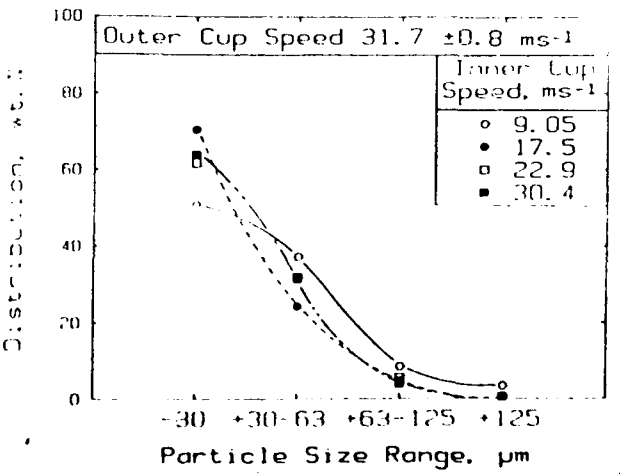


Fig. 14 Variation of particle size with inner cup speed when outer cup speed is nearly constant.

ACKNOWLEDGEMENTS

We are most appreciative of the help of Wayne Robey in building the apparatus and of Karin Rusin with the particle size analysis. Research support from the Navy Rapid Solidification Technology Program, administered by the Naval Air Development Center, is gratefully acknowledged.

REFERENCES

1. Duerig, T., Eseudin, M. and Keller, J, U.S. Patent 4,575,325.

2. Anderson, I. E. and Rath, B. B., "Rapid Solidification of Copper-Based Alloys," Rapidly Solidified Crystalline Alloys, S. K. Das, B. H. Kear and C. M. Adam, Eds., TMS-AIME, Warrendale, PA, 219-244 (1985).

3. Irving, R. J., "Injection Molding Takes on Powder Metallurgy Parts," Iron Age, 43-48 (Jan. 1985).

4. Erickson, A. R. and Wiech, R. E., "Injection Molding," Metals Handbook, Ninth Edition, Vol. 7, American Society for Metals, Metals Park, OH, 495-500 (1984).

5. Charles, S. W. and Popplewell, J, "Progress in the Development of Ferromagnetic Liquids," IEEE Transactions on Magnetics, Vol. MAG-16, No. 2, pp. 172-177 (March 1984).

6. Berkowitz, A. E. and Walter, J. L., "Ferrofluids Prepared by Spark Errosion," Journal of Magnetism and Magnetic Materials, 39, 75-78 (1983).

7. Yang, K. C. and Rowan, B. D., "Production of Gold, Platinum, and Palladium Powders," Metals Handbook, Ninth Edition, Vol. 7, American Society for Metals, Metals Park, OH, 148-151 (1984).

8. Lambert, J. B. and Droegkamp, R. E., "P/M High Temperature Materials, ibid, 765-772.

9. Dunkley, J. J., "The Production of Metal Powders by Water Atomization," Powder Met. Int., 10, 38-41 (1978).

10. Raman, R. V., Patel, A. N. and Carbonara, R. S., "Rapidly Solidified Powder Produced by a New Atomization Process," Metal Powder Report, 39, No. 2, 106-107 (1984).

11. Patel, A. N., Battelle Memorial Institute, Columbus, OH, private communication, (1985).

12. Adam, C. M. and Lewis, R. E., "High Performance Aluminum Alloys," Rapidly Solidified Crystalline Alloys, S. K. Das, B. H. Kear and C. M. Adam, Eds., TMS-AIME, Warrendale, PA, 157-183 (1985).

13. Lawley, A., "Preparation of Metal Powders," Ann. Rev. Mater. Sci., Ann. Revs. Inc., (8), 49-71 (1978).

No part of this paper may be reproduced, stored in a retrieval system, or transmitted, in any form or by any means, electronic, mechanical, photocopying, recording, or otherwise, without the prior written permission of the publisher.

Nothing contained in this paper is to be construed as a grant of any right of manufacture, sale, or use in connection with any method, process, apparatus, product, or composition, whether or not covered by letters, patent or registered trademark, nor as a defense against liability for the infringement of letters patent or registered trademark.

SAN: 204-7586
Copyright 1988 ASM INTERNATIONAL™
All rights reserved

This paper is subject to revision. Statements and opinions advanced in papers or discussion are the author's and are his responsibility, not ASM INTERNATIONAL; however, the paper has been edited by ASM INTERNATIONAL for uniform styling and format.

APPENDIX III

submitted to J. Amer. Ceram. Soc

Computer Modelling of Ceramic-Air PZT Composites

I: Bending and Fracture in Homogeneous Ceramics

M.S. Duesbery

GeoCenters Inc., Fort Washington MD 20744

and

M. Kahn

Naval Research Laboratory

Washington D.C. 20375

ABSTRACT

An interacting-particle method for computer simulation of deformation and fracture in polycrystalline ceramics is described and is applied to several simple cases. Models of the stress distribution produced in bending of a beam by terminal couples and by three-point loading are examined and compared with the predictions of Bernoulli-Euler elastic theory. It is shown that there can be significant deviations from theory in the case of three-point bending. The influence of an isolated void on the stress distribution in three-point bending is also considered. The failure mechanism of the model is considered in detail and compared with the basic experimental features of fracture and crack propagation.

1. Introduction

It is well-known that porosity in ceramic materials can affect physical properties such as elastic response, tensile strength and fracture behavior (1). It is widely accepted that modifications induced by the pores, or voids, in the internal stress distribution are responsible. For example, regions of enhanced stress associated with irregular voids or void clusters can reduce the fracture strength considerably (1). The relative importance of the size and surface roughness of the voids is not clear. Kahn et al. (2) showed that the transducing properties of PZT for hydrostatic pressure can be improved by the introduction of ordered arrays of disk-shaped voids. This was attributed to the cooperative stress concentrating effect of the void arrays, which enhances the piezoelectric response for a stress field normal to the disk plane (3). More recent work (4) on the mechanical properties of PZT containing ordered, disk-shaped voids suggests that the presence of void arrays can have an influence also on the tensile strength and fracture toughness.

It is important, both from a technological point of view and in the interest of basic knowledge, to understand the reasons for these effects. Analytic theoretical solutions are not available at present, so that a numerical approach is necessary. Techniques based on continuum mechanics, for example the finite-element method, have been used successfully to study the linear elastic and electric response of ceramic composites (e.g. 5-7). We will use an equivalent method derived from molecular dynamics (e.g. 8). The present manuscript will focus on an introduction to this model in a two-dimensional (2D) approximation and its performance in some elementary applications.

2. The Theoretical Model

The 2D polycrystalline ceramic solid will be modelled by a regular triangular lattice of particles or mass points bound by central pairwise forces. The particles, each representing a cluster of one or more grains, are taken to be non-deforming in a first approximation, so that strain accommodation and fracture are constrained to occur solely at the inter-particle bonds. The interparticle forces can thus be interpreted as an approximate representation of intergranular cohesion. This is a suitable model for the problem at hand, because experiment indicates that for PZT with fine-grained microstructure, failure occurs as a result of intergranular fracture (9). This suggests that the rate-controlling crack nucleation and propagation mechanisms operate at grain boundaries, i.e., the inter-particle bonds of the model.

This approach to fracture modelling is not new, but has been applied previously only at an atomistic level (10-14). The model is formally equivalent to FEM in the linear limit (14). Two aspects of the theoretical model deserve further discussion. The interparticle potential function, which governs the mechanical properties of the model, and the numerical solution of the problem will both be addressed below.

2.1 The Inter-Particle Potential Function

The particle binding forces are assumed to be derived from a central potential $V(|\underline{r}^{ij}|)$, such that the energy U^i of the ith particle is given by

$$U^i = \frac{1}{2}\sum_{j\neq i} V(|\underline{r}^{ij}|) \qquad [1$$

where $\underline{r}^{ij}$ is the relative position vector $\underline{r}^i$-$\underline{r}^j$ of particles i and j, and the summation extends over nearest neighbor particles only. The assumption of central forces is certainly a simplification, but the exact form of V(r) is unlikely to be of great importance for the present studies of stress distribution and fracture. It should be sufficient that the potential fit the elastic constants approximately and, beyond the linear limit, be somewhat harder in compression than tension, to reflect the behavior of the typical solid. In the case of fracture, a catastrophic phenomenon common to a wide range of materials with different binding forces, it is improbable that the details of the binding are of controlling importance.

Two different potential functions have been used. First, a standard Lennard-Jones form, smoothly truncated at a cut-off distance r_c, shown in fig. 1 as a function of r/a, where a is the lattice constant. For separations greater than r_c the particles no longer interact; therefore it seems reasonable to take $r>r_c$ as the criterion for breaking, or fracture, of a bond. The second potential considered was a bi-quadratic (piece-wise linear force) model. The latter potential parallels closely the atomistic model of Ashurst and Hoover (14).

The single free parameters in the potentials were fitted to the Young's modulus, using a value of 106GPa, representative of the largest values reported for dense polycrystalline PZT (15). Other elastic constants or characteristic properties could also be fitted by incorporating additional parameters into the potential, but this was considered an unnecessary complication; our intention is to examine the simplest possible model consistent with material properties. In the linear limit the two potentials describe identical models, predicting a value of 53GPa for the shear modulus, which compares well with a typical measured value (15) of 41GPa.

The lattice constant a determines the scale, or resolution of the model, and can be identified with the element size in FEM. The continuum limit is approached as a tends to zero. The model is scale-invariant; that is, the calculated stresses are independent of the value assigned to a, provided that the potential for each value of a is fitted to the same elastic constant. For the present problem, in which features on an intergranular scale are of primary importance, a will be considered to have a value of the same order as the grain, or crystallite size, about 4um for the experimental work (2,4) cited above.

2.2 Computational Methods

The total energy of the particle assembly, W, can be written as a sum over the individual particle energies [1] as

$$W = \sum_i U^i = \frac{1}{2} \sum_i \sum_{j \neq i} V(|\underline{r}^{ij}|) \qquad [2$$

To simulate deformation, appropriate boundary conditions in the form of fixed displacements or constraining forces must be applied to the model. It is usually convenient also to apply an initial, approximate displacement field, although this is not necessary. The assembly will then no longer be in equilibrium and the force $\underline{F}^i$ on the ith particle will be given by

$$F^i_\alpha = P^i_\alpha - \frac{\partial W}{\partial r^i_\alpha} = P^i_\alpha - \sum_{j \neq i} \frac{\partial V}{\partial r^{ij}_\alpha} \qquad [3$$

where $\underline{P}^i$ represents the constraint forces, if present, and . denotes a resolved vector component. The numerical problem is to adjust or "relax" the coordinates $\underline{r}$ until equilibrium is reached. This is done by the conventional molecular dynamic procedure of allowing the particles to execute Newtonian motion subject to the forces [3]. At periodic intervals the kinetic energy is quenched from the assembly, which therefore tends to a configuration of minimum potential energy.

The specific deformation to be modelled determines the form of the constraints. An example is provided by the case of a bent beam, which can be modelled with constraints of terminal couples (TC) (fig.2(a) or with three-point (TP) force constraints (fig. 2(b)). Consider first the case of TC

bending, with a beam bent into a circular arc of radius R, about an axis normal to the plane of the (2D) beam by couples M at each end, causing a central deflection normal to the length of the beam and parallel to the x_2 axis (see fig. 2(a)). The displacement field $\underline{u}$ is given approximately by (16,17)

$$u_1 = -r_1 r_2/R$$

$$u_2 = r_1^2/R \qquad [4$$

These displacements define an inhomogeneous strain field in the beam, but because it remains approximately in equilibrium, residual forces will be small, provided that boundary conditions appropriate to terminal couples (e.g. fixing of the positions at the ends of the beam) are satisfied. The same displacement field can be used as an initial solution for modelling of three-point bending. However, in this case the boundary conditions are that the particles in contact with the three constraining anvils (fig. 2(b)) are not permitted to move in the x_2 direction. For these boundary conditions the displacement field [4] is not a good representation of the equilibrium elastic solution, so that the residual forces on the displaced particles will be much larger.

Voids can be modelled by removing an appropriate set of particles from the model. Stress concentrations induced by flaws can be simulated by stretching inter-particle separations, either by applying constant constraint forces to specific particles or by breaking interparticle bonds.

3. Bending and Fracture Studies.

The behavior of simple cases will be examined, in order to demonstrate the reliability of the model in situations for which the approximate solution is known. The stress distributions produced by terminal couple and three-point bending of homogeneous specimens will be considered as well as that of a bent sample containing an isolated void. Fracture, crack propagation and crack stress enhancement for the case of uniaxial stress applied to homogeneous models will also be examined.

3.1 Deformation by Bending

As noted already, there are two distinct sets of bending constraints to be considered, TC (terminal couple) and TP (three-point) bending. While the latter case is more accurately descriptive of the experimental environment, the former has the advantage that periodic boundary conditions can be used, permitting use of a smaller model. The displacement field [4] is an approximation based on the Bernoulli-Euler theory of TC bending (16,17). The same theory is valid for bending by TP loading, but the elastic displacement field must be modified to accommodate the boundary conditions of vanishing normal stress at the specimen ends (18). The displacements for TP bending of a beam with length L are

$$u_1 = - r_1 r_2 (L - r_1)/R_0 L$$

$$u_2 = r_1^2 (3L/2 - r_2)/3R_0 L \qquad [5$$

in which the radius of curvature R_0 is that at the center of the bent beam.

TC and TP bending can be contrasted by comparing the maximum developed tensile stresses. Consider a beam with the geometry shown in fig. 2(c), i.e. of length L and thickness t, deflected centrally through a distance d either by couples M (TC loads, fig. 2(a)) or by TP loads F (fig. 2(b)). The thickness of the specimen normal to the plane of the figure will be denoted by w. For TC bending, the stored elastic energy W and maximum developed tensile stress are given in terms of the deflection d by

$$W = \frac{8}{3}.\frac{wEt^3}{L^3}.d^2 = M\theta \qquad [6$$

$$\sigma_m = 4.\frac{Et}{L^2}.d \qquad [7$$

where E is Young's modulus and θ is half the angle of arc into which the beam is bent. The moment can be estimated directly by numerically integrating the stress moments of the particles at the end surfaces of the specimen. An alternative is to calculate the moment using [6], from the stored energy and the known angle of bending.

For TP loading, the expressions analogous to [6] and [7] are

$$W = 2.\frac{wEt^3}{L^3}.d^2 = \frac{Fd}{2} \qquad [8$$

$$\sigma_m = 6.\frac{Et}{L^2}.d \qquad [9$$

The expressions [6-9] follow directly from Bernoulli-Euler bending theory; the energy [6,8] and stress [7,9] equations differ only in the numerical factors, because of the different loading conditions.

For the bending simulations, a 2D model of 150 x 32 particles was used. Results will be given for a deflection of 0.045a, which for TC bending would correspond to a maximum stress [12] of 31.6MPa or 2.25×10^{-4}E in terms of the model Young's modulus, within the linear regime. For TP bending the full model was allowed to relax. For the TC case, periodic boundary conditions were used and only a central, periodic region of 25 x 32 particles was relaxed. The values of maximum stress, stored elastic energy and applied moment or load are summarized in Table I for both TC and TP bending. The row labelled BE contains values calculated from the Bernoulli-Euler equations [6-9], while the numbers in the row marked NM have been calculated from the relaxed numerical model.

For TC bending, the energies and stresses are the same as the NM values within the accuracy of the model. For TP bending, on the other hand, the numerical values for load, maximum stress and elastic energy are each about 20% lower than predicted by BE theory. To understand the reason for this discrepancy it is necessary to examine the longitudinal displacement fields, in which most of the energy is stored. These are shown in fig. 3 for $x_2 = t/2$ (i.e the tensile edge), as a function of position along the half-length of the beam (the left and right ends of the abscissa in fig. 3 correspond respectively to the center and one end of the beam). All displacements have been normalised to the maximum value of Lt/4R (see [4]) expected for TC bending. The straight line in fig. 3 shows the longitudinal displacement variation for the TC-bent beam, for reference; there is no distinction between theory [4] and the numerical model in this case. The dash-dot and dashed curves in fig. 3 show, respectively, the theoretical [5] and numerical model displacements for TP bending. Both of these curves rise more sharply than the

TC line close to the beam center, because the central curvature is larger for TP than for TC bending, then drop below the TC line towards the end of the beam due to the absence there of normal loading. The displacements for the numerical model are consistently less than the Bernoulli-Euler theoretical values, by about 20% at the center, dropping to about 9% less at the end, of the beam. This accounts for the lower maximum stress, since this is determined solely by the conditions at the center of the bar. Whether or not this reduced tensile stress is observable experimentally is uncertain. The calculations were performed on the assumption that the anvil-specimen contacts are frictionless. Any resistance to sliding at these points would inhibit longitudinal displacements at the surface and thereby reduce the deviations from B-E theory.

The modelled ratio of load to maximum stress remains the same as in BE theory, confirming that for the central region of the bent specimen, which is the region of principal interest for ceramic fracture, BE elastic theory is applicable. This also suggests that the TC model, with its associated reduced computational needs, is an adequate approximation for fracture studies.

Tensile and compressive stress levels for a TP bent specimen are shown in fig. 4 as contours of constant stress; the values in both diagrams have been normalised to the maximum BE stress, with contour levels spaced at intervals of 0.2 of this reference figure. The minor irregularities in the contour plots in both figs. 4 and 5 are due to the approximations involved in numerical interpolation. Figs. 4(a) and (b), respectively, show the BE and NM tensile stresses. The analogous plots for TC bending would simply show a set of horizontal lines (to be precise, the contours would be circular arcs, but

the curvature would not be visible in the diagram). There is little difference between the two diagrams, except in the magnitude of the levels and at the ends of the beam, where the loading details become dominant (22). The stress components other than the tensile stress parallel to the length of the model are small for both BE and NM cases. For the BE approximation, the only other significant component is σ_{12}, with maximum magnitude about 5% of the maximum tensile stress. In the NM case, σ_{12} shear stresses of magnitude up to 10% of the maximum tensile stress are present, together with σ_{22} tensile or compressive stresses up to 30% of the maximum longitudinal stress in the immediate neighborhood of the anvil contacts.

The effect of introducing a void into the bent beam is illustrated in fig. 5, which shows stress contour plots for the TP bent specimen of fig. 4(b) with an enclosed void of dimensions 19 x 8 particles, positioned centrally lengthwise and close to the tensile surface. The full specimen is shown in fig. 5(a); in order to better resolve the detail around the void, the area outlined with broken lines in fig. 5(a) is magnified and displayed in fig. 5(b). The principal change in the tensile stress field involves shifts in the contours, conforming to the added boundary conditions of vanishing stress normal to the void surfaces. Noticeable is that the stress contours bulge in the region over the cavity, containing a small closed-contour area of enhanced stress. The contours can also be seen to be more densely packed immediately below the void.

The void in fig. 5 has relatively sharp corners and it is natural to inquire whether the numerical model develops stress concentrations at these corners. No such features are detectable at the resolution of figs. 5(a) and (b), but detailed examination of the particle stresses shows that the stress

at the upper corners of the void is about 10% larger than the stress at the center of the top edge of the void. At the bottom of the void the stress enhancement at the corners, defined in the same way, is smaller, with a magnitude of only 2%. This lower result is due to the overriding stress-concentrating effect of the narrow channel below the void; for the same void centered in a model stressed in uniaxial tension, the corner stress enhancement is 10% at each of the four corners.

3.2 Fracture in Uniaxial Stress

With the present technique it is not possible to model cracks with a tip radius smaller than about half the lattice spacing a. If a is considered to have grain-sized dimensions, cracks are intrinsically blunt, but this is not necessarily a disadvantage. In a real polycrystalline ceramic there will be flaws with dimensions ranging from the atomic, "microcrack" level to a grain-sized scale and larger. Confinement of crack propagation to intergranular paths suggests that pre-existent microcracks within grains do not control failure. Rather it is proposed that stress concentrations at the tips of larger-scale "macrocrack" flaws, in the grain boundaries, act locally to enhance microcrack stresses and thereby cause failure by a cascade process. Nucleation and propagation of such macrocracks will be the subject of this section.

Consider first the case of a uniform, uniaxial applied stress oriented parallel to one of the primitive vectors of the lattice, as shown in fig. 6(a). Tensile failure of the Lennard-Jones model occurs at an applied stress of 228MPa. This value, which will be called the cleavage or intrinsic fracture stress, is equal to the strength of a single bond for this particularly simple

case, as can be seen from the following argument. Fig. 6(a) shows the particle bonding scheme. The reference particle A is bonded to the six particles labelled B-G. Because each bond is shared by two particles, the binding of particle A can be considered due only to the three bonds AB, AC and AD. For a stress directed as shown, only the bond AC resists the pull, because the lengthening of the bonds AB and AD due to the horizontal extension is exactly cancelled by the vertical Poisson contraction (a consequence of the 60° angles and Poisson's ratio = 1/3 of the triangular lattice geometry). Hence the model fails when the applied stress reaches the strength of the AC bond.

Next consider the same stress applied to a Lennard-Jones model with an embryo macrocrack introduced by breaking a single bond on one stressed edge of the model. The initial state is depicted in fig. 6(b), which shows a small portion of the particle lattice, with the broken bond indicated by the absence of a bonding line. This model begins to fail at a level of 190 $\pm$ 15Mpa, about 15% lower than in the case of a virgin sample. The resulting crack propagates throughout the model without the need for further increase in the applied stress. This suggests that the stress required for crack propagation is less than the cleavage stress, presumably due to stress concentrations at the crack tip. In fact the stress at the tip of the embryo crack just prior to fracture is 270 $\pm$ 15MPa, not only larger than the applied stress but also substantially larger than the cleavage strength. The particle lattice can support this larger stress locally because when the deformation is inhomogeneous, as is the case at the crack tip, the balance between tensile extension and Poisson contraction discussed above is no longer operational (due to loss of triangular symmetry) and additional bonds resist the external forces. The same

behavior is found for the biquadratic potential, though at different stress levels due to the different non-linear properties.

It is worthwhile to look in more detail at the micromechanics of failure in the model. In the stress-free state, all bonds in the model of fig. 6(a) have a length equal to the lattice constant a, for which the potential function is a minimum as shown in fig. 1. When a horizontal tensile stress (fig. 6(a)) is applied, the parallel bonds increase in length and the bond energies increase, as can be seen from the potential curve in fig. 1. At the same time the Young's modulus, which is proportional to the second derivative of the potential, decreases. With continued increase in bond length this modulus will decrease to zero, leading to an instability towards a homogeneous increase in length of all the horizontal bonds.

This mechanism alone clearly does not model the essential inhomogeneity of fracture in real materials. However, consideration of the vibrational properties of the strained lattice shows that as the bonds lengthen beyond the Young's modulus instability, but before the fracture criterion ($r = r_c$) is reached, a dynamic instability intervenes, in which alternate horizontal bonds undergo opposite changes in length. For example, in the sequence of particles F-A-C in fig. 6(a), the bonds FA and AC will increase and decrease in length, respectively, with the total length FC remaining constant; a decrease in internal energy accompanies these changes. More generally, while the average particle spacing remains the same, a lowering of energy can be realised by increasing the length of one critical bond at the expense of a decrease in length of the remainder.

This dynamic instability signals the onset of inhomo-geneity, and represents the model analog of a crack nucleus. However, free surfaces have

not yet been formed and propagation does not necessarily occur. Further energy must be supplied before a critical bond can extend to meet the 'broken' criterion. As noted above, the lengthening critical bond receives energy from the shrinkage of other bonds in the model. How much of this energy can be transferred, and whether or not it is sufficient to complete the fracture process, determine whether the crack can propagate. Without this energy transfer mechanism or some extrinsic source of energy, fracture cannot proceed.

It is now possible to rationalise the interplay of cleavage stress and surface energy in the model. For a notched specimen, dynamic instability will first occur at the tip of the notch where the deformation is largest. One bond will begin to extend, drawing energy from the contraction of neighboring bonds. Provided that sufficient energy can be extracted, the process will continue until the bond length exceeds the critical fracture length; new surface will then have been formed and fracture will be complete. The same physical state which existed at the crack tip prior to fracture will then be reproduced, advanced by a distance of one particle spacing, so that propagation will continue. If the energy available is insufficient to stretch the extended bond to the critical fracture distance, then despite the presence of the instability the crack will not propagate until additional energy is supplied. In other words, although a crack has been nucleated, it is stable against propagation.

We have also calculated the stress enhancement at the tip of a macrocrack as a function of the crack length for cracks of length varying from a to 5a, inserted normal (or as closely normal as possible) to the stress direction in one edge of the specimen. The expected stress enhancement for

a sharp crack (i.e. one for which the length is much larger than the tip radius) in a continuum (e.g. 18) is

$$(\sigma_E - \sigma)/\sigma = 1.12\ (c/2r)^{0.5} \qquad [10$$

where σ_E is the stress at the crack tip, σ the applied stress, c the crack length and r the crack tip radius. The value of $(\sigma_E - \sigma)/\sigma$ calculated from the model is shown in a logarithmic plot against c in fig. 7. The calculated dependence is roughly linear; the ln(c) = 0 intercept of the straight line with slope 0.5 drawn in fig. 7 suggests an effective crack tip radius of 0.56a, quite consistent with the geometry of the model (fig. 6(b)). Bearing in mind that the length to tip radius ratio of the modelled macrocrack does not approach the limiting values required for validity of [10], the agreement is reasonable and demonstrates that macrocracks share the stress concentrating capability of sharp microcracks.

4. Summary and Discussion

An interacting particle computer modelling technique for the study of deformation and fracture processes in polycrystalline ceramics has been described. The method is intrinsically capable of accounting for non-linearity and for the extremes of deformation encountered in fracture.

The method has been used to model bending of homogeneous ceramics. For the case of bending by terminal couples, the deformed model agrees closely with the Bernoulli-Euler theory. For three-point bending, however, the maximum tensile stress and load in the numerical model are found to be about 20% lower than predicted by the theory. This discrepancy is traceable to reduced tensile displacements in the numerical model, a result of boundary conditions more accurately descriptive of the experimental environment.

The effect of an isolated rectilinear void on the stress distribution in three-point bending has been considered. The principal changes in the internal stress field are consistent with the boundary conditions of no load normal to the surfaces of the void and the channeling of isostress contours around the void to maintain elastic equilibrium.

Fracture by nucleation and propagation of macrocracks (i.e. cracks with tip radii of the same order as the model lattice constant) has been modelled in perfect and notched homogeneous ceramic specimens. For notched fracture, crack propagation begins and continues at a stress about 15% lower than the cleavage stress. The stress at the tip of the notch just before crack initiation reaches a level some 20% higher than the cleavage stress, due to the presence of inhomogeneous deformation at the notch tip. This variation in the critical stress required for failure has its origin in the micromechanics of the model. Two criteria must be satisfied for fracture to occur. First, at least one bond must be stretched to a critical, unstable level, which requires a local stress which dependent on the bond environment. Secondly, enough energy must be available to permit the instability to proceed to bond breakage.

The stress concentration at the tip of a macrocrack has been modelled as a function of crack length. Even for short, blunt cracks, the results are in fair agreement with the predictions of continuum elasticity for sharp cracks.

References

1. R.W. Rice, "Microstructure Dependence of Mechanical Behavior of Ceramics", pp199-381 in Treatises on Materials Science and Technology, vol. II: Properties and Microstructure. ed. R.K. MacCrone, Academic Press: New York, 1977.

2. M. Kahn, A. Dalzell and B. Kovell, pp273-276 in Proceedings of the Sixth IEEE International Symposium on Applications of Ferroelectrics, Lehigh University, Bethlehem PA, 1986.

3. M. Kahn, "Acoustic and Elastic Properties of PZT Ceramics with Anisotropic Pores", J. Am. Ceram. Soc., 68 [11] 623-628 (1985).

4. M. Kahn, B. Kovel and D. Lewis III, "Fracture Phenmena in PZT Ceramic containing Arrays of Flat Voids", to be published.

5. S. DaVanzo, Ph.D thesis, Penn. State University, 1986.

6. S. Davanzo, A. Safari and R.E. Newnham, "Finite Element Modelling of Perforated PZT-Polymer Composites", FerroelectricsLet. 3, 109-121 (1985).

7. W. B. Carlson, S.E. Trolier, A. Safari, R.E. Newnham and L.E. Cross, pp641-644 in Proceedings of the Sixth IEEE Symposium on Applications of Ferroelectrics, Lehigh University, Bethlehem PA, 1986.

8. W.G. Hoover, "Molecular Dynamics", Lecture Notes in Physics #258, (Springer-Verlag, New York, 1986).

9. A. Kishimoto, K. Koumoto and H. Yanagida, pp71-72 in the Third U.S.: Japan Seminar on Dielectric and Piezoelectric Ceramics, Toyama, Japan, 1986.

10. R. Thomson, C. Hsieh and V. Rana, "Lattice Trapping of Fracture Cracks", J. Appl. Phys. 42 (1971) 3154-3160.

11. J.E. Sinclair and B.R. Lawn, "An Atomistic Study of Cracks in Diamond-Structure Crystals", Proc. R. Soc. London A329 (1972) 83-103.

12. M.F. Kanninen and P.C. Gehlen, "A Study of Crack Propagation in alpha-Iron", in "Interatomic Potentials and the Simulation of Lattice Defects", edited by P.C. Gehlen, J.R. Beeler jr. and R.I. Jaffee, (Plenum Press, New York, 1972) 713-724.

13. C. Hsieh and R. Thomson, "Lattice Theory of Fracture and Crack Creep", J. Appl. Phys. 44 (1973) 2051-2063.

14. W.T. Ashurst and W.G. Hoover, "Microscopic Fracture Studies in the Two-Dimensional Triangular Lattice", Phys. Rev. B14 (1976) 1465.

15. pp. 66,78 in "Landolt-Bornstein Numerical Data and Functional Relationships in Science and Technology", New Series, Group III, vol. 1, edited by K.-H. Hellwege and A.M. Hellwege, Springer- Verlag: New York, 1966.

16. I.S. Sokolnikoff, pp101-107 in "Mathematical Theory of Elasticity", second edition, McGraw-Hill: New York, 1956.

17. S.P. Timoshenko and J.N. Goodier, pp284-287 in "Theory of Elasticity", third edition, McGraw-Hill: New York, 1970.

18. A.E.H. Love, pp138-140 in "A Treatise on the Mathematical Theory of Elasticity", fourth edition, Dover Publications: New York, 1944.

19. B.R. Lawn and T.R. Wilshaw, p52-65 in "Fracture of Brittle Solids", Clowes and Sons: London, 1975.

TABLE I

The load, maximum developed stress and elastic stored energy in bars deformed by terminal couples and by three-point bending to a central deflection of $3 \times 10^{-4} L$ (fig. 2(c)). Values are shown for the Bernoulli-Euler theory (BE) and for the numerical model (NM).

	Couple bending			Three-point bending		
	moment μN-m	max. stress MPa	energy nJ	load mN	max. stress MPa	energy nJ
BE	6.75	31.6	8.1	21.4	47.5	6.1
NM	6.70	30.5	8.1	17.9	37.7	5.1

Figure Captions

Fig. 1 The interparticle potential V(r) as a function of the interparticle spacing. The cutoff radius r_c is shown.

Fig. 2 (a) Schematic diagram of a beam bent by terminal couples M. Axes and sense of deflection are indicated. (b) Schematic diagram of a beam bent by three-point loading. The loads F and reference axes are shown. (c) Definitions of length L, thickness t and deflection d for a general bent beam.

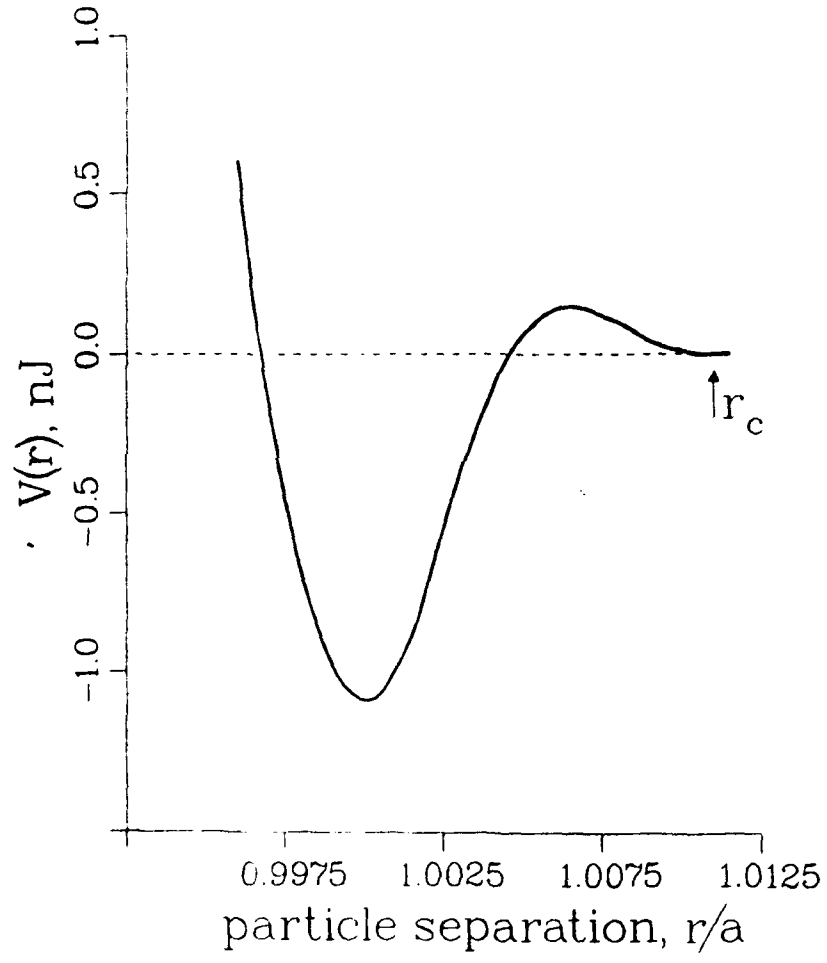
Fig. 3 The longitudinal displacement (in units of the maximum TC displacement u_{max}) in a bent beam as a function of position in units of the beam length (with center as origin). The straight line shows the variation for Bernoulli-Euler and numerical TC bending. The dash-dot and dashed curves show, respectively, displacements for Bernoulli-Euler and numerical TP bending.

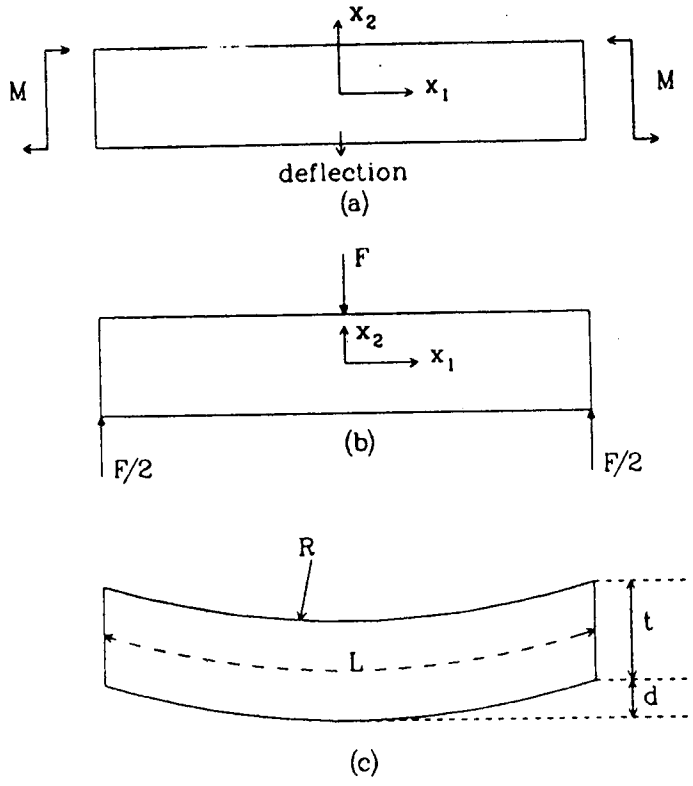
Fig. 4 Contours of constant tensile stress for a beam deformed by three-point bending in (a) the Bernoulli-Euler elastic approximation and (b) the numerical approximation. All stresses are normalised to the maximum tensile stress in the Bernoulli-Euler model.

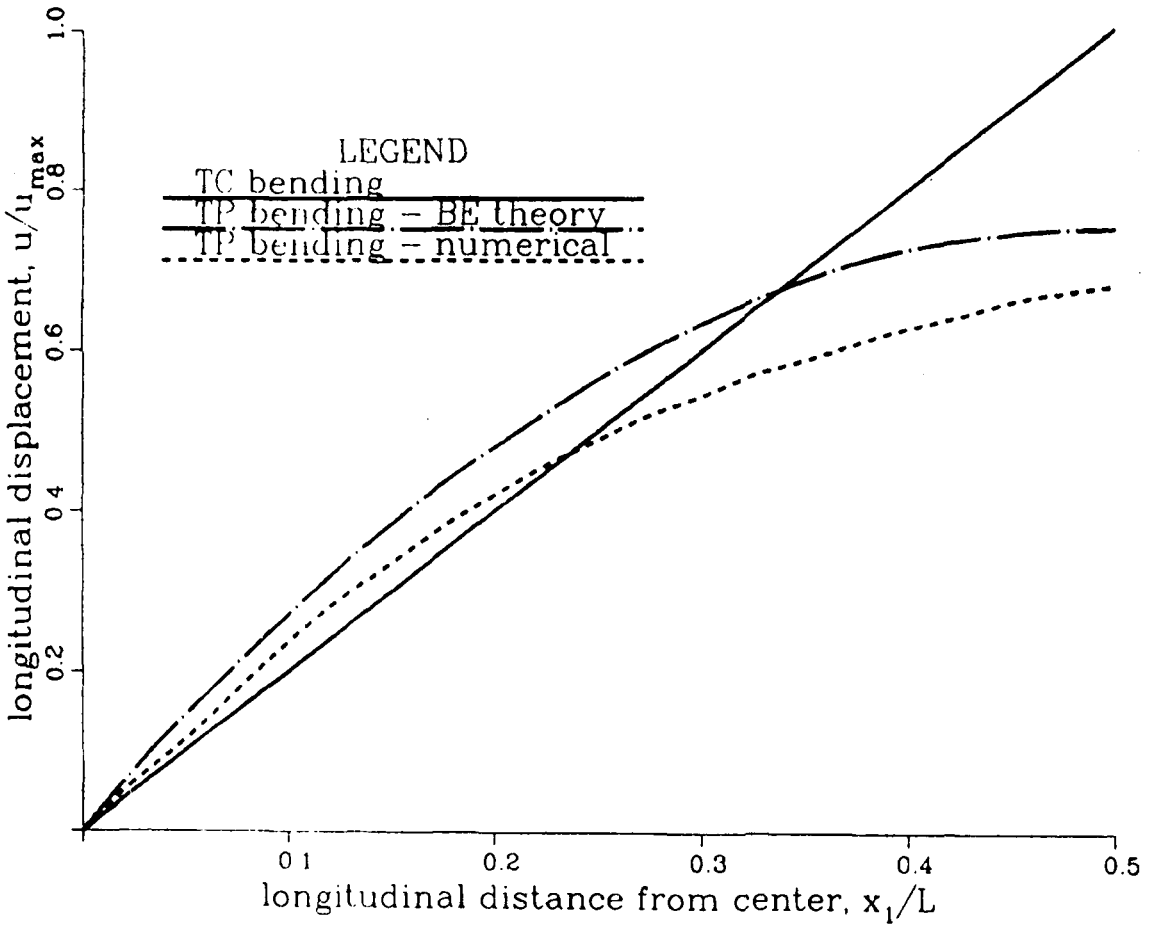
Fig. 5 Contours of constant tensile stress around an isolated void in a beam deformed by three-point bending. The diagram (a) shows the full beam; in (b) is shown an expanded view of the area shown in dashed outline in (a). All stresses are normalised to the maximum tensile stress in the Bernoulli-Euler model.

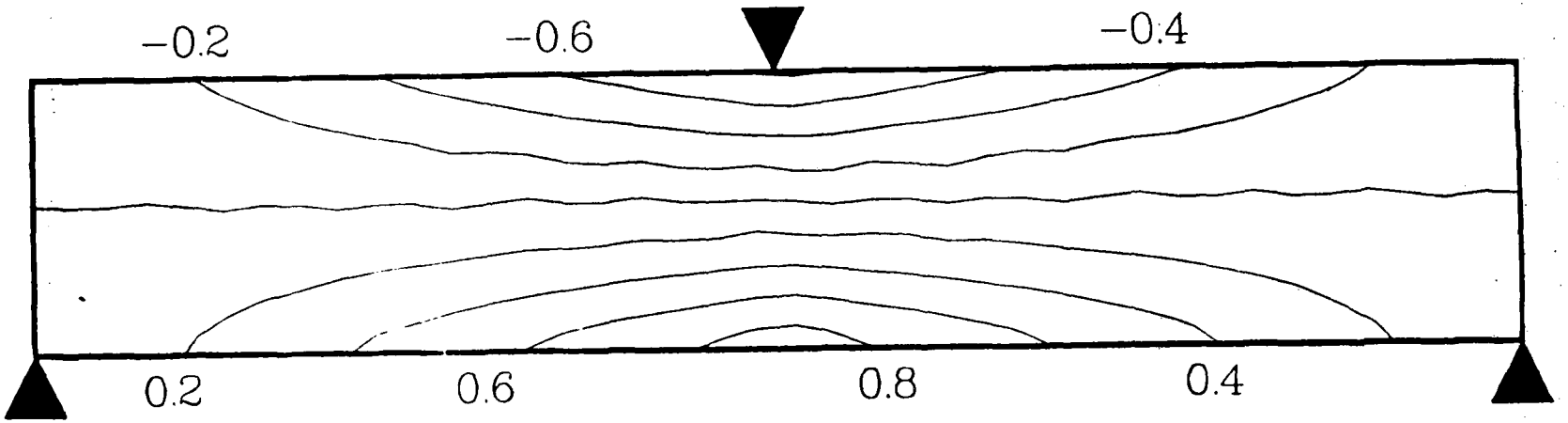
Fig. 6 (a) Schematic diagram of the bonding scheme of the reference particle A to the six neighboring particles B-G. The orientation of tensile stress for uniaxial or bending deformation is shown. (b) Schematic diagram of the triangular lattice showing the orientation of the tensile stress, the location of the broken bond and the fracture path for notched fracture.

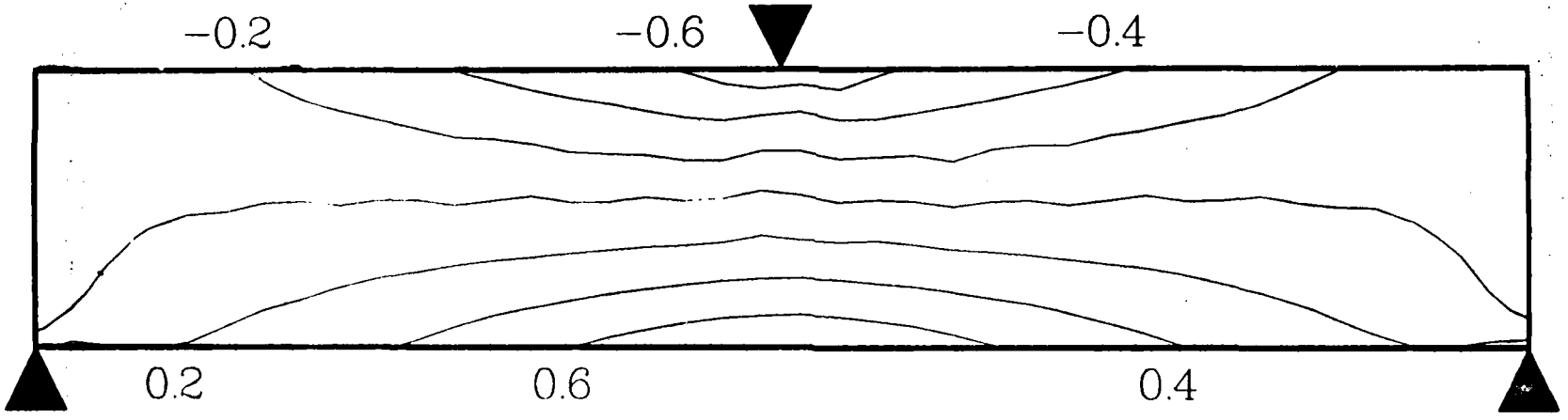
Fig. 7 The dependence of the calculated stress enhancement $\left(\frac{\sigma_\epsilon - \sigma}{\sigma}\right)$ at a crack tip on the length of the crack, c.

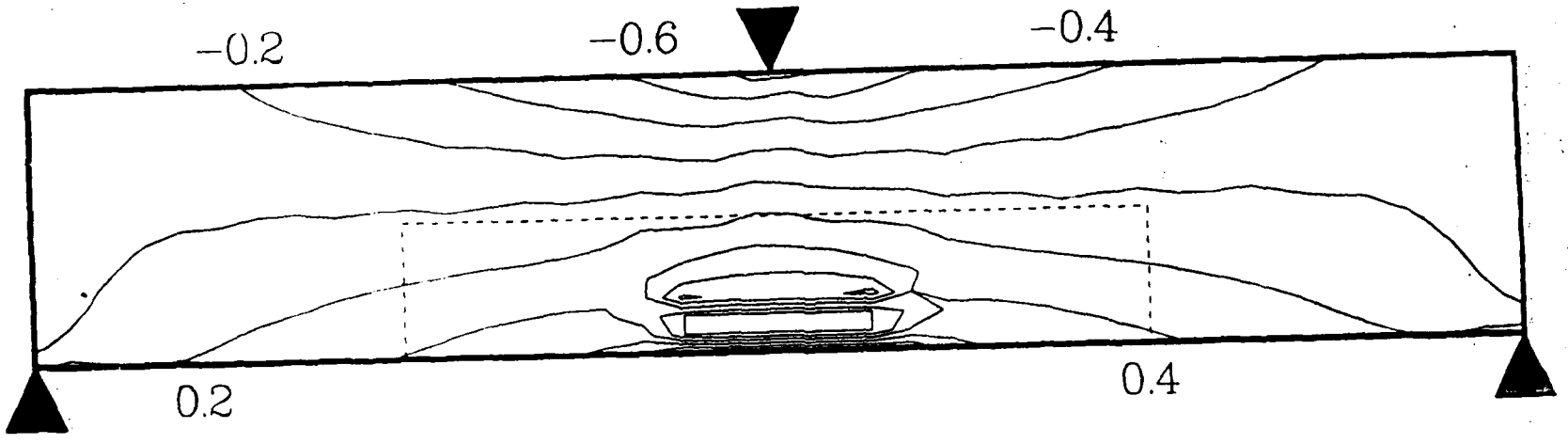

1.0
0.5
0.0
−0.5
−1.0
V(r), nJ
r_c
0.9975
1.0025
1.0075
1.0125
particle separation, r/a

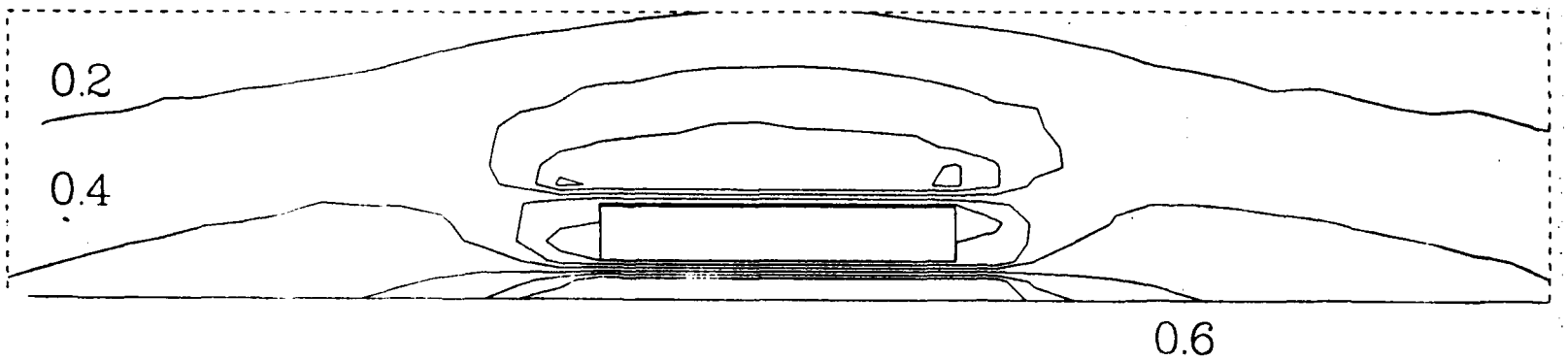

x2
x1
M
M
deflection
(a)
F
x2
x1
(b)
F/2
F/2
R
t
L
d
(c)

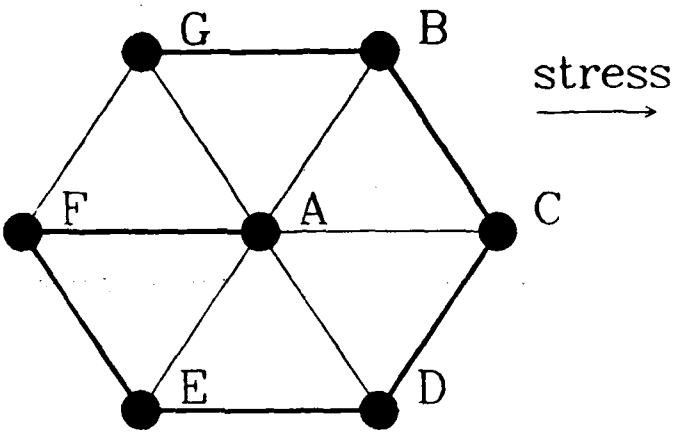

LEGEND
TC bending
TP bending – BE theory
TP bending – numerical
longitudinal displacement, u/u_{max}
0.2
0.4
0.6
0.8
1.0
0.1
0.2
0.3
0.4
0.5
longitudinal distance from center, x_1/L


−0.2
−0.6
−0.4
0.2
0.6
0.8
0.4

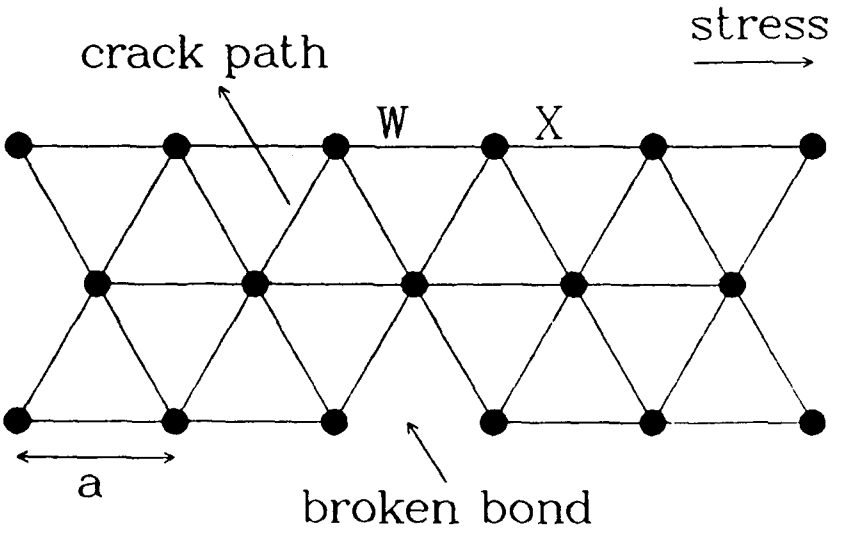

−0.2
−0.6
−0.4
0.2
0.6
0.4


−0.2
−0.6
−0.4
0.2
0.4


0.2
0.4
0.6



(a)



(b)

FIG

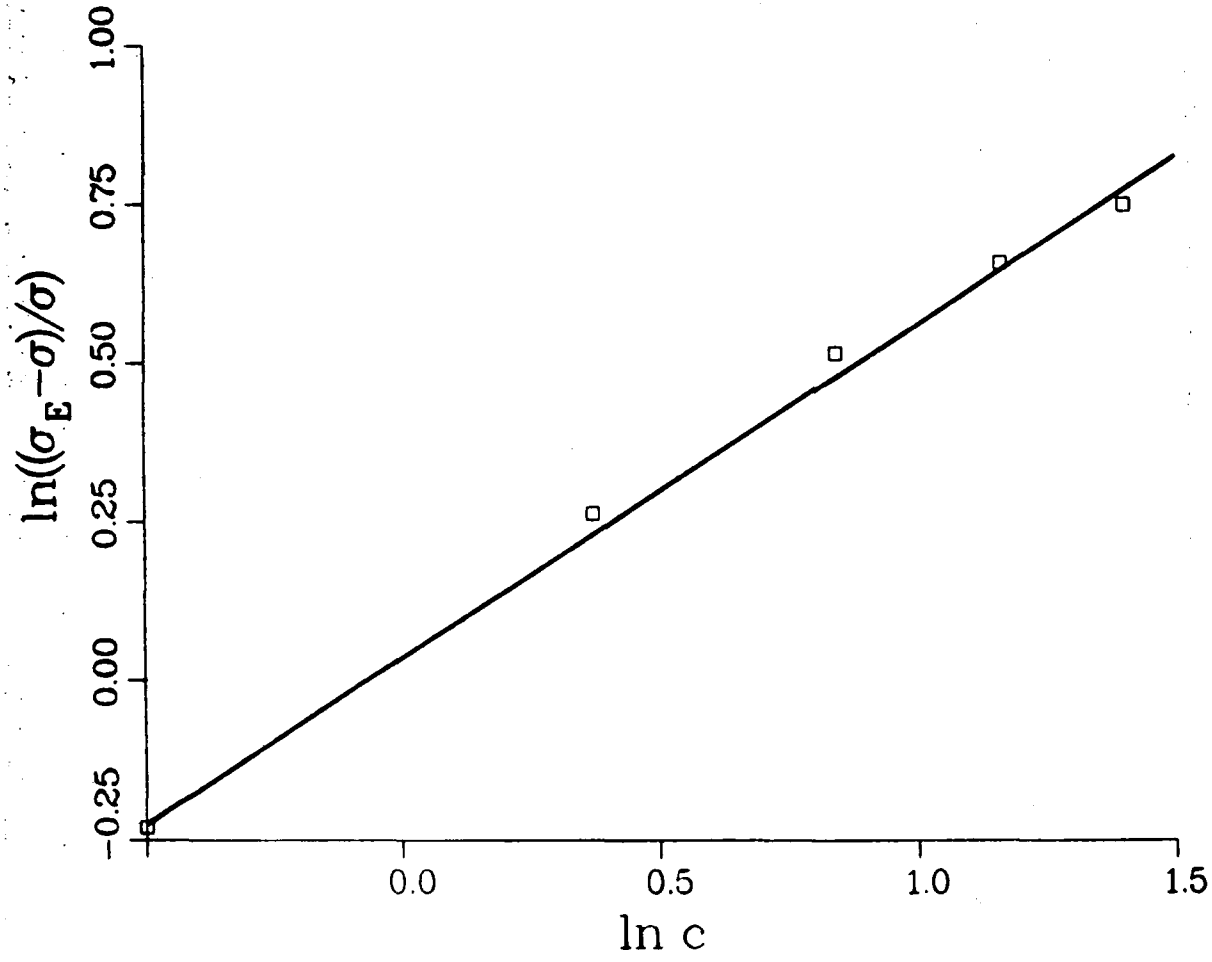


FIG. 7

Submitted to J. Amer. Ceram Soc.

Computer Modelling of Ceramic-Air PZT Composites
II: Two-Dimensional Deformation and Fracture.

M.S. Duesbery

GeoCenters Inc., 10903 Indian Head Highway,

Fort Washington MD 20744

and

M. Kahn

Naval Research Laboratory

Washington D.C. 20375

ABSTRACT

Computer modelling has been used to study deformation and fracture in two-dimensional ceramics containing isolated and ordered voids. Factors governing the void-induced changes in the internal stress fields are identified. The intervoid regions show depleted levels of elastic energy density and are effective barriers to crack movement. Design criteria are suggested both to minimise the intrinsic stress enhancement and to reduce the probability of surface flaw activation. The relevance of the results to experimental data is discussed.

1 Introduction

Porosity in ceramic materials can affect physical properties such as elastic response, tensile strength and fracture behavior (1). Stress concentrations at the pore surfaces, due either to the shape and size of the individual pores, or to intergranular and transgranular microcracks at the pore surfaces, are believed to cause degradation of the fracture strength. For example, regions of enhanced stress associated with irregular voids or void clusters can reduce the fracture strength considerably (1).

The relative importance of the size and surface roughness of the voids is not clear. Kessler et al. (2), explaining an increase in fracture energy with grain size in 1% porous MgO, suggested that for the smaller grain sizes, pores at grain boundaries were small and sharp, leading to large stress concentrations. For coarser-grained ceramics the pores were larger, located within the grains and were rounded, leading to lower stress enhancement and consequent less degradation of the fracture strength. On the other hand, Biswas and Fulrath (3), working on Nb doped lead zirconate titanate (PZT) with spherical pores, found a higher fracture strength for smaller pores.

The effect can be enhanced by deliberate control of the size, shape, orientation and spatial distribution of the voids. For example, Molnar and Rice (4) found that in lead zirconate titanate (PZT) ceramics with lenticular pores, the fracture strength in three-point bending was substantially less when the long axis of the pores was normal to the direction of the primary tensile stress than when parallel. Presumably this is because when the tensile stress acts normal to the long axis, there are larger stress concentrations at the sharp ends of the needle-shaped cavities. Kahn et al. (5) showed that the transducing properties of PZT for hydrostatic pressure can be improved by

the introduction of ordered arrays of disk-shaped voids. This was attributed to the cooperative stress concentrating effect of the void arrays, which enhances the piezoelectric response for an applied stress normal to the disk plane (6).

Perhaps the most comprehensive study of the effect of pores on the mechanical strength has been conducted by Kahn et al. (7), whose studies of PZT with controlled voids indicates that the presence of void arrays can have a strong influence on the tensile strength and fracture toughness. Three-point bending was used to test PZT samples containing ordered arrays of disk-shaped voids. Certain specific array geometries and void dimensions were found to give specimen strengths approaching that of hot pressed PZT (8), suggesting a suppression of the usual defect-induced strength decrement.

In an endeavor to understand the effect on mechanical properties of pores in general and of the ordered void arrays used in (7) in particular, we have used computer simulation to examine the internal stress profiles and fracture properties of numerical models with ceramic characteristics (i.e. brittleness). Most of the work will be confined to two dimensions (2D), because of numerical convenience and because the principal effects can be demonstrated more clearly in 2D systems.

2 Numerical Details

We use a particle dynamic model, described earlier (9), consisting of material points arranged in a triangular lattice with lattice constant *a*. The particles are bound by a central pair potential $V(|\underline{r}_{ij}|)$, where $\underline{r}_{ij}$ is the relative position vector of the particles i and j. The form of V(r) is chosen to match the elastic properties of the modelled material for small defor-

mations.

If we write the positional coordinates $\underline{r}_i$ as dimensionless multiples ρ_i of the scale constant a, then a change of scale from *a* to *ka* results in the identities

$$V(\rho,ka) = V(\rho,a)$$
$$S(\rho,ka) = k^{-3}S(\rho,a)$$
$$E(ka) = k^{-3}E(a)$$

where S(r) and E(a) are the stress and Young's modulus, respectively. Thus for a given potential function, the energies and the dimensionless stresses S/E are independent of the absolute magnitude of a; in other words, these quantities are *scale-invariant*.

For comparison with experiment it will be convenient at times to attach a magnitude and a physical meaning to the scale constant *a*. For example, one specific aim is to address the experiments described in (7), which deal with fine-grained (4μm) polycrystalline PZT ceramics containing disk-shaped voids with typical thickness and diameter of order 10μm and 250μm, respectively. In this case *a* should be considered to have a size small enough to model the minimum void dimension; a convenient size is about 10μm. The model particles would then each contain a few crystal grains and the interparticle forces would be interpreted as intergranular interactions.

Treatment of fracture modelling requires more careful consideration. The criterion for decohesion, or cracking, of a bond (9) is that the interparticle separation ρa must exceed a critical value $\rho_c a$; a modelled crack tip is limited to a diameter of order *a*. Therefore if *a* is considered to be of

granular dimensions, cracks on this scale would have a commensurate tip radius, much larger than the near-atomic size normally expected for failure cracks in ceramics. The stress concentrations at the crack tip are not similarly limited, because these depend only upon the ratio of the tip and length dimensions.

This problem can be addressed in two ways. Either we can consider that the fracture-controlling cracks do indeed have granular dimensions, in which case the model can directly address fracture on the experimental scale, or we can assign a much smaller value to a, one appropriate to an atomic-sized crack, in which case the modelled voids will have dimensions much smaller than those in (7). The calculation is the same in both cases; the problem is one of interpretation. Our aim will be to use the model to derive principles which are generally valid, independent of the scale.

Standard molecular dynamic numerical algorithms are used (9).

3 Stress Distributions

The stress distributions in 2D sections of ceramic models containing isolated voids and ordered void arrays have been calculated for deformation by uniaxial stress and by bending. The mechanisms are the same in both cases, but the results are more clearly demonstrated by reference to the simpler, uniaxially stressed state.

Comparisons between different configurations will be made at constant strain. This implies different applied stresses, since the effective Young's modulus will vary with the void content, but constant strain conditions are more representative of the conditions in a bulk cross-section. Constant uniaxial strain in the model is realised by applying the appropriate elastic

displacements and then preventing the particles at the stressed boundaries from moving in the direction of the strain axis.

Fig. 1a shows a schematic diagram of a void and a void lattice unit cell, defining the void length x and height y, together with the associated intervoid spacings u and v, parallel to x and y respectively. The cell dimensions X and Y are also indicated. The tensile stress direction in all figures will be in the horizontal direction, parallel to the X dimension of the unit cell as shown in fig. 1a.

3.1 Isolated Voids

Calculations of the stress distribution around isolated voids of various sizes have been performed for voids centered within a single cell of 50(X) x 32(Y) particles. The results are detailed in Table I, which details the stresses (in units of the applied stress) at the points A and B specified in fig. 1a. These are, respectively, the void corner and the center of the edge parallel to the applied stress.

Four distinct sources of internal stress modulation are identifiable and will be discussed in turn.

(a) Corner Effect. The sharpness of the modelled void corners is a source of stress concentration. Fig. 1b illustrates the triangular lattice particle stacking around a void. The particles are shown as filled circles; lines between the circles represent interparticle bonds. The void is shown in dashed outline. It is clear that the corner sharpness is determined simply by the triangular geometry of the lattice. By St. Venant's principle the effect of the corners will be short-ranged and independent of the shape of the void.

Confirmation of the shape-independence of the corner effect is provided by the observation that the stresses at all four void corners are the same, despite the differences in micro-geometry (compare, for example, the corners P and Q in fig. 1b).

(b) Channelling Effect. This effect occurs because of the equilibrium condition that the divergence of the stress must vanish, and can be visualised most easily by imagining "lines of force" (analogous to magnetic flux lines or hydrodynamic flow lines) which can end only at points of loading. The density of the force lines specifies the stress. In the presence of a void the lines of force must be deflected to pass around the void, resulting in a higher line density and consequent higher stress in these regions. The stress concentrating factor depends primarily on the dimension of the void normal to the applied stress direction. The stress enhancement is largest at the void corners (location A in fig. 1a and column A in Table I) and drops off with increasing distance from the void. Typically, a stress enhancement level of greater than 10% extends into the channel to a distance equal to the height y of the void. Column D in Table I shows the maximum extent of the 10% stress enhancement for each void, in units of *a* measured normal to and from the void edge parallel to the applied stress. Fig. 2a shows a graphic example of the channelling effect, using two voids for emphasis. The tensile stresses in figs. 2 and 3 are represented by open circles, centered on the particle positions, with radii proportional to the magnitude of the local stress.

(c) Shape Effect. The action of the external stress in deforming the void causes a stress concentration at the void surfaces parallel to the stress

direction (e.g. the point B in fig. 1a and column B in Table I), as shown by Inglis (10) for an elliptical void. The stress enhancement is largest when the small dimension of the void is parallel to the stress direction (cf. Molnar and Rice (4)) and increases with increasing void aspect ratio (y/x in fig. 1a). Examples are shown for isolated voids in the diagrams of figs. 2b and 2c, for which the maximum stresses (partly due to corner and channelling effects also) are, respectively, factors of 1.95 and 1.15 larger than the applied stress.

(d) Depletion Effect. The boundary conditions at internal voids require that there be no normal stress on the void surfaces (for example, at the points C in fig. 1a). For uniaxial stresses this means that there is a region of depleted stresses adjacent to the void surfaces normal to the applied tensile stress. An example can be seen in the diagram of fig. 2b. The spatial extent of the stress depletion depends on the height y of the void (compare figs. 2b and 2c). Typically, stresses are depleted below 50% of the applied stress to a distance y in the direction of the applied stress. The extent of this 50% depletion zone, measured normal to the unstressed void edge, is detailed in column E of Table I.

3.2 Void Arrays

The effects described above are modified when multiple, ordered voids are present. For ordering normal to the applied stress (i.e. a vertical array of voids for the geometry of fig. 1a) the changes in the stress fields are not very important. For large intervoid spacings v (fig. 1a) the internal stresses are given to a good approximation by linear superposition of the individual

void stress fields, but when the spacings become smaller than about four times the void height y, channelling effects are amplified (e.g. fig. 2a).

The influence of ordering parallel to the applied stress is more interesting. For closely-spaced voids, the intervoid spaces (adjacent to the points C in fig. 1a) can be nearly stress-free, due to overlap of the depletion zones. An example is shown in fig. 3a. This implies that there is little elastic energy stored in these regions; as will be seen below, this is important for the fracture properties.

The depletion effect for this type of ordering also interacts strongly with the shape effect. Stress enhancement due to the shape effect requires there to be a tensile stress acting on the void edges C in fig. 1a. The enhancement is reduced when the stress is relieved, as happens when there is an array of voids parallel to the applied stress. Fig. 3b shows the stress distribution for three voids, each of the same size as that shown in fig. 2b, aligned parallel to the applied stress. The stress concentration factor for all voids in fig. 3b is reduced. For the two outer voids the reduction is from 1.95 (fig. 2b) to 1.75. For the central void, which is 'shielded' on both sides, the stress concentration factor is reduced to 1.25.

This has immediate application to the case in which voids ordered parallel to the stress direction intersect the specimen edge (see fig. 3c). The depletion effect not only limits the stress concentrations at the upper ends of the voids, because of interaction with the shape effect, but also unloads the tensile edge of the specimen.

We have also modelled the stress distributions produced by three-point bending. The conclusions are unchanged,, the only difference being the additional complication presented by the tensile stress gradient across the

model.

4 Fracture Simulations.

In a homogeneous continuum, when a crack has been nucleated, propagation can continue unchecked because the crack tip fields, which by definition meet the fracture criteria, are invariant to translation. However, in a strongly inhomogeneous material, such as a ceramic void-array composite, the process of crack propagation is largely divorced from that of crack nucleation. In practical terms, this means that crack nucleation, although necessary, is not a sufficient condition for fracture failure. It is necessary also that the crack be able to move throughout the composite.

We have modelled bending failure by fracture for several void sizes and array spacings, considering both flaw-free models and models containing a controlled flaw (accomplished by breaking an interparticle bond, as for example at the point X in fig. 1b). Bending is the preferred deformation mode for fracture modelling because the most highly stressed regions, expected to be the source of crack nucleation, are localised at the tensile surface. Fig. 3d shows a schematic diagram of part of a bending model. The diagram is delimited at top and bottom by the neutral plane and tensile 'surface' respectively; the left and right boundaries define a single translationally periodic cell. For flaw-free models fracture begins always at the location of the largest tensile stress, either at the surface or at an adjacent void corner. The crack moves between void and surface and is arrested; further propagation proceeds strictly from void to void, requiring a load increase at each renucleation step (e.g. the sequence A to E in fig. 3d). Only when the void separation u (fig. 1a) is very large does crack propagation proceed

through the matrix between the voids.

The preference for crack propagation to proceed by this void "unzipping" mechanism has been demonstrated further by simulations in models with an induced, surface flaw situated at the tensile surface immediately below a void-free column (e.g. the location Y in fig. 3d). The stress at the tip of the flaw is enhanced to a level typically 15-20% greater than the most highly stressed void corners, but crack nucleation still occurs preferentially at the void corners and proceeds by the same unzipping mechanism.

The reason for this behavior is that crack propagation between voids is strongly inhibited by the low level of stored elastic energy in the inter-void regions adjacent to C in fig. 1a. In order for the crack to propagate, a virtual movement of the crack tip must be capable of releasing enough energy to create new surfaces. In the energy-depleted areas between the voids, this condition cannot be satisfied and the crack can propagate only with difficulty. Hence the preferred crack path lies through the voids. This explanation has been confirmed by using different interparticle potentials, each matching the same elastic properties, but with different surface energies. In models with lower surface energy, cracks can more readily penetrate the low-stress intervoid regions.

This property of fracture inhibition is of particular significance for composites in which the void arrays intersect the surface. The combination of deactivated surface flaws and inhibition of crack propagation should afford exceptional resistance to fracture failure.

We now return to the question of scale. As already noted, we cannot model microscopic cracks in a macroscopic void array. However, the conclusion that crack propagation through regions with low stored elastic energy is

inhibited is quite general and independent of the relative sizes of crack tip and void.

5. Summary and Discussion

The stress distributions in 2D ceramic models containing isolated and ordered voids have been calculated. Specific mechanisms leading to stress concentration and stress depletion have been identified. The overall conclusion is that stress concentrations cannot be avoided, but can be minimised by the judicious choice of void and array dimensions. Specifically, the void array spacings should be large in the direction normal to the applied tensile stress, to minimise channelling effects, and small in the parallel direction, to maximise stress depletion and reduce shape-induced concentrations. Particularly notable is the effect of void arrays which intersect the surface; in addition to the effects above, the surface is unloaded. This is of particular significance for ceramic devices, since common sources of mechanical weakness are surface flaws produced by machining.

We have performed some preliminary calculations for bulk (3D) models containing disk-shaped voids; these suggest that the mechanisms are the same, but that the stress concentrating effects are reduced.

Fracture in 2D has also been modelled. It is found that cracks nucleate preferentially at void corners and proceed from void to void. Movement of cracks through the stress-depleted regions is severely inhibited because of their low levels of stored elastic energy.

These results suggest that there are sound micromechanical reasons for the strengthening effects found in the experimental work of Kahn et. al (7), and suggest further avenues along which the phenomenon could be pursued

systematically.

Table I

The magnitude and range of internal stress concentrations in a model of size 50 x 32 particles containing isolated voids. The void size is quoted in particle units. Columns A and B show the internal stresses (in units of the applied stress) at the corner and at the upper edge center of the void (see fig. 1). Column D gives the distance from the void (in units of *a*) within which there is a channelling stress enhancement of at least 10% normal to the stress direction. Column E gives the analogous distance for a stress depletion of at least 50% parallel to the stress direction.

Void Size	A	B	D	E
6 x 4	1.55	1.45	4.4	3.0
12 x 8	1.75	1.45	6.1	6.0
18 x 12	1.65	1.35	5.2	10.0
12 x 2	1.25	1.15	2.6	2.0
12 x 4	1.45	1.25	4.4	3.0
12 x 12	1.85	1.55	5.2	11.0
8 x 12	1.95	1.65	5.2	10.0
4 x 12	2.15	1.95	5.2	9.0
2 x 12	2.25	2.25	5.2	9.0

References

1. R.W. Rice, "Microstructure Dependence of Mechanical Behavior of Ceramics", pp199-381 in Treatises on Materials Science and Technology, vol. II: Properties and Microstructure. ed. R.K. MacCrone, Academic Press: New York, 1977.

2. T.B. Kessler, T.E. Ritter Jr. and R.W. Rice, "The Effects of Microstructure on the Fracture Energy of Hot Pressed MgO", Mat. Sci. Res. vol. 7, "Surfaces and Interfaces of Glass and Ceramics", edited by V.D. Frechette et al., Plenum Press: New York, 1974, p529.

3. D.P. Biswas and R.M. Fulrath, "Mechanical Properties of Porous PNZT Polycrystalline Ceramics", pp933- in Fracture Mechanics of Ceramics, vol. 4: "Crack Growth and Microstructure", edited by R.C. Bradt et al., Plenum Press: New York, 1978.

4. B.K. Molnar and R.W. Rice, "Strength Anisotropy in Lead Zirconate Titanate Transducer Rings", Bull. Am. Ceram. Soc. 52 [6] 505(1973).

5. M. Kahn, A. Dalzell and B. Kovell, pp273-276 in Proceedings of the Sixth IEEE International Symposium on Applications of Ferroelectrics, Lehigh University, Bethlehem PA, 1986.

6. M. Kahn, "Acoustic and Elastic Properties of PZT Ceramics with Anisotropic Pores", J. Am. Ceram. Soc., 68 [11] 623-628 (1985).

7. M. Kahn, B. Kovel and D. Lewis III, "Fracture Phenmena in PZT Ceramic containing Arrays of Flat Voids", to be published.

8. R. Gerson, S.R. Burloge and D. Berlincourt, "Dynamic Tensile Strength of a Ferroelectric Ceramic", Trans. Acoust. Soc. Am. 33 [11] 1483 (1961).

9. M.S. Duesbery and M. Kahn, to be published.

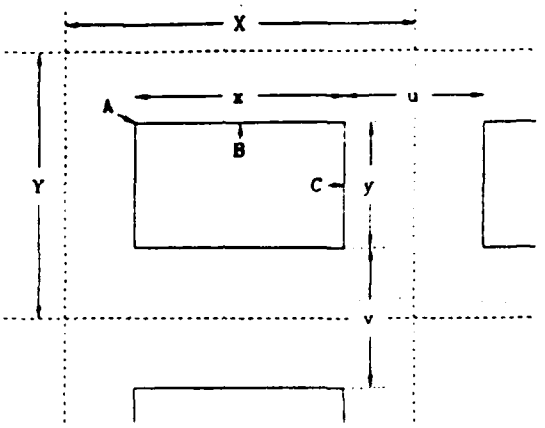
10. C.E. Inglis, "Stresses in a Plate due to the Presence of Cracks and Sharp Corners", Trans. Inst. Nav. Archit. 55 219 (1913).

Figure Captions

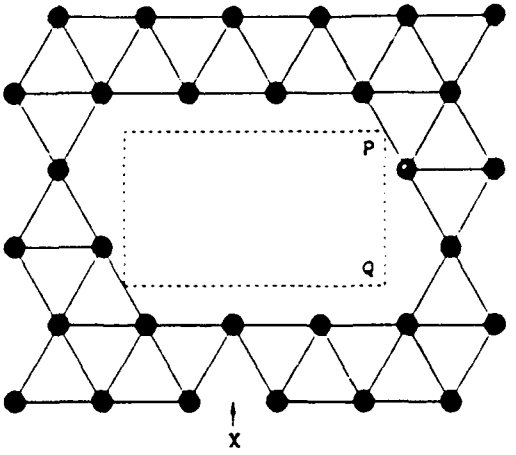
Fig. 1. (a) Void and void array dimensions are defined. Voids are drawn with solid lines and the void array unit cell is shown in broken outline. The applied stress acts parallel to the horizontal (X) direction. (b) Void corner geometry in the triangular lattice. Filled circles mark particle positions and full lines show interparticle bonds. A void is shown in broken outline. The arrow labelled X indicates a broken bond.

Fig. 2. Illustration of the channelling (a) and shape (b), (c) effects. Tensile stresses are represented by circles centered on the particle positions, with radii proportional to the magnitude of the stress.

Fig. 3. Illustration of the depletion effect (a) and the interaction of the depletion effect with the shape effect (b). Surface unloading is shown in (c). (d) shows a section of a bent specimen, with a typical fracture path indicated by the sequence A-E. Y marks a surface location lying below a void-free column.

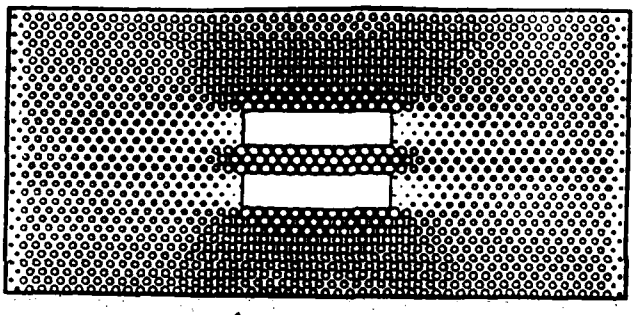


a

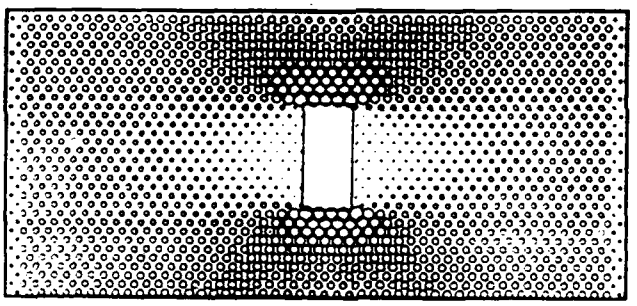


b

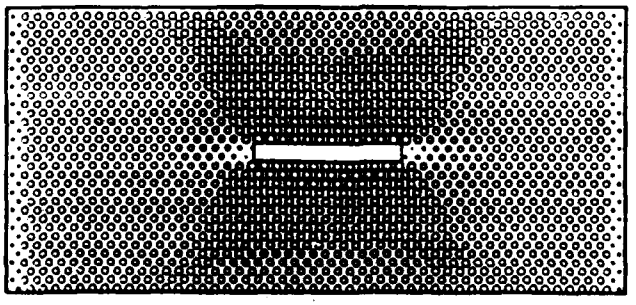
FIG. 1



a

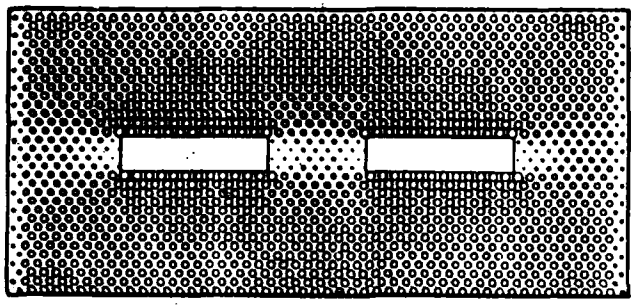


b

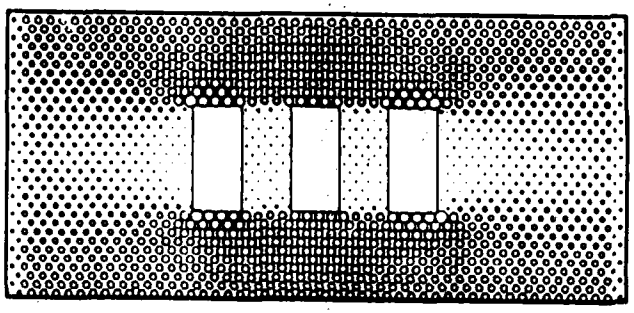


c

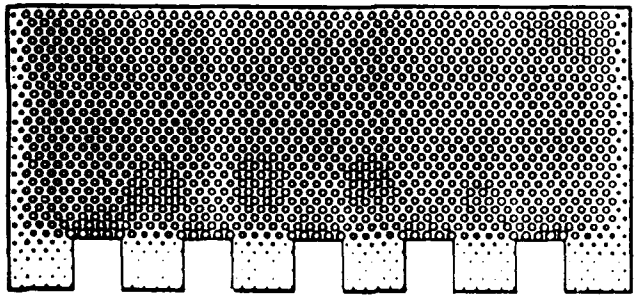
FIG. 2



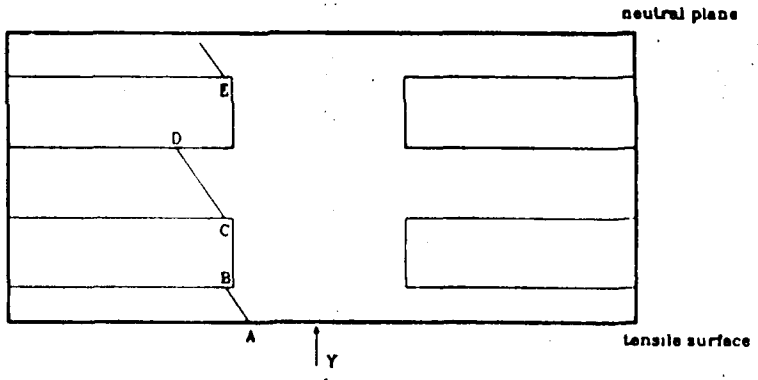
a



b



c



d

APPENDIX IV

Submitted to Phil. Mag.

The Interaction of Dislocations with Coherent Inclusions

I. Edge Dislocations and Repulsive Obstacles

by

M.S. Duesbery*, N. Louat* and K. Sadananda

Naval Research Laboratory, Washington D.C 20350

Abstract

The passage of an edge dislocation through an array of repulsive, coherent obstacles is simulated for several obstacle sizes, array dimensions and misfit values, using computer techniques adapted from molecular dynamic methods. For small misfit values bypass occurs by intersection of the obstacle and the bypass stress increases rapidly with the misfit. Above a critical misfit value, which varies with the size and separation of the obstacles, the bypass mechanism changes to Orowan loop formation; the passing stress continues to increase with misfit, but at a lower rate. It is found that there are two principal consequences of the obstacle stress field. Dipole-enhancing effects lead to a reduction in the breaking angle to between 40° and 70° from the near-90° expected for impenetrable obstacles, with a corresponding decrease in the bypass stress. However, the coherency stresses also renormalise the obstacle geometry to increase their effectiveness as barriers to dislocation motion.

* On-site contract employees of GeoCenters Inc., Fort Washington MD 20744

1. Introduction

It has been known for many years that metals can be hardened by the precipitation or dispersion of a second phase (Kelly and Nicholson 1953, Ashby 1970,1971, Brown and Ham 1971, Brown 1979, Gerold 1979, Lloyd 1985). The degree of hardening varies with many factors, including the size and distribution of the precipitates, their elastic strength relative to that of the matrix and the nature of the precipitate-matrix interface. The principles underlying the hardening effect are understood at a qualitative level. The precipitates impede the passage of dislocations, which must bypass the obstacles in order for plastic flow to proceed. Bypass can occur in several ways, depending on the detailed nature of the second phase particles and the character of the dispersion. For example, soft precipitates may be easily intersected by dislocations. A harder second phase, on the other hand, may force the dislocations to loop (Orowan 1948) or cross-slip (Hirsch 1957) around the inclusions.

Quantitative understanding, in contrast, is poor, because the configuration adopted by a dislocation in an arbitrary stress field is not, in general, amenable to analytic solution, so that numerical methods are necessary. The simplest approximation is the constant energy line tension model (e.g. Friedel, 1956), which treats a dislocation as an elastic string with a fixed energy per unit length E, taken to be $\mu b^2/2$, where μ is the shear modulus and b the Burgers vector. The line tension model is crude, completely ignoring the self-interaction of the dislocation (i.e. the elastic interaction between remote parts of the same dislocation), but nonetheless forms the predominant basis for current understanding of dispersion hardening. Refinements have been developed which take into account the variation of the line energy with dislocation character (DeWit and Koehler 1959, Kocks, Argon and Ashby

1975), replacing the constant energy E by the orientation-dependent quantity $E + E''$, where the double prime denotes the second derivative with respect to the angle between the dislocation line and the Burgers vector. This improved approximation takes into account the difference in line energy between edge and screw dislocations and was used by Gleiter (1967) to model the bypass mechanism for coherent obstacles, but falls short in not accounting for the non-local nature of the self-stress.

A numerical model was developed independently by Bacon (1967) and Foreman (1967) based on Brown's (1964,1967) self-stress theory, which accounts fully for the anisotropy of the line energy and the non-locality of the self-interaction. This model has been used (Foreman, Hirsch and Humphries 1970, Shtolberg 1971, Bacon, Kocks and Scattergood 1973) to investigate dislocation bowing between impenetrable (i.e. infinitely strong with no stress field) obstacles of varying shape. The most complete treatment was given by Bacon et al. (1973) (referred to below as BKS), who showed that the predictions of the full self-stress model can be very different from those of the line tension model.

The work reported below extends the Bacon-Foreman model to the case of penetrable, coherent obstacles. It will be shown that the behaviour differs substantially from that found by BKS for impenetrable obstacles, but can be characterised in a similar way by renormalisation of the obstacle geometry.

2. Modelling Methods

The shear stress field at a point P due to an element of length ds at C of a dislocation segment AB (fig. 1a) is (Brown 1967)

$$d\sigma = \frac{1}{b} \cdot \frac{(E + E'')}{|\underline{r}|^2} \cdot \sin\beta.ds \qquad (1)$$

where $\underline{r}$ is the vector joining C and P and ß is the angle between $\underline{r}$ and the tangent to the dislocation line at C. The stress at P due to the entire segment AB is obtained by integrating (1) along the contour AB. The self-stress of a dislocation at a specific point on the dislocation line is singular according to (1), but can be defined in terms of a cutoff parameter η (analogous to the 'core radius') as the average of the integral of (1) evaluated at distances $(+\eta, -\eta)$ normal to the dislocation line at the reference point (Brown 1964).

The Bacon-Foreman model approximates a continuous dislocation by a discrete set of N irregularly spaced vertices s_n (n=1,...,N) lying on the dislocation line (fig. 1b). The numerical computation of the self-stress has been treated in detail by BKS and will only be summarised here. The self-stress σ_n of the dislocation at the vertex s_n is considered to be comprised of two contributions. The first, due to a circular arc through the vertices s_{n-1}, s_n and s_{n+1}, is calculated from the known analytical expression (Brown 1964). The second, due to the remainder of the dislocation, is computed in a piece-wise linear approximation by summing the stresses at the vertex s_n due to all segments other than those forming the circular arc. In the work below the explicit approximations given by BKS (equations 11 and 12) to these two

terms have been used.

To accommodate the boundary conditions necessary to model coherent obstacles, some modification to the algorithm used by BKS, which depends upon pinning at the obstacle, is required. A procedure derived from standard molecular dynamic techniques has been used. Each dislocation segment is assigned a mass m^*ds proportional to its length ds and is permitted to move in accord with classical dynamics. A modified Verlet (1967) (central difference) algorithm is used; the position vector $\underline{r}$ of each dislocation segment is permitted to evolve during the time interval t to t+dt according to

$$\underline{r}(t+dt) = \lambda(\underline{r}(t) - \underline{r}(t-dt)) + \underline{F}.(dt)^2/(m^*ds) \qquad (2)$$

where $\underline{F}$ is the force on the dislocation segment and λ is a parameter which permits damping of the motion; for $\lambda = 1$, the Verlet algorithm is recovered exactly. The force $\underline{F}$ is calculated from the Peach-Koehler (1950) formula

$$\underline{F} = (\underline{b} \cdot \underline{\sigma}) \times d\underline{s} \qquad (3)$$

using a stress field $\underline{\sigma}$ comprised of the self-stress, the applied stress and the stress from the precipitates, each of which contributes a term

$$\begin{aligned} \sigma_{ij} &= 6\mu\epsilon R^3 \cdot x_i x_j / r^5 \qquad && r > R \\ \sigma_{ij} &= 0 && r < R \end{aligned} \qquad (4)$$

where μ is the shear modulus, ϵ is the particle-matrix specific size misfit, R is the precipitate radius and (x_i, r) define the position of the field point with respect to the centre of the precipitate. The x_1x_2 plane will be taken to be the primary slip plane. The sign and magnitude of the stress (4) then varies with x_3 (4), which is the height at which the slip plane intersects the precipitate. Since a variation of x_3 is entirely equivalent to variation of the sign and magnitude of ϵ, it will be assumed that the plane of intersection lies always at $x_3 = R/\sqrt{2}$, the position of maximum stress. The initial dislocation line will always be taken to lie along the x_1 direction.

In practice it is found that the discontinuity in stress at the particle surface leads to numerical instability; the stress field within the precipitate was therefore approximated by

$$\sigma_{ij} = \sigma(s) \cdot (\rho/R)^n \qquad r < R \qquad (4a)$$

where $\sigma(s)$ is the stress at the precipitate surface, ρ is the distance measured in the dislocation slip plane from the field point to the axis of the precipitate and n is a decay exponent. The value of n was taken as 2, but does not have a significant influence on the calculations.

The dislocation segments are permitted to have variable lengths, with the segment density largest in regions of strong curvature, a feature present also in the BKS treatment. A typical run was begun with 20 evenly spaced vertices along the dislocation line; additional vertices were added for small precipitates to ensure that at least ten initial segments were present to wrap around each obstacle. During the calculation, whenever the angle between two contiguous segments exceeded 0.5 radians, an additional vertex was inserted

on either side of the central vertex. The time step (dt^2/m^*) was adjusted *ad hoc* to preserve stability; a value of one quarter of the inter-obstacle spacing was found to be adequate in most cases.

The algorithm (2) is less efficient for impenetrable obstacles than that used by BKS, but has the advantage that arbitrary stress fields can be treated, that the motion of mechanically unstable configurations can be described with confidence and that finite temperatures can be simulated. It is found that undamped motion ($\lambda = 1$) leads to extensive oscillation, which is physically real, but inconvenient to the present purpose of determining equilibrium configurations; a value of $\lambda = 0.7$, which was found to give critical damping, was used.

The algorithm has been tested for impenetrable obstacles by turning off the precipitate interaction (4), instead pinning the dislocation at the matrix/precipitate interface. This procedure reproduces the BKS results.

The present work will consider only isotropic elasticity, because the intention is to determine the effect of coherent obstacles within the simplest possible framework. The effects of anisotropic elasticity on self-stress theory in general have been reviewed by Bacon (1985). The specific influence of anisotropy on the BKS results has been considered by Scattergood and Bacon (1974,1975,1976,1982). It was found that the isotropic elastic model can usually provide a fair approximation to the anisotropic case provided that effective values for μ and ν (ν is Poisson's ratio), fitted to anistropic energy factors, are used. In the present work no attempt has been made to do this.

3. Line Tension and Self-Stress Theory

It is worthwhile to consider briefly the history of the application of line tension and self-stress theories to passage of dislocations through obstacle arrays. A representative diagram of a dislocation bowed by an applied stress σ against an infinite array of impenetrable spherical precipitates each with diameter D and separation L is shown in fig. 2. Also defined in fig. 2 are the breaking angle θ (the angle of maximum slope of the dislocation), the maximum bowout distance Y_m and the parameter Y_c (to be discussed later), which is the distance by which the dislocation "stands off" from the obstacle. Conventional line tension theory identifies the force F exerted on each obstacle as $2T\sin\theta$, where T is the line tension acting along the dislocation line at the obstacle. This approximation is strictly valid only for point obstacles, but provides a convenient reference state and illustrates the importance of the line tension and the breaking angle θ in determining the bypass conditions. For penetrable obstacles F must exceed the obstacle 'strength' and for impenetrable obstacles a maximum in F signals an instability towards Orowan bypass. The force on the dislocation necessary to support the configuration shown in fig. 2 is evaluated in a similar approximation to be σbL, where σ is the applied resolved shear stress, so that for impenetrable obstacles, the constant energy line tension model ($T = E = \mu b^2/2$) predicts a bypass (Orowan) stress σ_o of

$$\sigma_o = 2T/bL = \mu b/L \qquad (5)$$

At this critical point the breaking angle $\theta = 90°$ and the bowed dislocation forms a semicircular arc with $Y_c = L/2$.

It is well-known that if the orientation dependence of the line energy

is taken into account, the breaking angle θ remains at 90°, but the maximum bowout and bypass stress become orientation-dependent, reflecting that, for example, the line tension at the obstacle for a screw dislocation in the critical configuration is equal to the line energy for an edge dislocation. In this approximation the bypass stress for a screw dislocation is larger by a factor $1/(1-\nu)$ than for an edge, and the maximum bowout correspondingly smaller. Adoption of the DeWit-Koehler (1959) expression for the line energy does not change these conclusions. The Orowan stress σ_o for an edge dislocation is the same for both line tension approximations and will be used as the reference unit.

The line tension approximations can be matched closely in the Bacon-Foreman model by permitting only the first (local curvature) term to contribute to the self-stress, ignoring the non-local integral over the dislocation line. The influence of the non-local term can be seen by noting that the line energy E is given by

$$E = A. \frac{\mu b}{4\pi} . \ln(R/r_0) \qquad (6)$$

where R and r_0 are outer and inner cutoff distances, respectively and A is an orientation factor. In the local approximation R is commensurate with the dislocation spacing in the bulk crystal. When non-local effects are taken into account, on the other hand, R depends on the shape assumed by the individual dislocation. The positive and negative arms of the bowed dislocation form dipoles of separation D and L (respectively XX and XX′ in fig. 2). The outer cutoff R should have a value between these two limits, as was pointed out by Ashby (1966,1968). Computations performed by Bacon (1967) and Foreman et al.

(1970) support this simple rationalisation. The BKS treatment, encompassing a wide range of relative obstacle sizes and spacings, showed that the real case is more complicated.

The BKS results were consistent with an Orowan stress given by

$$\sigma/\sigma_o = A(\ln X + B) \qquad (7)$$

where A is a constant equal to 1 for edge and $1/(1-\nu)$ for screw dislocations, X is the harmonic mean of L and D (i.e. $1/X = 1/L + 1/D$), B is an empirical constant of order unity and σ_o is given by (5). The physical interpretation of (7) is that for large obstacle separations, the logarithmic term is dominated by the obstacle size, reflecting the importance of the dipole interaction between the dislocation arms on either side of the obstacle. Conversely, for closely spaced large obstacles, it is the interaction of the dislocation arms between obstacles which governs the Orowan stress.

BKS found also that the breaking angle can differ from 90° by up to ±10°, with the smaller angles operative for small obstacles, for which the dipole effect is strongest.

4. The Effect of Coherency Strains

The influence on the edge dislocation bypass stress of repulsive obstacles (i.e. for dislocation-precipitate encounters on a plane with $x_3 > 0$ for $\epsilon > 0$ or on a plane $x_3 < 0$ for $\epsilon < 0$) with misfit parameters ϵ in the range $0.001 \leq |\epsilon| \leq 0.050$ has been considered for obstacle diameters D of 316b, 158b and 79b and separations L varying from 0.5D to 12D (the obstacle

and array sizes have been chosen, as far as possible, to match the values used by BKS). For each combination, Table I lists the stand-off distance Y_c (in units of D), the maximum bowout distance Y_m (in units of L), the breaking angle θ and the critical stress σ (in units of σ_o).

For small misfit values bypass occurs by intersection. For larger misfits Orowan looping occurs. The bypass stress in units of σ_o is shown in fig. 3 as a function of the misfit; the curves in fig. 3 are displaced along the y-axis in unit σ_o steps for clarity. The y-axis ticks are drawn at integral multiples of σ_o, but the numbering is omitted because of the curve displacement. Sets of points for different obstacles are displaced by an additional, similar step, with the obstacle diameter D indicated. The obstacle separation L is shown within a blanked region of each curve. Data points drawn as open circles indicate bypass by intersection; closed circles refer to Orowan bypass. As expected, each curve shows an initial high hardening rate in the intersection regime, reflecting a bypass stress determined directly by the backstress (4) exerted by the precipitate. The hardening rate drops as the Orowan mechanism becomes dominant, because bypass in this regime is governed by the line tension of the dislocation rather than by the precipitate backstress.

For each obstacle size, the intersection mechanism persists to a larger misfit value for larger obstacle separation. This occurs because the larger separations permit the dislocation to wrap more closely around the precipitate, with a consequent higher curvature and stronger forward force.

For precipitates without a stress field, such as the impenetrable obstacles used by BKS, the bypass stress is constant for a fixed obstacle diameter and separation. It is clear from fig. 3 that this is not true in general for coherent obstacles, even for Orowan bypass. In the Orowan regime

the hardening rate with increasing ϵ, although lower than in the intersection regime, is nonetheless significant and is larger for smaller obstacle separations. The general, low hardening rate in the Orowan regime occurs for reasons explained below, but the larger hardening for small obstacle separations is a consequence of overlap of the obstacle stress fields. Fig. 4 shows a three-dimensional perspective illustration of the σ_{32} shear stress field (i.e. the stress which acts on an incident edge dislocation) of an obstacle array. The x_1 and x_2 axes in fig. 4, which are the same as those in fig. 2, with the x_1 axis parallel to the initial dislocation and the length of the obstacle array, are labelled in units of D/(2√2) (i.e. the radius of the obstacle cross-section in the slip plane). The x_3 axis shows the shear stress normalised to the maximum value; values within the precipitate have no meaning. In fig 4a, for an obstacle separation of 2.5D, the stress fields of the individual obstacles are effectively independent. For a smaller separation of 0.5D (fig. 4b) there is a clear overlap, with a saddle-point midway between the obstacles. The absolute height of this saddle-point increases with misfit and leads to a backstress acting on the dislocation, causing the hardening shown in fig. 3.

This is not a complete explanation. The hardening with increasing ϵ is stronger for larger obstacles. For example, fig. 3 shows that for separations of half the obstacle diameter, the hardening rate for an obstacle diameter of 316 is nearly four times as large as for a diameter of 79. It seems reasonable to attribute this difference, at least in part, to the stronger, bypass-promoting precipitate dipoles (XX in fig. 2) for the smaller obstacles.

The magnitudes of the bypass stresses in the Orowan bypass limit may be compared with the BKS results for obstacles of similar size and separation.

For an obstacle diameter of 316, BKS find that the bypass stress for edge dislocatopns varies over a narrow range from $0.937\sigma_o$ to $1.025\sigma_o$ as the separation changes from 316 to 1000. For the same obstacle diameter and for separations 400 and 1000, fig. 3 and Table I show that for coherent obstacles, the bypass stresses at the onset of the Orowan process are $0.775\sigma_o$ in each case, somewhat lower than the BKS values. As the misfit rises to 0.040, the bypass stresses increase to $1.475\sigma_o$ and $2.475\sigma_o$ for L = 400 and 1000, respectively, both substantially larger than the BKS results. Thus within the Orowan limit, coherent obstacle arrays are weaker than their impenetrable analogues for small misfit, but harder for large misfit. The reasons for this behaviour will becom apparent below.

Typical examples of the dislocation configurations adopted during the intersection and looping processes are illustrated in figs. 5a and b. In both cases the dislocation is moving from bottom to top of the diagrams, through a periodic array of obstacles with diameter D = 316b and separation L = 1000b Only one obstacle, with central coordinates x_o, y_o and radius projected into the slip plane (D/2/2) is shown; translationally periodic boundary conditions operate at the lateral ends of the diagrams.

Fig. 5a shows successive equilibrium positions of the dislocation for an obstacle-matrix mismatch of ϵ = 0.001 as the stress is increased in steps of $0.05\sigma_o$ from $0.15\sigma_o$ to $0.40\sigma_o$, then to $0.438\sigma_o$, just below the bypass stress; non-equilibrium configurations for successive intervals of 25 time steps at an applied stress $0.1\sigma_o$ larger than critical are shown also (dashed lines) to illustrate the evolution of the bypass process. Bypass in this case occurs by intersection. A larger mismatch of ϵ = 0.010 forces the dislocation to pass the obstacle array by the Orowan process, leaving behind a loop which lies

partly inside the obstacle (fig. 5b; the loop lies inside the obstacle for $x_2 > y_o$ because the obstacle stress field (4) is attractive in this region). The equilibrium configurations shown in fig. 5b begin at a stress of $0.3\sigma_o$ and advance in steps of $0.1\sigma_o$ to $0.9\sigma_o$, then to the subcritical stress of $0.947\sigma_o$; subsequent non-equilibrium shapes are the result of time intervals as above at an additional stress increment of $0.1\sigma_o$.

Particularly notable from fig. 5b is that the breaking angle, even for Orowan bypass, is only 57°, much smaller than the line tension and BKS values. Reference to Table I shows that the breaking angle for all Orowan processes is of a similar magnitude, ranging from 40° to 70°. This is attributable to the obstacle stress field (4), which repels the dislocation for $x_2 < y_o$ but is attractive for $x_2 > y_o$, substantially strengthening the dipolar attraction between the dislocation arms on either side of the precipitate. This dipole enhancement is responsible for the lowering of the bypass stress levels for low-misfit Orowan bypass from the impenetrable obstacle BKS values. The low value of θ also has a bearing on the probability of bypass by cross-slip, a subject which will be discussed later.

It is evident from the discussion above, which demonstrates a strong variation of the bypass stress with misfit for constant obstacle size and separation, that the BKS expression (7) cannot hold. However, the diagram of fig. 5b shows that the dislocation configuration in the critical state forms a roughly circular arc concentric with the obstacle, but of larger diameter. This suggests that the dislocation "sees" a larger obstacle than is physically present, i.e. that the obstacle diameter D should be renormalised to an effective value D^* equal to the distance by which the dislocation "stands off" from the obstacle, denoted by Y_c in fig. 2. It can be seen from Table I that

Y_c increases monotonically with misfit, thereby decreasing the obstacle dipole enhancement; this effect is responsible for the hardening in the Orowan regime (except that caused by stress field overlap) and causes the obstacle array to be stronger for large misfit than the impenetrable analogue. The renormalised obstacle separation L^* is given by $L+D-D^*$ and the analogue of (7) is

$$\sigma/\sigma_o = (L/L^*) \cdot A^*(\ln X^* + B^*) \qquad (8)$$

in which the prefactor (L/L^*) is necessary to retain a consistent definition of σ_o (5) and X^* is the harmonic mean of D^* and L^*.

Fig. 6 shows the variation of the bypass stress in the Orowan regime with $(L/L^*)\ln X^*$. The data points obtained in BKS for edge dislocations are also shown in fig. 6 (for impenetrable obstacles $L = L^*$, so that the same plot can be used). The BKS points (open circles) show a linear dependence of stress on $\ln X$ with the slope of $1/2\pi$ expected from linear elasticity, covering a range of $\ln X$ from 1 to 6, and indicate a value of 0.7 for B. The data from the present calculation are shown as filled circles, and suggest an *apparent* approximately linear relation between passing stress and $(L/L^*)\ln X^*$ over a range from 2.5 to 25, with an initial slope of $0.7/2\pi$, decreasing with increasing $(L/L^*)\ln X^*$, and a value of 0 for B^*.

The dependence shown in fig. 6 must be strongly qualified. The evidence suggests that the data points belong to a single curve, or a set of closely spaced curves, indicating that the underlying physics is correct. However, the curves cannot be described by (8) unless the "constant" B^* is a near-linear function of (L^*/L), because a plot of $(\sigma/\sigma_o).(L^*/L)$ against $\ln X^*$ shows no apparent order. There seems to be no fundamental reason for a functional

dependence of B^* on (L^*/L); for the present the dependence will be accepted at face value.

Note should be made of the point marked A in fig. 6. This point clearly does not belong to the same curve as the remainder of the data; it pertains, together with two other points omitted from fig. 6 (because of even larger deviations in the same sense), to large, closely spaced obstacles with overlapping stress fields. In this limit, when the bypass process is dominated by the obstacle array backstress rather than the line tension of the dislocation, the philosophy of (7) breaks down.

5. Summary and Discussion

The passage of an edge dislocation through an array of coherent, spherical precipitates has been considered for the case of repulsive interactions and has been compared with the analogous calculations for impenetrable obstacles reported by BKS. Aside from the expected difference - that for low misfit values bypass of coherent obstacles takes place by intersection - there are two principal consequences of the coherency stresses. The force of attraction between the arms of the trans-obstacle dipole (XX in fig. 2) is augmented by the obstacle stress field (4) for that part of the dipole which protrudes beyond the centre-line of the array. In a similar way the mutual attraction of the inter-obstacle dipole (XX′ in fig. 2) arms is weakened. The combined effect is to reduce the bypass stress for small misfit values, particularly for small obstacles, for which the trans-obstacle dipole effect is dominant.

The second effect occurs for larger misfits and is strongest for large obstacles. The dislocation senses the physical dimensions of a obstacle only

indirectly, via the coherency stress field. The dislocation "stands off" from the obstacle of diameter D, forming a roughly circular arc with larger diameter D^*. The effective barrier seen by the dislocation resembles an array of impenetrable obstacles with renormalised diameter D^* and separation $L^* = L+D-D^*$. This effect causes the bypass stress to rise above the values for an array of impenetrable obstacles of the same *physical* dimensions and can be large; in the present work an array strength enhancement of a factor of 2.5 was observed for D = 316 and L = 400. An additional hardening effect for very closely spaced obstacles is caused by stress field overlap. When this happens the renormalisation procedure breaks down because the bypass stress and dislocation shape are perturbed severely by the backstress exerted by the combined obstacle stress fields .

Associated with the easier bypass of coherent obstacles is depression of the breaking angle from the near-90° values predicted by impenetrable obstacle theory to levels of 40° - 70° (the smaller angles pertain to smaller obstacles, as in the BKS work, reflecting the stronger trans-obstacle dipoles). This militates against the simple cross-slip mechanism (Hirsch,1957; Ashby and Smith, 1960; Humphreys and Martin, 1967; Gleiter, 1967; Duesbery and Hirsch, 1970; Humphreys and Hirsch, 1970) developed to explain the generation of prismatic loops as a result of dislocation bypass of coherent obstacles. Humphreys and Hirsch (1970) conclude that the cross-slip process necessary to create the (interstitial) prismatic loops must originate behind the obstacle (i.e. at $x_2 < 0$ in fig. 2). The present results suggest that for spherical precipitates, it is unlikely that a single undissociated edge dislocation can attain the necessary screw orientation before the bypass stress is reached, still less in the region behind the precipitate.

TABLE I

For obstacles of diameter D, separation L and misfit parameter ϵ, the critical values of the standoff distance Y_c (in units of D), the maximum bowout Y_m (in units of L), the breaking angle θ and the bypass stress σ (in units of σ_o) are tabulated. An asterisk after the stress value indicate bypass by intersection.

D	L	ϵ	Y_c	Y_m	θ_c	σ	ϵ	Y_c	Y_m	θ_c	σ
316	1000	.001	.351	.278	40	.438*	.002	.490	.381	51	.600*
		.003	.605	.398	51	.675	.005	.712	.494	61	.800
		.007	.845	.476	57	.875	.010	.932	.479	57	.947
		.020	1.165	.426	50	1.147	.030	1.273	.539	60	1.322
		.040	1.382	.448	52	1.475	.050	1.453	.447	52	1.625
	400	.001	.315	.361	36	.350*	.002	.294	.741	80	.550*
		.005	.646	.555	48	.775	.010	.783	.581	50	1.091
		.020	.914	.536	47	1.591	.030	.977	.597	52	2.044
		.040	1.019	.607	53	2.475					
	150	.001	.303	.526	29	.225*	.002	.400	.732	38	.369*
		.005	.539	.853	43	.650	.010	.627	.904	46	1.025
		.020	.697	.956	49	1.700	.030	.730	1.005	52	2.322
		.040	.751	1.001	52	2.925					
158	1000	.001	.250	.153	30	.286*	.002	.363	.270	49	.475*
		.005	.558	.357	58	.637*	.010	.783	.398	61	.725*
		.020	1.003	.440	65	.819	.030	1.183	.437	62	.875
		.040	1.268	.500	70	.937	.050	1.391	.447	61	.962
	400	.001	.285	.192	27	.250*	.002	.381	.303	40	.400*
		.005	.558	.465	56	.587	.010	.741	.499	56	.725
		.020	.948	.451	51	.894	.030	1.067	.428	48	1.025
		.040	1.139	.474	52	1.150	.050	1.203	.459	50	1.263
	160	.001	.273	.239	23	.184*	.002	.342	.407	36	.309*
		.005	.516	.539	44	.512	.010	.651	.555	44	.712
		.020	.768	.584	46	1.050	.025	.803	.595	47	1.200
		.030	.832	.578	46	1.337	.040	.871	.651	51	1.612
		.050	.904	.608	48	1.862					

D	L	ϵ	Y_c	Y_m	θ_c	σ	ϵ	Y_c	Y_m	θ_c	σ
79	1000	.001	.246	.092	19	.188*	.002	.287	.181	36	.363*
		.005	.593	.193	37	.400*	.010	.671	.291	53	.575*
		.020	.825	.380	69	.725	.030	.985	.377	67	.725
		.040	1.112	.373	62	.725					
	500	.001	.292	.092	18	.156*	.002	.286	.169	32	.281*
		.005	.443	.284	50	.463*	.010	.622	.348	56	.563
		.020	.835	.395	60	.650	.030	.941	.453	68	.706
		.040	1.067	.431	63	.738					
	250	.001	.275	.099	16	.138*	.002	.304	.192	29	.250*
		.010	.606	.418	55	.538*	.020	.798	.456	57	.650
		.030	.921	.457	55	.725	.040	1.011	.454	54	.788
	79	.001	.241	.144	14	.100*	.002	.306	.249	23	.175*
		.005	.406	.473	40	.331*	.010	.534	.569	45	.481
		.020	.679	.513	41	.663	.030	.740	.593	47	.837
		.040	.788	.582	46	.987					
	38	.001	.300	.154	9	.063*	.002	.332	.278	16	.112*
		.005	.391	.577	32	.237*	.010	.487	.704	37	.375
		.020	.575	.843	43	.587	.030	.629	.806	41	.762
		.040	.656	.905	47	.944	.050	.678	.950	49	1.112

References

Ashby, M.F., 1966, Acta Met. 14 679.

Ashby. M.F., 1968, Second Bolton Landing Conference on Oxide Dispersion Strengthening, (Gordon and Breach) p143.

Ashby, M.F., 1970, First International Conference on the Strength of Metals and Alloys, Asilomar, California, vol. II, p507.

Ashby, M.F., 1971, Strengthening Methods in Crystals, (Elsevier, Amsterdam), p137.

Ashby, M.F. and Smith, G.C., 1960, Phil. Mag. 5 298.

Bacon, D.J., 1967, Phys. Stat. Sol. 23 527.

Bacon, D.J., Kocks, U.F. and Scattergood, R.J., 1973, Phil. Mag. 28 1241.

Bacon, D.J., 1985, Fundamentals of Deformation and Fracture, (The University Press, Cambridge), p401.

Brown, L.M., 1964, Phil. Mag. 10 441.

Brown, L.M., 1967, Phil. Mag. 15 911.

Brown, L.M., 1979, Fifth International Conference on the Strength of Metals and Alloys, vol. III, p1551.

Brown, L.M. and Ham, R.K., 1971, Strengthening Methods in Crystals, (Elsevier, Amsterdam), p9.

DeWit, G and Koehler, J.S., 1959, Phys. Rev. 116 1113.

Duesbery, M.S. and Hirsch, P.B., 1970, Conference on Fundamental Aspects of Dislocation Theory, NBS publ. #317, p1115.

Foreman, A.J.E., 1967, Phil. Mag. 15 1011.

Foreman, A.J.E., Hirsch, P.B. and Humphreys, F.J., 1970, Conference on Fundamental Aspects of Dislocation Theory, NBS publ. #317, p1083.

Friedel, J., 1956, "Les Dislocations", (Gauthier-Villars, Paris).

Gerold, V., 1979, Dislocations in Solids, edited by F.R.N. Nabarro, vol. 4, (North Holland, Amsterdam), p219.

Gleiter, H., 1967, Acta Met. 15 1213.

Hirsch, P.B., 1957, J. Inst. Metals 86 13.

Humphreys, F.J. and Hirsch, P.B., 1970, Proc. R. Soc. Lond. A318 73.

Humphreys, F.J. and Martin, J.W., 1967, Phil. Mag. 16 927.

Kelly, A. and Nicholson, R.B., 1953, Prog. in Mater. Sci. 10 151.

Kocks, U.F., Argon, A.S. and Ashby, M.F., 1975, Prog. in Mater. Sci. 19 1.

Lloyd, D.J., 1985, Seventh International Conference on the Strength of Metals and Alloys, Montreal, Canada, (Pergamon Press, New York), vol. III, p1755.

Orowan,E., 1948, Symposium on Internal Stresses in Metals and Alloys, (Institute of Metals, London), p451.

Peach, M.O. and Koehler, J.S., 1950, Phys. Rev. 80 436.

Scattergood, R. and Bacon, D.J., 1974, Phys. Stat. Sol. (a) 25 395.

Scattergood, R. and Bacon, D.J., 1975, Phil. Mag. 31 179.

Scattergood, R. and Bacon, D.J., 1976, Acta Met. 24 705.

Scattergood, R. and Bacon, D.J., 1982, Acta Met. 30 1665.

Shtolberg, A.A., 1971, Phys. Stat. Sol. 43 523.

Verlet, L., 1967, Phys. Rev. 159 98.

Figure Captions

Fig. 1 a. Geometry of an arbitrary curved dislocation line AB. $\underline{r}$ is the vector from the field point P to the line element ds at C and 22 is the angle between $\underline{r}$ and the tangent to the line at C.

b. Piecewise representation of a general dislocation arc as a discrete set of line segments connecting vertices s_1 to s_N. To determine the self-stress at the vertex s_n the segments between s_{n-1} and s_{n+1} are treated as an arc of a circle, while the remaining segments are treated as linear.

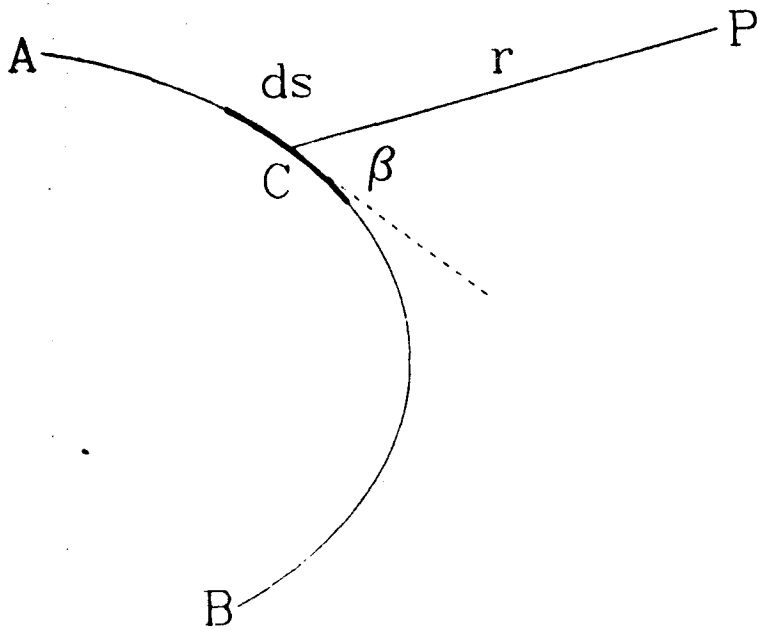
Fig. 2 Diagram of a dislocation bowed against an array of coherent obstacles. The diameter D and separation L characterise the obstacle array; the stand-off distance Y_c, the maximum bowout Y_m and the breaking angle θ describe the dislocation configuration in the critical state. The dislocation arms at XX form a trans-obstacle dipole, those at XX′ an inter-obstacle dipole.

Fig. 3 The variation of the passing stress σ/σ_o as a function of misfit ϵ for several obstacle array geometries. Each group of curves, for a specific obstacle diameter D, is offset from those below it by a two unit steps. The curves within each group are offset by a single unit step; the obstacle separation is listed in the blanked region of each curve. Calculated data points are represented by circles, open for bypass by intersection and filled for bypass by the Orowan mechanism.

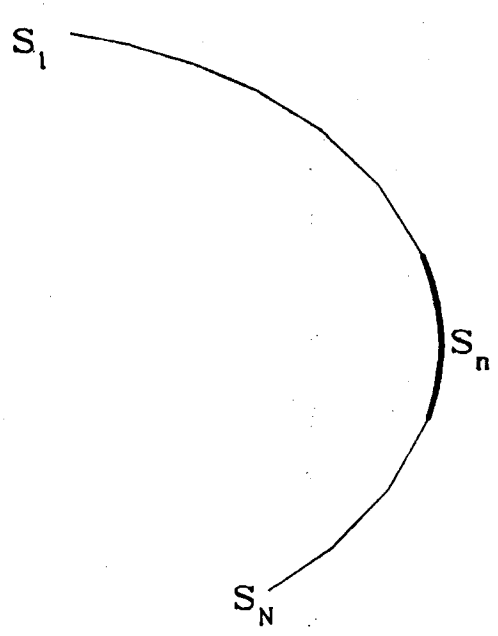
Fig. 4 A perspective view of the σ_{32} shear stress field of the repeat region between two obstacles from a periodic array parallel to the x_1 axis. Distances are given in units of D/2/2 (the radius of the obstacle in the slip plane and stresses are normalised to the maximum value. Stresses are shown for an obstacle separation of 5D/2/2 (a) and 2D/2/2 (b).

Fig. 5 Diagrams of dislocation configurations encountered during the bypass process. The circles show the obstacle cross-section in the slip plane; the vertical lines at the lateral edges of the diagrams delimit the repeat period. Full lines depict equilibrium dislocation configurations at equally-spaced stress levels up to the critical bypass stress. Dashed lines show non-equilibrium dislocation configurations at successive equally-spaced time intervals for a stress one level above the bypass stress. Axes referred to in the text are indicated. The intersection and Orowan bypass processes are illustrated in (a) and (b) respectively.

Fig. 6 The variation of the passing stress σ/σ_o with $(L/L^*)lnX^*$. Filled circles refer to the pressent alculations. Open circles refer to the edge dislocation data calculated by BKS for impenetrable obstacles. The isolated point labelled A is discussed in the text.

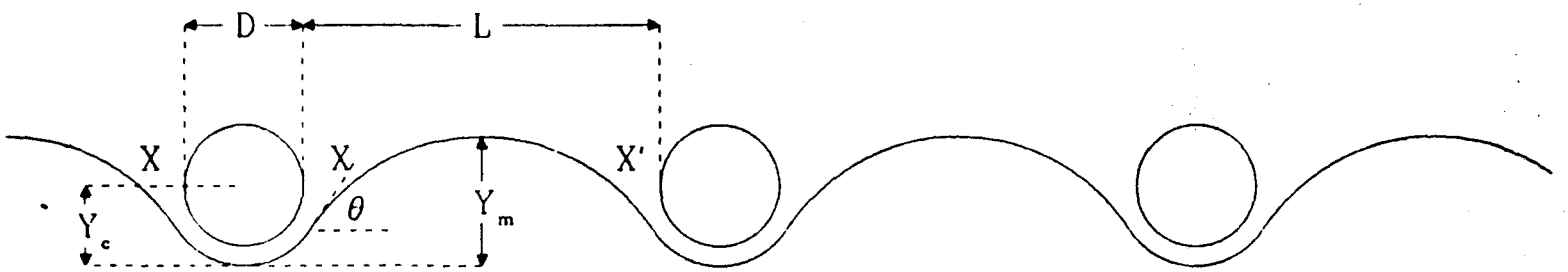


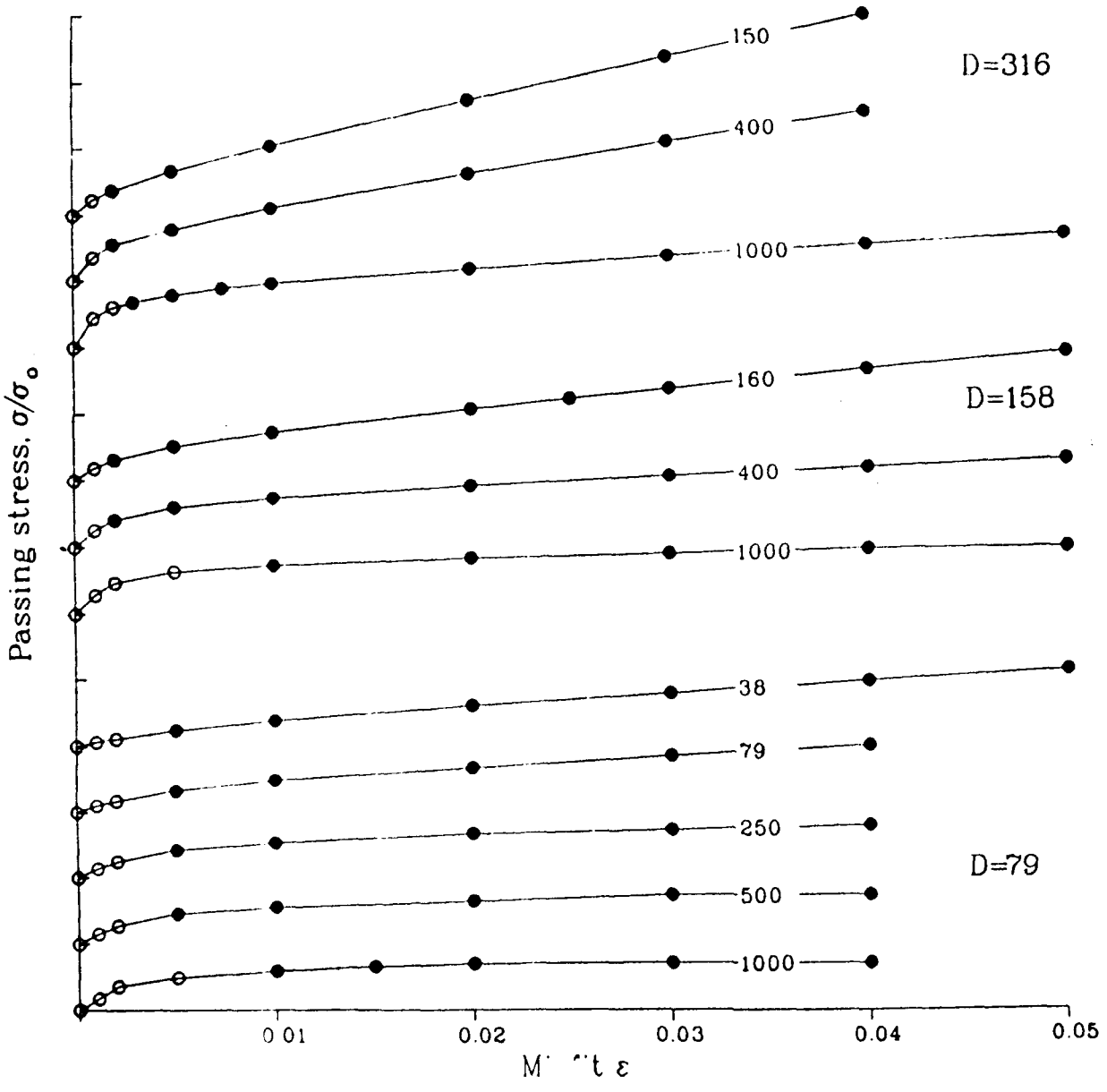
(a)

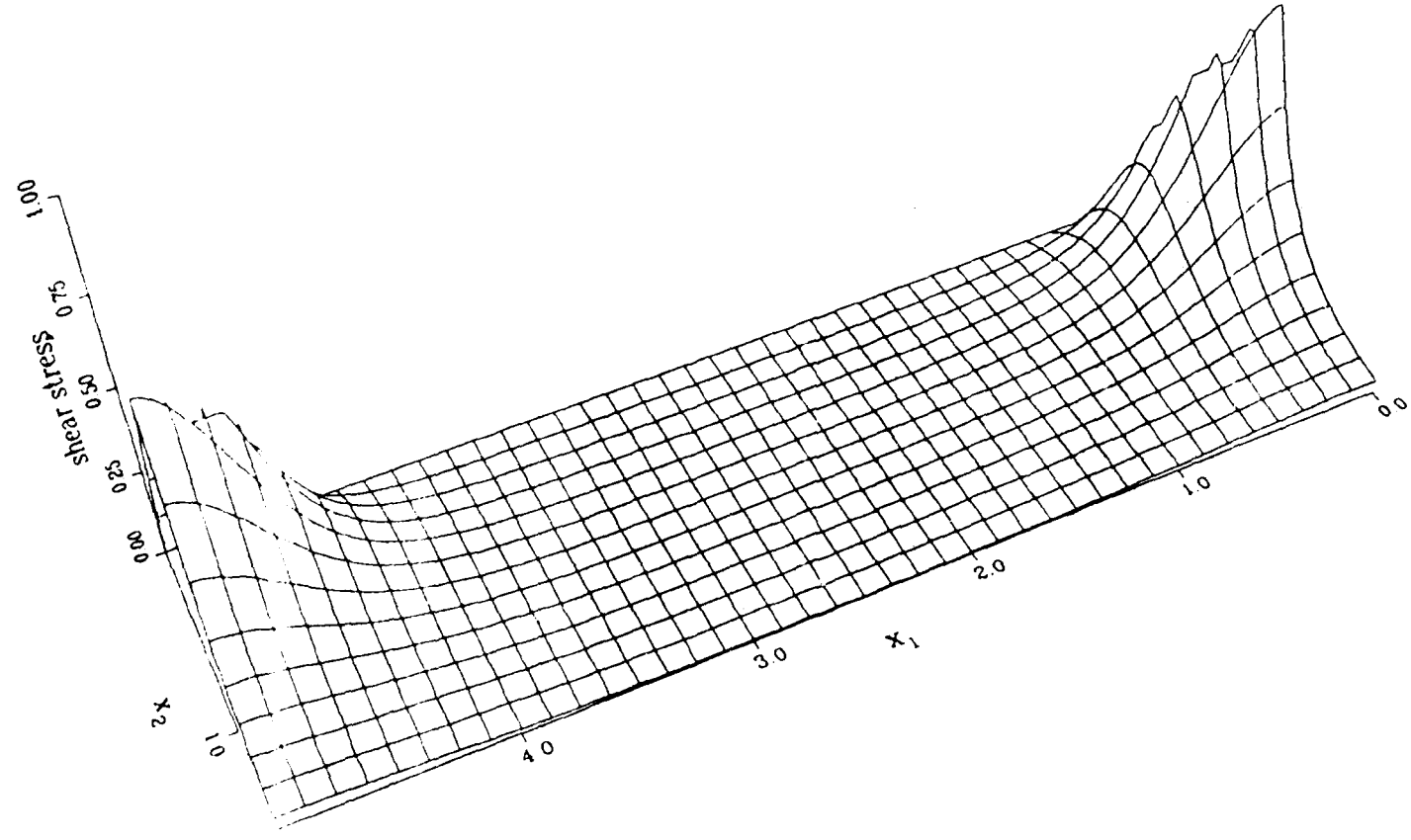


(b)

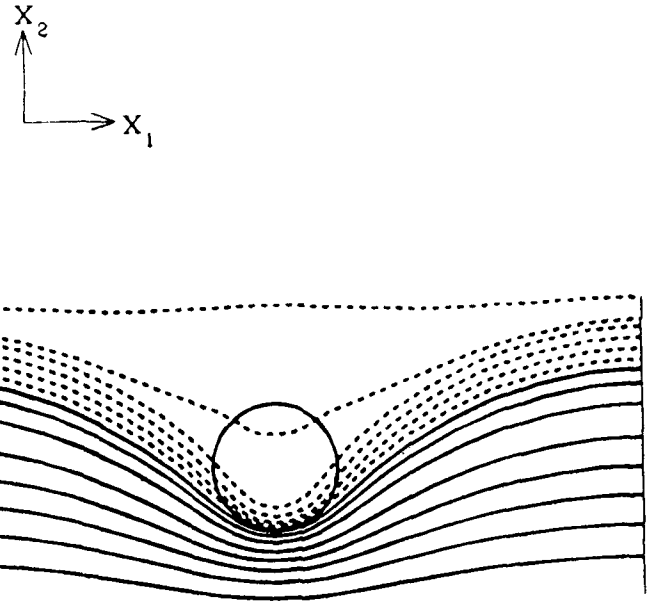
FIG. 1

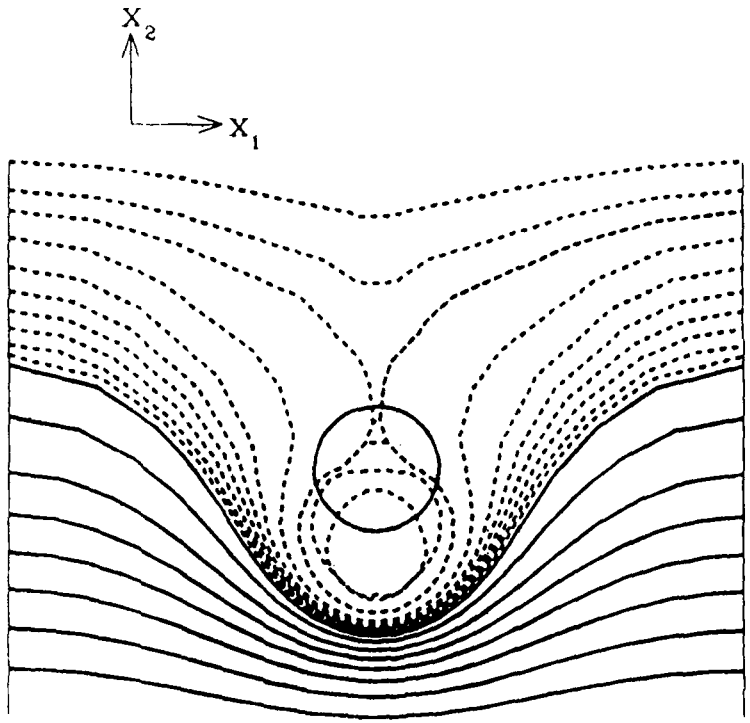

D
L
X
X
X'
θ
Y
c
Y
m

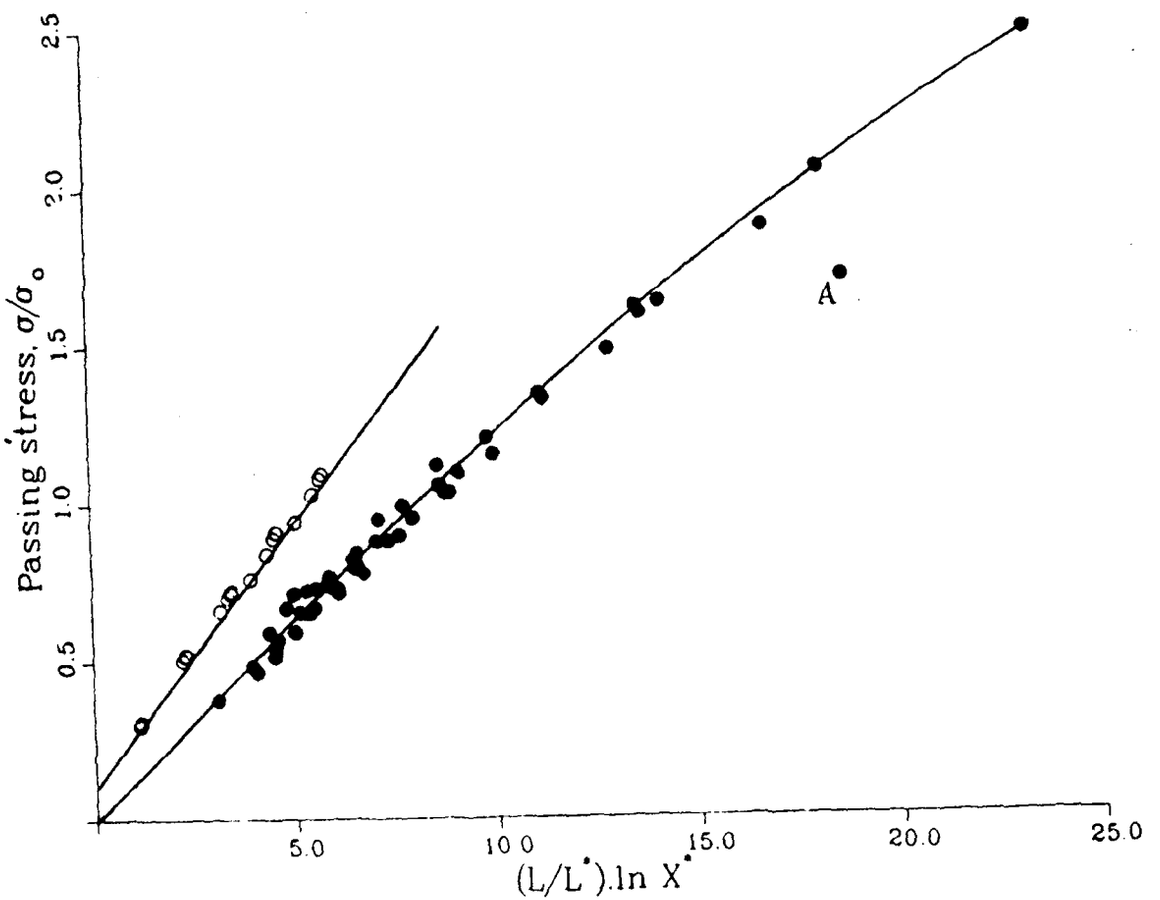

150
400
1000
160
400
1000
38
79
250
500
1000
D=316
D=158
D=79
Passing stress, σ/σ₀
0 01
0.02
0.03
0.04
0.05


shear stress
1.00
0.75
0.50
0.25
0.00
x_2
0.0
1.0
2.0
3.0
4.0
x_1

shear stress
0.00
0.25
0.50
0.75
1.00
x_2
0.0
0.5
1.0
1.5
x_1


X2
X1


X2
X1


Passing stress, σ/σ_o
0.5
1.0
1.5
2.0
2.5
A
5.0
10.0
15.0
20.0
25.0
$(L/L^*).\ln X^*$

APPENDIX V

Theoretical and Applied Fracture Mechanics 10 (1988) 177–189
North-Holland

DIRECTIONAL INSTABILITY OF CRACK PROPAGATION WITH ENERGY DISSIPATION

J.G. MICHOPOULOS *

Institute of Fracture and Solid Mechanics, Lehigh University, Bethlehem, PA 18015, U.S.A.

It was shown that the behavior of propagating curved and branched cracks is inherently governed by the dynamics of the crack system provided that dissipation in the potential energy is accounted for. A model is proposed by introducing the concept of an "equivalent crack particle" such that the deterministic aspect of the propagating crack in an idealized continuum and the stochastic nature of the micromechanical characteristics of the real material can be modelled. The Langevin equations of motion and the corresponding Fokker–Planck equations are thus derived.

1. Introduction

Instability associated with crack propagation can occur in the form of bifurcation where the crack tends to curve for no apparent reason. Numerous attempts have been made in the past to account for such a phenomenon by predicting the onset of branching and/or the curving. Among the criteria considered were the critical velocity and stress intensity factor, maximum tangential stress, and a combination of them. Dissipation, however, was not included.

The critical velocity criterion was first proposed by Yoffé [1] and later by Craggs [2] to study the behavior by dynamic fracture. It suggests that a crack would bifurcate when a critical velocity is reached. Clark and Irwin [3] and Congleton and his co-workers [4–7] proposed the critical stress intensity factor criterion. They made use of information from experiments for an advancing crack. Branching was also attributed to the driving energy for the propagating crack [8–10]. Even though Rabinovitch [11] showed errors in the numerical analysis, the criterion is still being referred to that of maximum energy release rate.

Maximum tangential stress for static [12–14] and dynamic loads [1,2,15] was also proposed as a possible criterion for crack branching. The direction of branch initiation was assumed to be normal to the maximum tangential stress near the crack front. The best results were obtained from the energy density criterion. In this approach, the location of minimum strain energy density was identified by Sih [15–17] with crack branching or change in the crack growth direction. The maximum dilatational energy density criterion by Theocaris and Andrianopoulos [18,19] was also applied for the running crack and gave the most accurate predictions for the crack bifurcation angles [20].

Attempts have also been made to apply various combinations of the different criteria. The critical velocity in conjunction with the maximum tangential stress or a critical energy density was employed for predicting the onset of branching and the branch angle [1,2,15,21]. Change in the crack growth direction has been distinguished from crack branching even though these two events may be governed by the same mechanism of instability. The kinked crack geometry has been investigated by application of the energy release rate criterion [22–25]. To the author's knowledge, the only consistent treatment of crack curving has been given by Sih [26] and by Ramulu and Kobayashi [27]. The maximum circumferential stress or the minimum strain energy density criterion were used for predicting a change in the direction of crack growth. Such a change was assumed to occur at an arbitrary distance ahead of the crack tip. Streit and Finnie [28] used a similar distance to study the influence of stress applied parallel to the crack extension direction.

Crack propagation consideration usually includes only the energy used in creating new crack surfaces, kinetic energy and that stored in the body. Energy dissipated as a result of microde-

* Currently, Senior Research Scientist, Geo-Centers, Inc., Materials Science and Technology Divsion, Code 6383, U.S. Naval Research Laboratory, Washington, DC 20375, U.S.A.

0167-8442/88/$3.50 © 1988, Elsevier Science Publishers B.V. (North-Holland)

fects created in the vicinity and away from the path of a running crack has generally been neglected. Even though this may not affect the prediction of terminal velocity and/or the angle of crack initiation, the overall pattern of bifurcation instability may be influenced.

The statistical character [1] of a real material may provide an explanation why reproducibility was lacking in many of the brittle fracture experiments [33–35]. Freudenthal [36] argued that failure can initiate in highly localized regions of the medium where defects prevail in the microstructure or produced during deformation. These defects can grow into flaws by destroying the cohesion of the material. The random inhomogeneity of the real material was reflected through the distribution function of fracture strength giving consideration to specimen size and stress state. Stochastic arguments were also applied to the qualitative and quantitative description of fracture in porous materials [37–39]. No information, however, was given to branching or curving.

Ravi-Chandar and Knauss [40–43] observed by high speed photography that cracks are generated ahead of the main crack in the fracturing Homalite-100 specimen. They showed that fracture is a continuous process of crack initiation as known by previous investigators [3,29,44]. Following the work of Congleton and Anthony [4–7] who explained branching by the presence of a small crack ahead of the main crack. Ravi-Chandar and Knauss [42] and Ramulu and Kobayashi [27,45] used similar arguments. Their models were based on the continuous interaction of the randomly distributed microcracks and voids in the material with the main crack. The directional instability of the running crack was shown to be affected by the stochastic nature of the material. Five specimens of identical geometries, subjected to identical load histories were tested [42], the point of branching had a variation of only ± 1 mm. However, the details of the branch evolution varied considerably.

The objective of this work is to derive a theoretical model free of inconsistencies. Both deterministic and stochastic characteristics will be introduced to describe dynamic fracture behavior in imperfect materials by including energy dissipation. A criterion will be developed to predict the onset of directional instability and location. The results will be compared with the experiments.

[1] The assumption of uniformity and homogeneity tends to preclude the triggering of dynamic instability. This may be a reason why crack propagation data in glass and polymers agree so well with experiments [3,29–32].

2. Dissipative micromechanics of dynamic fracture

The dynamic behavior of a moving crack depends on loading, geometry and material properties. Reference can be made to the known equations of motion for a crack [46–67]. Experimental observations can also provide insight into analytical modeling. According to the works in [40–43,45,68], microcracks are present in the material and they are nucleated as the main crack propagates. They can further coalesce near the crack tip leading to a decrease in the local stress intensity and increase in the local compliance. These flaws or defects can divert the direction of crack growth. It was suggested in [45] that the onset of bifurcation corresponds to the stress intensity factor reaching a critical value while deviation from the original path depends on the critical distance between the crack tips and the neighboring defects. In view of these observations, the following assumptions are made in developing the present model.

2.1. Reference systems

Crack motion is two-dimensional and reference is made to the $(O_m xy)$ coordinate system in the physical domain with Young's modulus E and Poisson's ratio ν as shown in Fig. 1(a). The fictitious ECP refers to the $(O_m q_1 q_2)$ system and is shown in Fig. 1(b).

2.2. Loading conditions

A stress pulse with magnitude σ and duration τ is applied at an angle β with the y-axis for $t \leq \frac{1}{2}\tau$. This corresponds to σ_{0_x} and σ_{0_y} in the x- and y-direction, respectively.

2.3. Micromechanical effect

Instantaneous forces acting on the ECP are introduced to simulate the random interaction of the main crack with the micromechanical structure

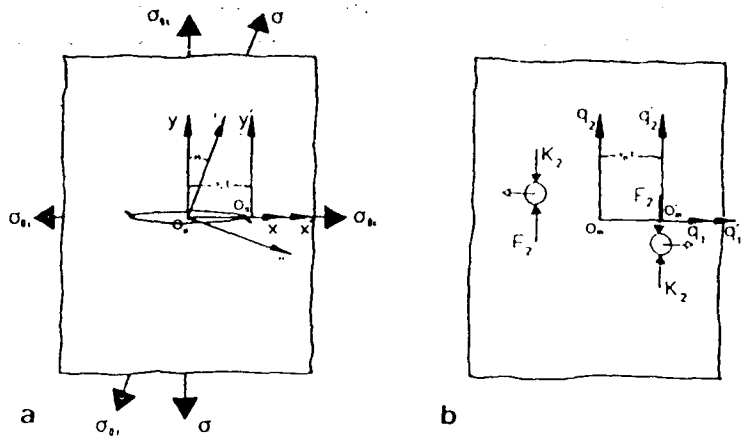


Fig. 1. Schematic representations of moving crack. (a) physical domain. (b) mathematical model.

of the material. These forces may have a nondissipative linear part and a dissipative nonlinear part.

3. Equivalent crack particle

Let the axes $(O_m q_1' q_2')$ be attached to the crack tip in the absence of any stochastic influence. This system moves with reference to the $(O_m q_1 q_2)$ axes with a constant speed v_p such that

$$q_1 = q_1' + v_p t, \quad q_2 = q_2'. \tag{1}$$

The dynamic equations of motion for the ECP referred to the moving frame of reference are

$$m_p \ddot{q}_i' + \gamma \dot{q}_i' = K_i(q_j') + \Phi_i(t), \quad i, j = 1, 2, \tag{2}$$

where γ is the damping coefficient while K_i and Φ_i represent the deterministic and the stochastic forces on the ECP, respectively. The deterministic force represents the influence of micromechanical defects near the crack tip which increases the inertia to keep the crack on its original path. It introduces a spring-like action opposing the deviations caused by the stochastic impulses accounted for by the constant ψ, i.e.,

$$K_i(q_i') = -\psi q_i'. \tag{3}$$

The random micromechanical interaction can be simulated by impulse-like action due to a stochastic force:

$$\Phi_{ij} = \phi_i \delta(t - t_j), \tag{4}$$

where ϕ_i is the strength and δ is the Dirac function. The time t_j is the occurrence of the jth pulse. The total force exerted by the microdefects can be obtained by the sum

$$\Phi_i = \phi_i \sum_{j=1} \delta(t - t_j). \tag{5}$$

Since the impulses are not unidirectional, Φ_i in eq. (2) can be generalized as

$$\Psi_i(t) = \phi_i \sum_{j=1} \delta(t - t_j)(\pm 1)_j. \tag{6}$$

If the acceleration in eq. (2) is negligible, the Langevin equations of motion [69] are obtained:

$$\dot{q}_i' = K_i(q_j') + F_i, \quad i, j = 1, 2, \tag{7}$$

in which

$$K_i(q_j') = \frac{K_i(q_j')}{\gamma} = -d_2 q_i', \quad d_2 = \frac{\psi}{\gamma} \tag{8}$$

$$F_i(t) = \frac{\phi_i}{\gamma} \sum_{j=1} \delta(t - t_j)(\pm 1)_j. \tag{9}$$

Since the impulses are random depending on the material microstructure, it is impossible to predict the actual paths of the ECP. The influence of the random forces on the velocity as a function of time can be described qualitatively in Fig. 2. However, it is possible to evaluate the average behavior. If F_i is averaged over the random sequence of plus and minus signs, then on the average

$$\langle F_i(t) \rangle = 0. \tag{10}$$

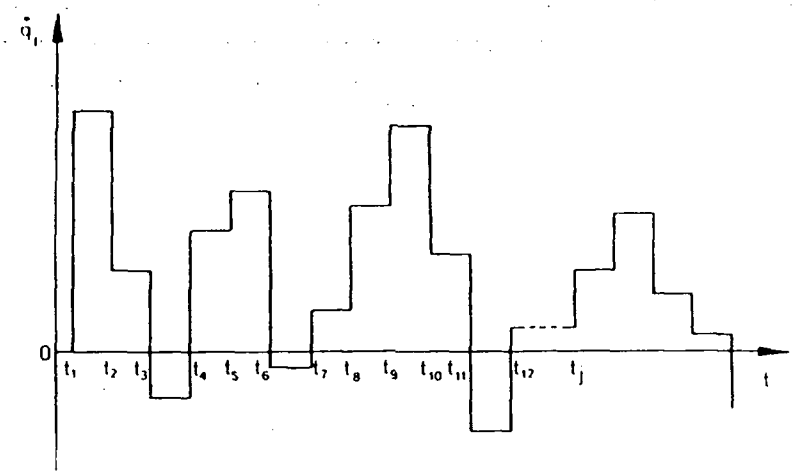


Fig. 2. Velocity time history due to random forces

Further, consider the product of F_i at t with F_i at t' and take the average over the duration of the pushes and their directions. Adopting a Poisson process, the following correlation function is derived:

$$\langle F_i(t) F_i(t') \rangle = Q\delta(t - t'), \tag{11}$$

with

$$Q = \frac{\phi_i^2}{\gamma^2 t_0} \tag{12}$$

Equations (7), (10) and (11) suggest that the motion of the ECP has the qualitative feature of the Brownian motion [70,71] of a particle being influenced by impulses of the neighboring particles. A deterministic form of eqs. (7) is

$$\dot{q}_i' = -d_2 q_i', \quad i = 1, 2. \tag{13}$$

They, however, do not describe the real stochastic dynamical system and are not integrable on account of the stochastic character of the forces F_i. A different approach would be required to incorporate the stochastic character of the ECP.

The deterministic equations of motion can be derived by applying eqs. (1) to eqs. (13). This gives

$$\dot{q}_i(t) = K_i(q_j), \quad i, j = 1, 2. \tag{14}$$

where q_i are referred to the global coordinates of the ECP and

$$K_1 = v_p - d_2(q_1 - v_p t), \quad K_2 = -d_2 q_2. \tag{15}$$

The Langevin equation of motion [69] can thus be written as

$$\dot{q}_i = K_j(q_j) + F_i, \quad i = 1, 2. \tag{16}$$

The components $F_i(t)$ correspond to the random impulses caused by the microdefects, and K_j are given by eqs. (15). The constants in eq. (9) would be altered. In what follows, it would be more expedient to solve the deterministic Fokker–Planck equation that expresses the continuity of the probability distribution for the ECP following a particular path. The correspondence of eq. (16) being nondeterministic with the Fokker–Planck equation [70–74] is given in the Appendix.

A uniform motion of the ECP prevails along the $(O_m q_1)$ axis when $\langle q_1 \rangle = v_p t$ in the first of eqs. (15). Only the second equation of motion needs to be investigated as a one-dimensional problem. It follows that the corresponding Fokker–Planck equation is also one-dimensional as given by eq. (A7). The q_1 coordinate, serving as a behavior parameter for the two-dimensional system, is deterministic. The combination of eqs. (14) and (15) yields

$$q_1 = \int_0^t v_p \, \mathrm{d}t. \tag{17}$$

The one-dimensional nature of the problem excludes information on stability.

4. Dissipative model

The natural boundary condition of the problem requires that $f \to 0$ for $q_2 \to \pm\infty$. It follows from eq. (A6) that $I \to 0$ for $q_2 \to \pm\infty$ and hence

$$\tfrac{1}{2}Q\frac{\mathrm{d}f}{\mathrm{d}q_2} = K_2 f. \tag{18}$$

This yields the probability density distribution function:

$$f(q_2) = N\exp\left[-\frac{2V(q_2)}{Q}\right]. \tag{19}$$

where the normalization constant N is determined by

$$\int_{-\infty}^{+\infty} f(q_2)\,\mathrm{d}q_2 = 1. \tag{20}$$

Here, K_2 is related to the function $V(q_2)$ of the deterministic system as

$$V(q_2) = -\int K_2(q_2)\,\mathrm{d}q_2. \tag{21}$$

The potential of the ECP can thus be determined from a knowledge of the deterministic force K_2. In the absence of dissipation, the linear force characteristics as shown in Fig. 3 would be represented by a second order surface in the (Vq_2d_2) space. It would always have a unique minimum trajectory.

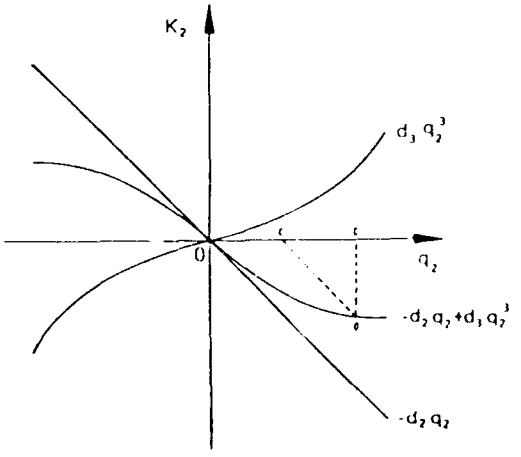


Fig. 3. Variations of deterministic force with q_2: conservative and dissipative.

For a system with dissipation, the additional coefficients d_2 and d_3 are introduced into K_2:

$$K_2 = -d_1 + d_2q_2 - d_3q_2^3, \tag{22}$$

in which d_1 corresponds to a constant force. The only nonlinear term being odd in q_2 is associated with d_3. Figure 3 shows that the area $OC'Q$ represents the energy spent for deviating the ECP from its average path along q_1 by an amount OC. The area $OC'Q$ is the amount dissipated by microcracks near the crack tip. Substituting eq. (22) into (21) yields

$$V(q_2) = d_1q_2 - \frac{d_2}{2}q_2^2 + \frac{d_3}{4}q_2^4. \tag{23}$$

Plotted in Figs. 4(a)–(c) inclusive are the potential surfaces Vq_2d_2 obtained from eq. (23) and Figs. 4(d)–(f) inclusive are the probability density distribution surfaces $f(q_2,d_2)$ computed from eq. (19) for fixed values of d_1, d_3 and Q. Note that the random force $F_2(t)$ drives the ECP upward as q_2 extends in the positive and negative direction. Restoration is provided by the deterministic force $K_2(q_2)$ such that the most probable positions of the ECP correspond to those points of minima V and maxima f. More specifically, the variations of $V(q_2)$ and $f(q_2)$ with q_2 in Figs. 4(b) and 4(e) are displayed in Fig. 5(a) for $d_2 < 0$ and Fig. 5(b) for $d_2 > 0$, respectively. Two fixed values of $(d_2)_1$ and $(d_2)_2$ are used such that $(d_2)_1 < (d_2)_2$. The force $K_2(q_2)$ tends to decrease with d_2. This results in a spread of the $V(q_2)$ and $f(q_2)$ curve. The final trajectory of the ECP is, therefore, expected to be more deterministic as d_2 increases.

The conditions $\mathrm{d}V/\mathrm{d}q_2 = 0$ or $\dot{q}_2 = 0$ lead to

$$q_2^3 - \frac{d_2}{d_3}q + \frac{d_1}{d_3} = 0, \tag{24}$$

which gives the steady-state equilibrium conditions. A plot of q_2 against d_2/d_3 is given in Fig. 6 for different d_1/d_3 ratios. They represent the stable and unstable trajectories of the ECP. Two different situations prevail, depending on whether $d_2/d_3 > 0$ or $d_2/d_3 < 0$. When $d_1 = 0$, $d_2 < 0$ and $d_3 > 0$, eq. (24) gives the only solution with V being minimum for $q_2 = 0$ which corresponds to a stable situation. If $d_2 > 0$ and $d_3 > 0$, there result three possibilities. The one with V being a local maximum and $q_2 = 0$ is unstable while the remaining two with $q_2 = \pm\sqrt{|d_2|/d_3}$ are stable and

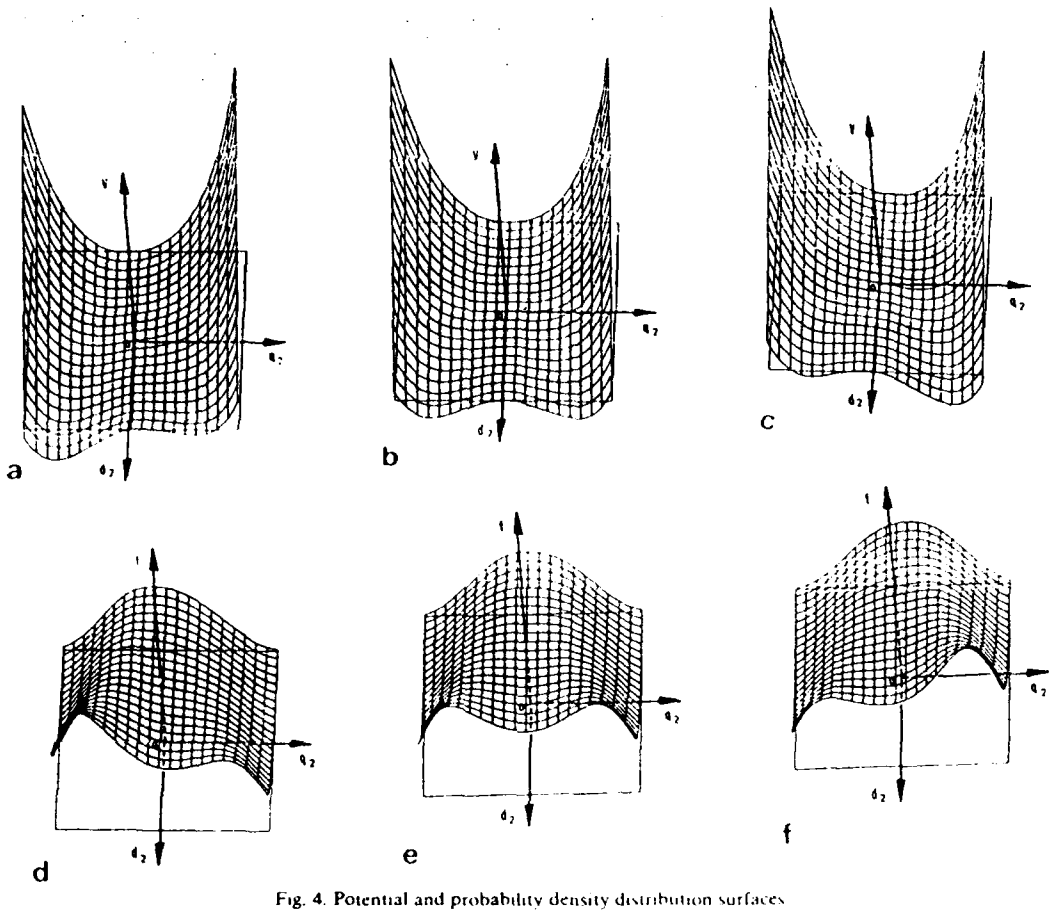


Fig. 4. Potential and probability density distribution surfaces

shown in Fig. 6. A bifurcation point is found at $d_2 = 0$. The ECP branches to two symmetric paths with reference to the d_2-axis as d_2 changes in sign from negative to positive.

The physical phenomenon of crack branching might be regarded as the development of two stable positions from an unstable one. This occurs when d_2 becomes positive. A set of critical points

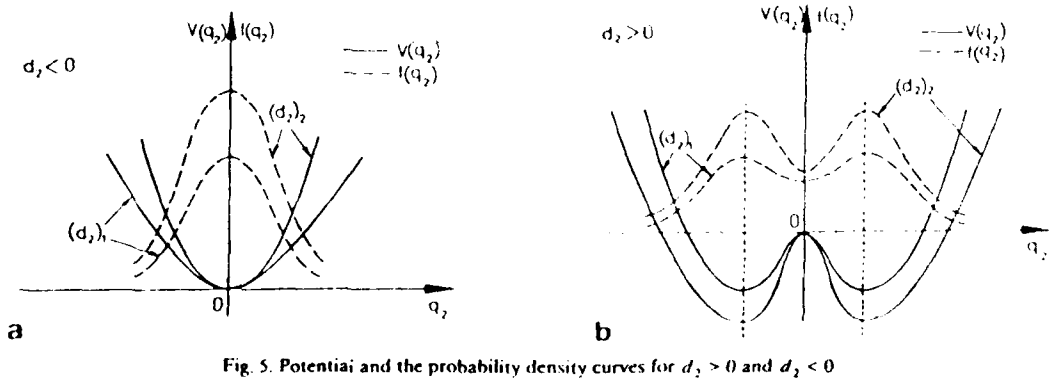


Fig. 5. Potential and the probability density curves for $d_2 > 0$ and $d_2 < 0$

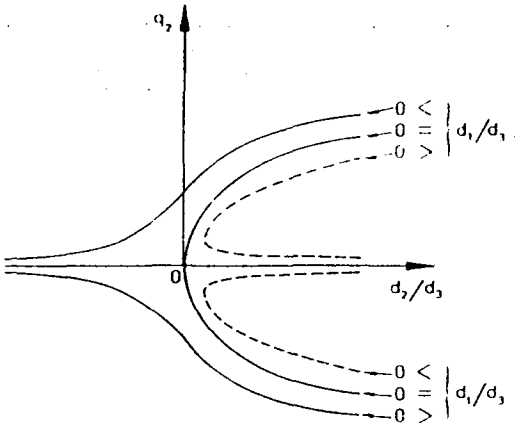


Fig. 6. Stable and unstable trajectories in d_2q_2-plane.

in the d_1d_2-plane may be determined that correspond to this transition. Differentiating eq. (24) with respect to q_2 and setting the result to zero renders

$$3q_2^2 - \frac{d_2}{d_3} = 0. \tag{25}$$

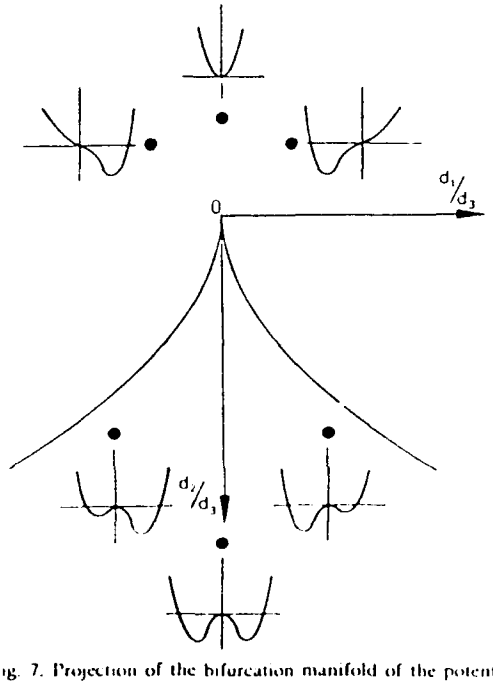


Fig. 7. Projection of the bifurcation manifold of the potential in d_2/d_3 versus d_1/d_3 space.

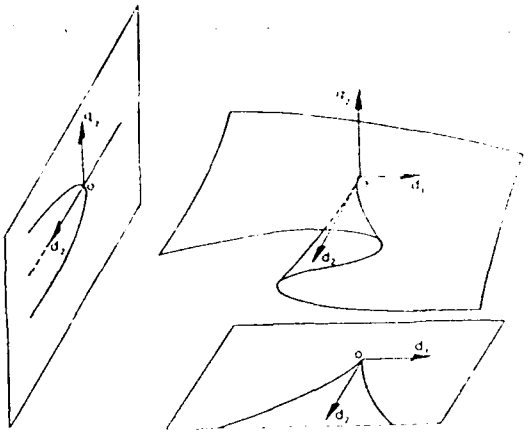


Fig. 8. Bifurcation manifold and d_2d_1-plane.

In view of eqs. (24) and (25), it is found that

$$-\left(\frac{d_2}{4d_3}\right)^3 + \left(\frac{d_1}{2d_3}\right)^2 = 0, \tag{26}$$

where d_3 influences the scaling. The cuspoid curve in Fig. 7 is a graphical representation of eq. (26). The region within the cuspoid corresponds to positive d_2. It represents two stable and one unstable paths. The region outside the cuspoid corresponds only to one stable path. All of them are steady-state. The manifold of the critical points in the $(q_2d_2d_1)$ space and their projections onto the d_2q_2- and d_2d_1-planes are shown in Fig. 8. The instability characteristics of the ECP correspond to the Riemann–Hugoniot cusp [75] in Fig. 8 and can be identified with eq. (23) [76].

Finally, the parameter d_3 controls the distance between the two bifurcated paths in Fig. 6 and it can be related to the crack bifurcation angle with the aid of a criterion.

5. Physics of equivalent crack particle

Consider the physical coordinates

$$x = q_1, \quad y = q_2 \tag{27}$$

such that the trajectories of the ECP coincide with those of the actual crack tip. The parabolic bifurcation scheme of Fig. 6 in the d_2q_2-plane will be transferred to the xy-plane. This is shown in Figs. 9(a) and 9(b) such that x_c specifies the location where the directional instability will occur and θ_c

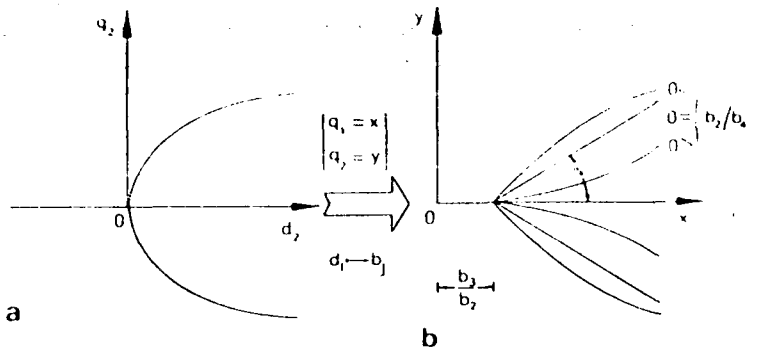


Fig. 9. Transformation of parabolic bifurcation to physical behavior.

is the crack branching angle. The analytical expression

$$y = U_+(x - x_c)\frac{b_2x - b_3}{\sqrt{b_4^2 + b_5x^2}} \tag{28}$$

describes the curve [77] in Fig. 9(b) with U_+ being the positive asymmetrical unit-step function. This eliminates the branches of the curve prior to the bifurcation point. The unstable path is obtained by rearranging eq. (28) into the form

$$\left(b_4^2 + b_5x^2\right)y^3 - \left[U_+(x - x_c)\right]^2(b_2x - b_3)^2y = 0. \tag{29}$$

The equilibrium trajectories of the ECP represented by eq. (29) will correspond to the minimae of the potential

$$V = b_1y - \tfrac{1}{2}\left[U_+(x - x_c)\right]^2(b_2x - b_3)^2y^2 + \tfrac{1}{4}\left(b_4^2 + b_5x^2\right)y^4, \tag{30}$$

in which

$$b_5 = \operatorname{sgn}\left(\frac{b_2}{b_4} - \tan\theta_g\right), \tag{31}$$

and the parameters associated with crack branching are

$$x_c = b_3/b_2, \qquad \tan\theta_c = b_2/b_4 \tag{32}$$

The sign function in eq. (31) depends on whether the bifurcation angle is smaller, equal or larger than the characteristic angle θ_g which corresponds to the bifurcation angle [78].

By comparing the coefficients of eqs. (23) and (30) and taking into consideration eqs. (32) and (27), it is found that

$$\begin{aligned} d_1 &= b_1, \\ d_2 &= \left[U_+\left(x - \frac{b_3}{b_2}\right)\right]^2(b_2x - b_3)^2, \\ d_3 &= b_4^2 + b_5x^2. \end{aligned} \tag{33}$$

This establishes a one-to-one continuous differentiable transformation of Figs. 9(a) and 9(b).

There remains the assessment of b_1. The stress intensity factor ratio K_{II}/K_I; the circumferential maximum stress [14,15]; the minimum strain energy density [15]; and the maximum dilatational strain energy density [18–20] have been all suggested as possible criteria for crack branching. A satisfactory approximation of θ_c is [31]:

$$\theta_c = -2\frac{K_{II}}{K_I}, \tag{34}$$

where K_{II} and K_I are defined in terms of their static counterparts $(K_{II})_s$ and $(K_I)_s$. Here, directional instability occurs in a distance that is small compared to the initial half crack length a. According to this assumption, the dynamic stress intensity factors are given by [79]:

$$\begin{aligned} K_I &= \bar{k}(v_c)(K_I)_s, \\ K_{II} &= \bar{k}(v_c)(K_{II})_s. \end{aligned} \tag{35}$$

Table 1
Variation of parameter h as a function of Poisson's ratio ν [79]

ν	0.1	0.2	0.25	0.33	0.4
v_2h	0.0452	0.9479	0.9486	0.9484	0.9469

in which [31]

$$(K_{\mathrm{I}})_{\mathrm{c}} = \left\{\left[(1+k_b)-(1-k_b)\cos 2\beta\right]\frac{\sigma_\eta}{2} + \sigma_{0_{\mathrm{c}}}\right\}\sqrt{\pi a},$$

$$(K_{\mathrm{II}})_{\mathrm{c}} = \left[\frac{\sigma_\eta}{2}(1-k_b)\sin 2\beta\right]\sqrt{\pi a}. \tag{36}$$

Note that $k_b = \sigma_\xi/\sigma_\eta$ and

$$\sigma_\xi = -\sigma, \quad \sigma_\eta = \frac{\nu}{\nu-1}\sigma, \quad \tau_{\xi\eta} = 0. \tag{37}$$

The quantity $\bar{k}(v_c)$ in eqs. (35) can be approximated within 2% by

$$\bar{k}(v_c) = \frac{\left(1-\frac{v_c}{v_R}\right)}{\sqrt{1-hv_c}}, \quad 0 < v_c < v_R. \tag{38}$$

Here, v_R is the velocity of the Rayleigh waves and h is a function of the Poisson's ratio ν as given in Table 1.

The ECP trajectory at the onset of crack bifurcation can be obtained by making use of eq. (30):

$$\frac{\mathrm{d}V}{\mathrm{d}y} = y^3 - \frac{\left[U_+\left(x-\frac{b_3}{b_2}\right)\right]^2}{b_4^2+b_5x^2}(b_2x-b_3)^2 y + \frac{b_1}{b_4^2+b_5x^2} = 0. \tag{39}$$

The only real root is found to be

$$y = \left[-A+\sqrt{A^2+\frac{B^3}{27}}\right]^{1/3} + \left[-A-\sqrt{A^2+\frac{B^3}{27}}\right]^{1/3}, \tag{40}$$

in which

$$A = \frac{b_1}{2\left(b_4^2+b_5x^2\right)}, \qquad B = \frac{\left[U_+\left(x-\frac{b_3}{b_2}\right)\right]^2(b_2x-b_3)^2}{\left(b_4^2+b_5x^2\right)^2}. \tag{41}$$

Differentiating eq. (40) with respect to x, the slope of the ECP trajectory at the instability is obtained:

$$\frac{\mathrm{d}y}{\mathrm{d}x} = \frac{1}{27}\left[A^2+\frac{B^3}{27}\right]^{-1/2}\frac{b_2B^3}{(b_2x-b_3)} \times\left\{\left[-A+\sqrt{A^2+\frac{B^3}{27}}\right]^{-1/3} + \left[-A-\sqrt{A^2+\frac{B^3}{27}}\right]^{-1/3}\right\}. \tag{42}$$

For small angles, eq. (42) becomes

$$\frac{\mathrm{d}y}{\mathrm{d}x} = -2\frac{K_{\mathrm{II}}}{K_{\mathrm{I}}}. \tag{43}$$

Eliminating $\mathrm{d}y/\mathrm{d}x$ in eqs. (42) and (43), a relation of the form

$$f_1(b_1, b_2, b_3, b_4, b_5, K_{\mathrm{II}}/K_{\mathrm{I}}) = 0 \tag{44}$$

can be obtained. It can be solved numerically with respect to b_1 when the remaining parameters are specified. The parameter d_2 depending on b_2 and b_3 tends to control crack bifurcation.

Suppose that d_2 is represented by

$$d_2 = -\left[d_{21}\left(K_{\mathrm{I}b}^p - K_{\mathrm{II}}^p\right)^2 + d_{22}\left(r_0^s - r_c^s\right)^2\right], \tag{45}$$

with p and s being exponents that are yet to be determined. The coefficients d_{21} and d_{22} are also unknown. In eq. (45), $K_{\mathrm{I}b}$ is a critical stress intensity factor associated with a critical crack tip core radius r_c at the onset of crack bifurcation [27,45]. The distance r_0 corresponds to the location of an imaginary small crack [4] ahead of the main crack. For a crack with its tip traveling to a distance x, K_{I} is obtainable from eqs. (35) and the first of eqs. (36):

$$K_{\mathrm{I}} = \bar{k}(v_c)\left\{\left[(1+k_b)-(1-k_b)\cos 2\beta\right]\frac{\sigma_\eta}{2} + \sigma_{0_{\mathrm{c}}}\right\}\sqrt{\pi x}. \tag{46}$$

For the sake of simplicity, r_0 will be found from the maximum circumferential stress [2] [27]:

$$r_0 = R(v_c, v_1, v_2)\left(\frac{K_{\mathrm{I}}}{\sigma_{0_{\mathrm{c}}}}\right)^2 \tag{47}$$

[2] A better choice would be the minimum strain energy density criterion.

The contraction R stands for

$$R(v_c, v_1, v_2) = -\frac{1}{128\pi}\int_0^{\pi} B_1(v_c)\left\{-(1+s_2^2)(2+3s_1^2) - \frac{4s_1s_2}{1+s_2^2}(14+3s_2^2) - 16s_1(s_1-s_2) + 16(1+s_1^2)\right\}^2, \quad (48)$$

in which

$$B_1(v_c) = \frac{1+s_2^2}{4s_1s_2-(1+s_2^2)^2}, \qquad s_i^2 = 1-\frac{v_c^2}{v_i^2}, \quad i=1,2. \quad (49)$$

The dilatational wave velocity is v_1 and distortional wave velocity is v_2. Substituting eqs. (46) and (47) into eq. (45) and retaining terms with degree less than or equal to two after expansion, eqs. (33) and (45) may be equated to obtain $p=2$ and $s=1$. Hence, eq. (45) becomes

$$d_2 = -(d'_{21}+d'_{22})x^2 + 2x_c(d'_{21}+d'_{22})x - x_c^2(d'_{21}+d'_{22}), \quad (50)$$

provided that

$$d'_{21} = d_{21}S(u_c, k_b, \beta, \sigma_\eta, \sigma_{0_v}),$$
$$d'_{22} = d_{22}\left[\frac{R(v_c, v_1, v_2)}{\sigma_{0_v}^2}\right]^2 S(u_c, k_b, \beta, \sigma_\eta, \sigma_{0_v}) \quad (51)$$

and

$$S(u_c, k_b, \beta, \sigma_\eta, \sigma_{0_v}) = \pi^2\left[\bar{k}(v_c)\right]^4\left\{\left[(1-k_b)+(1+k_b)\cos 2\beta\right]\frac{\sigma_\eta}{2} + \sigma_{0_v}\right\}^4. \quad (52)$$

Equating the coefficients for quantities in eqs. (50) and (45) with like powers of x yields

$$\frac{[U_+b_2]^2}{b_4^2+b_5x^2} = S\left[d_{21}+d_{22}\left(\frac{R}{\sigma_{0_v}^2}\right)^2\right],$$
$$\frac{[U_+b_3]^2}{b_4^2+b_5x^2} = d_{21}K_{1b}^4 + d_{22}r_c^2,$$
$$\frac{[U_+]^2}{b_4^2+b_5x^2}b_2b_3 = \sqrt{S}\left(d_{21}K_{1b}^2 + d_{22}r_c\frac{R}{\sigma_{0_v}^2}\right). \quad (53)$$

From the above relations, b_3/b_2 is determined:

$$\frac{b_3}{b_2} = \frac{d_{21}K_{1b}^4 + d_{22}r_c^2}{\sqrt{S}\left(d_{21}K_{1b}^2 + d_{22}r_cR/\sigma_{0_v}^2\right)}. \quad (54)$$

which corresponds to the first of eqs. (32) for x_c.

Accurate predictions of the crack bifurcation have been made by the maximum dilatational energy density criterion [21]. A slightly nonlinear relationship between the angle θ_c and ratio v_c/v_2 can be approximated by

$$\theta_c = -200\frac{v_c}{v_2} + \alpha, \quad \alpha = \begin{cases} 138 & \text{for plane strain,} \\ 140 & \text{for plane stress.} \end{cases} \quad (55)$$

This linearization gives an error of 7% in one region for $v_c/v_2 = 0.623$. With the aid of eq. (55) and the second of eq. (32), b_2/b_4 is found for plane stress:

$$\frac{b_2}{b_4} = \tan\left[\pi\left(-\frac{10}{9}\frac{v_c}{v_2}+\frac{7}{9}\right)\right]. \quad (56)$$

Equations (53) can be further applied to give

$$d_{22} = \frac{[U_+]^2\sigma_{0_v}C}{b_4^2+b_5x^2SR},$$
$$d_{21} = \frac{[U_+]^2}{b_4^2+b_5x^2}\left[\frac{b_2^2}{S}-\frac{RC}{S}\right], \quad (57)$$

in which C is given by

$$C = \frac{\sqrt{S}\,b_2b_3 - K_{1b}^2}{r_c\sigma_{0_v}^2 - RK_{1b}^2}. \quad (58)$$

Without loss in generality, b_4 may be arbitrarily set to unity. The critical stress intensity factor K_{1b} and critical distance r_c can be taken as [7]:

$$K_{1b} = \sqrt{2n}\,K_{1c}, \quad n = r_c/a_0. \quad (59)$$

in which a_s is the effective microcrack length at a distance r_c ahead of the running crack. The static critical stress intensity factor is K_{1c}. Values of n for some metals and Plexiglas (PMMA) can be found in [7]. Reported in [27] are r_c values for Homalite-100 and in [21] for Plexiglas.

Finally, the parameter Q controlling the stochastic characteristics of the crack instability problem is also an unknown. Sharpness of the probability density distribution density surface tends to increase with decreasing Q. It controls the stochasticity of the directional instability geometry after bifurcation and is anticipated to depend on microdefects in the material.

6. Discussion

Presented in this work is a crack bifurcation model that incorporates the influence of microcracks stochastically and dissipation. An equivalent crack particle is defined whose probabilistic unstable behavior is shown to be governed by the Fokker–Planck equation. The coefficients in the mathematical model are determined from available experimental observations and are related to parameters made use by previous investigators.

Mathematical inconsistencies [27,45] in previous works have been removed by incorporating K_{1b} and r_c into a single statement as given by eq. (45). The necessary and sufficient conditions for the onset of crack bifurcation are satisfied simultaneously.

Acknowledgment

The author wishes to express his gratitude to Professors G.C. Sih and P.S. Theocaris for their inspiring discussions and support during the course of the present work.

Appendix

Fokker–Planck equation

Consider a probability density in terms of Dirac's δ-function as follows:

$$P(q, t) = \delta[q - q(t)] = \delta[q_1 - q_1(t)]\,\delta[q_2 - q_2(t)]. \tag{A1}$$

where q is a random position vector of the ECP and is a solution of eq. (14). Differentiation with respect to time gives

$$\dot{P}(q, t) = -\nabla(P\dot{q}(t)) = \dot{P}(q, t) = -\nabla(PK). \tag{A2}$$

with P being a density in the q-space. The velocity vector K describes the deterministic motion governed by eq. (14).

A one-dimensional motion of the ECP in the qt-space can be obtained by

$$P_j = \delta[q - q_j(t)], \tag{A3}$$

for a given path j according to eq. (A1). The average, over all these paths, may be expressed as:

$$f(q, t) = \langle P(q, t)\rangle = \sum_j p_j \delta[q - q_j(t)] = \langle \delta[q - q_j(t)]\rangle. \tag{A4}$$

where use has been made of eq. (20). An equation governing the probability distribution $f(q, t)$ that is amenable to evaluation will be found.

It has been established [70–72] that for every Langevin equation, there is always a corresponding Fokker–Planck equation [73,74]. The Fokker–Planck equation that corresponds to the Langevin equation (16) in one dimension is given by

$$\dot{f} = \frac{\mathrm{d}}{\mathrm{d}q}(Kf) + \tfrac{1}{2}Q\frac{\mathrm{d}^2 f}{\mathrm{d}q^2}. \tag{A5}$$

The force K sometimes is referred to as the drift coefficient while Q is known as the diffusion coefficient as defined by an expression similar to eq. (12). If the probability current I is defined as

$$I = Kf - \tfrac{1}{2}Q\frac{\mathrm{d}f}{\mathrm{d}q}, \tag{A6}$$

then the Fokker–Planck equation takes the form

$$\dot{f} + \frac{\mathrm{d}I}{\mathrm{d}q} = 0. \tag{A7}$$

For the problem at hand, the Langevin equation in two dimensions may be written in terms of the components of the vector q:

$$\dot{q}_1 = K_1 + F_1(t), \qquad \dot{q}_2 = K_2 + F_2(t). \tag{A8}$$

References

[1] E.H. Yoffé, "The moving Griffith crack", *Phil. Mag. 42*, pp. 739–750 (1951).

[2] J.W. Craggs, "On the propagation of a crack in an elastic-brittle material", *J. Mech. Phys. Solids 8*, pp. 66–75 (1960).

[3] A.B.J. Clark and G.R. Irwin, "Crack-propagation behaviors", *Exp. Mech. 6*, pp. 321–330 (1966).

[4] J. Congleton and N.J. Petch, "Crack-branching", *Phil. Mag. 16*, pp. 749–760 (1967).

[5] S.R. Anthony and J. Congleton, "Crack branching in strong metals", *Metal Sci.* pp. 158–160 (1968).

[6] S.R. Anthony, J.P. Chubb and J. Congleton, "The crack-branching velocity", *Phil. Mag. 22*, pp. 1201–1216 (1970).

[7] J. Congleton, "Practical applications of crack-branching measurements", in: *Dynamic Crack Propagation*, Noordhoff, Leyden, pp. 427–483 (1973).

[8] J.W. Johnson and G.W. Holloway, "On the shape and size of the fracture surfaces", *Phil. Mag. 14*, pp. 731–743 (1966).

[9] J.W. Johnson and G.W. Holloway, "Microstructure of the mist zone on glass fracture surfaces", *Phil. Mag. 17*, pp. 899–910 (1968).

[10] G.K. Bansal, "On fracture mirror formation on glass and polycrystalline ceramics", *Phil. Mag. 35*, pp. 935–944 (1977).

[11] A. Rabinovitch, "A note on the fracture branching criterion", *Phil. Mag. 40*, pp. 873–874 (1979).

[12] M.L. Williams, "On the stress distribution at the base of a stationary crack", *J. Appl. Mech. 24*, pp. 109–114 (1957).

[13] F. Kerkhof, in: K.A. Wolf, ed., *Vorgange beim bruch struktur und physikalishes verhalten der kunstoffe*, Springer, Berlin, pp. 440–484 (1962).

[14] F. Erdogan and G.C. Sih, "On the crack extension in plates under plane loading and transverse shear", *J. Basic Engrg., Trans. ASME, Ser. E, 35*, pp. 519–527 (1963).

[15] G.C. Sih, "Dynamic crack problems: strain energy density fracture theory", in: G.C. Sih, ed., *Elastodynamic Crack Problems*, Noordhoff, Leyden, pp. 17–46 (1977).

[16] G.C. Sih, "Some basic problems in fracture mechanics and new concepts", *Engrg. Fracture Mech. 5*, pp. 365–377 (1973).

[17] G.C. Sih, "Strain energy density factor applied to mixed mode crack problems", *Internat. J. Fracture 10*, pp. 305–321 (1974).

[18] P.S. Theocaris and N.P. Andrianopoulos, "The Mises elastic-plastic boundary as the core region in fracture criteria", *Engrg. Fracture Mech. 16*, pp. 425–432 (1982).

[19] N.P. Andrianopoulos, "Crack initiation conditions in ductile materials – a new criterion", Ph.D. Diss., Department of Engineering Sciences, National Technical University of Athens (1983).

[20] P.S. Theocaris and N.P. Andrianopoulos, "A modified strain energy density criterion applied to crack propagation", *J. Appl. Mech. 49*, pp. 81–86 (1982).

[21] P.S. Theocaris and H.G. Georgiadis, "Bifurcation predictions for moving cracks by the *T*-criterion", *Internat. J. Fracture 29*, pp. 181–190 (1985).

[22] M.A. Hussain, S.L. Pu and J. Underwood, "Strain-energy release rate for a crack under Mode I and Mode II", *ASTM STP 560*, pp. 2–28 (1974).

[23] K. Palaniswamy and W.G. Knauss, "On the problem of crack extension in brittle solids under general loading", in: S. Nemat-Nasser, ed., *Mechanics Today*, Pergamon Press, pp. 87–148 (1978).

[24] C.H. Wu, "Elasticity problems of slender *Z*-crack", *J. Elast. 8*, pp. 183–205 (1978).

[25] B.L. Karihaloo, L.M. Keer and S. Nemat-Nasser, "Crack kinking under non-symmetric loading", *Engrg. Fracture Mech. 13*, pp. 879–888 (1980).

[26] G.C. Sih, "Some elastodynamic problems of cracks", *Internat. J. Fracture 4*, pp. 51–68 (1968).

[27] M. Ramulu and A.S. Kobayashi, "Dynamic crack curving – A photoelastic evaluation", *Exp. Mech. 23*, pp. 1–9 (1983).

[28] R. Streit and I. Finnie, "An experimental investigation of crack path directional stability", *Exp. Mech. 20*, pp. 17–23 (1980).

[29] H. Schardin, "Velocity effects in fracture", Conf. on Fracture, Swampscott, USA, Wiley, New York, 12–16 April (1959).

[30] F. Kerkhof, Bruchvorgange in Glasern, Verlag der Deutschen Glastechnischen Gesellschaft, Frankfurt (1970).

[31] F. Kerkhof, "Wave fractographic investigations of brittle fracture dynamics", in: *Dynamic Crack Propagation*, pp. 3–35 (1973).

[32] L.J. Broutmann and T. Kobayashi, "Dynamic crack propagation studies in polymers", in: *Dynamic Crack Propagation*, pp. 215–225 (1973).

[33] E.F. Poncelet, "Nature of strength and failure in brittle solids", *Colloid Chem. 6*, pp. 77–88 (1946).

[34] E.F. Poncelet, "A theory of static fatigue for brittle solids", *Fracturing of Metals, ASM*, pp. 201–227 (1948).

[35] S.N. Zhurkov, "Kinetic concept of the strength of solids", *Internat. J. Fracture 1*, pp. 311–323 (1965).

[36] A.M. Freudenthal, "Statistical approach to brittle fracture", in: H. Liebowitz, ed., *Fracture*, Academic Press, New York, pp. 591–619 (1968).

[37] R.F. Smalley Jr., D.L. Turcotte and S.A. Solla, "A renormalization group approach to the stick-ship behavior of faults", *J. Geoph. Res. 90*, pp. 1894–1900 (1985).

[38] D.L. Turcotte, R.F. Smalley, Jr. and S.A. Solla, "Collapse of loaded fractal trees", *Nature 313*, p. 671 (1985).

[39] S.A. Solla, "Crack propagation and onset of failure", *Growth and Form*, pp. 260–262 (1986).

[40] K. Ravi-Chandar and W.G. Knauss, "An experimental investigation into dynamic fracture: I. Crack initiation and arrest", *Internat. J. Fracture 25*, pp. 247–262 (1984).

[41] K. Ravi-Chandar and W.G. Knauss, "An experimental investigation into dynamic fracture: II. Micro-structural aspects", *Internat. J. Fracture 26*, pp. 65–80 (1984).

[42] K. Ravi-Chandar and W.G. Knauss, "An experimental investigation into dynamic fracture: III. On steady-state crack propagation and crack branching", *Internat. J. Fracture 26*, pp. 141–154 (1984).

[43] K. Ravi-Chandar and W.G. Knauss, "An experimental investigation into dynamic fracture: IV. On the interac-

tion of stress waves with propagation cracks", *Internat. J. Fracture 26*, pp. 189–200 (1984).

[44] J.W. Dally, "Dynamic photoelastic studies of fracture", *Exp. Mech. 19*, pp. 349–367 (1979).

[45] M. Ramulu and A.S. Kobayashi, "Mechanics of crack curving and branching — A dynamic fracture analysis", *Internat. J. Fracture 27*, pp. 187–201 (1985).

[46] G.C. Sih, "Dynamic aspects of crack propagation", in: M.F. Kanninen, ed., *Elastic Behavior of Solids*, McGraw-Hill, New York, pp. 607–639 (1969).

[47] J.J. Gilman, "Cleavage, ductility and tenacity in crystals", in: B.L. Averbach et al., eds., *Fracture: Proc. Int. Conf. on the Atomic Mechanisms of Fracture*, MIT Techn. Press, Cambridge, MA, pp. 193–224 (1959).

[48] D.K. Roberts and A.A. Wells, "The velocity of brittle fracture", *Engineering 178*, pp. 820–821 (1954).

[49] J.P. Berry, "Some kinetic considerations of the Griffith criterion for fracture: I. Equations of motion at constant force", *J. Mech. Phys. Solid. 8*, pp. 194–206 (1960).

[50] J.P. Berry, "Some kinetic considerations of the Griffith criterion for fracture: II. Equations of motion at constant deformation", *J. Mech. Phys. Solid. 8*, pp. 207–216 (1960).

[51] J.J. Gilman, "Direct measurements of the surface energies of crystals", *J. Appl. Phys. 31*, pp. 2208–2218 (1960).

[52] P.P. Gillis and J.J. Gilman, "Double cantilever cleavage mode of crack propagation", *J. Appl. Phys. 35*, pp. 647–658 (1964).

[53] S.J. Burns and W.W. Webb, "Fracture surface energies and dislocation processes during dynamical cleavage of Lif. I", *J. Appl. Phys. 41*, pp. 2078–2085 (1970).

[54] B. Steverding and S.H. Lehnigk, "The propagation law of cleavage fracture", *Internat. J. Fracture 6*, pp. 223–232 (1970).

[55] B. Steverding and S.H. Lehnigk, "Response of cracks to impact", *J. Appl. Phys. 41*, pp. 2096–2099 (1970).

[56] B. Steverding and S.H. Lehnigk, "Dynamics of brittle fracture", *Internat. J. Fracture Mech. 8 (1)*, pp. 59–73 (1972).

[57] S.H. Lehnigk, "A microscopic dynamic theory of stability and instability of cracks under impulsive loading", in: *Dynamic Crack Propagation*, pp. 333–347 (1973).

[58] B. Steverding, "Fracture and dislocation dynamics", in: *Dynamic Crack Propagation*, pp. 349–361 (1973).

[59] Z.J. Bilek and S.J. Burns, "The dynamics of crack propagation in double cantilever beam specimens", in: *Dynamic Crack Propagation*, pp. 371–385 (1973).

[60] M.F. Kanninen, "A dynamic analysis of unstable crack propagation and arrest in the DCB test specimen", *Internat. J. Fracture 10*, pp. 415–430 (1974).

[61] L.B. Freund, "A simple model of the double cantilever beam crack propagation specimen", *J. Mech. Phys. Solid 25*, pp.69 (1977).

[62] J.G. Michopoulos, "A beam model for the dynamic propagation of oblique cracks" in: G.C. Sih and P.S. Theocaris, eds., *Mixed Mode Crack Propagation*, Noordhoff, Leiden, Netherlands, pp. 133–162 (1981).

[63] J.D. Achenbach, "Elastodynamic fracture mechanics", *SIAM-AMS Proc.*, Vol. 12, pp. 3–20 (1979).

[64] L.B. Freund, "Crack propagation in an elastic solid subjected to general loading: I. Constant rate of extension", *J. Mech. Phys. Solid 20*, pp. 129–140 (1972).

[65] L.B. Freund, "Crack propagation in an elastic solid subjected to general loading: II. Non-uniform rate of extension", *J. Mech. Phys. Solid 20*, pp. 141–152 (1972).

[66] L.B. Freund, "Crack propagation in an elastic solid subjected to general loading: III. Stress wave loading", *J. Mech. Phys. Solid 2*, pp. 47–61 (1973).

[67] L.B. Freund, "Crack propagation in an elastic solid subjected to general loading: IV. Obliquely incident stress pulse", *J. Mech. Phys. Solid 22*, pp. 137–146 (1974).

[68] M. Ramulu, A.S. Kobayashi and B.S.J. Kang, "Dynamic crack curving and branching in line-pipe", *J. Pressure Vessel Tech. 104*, pp. 317–322 (1983).

[69] P. Langevin, "Sur la theorie du mouvemont Brownien", *Comptes Rendus 146*, pp. 530–533 (1908).

[70] R.L. Stratonovich, *Topics in the Theory of Random Noise*, Gordon and Breach, New York (1963).

[71] H. Haken, *Synergetics: An Introduction*, Springer, Berlin (1978).

[72] G.E. Uhlenbeck and L.S. Ornstein, "On the theory of the Brownian motion", *Phys. Rev. 36*, pp. 823–841 (1930).

[73] A.D. Fokker, "Die mittere energie rotierender elektrischen dipole im strahlungungsfeld", *Ann. Physik Chemie 43*, pp. 810–820 (1914).

[74] M. Planck, "The Fokker–Planck equation", *Sitzber Preub. Akad. Wiss.*, p. 324 (1917).

[75] J.G. Michopoulos and P.S. Theocaris, "Dynamic fracture and catastrophe theory", in preparation.

[76] R. Thom, *Structural Stability and Morphogenesis*, Benjamin, Reading, MA (1975).

[77] J.D. Lawrence, *A Catalog of Special Plane Curves*, Dover, New York (1972).

[78] J.F. Kalthoff, "On the characteristic angle for crack branching in brittle materials", *Internat. J. Fracture 7*, pp. 478–480 (1971).

[79] L.R.F. Rose, "Recent theoretical and experimental results on fast brittle fracture", *Internat. J. Fracture 12*, pp. 799–813 (1976).

SYSTEM'S IDENTIFICATION APPROACH FOR THE DIRECTIONAL INSTABILITY OF THE DYNAMIC CRACK IN COMPOSITES

John G. Michopoulos
Geo-Centers, Inc.
Ft. Washington, MD. 20744
at
Mechanics of Materials Branch, Code 6380
Materials Science and Technology Division
U.S. Naval Research Laboratory
Washington, D.C. 20375, U.S.A

Abstract.

The propagating crack in a particulate composite, has been treated as a system to be identified, such as a model can be built to be used as a predictive tool. The identification process is being applied in both the space of morphology of the bifurcated cracks as well as the space of the behavior parameters characterizing the cracks.

It is shown that a simple of topologicaly singular polynomial has all the properties needed to capture the morphology of the crack after the critical point. The isomorphic relationship of this polynomial to the potential characterizing the equilibrium of an equivalent particle is also presented.

The model represented by this polynomial is trained to the actual experimental results gathered by several investigators, in the form of a diffeomorphic tuning of the coefficients.

In order to extend the modelling such as the stochastic character of the particle-matrix interaction will be incorporated, the *Fokker-Planck* equation has been proposed to replace the classical *Langevin* equations of motion. Thus, the probality density distribution function for the crack tip to be on an exact path is proposed to more efficiently capture the non-deterministic attributes of the crack propagation.

Presented at COMP'98 [illegible] Athens, Greece

1 Introduction

The instability associated with crack propagation occurs in the form of sudden curving or sudden bifurcation in two or more branches for no apparent reason. Answers to the questions why it is happening and when it is happening have been attempted by a host of investigators since the very early days of dynamic fracture. A historical review of the proposed theories on the subject is presented in [1]. The common characteristic of all these approaches can be detected to be that they employ one physical quantity which when exceeds a critical value directional instability occurs. A plethora of different quantities were introduced to be responsible (i.e. crack speed, dynamic stress intensity factor, energy release rate, strain energy density, dilatational strain energy density, e.t.c), without a clear specification of which conditions were including the simultaneous satisfaction of conditions related to the rest of them. No negative experiment was ever reported, such as refutation of the criticality or participation of a given parameter would be deducted. It seemed that all theories were yielding relatively accurate predictions for narrow classes of materials (i.e. very brittle isotropic and homogeneous materials and in some cases ductile materials), and they could only judged on the basis of their prediction's accuracy when compared with the experimental observations.

The underlined skeletal mechanism of these approaches involves the application of the traditional steps of the scientific method:

- Initial observation of the phenomenon in the physical world.
- Initial theory formation involving hypotheses in terms of the perceived physical parameters which are juged to control the originally observed phenomenon.
- Recreate the original phenomenon in the laboratory by devising an experiment as closely to the actual conditions as possible by mesuring the quantities participating in the initial theory.
- If the measurements agree with the predictions of the theory then the theory is judged to be acceptable otherwise it is modified to a new form and the process is repeated.

The second step of this program for scientific research introduces the assumptions needed for the theory which can only be based on the researcher's experience, judgement, and understanding. The subjectiveness of this approach, together with the inherent charateristics of the research media used, create a strongly user-media depented situation. As a result redudancy seems to be the obvious by-product characteristic of these theories. Issues concerning the attributes characterizing the theories themselves (i.e. consistency completness and decidability) have been traditionaly ignored.

The substantial number of parameters involved in the dynamic crack propagation process increased by the host of parameters characterizing more complex material like composite and non-homogeneous materials in general, together with the inherent weaknesses of the traditional method, call for an alternative approach.

The particular approach suggested here is a system's identification approach. The methodology involved in this approach will guarantee the objectivity of the established model since it will be based on facts, and will carry the merits of the formal '*Model Theory* ', in terms of the consistency, completeness and decidability issues involved. The program of a system's identification methodology considers the to be predicted or explained phenomenon of the physical world as a process or a system to be identified. It can be briefly described by the following steps:

- Establish the dimensionality of the observation space in terms of the number of the state (or behavior) and input (or control) parameters involved in the actual process to be identified.
- Create a laboratory experiment of gathering facts from the physical world, by simply exposing the process to discrete paths in the control space and simultaneously measuring the coresponding paths in the state space.
- Develop a model in the form of figure 1 relating the state parameters involved to the control ones, and train it to the gathered facts observed.
- Use the obtained model to predict the state of the process for a given excitation in the control space.

No assumptions related to the homogeneity of the material or the non-dissipative character of the propagation, or the stochasticity of the void-particle-crack interaction processes will be made. Traditionally introduction of this type of assumptions introduced undesirable redudancy. In our formulization, the actual behavior of the system will 'inform' the system via its training process what actually happens.

In the approach followed all available knowledge based on observation will be used to construct the minimal functional form of the process of dynamic fracture, such as all of the observed behavior characteristics will be derivable from this formulation.

2 Modeling the Stability of Dynamic Fracture.

2.1 Problem Definition.

The actual physical definition of the system to be identified, is described by the following postulates:

Postulates.

1. The crack propagation process will be considered in two dimensional media. The equations of motion for the crack tip and the will be referred to a cartesian frame of reference $O_n - x_1 - x_2$, as in figure 2.

2. The loading conditions will be a rectangular stress pulse of amplitude σ and duration τ applied along the ξ - axis rotated by an angle β relative to the x_2 - axis, and the static remotely applied loads σ_{01} and σ_{02} along the x_1- and x_2- axes respectively. The analysis will be restricted for times $t \leq \tau/2$.

3. The medium will correspond to an infinite specimen, made of a particulate composite material with Young's modulus E_c and a Poisson's ratio ν_c.

4. The crack tip moves with an average constant velocity, which can be considered to be the terminal velocity of the crack.

The dimensionality of the behavior space determines the number of the dynamic equations needed. The functional form of this equations will be selected to mach the actual bifurcation morphology and the control parameters of participating in this form will be mached with the actual physical parameters for which measurements exist or other qualitative facts have been gathered.

In figure (2) we can see a schematic representation of the specimen and loadings as well as the respective crack.

The behavior of any dynamical system, can be expressed by its spatio-temporal characteristics represented by its behavior parameters. These behavior parameters are governed by a set of control parameters, via the differential equations of evolution governing the system.

Existence of accurate dynamical equations would define the relationship between control and behavior parameters. However, the equations derived up to now [2-23] for homogeneous media, were proved inefficient on capturing the directional instability of the crack, as well as the stochastic attributes of the inhomogeneous continuum.

A typical representation of generalized equations of motion is described by the classical dynamic equations of the form:

$$\ddot{x}_i + y_i \dot{x}_i = \mathcal{F}_i(c_j; x_i), \; i = 1, 2 \qquad (1)$$

Here g_i represent the damping constants, and $\mathcal{F}_i$ represent the generalized forces driving the motion of the system, whereas x_i and c_j are the state and control variables respectively. From the systems' identification point of view, these equations could be trivially extracted as the system's equations, assuming a Taylor expansion of the forces $\mathcal{F}_i$ in terms of the state variables x_i is available. Provided an extensive set of data referring to input-output (control-behavior) pairs from the corresponding spaces were available, the coefficients c_j of the Taylor expansion would be evaluated by following standard identification techniques like regression , quasilinerization and heuristic identification [24]. Since no such a data base is readily available, utilization of what already exists in terms of quatitative and qualitative information, will be invoked.

A primary characteristic of the crack branching phenomenon is that it occurs after the crack has reached its terminal constant velocity. This fact has also been verified for particulate composites [25,26]. The physicaly two dimensional problem is reduced to a mathematically one dimensional problem, since the first of eqs. 1 reduces to :

$$\dot{x}_1 = v_c \tag{2}$$

Here v_c represents the constant terminal velocity of the crack along the x_1 axis. This equation is uncoupled from the other one and therefore the speed along the x_1 axis and the quantities associated with it can be treated as paramaters for the system represented by the second equation. The remaining equation of motion after elimination of the acceleration term without loss of generality reduces to

$$\dot{x}_2 = \mathcal{F}(d_j; x_2) \tag{3}$$

It remains to establish the functional form $\mathcal{F}$ capturing the behavior of the system as it is shown in figure 1, by insuring that crack bifurcation and stochasticity of material-crack interaction facts have been accounted for in the identification process.

2.2 Bifurcation Characteristics of Dynamic Fracture.

The traditional theory of dynamic modeling indicates that only non-linear dynamic systems where the driving forces are non-linear functions of the state variables, exhibit bifurcational and/or chaotic behavior [27,28]. It seems therefore appropriate to utilize the simplest non-linear system which will exhibit the bifurcation pattern.

Observation of fractured specimens after bifurcation indicates, that the geometry of the travelled trajectories can fall in any of the three types shown in figure (3b) when they are viewed on the $x_1 - x_2$ plane. A characteristic functional form describing these three modes of bifurcation corresponding to three different ranges of the parameters involved can be generated by appropriate combination of the positive assymetrical

unit-step function U_+ [29] and the *bullet-nose* function [30] as follows :

$$y = U_+(x - x_c)\frac{b_2 x - b_3}{(b_4^2 + b_5 x^2)^{1/2}} \quad (4)$$

The use of the unit-step function eliminates the branches of the bullet-nose function prior to the bifurcation point which is located at a distanse x_c from the origin. It can be verified that the parameters associated with crack branching (the critical distance from the origin and the bifurcation angle) are

$$x_c = b_3/b_2 \ , \quad (5)$$

$$\tan\theta_c = b_2/b_4 \ , \quad (6)$$

The constant b_5 actually represents the sign function

$$b_5 = \mathrm{sgn}(\frac{b_2}{b_4} - \tan\theta_g) \ , \quad (7)$$

which depends on whether the bifurcation angle is smaller, equal or larger than the characteristic angle θ_g as it has been defined in [31]. In order for the trajectory equation to be meaningful, the constants b_i have to be determined in terms of observable and measurable quantities, as well as the dynamical equations to which this behavior corresponds. To achieve this we rely on standard statements of the Bifurcation [32] or/and Catastrophe theory [33]. Indeed, according to these theories the simplest dynamical system with one state variable ($q_2 \in \mathcal{Q}$ in correspondance to $x_2 \in \mathcal{B}$) exhibiting bifurcational behavior, is the autonomous gradient system of the form:

$$\dot{q}_2 = K_2(q_2)$$

where $K_2(q_2)$ is the force corresponding to the potential

$$V(q_2) = d_1 q_2 - \frac{d_2}{2}q_2^2 + \frac{d_3}{4}q_2^4$$

trough the gradient condition

$$K_2(q_2) = -\frac{dV}{dq_2} \quad (10)$$

Here $d_i \in \mathcal{D}$ are the control parameters of the system.

The equilibrium (steady state) points corresponding to the minimae of the potential surfaces are determined by the condition $\dot{q}_2 = 0$ or $dV(q_2)/dq_2 = 0$ (since the system is a gradient one). The resulting equation will be

$$q_2^3 - \frac{d_2}{d_3}q_2 + \frac{d_1}{d_3} = 0 \ , \quad (11)$$

The graph of this equation in the $q_2 - d_2/d_3$ plane (see Fig. 4) for different values of the parameter d_1/d_3, will correspond to the projection of the locii of the critical points of the potential surface on this plane, thus defining, the stable and unstable trajectories of the system.

For the case where $d_1 = 0$, the only solution of equation (11), in the case $d_2 < 0$, $d_3 > 0$, is the stable one (corresponding to the minimae of the potential surface) where $q_2 = 0$. On the other hand, in the case where $d_2 > 0$, $d_3 > 0$, we find three solutions, one corresponding to $q_2 = 0$, which evidently is unstable (since it corresponds to the local maximae of the potential surface), and two other stable solutions $q_2 = \pm(\mid d_2 \mid /d_3)^{1/2}$, corresponding to the two local minimae trajectories in the positive d_2/d_3 half plane of figure (4). Clearly the point where $d_2 = 0$ is the bifurcation point. After following a single path, the system may follow two symmetric to the d_2-axis paths when the control parameter d_2 from negative becomes positive. Therefor the necessary and sufficient condition for bifurcation to occur is the zeroing of d_2.

Depending on the sign of the control parameter d_1, as it can be seen in figure (4), we may have a curved non symmetric path followed by the system instead of the bifurcated situation mentioned previously. The symmetric behavior is broken due to the non symmetric minimae paths for the negative d_2.

For the case of broken symmetry, when we gradually change d_2 from negative to positive values, we arrive to $d_2 = 0$, where the stable steady-state, becomes unstable. Therefore, during this transition, the stable equilibrium positions are exchanged and new stable positions are created, i.e. we have the so called *exchange of stability*. The initially steady state position after the bifurcation point reduces to an unstable steady-state and two stable steady-state positions. This scheme may very well describe the crack branching process.

To justify whether two stable and one unstable positions will always occur for positive values of d_2, the set of the critical points in the control parameter space is determined. Since the parameter d_3 has only a scaling role (see equation (11)), the critical points can be established on the $d_2 - d_1$ plane. Differentiating one more time equation (11), we obtain :

$$3q_2^2 - \frac{d_2}{d_3} = 0. \qquad (12)$$

Eliminating now the behavior parameter q_2 from equations (11) and (12) we have

$$\left(\frac{d_2}{3d_3}\right)^3 + \left(\frac{d_1}{2d_3}\right)^2 = 0 \qquad (13)$$

The graphical representation of this equation is the cuspoid curve indicated in figure (5), and it divides the control parameter plane in two regions. The region within the cuspoid corresponds to potentials which for positive values of d_2, present two stable steady-state and one unstable steady-state paths, while every other point outside the cuspoid, corresponds only to one stable steady-state path. In figure (5) we can also see for different combinations of the control parameters corresponding to the location of the black dots, the

form of the potential.

In Figure (6) we may observe the manifold of the critical points of the potential in the $q_2 - d_2 - d_1$ space, and its projections onto the $d_2 - q_2$ and $d_2 - d_1$ planes.

It has been shown [33,27,32], that all of the above mentioned characteristics of the instability of the system correspond to the *Riemann-Hugoniot* cusp catastrophe shown in figure (6), which has a universal unfolding identical to the potential.

The dependence of the stable paths of the system is therefore summurized as follows. The control parameter d_1 according to figure (4), controls the location of the dominating steady-state stable trajectory which has the characteristics of a curved crack. The control parameter d_2, according to figure (2), controls the location of the bifurcation point, since for its sign change we obtain different set of stable trajectories. Finally, the parameter d_3 controls the distance between the two bifurcated paths in figure (2), and it can be therefore, correlated to the criteria yielding the crack bifurcation angle.

The next step is to establish a transition from the gradient system of the bifurcation behavior of figure (3a), to a system with a bifurcation behavior of figure (3b). In terms of model theory what is needed can be described by the comutation properties of the diagrams in figures (1a) and (1b) when refering to the dynamic equations which can be equivalenced to the figure (1c) when refering to the potential formulation. The main difference between the two systems resides in that in figure (1b) the state or behavior parameters are the time velocities, while in figure (1c) the state parameters are the average trajectories as they represent the stable trajectories of the system. Therefore, instead of identifying directly the actual system represented by the upper morhisms of figures (1b,c), the functional form of the system corresponding to the lower morphisms of figures (1b,c) has been established in terms of our bifurcational requirements. A smooth differential transformation is needed to map the bifurcation behavior of the modelled system to the one of the actual system, such as a transition from figure (3a) to figure (3b) can be achieved.

It is trivial to show that the potential corresponding to the gradient system with trajectories given by the rearrangement of equation (4) such as it will include the unstable path along the x_2 axis

$$(b_1^2 + b_3 x_1^2)x_2^3 - [U_*(x_1 - x_*)]^2(b_3 x_2 - b_1)^2 x_2 = 0 \tag{5}$$

will be the one given by

$$V(x_2) = b_1 x_2 - \frac{1}{2}[U_*(x_1 - x_*)]^2 x_2^2 + \frac{(b_1^2 + b_3 x_1^2)}{4} x_2^4 \tag{6}$$

Employment of $x_1 = q_1$ for the morphism h_b implies through the composition rules of partial functions of polynomial form that, $V(q_2) = V(x_2)$ for the morphism h_a. As a result the morphism h_c can be deduced

by comparing the coefficients of equations (9) and (15):

$$d_1 = b_1 \,,$$
$$d_2 = [U_+(x_1 - \frac{b_3}{b_2})] \,, \tag{16}$$
$$d_3 = b_4^2 + b_5 x_1^2 \,.$$

The maps expressed by the morphisms h_c and h_b in figure (1c), represent an injective continuous differentiable transformation of the figure (8a) to the figure (8b) and therefore it constitutes a diffeomorphic transformation. Also all the maps needed for establishing the comutability of the diagram in figure (1c) have been established.

The deterministic bifurcational morphology of the average path of the crack has been identified to be represented by the functional form of the deterministic force $K_2(q_2)$ as it is defined through relations (9) and (10).

2.3 Stochastic Characteristics of Dynamic Fracture.

Experimental works [34-38], have indicated that microcracks and microvoids are present in the material and they are nucleated as the main crack propagates. They can further coalesce near the crack tip, leading to a decrease in the local stress intensity and increase in the local compliance. The shape and the size as well as the spatial distribution of these defects are certainly parameters with stochastic characteristics. Moreover, it has also been observed [25,26], that in particulate composites an additional set of stochastic parameters contribute to the characteristics of the dynamic fracture. Such parameters are the ones characterizing the shape, the size of the particles, the adhesion quality between the particles and the matrix mainly controlled by the interphase, the type of dispersion and the amount of particle agglomeration. All of these parameters seem to possess nonuniform distributions over the spatial domain of the material.

To account of all these different stochastic effects the driving force will be considered to have a stochastic component $F(t)$. The deterministic part accounting for the loading and geometry interactions will be K_2 as it defined by relations (10) and (9). Equation (8) as the isomorphic expression of equation (3) can thus be presented as a semistochastic *Langevin* equation of motion:

$$q_2 = K_2(q_2) + F(t) \tag{17}$$

The stochastic force $F(t)$ can be considered to represent the impulses applied by the microdefects and the particles. If the duration of each single impulse interaction is very small such as *Dirac's* δ - function can be employed, it has been shown [1] the total force exerted by all sources in the course of time is derived by

summation over the sequence of j pushes, and is given by:

$$F(t) = o \sum_{j=1}^{m} \delta(t - t_j)(\pm 1)_j \,. \tag{18}$$

Here o represents the strength of the δ function.

Instead of solving the stochastic *Langevin* equation (17) for q_2, adaptation of a *Poisson's* process allows for the formation [40,41,1] of the corresponding *Fokker-Planck* equation :

$$\dot{f} + \frac{dj}{dq_2} = 0 \,, \tag{19}$$

with j being the propability current defined by:

$$j = K(q_2)f - \frac{1}{2}Q\frac{df}{dq_2} \,. \tag{20}$$

Here the essential quantity governed by equation (19) is the probability distribution function $f(q_2,t)$ expressing the probability of the system to be at coordinate q_2 at time t.

The quantity Q plays the role of the diffusion constant in the continuity equation (19) and it is defined by [1,40] :

$$Q = \frac{o^2}{t_0} \,, \tag{21}$$

corelating thus the amplitute of δ- function used in the formation of the *Langevin* equation, with the *Fokker-Planck* equation.

For a stationary solution of equation (19), where $\dot{f} = 0$, i.e., f is time-independent, direct integration of this equation is possible:

$$j = \text{const} \,. \tag{22}$$

Imposing now the phenomenologically obvious 'natural boundary condition' on f, which means that f vanishes for $q_2 \to \pm\infty$, leads to $j \to 0$ for $q_2 \to \pm\infty$. As a result, the constant in equation (22) must vanish. Under these circumstances the probability current equation (20), yields:

$$\frac{1}{2}Q\frac{df}{dq_2} = K_2 f \,. \tag{23}$$

Under the condition given by equation (10), equation (23) can be solved to to give the probability density distribution function :

$$f(q_2) = N \exp[-\frac{2V(q_2)}{Q}] \,, \tag{24}$$

where the normalization constant N is determined by the relation

$$\int_{-\infty}^{+\infty} f(q_2)dq_2 = 1 \,. \tag{25}$$

The stability analysis in terms of the potential V of the deterministic system, can be reduced to the stability analysis of the real semi-stochastic system, since the probability density distribution function f, has been expressed in terms of V , through equation (24). The equivalence between the modeled and the original system is now guaranteed through the commutative diagram of figure (1c).

Plotted in Figures 7(a) to 7(c) inclusive are the potential surfaces in the $V - q_2 - d_2$ space obtained from equation (9) and Figures 7(d) to 7(f) inclusive are the probability density distribution surfaces in the $f - q_2 - d_2$ space, computed from equation (24) for fixed values of $d_1, d_3$and$Q$. Note that the random force $F(t)$ drives the system upward as q_2 extends in the positive or negative direction. Restoration is provided by the deterministic force $K_2(q_2)$ such as the most probable positions of the system correspond to those points where V is minimum and f is maximum. For the sake of the real crack system the statement closer to reality should the one refering to the maximum points of f.

TABLE I

ν_r	0.1	0.2	1/4	1/3	0.4
$v_2 h$	0.9452	0.9479	0.9486	0.9484	0.9469

Table 1: Variation of parameter h as a function of Poisson's ratio ν_r according to Ref. [48]

3 Model Training.

The training process involves the calibration of the control parameters b_i, such as the already existing experimental observations and experience in the form of valid and quantitavely accurate criteria can be utilized.

It has been already verified from figures (4), (6), and (7), that the asymmetry characteristics of the directional instability of the potential, are essentially governed by the d_1 control parameter. Therefore, the crack curving mechanism can directly be associated with the values of this parameter. It has been claimed many times in the past that the more essential parameter controling the crack curving process is the ratio of the stress intensity factors K_{II}/K_I Most of the available criteria conclude this result either by solving analytically the trigonometric equation expressing the maximum of the circumferencial stress [42,43], or solving numerically the transcentental equations expressing the minimum strain energy density [43] or the maximum dilatational strain energy density [44,45,46]. A satisfactory approximation of the crack curving angle θ_c will be given by the relationship [47]

$$\theta_c = -2\frac{K_{II}}{K_I} \quad (26)$$

where the stress intensity factors of the propagating crack will be defined in terms of their static values K_{IIs}, K_{Is}, case the directional instability occurs in a distance which is small compared to the initial semi-length a of the crack. According to this assumption the dynamic stress intensity factors will be defined from the expressions [48] :

$$K_I = \bar{k}(v_c)K_{Is} \ , K_{II} = \bar{k}(v_c)K_{IIs} \ , \quad (27)$$

where $\bar{k}(v_c)$ can be approximated within 2% in the range $0 < v_c < v_R$, by

$$\bar{k}(v_c) \simeq \frac{(1 - \frac{v_c}{v_R})}{(1 - hv_c)^{1/2}} \quad (28)$$

Here, v_R is the velocity of the *Rayleigh* waves, and h is a function of the Poisson's ratio ν_r according to Table I.

The static values of the stress intensity factors, according to the geometry of figure (2a) can be found in

a manner analogous to that followed by Kerkhoff [47], to be:

$$K_{I_s} = \{[(1+k_b)-(1-k_b)\cos 2\beta]\frac{\sigma_\eta}{2} + \sigma_{0y}\}\sqrt{\pi a}\ .\ \ K_{II_s} = [\frac{\sigma_\eta}{2}(1-k_b)\sin 2\beta]\sqrt{\pi a}\ , \tag{29}$$

with,

$$\sigma_\xi = -\sigma\ ,\ \sigma_\eta = \frac{\nu_c}{\nu_c - 1}\sigma\ ,\ \tau_{\xi\eta} = 0\ , \tag{30}$$

and the biaxility factor defined by :

$$k_b = \frac{\sigma_\xi}{\sigma_\eta} = \frac{\nu_c - 1}{\nu_c}\ . \tag{31}$$

Therefore, the ratio of the stress intensity factors is completely defined in terms of the external loading geometry through relations (26-29) This can help establish the first of the control parameters. Indeed, the equilibrium condition for the potential expressed by equation (15), yields to the cubic equation of the form.

$$\frac{dV}{dx_2} = x_2^3 - \frac{[U_+(x_1 - \frac{b_3}{b_2})]^2}{b_4^2 + b_5 x_1^2}(b_2 x_1 - b_3)^2 x_2 + \frac{b_1}{b_4^2 + b_5 x_1^2} = 0\ . \tag{32}$$

and the only real root of it will be given by :

$$x_2 = [-A + (A^2 + \frac{B^3}{27})^{1/2}]^{1/3} + [-A - (A^2 + \frac{B^3}{27})^{1/2}]^{1/3}\ , \tag{33}$$

with,

$$A = \frac{b_1}{2(b_4^2 + b_5 x_1^2)}\ ,\ B = \frac{[U_+(x_1 - \frac{b_3}{b_2})]^2}{b_4^2 + b_5 x_1^2}(b_2 x_1 - b_3)^2 \tag{34}$$

Differentiating now equation (33), with respect of x_1, we obtain the slope of the system's trajectory at the instability point corresponding to the curving point of the crack :

$$\begin{aligned}\frac{dx_2}{dx_1} &= \frac{1}{27}\{A^2 + \frac{B^3}{27}\}^{-1/2}\frac{b_2 B^3}{(b_2 x_1 - b_3)} \\ &\{[-A + (A^2 + \frac{B^3}{27})^{1/2}]^{-1/3} + [-A - (A^2 + \frac{B^3}{27})^{1/2}]^{1/3}\}\end{aligned} \tag{35}$$

This slope for small angles can be approximated by the value of the angle itself:

$$\frac{dx_2}{dx_1} = -2\frac{K_{II}}{K_I}\ . \tag{36}$$

By equating now the right hand sides of equations (35,36), we obtain a highly nonlinear algebraic equation of the type,

$$\Gamma_1(b_1, b_2, b_3, b_4, K_{II}/K_I) = 0\ , \tag{37}$$

which can only be solved numerically with respect of b_1, provided that the rest of the b_i parameters are known.

Compared to the critical velocity, the concept of the critical stress intensity factor, seems functioning better as the quantity which if exceeded yields to bifurcation of the crack or directional instability in general [49-52]. A fact which has been also observed experimentally by Ravi-Chandar and Knauss [36] as well as by Ramulu and Kobayashi [53,38]. A second quantity participating in the instability making mechanism of the crack seems to be the characteristic distance of the crack tip from a point ahead of it, where the stresses have some characteristic values such as the micromechanical inhomogeneities at this range become active enough to bother the crack propagation trajectory. Although, this distance r_0 was initially proposed by Congleton [49] as the distance of an imaginary small crack ahead of the tip of the main crack, it has been recently associated with the radius r_c, of the so-called *core region* by Ramulu and Kobayashi [53,38]. In fact, they proposed a criterion [38], to describe the directional instability of the crack, which utilizes both the critical stress intensity factor K_{Ib} and the critical distance r_c. This was expressed in terms of the following relationships :

$$K_I \geq K_{Ib} , \tag{38}$$

$$r_0 \leq r_c . \tag{39}$$

Relation (38) is the necessary condition and relation (39) is a sufficient condition for this criterion. It is unfortunate that we have two separate equations for the necessary and sufficient condition , and therefore, the criterion lacks of mathematical consistency, although it is physically consistent and produces very good predictions.

One way to remove the inconsistency , is to utilize the two separate conditions of the criterion proposed by Ramulu and Kobayashi, to derive one single necessary and sufficient condition, by expressing the control parameter d_2 , in terms of the stress intensity factor and the critical distance, such as relations (38,39) will still be satisfied simultaneously. Since at the bifurcation point the control parameter d_2 becomes zero, it has to be linearly dependent on a term containing the sum of the squares of the quantities corresponding to the conditions (38), and (39). It can be proven fairly easy , that such a result can be obtained by introducing a relation of the form :

$$d_2 = -[d_{21}(K_{Ib}^p - K_{II}^p)^2 + d_{22}(r_c^s - r^s)^2]$$

The exponents p, s and the unit compatibility coefficients d_{21}, d_{22} are to be determined.

The instantaneous stress intensity factor of the propagating crack with its tip in a distance r can be found for mode one, by combining relations (27) and (28),

$$K_I = \bar{k}(v_r)\{[(1 + k_b) - (1 - k_b)\cos 2\beta]\frac{\sigma_\eta}{2} + \sigma_{0y}\}\sqrt{\pi r} . \tag{41}$$

For the sake of simpicity the maximum circumferential stress criterion was used for determining r_o [1,38]

$$r_o = R(v_c, v_1, v_2)(\frac{K_I}{\sigma_{01}})^2 . \tag{42}$$

The contraction R represents a quantity which is a function of the dilatational, and the distortional wave velocities v_1 and v_2, and it is defined in [1]. Substitution of equations (41 and 42) into equation (40), and truncation of terms above second degree, yields $p = 2$ and $s = 1$, and :

$$d_2 = -(d_{21}^{'} + d_{22}^{'})x_1^2 + 2x_c(d_{21}^{'} + d_{22}^{'})x_1 - x_c^2(d_{21}^{'} + d_{22}^{'}) , \tag{43}$$

provided that

$$d_{21}^{'} = d_{21}S(v_c, k_b, \beta, \sigma_\eta, \sigma_{02}),\ d_{22}^{'} = d_{22}[\frac{R(v_c, v_1, v_2)}{\sigma_{01}^2}]^2 S(v_c, k_b, \beta, \sigma_\eta, \sigma_{02}) , \tag{44}$$

and

$$S(v_c, k_b, \beta, \sigma_\eta, \sigma_{02}) = \pi^2[\overline{k}(v_c)]^4\{[(1 - k_b) + (1 + k_b)\cos 2\beta]\frac{\sigma_\eta}{2} + \sigma_{02}\}^4 . \tag{45}$$

Equating the coefficients of like powers of x_1, between equations (43) and (40), and after some algebra the ratio b_3/b_2 is defined :

$$\frac{b_3}{b_2} = \frac{d_{21}K_{Ib}^4 + d_{22}r_c^2}{\sqrt{S}(d_{21}K_{Ib}^2 + d_{22}r_c R/\sigma_{01}^2)} . \tag{46}$$

which corresponds to equation (5) for x_c.

The most accurate predictions of the crack bifurcation have been made by the maximum dilatational energy criterion [46] . The slightly nonlinear relationship deduced from this criterion between the angle θ_c and the ratio v_c/v_2 can be approximated by:

$$\theta_c = -200\frac{v_c}{v_2} + \alpha ,\ \alpha = \begin{cases} 138 & \text{for plane stram} \\ 140 & \text{for plane stress} \end{cases} \tag{47}$$

With the aid of this equation and equation (6), b_2/b_4 is determined for plane stress:

$$\frac{b_2}{b_4} = \tan[\pi(-\frac{10}{9}\frac{v_c}{v_2} + \frac{7}{9})] . \tag{48}$$

The additional constants can be determined also to be [1]

$$d_{22} = \frac{[U_+]^2\sigma_{01}C^*}{b_1^2 + b_5x_1^2SR} ,\ d_{21} = \frac{[U_+]^2}{b_1^2 + b_5x_1^2}[\frac{b_5^2 - RC^*}{S}] \tag{49}$$

in which C^* is given by

$$C^* = \frac{\sqrt{S}b_2b_3 - K_{Ib}^2}{r_c\sigma_{01}^2 - RK_{Ib}^2} . \tag{50}$$

Without loss of generality, b_4 may be arbitrarily set to unity. The critical stress intensity factor K_{Ib} and critical distance can be taken as [52] :

$$K_{Ib} = \sqrt{2n} K_{Ic} \ , \ n = \frac{r_c}{a_a} \tag{51}$$

in which a_a is the effective microcrack length at a distance r_c ahead of the running crack. The static critical stress intensity factor is K_{Ic}. Values of n for some metals and Plexiglass (PMMA) can be found in [52]. Reported in [53] are r_c values for Homalite-100 and in [54] for Plexiglas.

Finally, the paramater Q controlling the stochastic characteristics of the crack instability problem is also an uknown to be determined. Decreasing Q results to an increase the sharpness of the probability density distribution surface. It therefore, controls the stochasticity of the directional instability geometry after bifurcation and it will depend on the the distribution of the microdefects the particles and their size as well as volume fraction. Unfortunately this is the essential parameter which cannot be matched to experimental data, suggesting the need of an extensive experimental program.

In the training process described up to now the minimal set of required control parameters b_i, $i = 1,2,3,4$ has been trained to match a host of material characterizing quantities and geometry and loading parameters. More specifically equations (37,46,48,49,50) can be viewed as the partial functions mapping the physical control parameter space to the mathematically required control space. Thus the quantities $v_c, r_c, a_a, v_1, v_2, K_{Ic}$ (material) and $\sigma_{01}, \sigma_{02}, \sigma_\eta, \sigma_\xi$ (loading) and β, a (geometry), have been matched with the b_i parameters. With the emphasis here being on particulate composites, it seems that the material control parameter space can be furthermore parsed to those of the filler, to those of the matrix and to those of the interphase. For this consideration mixture theories are necessary. Sometimes these theories introduce empirical quantities which as a result increase the dimensionality of the actual control space. In [55,56] the possible ways of implemanting the characteristics of the three phases involved in the composite to derive the bulk properties of the composite, are given. In [25,26] has been established that the critical terminal velocity of the crack in the composite v_c is a linear function of the filler volume fraction for Fe particle composites

4 The Dissipative Oscilating System - Discussion.

The system identified to posess all the phenomenological characteristics of the crack instability observations, as given by the equations of motion (2) and (17), with a driving deterministic force given by equations (10) and (9):

$$K_2(q_2) = -d_1 + d_2 q_2 - d_3 q_2^3 \,, \tag{52}$$

is nothing but a non-linearly oscilating system. A system which is isomorphic to an oscilating (about the q_1 or x_1 axis) particle which in the same time travels along the x_1 axis with a constant velocity v_c as equation (2) suggests. This particle oscilates and the influence of the recovering linear spring-like force $d_2 q_2$ corresponding to a perfect material without deffects and particles, and under the influence an opposing non linear spring-like force $d_3 q_2^3$. Figure 9 shows that the area OCQ represents the energy spent for deviating the particle from its average path along q_1 or x_1 by an amount OC. The area OC'Q represents the amount dissipated by the microcracks and filler particle interaction with the crack tip.

It is of dramatic importance to realize here that it is this nonlinear term which can be attributed to the dissipative mechanisms of the dynamic fracture, which is responsible for obtaining the topologically singular potential exhibiting the bifurcation and curving behavior.

The semi-stochastic character of the bifurcation process has been captured by the implementation of the probabiltity density distribution for the crack tip to be at a given trajectory. This probability function has been derived to be the solution of a *Fokker-Planck* equation corresponding to a *Langevin*equation of motion, and it has been expressed in terms of the potential corresponding to the deterministic gradient system.

All necessary control parameters have been matched to the physical parameters controlling the behavior of the system by appropriate training of the model through diffeomorphic tuning techniques.

Finally the described model is completely based on actual experimental observations or theories and criteria fitting experimental observations. Therefore, if the behavior surface established by appropriate combinations of the control parameters, is continuous (locally flat), and the characterizing the observations are of zero order of reality, and as composition rule the ususal functional composition is used then the model is guaranteed to give accurate predictions for every combination of the physical control parameters lying between those combinations used for the training process.

Aknowledgment.

Drs. P.W. Mast and G.E. Nash are gratefully aknowledged for the exuberant joy following the mental growth, after the infliction of the pain following their restless stimulation on the issues of pushing towards the objective scientific method as an instance of the general process of research industrialization as a product

of our "Meta-research" activities. Drs. R. Badaliance and I. Wollock are also gratefully aknowledged for giving me the opportunity to exist in the process of building rational plants. and to let me exercise the power of the daily new-found boundaries on them.

References

[1] Michopoulos J. G. Directional instability of crack propagation with energy dissipation. *International Journal of Theoretical and Applied Fracture Mechanics*, 9(To appear), 1988.

[2] J. D. Achenbach. Elastodynamic fracture mechanics. In *Fracture Mechanics*, pages 3–20, SIAM-AMS, 1979.

[3] G. C. Sih. *Dynamic Aspects of Crack Propagation*, pages 607–639. Graw Hill Co., New York, 1969.

[4] L. B. Freund. Crack propagation in an elastic solid subjected to general loading - i. constant rate of extension. *Journal of the Mechanics and Physics of Solids*, 20:129–140, 1972.

[5] L. B. Freund. Crack propagation in an elastic solid subjected to general loading - ii. non-uniform rate of extension. *Journal of the Mechanics and Physics of Solids*, 20:141–152, 1972.

[6] L. B. Freund. Crack propagation in an elastic solid subjected to general loading - iii. stress wave loading. *Journal of the Mechanics and Physics of Solids*, 21:47–61, 1973.

[7] L. B. Freund. Crack propagation in an elastic solid subjected to general loading - iv. obliquely incident stress pulse. *Journal of the Mechanics and Physics of Solids*, 22:137–146, 1974.

[8] J. J. Gilman. Cleavage ductility and tenacity in crystals. In Averbach B.L. et al., editor. *The Atomic Mechanisms of Fracture*, pages 193–224. MIT Techn. Press, Swampscott Mass., 1959.

[9] D. K. Roberts and A. A. Wells. The velocity of brittle fracture. *Engineering*, 178:820–821, 1954.

[10] J. P. Berry. Some kinetic considerations of the griffith criterion for fracture - i: equation of motion at constant force. *Journal of the Mechanics and Physics of Solids*, 8:194–206, 1960.

[11] J. P. Berry. Some kinetic considerations of the griffith criterion for fracture - ii: equations of motion at constant deformation. *Journal of the Mechanics and Physics of Solids*, 8:207–216, 1960.

[12] J. J. Gilman. Direct measurements of the surface energies of crystals. *Journal of Applied Physics* 31:2208–2218, 1960.

[13] P. P. Gillis and J. J. Gilman. Double cantilever cleavage mode of crack propagation. *Journal of Applied Physics*, 35:647–658, 1964.

[14] S. J. Burns and W. W. Webb. Fracture surface energies and dislocation processes during dynamical cleavage of lif. i. *Journal of Applied Physics*, 41:2078–2085, 1970.

[15] B. Steverding and S. H. Lehnigk. The propagation law of cleavage fracture. *International Journal of Fracture*, 6:223–232, 1970.

[16] B. Steverding and S. H. Lehnigk. Response of cracks to impact. *Journal of Applied Physics*, 41:2096–2099, 1970.

[17] B. Steverding and S. H. Lehnigk. Dynamics of brittle fracture. *International Journal of Fracture*, 8:59–73, 1972.

[18] S. H. Lehnigk. A microscopic dynamic theory of stability and instability of cracks under impulsive loading. In G. C. Sih, editor, *Dynamic Crack Propagation*, pages 333–347, Noordhoff Int. Publ., Leyden, 1973.

[19] B. Steverding. Fracture and dislocation dynamics. In G. C. Sih, editor, *Dynamic Crack Propagation*, pages 349–361, Noordhoff Int. Publ., Leyden, 1973.

[20] Z. J. Bilek and S. J. Burns. The dynamics of crack propagation in double cantilever beam specimens. In G. C. Sih, editor, *Dynamic Crack Propagation*, pages 371–385, Noordhoff Int. Publ., Leyden, 1973.

[21] M. F. Kanninen. A dynamic analysis of unstable crack propagation and arrest in dcb test specimen. *International Journal of Fracture*, 10:415–430, 1974.

[22] L. B. Freund. A simple model of the double cantilever beam crack propagation specimen. *Journal of the Mechanics and Physics of Solids*, 25:69, 1977.

[23] Michopoulos J.G. A beam model for the dynamic propagation of oblique cracks. In G. C. Sih and P. S. Theocaris, editors, *Mixed Mode Crack Propagation*, pages 143–162, Sijthoff and Noordhoff Publ., Netherlands, 1981.

[24] Graupe D. *Identification of Systems*. Robert E. Krieger Publ. Co., Florida, 1976.

[25] Papanicolaou G.C. Papadopoulos G.A. Dynamic crack propagation in particulate composites by the method of transmitted caustics. In Sih G.C. and Theocaris P.S., editors, *Mixed Mode Crack Propagation*, pages 367–384, Sijthoff and Noordhoff Publ. Co., Netherlands, 1981.

[26] Theocaris P.S. Papanicolaou G.C. Papadopoulos G.A. The effect of filler volume fraction on crack propagation behavior of particulate composites. *Journal of Composite Materials*, 15:41–54, 1981.

[27] Guckenheimer J. Holmes P. *Nonlinear Oscillations, Dynamical Systems, and Bifurcations of Vector Fields*. *Applied Mathematical Sciences 42*. Springer-Verlag, New York, 2nd edition, 1986.

[28] Beltrami E. *Mathematics for Dynamic Modeling.* Academic Press, Inc., Boston, 1987.

[29] Korn G.A. Korn T.M. *Mathematical Handbook for Scientist and Engineers.* McGraw-Hill Book Co., New York, 1968.

[30] J. D. Lawrence. *A Catalog of Special Plane Curves.* Dover Publications, New York, 1972.

[31] J. F. Kalthoff. On the characteristic angle for crack branching in brittle materials. *International Journal of Fracture*, 7:478–480, 1971.

[32] Iooss G. Joseph D. *Elementary Stability and Bifurcation Theory.* Springer-Verlag, New York, 1980.

[33] R. Thom. *Structural Stability and Morphogenesis.* Benjamin, Reading Mass., 1975.

[34] K. Ravi-Chandar and W. G. Knauss. An experimental investigation into dynamic fracture : i. crack initiation and arrest. *International Journal of Fracture*, 25:247–262, 1984.

[35] K. Ravi-Chandar and W. G. Knauss. An experimental investigation into dynamic fracture : ii. microstructural aspects. *International Journal of Fracture*, 26:65–80, 1984.

[36] K. Ravi-Chandar and W. G. Knauss. An experimental investigation into dynamic fracture : iii. on steady-state crack propagation and crack branching. *International Journal of Fracture*, 26:141–154, 1984.

[37] K. Ravi-Chandar and W. G. Knauss. An experimental investigation into dynamic fracture : iv. on the interaction of stress waves with propagation cracks. *International Journal of Fracture*, 26:189–200, 1984.

[38] M. Ramulu and A. S. Kobayashi. Mechanics of crack curving and branching - a dynamic fracture analysis. *International Journal of Fracture*, 27:187–201, 1985.

[39] A. S. Kobayashi M. Ramulu and B. S.-J. Kang. Dynamic crack curving and branching in line-pipe. *Journal of Pressure Vessel Technology*, 104:317–322, 1983.

[40] H. Haken. *Synergetics — An Introduction.* Springer-Verlag, Berlin, 1978.

[41] Risken H. *The Fokker Planck Equation.* Springer Verlag, Berlin, 1984.

[42] F. Erdogan and G. C. Sih. On the crack extension in plates under plane loading and tnsverse shear. *Journal of Basic Engineering Trans. A.S.M.E., Series D*, 35:519–527, 1963.

[43] G. C. Sih. *Dynamic Crack Problems: Strain Energy Density Fracture Theory*, pages 17–37. Volume 4. Noordhoff Int. Publ., Leyden, 1977.

[44] P. S. Theocaris and N. P. Andrianopoulos. The mises elastic-plastic boundary as the core region in fracture criteria. *Engineering Fracture Mechanics*, 16:425–432, 1982.

[45] P. S. Theocaris and N. P. Andrianopoulos. A modified strain energy density criterion applied to crack propagation. *Journal of Applied Mechanics*, 49:81–86, 1982.

[46] P. S. Theocaris and H. G. Georgiadis. Bifurcation predictions for moving cracks by the t-criterion. *International Journal of Fracture*, 29:181–190, 1985.

[47] F. Kerkhof. Wave fractographic investigations of brittle fracture dynamics. In G. C. Sih, editor. *Dynamic Crack Propagation*, pages 3–35, Noordhoff Int. Publ., 1973.

[48] L. R. F. Rose. Recent theoretical and experimental results on fast brittle fracture. *International Journal of Fracture*, 12:799–813, 1976.

[49] J. Congleton and N. J. Petch. Crack branching. *Philosophical Magazine*, 16:749–760, 1967.

[50] S. R. Anthony and J. Congleton. Crack branching in strong metals. *Metal Science*, 158–160, 1968.

[51] J. P. Chubb S. R. Anthony and J. Congleton. The crack branching velocity. *Philosophical Magazine*, 22:1201–1216, 1970.

[52] J. Congleton. Practical applications of crack-branching measurements. In G. C. Sih, editor. *Dynamic Crack Propagation*, pages 427–483, Noordhoff Int. Publ., Leyden, 1973.

[53] M. Ramulu and A. S. Kobayashi. Dynamic crack curving - a photoelastic evaluation. *Experimental Mechanics*, 23:1–9, 1983.

[54] Theocaris P.S. and Papadopoulos G. *Journal of Applied Mechanics*, 81–86, 1982.

[55] Theocaris P.S. Papanicolaou G.C. Kontou E.A. The effect of filler-volume fraction and strain rate on the tensile properties of glass/epoxy particulate composites. *Journal of Reinforced Plastics and Composites* 206–224, 1982.

[56] Papanicolaou G.C. Paipetis S.A. Theocaris P.S. The concept of boundary interphase in composite mechanics. *Colloid and Polymer Science*, 625–630, 1978.

Figure Captions

1. Diagramatic comutative descriptions of the equivalence between the natural and the modeled problem. in a qualitative (a), a functional for the equations of motion (b), and a functional for the potentials of the corresponding gradient systems (c), domains.

2. Schematic representations of the problem and the associated geometry, loading and micromechanical characteristics.

3. Diffeomorphic transformation of the bifurcation scheme, from the parabolic (a) to the actually realized experimentally, *bullet nose* scheme (b) .

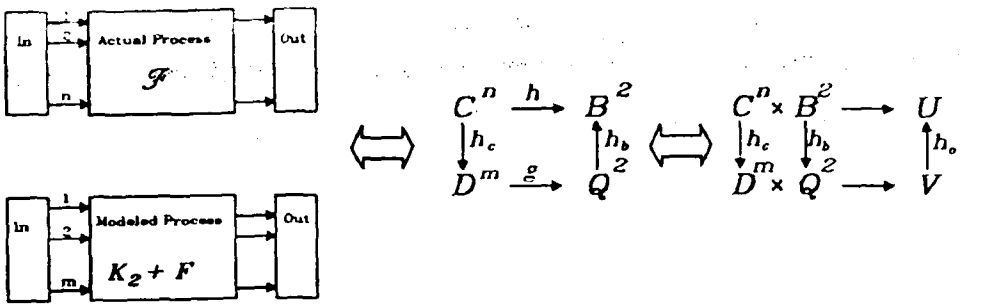
4. The stable and unstable trajectories of the system in the $d_2 - q_2$ plane.

5. Projection of the bifurcation manifold of the potential, in the $d_2/d_3 - d_1/d_3$ space, deciding for the stable and unstable combinations of the control parameters.

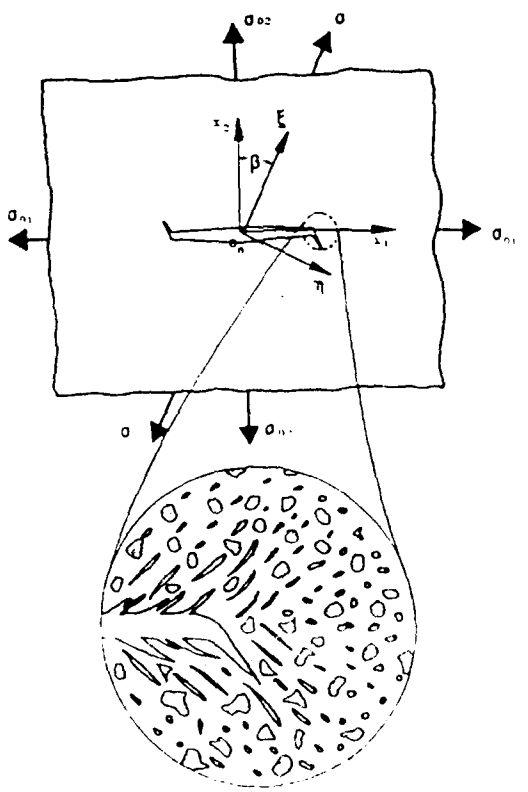
6. The equilibrium manifold of the potential as it is represented from its bifurcation set with its projections.

7. The potential (a,b,c) and probability density distribution (d,e,f) surfaces in the $d_2 - q_2$, for $d_1 < , = , > 0$ respectively.

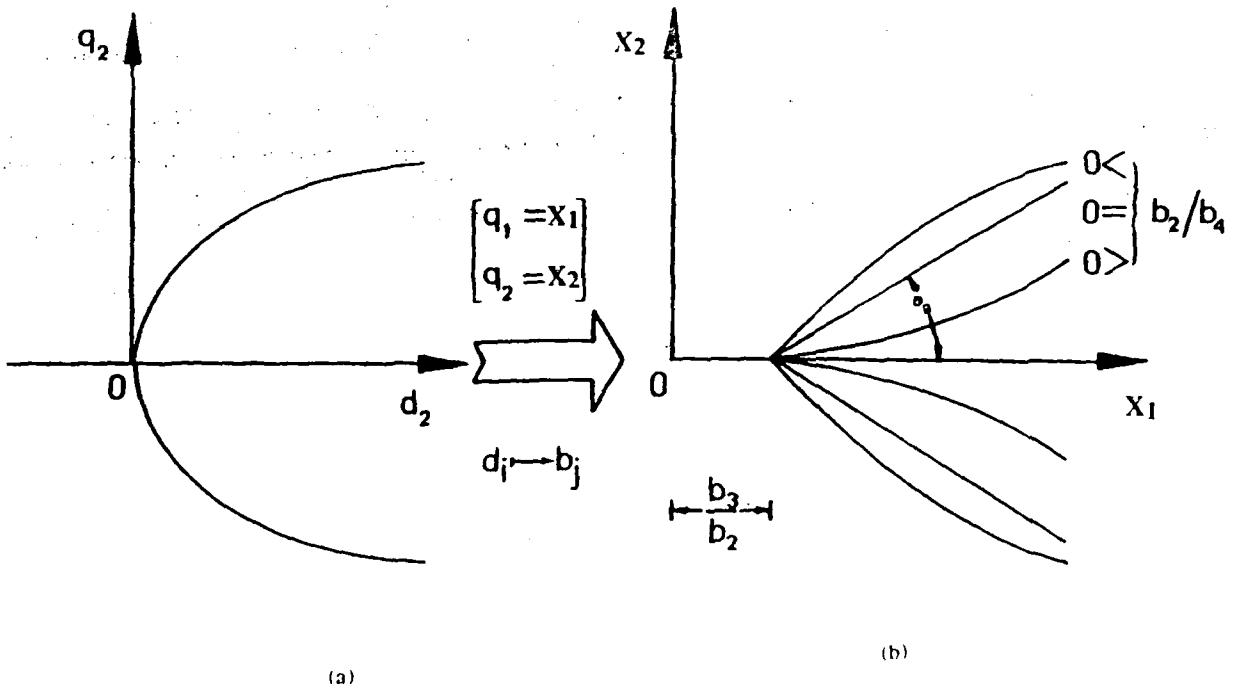
8. Variations of deterministic force for q_2: conservative and dissipative.



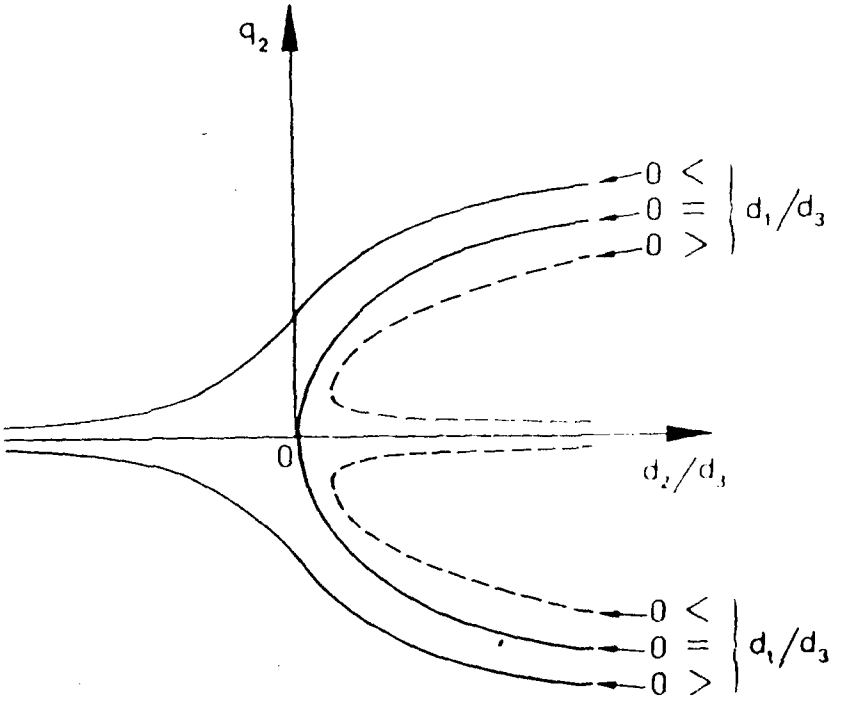
1. Diagramatic comutative descriptions of the equivalence between the natural and the modeled problem. in a qualitative (a), a functional for the equations of motion (b), and a functional for the potentials of the corresponding gradient systems (c), domains.



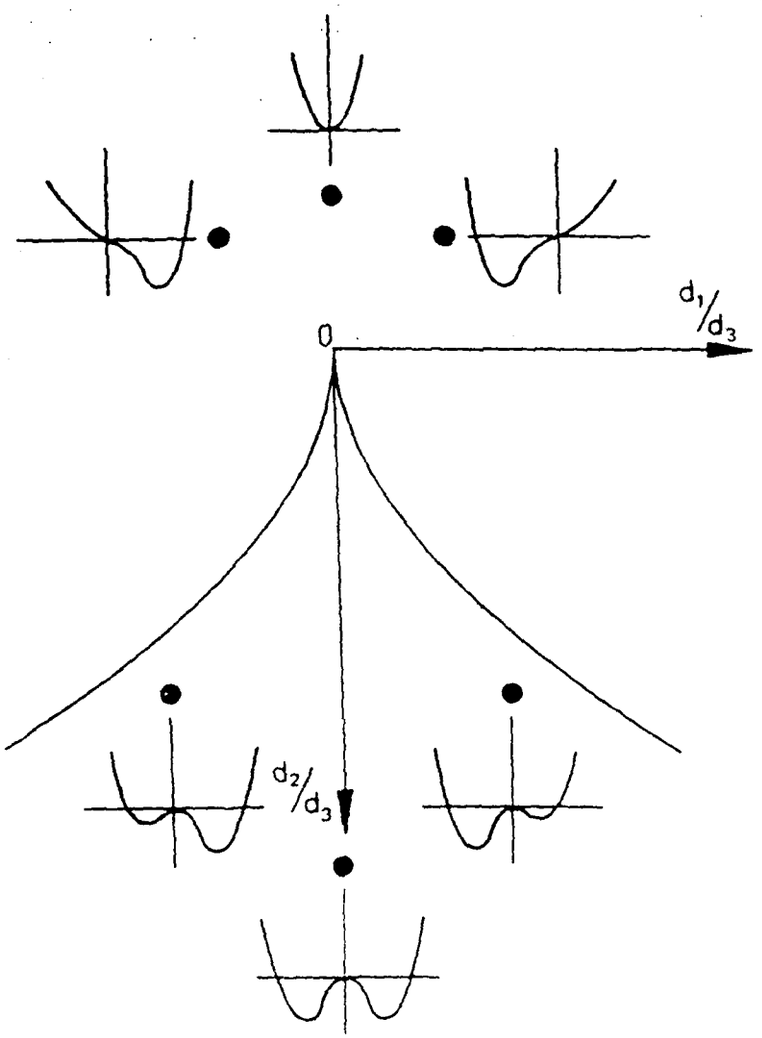
2. Schematic representations of the problem and the associated geometry, loading and micromechanical characteristics.



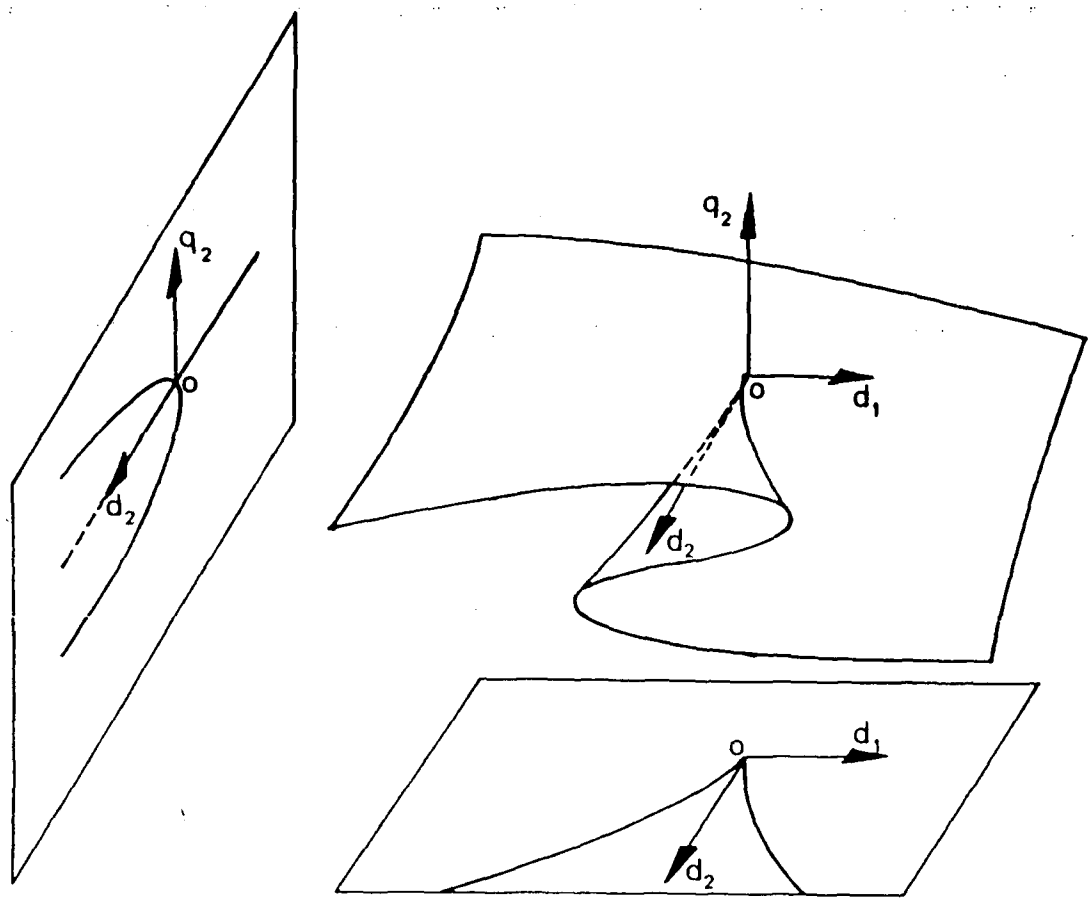
3. Diffeomorphic transformation of the bifurcation scheme, from the parabolic (a) to the actually realized experimentally, *bullet nose* scheme (b).



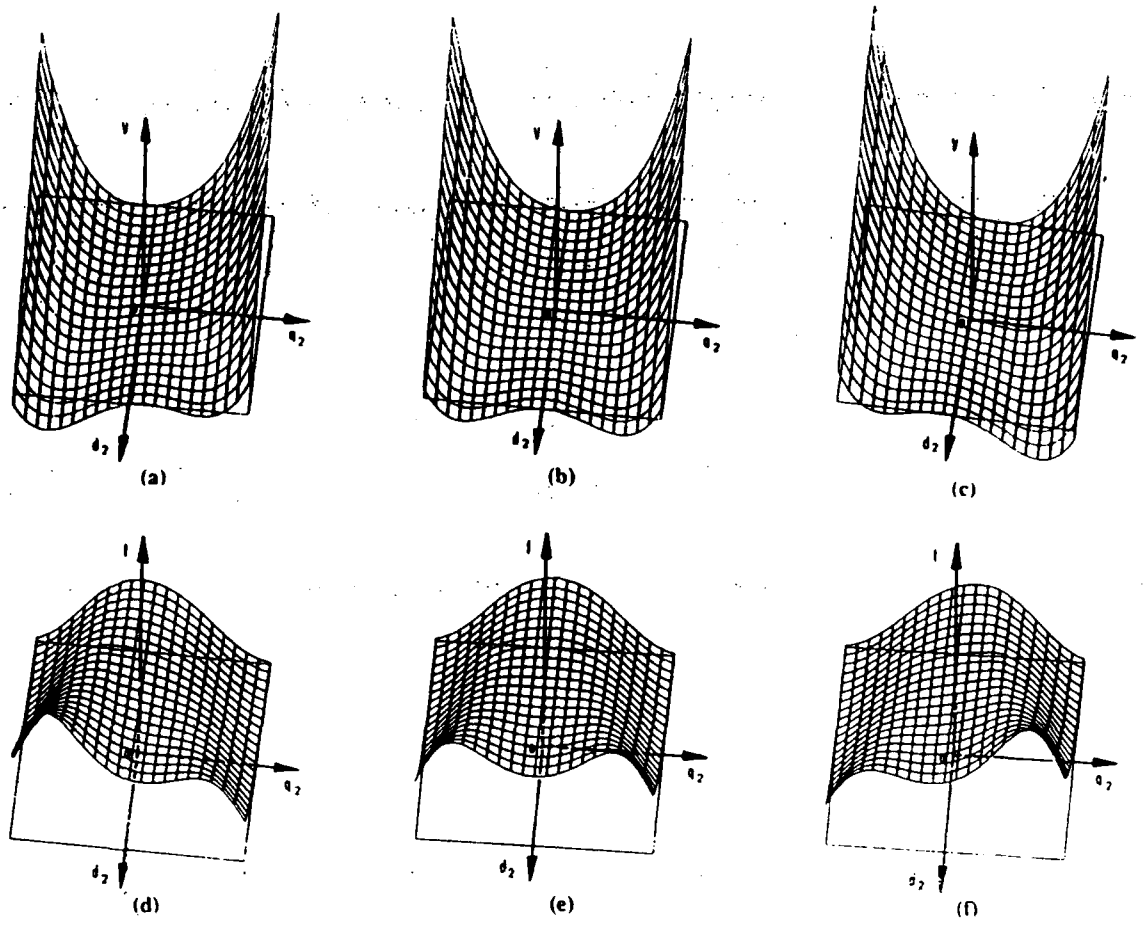
4. The stable and unstable trajectories of the system in the $d_2 - d_3$ plane.



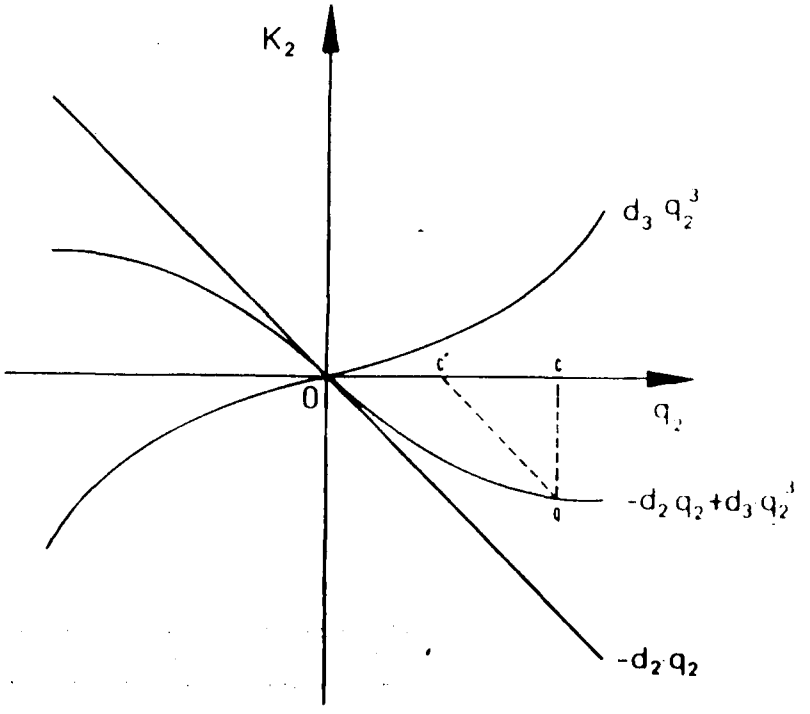
5. Projection of the bifurcation manifold of the potential, in the $d_2/d_3 - d_1/d_3$ space, deciding for the stable and unstable combinations of the control parameters.



The equilibrium manifold of the potential as it is represented from its bifurcation set with its projections.



7. The potential (a,b,c) and probability density distribution (d,e,f) surfaces in the $d_2 - q_2$, for $d_1 <$, = , > 0 respectively.



8. Variations of deterministic force for q_2 conservative and dissipative.

APPENDIX VI

FAILURE BEHAVIOR OF COMPOSITE MATERIALS FOR SHIP APPLICATIONS.

P. W. Mast G. E. Nash J. G. Michopoulos
R. Thomas I. Wolock

February 5, 1988

Abstract

A completely phenomonological approach is formulated for identifying the nonlinear constitutive behavior of composite materials and characterizing the degree of load-induced internal damage in arbitrary structures. The constitutive behavior and the energy dissipated by internal failure mechanisms, the latter being characterized by an ***energy dissipation function***, are deduced by means of a deconvolution procedure using an extensive set of data furnished by NRL's automated in-plane loader. Use of this information as a failure analysis and prediction tool is demonstrated by simulating the structural response of a ship's mast made from several different composite materials.

æ

1 Introduction.

The use of composite materials in structural components has increased dramatically in recent years and they are currently being employed in a large number of applications. Moreover, this trend is expected to accelerate as the cost of producing these materials declines because they offer many significant advantages over the more frequently used monolithic materials. Some of the more prominent features of composites are

- The ability to readily modify the material and tailor its mechanical, electromagnetic, and thermal properties to specific applications.
- Tolerence of extreme environments.
- Significant weight savings.
- Superior damage tolerence.

As desirable as these features may be, however, they can be fully exploited in a structural setting only by having a highly developed understanding of the innate mechanical and failure behavior — an understanding far in excess of what is currently known.

The basic obstacle in reaching the required degree of understanding is the sheer complexity of the observed mechanical behavior. In particular, composites are generally highly anisotropic, strongly nonlinear, and, unlike metals, usually fail in an extremely complicated spatially diffuse noncatastrophic manner [1-3]. Past approaches to failure characterization and prediction for these materials have not adequately addressed this complexity and typically represent attempts to apply extensions of the time-tested techniques developed for metals using overly simplistic models based on linear elastic fracture mechanics and/or deterministic or statistical micromechanics. These analyses have proved largely unsuccessful because, to a great extent, they are based not on observed fact, but rather tend to utilize models defined over low dimensional parameter spaces which reflect preconceived notions of the dominent failure mechanisms.

Unfortunately, this methodology is not adequate when dealing with composites (and probably metals as well) because the failure events are

1 Introduction.

The use of composite materials in structural components has increased dramatically in recent years and they are currently being employed in a large number of applications. Moreover, this trend is expected to accelerate as the cost of producing these materials declines because they offer many significant advantages over the more frequently used monolithic materials. Some of the more prominent features of composites are

- The ability to readily modify the material and tailor its mechanical, electromagnetic, and thermal properties to specific applications.
- Tolerence of extreme environments.
- Significant weight savings.
- Superior damage tolerence.

As desirable as these features may be, however, they can be fully exploited in a structural setting only by having a highly developed understanding of the innate mechanical and failure behavior — an understanding far in excess of what is currently known.

The basic obstacle in reaching the required degree of understanding is the sheer complexity of the observed mechanical behavior. In particular, composites are generally highly anisotropic, strongly nonlinear, and, unlike metals, usually fail in an extremely complicated spatially diffuse noncatastrophic manner [1-3]. Past approaches to failure characterization and prediction for these materials have not adequately addressed this complexity and typically represent attempts to apply extensions of the time-tested techniques developed for metals using overly simplistic models based on linear elastic fracture mechanics and/or deterministic or statistical micromechanics. These analyses have proved largely unsuccessful because, to a great extent, they are based not on observed fact, but rather tend to utilize models defined over low dimensional parameter spaces which reflect preconceived notions of the dominent failure mechanisms.

Unfortunately, this methodology is not adequate when dealing with composites (and probably metals as well) because the failure events are

far too varied and complicated to be well represented by a model involving only a few parameters; rather, an appropriate model requires a much larger parameter space for its description if it is to represent physical fact in a high fidelity objective manner consistent with the scientific method. Moreover, because the phenomona are so complex, the model cannot be formulated at the level of the individual failure events, but instead must be generic and phenomonological in nature, relying on massive amounts of experimental data to identify the model parameters. Only after these parameters are determined can the model be related to particular failure mechanisms. This can generally be accomplished by using a various assortment of transformation techniques, for instance, a combination of symbolic programming and systems identification methods, and leads to a sort of phenomonological micromechanics.

The purpose of this report is to describe an approach to modeling the mechanical behavior of composite materials consistent with the aforementioned standards. This approach, which, in the spirit of the prior discussion is completely phenomonological, provides quantitative procedures for identifying the constitutive behavior of any particular composite material and for characterizing the degree of internal damage the material undergoes when it is part of a structural component subjected to arbitrary loads.

The crux of the procedure involves the determination of an *energy dissipation function* which we regard as a property of the material. This quantity completely determines both the nonlinear aspect of the constitutive behavior and the associated load-induced internal damage. The data from which the dissipation function is determined is obtained from an extensive series of tests performed with NRL's in-plane loader. This is a completely computer controlled testing machine capable of producing arbitrary combinations of opening/closing, sliding, and rotating boundary displacements and is fully described in Section 2. The dissipation function and the concommitant constitutive behavior are extracted from the data using a mathematically well-founded deconvolution procedure which is presented in Section 3.

The identification of the dissipation function and constitutive behavior provides the information required to compute the stresses, strains, and displacements and characterize the load-induced damage in a given structural component. Specifically, once the dissipation function has been deter-

mined, the stresses, strains, and displacements may be found by integrating the equilibrium and strain-displacement equations subject to appropriate boundary conditions and the energy dissipation per unit volume computed at all points in the structure. A demonstration of this capability is provided in Section ?? where we simulate the structural response of a ship's mast made from a number of different composite materials using a finite element procedure and produce spatial maps which illustrate how energy is dissipated within the structure under various systems of external loads.

2 The In-plane Loader System.

The in-plane loader system, shown schematically in Fig. 1, is the hardware manifestation of our research plant whose primary function is to produce reliable data from which the composite constitutive behavior can be deduced with a minimum of ancillary hypotheses. The main components of the system are ennumerated below:

The in-plane loader :

This is a sophisticated automated testing machine capable of subjecting test specimens to arbitrary displacement controlled in-plane loading corresponding to combinations of pulling/pushing, sliding, and rotating boundary displacements.

A minicomputer :

The computer serves as a controller by sending commands to the hydraulic actuators of the in-plane loader through digital-to-analog converters, and by receiving gauge measurements from the in-plane loader via the analog-to-digital converters. It is also used for real time data collection and reduction during the tests as well as for various post-testing analyses. Among the latter are the determination of the energy dissipation function and consequent constitutive behavior for the material and finite element analysis of specific structural components.

A graphics processor :

The graphics processor is used to facilitate the pre and post-processing requirements of the finite element analyses. Specifically, it is employed in conjunction with solid modeling and rendering software to produce finite element models of the specimen itself and specific structural components. It is also used to generate rendered images showing the spatial distribution of dissipated energy.

The specimen :

The last and most important component of the system is the specimen itself. The specimens were designed to meet the following requirements:

1. The characteristic dimensions be sufficiently large relative to fiber diameter and lamina thickness to ensure that the material could be analyzed as either a single mechanically equivalent homogeneous anisotropic monolithic material, or a collection of layers of varying orientations of such materials.
2. The overall specimen size be small enough to keep material costs at a managable level.
3. A strain riser be present to guarantee that high strain regions ocur well away from all specimen boundaries.

The single edge-notched specimen which resulted is shown in Fig. 2. Here it is important to note that the primary function of the notch is only to act as a strain riser in order to ensure satisfaction of requirement (3) above, and *not* to mimic a crack in the fracture mechanics sense.

2.1 In-plane Loader Description.

Although the in-plane loader has been described previously [1], its design has since evolved sufficiently to warrent an updated description. The in-plane loader in its current incarnation is shown in Fig. 1 with a more detailed portrayal in the vacinity of the specimen grips shown in Fig.3. Basically it consists of three independent computer controlled hydraulic actuators connected to a movable head. The loading path of each actuator can be independently prescribed, thereby producing arbitrary combinations of opening/closing, sliding, and in-plane rotating displacements.

Each actuator unit is composed of

1. A 2-Kip hydraulic linear actuator witha 6-in. stroke.
2. A d.c. powered linear displacement transducer (DCLVDT) which is mounted on the actuator and measures ram motion relative to the actuator cylinder.
3. An operational amplifier which serves to compute the difference between the actual ram displacement and the programmed one.

4. An electrically controlled hydraulic servo valve which receives the displacement error output of the operational amplifier and delivers conttrolled hydraulic power to the actuator — forcing the ram to displace the amount nessessary to minimze the displacement error.

5. A 2-Kip strain gauge load cell mounted on the ram end.

6. An instrument amplifier to amplify the millivolt output of the load cell.

Relative displacements between the two grips are monitored by a specially designed six component DCLVDT transducer mounted on the specimen side of the movable head. A three component strain gauged load cell is used to monitor the movable head reaction forces.

Two actuator configurations deserve special attention. The first is when any of the acuators is colinear with another, while the second occurs when the line of action of the actuators intersects at a common point. Both of these configurations prevent the application of the full range of opening/closing, sliding, and rotation, and, consequently, were avoided in the design.

The hydaulic grips are computer controlled and operate like a pair of pliers whose handles are forced together by a compact servo-controlled jack built into the head. Specimens are inserted in the grips from a loading magazine via a mechanical feeding device. This ensures uniformity in the gripping conditions and allows for a rapid throughput (currently 340 specimens/hour). A hydraulic power control unit consisting of of an operational amplifier, a pressure transducer, and a electrohydraulic valve, maintains a constant gripping pressure as the test proceeds. The magnitude of the gripping force is sufficient to prevent specimen slippage, and yet not so great as to cause failure at the grips.

The digital imaging system is to provided to give the operator an efficient and accurate method of performing initial specimen geometry measurements and calibrations. A video camera with a long focal length, positioned by a motor driven three axis stage, is mounted over the specimen and provides a magnified ($15\times$) view of the specimen on a TV monitor. Horizontal and vertical cursor lines are superposed on the TV image and can be used to mark various features such as the initial position of the

notch tip. The cursor digital output signals are continuously monitored and saved on command.

The block diagram of the entire system is shown in Fig. 4 together with a schematic representation of the information paths from and to the in-plane loader relative to the computer controller. Twenty one measuring channels are interfaced with a multiplexer connected to the analog-to-digital converter which is connected to the computer through DMA access via the computer bus. Similarly, the digital-to-analog converter has its output connected to the servo valves of the actuators and its input communicates with the computer via the bus in a DMA fashion.

2.2 Operational Aspects.

The objective of the in-plane loader system is to control the rigid body motion of the boundary of the specimen which is held by the moveable grip. Because the actuators are constrained to move in a plane parallel to the specimen, the resulting motion involves only three degrees of freedom relative to any frame of reference on that plane. The relation between the prescribed actuator displacements and the resulting grip motion is illustrated in Figs. 5a and 5b. The important point to note here is that the grip motion can be resolved into three basic components, namely, sliding u_x, opening/closing u_y, and rotation ω. Specified combinations of actuator displacements therefore map into particular combinations of these three basic motions.

It is convenient to employ a reference frame which is located at the initial position of the notch tip for both the boundary displacements (which are denoted by $\boldsymbol{d}$ relative to this frame) and the resulting reaction forces t. Fig. 5c illustrates these displacements and tractions and the resulting deformation of the specimen. The decomposition of the applied displacements relative to this frame into a sliding motion d_0, an opening/closing motion d_1, and a rotational motion d_2 is shown in Figs. 5(d,e,f), respectively. For the purpose of dimensional homogeneity , d_2 is defined as the length of the arc traveled by a point 1 inch away from the notch tip rigidily connected with the moving grip along the direction of the rotation, instead of using the actual rotation in radians.

Subsequent analysis requires that we compute the energy dissipated

within the material at a discrete set of observation points as the specimen is loaded by applying a predetermined series of boundary displacements d^i. Here $i = 1, \ldots, n$ and n denotes the number of observation points. The details of these computations will be discussed in the next section; here we attend to the sampling strategy. It is advantageous to think in terms of a three dimensional displacement space with coordinates (d_0, d_1, d_2). Then a particular test in which the actuator motions are continuously varied corresponds to a specific path in this space. The issue then is how to select a representative family of paths which cover the space and how to sample along each path.

As will be discussed in the following section, we do not expect to observe any significant path dependent behavior during loading. By this we mean that the mechanical response of the material at any point in this space should depend only on the current state of internal strain and be independent of the particular path followed to achieve this state. This type of behavior greatly simplifies matters because it permits us to cover the displacement space with a family of loading paths selected soley on the basis of convenience. Towards this end, it was decided to cover the space with a set of 15 uniformly distributed radial loading paths as indicated in Fig 6a. Note that because of symmetry only the half space corresponding to positive shear ($d_0 \geq 0$) need be considered. The required set of observation points are generated by uniformly sampling each path at 50 distinct points starting from a prescribed minimum and terminating at a prescribed maximum yielding a total of 750. Only 15 specimens are required, however, because the 50 observations per loading path are obtained from a single specimen.

Since our concern is limited exclusively to radial loading paths, it is natural to describe them in terms of spherical coordinates as shown in Fig. 6b. Thus the direction of each path is specified by prescribing the coordinates θ_1 and θ_2 and the location of any point on the path is determined by the value of r. As an aid in visualization, it helps to display the spherical coordinate representation in a cartesian frame with axes (θ_1, θ_2, r) as shown in Fig. 6c. Then each loading path with direction (θ_1, θ_2) is represented by a vertical line which intersects the plane $r = 0$ at the point (θ_1, θ_2). A graphical representation of the transformation which maps the spherical coordinate system in its usual form into the cartesian reference

frame is shown in Fig. 6c. Points along the θ_1 axis correspond to rotation-free deformations with the points at $\theta_1 = \pi/2, 0, -\pi/2$ representing pure opening, sliding, and closing, respectively. Similiarly, points along the θ_2 axis represent extension/compression free deformations with the points at $\theta_2 = \pm\pi/2$ corresponding to pure rotation. The three loading paths coresponding to pure sliding, opening and rotation together with a rendition of the deformed specimen for three equally spaced points on each path are also shown in Fig. 6c.

The representation in Fig. 6c is particularly convenient in situations where the major concern is to determine the distance r along each path corresponding to some critical event such as the attainment of a threshold value of dissipated energy or the occurence of a maximum in one of the boundary tractions [1]. The locus of these critical points then define a surface in the space (θ_1, θ_2, r) which serves to characterize that aspect of the material response. A typical surface defined in this manner is shown in Fig. 7. This concept of a response surface provides an effective tool for comparing the mechanical characteristics of different materials and assessing the effects of aging and various preconditioning regimens. Any variation in prospective mechanical behavior is quickly detected by a simple visual comparison of these surfaces. Approaches based on this procedure have been successfully implemented to investigate the effects of aging, resin type, and fatigue preconditioning on Kevlar and graphite/epoxy. We refer the reader to Refs.[1-3] for further discussion of these results.

We conclude this section by outlining the sequence of events involved in a typical test. Thus, one of the loading paths is selected and initial measurements regarding the specimen geometry, such as notch tip location, are performed by the operator using the digital imaging system. The specimen is inserted in the grips via the feeding mechanism and the remainder of the test is performed automatically, with the computer control system measuring specimen thickness and controlling the grip pressure, loading the specimen, and monitoring and storing boundary forces and displacements (t, d) at the 50 sampling points along the loading path. An entire test takes about 10 sec. Each test is generally performed twice to establish reproducibility. Typically it is found that the data is reproducible to within an RMS error of 5%.

3 Constitutive Equation Determination and Load-Induced Internal Damage Characterization.

Composite materials tend to fail in a gradual but complex manner under static loading conditions [2]. In particular, these materials tend to undergo progressive damage over a diffuse volume induced by such events as debonding, delamination, fiber breakage, matrix cracking, etc. resulting in pronounced nonlinear load–deformation behavior until the structure is rendered unusable [3]. As discussed in the Introduction, it is now apparent that a "micromechanical" approach or a simple one or two parameter "failure criterion" is not sufficient to either describe the failure process or provide realistic failure assessments and predictions. Rather, a phenomonological approach is required which is ammenable to quantitative characterization and portrays more accurately the physical situation.This is the methodology followed here. Specifically, we regard the effects of load-induced internal damage as being directly reflected in the mechanical constitutve behavior. Identifying the entire range of nonlinear behavior then makes possible a quantitative understanding of the consequences of the various failure mechanisms and their impact on structural response.

In order to determine the nonlinear constitutive behavior, it is generally sufficient to regard the composite as being composed of either a single mechanically equivalent homogeneous anisotropic material, or a collection of layers of varying orientations of such materials, provided that the loads are either quasi-static or dominated by low temporal frequencies. It is neccesary to impose this restriction on the loads to insure that the wave lengths corresponding to the spatial variation of the stresses, strains, etc. are large compared to the microstructural characteristic lengths; otherwise events on the micro scale take on a predominant role and this homogenization procedure cannot be expected to provide a high fidelity model. If, furthermore, the material is known not to exhibit any significant rate or path dependent behavoir, then, at least during loading, it may be regarded as behaving in a manner similiar to that of a hyperelastic material (nonlinearly elastic with a strain energy potential). It is then possible to describe its mechanical behavior in terms of a constitutive relation which involves *only* stresses and

strains and is independent of time and loading history.

Knowledge of this relation, which is generally a nonlinear fourth order anisotropic tensor function of the form

$$\sigma = \mathcal{F}(\epsilon),$$

where σ and ϵ denote the stress and strain tensors, respectively, is the key ingredient to computing the stresses, strains, and displacements in any given structural component under arbitrary loadings. Indeed, once this relation is determined, the stresses, strains, and displacements may be found by integrating the equilibrium and strain-displacement equations subject to appropriate boundary conditions. Moreover, if we assume that the stored energy is composed of the sum of a reversible and irreversible part, then the irreversible component (the energy dissipated by load-induced internal damage) may also be computed using this information.

The remainder of this section is devoted to a description of a procedure for determining the constitutive relation and characterizing the degree of load-induced internal damage using boundary force and displacement data observed in a series of in-plane loader tests. This process is in actuality a *deconvolution* process because the observations reflect both the effects of material behavior *and* specimen geometry. In order to obtain information relating to the material response alone, the geometric effects must be factored out of the observations, or, equvilently, the constitutive information must be deconvolved from the data. An important point to note here is that the deconvolution process requires an extremely large amount of multiaxial test data; the only feasible way to obtain data in such quantity is by the use of an automated testing machine such as the in-plane loader. With this in mind, we proceed to discuss the deconvolution procedure in some detail.

3.1 Caveats.

In performing the deconvolution we introduce a number of assumptions and simplifications which are itemized below.

- The material can be regarded as a mechanically equivalent homogeneous anisotropic material as discussed above. In an angle-ply com-

posite this assumption can be applied either on a ply-by-ply basis or to the collection, as appropiate.

- Loading is either static or slowly varying in accordance with the considerations discussed above.

- The material behaves as if it were hyperelastic during loading. This assumption by definition precludes consideration of materials which exhibit marked viscous, rate, and load history dependencies. Moreover, given this assumption, there exists a strain energy density potential (strain energy per unit volume), $\psi(\boldsymbol{\varepsilon})$, such that $\boldsymbol{\sigma} = \text{grad}_{\boldsymbol{\varepsilon}}\psi(\boldsymbol{\varepsilon})$.

- Only an initial loading phase is considered with no unloading permitted. This restriction is necessary in order to maintain consistancy with the previous assumption since most composites tend to unload along paths which are different than the initial loading paths.

- The energy absorbed by the material can be regarded as being composed of the sum of a reversible and irreversible part. The reversible component is the energy which would be recovered if the material were to unload. The irreversible part represents the energy which is dissipated by the internal damage mechanisms and can be described by a dissipation function $\varphi(\boldsymbol{\varepsilon})$ (dissipation energy per unit volume).

- The constitutive relation is continuous; i.e., no jumps are permitted.

- The deformations are sufficiently small so that infinitesimal stress and strain tensors may be employed.

- Only shell-like structures are considered so that the stress and strain fields in either the entire material or in each ply are two-dimensional with no transverse components, i.e. $\boldsymbol{\sigma} = (\sigma_\eta, \sigma_{\eta\varsigma}, \sigma_{\varsigma\varsigma})^T$, and $\boldsymbol{\varepsilon} = (\varepsilon_\eta, \varepsilon_{\eta\varsigma}, \varepsilon_{\varsigma\varsigma})^T$, where (η, ς, ξ) is a coordinate system embedded in the material or layer with one axis along the fiber direction as shown in Fig. 3.

- Displacement continuity is maintained between layers.

It should be stressed here that unlike the typical micromechanical treatments [4], we make no explicit assumptions concerning the detailed nature of the various failure processes, rather our approach is to introduce a minimal number of hypotheses which we feel are in accordance with physical fact and are readily defensible. Moreover, many of the above restrictions can be easily relaxed when the situation warrents.

3.2 Analysis.

The primary issue is the estimation of the tensor function $\mathcal{F}(\boldsymbol{\varepsilon})$ and the dissipation function $\varphi(\boldsymbol{\varepsilon})$, or, because of the above hyperelasticity hypothesis, $\psi(\boldsymbol{\varepsilon})$ and $\varphi(\boldsymbol{\varepsilon})$ since $\boldsymbol{\sigma} = \mathrm{grad}_{\boldsymbol{\varepsilon}}\psi(\boldsymbol{\varepsilon})$. The procedure by which both quantities are computed is conceptually simple, yet based firmly on established principles in the areas of applied mathematics and systems identification [5]. We summarize the steps below and provide more detailed explanations in the remaining subsections.

1. A representation is chosen for the strain energy density potential in terms of a set of m basis functions $\chi = (\chi_1, \chi_2, \ldots, \chi_m)^T$ and an initially unknown parameter vector $\alpha = (\alpha_1, \alpha_2, \ldots, \alpha_m)^T$. Similiarly, a representation is chosen for the dissipation function in terms of the same set of basis functions and a parameter vector $\beta = (\beta_1, \beta_2, \ldots, \beta_m)^T$.

2. A uniform set of loading paths in displacement space is selected (15 for each material or 15 for each of a set of layup configurations for angle-ply composites), boundary forces and displacements (t, u) are measured at 50 equally spaced points on each loading path as described in the previous chapter, and the energy imparted to the specimen, U^i, is computed for each observation point i. If the composite is regarded as a single equvilent homogenous material (in the case of an angle-ply composite, this implies that each layup configuration is to be counted as a seperate material), then this procedure yields $n = 750$ values of U^i per material. If the material is an angle-ply composite and we wish to analyze the constitutive behavior on a ply-by-ply basis, then the procedure yields $n = 750 \times np$ values of U^i for each material, where np denotes the number of layup configurations.

3. **The fact that the energy imparted to the specimen is equal to the integral of $\psi(\boldsymbol{\varepsilon}(\boldsymbol{x}))$ over the volume of the specimen, where $\boldsymbol{x} = (\eta, \varsigma, \xi)$, is applied at each of the n observation points and results in a highly overdetermined set of equations for the m components of the parameter vector $\boldsymbol{\alpha}$ (a system of $n \times m$ equations with $n \gg m$).**

4. **These equations, in conjunction with the strain-displacement and equilibrium relations and any appropriate constraints, are solved numerically for $\boldsymbol{\alpha}$ and the constitutive relation computed.**

5. The irreversible portion of the imparted energy, V^i, is computed for each observation point and the fact that V^i equals the integral of $\varphi(\boldsymbol{\varepsilon}(\boldsymbol{x}))$ over the volume of the specimen is used to obtain an $n \times m$ system of equations for the components of the parameter vector $\boldsymbol{\beta}$. This equation, along with any appropriate constraints, is solved numerically allowing us to compute the dissipation function. $\varphi(\boldsymbol{\varepsilon})$.

3.2.1 Representation of the Strain Energy Density Potential and Dissipation Function.

The strain energy density potential $\psi(\boldsymbol{\varepsilon})$ and the dissipation function $\varphi(\boldsymbol{\varepsilon})$ are represented by the linear combination

$$\left\{ \begin{array}{c} \psi(\boldsymbol{\varepsilon}) \\ \varphi(\boldsymbol{\varepsilon}) \end{array} \right\} = \left\{ \begin{array}{c} \boldsymbol{\alpha} \\ \boldsymbol{\beta} \end{array} \right\} \cdot \chi(\boldsymbol{\varepsilon}), \tag{1}$$

where $\chi(\boldsymbol{\varepsilon})$ is a vector of suitable C^0 (or smoother basis) functions over the 3-space $(\varepsilon_{\eta\eta}, \varepsilon_{\eta\varsigma}, \varepsilon_{\varsigma\varsigma})$, and $(\boldsymbol{\alpha}, \boldsymbol{\beta})$, are the parameter vectors to be determined. This representation is quite general in the sense that χ_i may be chosen more or less arbitrarily, for instance, as interpolation basis functions over a suitable mesh defined on $(\varepsilon_{\eta\eta}, \varepsilon_{\eta\varsigma}, \varepsilon_{\varsigma\varsigma})$, in which case any of the usual three dimensional finite element shape functions may be used; as B-splines or cardinal splines; or as locally defined or global orthogonal polynomials. The only significant restriction on the form of the basis functions is that positivity of the quantities $\psi(\boldsymbol{\varepsilon})$ and $\varphi(\boldsymbol{\varepsilon})$ must be assured in order to maintain agreement with physical fact. When χ is an interpolation basis, the components of the parameter vectors $(\boldsymbol{\alpha}, \boldsymbol{\beta})$ are simply the values of (ψ, φ) at the node points; however, this is not true when the later two

The quantity $\boldsymbol{\varepsilon}^i(\boldsymbol{\alpha}, \boldsymbol{x})$ which appears in Eq.(2) is the specimen strain field corresponding to the ith observation and is not known explicitly; however, it must satisfy the following equilibrium, strain-displacement, and constitutive requirements:

$$\text{div } \boldsymbol{\sigma}^i = 0 \tag{3}$$

$$\boldsymbol{\varepsilon}^i = \text{sym}(\text{grad } \boldsymbol{u}^i) \tag{4}$$

$$\boldsymbol{\sigma}^i = \boldsymbol{\alpha} \cdot \text{grad}_{\boldsymbol{\varepsilon}} \chi(\boldsymbol{\varepsilon}^i), \tag{5}$$

where $\boldsymbol{u}$ is the displacement field. The appropriate boundary conditions are free surface conditions (no tractions) except on the gripped surfaces where displacements are prescribed. Equations(2)-(5) form a coupled system of nonlinear equations whose solution yields the quantities $(\boldsymbol{\alpha}, \boldsymbol{\varepsilon}, \boldsymbol{\sigma}, \boldsymbol{u})$.

Finally, by an argument identical to that given above, a relation similiar to Eq.(2) must hold for the dissipated energy V^i and the dissipated energy function $\varphi(\boldsymbol{\varepsilon})$; namely,

$$V^i = \beta^j \int_{vol} \chi_j(\boldsymbol{\varepsilon}^i(\boldsymbol{x}))d\boldsymbol{x} \tag{6}$$

where V^i (the irreversible portion of U^i) is given by

$$V^i = U^i - \frac{1}{2} t^i \cdot d^i.$$

A graphical depiction of V^i for a hypothetical one dimensional loading siuation is given in Fig. 1. Since the strain field $\varepsilon(\boldsymbol{x})$ is known from the solution of Eqs.(2)-(5), the parameter vector $\boldsymbol{\beta}$ may be determined by solving Eq.(6) enabling $\varphi(\boldsymbol{\varepsilon})$ to be computed.

3.2.3 Method of Solution.

The nature of the system (2)-(6) suggests solution by the following iterative procedure:

1. An initial estimate of the strain field, i.e., $\varepsilon_0^i(\boldsymbol{x})$, is obtained by solving Eqs.(3) and (4) using the constitutive relation

$$\boldsymbol{\sigma} = K\boldsymbol{\varepsilon},$$

where $\boldsymbol{K}$ is the stiffness matrix for the unstressed material and can either be obtained from the literature (when available) or estimated from mixture theory. The problem defined here is linear and is readily solved by finite element methods, or, in certain cases, by closed-form procedures.

2. Using the estimate $\boldsymbol{\varepsilon}_0^i(\boldsymbol{x})$ for $\boldsymbol{\varepsilon}^i(\boldsymbol{\alpha}, \boldsymbol{x})$, an estimate of the parameter vectors $(\boldsymbol{\alpha}, \boldsymbol{\beta})$ is obtained from Eqs.(2) and (6) subject to the constraints that each component of the imparted energy be monotonically increasing along every loading path. This involves solving a linear or quadratic programming problem as will be explained shortly.

3. Equations(3)-(5) are solved numerically with the value of $\boldsymbol{\alpha}$ in Eq.(5) taken as $\boldsymbol{\alpha}_0$; the new estimate of $\boldsymbol{\varepsilon}$ is utilized in Eqs.(2) and (6) to obtain an updated estimate of $\boldsymbol{\alpha}$ and $\boldsymbol{\beta}$; and the process is repeated until successive estimates differ by a sufficiently small amount.

Note that except for the initial step, determining the estimate of $\boldsymbol{\varepsilon}^i(\boldsymbol{\alpha}, \boldsymbol{x})$ always involves solving a set of *nonlinear* boundary value problems. Although this is in general difficult and time-consuming, as a practical matter, unless one is interested in venturing deeply into the nonlinear regime where significant strain redistribution occurs due to spatially wide spread material stiffness changes, sufficient accuracy should be attainable by implementing only a single cycle of the iteration procedure. Thus we usually need only to solve the *linear* problem described in Item 1 above, and the difficulties mentioned above should be of little concern. If the need does arise to implement more than one cycle of the iteration procedure, techniques such as homotopic continuation methods [6] applied along each loading path are available to help alleviate the difficulties.

3.2.4 Initial Estimates of the Parameter Vectors.

As mentioned previously, $\boldsymbol{\varepsilon}_0^i(\boldsymbol{x})$ is computed by solving a *linear* boundary value problem. Indeed, using the fact that any boundary displacement d produced by the in-plane loader can be represented by a linear combination of opening/closing (d_1), sliding (d_0), and rotating (d_2) displacements, only *three* finite element analyses need be performed in this step since any strain

field $\epsilon_0^i(x)$ can be represented as

$$\epsilon_0^i = d^k \epsilon_{k0}^i,$$

by linear superposition. Here, ϵ_{k0}^i are the strain fields corresponding to the unit boundary displacements $\hat{d}_j = \delta_j^k$ and δ_j^k is the Kronecker delta.

With $\epsilon_0^i(x)$ known the quantity $\int_{vol} \chi_j(\epsilon_0^i(x))dx$ in Eqs.(2) and (6) may be computed. Thus, setting

$$\int_{vol} \chi_j(\epsilon_0^i(x))dx \equiv F_j^i,$$

eqs.(2) and (6) may be written as the *linear* set of equations

$$Fz = W, \tag{7}$$

where $W \equiv (U^1, \ldots, U^n)^T$ or $(V^1, \ldots, V^n)^T$, $z \equiv \alpha_0$ or β_0, and

$$F = \begin{pmatrix} F_1^1 & \cdots & F_m^1 \\ \vdots & & \vdots \\ \vdots & & \vdots \\ \vdots & & \vdots \\ \vdots & & \vdots \\ F_1^n & \cdots & F_m^n \end{pmatrix}.$$

As long as $\text{rank}(F) < \text{rank}(\overline{F})$, where $\overline{F}$ is the augmented matrix

$$\begin{pmatrix} F_1^1 & \cdots & F_m^1 & W^1 \\ \vdots & & \vdots & \vdots \\ \vdots & & \vdots & \vdots \\ \vdots & & \vdots & \vdots \\ \vdots & & \vdots & \vdots \\ F_1^n & \cdots & F_m^n & W^n \end{pmatrix},$$

Eq.(7) is an overdetermined system and there exists no value of z which satisfies (7) exactly. Rather one must seek to minimize the norm of the error vector $e = W - Fz$ to obtain a best approximation to the solution.

This is the usual state of affairs in parameter estimation; indeed, the more highly overdetermined the system the better since one generaly wants to work with as many independent observations as possible in order to filter out any undesirable stochastic variations (noise). If enough observations are linearly dependent then it can happen that $\text{rank}(\boldsymbol{F}) = \text{rank}(\overline{\boldsymbol{F}}) < m$, in which case there exists $m - \text{rank}(\boldsymbol{F})$ solutions to Eq.(7). A little thought reveals that this situation is most likely to occur when the material response is linear over most of the range of imposed loads and is something we try to avoid.

Assuming for the moment that Eq.(7) is indeed overdetermined, we seek to minimize the norm of $\boldsymbol{e} = \boldsymbol{W} - \boldsymbol{F}\boldsymbol{z}$ subject to the constraints

1. The values of (ψ, φ) be positive at the node points of the interpolation mesh, i.e.

$$z^i > 0, \tag{8}$$

   to maintain positivity.

2. The absorbed and dissipated energy be monotonically increasing along each radial loading path in displacement space, i.e.,

$$\begin{aligned} &\text{row}(\boldsymbol{F})_{i_p} \cdot \boldsymbol{z} > 0, \\ &(\text{row}(\boldsymbol{F})_{i+1} - \text{row}(\boldsymbol{F})_i) \cdot \boldsymbol{z} \geq 0, \quad i = i_p, \ldots, i_q - 1, \end{aligned} \tag{9}$$

   where (9) applies to each loading path, i_p is a point at the beginning the the path, and i_q is the end point.

Note that the above constraints are *linear* inequality constaints in z, and as such are readily dealt with.

Two widely used measures of vector magnitude are the L^2 (Euclidean) and L^∞ (Chebychev) norms given by

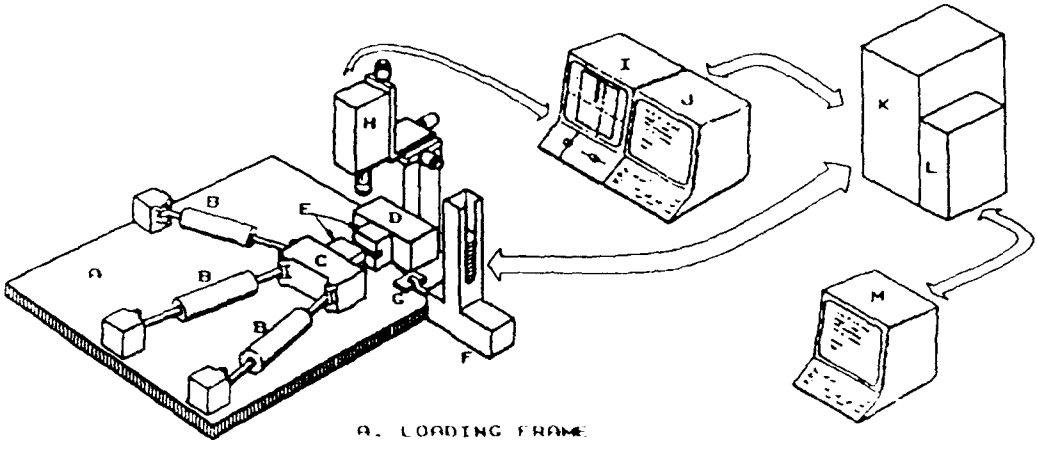
$$\| \boldsymbol{x} \|_{L^2}^2 = (x_1^2 + x_2^2 + \ldots + x_n^2)^2$$

and

$$\| \boldsymbol{x} \|_{L^\infty} = \max_{x_i} (|x_1|, |x_2|, \ldots, |x_n|),$$

respectively. Minimizing $\| \boldsymbol{e} \|$ in Eq.(7) under the L^2 norm subject to the constraints (8) and (9) is a problem in *quadratic programming* since the objective function $\| \boldsymbol{W} - \boldsymbol{F}\boldsymbol{z} \|_{L^2}$ is quadratic in the variables $(z^1, z^2, \ldots, z^n)$.

This is a well-established discipline and many efficient procedures are available to deal with such problems [7]. Minimizing $\| e \|$ under the L^∞ norm is just as straightforward, and perhaps easier, because there exists a well-known technique [8] for converting such problems into *linear prgramming* problems which can be solved using the simplex method or one of its variants [8].



A. LOADING FRAME
B. HYDRAULIC ACTUATORS
C. MOVABLE HEAD
D. FIXED HEAD
E. SPECIMEN GRIPS
F. SPECIMEN LOADER/UNLOADER
G. TEST SPECIMEN
H. VIDEO CAMERA
I. VIDEO MONITOR FOR POSITIONING DEVICE
J. MAIN TERMINAL
K. COMPUTER
L. GRAPHICS PROCESSOR
M. GRAPHICS TERMINAL

Fig. 1 The in plane loader system

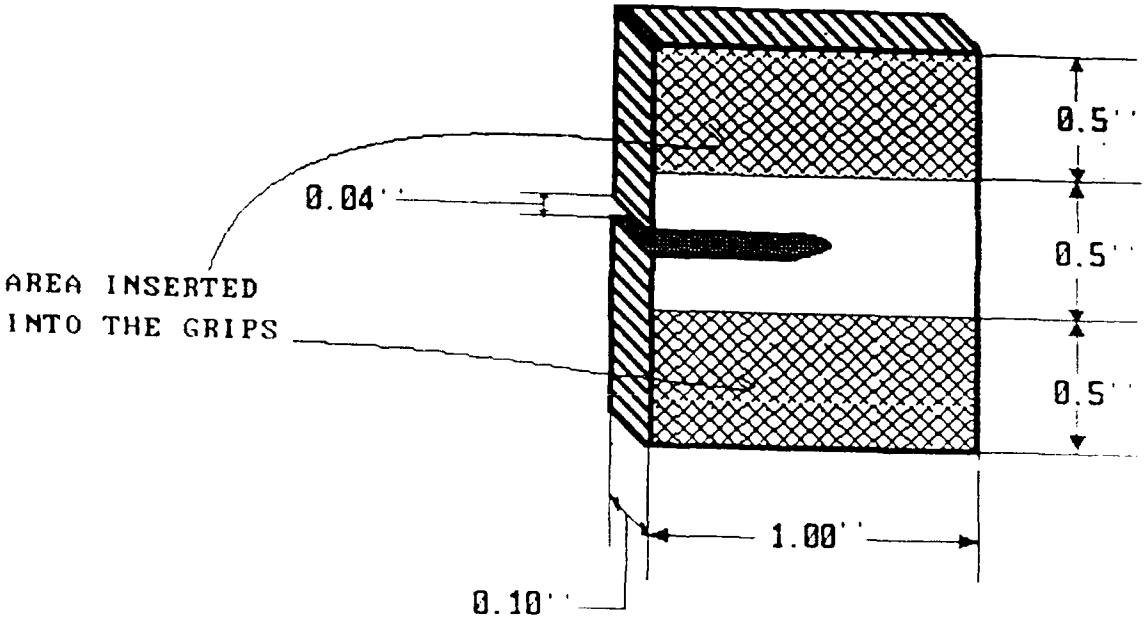


Fig. 2 The test specimen

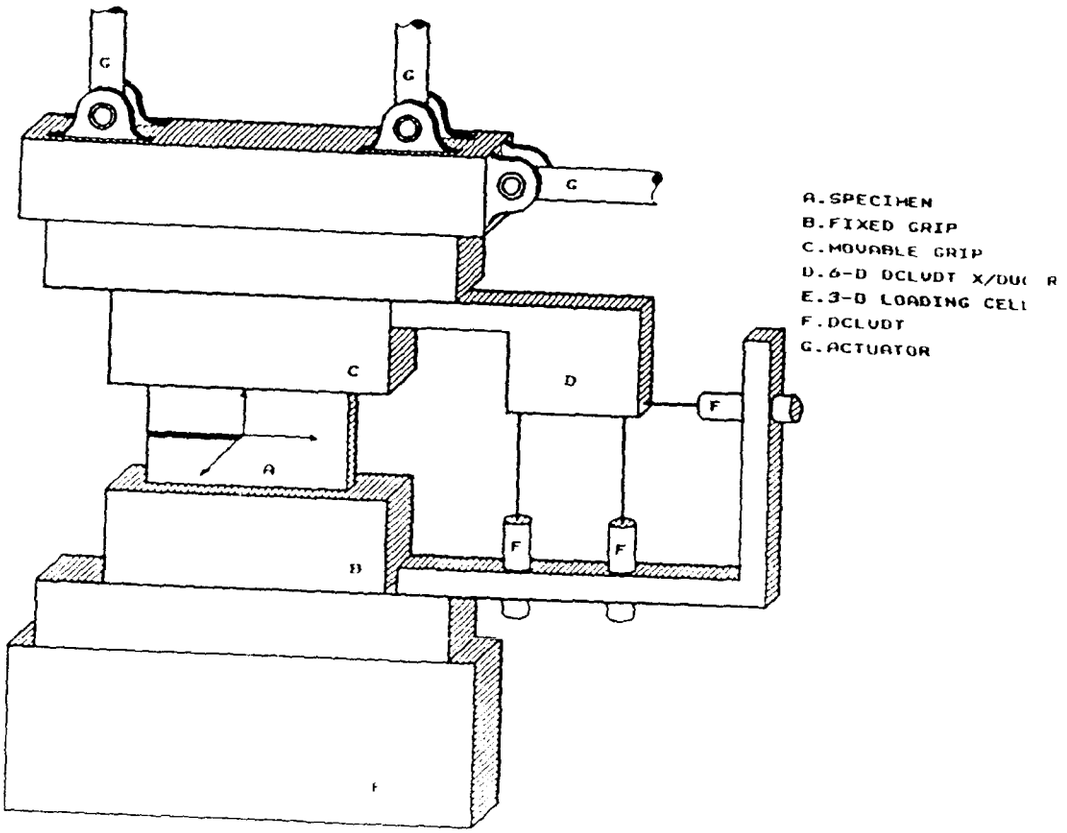


Fig. 3 The grip region of the in-plane loader

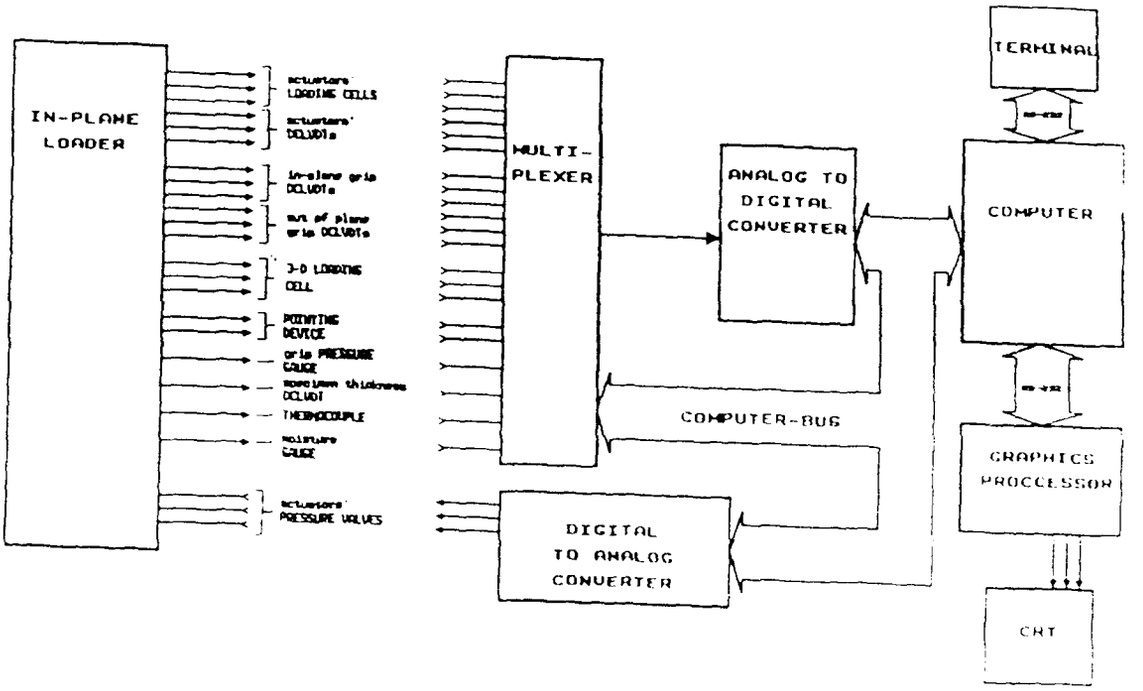


Fig. 4 Block diagram of the control and measurement system

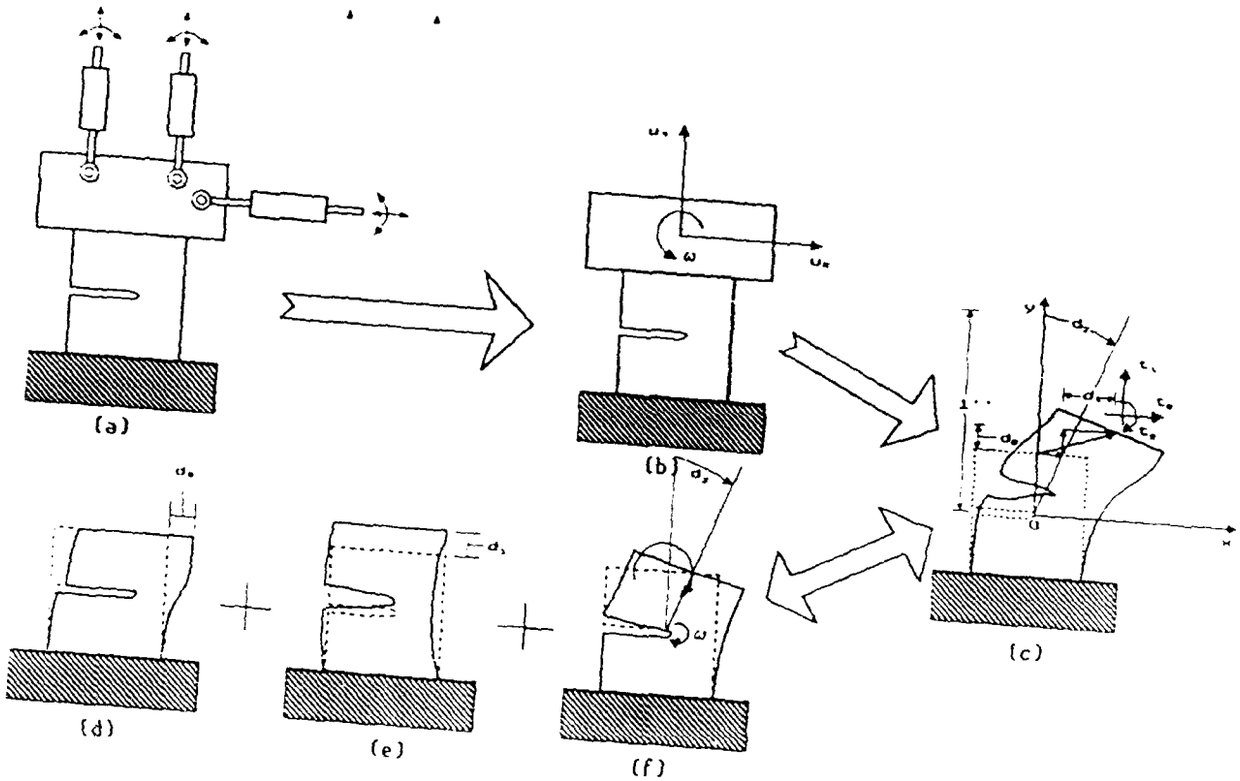


Fig. 5 Relation between prescribed actuator displacements, resulting grip motion and equivalent boundary displacements and tractions on the specimen

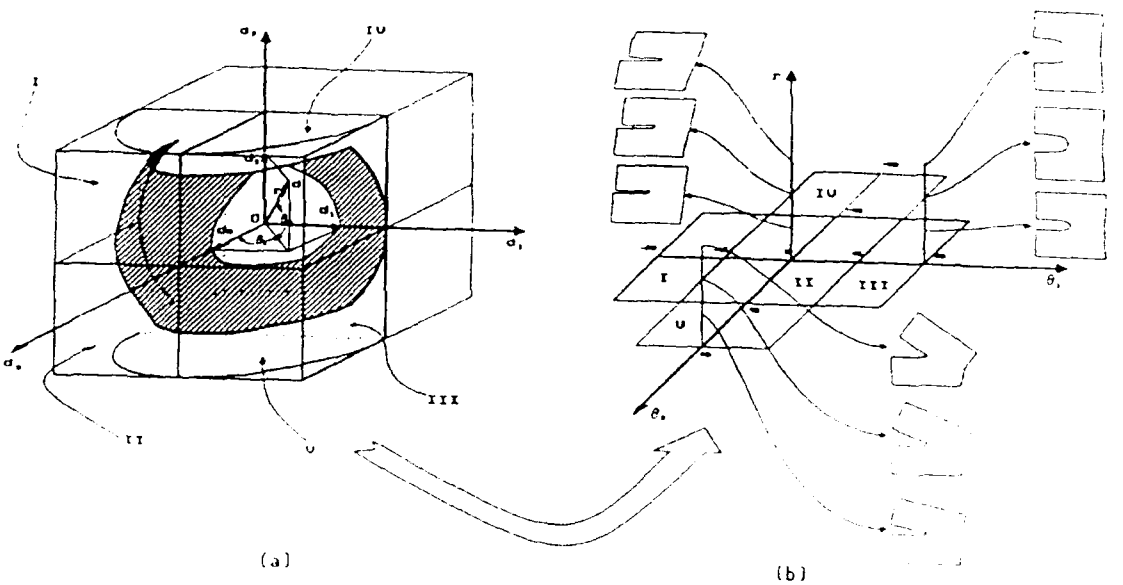
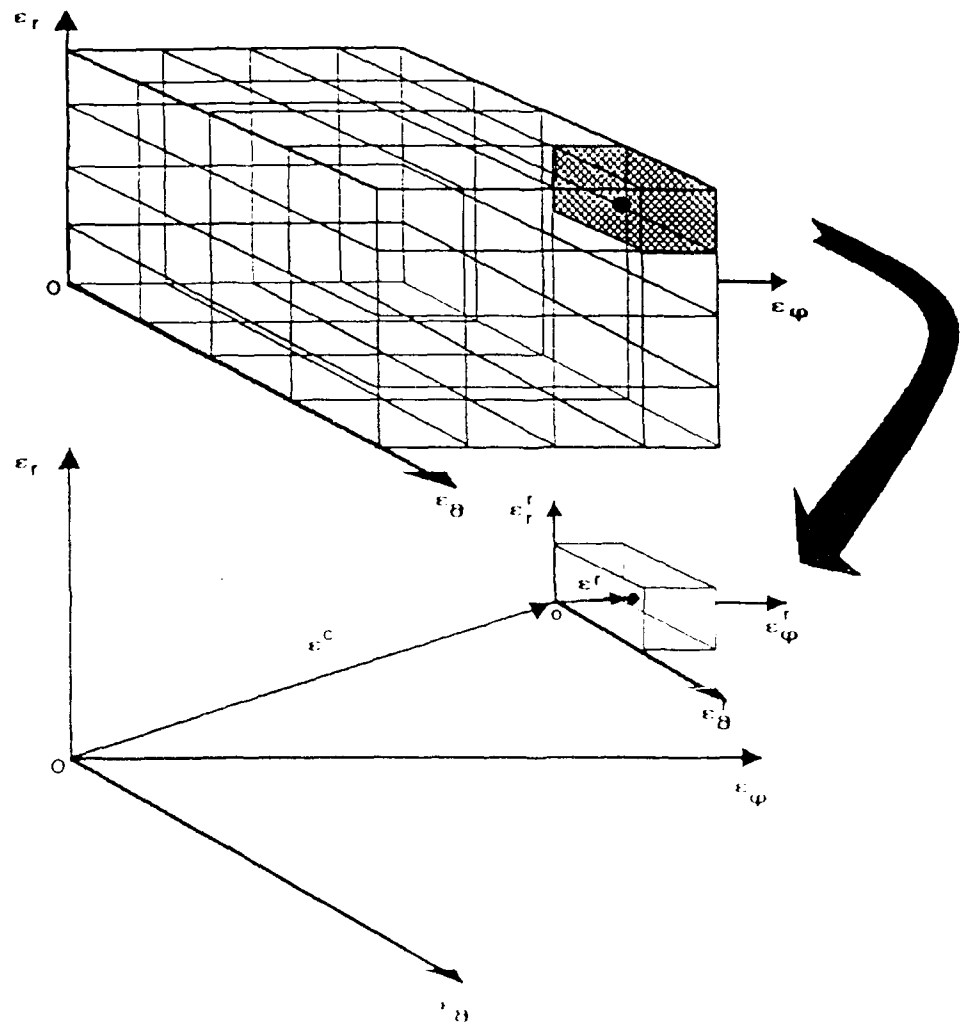


Fig. 6. Selected loading paths and displacement space



$$\Psi(\varepsilon^c, \varepsilon^r) \quad N_{\alpha\alpha}(\varepsilon^r)\phi^\alpha(\varepsilon^{c\,\alpha}, 0)$$

Fig. 8. Illustration of the interpolation procedure

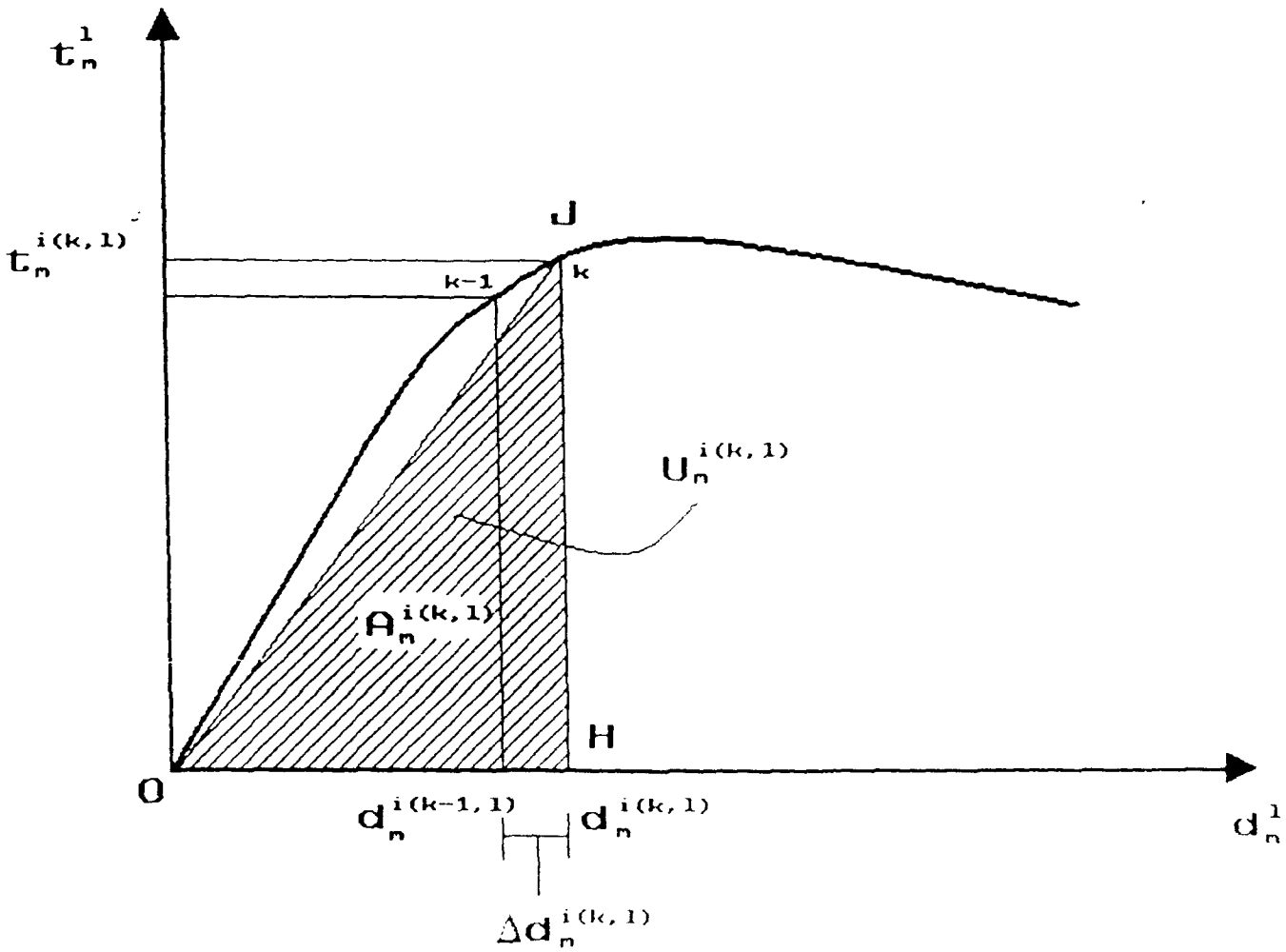


Fig 1

APPENDIX VII

RECORD AND DISCLOSURE OF INVENTION

DIRECTIVE: ONRINST 5870.1C

DEPARTMENT OF THE NAVY
OFFICE OF NAVAL RESEARCH
ARLINGTON, VA. 22217

INSTRUCTIONS. A Navy inventor or an employee of a Navy contractor should use this form when submitting an invention disclosure to the Department of the Navy. Original and two copies should be printed or typed and forwarded to the Navy Patent representative in the area or directly to the Office of Naval Research at the above address. Where space on form is inadequate, enter "see attached page", identify item by number and use plain pages as needed. When completely executed, this form becomes an important legal document useful in proving priority of invention.

FOR USE BY NAVY PATENT ACTIVITY	
PATENT ACTIVITY (Name)	NAVY CASE NO
DATE DISCLOSURE RECEIVED	LOCAL CASE NO

PART I. RECORD OF INVENTION

1. INVENTOR(S)	ADDRESS	POSITION TITLE	EMPLOYER (Activity & Code No. or Company & address)
J.C.M. Li		Summer Faculty	Naval Research Laboratory Code 6390, Wash, DC 20375-5000
Hsiang Y. Yu		Senior Scientist	Geo-Centers, Ft. Wash., MD 20744
V. Provenzano		Research Physicist	Naval Research Laboratory Code 6372, Wash, DC 20375-5000
J. M. Wolla		Matls Research Engr.	Naval Research Laboratory Code 6372, Wash, DC 20375-5000

2. DESCRIPTIVE TITLE OF INVENTION (Disclosure details of invention in Part II or reverse)

High Damping Materials with Nanometer Voids

RECOMMENDED SECURITY CLASSIFICATION AND AUTHORITY ON INVENTION DISCLOSURE

UNCLASSIFIED

3. CONCEPTION, INITIAL RECORDS AND RESULTS OF FIRST MODEL

a. EARLIEST DATE AND PLACE INVENTION WAS CONCEIVED (Identify persons and records to support date and place)

Theoretical prediction of high damping due to voids and the fact that damping is independent of the size of the voids(July 13, 1988).

b. DATE AND PRESENT LOCATION OF FIRST SKETCH, DRAWING OR PHOTO AND FIRST WRITTEN DESCRIPTION (Such as notebook entries, etc.)

July 14, 1988, attached.

c. DATE AND PLACE OF COMPLETION OF FIRST OPERATING MODEL OR FULL SIZE DEVICE AND ITS PRESENT LOCATION

not yet

d. DATE AND PLACE OF FIRST TEST OR OPERATION AND THE RESULTS (Give name and address of witnesses, and present location of records)

not yet

4. OTHER RECORDS (Notebook entries, descriptions, reports, drawings, etc.)

IDENTIFICATION	DATE OF DOCUMENT	PRESENT LOCATION
Notebook records	7/12/88 - 7/15/88	Naval Research Laboratory Washington, DC 20375-5000

5. OTHER INDIVIDUALS TO WHOM INVENTION WAS DISCLOSED

NAME	ACTIVITY OR COMPANY INDIVIDUAL REPRESENTS	DATE DISCLOSED	TYPE (Oral or written disclosure)

NAVONR 5870/35 (Rev. 4-81)

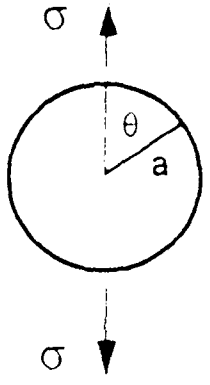
3. Description of invention:

It is proposed to mix nanometer sized particles of two metals: a structural metal such as iron or copper and a soft metal such as gallium or tin. The two metals must be insoluble with each other and the volume fraction of the soft metal should be small (1% or less). If the thermal expansion of the soft metal is larger than the strong metal, the mixture should be compacted at some high temperature and cooled down to room temperaure . Otherwise, compact at a low temperature and warm up to room temperature. The presence of the soft metal will stabilize the voids and prevent them from disappearing by sintering. The soft metal should also provide a path for interface diffusion of atoms.

4. Advantages and new features:

If successful, the result should be a strong structural material with large damping - something not available currently. With this material, noise and vibration reduction capacity can be incorporated into machinery designs. The material can also be used as a substitute or replacement material in machinery that has been poorly designed and subject to vibration. In this case, the vibrational energy would dissipated in the form of heat in the material.

DAMPING DUE TO SPHERICAL VOID - DIFFUSION



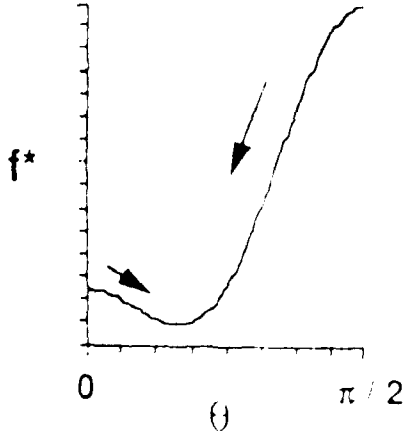
STRAIN ENERGY DENSITY ALONG INNER SURFACE

$$f = \left[50\cos^4\theta - 10(9 - 5\nu)\cos^2\theta + \frac{16 + 25(1 - \nu^2)}{(1 + \nu)} \right] \frac{9(1 - \nu)\sigma^2}{8G(7 - 5\nu)^2}$$

ATOM FLUX CAUSED BY STRAIN ENERGY GRADIENT

$$J = -\frac{Dc}{kT}\frac{\partial \mu}{\partial x} = \frac{Dcv}{akT}\frac{df}{d\theta}$$

D: surface diffusivity
c: surface concentration
v: atomic volume
k: Boltzmann constant
T: absolute temperature



DAMPING PER VOID PER SECOND

$$\Delta W = 2\int_0^{\pi/2} J(2\pi a \sin\theta)\, v \frac{df}{d\theta}\, d\theta$$

$$= \frac{4\pi Dcv^2}{kT}\left(\frac{664}{45} - \frac{176}{7}\nu + \frac{40}{3}\nu^2\right)\left[\frac{45(1 - \nu)\sigma^2}{8G(7 - 5\nu)^2}\right]^2$$

- INDEPENDENT OF SIZE OF VOID
- PROPORTIONAL TO SURFACE DIFFUSIVITY

NRL

5. Execution of Disclosure:

Signature of Inventors	Date
J.C.M. LI	Aug. 19, 1988
H.Y. YU	Aug. 19, 1988
V. PROVENZANO	Aug. 19, 1988
J.M. WOLLA	Aug 19, 1988

"Disclosed and understood by me on August 19, 1988"

J.C.M. KAMPE — August 1988

"Disclosed and understood by me on August 19, 1988"

S.C. SANDAY — August 1988

RECORD AND DISCLOSURE OF INVENTION

DIRECTIVE OPNAVINST 5870

DEPARTMENT OF THE NAVY
OFFICE OF NAVAL RESEARCH
ARLINGTON, VA. 22217

INSTRUCTIONS. A Navy inventor or an employee of a Navy contractor should use this form when submitting an invention disclosure to the Department of the Navy. Original and two copies should be printed or typed and forwarded to the Navy Patent representative in the area or directly to the Office of Naval Research at the above address. Where space on form is inadequate, enter "see attached page", identify item by number and use plain pages as needed. When completely executed, this form becomes an important legal document useful in proving priority of invention.

FOR USE BY NAVY PATENT ACTIVITY	
PATENT ACTIVITY *(Name)*	NAVY CASE NO
DATE DISCLOSURE RECEIVED	LOCAL CASE NO

PART I. RECORD OF INVENTION

1. INVENTOR(S)	ADDRESS	POSITION TITLE	EMPLOYER *(Activity & Code No., or Company & address)*
Hsiang-Yung Yu		Senior Scientist	Geo-Centers, Ft.Wash., MD 20744
S. Carlos Sanday		Supv. Physical Scientist	Naval Research Laboratory Code 6370 Washington, DC 20375

2. DESCRIPTIVE TITLE OF INVENTION *(Disclosure details of invention in Part II on reverse)*

Micro-mechanics Tester with Passive Loading Mechanism

RECOMMENDED SECURITY CLASSIFICATION AND AUTHORITY ON INVENTION DISCLOSURE

UNCLASSIFIED

3. CONCEPTION, INITIAL RECORDS AND RESULTS OF FIRST MODEL

a. EARLIEST DATE AND PLACE INVENTION WAS CONCEIVED *(Identify persons and records to support date and place)*

3/1/89, Naval Research Laboratory, witnessed by C. Kim on this date and by V. Provenzano, 3/28/89

b. DATE AND PRESENT LOCATION OF FIRST SKETCH, DRAWING OR PHOTO AND FIRST WRITTEN DESCRIPTION *(Such as notebook entries, etc.)*

3/1/89, NRL notebook entry

c. DATE AND PLACE OF COMPLETION OF FIRST OPERATING MODEL OR FULL SIZE DEVICE AND ITS PRESENT LOCATION

not yet

d. DATE AND PLACE OF FIRST TEST OR OPERATION AND THE RESULTS *(Give name and address of witnesses, and present location of records)*

not yet

4. OTHER RECORDS *(Notebook entries, descriptions, reports, drawings, etc.)*

IDENTIFICATION	DATE OF DOCUMENT	PRESENT LOCATION
notebook records	3/1/89 - 3/28/89	Naval Research Laboratory Washington, D.C. 20375

5. OTHER INDIVIDUALS TO WHOM INVENTION WAS DISCLOSED

NAME	ACTIVITY OR COMPANY INDIVIDUAL REPRESENTS	DATE DISCLOSED	TYPE *(Oral or written disclosures)*

1. General purpose:

Simple, inexpensive method to design a compact micro-mechanics tester to study the mechanical properties, specially the Young's modulus of thin films, fibers and whiskers.

2. Background:

The techniques engaged to measure the tensile properties of a very small sample such as thin films, fibers and whiskers are High Speed Rotor, Bulge Method, Electron-microscope Devices, Direct Measurement of Strain by Diffraction Method and Tensile Test. A number of micro-tensile testers have been built for the observation of small load and small elongations typical of thin film work. "Soft" testers, which are common in thin film studies, are those in which the load is given and the elongation is measured, whereas "hard" types prescribe the strain rate and measure the load. For softer testers, the existing methods for apply the uniaxial load are magnetically, electromagnetically or gravimetrically. The elongation is measured by direct observation through an optical microscope, interferometrically, or with a differential transducer.The hard machines described in the literature use a strain-gauge-proof ring to measure the load while the strain is observed using a differential transducer or an optical arrangement. The various tensile--tester apparatuses are summarized by Hoffman (R. W. Hoffman, in "Physics of Thin Films", G. Hass and R. E. Thun eds., vol. 3, p. 211, Academic Press Inc., New York, 1966). In all these existing techniques, an active apparatus is need either to apply the load or to apply the strain to the grips which hold the sample. The disadvantage are connected with the fact that this kind of design is costly and the dimension of the tester can not be easily reduced.

3. Description and operation:

The following is our new micro-mechanics tester design. The load which apply to the sample is provided by the thermal expansion of the two parallel rods as shown in figure 1 which are thermal insulated, therefore, it is a passive element. The sample is parallel to the rods such that the tension load due to the thermal expansion of the rods is transmitted by two parallel rigid bars which attached to the rods perpendicularly. The sample is mount at the center of the rigid bars with the method same as the conventional micro-tensile testing. The elongation is measured by direct observation through an optical microscope, interferometrically, or with a differential transducer. Due to the constrain of the sample, the thermal elongation of the system is different from the value which obtained without the sample mounted. By knowing the relations between this strain difference and the temperature, the stress strain relation can be obtained. The equation for obtained the Young's modulus of the film through the testing is shown in equation (1).

$$Y_s = Y_r \frac{A_r}{A_s} \frac{\beta(x-1)}{1+\alpha\Delta T} \qquad (1)$$

where

An numerical example is provided as follows. For typical thin film sample with gauge length 1 cm, cross-section area 1 cm x 1 μm and Young's modulus of order of 1×10^{11} N/m^2 and by assuming the rods is made by crystalline polyethylene with Young's modulus 4×10^8 N/m^2 and linear thermal expansion coefficient 300×10^{-6} /^{o}k. The dimension of the rod are assumed to be 5 cm (L) long and 5 mm in diameter. When the temperature increases 5°k from room temperature, the elongation is 75 μm before the sample mounted and is 56.9 μm after the sample mounted (with $\Delta L_0/\Delta L$ = 132%). Both the elongations and the change of the elongation are very easy to measured. The strain applied to the specimen is 0.57% in presence example which is suitable to measure the Young's modulus and yield strength of the sample.

4. Advantages and new features:

This is a simple, compact and inexpensive approach for constructing micro-mechanical tester. The innovation feature of present method is in the loading mechanism. A passive element is used instead of conventional active element to apply the load. This passive element consists of a high thermal expansion rod with a heating wire which are thermally insulate from outside environment. It's technical advantages are: (a) no moving part involved in this tester, therefore simplified the design and the cost, (b) except the elongation measuring device, no instrument is required to apply the load, thus the whole dimension of the system can be reduced dramatically, and (c) It is easy to modify to different load range by simply changing the passive element.

5. Alterntives:

Any alternative design which utilize the fundamental feature of present invention, that is using the material thermal expansion property to be the loading mechanism, is claimed under this disclosure. The alternative design may include the shape, size of the system, the material used for the passive element and the instrument used for measuring the elongation and the temperature. For example the shape of the passive element can changed into a disc and the thin film is attached to the circumference. The polyethylene rod can be replace by any other material with high thermal expansion coefficient and suitable stiffness.

$$x = \frac{\Delta L_0}{\Delta L} \qquad (2)$$

and

L : the original distance of the two rigid-bar/rod joint points,

βL : the original length of the sample (gauge length),

ΔL_0 : linear expansion without sample attached,

ΔL : linear expansion with sample attached,

A_s : the cross section area of the sample,

A_r : the total cross section area of the expansion rods,

Y_s : Young's modulus of the sample,

Y_r : Young's modulus of the rod,

α : thermal expansion coefficient of the bar,

ΔT : temperature difference.

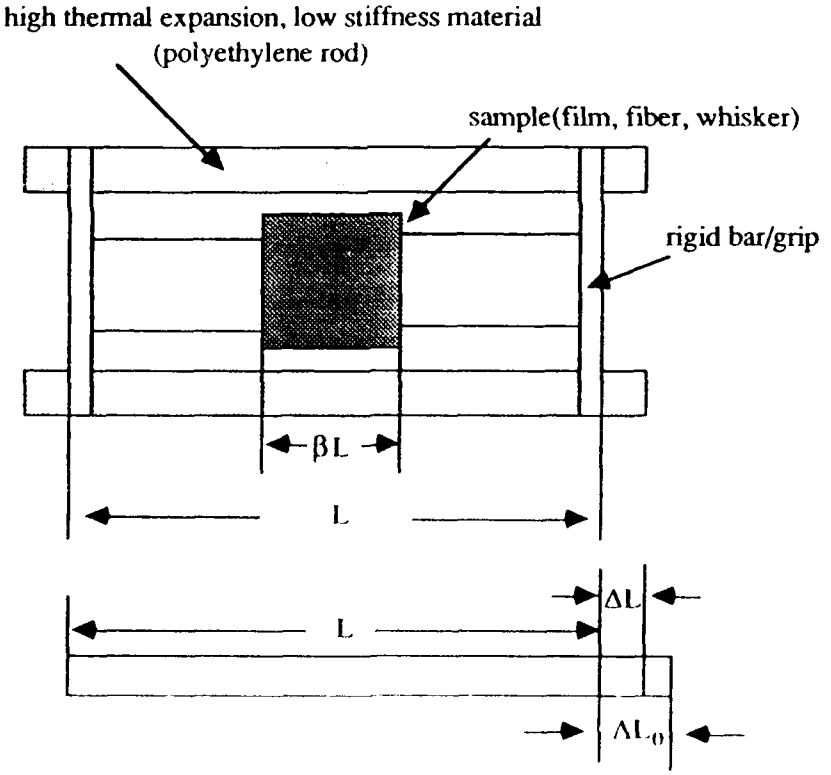


Fig. 1 Schematic diagram showing the principle of the thermal activated micro-testing machine.

6. **Execution of Disclosure:**

Signature of Inventors	Date
H. Y. YU	3/28/89
S. C. SANDAY	3/28/89

"Disclosed and understood by me on March 28, 1989"

C. KIM	3/28/89

"Disclosed and understood by me on March 28, 1989"

V. PROVENZANO	3/28/89

ELLIPSOIDAL INCLUSION IN A HALF SPACE

H. Y. Yu* and S. C. Sanday

Naval Research Laboratory, Washington, D.C. 20375-5000

Accepted by
ASME Journal of Applied Mechanics

*On-site contract employee from Geo-Centers Inc., Fort Washington, MD, U.S.A.

ABSTRACT

An alternate method of approach for solving the elastic fields in the half space with an isotropic ellipsoidal inclusion is proposed. This new approach involves the application of the Hankel transformation method for the solution of prismatic dislocation loops and Eshelby's solution for ellipsoidal inclusions. Existing solutions by other method for the inclusion with pure dilatational misfit in a half space are shown to be the special cases of the present, more general solution.

1. INTRODUCTION

The elastic fields caused by an ellipsoidal inclusion with thermal expansion stress-free transformation strains (eigenstrains) in an isotropic infinite body were investigated by Goodier (1937). For more general eigenstrains, solutions were obtained by Eshelby (1957, 1959, 1961). By using the Galerkin vector, Mindlin and Cheng (1950) obtained the solution of the thermoelastic stress field in the semi-infinite solid when a uniform dilatational thermal expansion is given inside a spherical domain. Mindlin's solution (1953) for Green's function in a half space was used by Seo and Mura (1979) to solve the same problem for the domain in the shape of an ellipsoid. By combining an application of potential theory with the stress-function approach of Papkovitch and Neuber, and starting with Eshelby's solution for the homogeneous infinite solid, Aderogba (1976) generalized the solution of Mindlin and Cheng to the case of a spherical inclusion in half-space undergoing a general uniform transformation.

The method of Hankel transformations, elaborated for cylindrically symmetrical problems of the theory of elasticity in Sneddon's book (1951), has been used to solve the stress field of a circular edge dislocation loop with Burger's vector normal to the plane of the loop (prismatic loop) in an unbounded solid (Kroupa, 1960) and in the half space (Bastecka, 1964). The elastic solution of a dislocation loop in a two phase material had been given by Salamon and Dundurs (1971).

In the present study, Eshelby's method for the ellipsoidal inclusion and the Hankel transformation method for the prismatic loop are used for the analysis of the elastic solution of an ellipsoidal inclusion in the half space when a uniform axisymmetric principle eigenstrain is given inside the inclusion, which in the absence of the surrounding half space would result in a uniform homogeneous strain, not accompanied by stress. This approach provides an alternate way for obtaining a more general solution of the stresses in the half

space with an ellipsoidal inclusion. Existing solutions are shown to be special cases of the present one.

2. FUNDAMENTAL EQUATIONS

A semi-infinite domain is defined by $x_3 \geq 0$ as shown in Fig.1. The surface $x_3 = 0$ is free from external tractions. The present problem is to express the elastic field when the eigenstrain e^T_{ij} in an ellipsoidal subdomain Ω_1 (with semi-axes a_1, a_2, a_3 and center at $x_1 = x_2 = 0$ and $x_3 = c$) of the half space is made up of a uniform dilatation 3e and an extension b parallel to the x_3 axis which in the absence of the surrounding half space would result in a uniform homogeneous strain as

$$e^T_{ij} = \delta_{ij}(\varepsilon + \beta\delta_{i3}) \quad i, j = 1, 2, 3, \tag{1}$$

where δ_{ij} is the Kronecker delta (the usual summation convention does not apply to any of the expressions in this paper).

For an inclusion Ω centered at $x_1 = x_2 = x_3 = 0$ and with uniform eigenstrain described by Eq.(1), the stress field in an isotropic infinite body outside Ω can be obtained by using Eshelby's method (1961). The result is given by

$$\sigma_{ij} = \frac{\mu\beta}{4\pi(1-\nu)}[\psi_{,ij33} - 2\nu(1-\delta_{i3})(1-\delta_{j3})(\phi_{,ij} + \delta_{ij}\phi_{,33}) - 2(\delta_{i3}+\delta_{j3})\phi_{,ij}] - \frac{(1+\nu)\mu\varepsilon}{2\pi(1-\nu)}\phi_{,ij}, \tag{2}$$

where the numerical suffixes, i, j = 1, 2, 3, following a comma denote differentiation with respect to the Cartesian coordinates x_1, x_2, x_3, respectively; m and n are the shear modulus and Poisson's ratio, respectively; and y and f are the biharmonic and harmonic potential of attracting matter of unit density filling the volume Ω, respectively. For a spheroidal inclusion, that is $a_1 = a_2$, equation (2) can be transformed into cylindrical coordinates (r,θ,z) as follows:

$$\sigma_{rr} = -\frac{\mu\beta}{4\pi(1-\nu)}\left[\phi_{,zz} + z\phi_{,zzz} + \frac{1-2\nu}{r}\phi_{,r} + \frac{z}{r}\phi_{,rz} + f\left(\frac{1}{r}\phi_{,r} + 2\phi_{,zz}\right.\right.$$

$$\left.\left. + r\phi_{,rzz} + z\phi_{,zzz} + \frac{z}{r}\phi_{,rz}\right]\right] + \frac{(1+\nu)\mu\varepsilon}{2\pi(1-\nu)}\left[\frac{\phi_{,r}}{r} + \phi_{,zz}\right],$$

$$\sigma_{\theta\theta} = -\frac{\mu\beta}{4\pi(1-\nu)}\left[2\nu\phi_{,zz} - \frac{1-2\nu}{r}\phi_{,r} - \frac{z}{r}\phi_{,rz} + f\left(\phi_{,zz} - \frac{1}{r}\phi_{,r} - \frac{z}{r}\phi_{,rz}\right)\right]$$

$$- \frac{(1+\nu)\mu\varepsilon}{2\pi(1-\nu)}\frac{\phi_{,r}}{r}, \qquad (3)$$

$$\sigma_{zz} = -\frac{\mu\beta}{4\pi(1-\nu)}\left[\phi_{,zz} - z\phi_{,zzz} - f\left(3\phi_{,zz} + z\phi_{,zzz} + r\phi_{,rzz}\right)\right] - \frac{(1+\nu)\mu\varepsilon}{2\pi(1-\nu)}\phi_{,zz},$$

$$\sigma_{rz} = -\frac{\mu\beta}{4\pi(1-\nu)}\left[z\phi_{,rzz} + f\left(2\phi_{,rz} + z\phi_{,rzz} - r\phi_{,zzz}\right)\right] - \frac{(1+\nu)\mu\varepsilon}{2\pi(1-\nu)}\phi_{,rz},$$

$$\sigma_{r\theta} = \sigma_{z\theta} = 0,$$

where $f = \dfrac{a_3^2}{a_1^2 - a_3^2}$.

Equations (3) are obtained with the aid of the relationships between the derivatives of the functions ψ and ϕ given by Eshelby (1962) and the following relationships

$$\nabla^2\phi = 0,$$

$$x_1\phi_{,2} = x_2\phi_{,1}, \qquad (4)$$

and

$$\phi_{,r} = \frac{x_1\phi_{,1} + x_2\phi_{,2}}{r},$$

where the letter suffixes following a comma denote differentiation with respect to the cylindrical coordinates r, θ, and z.

For a circular edge dislocation loop with the z-axis (or x_3-axis) as the axis of symmetry in an unbounded medium, the stress field is found by Kroupa (1960) by using Hankel transformations. For $z > 0$, Kroupa's solution can be rewritten as

$$\sigma_{rr} = -\frac{\mu ba}{2(1-\nu)}\left[(I_0^{-1})_{,zz} + z(I_0^{-1})_{,zzz} + \frac{1-2\nu}{r}(I_0^{-1})_{,r} + \frac{z}{r}(I_0^{-1})_{,rz} \right],$$

$$\sigma_{\theta\theta} = -\frac{\mu ba}{2(1-\nu)}\left[2\nu(I_0^{-1})_{,zz} - \frac{1-2\nu}{r}(I_0^{-1})_{,r} - \frac{z}{r}(I_0^{-1})_{,rz} \right],$$

$$\sigma_{zz} = -\frac{\mu ba}{2(1-\nu)}\left[(I_0^{-1})_{,zz} - z(I_0^{-1})_{,zzz} \right], \qquad (5)$$

$$\sigma_{rz} = \frac{\mu ba}{2(1-\nu)}\left[z(I_0^{-1})_{,rzz} \right],$$

$$\sigma_{r\theta} = \sigma_{z\theta} = 0,$$

where

$$I_m^n = I(m,1;n),$$

$$I(m,p;n) = \int_0^\infty t^n J_m(rt/a) J_p(t)\, e^{-zt/a}\, dt,$$

$$I_m^n = -a(I_m^{n-1})_{,z}, \qquad (6)$$

$$= -ar^{m-1}(r^{-m+1} I_{m-1}^{n-1})_{,r} \qquad (m = 0,1,2,..;\ n = -1,0,1,2,..),$$

and J_m is the Bessel function of the mth order, a is the radius of the circular dislocation loop, and b is the Burger's vector which is normal to the plane of the loop z = 0.

For the penny shape inclusion ($a_1 = a_2 = a$ and $a_3 \to 0$) without shear and dilatation eigenstrains (penny shape prismatic inclusion), the eigenstrains are $e_{11}^T = e_{22}^T = 0$ and $e_{33}^T = \beta$. If we reduce Eq.(3) for the penny shape prismatic inclusion , it is interesting to note the similarity between Eqs.(3) and (5). By putting

$$\phi = kI_0^{-1} \qquad (a_3 \to 0), \qquad (7)$$

where $k = 2\pi ba/\beta$, the elastic solutions of the penny shape prismatic inclusion (Eq. 3) and the prismatic loop (Eq.5) are identical. This suggests that the method used to obtain the stress field of a prismatic loop in the half space due to the presence of the free surface can be adapted to solve the elastic field caused by an axisymmetrical inclusion in the half space

with its axis of symmetry normal to the plane of the free surface. This approach is believed to be quite reasonable since the solution for the axisymmetrical inclusion can be applied to the penny shape inclusion after a tedious passage to the limit and the fact that if the inclusion has the same elastic moduli as the matrix, the stress field is the same as that of a small dislocation loop when both the dislocation loop and the inclusion are infinitesimally small (Eshelby, 1961). For example, a small inclusion of volume V and an eigenstrain e_{33}^{T} in the x_3 direction has the same stress field as that of a prismatic interstitial dislocation loop of area A and Burger's vector b provided that $Ve_{33}^{T} = Ab$. By using the recurrence relations Eq.(7), it can be shown that function I_0^{-1} satisfied the Laplace equation $\nabla^2 I_0^{-1} = 0$.

3. ELASTIC SOLUTIONS

Consider the half space $x_3 = z > 0$ (Fig.1) with an ellipsoidal inclusion with its center at the point (0,0,c). In order that the plane z = 0 be a surface free of external tractions, the stress components on this plane must satisfy the following boundary conditions

$$(\sigma_{rz})_{z=0} = 0 \quad , \quad (\sigma_{zz})_{z=0} = 0, \tag{8}$$

and the equilibrium condition

$$\sum_{j=1}^{3} \sigma_{ij,j} = 0. \tag{9}$$

Similar to the work of Bastecka(1964), the stress σ_{ij} in the half space $z \geq 0$ outside the axisymmetric ellipsoidal inclusion centered at the point (0,0,c) can be expressed as

$$\sigma_{ij} = \sigma_{ij}^{I} + \sigma_{ij}^{II} + \sigma'_{ij}, \tag{10}$$

which satisfies the required boundary conditions, Eq.(8), the equilibrium condition, Eq.(9), and also converges to zero for x_1 and x_2 approaching $\pm\infty$ and x_3 approaching ∞.

In Eq.(10), the term σ^{I}_{ij} is the stress caused by the axisymmetric inclusion Ω_1 centered at (0,0,c), σ^{II}_{ij} is the stress due to the image inclusion Ω_2 centered at the point (0,0,-c), with eigenstrain

$$(e^{T}_{ij})^{II} = -(e^{T}_{ij})^{I} = -\delta_{ij}(\varepsilon + \beta\delta_{i3}). \tag{11}$$

The solution for the stresses σ^{I}_{ij} and σ^{II}_{ij} are obtained by translating the origin of coordinates in Eq.(2) and Eq.(3) to points (0,0,c) and (0,0,-c) respectively. The expressions of the Newtonian potential functions ϕ^{I} and ϕ^{II} for the solutions of σ^{I}_{ij} and σ^{II}_{ij} can be found in Seo and Mura's paper (1979). The additional stress σ'_{ij} in Eq.(10) is the fictitious stress necessary to make the surface of the half space free of stresses and it satisfies the boundary conditions

$$(\sigma'_{zz})_{z=0} = 0, \tag{12}$$

$$(\sigma'_{rz})_{z=0} = -(\sigma^{I}_{rz} + \sigma^{II}_{rz})_{z=0} \tag{13}$$

When $a_1 = a_2$, substituting Eq.(3) into Eq(13) gives

$$(\sigma'_{rz})_{z=0} = \frac{\mu}{2\pi(1-\nu)}\left[c\beta\phi^{II}_{,rzz} + f\beta(c\phi^{II}_{,rzz} + 2\phi^{II}_{,rz} - r\phi^{II}_{,zzz}) - 2(1+\nu)\varepsilon\phi^{II}_{,rz}\right]_{z=0}, \tag{14}$$

where, for $z = 0$, $\phi^{I}_{,rzz} = \phi^{II}_{,rzz}$, $\phi^{I}_{,rz} = -\phi^{II}_{,rz}$, $\phi^{I}_{,zzz} = -\phi^{II}_{,zzz}$. Now, in the limit when a_3 approaches zero, that is, for the penny shape inclusion, we can substitute Eq.(7) into Eq.(14) to obtain

$$(\sigma'_{rz})_{z=0} = \frac{\mu\beta k}{2\pi(1-\nu)}\left[-(1+f)\frac{c}{a^3}\int_0^\infty t^2 J_1(\rho t)J_1(t)e^{-ct/a}dt + \frac{2f}{a^2}\int_0^\infty t J_1(\rho t)J_1(t)e^{-ct/a}dt\right.$$
$$\left. + \frac{f\rho}{a^2}\int_0^\infty t^2 J_0(\rho t)J_1(t)e^{-ct/a}dt\right] - \frac{(1+\nu)\mu\varepsilon}{\pi(1-\nu)}\frac{k}{a^2}\int_0^\infty t J_1(\rho t)J_1(t)e^{-ct/a}dt \tag{15}$$

where $\rho = r/a$.

For the axisymmetric problem, by the appropriate expression of the elastic displacement as the derivatives of certain function $\varphi(r,z)$ in cylindrical coordinates, the equilibrium and Beltrami equations are replaced by a single equation (Sneddon, 1951),

$$\nabla^4 \varphi(r,z) = 0, \tag{16}$$

whose general solution is carried out by the method of integral transformations. The function ψ is replaced by its Hankel transform of zeroth order,

$$G(\zeta,z) = \int_0^\infty r\varphi(r,z)J_0(\zeta r)\, dr, \tag{17}$$

and it can be shown that $G(\zeta,z)$ is in general given by the expression

$$G(\zeta,z) = (A + Bz)e^{-\zeta z} + (C + Dz)e^{\zeta z}, \tag{18}$$

where A, B, C and D are unknown functions of ζ which are determined from the boundary conditions. The stress components are expressed by means of the function $G(\zeta,z)$.

In the present case, we consider the solution to converge to zero for z approaching ∞. Thus we set $C = D = 0$. In order to determine A and B, from the first boundary condition (Eq.12), we obtain the following relationship

$$A(\zeta) = -\frac{\mu}{\lambda+\mu}\frac{B(\zeta)}{\zeta}, \tag{19}$$

where $\lambda = 2\mu\nu/(1-2\nu)$ is Lame's constant. From the relationship between the stress components and the function $G(\zeta,z)$, we have

$$(\sigma'_{rz})_{z=0} = \int_0^\infty \zeta F(\zeta)J_1(\zeta r)d\zeta, \tag{20}$$

where $F(\zeta)$ is the Hankel transformation of the first order of the function $(\sigma'_{rz})_{z=0}$ and

$$F(\zeta) = -2(\lambda+\mu)\zeta^2 B(\zeta). \tag{21}$$

By letting $t = a\zeta$, and using Eqs.(15) and (19), $F(\zeta)$ becomes

$$F(\zeta) = -\frac{k\mu\beta}{2\pi(1-\nu)} [\, (c\zeta - 2f)J_1(a\zeta) + af\zeta J_0(a\zeta) \,]e^{-c\zeta} - \frac{(1+\nu)k\mu\varepsilon}{\pi(1-\nu)} J_1(a\zeta)e^{-c\zeta}. \tag{22}$$

This equation is used to calculate the function G which is substituted into the expressions for stress σ'_{ij} (Sneddon, 1951). In the calculation, in addition to the recurrence relations Eq.(6), the following recurrence (Eason, Noble and Sneddon, 1955) relation is also used

$$I^{II}(m,p-1;n) = (m+p-n)\, I^{II}(m,p;n-1) - \frac{r}{a} I^{II}(m-1,p;n) + \frac{z+c}{a} I^{II}(m,p;n) \qquad (m+n+p > 0), \tag{23}$$

where

$$I^{II}(m,p;n) = \int_0^\infty t^n J_m(\rho t) J_p(t) e^{-t(z+c)/a}\, dt, \tag{24}$$

and the transformation relation between two-dimensional harmonic potential $(I_0^{-1})^{II}$ and three-dimensional harmonic potential $(\phi)^{II}$ is

$$(\phi)^{II} = k\,(I_0^{-1})^{II}. \tag{25}$$

The resulting expressions for the fictitious stresses σ'_{ij} are

$$\sigma'_{rr} = -\frac{\mu\beta c}{2\pi(1-\nu)} [\, 2\phi^{II}_{,zzz} + z\phi^{II}_{,zzzz} + \frac{2(1-\nu)}{r}\phi^{II}_{,rz} + \frac{z}{r}\phi^{II}_{,rzz} \,]$$
$$- \frac{\mu\beta f}{2\pi(1-\nu)} [\, 2(2+\nu)\phi^{II}_{,zz} + (5z+2c)\phi^{II}_{,zzz} + z(z+c)\phi^{II}_{,zzzz} + \frac{2(1-\nu)}{r}\phi^{II}_{,r}$$
$$+ 2\frac{(1-\nu)(z+c)}{r} + z\,\phi^{II}_{,rz} + \frac{2r^2 + z(z+c)}{r}\phi^{II}_{,rzz} + rz\,\phi^{II}_{,rzzz} \,]$$

$$\sigma'_{rr} = -\frac{\mu\beta c}{2\pi(1-\nu)}\left[2\phi^{II}_{,zzz} + z\phi^{II}_{,zzzz} + \frac{2(1-\nu)}{r}\phi^{II}_{,rz} + \frac{z}{r}\phi^{II}_{,rzz}\right]$$

$$-\frac{\mu\beta f}{2\pi(1-\nu)}\left[2(2+\nu)\phi^{II}_{,zz} + (5z+2c)\phi^{II}_{,zzz} + z(z+c)\phi^{II}_{,zzzz} + \frac{2(1-\nu)}{r}\phi^{II}_{,r}\right.$$

$$\left. + 2\frac{(1-\nu)(z+c)+z}{r}\phi^{II}_{,rz} + \frac{2r^2 + z(z+c)}{r}\phi^{II}_{,rzz} + rz\,\phi^{II}_{,rzzz}\right]$$

$$+\frac{(1+\nu)\mu\varepsilon}{\pi(1-\nu)}\left[2\phi^{II}_{,zz} + z\phi^{II}_{,zzz} + \frac{2(1-\nu)}{r}\phi^{II}_{,r} + \frac{z}{r}\phi^{II}_{,rz}\right],$$

$$\sigma'_{\theta\theta} = -\frac{\mu\beta c}{2\pi(1-\nu)}\left[2\nu\phi^{II}_{,zzz} - \frac{2(1-\nu)}{r}\phi^{II}_{,rz} - \frac{z}{r}\phi^{II}_{,rzz}\right] \qquad (26)$$

$$-\frac{\mu\beta f}{2\pi(1-\nu)}\left[2(1+2\nu)\phi^{II}_{,zz} + [(1+2\nu)z + 2\nu c]\phi^{II}_{,zzz} - \frac{2(1-\nu)}{r}\phi^{II}_{,r}\right.$$

$$\left. -2\frac{(1-\nu)(z+c)+z}{r}\phi^{II}_{,rz} + \frac{2\nu r^2 - z(z+c)}{r}\phi^{II}_{,rzz}\right]$$

$$+\frac{(1+\nu)\mu\varepsilon}{\pi(1-\nu)}\left[2\nu\phi^{II}_{,zz} - \frac{2(1-\nu)}{r}\phi^{II}_{,r} - \frac{z}{r}\phi^{II}_{,rz}\right],$$

$$\sigma'_{zz} = \frac{\mu\beta c}{2\pi(1-\nu)}\left[z\phi^{II}_{,zzzz}\right] + \frac{\mu\beta f}{2\pi(1-\nu)}z\left[4\phi^{II}_{,zzz} + (z+c)\phi^{II}_{,zzzz} + r\phi^{II}_{,rzzz}\right]$$

$$-\frac{(1+\nu)\mu\varepsilon}{\pi(1-\nu)}\left[z\phi^{II}_{,zzz}\right],$$

$$\sigma'_{rz} = \frac{\mu\beta c}{2\pi(1-\nu)}\left[\phi^{II}_{,rzz} + z\phi^{II}_{,rzzz}\right] - \frac{\mu\beta f}{2\pi(1-\nu)}\left[r\phi^{II}_{,zzz} + rz\phi^{II}_{,zzzz} - 2\phi^{II}_{,rz}\right.$$

$$\left. -(4z+c)\phi^{II}_{,rzz} - z(z+c)\phi^{II}_{,rzzz}\right] - \frac{(1+\nu)\mu\varepsilon}{\pi(1-\nu)}\left[\phi^{II}_{,rz} + z\phi^{II}_{,rzz}\right],$$

$$\sigma'_{r\theta} = \sigma'_{rz} = 0.$$

Again, with the aid of the relationships between the derivatives of the functions ψ and ϕ given by Eshelby (1962) , the stress outside the inclusion can be obtained by substitute Eq.(2) and Eq.(26) into Eq.(10). In Cartesian coordinates, the stresses are

$$\sigma_{11} = \frac{\mu\beta}{4\pi(1-\nu)}\left[\psi^{I}_{,1133} + 2\nu\phi^{I}_{,22} + 2z\psi^{II}_{,11333} + (3-4\nu)\psi^{II}_{,1133} - 4\nu\psi^{II}_{,3333}\right.$$

$$
\begin{aligned}
&- \frac{(1+\nu)\mu\varepsilon}{2\pi(1-\nu)}\left[\phi^{I}_{,22} + 2z\phi^{II}_{,223} + (3-4\nu)\phi^{II}_{,22} - 4\nu\phi^{II}_{,33}\right],\\
\sigma_{33} &= \frac{\mu\beta}{4\pi(1-\nu)}\left[\psi^{I}_{,3333} - 4\phi^{I}_{,33} + 2z\psi^{II}_{,33333} - \psi^{II}_{,3333} - 2z^2\phi^{II}_{,3333} - 8z\phi^{II}_{,333} + 4\phi^{II}_{,33}\right]\\
&- \frac{(1+\nu)\mu\varepsilon}{2\pi(1-\nu)}\left[\phi^{I}_{,33} - \phi^{II}_{,33} + 2z\phi^{II}_{,333}\right], \qquad (27)\\
\sigma_{12} &= \frac{\mu\beta}{4\pi(1-\nu)}\left[\psi^{I}_{,1233} - 2\nu\phi^{I}_{,12} + 2z\psi^{II}_{,12333} + (3-4\nu)\psi^{II}_{,1233}\right.\\
&\qquad \left. - 2z^2\phi^{II}_{,1233} - 4(2-\nu)z\phi^{II}_{,123} - 2(2-3\nu)\phi^{II}_{,12}\right]\\
&- \frac{(1+\nu)\mu\varepsilon}{2\pi(1-\nu)}\left[\phi^{I}_{,12} + 2z\phi^{II}_{,123} + (3-4\nu)\phi^{II}_{,12}\right],\\
\sigma_{23} &= \frac{\mu\beta}{4\pi(1-\nu)}\left[\psi^{I}_{,2333} - 2\phi^{I}_{,23} + 2z\psi^{II}_{,23333} + \psi^{II}_{,2333} - 2z^2\phi^{II}_{,2333} - 8z\phi^{II}_{,233} - 2\phi^{II}_{,23}\right]\\
&- \frac{(1+\nu)\mu\varepsilon}{2\pi(1-\nu)}\left[\phi^{I}_{,23} + 2z\phi^{II}_{,233} + \phi^{II}_{,23}\right],\\
\sigma_{31} &= \frac{\mu\beta}{4\pi(1-\nu)}\left[\psi^{I}_{,1333} - 2\phi^{I}_{,13} + 2z\psi^{II}_{,13333} + \psi^{II}_{,1333} - 2z^2\phi^{II}_{,1333} - 8z\phi^{II}_{,133} - 2\phi^{II}_{,13}\right]\\
&- \frac{(1+\nu)\mu\varepsilon}{2\pi(1-\nu)}\left[\phi^{I}_{,13} + 2z\phi^{II}_{,133} + \phi^{II}_{,13}\right],
\end{aligned}
$$

and the dilatational stress is

$$
\sigma = \frac{(1+\nu)\mu\beta}{2\pi(1-\nu)}\left[-\phi^{I}_{,33} + 7\phi^{II}_{,33} - 2\psi^{II}_{,3333} + 2z\phi^{II}_{,333}\right] + \frac{2(1+\nu)^2\mu\varepsilon}{\pi(1-\nu)}\phi^{II}_{,33}. \qquad (28)
$$

It can be easily shown that these stress components shown in Eq.(27) satisfy the equilibrium condition, Eq.(9). For points inside inclusion Ω_1, the elastic stress σ^{*}_{ij} is given by

$$
\sigma^{*}_{ij} = (\sigma^{I}_{ij} - \sigma^{**}_{ij}) + \sigma^{II}_{ij} + \sigma'_{ij}, \qquad (29)
$$

where the stress $(\sigma^{I}_{ij} - \sigma^{**}_{ij})$ is the uniform stress inside the inclusion Ω_1 when the medium is infinite and whose solution has been given by Mura'(1982, Eq.11.20).

For the elastic field in a half space caused by an ellipsoidal inclusion ($a_1 = a_2$) with uniform dilatational eigenstrain only , i.e. $\beta = 0$, Eq.(28) becomes

$$\sigma_{ij} = -\frac{(1+\nu)\mu\varepsilon}{2\pi(1-\nu)}\{\phi^{I}_{,ij} + \phi^{II}_{,ij} - 2(1-2\nu)(\delta_{i3}+\delta_{j3}-1)\phi^{II}_{,ij} - 4\nu\delta_{ij}\phi^{II}_{,33} + 2x_3\phi^{II}_{,ij3}\}. \quad (30)$$

Equation (30) is the same as Seo and Mura's result (1979) for the elastic field in a half space caused by an ellipsoidal inclusion with uniform dilatational eigenstrain. The Mindlin and Cheng's result (1950) for a sphere with a uniform dilatational thermal expansion can also obtained by Eq.(30).

For the elastic field in a half space caused by a penny shape inclusion ($a_1 = a_2 = a$ and $a_3 \rightarrow 0$) without shear and dilatation eigenstrains (penny shape prismatic inclusion), the eigenstrains are $e^{T}_{11} = e^{T}_{22} = 0$ and $e^{T}_{33} = \beta$. Eq.(26) becomes (in Cartesian coordinates)

$$\sigma'_{ij} = -\frac{\mu\beta c}{2\pi(1-\nu)}\{(1-2\nu)(\delta_{i3}+\delta_{j3}-1)\phi^{II}_{,ij3} - \phi^{II}_{,ij3} + 2\nu\delta_{ij}\phi^{II}_{,333} - x_3\phi^{II}_{,ij33}\}, \quad (31)$$

and the stress field for exterior point of Ω_1 is

$$\sigma_{ij} = \frac{\mu\beta}{4\pi(1-\nu)}\{(x_3-c)(\phi^{I}_{,ij3} - \phi^{II}_{,ij3}) - (1-2\nu)(\delta_{i3}+\delta_{j3}-1)(\phi^{I}_{,ij} - \phi^{II}_{,ij} + 2c\phi^{II}_{,ij3}) - 2\nu\delta_{ij}(\phi^{I}_{,33} - \phi^{II}_{,33} + 2c\phi^{II}_{,333}) + 2cx_3\phi^{II}_{,ij33}\}. \quad (32)$$

By using the relationship Eq.(7) and transformed into cylindrical coordinates, Eq.(32) gives the same results as obtained by Bastecka (1964) for a circular edge dislocation loop in the half space.

4. SUMMARY

The stress field in the half space ($z \geq 0$) caused by an ellipsoidal inclusion Ω_1 centered at (0,0,c) with eigenstrain $e^T_{ij} = \delta_{ij}(\varepsilon + \beta\delta_{i3})$ which in the absence of the surrounding half space would result in a uniform homogeneous strain, not accompanied by stress, is found by the superposition of the following three stress fields: (a) the stress field of the inclusion Ω_1 centered at (0,0,c) with eigenstrain e^T_{ij} in an infinite medium, (b) the stress field of the image inclusion Ω_2 centered at (0,0,-c) with eigenstrain $-e^T_{ij}$, and (c) the additional fictitious stress field that makes all stress fields satisfy the equilibrium and boundary conditions.

The stress field of the inclusion in an infinite medium obtained by Eshelby is compared with the stress field of a prismatic loop in an infinite medium as obtained by Kroupa. A relationship is found between the potential function ϕ of the inclusion and the integral function I_0^{-1}, which involves the product of Bessel functions J_m, for the solution of the prismatic loop.

The fictitious stress field is solved first for the two dimensional problem by using the Hankel transformation method and then it is transformed into the three dimensional case by use of the relationship between ϕ and I_0^{-1}.

The solution of the elastic field in the half space with ellipsoidal inclusions with uniform dilatational eigenstrains obtained by Seo and Mura (1979) has been rearranged into three terms corresponding to the stress field of the inclusion Ω_1 in an infinite medium centered at (0,0,c) with eigenstrain $\delta_{ij}\varepsilon$, the stress field of the image inclusion Ω_2 centered at (0,0,-c) with eigenstrain $-\delta_{ij}\varepsilon$, and the additional fictitious stress field. It has also been shown that Seo and Mura's results are a special case of the present solution.

REFERENCES

Aderogba, K., 1976, "On Eigenstresses in a Semi-Infinite Solid," Math. Proc. Camb. Phil. Soc., Vol. 80, pp. 555-562.

Bastecka, J., 1964, "Interaction of Dislocation Loop with Free Surface," Czechoslovak Journal of Physics, Vol. B14, pp. 430-442.

Eason, G., Noble, B., and Sneddon, J.N., 1955, "On Certain Integrals of Lipschitz Hankel Type Involving Products of Bessel Functions," Philosophical Transactions of the Royal Society of London , Vol. A247, pp. 529-551.

Eshelby, J.D., 1957, "The Determination of the Elastic Field of an Ellipsoidal Inclusion and Related Problems," Proceedings of the Royal Society of London, Vol. A241, pp. 376-396.

Eshelby, J.D., 1959, "The Elastic Field Outside an Ellipsoidal Inclusion," Proceedings of the Royal Society of London, Vol. A252, pp. 561-569.

Eshelby, J.D., 1961, "Elastic Inclusions and Inhomogeneities," in Progress in Solid Mechanics, eds., I.N. Sneddon and R. Hill, North-Holland, Amsterdam, Vol.2 pp.89-140.

Goodier, J.N., 1937, "On the Integration of the Thermo-Elastic Equations," Philosophical Magazine and Journal of Science, Vol. 23, pp. 1017-1032.

Kroupa, F., 1960, "Circular Edge Dislocation Loop," Czechoslovak Journal of Physics, Vol. B10, pp. 284-293.

Mindlin, R.D., and Cheng, D.H., 1950, "Thermoelastic Stress in the Semi-Infinite Solid," Journal of Applied Physics, Vol. 21, pp. 931-933.

Mindlin, R.D., 1953, "Force at a Point in the Interior of a Semi-Infinite Solid," Proceedings, 1st Midwestern Conference on Solid Mechanics, pp. 55-59.

Mura, T., 1982, Micromechanics of Defects in Solid, Martinus-Nijhoff, Hague.

Salamon, N.J. and Dundurs, J., 1971, "Elastic Fields of a Dislocation Loop in a Two-Phase Material," J. Elasticity, Vol. 1, pp. 153-164.

Seo, T., and Mura, T., 1979, "The Elastic Field in Half Space Due to Ellipsoidal Inclusions with Uniform Dilatational Eigenstrains," ASME Journal of Applied Mechanics, Vol. 46, pp. 568-572.

Sneddon, I.N., 1951, Fourier Transforms, McGraw Hill, New York.

FIGURE CAPTION

Fig. 1 - Ellipsoidal inclusion Ω_1 with principal half-axes a_1, a_2, a_3 in a half space and its image Ω_2.

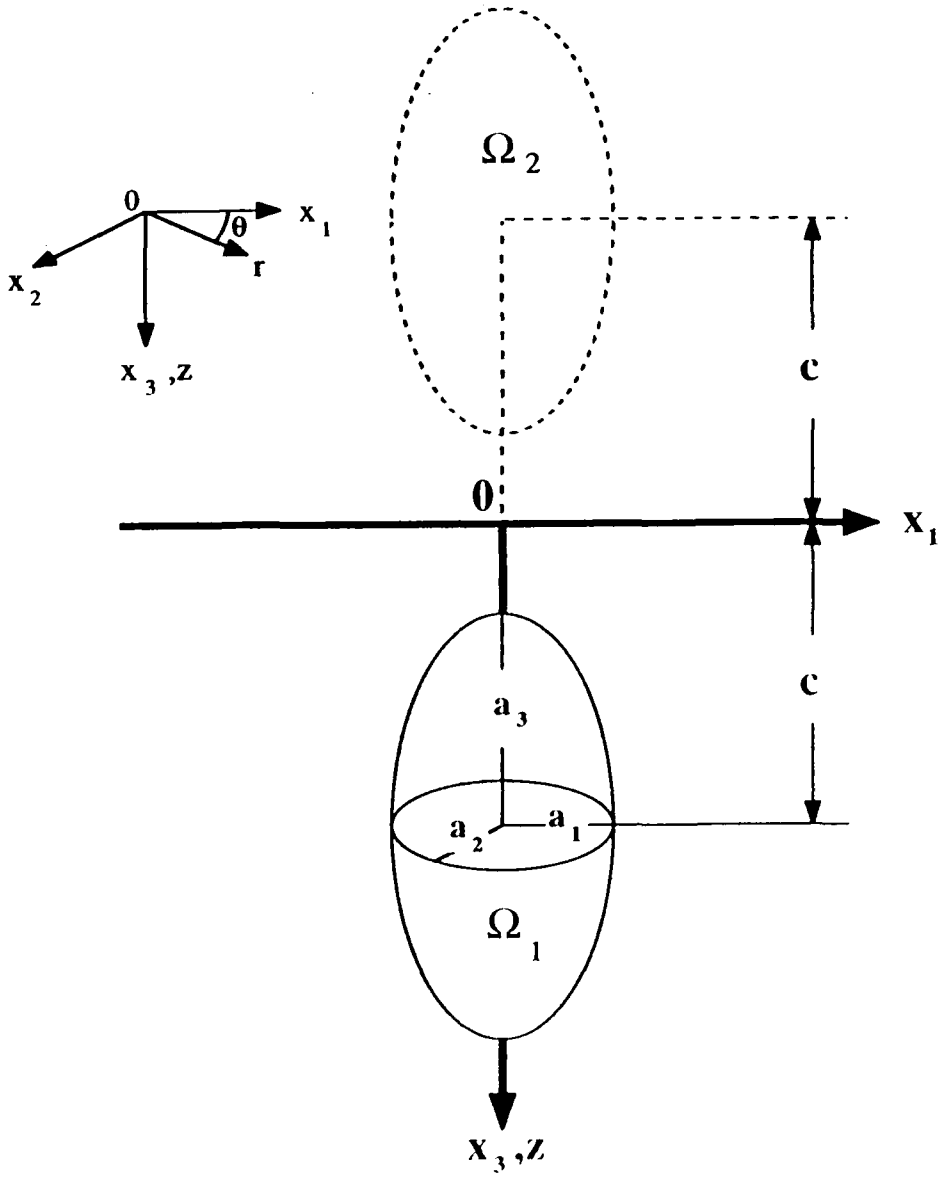


Fig. 1 - Ellipsoidal inclusion Ω_1 with principal half-axes a_1, a_2, a_3 in a half space and its image Ω_2.

Naval Research Laboratory
Washington, DC 20375-5000

NRL Report 9134

Three-Dimensional Stresses in a Half Space Caused by Penny-Shaped Inclusions

H. Y. Yu

Geo-Centers Inc.
Fort Washington, MD 20744

AND

S. C. Sanday

Composites and Ceramics Branch
Materials Science and Technology Division

August 19, 1988

Approved for public release, distribution unlimited

SECURITY CLASSIFICATION OF THIS PAGE

REPORT DOCUMENTATION PAGE

Form Approved
OMB No. 0704-0188

1a REPORT SECURITY CLASSIFICATION UNCLASSIFIED	1b RESTRICTIVE MARKINGS
2a SECURITY CLASSIFICATION AUTHORITY	3 DISTRIBUTION/AVAILABILITY OF REPORT Approved for public release; distribution unlimited
2b DECLASSIFICATION/DOWNGRADING SCHEDULE	
4 PERFORMING ORGANIZATION REPORT NUMBER(S) NRL Report 9134	5 MONITORING ORGANIZATION REPORT NUMBER(S)
6a NAME OF PERFORMING ORGANIZATION Naval Research Laboratory	6b OFFICE SYMBOL (If applicable) Code 6370
6c ADDRESS (City, State, and ZIP Code) Washington, DC 20375-5000	7b ADDRESS (City, State, and ZIP Code)
8a NAME OF FUNDING/SPONSORING ORGANIZATION Office of Naval Research	8b OFFICE SYMBOL (If applicable)
8c ADDRESS (City, State, and ZIP Code) Arlington, VA 22217	9 PROCUREMENT INSTRUMENT IDENTIFICATION NUMBER 10 SOURCE OF FUNDING NUMBERS PROGRAM ELEMENT NO: 61153N; PROJECT NO: RR0220441; TASK NO: ; WORK UNIT ACCESSION NO: DN280-063

11 TITLE (Include Security Classification)
Three-Dimensional Stresses in a Half Space Caused by Penny-Shaped Inclusions

12 PERSONAL AUTHOR(S)
Yu,* H.-Y. and Sanday, S.C.

13a TYPE OF REPORT	13b TIME COVERED	14 DATE OF REPORT (Year, Month, Day)	15 PAGE COUNT
Interim	FROM ___ TO ___	1988 August 19	18

16 SUPPLEMENTARY NOTATION
*Geo-Centers, Inc., Fort Washington, MD 20744

17 COSATI CODES			18 SUBJECT TERMS (Continue on reverse if necessary and identify by block number)		
FIELD	GROUP	SUB GROUP	Elastic solution	Orthotropic misfit	Half space
			Inclusion	Image stress	

19 ABSTRACT (Continue on reverse if necessary and identify by block number)

Elastic stress fields caused by isotropic penny-shaped inclusions and axisymmetric ellipsoidal inhomogeneties in a semi-infinite solid are investigated. The analytical solution for these problems is obtained by applying Hankel transformations and Eshelby's solution for ellipsoidal inclusions. This new approach can also be applied to other axisymmetric potential function-related problems in the half space.

20 DISTRIBUTION/AVAILABILITY OF ABSTRACT	21 ABSTRACT SECURITY CLASSIFICATION
[x] UNCLASSIFIED/UNLIMITED [ ] SAME AS RPT [ ] DTIC USERS	UNCLASSIFIED
22a NAME OF RESPONSIBLE INDIVIDUAL S. C. Sanday	22b TELEPHONE (Include Area Code) (202) 767-2264 / Code 6320

DD Form 1473, JUN 86 Previous editions are obsolete

S/N 0102-LF-014-6603

CONTENTS

INTRODUCTION 1

BASIC APPROACH 1

SOLUTION FOR σ'_{ij} 7

ELASTIC STRAIN ENERGY 11

THE ELLIPSOIDAL INHOMOGENEITY 11

SURFACE DISTORTION AND DILATATION FIELD 12

SUMMARY 12

REFERENCES 13

THREE-DIMENSIONAL STRESSES IN A HALF SPACE CAUSED BY PENNY-SHAPED INCLUSIONS

INTRODUCTION

Elastic fields caused by inclusions in infinite media have been extensivley investigated by several authors [1-5] after Eshelby's work [6-8]. Other research efforts have addressed the half-space problem with an inclusion located near the free surface [9-12]. In these studies, the following methods were used: Galerkin vector [9], Papkovich-Neuber displacement potential [10], image stress caused by two cuboidal inclusions with uniform eigenstrains [11], and Green's function in the half space [12]. Mura has recently reviewed these research efforts [13].

When the elastic moduli of an ellipsoidal subdomain of a material differs from those of the remainder (matrix), the subdomain is called an ellipsoidal inhomogeneity. Cracks, voids, and precipitates are examples of these inhomogeneities. A material containing inhomogeneities is assumed to be free from any stress field unless an external stress field σ_{ij}^{a} is applied. On the other hand, a material containing inclusions is subjected to an internal stress caused by the eigenstrain e_{ij}^{T} even if it is free from any external loads. The definition of eigenstrains has been given by Mura [13] and is the same as the stress-free-transformation strain described by Eshelby [6].

The solutions for ellipsoidal inhomogeneities can be reduced to the penny-shaped or elliptical crack case by setting the elastic constants λ and μ for the inhomogeneities equal to zero. The solution of the three-dimensional problems for these cracks has received considerable attention [14-19]. The stress field of a penny-shaped crack in the half space can be solved by obtaining the relevant system of integral equations for the problem formulated by Erdogan and Gupta [20] for the stress analysis of multilayered composites with a flaw.

In the present study, Eshelby's method for ellipsoidal inclusions [6-8] and Hankel's transformation method, used to obtain the elastic solutions of a circular dislocation loop in an unbounded media [21] and in the half space [22], are used for the analysis of the elastic solution of axisymmetric inclusions and axisymmetric-ellipsoidal inhomogeneities in the half space. The method provides a novel way for obtaining the image stresses of an ellipsoidal inclusion in the half space. It is used to find a more general solution of an ellipsoidal inclusion with anisotropic eigenstrain. Existing solutions are shown to be special cases of the present result. This method can also be used to obtain the stress field of a penny-shaped crack in the half space.

BASIC APPROACH

In this report, we consider an axisymmetric ellipsoidal inclusion Ω_1 in a half space (Fig. 1). In general, the inclusion Ω_1 is given by

$$\frac{x_1^2}{a_1^2} + \frac{x_2^2}{a_2^2} + \frac{x_3^2}{a_3^2} \leq 1 \qquad (1)$$

Manuscript approved March 10, 1988.

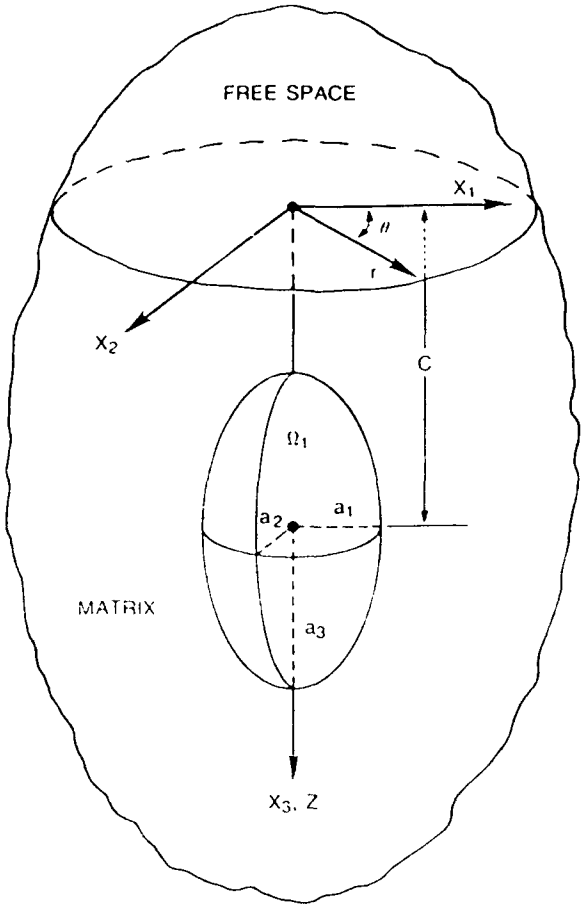


Fig. 1 — Ellipsoidal inclusion with principal half axis $a_1 = a_2$, a_3 in a half space

Symmetry with respect to the x_3-axis is then defined by $a_1 = a_2$, and the anisotropic eigenstrain of the inclusion

$$e_{ij}^T = \delta_{ij}(e + b\delta_{i3}) \qquad i,j = 1, 2, 3, \tag{2}$$

where δ_{ij} is Kronecker delta. (Note that the usual summation convention does not apply to any of the expressions in this report.) Equation (2) states that only normal eigenstrains appear, and $e_{11}^T = e_{22}^T = e$ and $e_{33}^T = e + b$.

For the inclusion Ω_1 defined by Eq. (1) with the uniform eigenstrain described by Eq. (2) with $a_3 = 0$, the stress field in the unbounded medium outside Ω_1 is obtained by using Eshelby's method [6-8]. The result is given by

$$\sigma_{ij} = \frac{\mu b}{4\pi(1-\nu)}\left[x_3\phi_{,ij3} - (1-2\nu)(\delta_{i3}\phi_{,j3} + \delta_{j3}\phi_{,i3}) - \phi_{,ij} - 2\nu\delta_{ij}\phi_{,33}\right]$$

$$- \frac{\mu(1+\nu)e}{2\pi(1-\nu)}\phi_{,ij}, \tag{3}$$

where the numerical suffixes, $i, j = 1, 2, 3$, following a comma denote differentiation with respect to the Cartesian coordinates x_1, x_2, x_3, e.g. $\phi_{,ij} = \partial^2\phi/\partial x_i \partial x_j$, and ϕ is the Newtonian potential function that is given by

$$\phi = \pi a_1^2 a_3 \int_{\lambda_0}^{\infty} \frac{U}{\Delta}\, ds , \tag{4}$$

where

$$U = 1 - \left[\frac{x_1^2 + x_2^2}{a_1^2 + s} + \frac{x_3^2}{a_3^2 + s} \right],$$

$$\Delta = (a_1^2 + s)(a_3^2 + s)^{1/2},$$

and λ_0 is the largest root of $U = 0$ outside of Ω_1 and $\lambda_0 = 0$ inside of Ω_1. For inclusions with uniform dilatation eigenstrain only ($b = 0$), Eq. (3) is valid for any a_3 value. The detailed expression of ϕ for both the oblate spheroid ($a_1 > a_3$) and the prolate spheroid ($a_1 < a_3$) are given by Yu [23]. Equation (3) can be transformed into cylindrical coordinates (r, θ, z) as follows:

$$\sigma_{rr} = -\frac{\mu b}{4\pi(1-\nu)} \left[\phi_{,zz} + z\phi_{,zzz} + \frac{1-2\nu}{r}\phi_{,r} + \frac{z}{r}\phi_{,rz} \right] + \frac{\mu(1+\nu)e}{2\pi(1-\nu)} \left(\frac{\phi_{,r}}{r} + \phi_{,zz} \right),$$

$$\sigma_{\theta\theta} = -\frac{\mu b}{4\pi(1-\nu)} \left[2\nu\phi_{,zz} - \frac{1-2\nu}{r}\phi_{,r} - \frac{z}{r}\phi_{,rz} \right] - \frac{\mu(1+\nu)e}{2\pi(1-\nu)} \frac{\phi_{,r}}{r},$$

$$\sigma_{zz} = -\frac{\mu b}{4\pi(1-\nu)} [\phi_{,zz} - z\phi_{,zzz}] - \frac{\mu(1+\nu)e}{2\pi(1-\nu)}\phi_{,zz}, \tag{5}$$

$$\sigma_{rz} = \frac{\mu b}{4\pi(1-\nu)} [z\phi_{,rzz}] - \frac{\mu(1+\nu)e}{2\pi(1-\nu)}\phi_{,rz},$$

$$\sigma_{r\theta} = \sigma_{z\theta} = 0.$$

Equations (5) are obtained with the aid of the following relationships:

$$\nabla^2\phi = 0,$$

$$x_1\phi_{,2} = x_2\phi_{,1},$$

and

$$\phi_{,r} = \frac{1}{r}(x_1\phi_{,1} + x_2\phi_{,2}), \tag{6}$$

where the letter suffixes following a comma denote differentiation with respect to the cylindrical coordinates r, θ, and z, e.g. $\phi_{,rz} = \partial^2\phi/\partial r\,\partial z$.

For a circular-edge dislocation loop with the z-axis as the axis of symmetry in an unbounded medium (Fig. 2), the stress field is found by Kroupa [21] by using Hankel transformations. For $z > 0$, Kroupa's solution can be rewritten as

$$\sigma_{rr} = -\frac{\mu b'}{2(1-\nu)}\, a\,[(I_0^{-1})_{,zz} + z(I_0^{-1})_{,zzz} + \frac{1-2\nu}{r}\,(I_0^{-1})_{,r} + \frac{z}{r}(I_0^{-1})_{,rz}],$$

$$\sigma_{\theta\theta} = -\frac{\mu b'}{2(1-\nu)}\, a\left[2\nu(I_0^{-1})_{,zz} - \frac{1-2\nu}{r}\,(I_0^{-1})_{,r} - \frac{z}{r}\,(I_0^{-1})_{,rz}\right],$$

$$\sigma_{zz} = -\frac{\mu b'}{2(1-\nu)}\, a\,[(I_0^{-1})_{,zz} - z(I_0^{-1})_{,zzz}], \tag{7}$$

$$\sigma_{rz} = \frac{\mu b'}{2(1-\nu)}\, a\,[z(I_0^{-1})_{,rzz}],$$

$$\sigma_{r\theta} = \sigma_{z\theta} = 0,$$

where

$$I_m^n = \int_0^\infty t^n J_m(rt/a)\, J_1(t) e^{-zt/a}\, dt,$$

$$I_m^n = -a(I_m^{n-1})_{,z},$$

$$= -ar^{m-1}(r^{-m+1} I_{m-1}^{n-1})_{,r} \qquad (m = 0, 1, 2\ldots;\ n = -1, 0, 1, 2\ldots),$$

and J_m is the Bessel functin of the mth order, a is the radius of the circular dislocation loop, and b' is the Burger's vector. Equation (7) is obtained by the method of Hankel transformation as used for cylindrically symmetric problems of the theory of elasticity in Sneddon's book [24] and subjected to the following boundary conditions:

$$u_z(r, 0) = \frac{1}{2}\, b' \quad \text{for } 0 \le r < a,$$

$$0 \quad \text{for } r > a, \tag{8}$$

$$\sigma_{rz}(r, 0) = 0 \quad \text{for } 0 \le r < \infty.$$

For the penny-shaped inclusion without shear and dilatation eigenstrains (penny-shaped prismatic inclusion), which is the axisymmetric inclusion when a_3 approaches zero, the equivalent eigenstrains

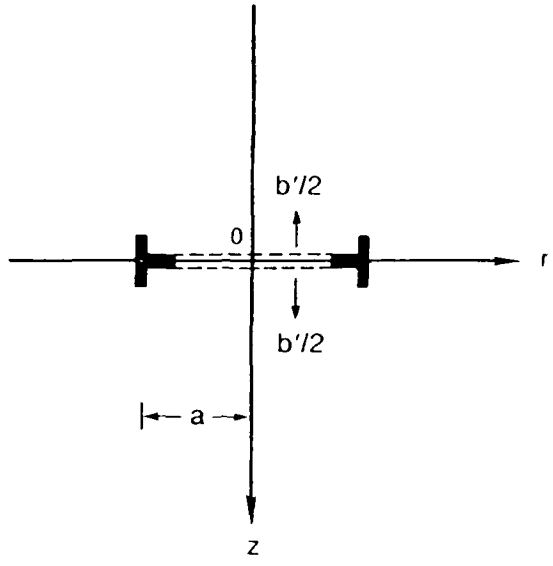


Fig. 2 - Circular edge dislocation loop in infinite solid

are $e_{11}^T = e_{22}^T = 0$, $e_{33}^T \neq 0$. If we reduce Eq. (5) for a penny-shaped prismatic inclusion, that is, $a_3 \to 0$ and $e = 0$, it is interesting to note the similarity between Eqs. (5) and (7). By putting

$$\phi = kI_0^{-1} \qquad (a_3 \to 0), \tag{9}$$

where $k = 2\pi b'a/b$, and $a_1 = a$, the elastic solutions of both the penny-shaped prismatic inclusion (Eq. 5) and the circular-edge dislocation loop (Eq. 7) are identical. This suggests that the method used to investigate the elastic solution of a circular-edge dislocation loop in the half space [22] can be applied to solve the elastic field caused by an axisymmetrical inclusion in the half space. This approach is resonable since the solution of the axisymmetrical inclusion can be obtained by the integration of the results of a penny-shaped prismatic inclusion and the fact that if the inclusion has the same elastic moduli as the matrix, the stress field is the same as that of a small dislocation loop when both the dislocation loop and the inclusion are infinitesimally small [8]. For example, a small inclusion of volume V and an eigenstrain e_{33}^T in the x_3 direction has the same stress field as that of a prismatic interstitial dislocation loop of area A and Burgers vector b_1 provided that $Ve_{33}^T = Ab_1$.

Consider the half space $x_3 = z > 0$ (Fig. 1), an axisymmetric inclusion with the center at the point (0, 0, c) in such a way that its axis of symmetry (z-axis) is perpendicular to the plane of the free surface $z = 0$. In order that the plane $z = 0$ be a free surface, no force must act on it, thus the stress components at $z = 0$ must satisfy the boundary conditions

$$(\sigma_{rz})_{z=0} = 0, \tag{10}$$

$$(\sigma_{zz})_{z=0} = 0,$$

and the equilibrium condition

$$\sum_{j=1}^{3} \sigma_{ij,j} = 0. \tag{11}$$

Similar to the work of Bastecka [22], the stress σ_{ij} outside the axisymmetric ellipsoidal inclusion centered at the point $(0, 0, c)$ but in the half space $z > 0$ is

$$\sigma_{ij} = \sigma_{ij}^{I} + \sigma_{ij}^{II} + \sigma_{ij}^{s}, \tag{12}$$

which will satisfy the required boundary conditions (Eq. 10) and the equilibrium condition (Eq. 11). This converges to zero for x_1 and x_2 approaching $\pm\infty$ and x_3 approaching ∞. In Eq. (12), the term σ_{ij}^{I} is the stress caused by the axisymmetric inclusion Ω_1 (and outside of it) centered at the point $(0, 0, c)$; σ_{ij}^{II} is the stress caused by the image inclusion Ω_2 centered at the point $(0, 0, -c)$ (Fig. 3) with eigenstrain

$$(e_{ij}^{T})^{II} = -(e_{ij}^{T})^{I} = -\delta_{ij}(e + b\delta_{i3}). \tag{13}$$

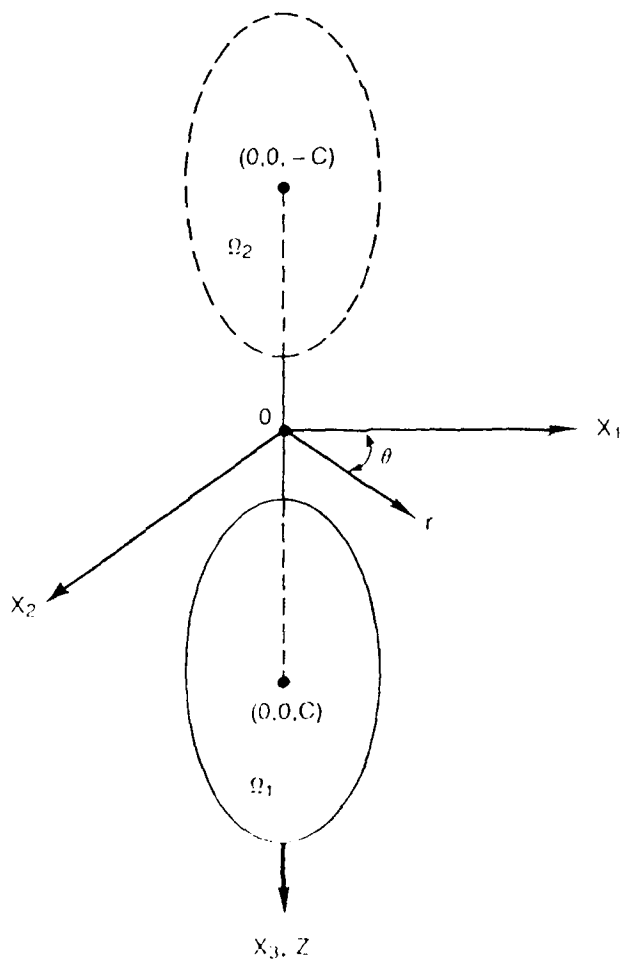


Fig. 3 — Semi-infinite solid containing an ellipsoidal inclusion Ω_1 and its image Ω_2

Equation 13 shows that σ'_{ij} is an additional stress that satisfies the boundary condition

$$(\sigma'_{zz})_{z=0} = -(\sigma^I_{zz} + \sigma^{II}_{zz})_{z=0} = 0; \tag{14a}$$

$$(\sigma'_{rz})_{z=0} = -(\sigma^I_{rz} + \sigma^{II}_{rz})_{z=0}. \tag{14b}$$

The solutions for the stresses σ^I_{ij} and σ^{II}_{ij} are obtained by translating the origin of coordinates in Eq. (3) and Eq. (5) to points (0, 0, c), and (0, 0, $-(c)$ respectively. The Newtonian potential function ϕ^I and ϕ^{II} for the solutions of σ^I_{ij} and σ^{II}_{ij} respectively are given by

$$\phi^I = \pi a_1^2 a_3 \int_{\lambda_1}^{\infty} \frac{U_1}{\Delta}\, ds\,,$$

$$\phi^{II} = \pi a_1^2 a_3 \int_{\lambda_2}^{\infty} \frac{U_2}{\Delta}\, ds\,, \tag{15}$$

where

$$U_1 = 1 - \left[\frac{x_1^2 + x_2^2}{a_1^2 + s} + \frac{(x_3 - c)^2}{a_3^2 + s}\right],$$

$$U_2 = 1 - \left[\frac{x_1^2 + x_2^2}{a_1^2 + s} + \frac{(x_3 + c)^2}{a_3^2 + s}\right],$$

$$\Delta = (a_1^2 + s)\,(a_3^2 + s)^{1/2},$$

and where

λ_1 is the largest root of $U_1 = 0$ for exterior points of Ω_1,

$\lambda_1 = 0$ for interior points of Ω_1, and

λ_2 is the largest root of $U_2 = 0$.

SOLUTION FOR σ'_{ij}

Substituting Eqs. (5) and (15) into Eq. (14) gives

$$(\sigma'_{zz})_{z=0} = 0; \tag{16a}$$

$$(\sigma'_{rz})_{z=0} = -\frac{\mu}{2\pi(1-\nu)}\left[cb\phi^{II}_{,rzz} - 2(1+\nu)e\phi^{II}_{,rz}\right]_{z=0}. \tag{16b}$$

where for $z = 0$, $\phi_{,rzz}^{I} = \phi_{,rzz}^{II}$ and $\phi_{,rz}^{I} = -\phi_{,rz}^{II}$. Now, in the limit when a_3 approaches zero, that is, for the penny-shaped inclusion ($a_1 = a_2 = a$), we can substitute Eq. (9) into Eq. (16b) to obtain

$$(\sigma_{rz}')_{z=0} = -\frac{\mu bc}{2\pi(1-\nu)} \frac{k}{a^3} \int_0^\infty t^2 J_1(\rho t) J_1(t) e^{-ct/a} dt$$

$$-\frac{\mu(1+\nu)e}{\pi(1-\nu)} \frac{k}{a^2} \int_0^\infty t J_1(\rho t) J_1(t) e^{-ct/a} dt , \tag{16c}$$

where $\rho = r/a$.

For the axisymmetric problem, by the appropriate expression of the elastic displacements as the derivatives of certain function $\psi(r,z)$ in cylindrical coordinates, the equilibrium and Beltrami equations are replaced by a single equation [24]

$$\nabla^4 \psi(r,z) = 0 , \tag{17}$$

whose general solution is carried out by the method of integral transformations. The function ψ is replaced by its Hankel transform of *zero*th order,

$$G(\zeta,z) = \int_0^\infty r\psi(r,z) J_0(\zeta r)\, dr , \tag{18}$$

and it can be shown that $G(\zeta,z)$ is generally given by the expression

$$G(\zeta,z) = (A + Bz)e^{-\zeta z} + (C + Dz)e^{\zeta z} , \tag{19}$$

where A, B, C and D are unknown functions of ζ, which are determined from the boundary conditions. The stress components are expressed by means of the function $G(\zeta,z)$.

In the present case, we consider the solution to converge to zero for z approaching ∞. Thus we set $C = D = 0$. To determine A and B from the first boundary condition (Eq. 16a), we obtain the following relationship

$$A = -\frac{\mu}{\lambda + \mu} \frac{B}{\zeta} , \tag{20}$$

where $\lambda = 2\mu\nu/(1-2\nu)$ is Lame's constant. From the second boundary condition (Eq. 16b), as modified in Eq. (16c), we have

$$(\sigma_{rz}')_{z=0} = f(r)$$

$$\int_0^\infty \zeta F(\zeta) J_1(\zeta r)\, d\zeta , \tag{21}$$

where

$$F(\zeta) = -2(\lambda + \mu)\zeta^2 B(\zeta) , \tag{22}$$

and

$$f(r) = -\frac{\mu bc}{2\pi(1-\nu)}\frac{k}{a^3}\int_0^\infty t^2 J_1(\rho t)J_1(t)e^{-ct/a}dt$$

$$-\frac{\mu(1+\nu)e}{\pi(1-\nu)}\frac{k}{a^2}\int_0^\infty tJ_1(\rho t)J_1(t)e^{-ct/a}dt. \tag{23}$$

By letting $t = a\zeta$, Eqs. (21) and (23) give

$$F(\zeta) = -\frac{k\mu}{2\pi(1-\nu)}[cb\zeta + 2(1+\nu)e]J_1(a\zeta)e^{-c\zeta}. \tag{24}$$

By substituting Eqs. (24), (22), and (20) into Eq. (19), the function $G(\zeta,z)$ is found that can then be substituted in the expressions for the stress σ'_{ij} [24, §51]. After substituting the relationship again,

$$\phi^{II} = k(I_0^{-1})^{II} = k\int_0^\infty t^{-1}J_0(\rho t)J_1(t)e^{-t(z+c)/a}dt, \tag{25}$$

these stresses σ'_{ij} are as follows.

$$\sigma'_{rr} = -\frac{\mu bc}{2\pi(1-\nu)}\left[2\phi_{,zzz}^{II} + z\phi_{,zzzz}^{II} + \frac{2(1-\nu)}{r}\phi_{,rz}^{II} + \frac{z}{r}\phi_{,rzz}^{II}\right]$$

$$+\frac{\mu(1+\nu)e}{\pi(1-\nu)}\left[2\phi_{,zz}^{II} + z\phi_{,zzz}^{II} + \frac{2(1-\nu)}{r}\phi_{,r}^{II} + \frac{z}{r}\phi_{,rz}^{II}\right],$$

$$\sigma'_{\theta\theta} = -\frac{\mu bc}{2\pi(1-\nu)}\left[2\nu\phi_{,zzz}^{II} - \frac{2(1-\nu)}{r}\phi_{,rz}^{II} - \frac{z}{r}\phi_{,rzz}^{II}\right]$$

$$+\frac{\mu(1+\nu)e}{\pi(1-\nu)}\left[2\nu\phi_{,zz}^{II} - \frac{2(1-\nu)}{r}\phi_{,r}^{II} - \frac{z}{r}\phi_{,rz}^{II}\right], \tag{26}$$

$$\sigma'_{zz} = \frac{\mu bc}{2\pi(1-\nu)}\left[z\phi_{,zzzz}^{II}\right] - \frac{\mu(1+\nu)e}{\pi(1-\nu)}\left[z\phi_{,zzz}^{II}\right],$$

$$\sigma'_{rz} = \frac{\mu bc}{2\pi(1-\nu)}\left[\phi_{,rzz}^{II} + z\phi_{,rzzz}^{II}\right] - \frac{\mu(1+\nu)e}{\pi(1-\nu)}\left[\phi_{,rz}^{II} + z\phi_{,rzz}^{II}\right],$$

$$\sigma'_{r\theta} = \sigma'_{\theta z} = 0.$$

When $c = 0$ and $\phi'' = k(I_0^{-1})''$, Eq. (26) reduces to the same results obtained by Bastecka [2] for a circular-edge dislocation loop in the half space. In Cartesian coordinates, Eq. (26) becomes

$$\sigma'_{ij} = -\frac{\mu bc}{2\pi(1-\nu)}\left[(1-2\nu)(\delta_{3i}+\delta_{3j}-1)\phi^{II}_{,ij3} - \phi^{II}_{,ij3} + 2\nu\delta_{ij}\phi^{II}_{,333} - x_3\phi^{II}_{,ij33}\right] + \frac{\mu(1+\nu)e}{\pi(1-\nu)}\left[(1-2\nu)(\delta_{3i}+\delta_{3j}-1)\phi^{II}_{,ij} - \phi^{II}_{,ij} + 2\nu\delta_{ij}\phi^{II}_{,33} - x_3\phi^{II}_{,ij3}\right]. \tag{27}$$

It can be shown that σ'_{ij} satisfies the equation of equilibrium, that is,

$$\sum_{j=1}^{3}\sigma'_{ij,j} = 0. \tag{28}$$

Therefore, for points outside Ω_1, the stress field caused by the presence of a penny-shaped inclusion in the half space can be obtained by Eqs. (3), (12), and (27). Thus,

$$\sigma_{ij} = \frac{\mu b}{4\pi(1-\nu)}[(x_3-c)(\phi^{I}_{,ij3}-\phi^{II}_{,ij3}) - (1-2\nu)(\delta_{3i}+\delta_{3j}-1)(\phi^{I}_{,ij}-\phi^{II}_{,ij}+2c\phi^{II}_{,ij3}) - 2\nu\delta_{ij}(\phi^{I}_{,33}-\phi^{II}_{,33}+2c\phi^{II}_{,333}) + 2cx_3\phi^{II}_{,ij33}] - \frac{\mu(1+\nu)e}{2\pi(1-\nu)}[\phi^{I}_{,ij}+\phi^{II}_{,ij} - 2(1-2\nu)(\delta_{3i}+\delta_{3j}-1)\phi^{II}_{,ij} - 4\nu\delta_{ij}\phi^{II}_{,33} + 2x_3\phi^{II}_{,ij3}]. \tag{29}$$

For points inside Ω_1, the elastic stress σ^*_{ij} is given by

$$\sigma^*_{ij} = \sigma_{ij} - \sigma^{**}_{ij} = (\sigma^{I}_{ij} - \sigma^{**}_{ij}) + \sigma^{II}_{ij} + \sigma'_{ij} \tag{30}$$

where $-\sigma^{**}_{ij}$ is the uniform stress that exists in the inclusion caused by the uniform eigenstrain e^{I}_{ij} (Eq. 2). The stress $(\sigma^{I}_{ij} - \sigma^{**}_{ij})$ is the uniform stress inside the inclusion Ω_1 when the medium is infinite. The solution is expressed explicitly by Mura ([13], Eq. 11.20). Equations (5), (12), and (26) give the stress field in cylindrical coordinates.

Seo and Mura's results [12] for the elastic field in a half space caused by an ellipsoidal inclusion with uniform dilatational eigenstrain (obtained by using Mindlin's solution [25] for Green's function in the half space) can be obtained as a special case by taking $b = 0$ (and $a_1 = a_2$) in Eqs. (29) and (30). Mindlin and Cheng's results [9] for a sphere can also be obtained as a special case by taking $a_1 = a_2 = a_3$ and $b = 0$ in Eq. (29).

ELASTIC STRAIN ENERGY

The elastic strain energy can be expressed as

$$W = -\frac{1}{2}\int_{\Omega_1}\sigma_{ij}^{*}\, e_{ij}^{T}\, d\bar{V},$$

$$= -\frac{1}{2}\int_{\Omega_1}\sum_{i=1}^{3}\sigma_{ii}^{*}\, e d\bar{V} - \frac{1}{2}\int_{\Omega_1}\sigma_{33}^{*}\, b d\bar{V}, \tag{31}$$

where $\sum_{i=1}^{3}\sigma_{ii}^{*}$ is the dilation stress field in the inclusion. It is given by

$$\sum_{i=1}^{3}\sigma_{ii}^{*} = -\frac{2\mu(1+\nu)e}{(1-\nu)}\left[2 - \frac{1}{\pi}(1+\nu)\phi_{,33}^{II}\right]$$

$$-\frac{2\mu(1+\nu)b}{(1-\nu)}\left[1 + \frac{1}{4\pi}(\phi_{,33}^{I} - \phi_{,33}^{II} + 2c\phi_{,333}^{II})\right]. \tag{32}$$

when $b = 0$, the strain energy obtained is the same as that obtained by Seo and Mura [12].

THE ELLIPSOIDAL INHOMOGENEITY

When an inhomogeneity contains an eigenstrain, it is called an inhomogeneity inclusion. Eshelby [6] first pointed out that the stress-field changes caused by an inhomogeneity when the remotely applied stress is σ_{ij}^{a} can be simulated by the eigenstress caused by an inclusion, if the eigenstrain e_{ij}^{T} is properly chosen. This eigenstrain is sometimes referred to as the equivalent eigenstrain, or the equivalent stress-free transformation strain. For a given uniformly applied stress σ_{ij}^{a} and a uniform eigenstrain $e_{ij}^{T^*}$, the normal components of the equivalent eigenstrains e_{ij}^{T} are given by [23]

$$(\lambda - \lambda^*)e^c + \lambda e^T + 2\mu e_{ij}^T + 2(\mu^* - \mu)\sum_{kl=11}^{33} S_{ijkl}\, e_{kl}^T$$

$$= \lambda^* e^{T^*} + (\lambda - \lambda^*)e^a + 2\mu^* e_{ij}^{T^*} + 2(\mu - \mu^*)e_{ij}^a, \tag{33}$$

where $ij = 11, 22, 33$ and kl denotes summation over 11, 22, 33 only; e^T, e^{T^*} and e^a are the sum of three normal components of strains e_{ij}^T, $e_{ij}^{T^*}$, and e_{ij}^a respectively;

$$e^c = \frac{1-2\nu}{4\pi(1-\nu)}(I_1 e_{11}^T + I_2 e_{22}^T + I_3 e_{33}^T) + \frac{\nu}{1-\nu}e^T. \tag{34}$$

In this equation, μ, λ are the elastic constants of the matrix; μ^*, λ^* are the elastic constants of the inhomogeneity; and I_1, I_2, I_3, and S_{ijkl} are constants whose values depend on the shape of the inclusion as given by Eshelby [6-8]. Some detailed expressions for these constants for the inclusions of special shapes are given by Mura [13]. Therefore, by solving the set of three simultaneous equations in Eq. (33), the equivalent eigenstrains e_{11}^T, e_{22}^T, and e_{33}^T are obtained once the uniform eigenstrain e_{ij}^T and uniformly applied stress σ_{ij}^a are given. If both e_{ij}^T and σ_{ij}^a are axisymmetric for an axisymmetrical inclusion, the resultant equivalent eigenstrain e_{ij}^T is also axisymmetric and can be represented in the form of Eq. (2). Then the results of Eqs. (3), (5), (12), (26), (27), (29), and (30) can be applied accordingly to solve the stress field and strain energy of an axisymmetrical inhomogeneous inclusion in the half space.

SURFACE DISTORTION AND DILATATION FIELD

The roughness of solid surfaces is a second-order effect, but it has profound practical consequences in many fields of engineering and pure science. In many practical situations, the presence of inclusions or inhomogeneities under an external load will change the surface profile. The displacement of the free surface ($z = 0$) solved by the present method is:

$$u_r = \frac{bc}{\pi}(\phi_{,rz}^{II})_{z=0} - \frac{(1+\nu)c}{\pi}(\phi_{,r}^{II})_{z=0},$$

$$u_z = \frac{b}{2\pi}[(\phi_{,z}^{II})_{z=0} - c(\phi_{,zz}^{II})_{z=0}] + \frac{c}{\pi}(\phi_{,z}^{II})_{z=0}. \tag{35}$$

The presence of inclusions or inhomogeneities under an external load will also produce a dilatational field. The dilatational field in the matrix obtained in the present study is:

$$\frac{\Delta V}{V} = -\frac{(1-2\nu)b}{4\pi(1-\nu)}[\phi_{,zz}^{I} - \phi_{,zz}^{II} + 2c\phi_{,zzz}^{II}]$$

$$+ \frac{(1-2\nu)(1+\nu)e}{\pi(1-\nu)}\phi_{,zz}^{II}. \tag{36}$$

The important relationships between the dilatation field and the equilibrium-concentration distribution for dilute solutions in stressed solid are given by Li [26].

SUMMARY

The stress field in the half space ($z \geq 0$) caused by a penny-shaped inclusion Ω_1 centered at $(0, 0, c)$ with eigenstrain $e_{ij}^T = \delta_{ij}(e + b\delta_{i3})$ is found by the superposition of the following three stress fields: (a) the stress field of the inclusion Ω_1 centered at (0,0,c) with eigenstrain e_{ij}^T in an infinite medium; (b) the stress field of the image inclusion Ω_2 centered at $(0, 0, -c)$ with eigenstrain $-e_{ij}^T$; and (c) the additional fictitious stress field that makes all stress fields satisfy the equilibrium and boundary conditions.

The stress field of the penny-shaped prismatic inclusion in an infinite medium obtained by Eshelby is compared with the stress field of a prismatic loop in an infinite medium as obtained by Kroupa [21]. A relationship is found between the potential function ϕ of the inclusion and the integral function I_0^{-1}, which involves the product of the Bessel functions J_m for the solution of the prismatic loop.

The fictitious stress field is solved first for the two-dimensional problem by using the Hankel transformation method and then it is transformed into the three-dimensional case by use of the relationship between ϕ and I_0^{-1}.

The solution of the elastic field in the half space with ellipsodial inclusions with uniform dilatational eigenstrains obtained by Seo and Mura (1979) has been rearranged into three terms corresponding to the sress field of the inclusion Ω_1 in an infinite medium centered at (0,0,-c) with eigenstrain $\delta_{ij}e$, the stress field of the image inclusion Ω_2 centerd at (0,0,-c) with eigenstrain $-\delta_{ij}e$, and the additional fictitious stress field. It has also been shown that when $a_1 = a_2$, Seo and Mura's results are a special case of the present solution.

REFERENCES

1. L.J. Walpole, "The Elastic Field of an Inclusion in an Anisotropic Medium," *Proc. R. Soc. London* **A300**, 270-289 (1967).

2. N. Kinoshita and T. Mura, "Elastic Fields of Inclusions in Anisotropic Media," *Phys. Status Solidi* **A5**, 759-768 (1971).

3. R.J. Asaro and D.M. Barnett, "The Nonuniform Transformation Strain Problem for an Anisotropic Ellipsoidal Inclusion," *J. Mech. Phys. Solids* **23**, 77-83 (1975).

4. T. Mura and D.C. Cheng, "The Elastic Field Outside an Ellipsoidal Inclusion," *J. Appl. Mech.* **44**, 591-594 (1977).

5. Y.P. Chiu, "On the Stress Field Due to Initial Strains in Cuboid Surrounded by an Infinite Elastic Space," *J. Appl. Mech.* **44**, 587-590 (1977).

6. J.D. Eshelby, "The Determination of the Elastic Field of an Ellipsoidal Inclusion and Related Problems," *Proc. R. Soc. London* **A241**, 376-396 (1957).

7. J.D. Eshelby, "The Elastic Field Outside an Ellipsoidal Inclusion," *Proc. R. Soc. London* **A252**, 561-569 (1959).

8. J.D. Eshelby, "Elastic Inclusion and Inhomogeneities," in *Prog. Solid Mech. 2*, I.N. Sneddon and R. Hill, eds. (North-Holland, Amsterdam, 1961), pp. 89-140.

9. R.D. Mindlin and D.H. Cheng, "Thermoelastic Stress in the Semi-Infinite Solid," *J. Appl Phys.* **21**, 931-933 (1950).

10. D.L. Guell and J. Dundurs, "Further Results on Center of Dilatation and Residual Stresses in Joined Elastic Half-Space," *Dev. Theor. Appl. Mech.* **3**, 105-115 (1967).

11. Y.P. Chiu, "On the Stress Field and Surface Deformation in a Half Space with a Cuboidal Zone in Which Initial Strains Are Uniform," *J. Appl. Mech.* **45**, 302-306 (1978).

12. K. Seo and T. Mura, "The Elastic Field in a Half-Space Due to Ellipsoidal Inclusions with Uniform Dilatational Eigenstrains," *J. Appl. Mech.* **46**, 568-572 (1979).

13. T. Mura, *Micromechanics of Defects in Solids* (Martinus-Nijhoff, The Hague, 1982).

14. I.N. Sneddon and M. Lowengrub, *Crack Problems in the Classical Theory of Elasticity* (Wiley, New York, 1969).

15. M.K. Kassir and G.C. Sih, *Three-Dimensional Crack Problems: A New Selection of Crack Solutions in Three-Dimensional Elasticity* (Mechanics of Fracture, Vol. 2, Noordhoff, 1975).

16. M.K. Kassir and G.C. Sih, "Three-Dimensional Stress Distribution Around an Elliptical Crack Under Arbitrary Loading," *J. Appl. Mech.* 33, 601-611 (1966).

17. J.R. Willis, "The Stress Field Around an Elliptical Crack in an Anisotropic Medium," *Int. J. Eng. Sci.* 6, 253-263 (1968).

18. L.M. Keer and T. Mura, "Stationary Crack and Continuous Distribution of Dislocations," Proc. 1st Intl. Conf. Fracture I, 1966, pps. 99-115.

19. H. Sekine and T. Mura, "The Elastic Field Around an Elliptical Crack in an Anisotropic Medium Under an Applied Stress of Polynomial Forms," *Int. J. Eng. Sci.* **17**, 641-649 (1979).

20. F. Erdogan and G. Gupta, "The Stress Analysis of Multi-Layered Composites with a Flaw," *Int. J. Solids Struc.* 7, 39-61 (1971).

21. F. Kroupa, "Circular Edge Dislocation Loop," *Czech. J. Phys.* **B10**, 284-293 (1960).

22. J. Bastecka, "Interaction of Dislocation Loop with Free Surface," *Czech. J. Phys.* **B14**, 430-442 (1964).

23. H.-Y. Yu, "Some Interactions Between Microstructure Defects," Ph.D. Dissertation, University of Rochester, 1977.

24. I.N. Sneddon, *Fourier Transforms* (McGraw Hill, New York, 1951).

25. R.D. Mindlin, "Force at a Point in the Interior of a Semi-Infinite Solid," Midwestern Conf. Solid Mech., 1953, pp. 56-59.

26. J.C.M. Li, "Physical Chemistry of Some Microstructural Phenomena," *Met. Trans.* **94**, 1353-1380 (1978).

Naval Research Laboratory
Washington, DC 20375-5000

NRL Report 9168

Film Elastic Properties Determined by the Indentation Test—Theoretical Considerations

H. Y. YU

Geo-Centers Inc.
Fort Washington, MD 20744

S. C. SANDAY

Composites and Ceramics Branch
Materials Science and Technology Division

and

B. B. RATH

Materials Science and Component
Technology Directorate

January 12, 1989

Approved for public release, distribution unlimited

SECURITY CLASSIFICATION OF THIS PAGE

REPORT DOCUMENTATION PAGE

Form Approved OMB No. 0704-0188

1a REPORT SECURITY CLASSIFICATION: UNCLASSIFIED	1b RESTRICTIVE MARKINGS
2a SECURITY CLASSIFICATION AUTHORITY	3 DISTRIBUTION/AVAILABILITY OF REPORT: Approved for public release; distribution unlimited
2b DECLASSIFICATION/DOWNGRADING SCHEDULE	
4 PERFORMING ORGANIZATION REPORT NUMBER(S): NRL Report 9168	5 MONITORING ORGANIZATION REPORT NUMBER(S)
6a NAME OF PERFORMING ORGANIZATION: Naval Research Laboratory; 6b OFFICE SYMBOL (If applicable): Code 6370	7a NAME OF MONITORING ORGANIZATION
6c ADDRESS (City, State, and ZIP Code): Washington, DC 20375-5000	7b ADDRESS (City, State, and ZIP Code)
8a NAME OF FUNDING/SPONSORING ORGANIZATION: Office of Naval Research; 8b OFFICE SYMBOL (If applicable)	9 PROCUREMENT INSTRUMENT IDENTIFICATION NUMBER
8c ADDRESS (City, State, and ZIP Code): Arlington, VA 22217	10 SOURCE OF FUNDING NUMBERS: PROGRAM ELEMENT NO 61153N; PROJECT NO RR0220441; TASK NO; WORK UNIT ACCESSION NO DN280 063

11 TITLE (Include Security Classification)

Film Elastic Properties Determined by the Indentation Test—Theoretical Considerations

12 PERSONAL AUTHOR(S)

Yu, H. Y., Sanday, S. C., and Rath, B. B.

13a TYPE OF REPORT	13b TIME COVERED	14 DATE OF REPORT (Year, Month, Day)	15 PAGE COUNT
Interim	FROM _____ TO _____	1989 January 12	34

16 SUPPLEMENTARY NOTATION

17 COSATI CODES			18 SUBJECT TERMS (Continue on reverse if necessary and identify by block number)
FIELD	GROUP	SUB GROUP	Indentation; Layered material; Elastic solution; Elastic constants

19 ABSTRACT (Continue on reverse if necessary and identify by block number)

The elastic solutions of axisymmetric mixed boundary value problems are considered. An elastic layer is assumed to be either in smooth contact or perfectly bonded to a semi-infinite elastic half-space. The elastic field caused by the indentation of the elastic layer by a rigid indenter is solved for spherical, conical, and flat-ended-cylindrical indenters. The results are obtained by solving a Fredholm integral equation of the second kind with a continuous symmetrical kernel that depends on the bonding conditions. Numerical results are given for several combinations of film and substrate elastic moduli and film thicknesses. These results provide a guideline for selecting appropriate film thickness and substrates to determine the elastic constants of thin films.

20 DISTRIBUTION/AVAILABILITY OF ABSTRACT	21 ABSTRACT SECURITY CLASSIFICATION
[X] UNCLASSIFIED/UNLIMITED [ ] SAME AS RPT [ ] DTIC USERS	UNCLASSIFIED
22a NAME OF RESPONSIBLE INDIVIDUAL: S. C. Sanday	22b TELEPHONE (Include Area Code): (202) 767-2264; 22c OFFICE SYMBOL: Code 6370

DD Form 1473, JUN 86 *Previous editions are obsolete* SECURITY CLASSIFICATION OF THIS PAGE

CONTENTS

INTRODUCTION 1

FORMULATION OF THE PROBLEM 2

NUMERICAL RESULTS 10

SUMMARY 22

REFERENCES 22

APPENDIX A — Determination of the Function $g(\lambda)$ 24

APPENDIX B — Comparison of Numerical Results 27

FILM ELASTIC PROPERTIES DETERMINED BY THE INDENTATION TEST—THEORETICAL CONSIDERATIONS

INTRODUCTION

Intense interest in thin-film technology has been spurred by the growing importance of microelectronics, metal matrix composites, ceramic matrix composites, high transition temperature superconducting films, and compositionally modulated materials. Correspondingly, the determination of film properties has become of greater importance. The need for techniques to study the mechanical properties of thin films, which are usually defined as coatings of thickness of up to a few micrometers, has recently rekindled an interest in microhardness and submicroindentation devices. The continuous indentation test, also known as the impression test, measures the elastic constants of bulk materials [1-3]. In these tests, the displacement and the load of the indenter, which is pressed onto a specimen at a predetermined speed, is recorded. The slope of the unloading curves in the load vs depth plot determines the elastic modulus of the specimen. Recently, a high-resolution nanoindenter was used to determine the Young's modulus of thin films [4] from the linear unloading portion of the indentation load vs depth curves. It was also shown that, as the indentation depth d approaches the dimension of the film thickness h, the influence of the substrate can be detected because of the changing contributions of the film and the substrate to the measured elastic constant. For small indentation depth relative to the film thickness, the data approach that expected for bulk film material since the indenter interrogates the film near its surface only. For deep indentations, the data approach that expected for bulk substrate material.

The indentation problem is a mixed boundary value problem, more commonly known as Boussinesq's problem. Harding and Sneddon [5], Sneddon [6], and Miki [7] have considered this problem when a semi-infinite space is indented by a cone, a sphere, and a flat-ended cylindrical punch. The flat-ended cylindrical punch problem for an elastic layer resting frictionlessly on a rigid foundation has been considered by Lebedev and Ufliand [8]. The rigid substrate supporting the elastic layer is, of course, a mathematical artifice that simplifies the analysis. Some investigators considered the indentation of an elastic layer perfectly bonded to an elastic half-space made up of different materials. Wu and Chiu [9] considered the plane strain problem and reduced the mixed boundary value problem to a single Fredholm integral equation of the second kind. Dhaliwal [10] was able to reduce the axisymmetric problem of a flat-ended cylindrical punch on a layered elastic medium to a Fredholm integral equation, which he solved approximately to estimate the safety of foundations supporting cylindrical columns. Subsequently Dhaliwal and Rau [11] extended the analysis of Dhaliwal to punches of arbitrary profile but did not present any numerical results.

A second approach to the solution of mixed boundary value problems is to replace the exact boundary condition by an approximate one and solve the new elasticity problem. Chen and Engel [12] used this approach to study the impact and contact stresses caused by flat-ended cylindrical and parabolic punches on a composite medium consisting of one or two elastic layers perfectly bonded to each other and to an elastic homogeneous half-space.

Manuscript approved August 16, 1988

The punch problem (for any shape punch) for an elastic layer resting frictionlessly on an elastic substrate (half-space) has not been considered. The punch problems for conical or spherical punches for a layer perfectly bonded to an elastic substrate have not been considered either. The need for the solution of these problems for determining the elastic properties of thin films by the indentation test is obvious. The contact between the thin film and the substrate is neither frictionless nor perfectly bonded. The solutions and numerical values for both ideal cases should be obtained to set guidelines for the indentation test, i.e., to determine what the proper substrate is and what the required film thickness is so that the film's elastic constants may be measured within a predetermined degree of accuracy. These are goals of this investigation.

FORMULATION OF THE PROBLEM

Consider an infinite layer of thickness h with elastic constants μ_1, ν_1, overlaying a half-space substrate with elastic constants μ_2, ν_2, and a rigid axisymmetric indenter (punch) with a flat, conical, or hemispherical end (Figs. 1 to 3, respectively) and axis normal to the layer surface, pressing frictionlessly on the layer. Choose cylindrical coordinate axes (r, θ, z) such that z is parallel to the generatrix of the indenter, r is perpendicular to z, θ is the angular distance between a reference line and r, and the origin of coordinates is located at the first point of contact between the indenter and the layer (center of first contact area for the flat-ended indenter).

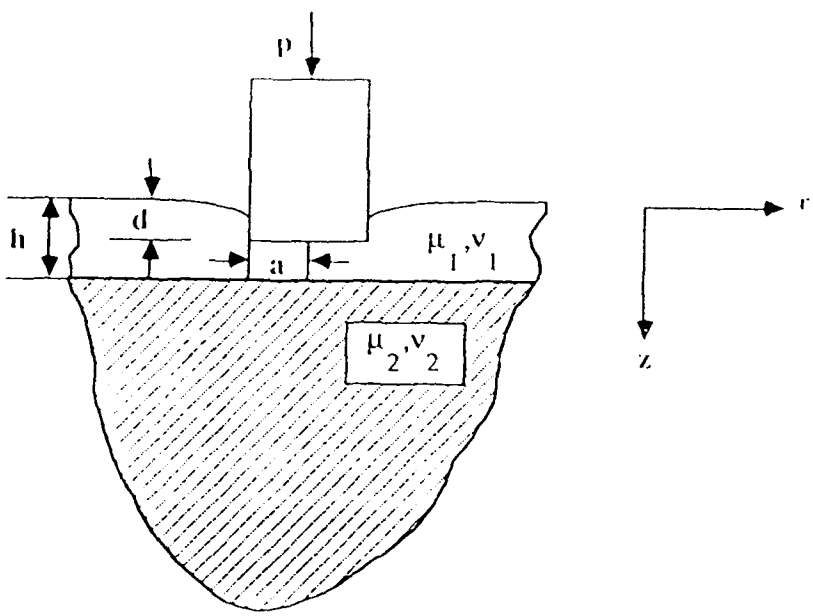


Fig. 1 — A composite medium consisting of an elastic layer either perfectly bonded to or smoothly overlaying an elastic semi-infinite substrate indented by a rigid flat-ended cylindrical indenter

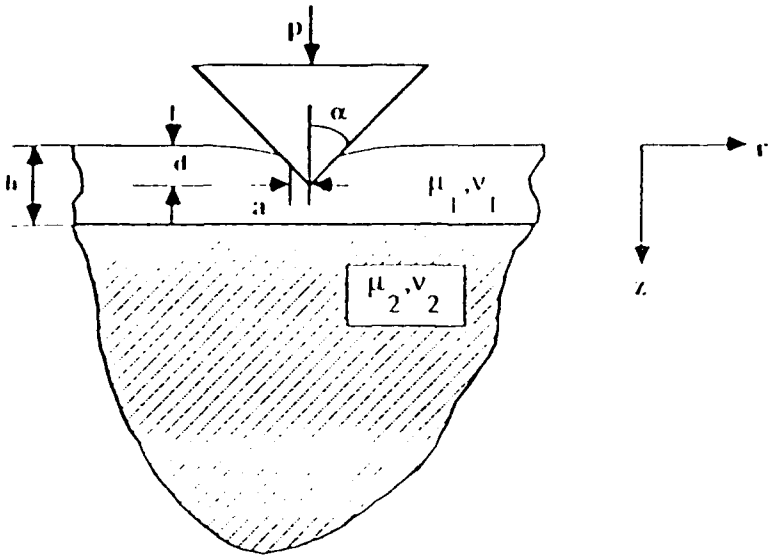


Fig. 2 — A composite medium consisting of an elastic layer either perfectly bonded to or smoothly overlaying an elastic semi-infinite substrate indented by a rigid conical indenter

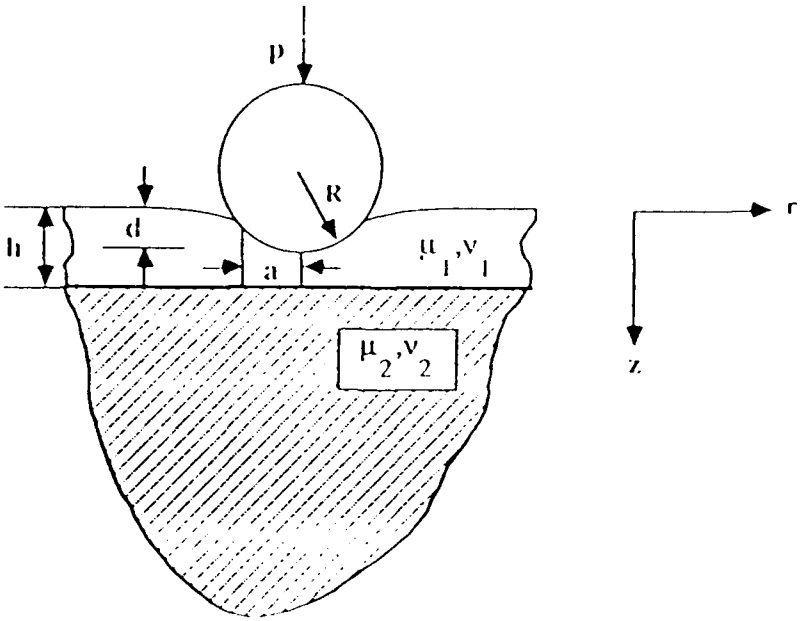


Fig. 3 — A composite medium consisting of an elastic layer either perfectly bonded to or smoothly overlaying an elastic semi-infinite substrate indented by a rigid spherical indenter

The Papkovich-Neuber functions may then be used to formulate the problem. Thus, in terms of a pair of harmonic functions $\varphi_j(r, z)$ and $\Psi_j(r, z)$ $(j = 1, 2)$, the displacement and stress components of interest may be written as

$$\begin{aligned} 2\mu_j u_{rj} &= -\varphi_{j,r} - z\Psi_{j,r}, \\ 2\mu_j u_{zj} &= k_j\Psi_j - \varphi_{j,z} - z\Psi_{j,z}, \\ \sigma_{zj} &= 2(1-\nu_j)\Psi_{j,z} - \varphi_{j,zz} - z\Psi_{j,zz}, \\ \tau_{rzj} &= (1-2\nu_j)\Psi_{j,r} - \varphi_{j,rz} - z\Psi_{j,rz}, \text{ and} \\ j &= 1, 2, \ k_j = 3 - 4\nu_j, \end{aligned} \tag{1}$$

where the letter subscripts following a comma denote differentiation with respect to the indicated cylindrical coordinates, e.g., $\varphi_{j,rz} = \partial^2\varphi_j/\partial r\,\partial z$.

The harmonic functions $\varphi_j(r, z)$, $\Psi_j(r, z)$ may be expressed in terms of a new set of unknown functions $A_i(\lambda)$, $(i = 1, 2, \ldots, 6)$ as the following Hankel integrals

$$\begin{aligned} \Psi_1(r, z) &= \int_0^\infty (A_1 \operatorname{ch}\lambda z + A_2 \operatorname{sh}\lambda z)\frac{J_0(\lambda r)}{\operatorname{sh}\lambda h}\,d\lambda, \\ \varphi_1(r, z) &= \int_0^\infty (A_3 \operatorname{sh}\lambda z + A_4 \operatorname{ch}\lambda z)\frac{J_0(\lambda r)}{\lambda \operatorname{sh}\lambda h}\,d\lambda, \\ \Psi_2(r, z) &= \int_0^\infty A_5 e^{-\lambda(z-h)}J_0(\lambda r)\,d\lambda, \\ \varphi_2(r, z) &= \int_0^\infty A_6 e^{-\lambda(z-h)}\frac{J_0(\lambda r)}{\lambda}\,d\lambda, \end{aligned} \tag{2}$$

where $\operatorname{ch}\lambda z$ and $\operatorname{sh}\lambda z$ are hyperbolic cosine of λz and hyperbolic sine of λz respectively and $J_0(\lambda r)$ is the Bessel function of the first kind of order 0. It may be readily be seen that Eqs. (2) satisfy the boundary conditions that the stresses and their derivatives in both media vanish for $r \geq 0$, $z \to \infty$, and for $z > 0$, $r \to \infty$.

Regardless of type of contact between layer and substrate the displacement and traction boundary conditions of the surface may be expressed as

$$u_{z1}(r, 0) = d - \delta(r/a) \qquad (0 \leq r \leq d), \tag{3.1}$$

$$\sigma_{z1}(r, 0) = 0 \qquad (a < r < \infty), \text{ and} \tag{3.2}$$

$$\tau_{rz1}(r, 0) = 0 \qquad (0 \leq r < \infty). \tag{3.3}$$

where d is the depth of penetration of the indenter, a is the radius of the circle of contact, and the function $\delta(r/a)$ is prescribed by the fact that, in reference to the tip of the indenter as origin, the punch has equation $z = \delta(r/a)$ so that $\delta(0) = 0$. The function $\delta(r/a)$ for conical, hemispherical, and flat-ended cylindrical indenters on the half-space have been given by Sneddon [6].

With the functions $\varphi_j(r, z)$ and $\Psi_j(r, z)$ $(j = 1, 2)$ as shown in Eq. (2), the boundary conditions Eq. (3.1) to (3.3) may be expressed by using Eq. (1) as follows.

$$\int_0^\infty \frac{A_1(\lambda)}{\operatorname{sh} \lambda h} J_0(\lambda r)\, d\lambda = \frac{\mu_1}{1 - \nu_1} [d - \delta(r/a)] \qquad (0 \le r \le a), \tag{4.1}$$

$$\int_0^\infty \frac{A_4(\lambda) - 2(1 - \nu_1)A_2(\lambda)}{\operatorname{sh} \lambda h} \lambda J_0(\lambda r)\, d\lambda = 0 \qquad (a < r < \infty), \tag{4.2}$$

and

$$A_3(\lambda) = (1 - 2\nu_1)A_1(\lambda) \qquad (0 < r < \infty). \tag{4.3}$$

Defining

$$M(\lambda) = \frac{A_1(\lambda)}{\operatorname{sh} w}, \quad 1 - g(\lambda) = \frac{A_1(\lambda)}{A_4(\lambda) - 2(1 - \nu_1)A_2(\lambda)}, \tag{5}$$

where $w = \lambda h$, and the conditions Eqs. (4.1) and (4.2) lead to a system of two integral equations for $M(\lambda)$:

$$\int_0^\infty M(\lambda) J_0(\lambda r)\, d\lambda = f(r) \qquad (0 \le r \le a), \tag{6.1}$$

and

$$\int_0^\infty \frac{\lambda M(\lambda)}{1 - g(\lambda)} J_0(\lambda r)\, d\lambda = 0 \qquad (a < r < \infty), \tag{6.2}$$

where

$$f(r) = \frac{\mu_1}{1 - \nu_1} [d - \delta(r/a)]. \tag{7}$$

The function $g(\lambda)$ can be obtained, as shown in detail in the Appendix A, by expressing the unknown functions $A_i(\lambda)$ $(i = 1, 2, \ldots, 6)$ in terms of $A_1(\lambda)$ for different boundary conditions between the layer and the semi-infinite half-space. This is, for the case of perfect bonding, continuity of components of displacements and tractions at $z = h$ requires that

$$\begin{aligned} u_{r1}(r, h) &= u_{r2}(r, h), \\ u_{z1}(r, h) &= u_{z2}(r, h), \\ \sigma_{z1}(r, h) &= \sigma_{z2}(r, h), \text{ and} \\ \tau_{rz1}(r, h) &= \tau_{rz2}(r, h), \end{aligned} \tag{8}$$

for $0 \leq r \leq \infty$, while for the case when the two surfaces are in smooth contact (frictionless), continuity of normal components of displacement and tractions and the conditions of vanishing shear stress components at the interface may be expressed by

$$u_{z1}(r, h) = u_{z2}(r, h),$$

$$\sigma_{z1}(r, h) = \sigma_{z2}(r, h), \text{ and} \tag{9}$$

$$\tau_{rz1}(r, h) = \tau_{rz2}(r, h) = 0,$$

for $0 \leq r < \infty$.

The solution of Eq. (6) is sought in the form [9]

$$M(\lambda) = [1 - g(\lambda)] \int_0^a \varphi(t) \cos \lambda t \, dt, \tag{10}$$

where $\phi(t)$ is the solution of the following Fredholm integral equation of the second kind with a continuous symmetrical kernel:

$$\phi(t) - \frac{1}{\pi} \int_0^a [G(s + t) + G(s - t)] \phi(s) \, ds = F(t) \qquad (0 \leq t \leq a), \tag{11}$$

where

$$G(x) = \int_0^\infty g(\lambda) \cos \lambda x \, d\lambda, \tag{12}$$

$$F(t) = \frac{2}{\pi} [f(0) + t \int_0^{\frac{\pi}{2}} f'(t \sin \theta) \, d\theta], \tag{13}$$

and

$$f'(x) = \frac{d}{dx} f(x).$$

After determining $F(t)$, the unknown function $\phi(t)$ can be solved by using Eq. (11). Then by using Eq. (10) and the solutions of the simultaneous equations of $A_i(\lambda)$, Eqs. (1) and (2) give a complete solution to the contact problem under consideration. For instance, by using Eq. (2) and the known formula

$$\int_0^\infty J_0(\lambda r) \sin \lambda t \, d\lambda = 0 \qquad (0 < t < r), \tag{14}$$

$$= (t^2 - r^2)^{-1/2} \qquad (t > r),$$

it is easy to obtain the equation for the distribution of the normal stresses under the punch

$$\sigma_{z1}(r, 0) = \int_r^a \frac{\phi'(t)}{(t^2 - r^2)^{1/2}} \, dt - \frac{\phi(a)}{(a^2 - r^2)^{1/2}}, \qquad (r < a). \tag{15}$$

Substituting Eq. (7) into Eq. (13) we have

$$F(t) = \frac{2\mu_1 d}{\pi(1 - \nu_1)} F_0(\tau), \tag{16}$$

where

$$F_0(\tau) = 1 \quad \frac{\delta(0)}{d} \quad \frac{\tau}{d} \int_0^{\pi/2} \delta'(\tau \sin\theta)\, d\theta, \tag{17}$$

and $\tau = t/a$. Introducing the dimensionless quantities

$$\frac{s}{a} = y \quad \text{and} \quad \phi(t) = \frac{2\mu_1 d}{\pi(1 - \nu_1)} H(\tau), \tag{18}$$

Eq. (11) then assumes the form

$$H(\tau) - \frac{1}{\pi} \int_0^1 [K(y + \tau) + K(y - \tau)]\, H(y)\, dy = F_0(\tau) \qquad (0 \le \tau \le 1), \tag{19}$$

where

$$K(u) = \frac{a}{h} \int_0^\infty g(w) \cos\left(\frac{auw}{h}\right) dw. \tag{20}$$

The magnitude of the applied load p can be obtained by integrating the pressure of the indenter on the layer over the area of contact, i.e., integrating Eq. (15) over the area of the circle of radius a. Thus,

$$p = \frac{4\mu_1 ad}{1 - \nu_1} \int_0^1 H(\tau)\, d\tau, \tag{21}$$

where $H(\tau)$ is known after $F_0(\tau)$ in Eq. (19) is determined.

The function $F_0(\tau)$ can be obtained from Eqs. (9), (13), (16), and (17) for an indenter of arbitrary axisymmetric profile. Intuitively, the contact pressure for the top surface of the layered half-space and that for the homogeneous half-space are similar in many respects if the indenter profile remains the same in both cases. For example, if the indenter has a sharp corner, the stress will be singular there. If the identer profile is smooth, then the normal stress σ_{z1} must, on physical grounds, remain finite around the circle $r = a$ ($\tau = 1$). This continuity of normal stresses gives an additional equation

$$\phi(a) = H(1) = 0, \tag{22}$$

which is a consequence of Eqs. (15) and (18). Therefore, in the case of indenters with smooth profile, such as conical or hemispherical, Eqs. (19) and (22) have to be solved first to find the relationships between the penetration depth d and the radius of contact area a. For convenience, let us define a dimensionless parameter γ, which is a function of h, μ_1, ν_1, μ_2, ν_2, and the indenter profile,

$$\gamma = \frac{a}{a_H}, \tag{23}$$

where a_H is the radius of the contact area for a homogeneous half-space with elastic constants μ_1 and ν_1. The relationships between a_H and d for different indenters are [5]:

$$a_H = a, \tag{24}$$

for a flat-ended cylindrical indenter of radius a (note that this equation is independent of d);

$$a_H = \frac{2}{\pi} d \tan \alpha, \tag{25}$$

for a conical indenter with included angle 2α; and

$$a_H = 2d \left(\ln \frac{1 + \rho}{1 - \rho} \right)^{-1} \qquad (\rho = a_H/R),$$

$$= (Rd)^{1/2} \qquad (a_H << R), \tag{26}$$

for a hemispherical tip indenter of radius R.

Since when using the indentation test to determine elastic constants, such as Young's modulus, shear modulus, or Poisson ratio, each constant is not measured directly but in any combinations of pairs, it is convenient to define a new elastic constant, say

$$\zeta = \frac{4\mu}{1 - \nu}, \tag{27}$$

which may be called the impression elastic modulus, or the impression modulus for short. Now the relationship between p and z for each type of indenter may be obtained as follows.

Flat-ended Cylindrical Indenter

For the flat-ended cylindrical indenter of radius a (Fig. 1), the boundary condition Eq. (3.1) is

$$u_{z1}(r, 0) = d \qquad (0 \le r \le d),$$

which gives

$$\delta(r/a) = 0, f(r) = \frac{1}{4} \zeta_1 d \qquad (0 \le r \le a),$$

and

$$F_0(\tau) = 1 \qquad (0 \le \tau \le 1), \tag{28}$$

where ζ_1 is the impression modulus for the homogeneous half-space with elastic constants μ_1 and ν_1. According to Eq. (21), the relationship between the p and the d can be written as

$$p = \zeta_1 a d \int_0^1 H(\tau)\, d\tau, \tag{29}$$

and

$$p_i = \zeta_i a d \qquad (i = 1, 2), \tag{30}$$

where $i = 1$ when $h \to \infty$ and $i = 2$ and $h \to 0$.

Conical Indenter

For normal penetration by a rigid cone of included angle 2α (Fig. 2), the boundary condition, Eq. (3.1), gives

$$\delta(r/a) = r \cot \alpha \qquad (0 \le r < a), \tag{31}$$

then Eqs. (7) and (13) become

$$f(r) = \frac{1}{4}\, \zeta_1 d \left(1 - \frac{2\gamma_c}{\pi a} r \right) \qquad (0 \le r \le a),$$

and

$$F_0(\tau) = 1 - \gamma_c \tau \qquad (0 \le \tau \le 1), \tag{32}$$

where $\gamma_c = a/a_H$. The relationships between p, d, and a are

$$\begin{aligned} p &= \frac{2}{\pi}\, \gamma_c \zeta_1 d^2 \tan \alpha \int_0^1 H(\tau)\, d\tau, \\ &= \frac{\pi}{2}\, \gamma_c \zeta_1 a_H^2 \cot \alpha \int_0^1 H(\tau)\, d\tau, \end{aligned} \tag{33}$$

and

$$p_i = \zeta_i d^2 \tan \alpha \qquad (i = 1, 2). \tag{34}$$

Spherical Indenter

For normal penetration by a rigid spherical indenter of radius R (Fig. 3), the same as before, the strained surface of the elastic layer conforms to the sphere between the first point of contact and the section of radius a. From the geometry of Fig. 3 we find that

$$\delta(r/a) = R \left[1 - \left(1 - \frac{r^2}{R^2} \right)^{1/2} \right] \qquad (0 \le r \le a). \tag{35}$$

which gives

$$f(r) = \frac{1}{4}\, \zeta_1 d \left[1 - \frac{2}{\gamma_1^2 \rho} \frac{1 - \left(1 - \dfrac{r^2}{R^2} \right)^{1/2}}{\ln(1+\rho) - \ln(1-\rho)} \right] \qquad (0 \le r \le a), \tag{36}$$

and

$$F_0(\tau) = 1 - \frac{\tau}{\gamma_s^2} \frac{\ln(1+\rho\tau) - \ln(1-\rho\tau)}{\ln(1+\rho) - \ln(1-\rho)} \qquad (0 \le \tau \le 1), \tag{37}$$

where $\gamma_s = a/a_H$ and $\rho = a/R$. If the indentation is small ($a << R$ or $\rho << 1$), then approximately

$$a = \gamma_s (Rd)^{1/2} \qquad (a << R), \tag{38}$$

and

$$F_0(\tau) = 1 - \gamma_s^2 \tau^2 \qquad (0 \le \tau \le 1, \rho << 1), \tag{39}$$

and from Eqs. (38) and (21)

$$p = \gamma_s \zeta_1 R^{1/2} d^{3/2} \int_0^1 H(\tau) d\tau,$$

$$= \gamma_s \zeta_1 R^{-1} a_H^3 \int_0^1 H(\tau)\, d\tau, \tag{40}$$

and

$$p_i = \frac{2}{3} \zeta_i R^{1/2} d^{3/2} \qquad (i = 1, 2) \tag{41}$$

The formulation of the problem is now complete for each of the three types of indenter considered. Numerical results for some cases of interest are presented and discussed in the following section.

NUMERICAL RESULTS

The mixed boundary value problem is represented by the Fredholm integral equation of the second kind as shown in Eq. (19). For a given function $k(u)$ (Eq. (20)) and $F_0(\tau)$ (Eqs. (28), (31), or (35) depending on the shape of the indenter), the function $H(\tau)$ is solved numerically in the form of a Chebyshev series of N terms ($N \ge 5$) [13]. The load on the indenter is then obtained by integration as indicated in Eq. (21). The calculations of the load and the function $K(u)$ for the given function $g(\lambda)$ (see Appendix A, Eqs. (A2) and (A10)) are also carried out numerically by using a Cray supercomputer.

For the conical and the spherical indenters, Eq. (19) is first solved by setting the parameter γ equal to 1 and then iterating until a proper value for γ is obtained such that $H(1) = 0$. Then the correct γ values are used to solve the function $H(\tau)$ and the load p.

The papers of Lebedev and Ufliand [8], Dhaliwal [9], and Chen and Engel [12] contain some numerical results and thus provide an excellent opportunity for comparison with the results obtained here. The kernel $K(u)$, as defined by Eq. (20), is computed first for both an elastic layer in smooth contact with a rigid substrate and an elastic layer perfectly bonded to an elastic substrate. The results obtained are the same as those in Refs. 8 and 9 (Tables B1 and B2 in Appendix B). The computer program used to solve the Fredholm integral equation (Eq. 19) was further checked by computing $H(\tau)$ values for a flat-ended cylindrical indenter pressing on an elastic layer in smooth contact with a rigid substrate and comparing the results with those given by Lebedev and Ufliand [8]. The excellent agreement (Table B3) provided confidence in the correctness of the present analysis.

When the layer and the substrate are perfectly bonded and the indenter is a flat-ended cylinder, the $H(\tau)$ values calculated by using the same set of $K(u)$ values (Table B2) show substantial disagreement between our results and Dhaliwal's published results (Table B4), as noted, for example, for the case when $h/a = 0.25$ and $\mu_1/\mu_2 = 0$ where values for $H(\tau)$ differ by approximately an order of magnitude. However, the results of Chen and Engel [12] for the spherical indenter when $a << R$ were reproduced (Table B5). The details of these comparisons are given in Appendix B.

In the present calculation, the number of terms N in the Chebyshev series that approximate the solution $H(\tau)$ is taken to be 5 when $h/a > 0.5$. For values of h/a smaller than 0.5, the number of terms should be increased to get accurate values for $H(\tau)$. For example, in our calculation, N was chosen to be 25 when $h/a = 0.1$.

Figures 4 to 7 give the relationships between the parameter γ (Eq. 23) and the layer thickness h for different indenter shapes, layer and substrate elastic properties, and bonding conditions. The parameter γ is the radius of contact a normalized with respect to the Hertz contact radius a_H for a homogeneous half-space of shear modulus μ_1 and Poisson ratio ν_1. For conical and spherical indenters with smooth contact between layer and substrate, the results for $\eta = 0, 0.2, 1, 2$, and 10 (where $\eta = (1 - \nu_2)\mu_1/(1 - \nu_1)\mu_2$) are plotted in Figs. 4 and 5, respectively. Figures 6 and 7 show the relationship between γ and h/a for a layer perfectly bonded to the substrate when $\beta = 0, 0.2, 1, 2$, and 10 (where $\beta = \mu_1/\mu_2$), and $\nu_1 = \nu_2 = 0.3$ for the conical and spherical indenters, respectively. These results show that $\gamma > 1$ when the substrate is stiffer than the layer ($\eta > 1$ or $\beta > 1$), and $\gamma < 1$ when the layer is stiffer than the substrate ($\eta < 1$ or $\beta < 1$). For a given depth of penetration, the radius of contact between the indenter and the composite medium increases with increasing stiffness of substrate materials. For a layer/substrate stiffness ratio (η or β) smaller than 1, the radius of contact increases from the value a_H to a certain maximum value and then decreases asymptotically back to the value a_H as the layer thickness increases from 0 to ∞. The layer thickness at which the maximum radius of contact occurs is always less than the radius of contact itself, i.e., $h/a < 1$. On the other hand, when the substrate is less stiff than the layer, the radius of contact decreases from its homogeneous half-space value a_H to a minimum value and then increases toward a_H asymptotically as the layer thickness h increases from 0 to ∞. The minimum value occurs in the range where $1 < h/a < 2$. Note that when the layer and the substrate are identical and there is no friction force at the interface, the radius of contact is not always the same as the homogeneous half-space, but it increases first, then decreases to a minimum value and increases again toward the homogeneous value a_H.

For the purpose of setting up a guideline for choosing the appropriate layer thickness and substrate properties to determine the elastic constants of thin films by the indentation test, it is convenient to define a nondimensional quantity p/p_1, which is the radio between p, the load needed to penetrate to a depth d into the composite (layered half-space) and p_1 the load needed to penetrate the same depth d into the homogeneous half-space consisting of the top layer material. This ratio p/p_1 is then plotted against h/a. For different shapes of indenter p/p_1 are given as follows:

$$\frac{p}{p_1} = \int_0^1 H(\tau)\, d\tau \qquad \text{(cylindrical indenter)},$$

$$\frac{p}{p_1} = 2\gamma_c \int_0^1 H(\tau)\, d\tau \qquad \text{(conical indenter)}, \tag{42}$$

and

$$\frac{p}{p_1} = \frac{3}{2}\gamma_s \int_0^1 H(\tau) d\tau \qquad \text{(spherical indenter)}$$

Figures 8 through 13 show the p/p_1 vs h/a curves for the smooth contact condition ($\eta = 0, 0.2, 0.5, 1, 2,$ and 10) and for perfectly bonded condition ($\beta = 0, 0.2, 0.5, 1, 2,$ and 10, $\nu_1 = \nu_2 = 0.3$) for the flat-ended cylindrical indenter, the conical indenter, and the spherical indenter, respectively. When the layer is perfectly bonded to, and softer than the substrate, the load p on the composite decreases more or less exponentially from p_2 (the load for the homogeneous half-space with elastic constants μ_2 and ν_2) to p_1 (the load for the homogeneous half-space with elastic constants μ_1 and ν_1) as the thickness of the layer increases from 0 to ∞. On the other hand, when the layer is stiffer than the substrate, p increases asymptotically from p_2 to p_1. When the layer is in smooth contact with and stiffer than the substrate, p decreases from p_2 to a minimum value, then increases toward p_1 as the layer thickness varies from 0 to ∞. When the layer is softer than the substrate, p does not decrease asymptotically from p_2 to p_1; for μ_2/μ_1 less than certain value (for example 0.63 for the flat-ended cylindrical indenter as shown in Fig. 14), the p values decrease from p_2 to a minimum value less than p_1, then increase and approach p_1 as the thickness increases.

When the indenter is a flat-ended cylinder of radius a, the radius of the contact area is always equal to a regardless of the composite medium material and layer thickness. This means the parameter γ is always equal to 1. When the indenter is conical or spherical, the radius of the contact area is no longer a constant, but is a function of the penetration depth d, the layer thickness h, the elastic constants of the layer and the substrate, and the shape of the indenter. Therefore, the scale of the absissa h/a, in Figs. 10 to 13, are not the same for all the curves. To compare the results for different conditions, it is necessary to express h in units of the constant value a_H instead of the variable a. Figures 15 to 18 show the p/p_1 vs h/a_H curves that are converted from Figs. 9, 10, 12, and 13 by using the corresponding γ values from Figs. 4 to 7, respectively.

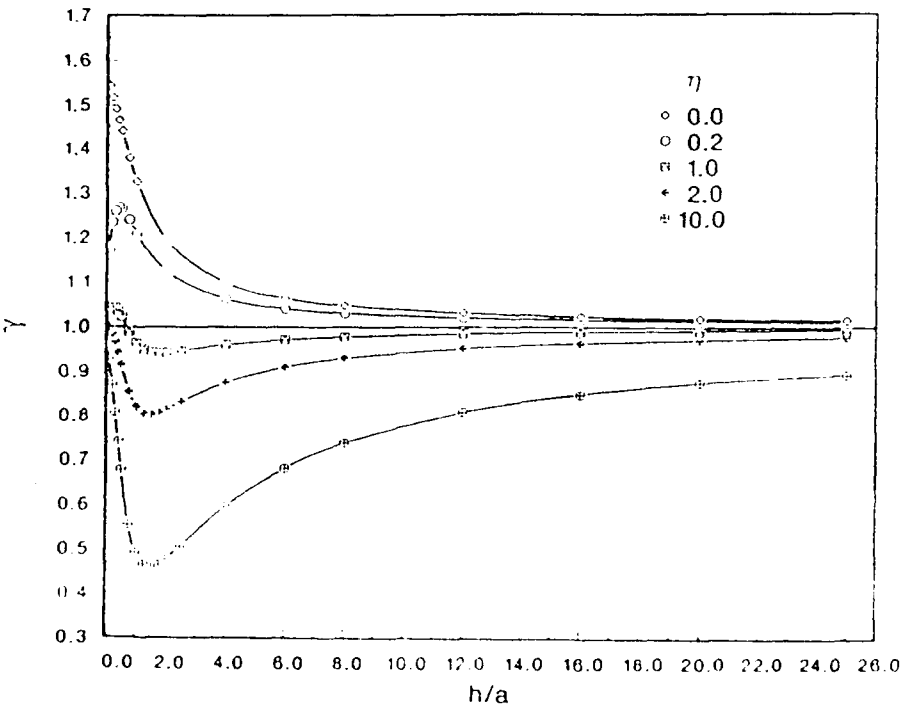


Fig. 4 — Variation of the normalized radius of the contact area between the conical indenter and the smooth contact composite medium γ, with layer thickness h/a, as a function of layer/substrate stiffness ratio η

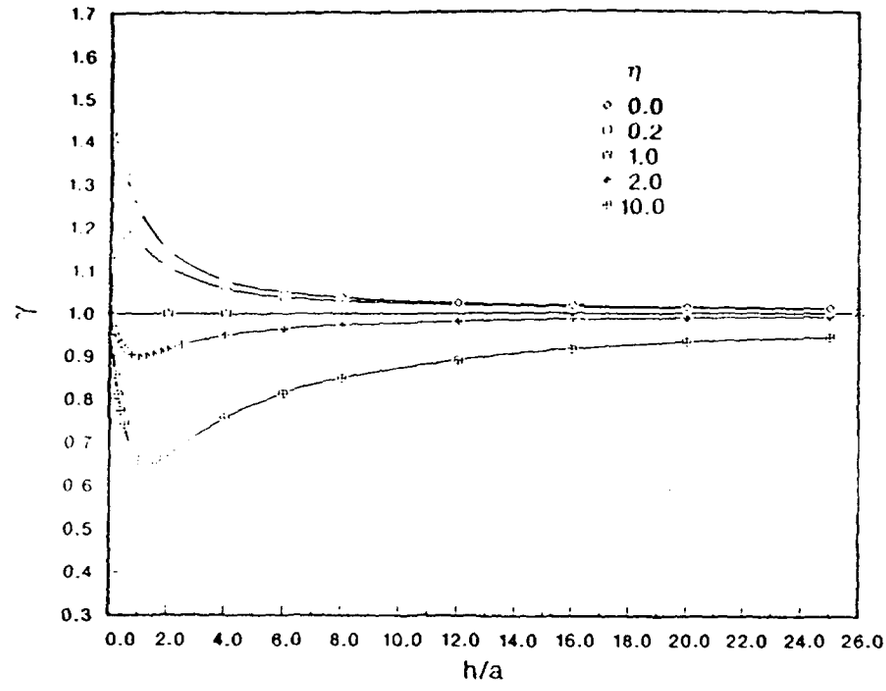


Fig. 5 — Variation of the normalized radius of the contact area between the spherical indenter and the smooth contact composite medium γ, with layer thickness h/a, as a function of layer/substrate stiffness ratio η

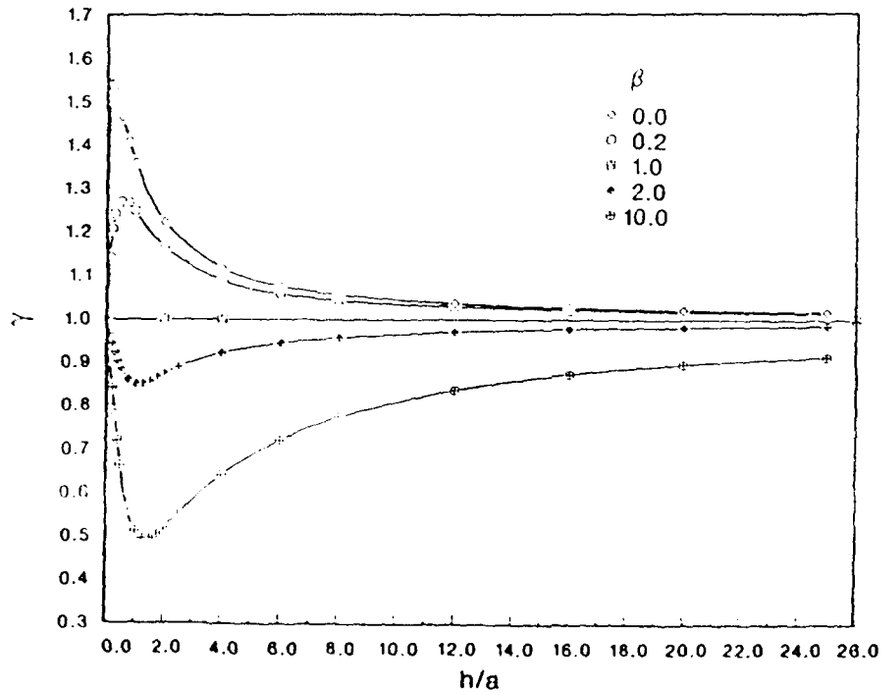


Fig. 6 — Variation of the normalized radius of the contact area between the conical indenter and the perfectly bonded composite medium γ, with layer thickness h/a, as a function of layer/substrate stiffness ratio β ($\nu_1 = \nu_2 = 0.3$)

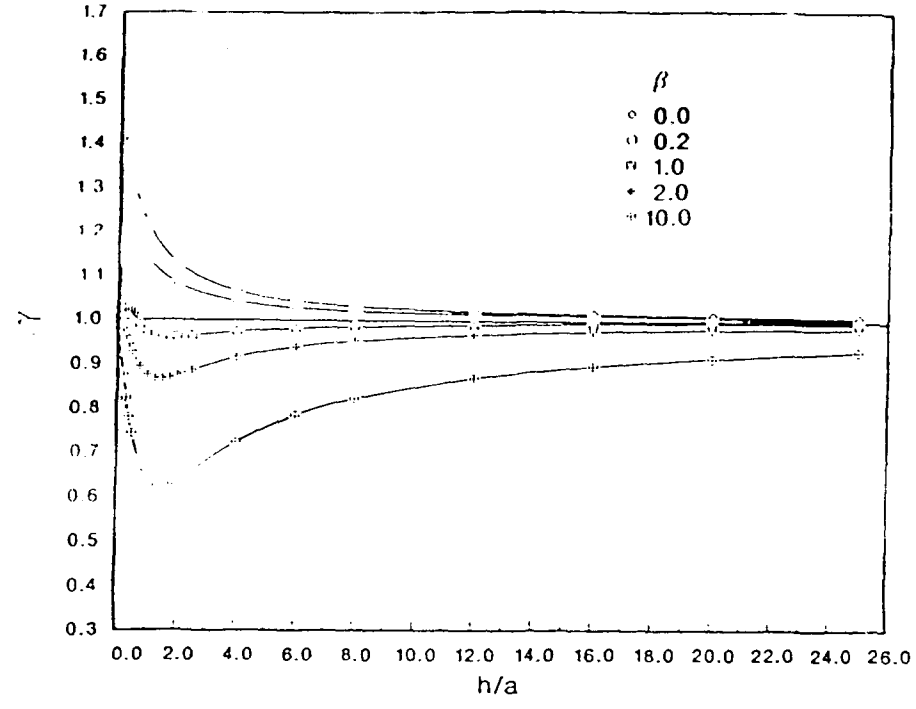


Fig. 7 — Variation of the normalized radius of the contact area between the spherical indenter and the perfectly bonded composite medium γ, with layer thickness h/a as a function of layer/substrate stiffness ratio β ($\nu_1 = \nu_2 = 0.3$)

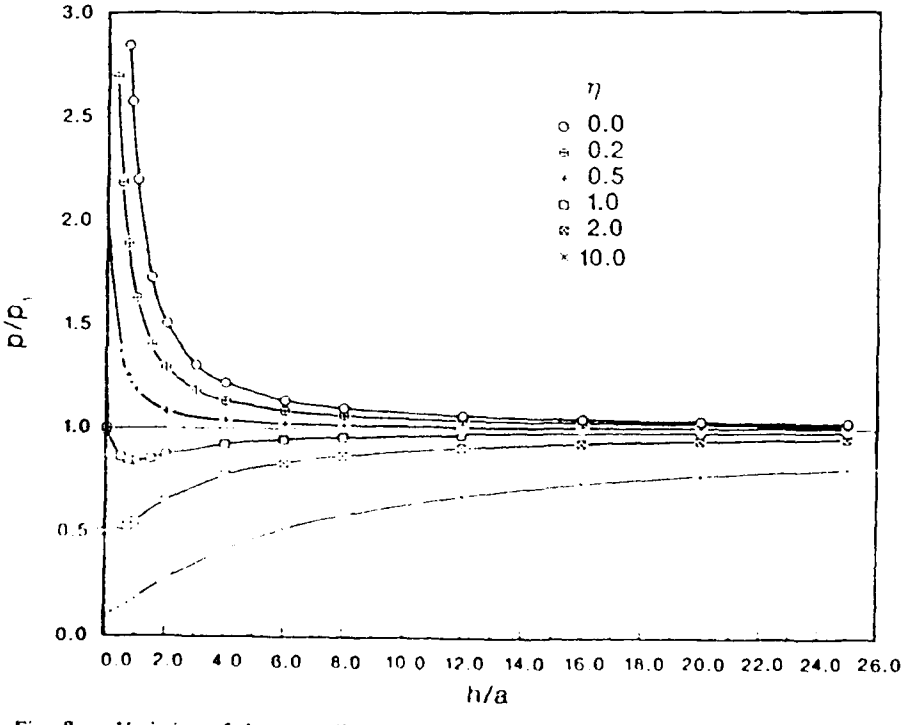


Fig. 8 — Variation of the normalized load p/p_1 for the flat-ended cylindrical indenter with layer thickness h/a for a smooth contact composite medium as a function of layer/substrate stiffness ratio, η

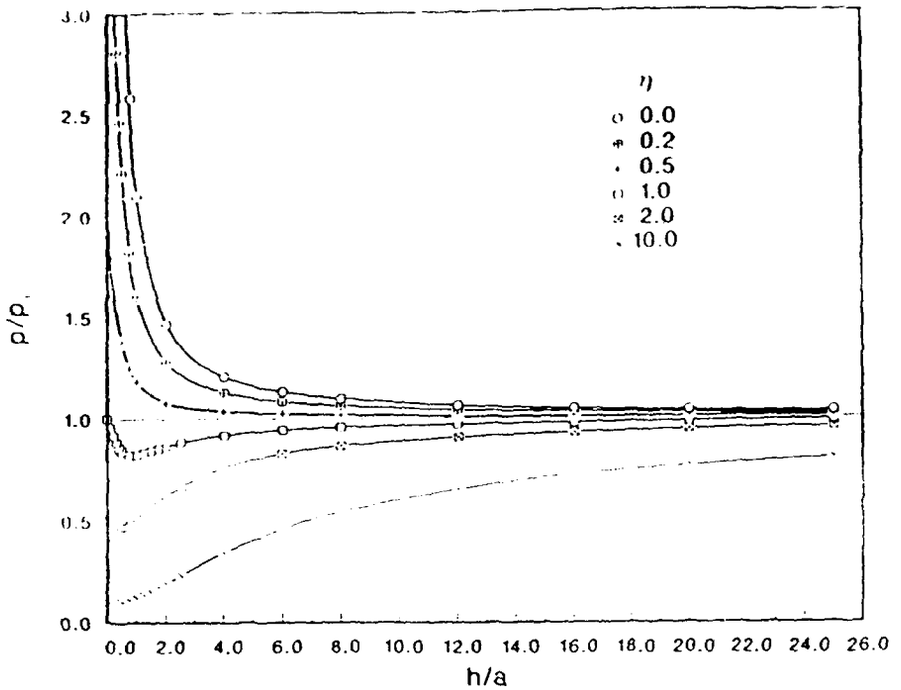


Fig. 9 — Variation of the normalized load p/p_1 for the conical indenter with layer thickness h/a for a smooth contact composite medium as a function of layer/substrate stiffness ratio η

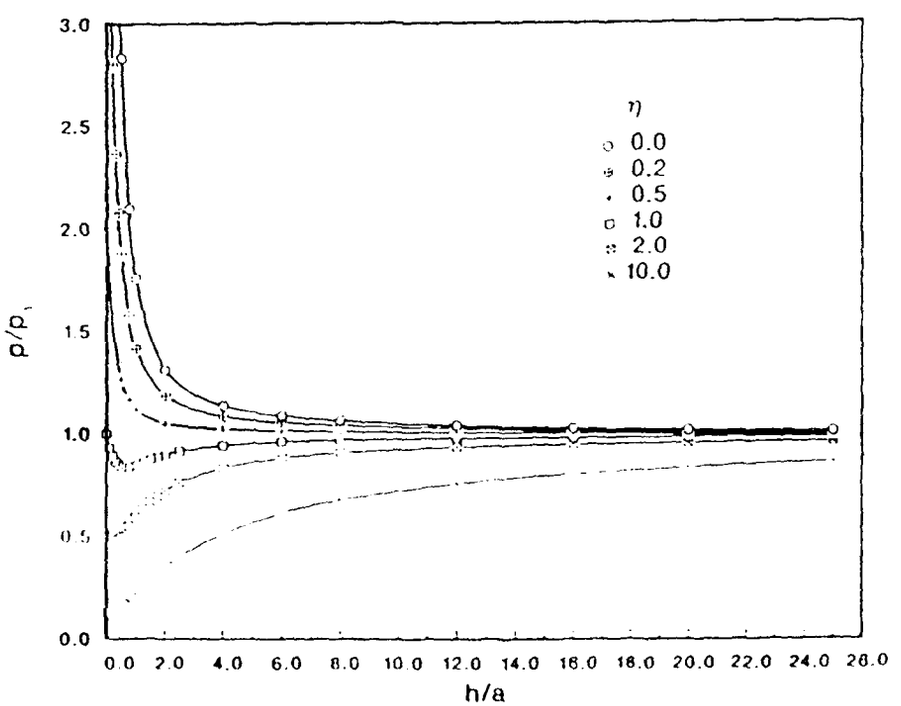


Fig. 10 — Variation of the normalized load p/p_1 for the spherical indenter with layer thickness h/a for a smooth contact composite medium as a function of layer/substrate stiffness ratio η

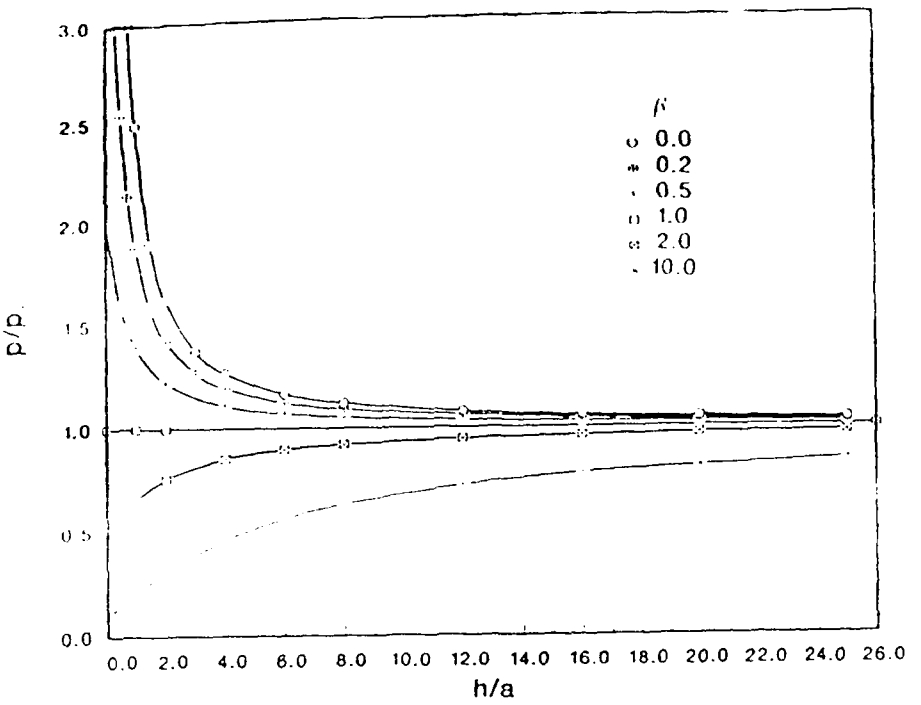


Fig. 11 — Variation of the normalized load p/p_1 for the flat-ended cylindrical indenter with layer thickness h/a for a perfectly bonded composite medium as a function of layer/substrate stiffness ratio β ($\nu_1 = \nu_2 = 0.3$)

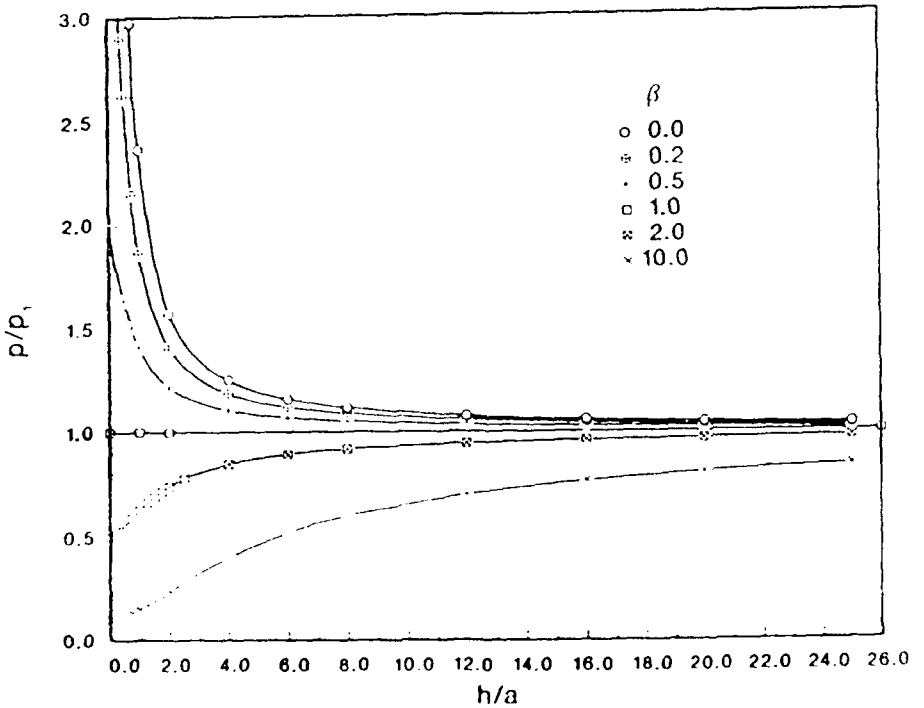


Fig. 12 — Variation of the normalized load p/p_1 for the conical indenter with layer thickness h/a for a perfectly bonded composite medium as a function of layer/substrate stiffness ratio β ($\nu_1 = \nu_2 = 0.3$)

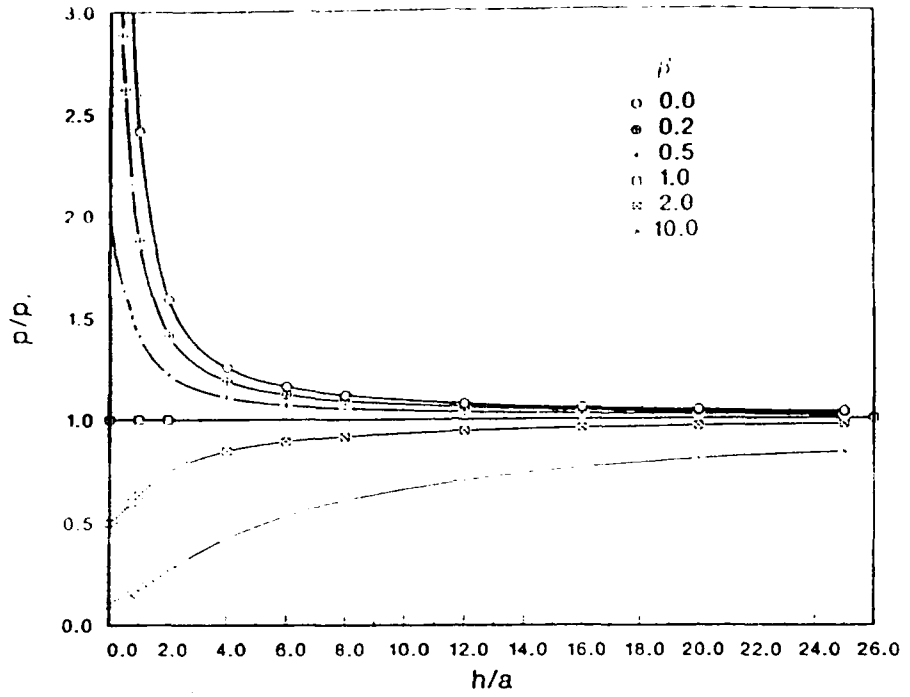


Fig. 13 — Variation of the normalized load p/p_1 for the spherical indenter with layer thickness h/a for a perfectiy bonded composite medium as a function of layer/substrate stiffness ratio β ($\nu_1 = \nu_2 = 0.3$)

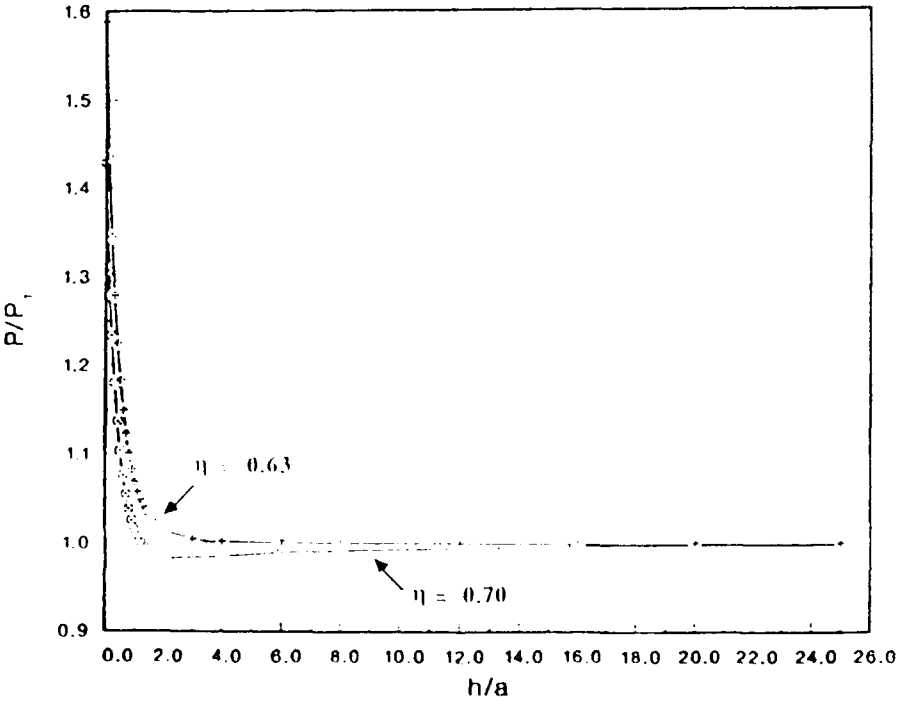


Fig. 14 — Variation of the normalized load p/p_1 for the flat-ended cylindrical indenter with layer thickness h/a for a smooth contact composite medium as a function of layer/substrate stiffness ratio η

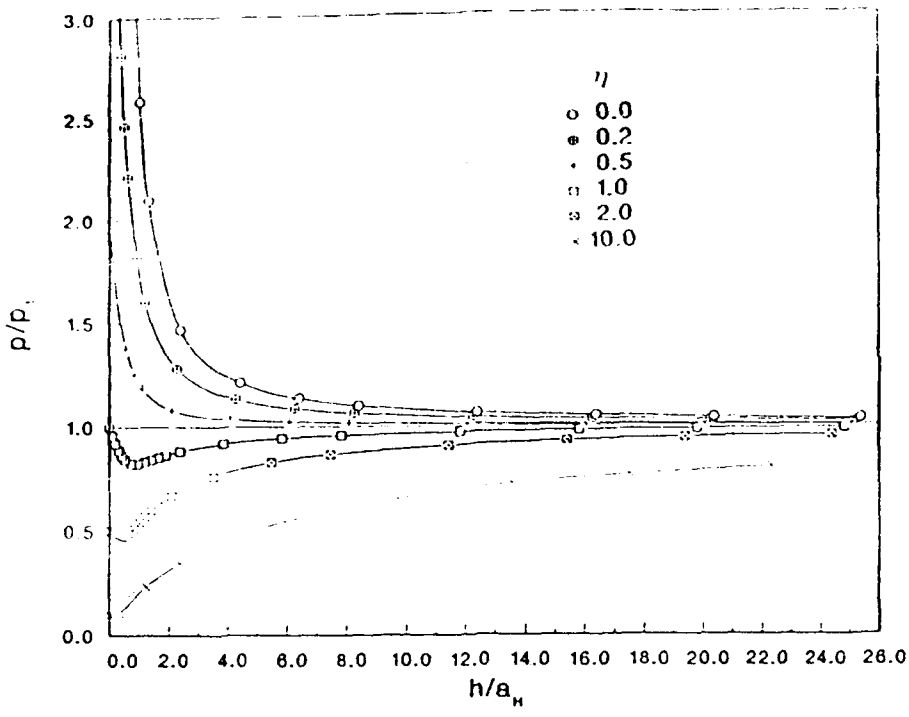


Fig. 15 — Variation of the normalized load p/p_1 for the conical indenter with layer thickness h/a_H for a smooth contact composite medium as a function of layer/substrate stiffness ratio η

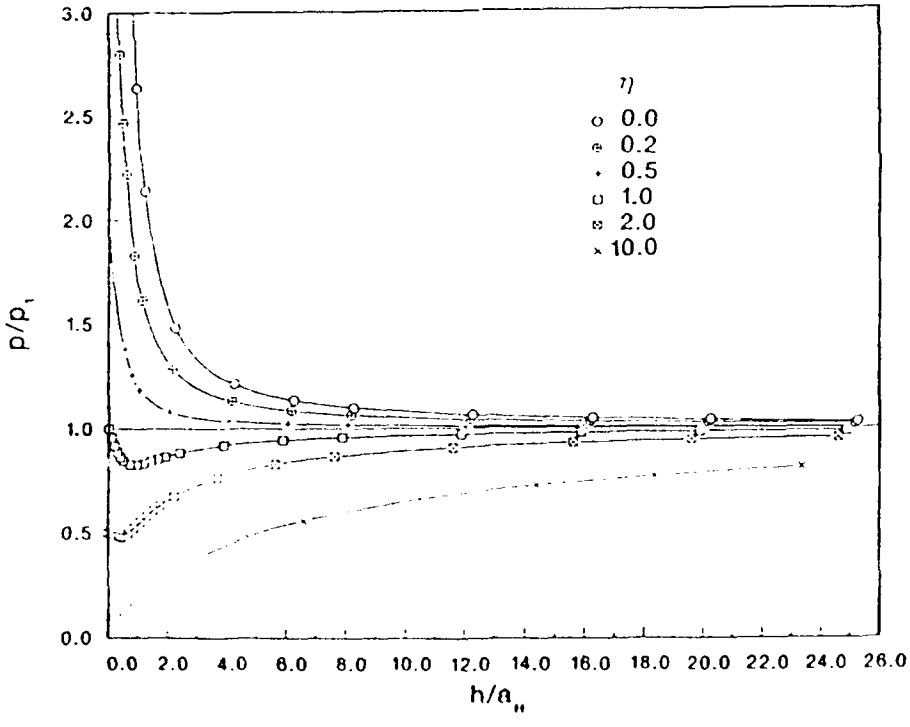


Fig. 16 — Variation of the normalized load p/p_1 for the spherical indenter with layer thickness h/a_H for a smooth contact composite medium as a function of layer/substrate stiffness ratio η

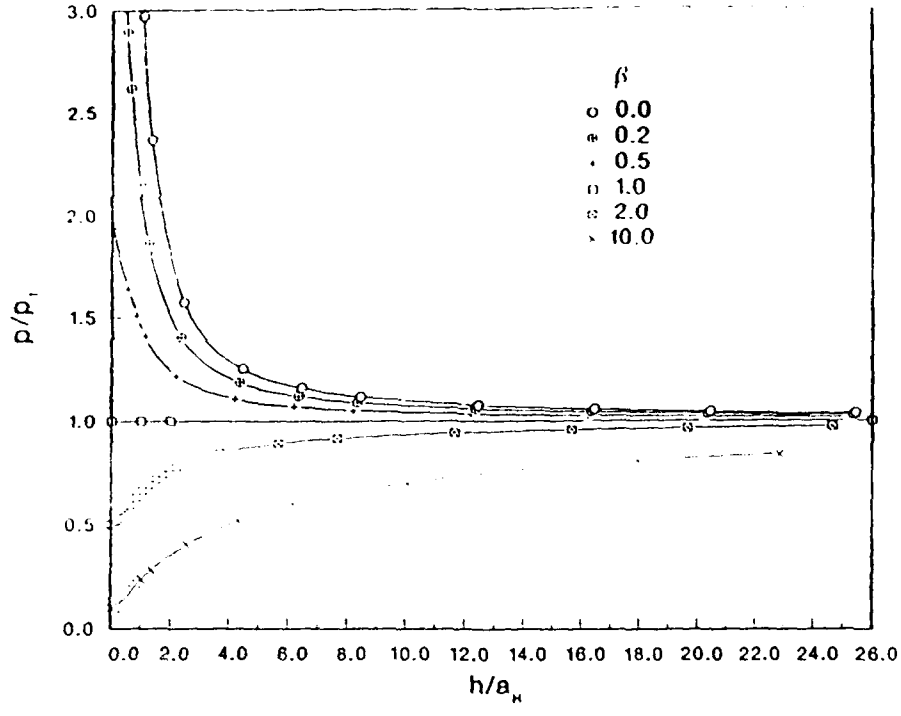


Fig. 17 — Variation of the normalized load p/p_1 for the conical indenter with layer thickness h/a_H for a perfectly bonded composite medium as a function of layer/substrate stiffness ratio β ($\nu_1 = \nu_2 = 0.3$)

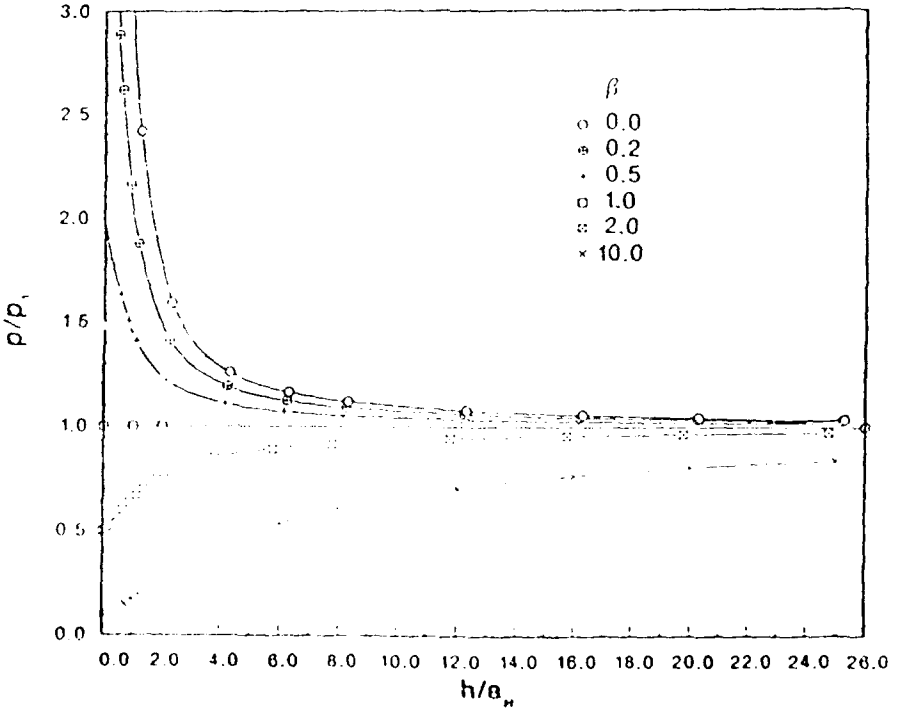


Fig. 18 — Variation of the normalized load p/p_1 for the spherical indenter with layer thickness h/a_H for a perfectly bonded composite medium as a function of layer/stiffness ratio β ($\nu_1 = \nu_2 = 0.3$)

In comparing these results, it is noted that the curves are quite similar for all three types of indenters despite the large differences in values of p and p_1 for the different indenters. This similarity allows us to establish guidelines for choosing a priori the approximate film thickness and substrate elastic properties for determining the elastic constants of the film within a given degree of accuracy. Figures 19 and 20 show, for the perfectly bonded and smooth contact conditions respectively, the film thickness needed so that the absolute values of $(p - p_1)/p_1$ are equal to 2%, 5%, and 10%. Note that the absolute value of the ratio $(p - p_1)/p_1$ has the same value as the ratio of the impression modulus $(\zeta_e - \zeta_1)/\zeta_1$, where ζ_e is the experimentally measured impression modulus obtained according to Eqs. (30), (34), or (41).

To determine the elastic constants of a perfectly bonded layer by the indentation test, as one may expect, the most proper substrate is the one that has the same elastic constants as the layer itself, i.e., $\beta = 1$. Figure 19 shows that when the β value is different from 1, the normalized layer thickness, h/a_H, needed to obtain a given accuracy varies almost linearly with β. The slope of the variation is dependent on the accuracy. The higher the accuracy required the steeper the slope is. When the layer is in smooth contact with the substrate, the best candidate substrate is no longer the one that has the same elastic constants as that of the layer. In this case, the substrate should be slightly stiffer than the layer. By assuming $\nu_1 = \nu_2 = 0.3$, η (in this case equal to β) is found to range from 0.87 (for 10% accuracy) to 0.71 (for 2% accuracy). For values of h/a_H greater than approximately 3, the layer normalized thickness h/a_H needed to obtain a given accuracy also varies almost linearly with η.

In preparing thin films, the film is neither perfectly bonded to the substrate, nor in perfectly smooth contact with the substrate. Figure 21 gives the upper bound h/a_H vs μ_1/μ_2 (by assuming $\nu_1 = \nu_2 = 0.3$) relations to ensure one can measure the film's elastic constants on the composite by the indentation test to a given degree of accuracy. Figure 21 is obtained by taking the upper ranges of the curves from Figs. 19 and 20. This result suggests that a good substrate candidate material is about 25% stiffer than the film material regardless of bonding conditions.

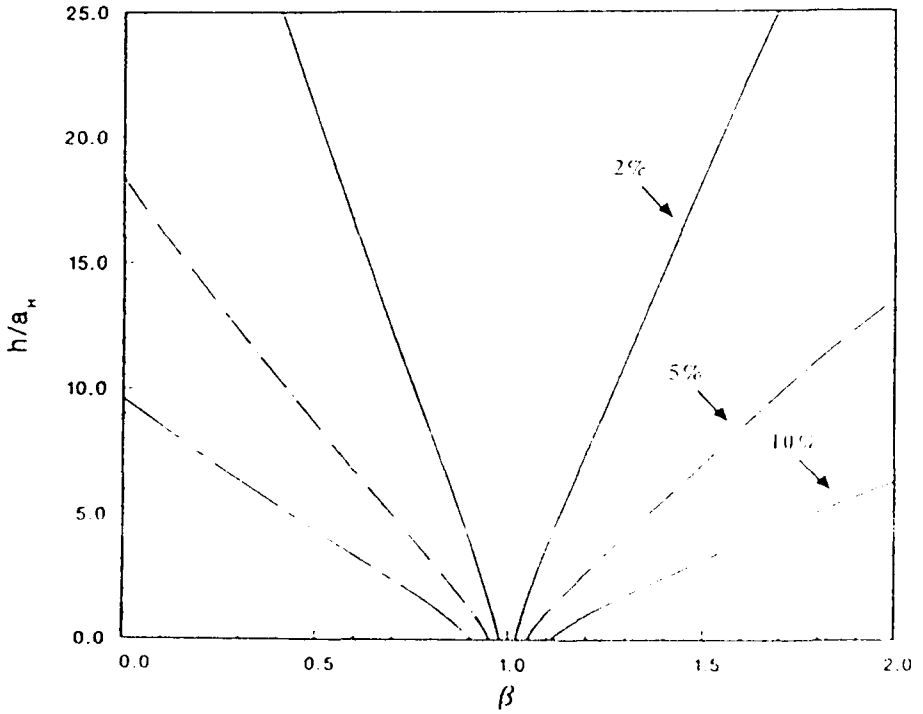


Fig. 19 — Relationships between the layer thickness h/a_H and layer/substrate stiffness ratio β such that $|(p - p_1)/p_1|$ is equal to 2%, 5%, and 10%

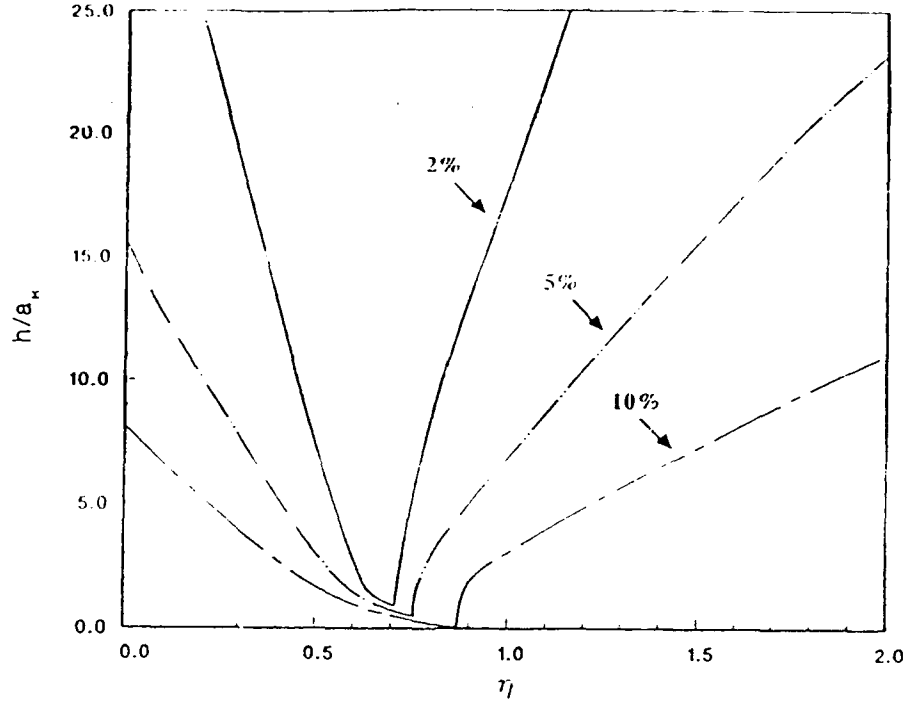


Fig. 20 — Relationships between the layer thickness h/a_H and layer/substrate stiffness ratio η such that $|(p - p_1)/p_1|$ is equal to 2%, 5%, and 10%

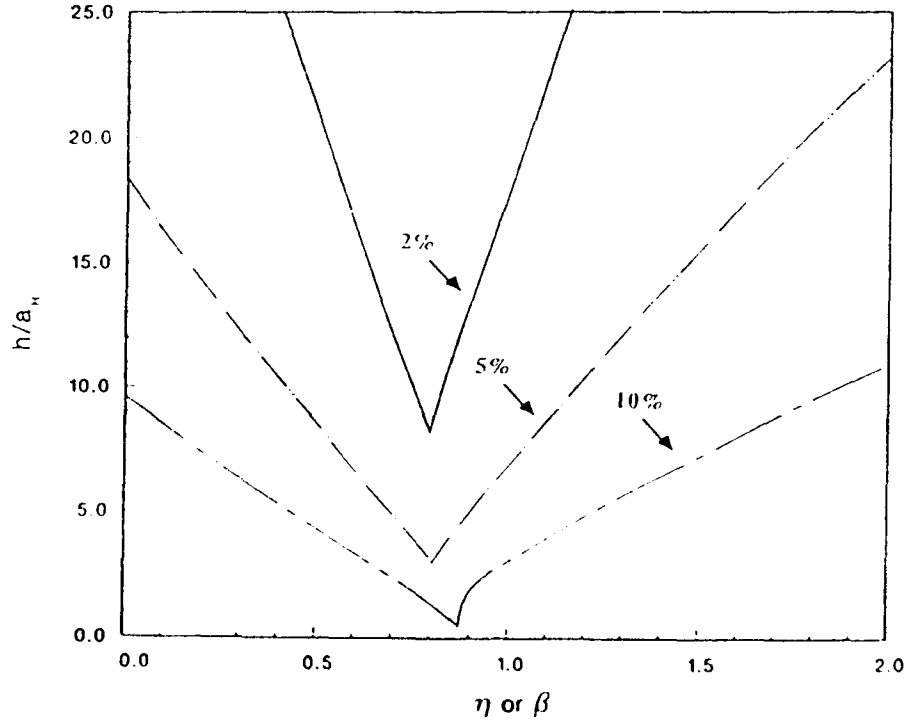


Fig. 21 — Relationships between the layer thickness h/a_H and layer/substrate stiffness ratio η or β such that $|(p - p_1)/p_1|$ is equal to 2%, 5%, and 10%

SUMMARY

The elastic solutions for the stress fields in a composite medium consisting of an elastic layer either perfectly bonded or smoothly overlaying an elastic semi-infinite substrate have been obtained for the cases when the composite medium is indented by rigid spherical, conical, and flat-ended cylindrical indenters. Numerical results were presented, and guidelines were suggested for the proper choice of approximate layer thickness and substrate elastic properties to determine the elastic constants of the layer within certain predetermined accuracy by using the indentation test.

The following comments may be offered in conclusion:

1. For a given minimum film thickness and a given substrate stiffness, the elastic constants of the film may be determined within a calculated accuracy for the cases when the film is perfectly bonded to or in frictionless contact with the substrate. Conversely, if a given accuracy is desired, the required substrate stiffness for a given film thickness or the required minimum film thickness for a given substrate stiffness may be calculated.

2. In presenting the effect of film thickness on indenter load, the film thickness h should be normalized with respect to the Hertz radius a_H of the contact area for the homogeneous half-space instead of normalizing it with respect to the actual radius a of contact area for the composite. The reasons for this are: the value a is not a readily measured quantity because of its dependence on the film thickness and the elastic constants of each component of the composite, whereas a_H can be obtained simply by knowing the penetration depth and the indenter geometry.

3. When $h/a \geq 4$, the load vs film thickness for the composite depends on the film/substrate stiffness ratio and it is not the same as for the homogeneous half-space as suggested elsewhere [12].

4. The p/p_1 vs h/a_H relationships for three different shapes of indenters—conical, spherical, and flat-ended cylindrical—are quite similar despite the large differences in values of p and p_1 for the different indenters.

5. It should be pointed out that this analytical approach is directly applicable to problems in other engineering disciplines such as, for example, the design of large columns on elastic foundations.

REFERENCES

1. R.W. Armstrong and W.H. Robinson, *N.Z. J. Sci.* **17**, 429 (1974).

2. R.W. Armstrong and W.H. Robinson, *J. Mater. Sci.* **10**, 1655 (1975).

3. H.Y. Yu, M.A. Imam, and B.B. Rath, *J. Mater. Sci.* **20**, 636 (1985).

4. M.F. Doerner and W.D. Dix, *J. Mater. Res.* **1**, 601 (1986).

5. J.W. Harding and I.N. Sneddon, *Proc. Cambridge Philos. Soc.* **41**, 16 (1945).

6. I.N. Sneddon, *Int. J. Eng. Sci.* 3, 47 (1965)

7. R. Muki, *Progress in Solid Mechanics* (North Holland Co., 1960), Vol. 1.

8. N.N Lebedev and I.S. Ufliand, *PPM* 22, 320 (1958).

9. T.S Wu and Y.P. Chiu, *Q. Appl. Math* 25, 233 (1967).

10. R. Dhaliwal, *Int. J. Eng. Sci.* 8, 273 (1970).

11. R. Dhaliwal and I. Rau, *Int. J. Eng. Sci.*, 8, 483 (1970).

12. W.T. Chen and P.A. Engel, *Int. J. Solids Structures* 8, 1257 (1972).

13. S.E. El-gendi, *Computer J.* 12, 282 (1969).

Appendix A

DETERMINATION OF THE FUNCTION $g(\lambda)$

THE PERFECTLY BONDED CASE

When the elastic layer is perfectly bonded to the elastic half-space (substrate), the boundary conditions at the interface $z = h$ are given by Eq. (8). By substituting Eqs. (1) and (2) into Eq. (8), the following simultaneous linear equations of the functions $A_i(\lambda)$, $(i = 1, 2, \ldots, 6)$ can be obtained:

$$w \operatorname{cth} w A_1 + w A_2 + A_3 + \operatorname{cth} w A_4 - \beta w A_5 - \beta A_6 = 0,$$

$$(k_1 \operatorname{cth} w - w)A_1 + (k_1 - w \operatorname{cth} w)A_2 - \operatorname{cth} w A_3 - A_4$$

$$- \beta(k_2 + w)A_5 - \beta A_6 = 0,$$

$$[2(1 - \nu_1) - w \operatorname{cth} w] A_1 + [2(1 - \nu_1) \operatorname{cth} w - w]A_2 - A_3 - \operatorname{cth} w A_4 \qquad \text{(A1)}$$

$$+ [2(1 - \nu_2) + w] A_5 + A_6 = 0,$$

$$[w - (1 - 2\nu_1) \operatorname{cth} w] A_1 + [w \operatorname{cth} w - (1 - 2\nu_1)] A_2 + \operatorname{cth} w A_3 + A_4$$

$$+ [(1 - 2\nu_2) + w] A_5 + A_6 = 0,$$

where $\beta = \mu_1/\mu_2$ and $w = \lambda h$. By solving Eqs. (4.3), (5), and (A1), the function $g(\lambda)$ for the perfectly bonded condition can be expressed as:

$$g(\lambda) = 1 - \frac{(B_1 + B_2 w + B_3 \operatorname{sh}^2 w)\, e^{-w} + (B_4 + B_5 w + B_6 \operatorname{sh}^2 w) \operatorname{sh} w}{(C_1 + C_2 w^2 + C_3 \operatorname{sh}^2 w)e^{-w} + (C_4 + C_5 w^2 + B_6 \operatorname{sh}^2 w) \operatorname{sh} w}, \qquad \text{(A2)}$$

where

$$B_1 = 4a_1 a_2 (1 + b_2\beta)\beta,$$

$$B_2 = -1 - 3b_2\beta + (k_2 - 2b_2^2)\beta^2 + b_2 k_2 \beta^3,$$

$$B_3 = 2a_2(1 + 2k_1 + 2b_2 k_1 \beta + k_2\beta^2)\beta,$$

$$B_4 = k_1 + (-b_2 + 2b_2 k_1 + 4a_1 a_2)\beta + (k_1 + 4a_1 a_2 k_2 + 2b_1 b_2^2)\beta^2 + b_2 k_2 \beta^3,$$

$$B_5 = -1-(1 + 4b_2)\beta + (1 - 2b_2)k_2\beta^2 + k_2^2\beta^3,$$

$$B_6 = k_1 + (1 + 2k_1k_2)\beta + (k_2 + 4a_2b_2k_1 + 16a_1a_2^2 + 2b_1b_2^2)\beta^2 + k_2^2\beta^3,$$

$$C_1 = 4a_1^2(1 + b_2\beta),$$

$$C_2 = 1 + 3b_2\beta - (k_2 - 2b_2^2)\beta^2 - b_2k_2\beta^3, \tag{A3}$$

$$C_3 = k_1 - (1 - 2k_1)b_2\beta + (k_2 + 16a_1a_2^2 + 2b_1b_2^2)\beta^2 + b_2k_2\beta^3,$$

$$C_4 = 4a_1^2 + 4a_1(2a_2 + a_1k_2)\beta - 8a_1a_2b_2\beta^2,$$

$$C_5 = 1 + (k_2 + 2b_2)\beta - (1 - 2b_2)k_2\beta^2 - k_2^2\beta^3,$$

and

$$a_1 = 1 - \nu_1,\ a_2 = 1 - \nu_2,\ b_1 = 1 - 2\nu_1,\ b_2 = 1 - 2\nu_2,\ k_1 = 3 - 4\nu_1, \text{ and } k_2 = 3 - 4\nu_2.$$

For the homogeneous half-space consisting of layer material, i.e., $h \to \infty$, Eq. (A2) gives $g(\lambda) = 0$. Then by Eq. (20) we have $k(u) = 0$ and Eq. (6) becomes

$$\begin{aligned} &\int_0^\infty M(\lambda)J_0(\lambda r)\,d\lambda = f(r) && (0 \le r \le a), \\ &\int_0^\infty \lambda M(\lambda)J_0(\lambda r)\,d\lambda = 0 && (a < r < \infty), \end{aligned} \tag{A4}$$

and Eqs. (17) and (19) give an explicit expression for the function $H(\tau)$, namely

$$H(\tau) = F_0(\tau) = 1 - \frac{\delta(0)}{d} - \frac{\tau}{d}\int_0^{\frac{\pi}{2}} \delta'(\tau \sin\theta)d\theta. \tag{A5}$$

This result is the same as those obtained by many authors [A1] for the homogeneous half-space. On the other hand, when $h \to 0$, i.e., a homogeneous half-space with elastic constants μ_2 and ν_2, Eq. (A2) gives

$$g(\lambda) = 1 - \eta, \tag{A6}$$

where

$$\eta = \frac{(1 - \nu_2)\mu_1}{(1 - \nu_1)\mu_2}. \tag{A7}$$

Substituting Eq. (A6) into Eq. (6) gives

$$\int_0^\infty M^*(\lambda)J_0(\lambda r)\,d\lambda = f(r)/\eta \qquad (0 \le r \le a),$$

and

$$\int_0^\infty \lambda M^*(\lambda) J_0(\lambda r)\, d\lambda = 0 \qquad (a < r < \infty), \tag{A8}$$

where

$$M^*(\lambda) = M(\lambda)/\eta.$$

By using Eq. (A7) for η and Eq. (7) for $f(r)$, Eq. (A8) assumes the same form as Eq. (A4) for the homogeneous half-space with elastic constants μ_2 and ν_2.

THE SMOOTH CONTACT CASE

When the elastic layer is in smooth (frictionless) contact with the surface of the elastic substrate, the simultaneous linear equations of the functions $A_i(\lambda)$, $(i = 1, 2, \ldots, 6)$ can be obtained by substituting Eqs. (1) and (2) into Eq. (9), thus

$$(k_1 \operatorname{cth} w - w) A_1 + (k_1 - w \operatorname{cth} w) A_2 - \operatorname{cth} w\, A_3 - A_4 - \beta(k_2 + w) A_5 - \beta A_6 = 0,$$

$$[2(1 - \nu_1) - w \operatorname{cth} w] A_1 + [2(1 - \nu_1) \operatorname{cth} w - w] A_2 - A_3 - \operatorname{cth} w\, A_4$$

$$+ [2(1 - \nu_2) + w] A_5 + A_6 = 0, \tag{A9}$$

$$[w - (1 - 2\nu_1) \operatorname{cth} w] A_1 + [w \operatorname{cth} w - (1 - 2\nu_1)] A_2 + \operatorname{cth} w\, A_3 + A_4 = 0,$$

$$[(1 - 2\nu_2) + w] A_5 + A_6 = 0.$$

Equations (4.3) and (A9) give

$$g(\lambda) = 1 - \frac{\operatorname{sh}^2 w + \eta (w + \operatorname{sh} w \operatorname{ch} w)}{w + \operatorname{sh} w \operatorname{ch} w + \eta (\operatorname{sh}^2 w - w^2)}. \tag{A10}$$

For the homogeneous half-space, Eq. (A10) gives

$$g(\lambda) = 0 \qquad h \to \infty$$

and

$$g(\lambda) = 1 - \eta \qquad h \to 0,$$

which are the same as for the case when the layer is perfectly bonded to the substrate.

REFERENCES

A1. T.S. Wu and Y.P. Chin, *Q. Appl. Math.* 25, 233 (1967).

Appendix B

COMPARISON OF NUMERICAL RESULTS

The following tables list some of the numerical results obtained by the authors and those given by other authors [B1-B3]. Tables B1 and B2 show the numerical values of the kernel $K(u)$ and function $H(\tau)$, respectively, for a flat-ended cylindrical indenter on a layer that is in smooth contact to a rigid substrate. In these two tables, the data on the second and the fourth columns are obtained by the present analysis and data on the first and the third columns are those listed on the first and the fourth columns of Tables I and II of Lebedev and Ufliand paper [B1]. The agreement among these data shows that we can reproduce their results in this special case.

Table B3 shows our values and those of Dhaliwal's [B2] (the first and the last columns on Table 2 for $\beta = 0$ and 0.25 in Ref. B2) for the Kernel $K(u)$ for a flat-ended cylindrical indenter on a layer that is perfectly bonded to an elastic half-space. The good agreement between these results provided a check of our formulation of the function $g(w)$ for the perfectly bonded condition, which is rather complicated to check otherwise. However, by using the same set of values of the kernel $K(u)$ shown in Table B3, we cannot reproduce Dhaliwal's results for the $H(\tau)$ values. These two sets of data are compared in Table B4. In some cases (e.g., $h/a = 0.25$), there are order of magnitude differences. Chen and Engel [B3] have pointed out that they could not reproduce all of Dhaliwal's results.

Table B1 — Numerical Value of the Kernel $K(u)$ for a Flat-Ended Cylindrical Indenter on a Film in Smooth Contact with a Rigid Half-Space.

u	$h/a = 2.0$		$h/a = 0.5$	
	LU[a]	YSR[b]	LU	YSR
0.0	0.5837	0.58379	2.3349	2.33515
0.2	0.5798	0.57985	2.0990	2.09873
0.4	0.5682	0.56824	1.5513	1.55130
0.6	0.5496	0.54955	0.9875	0.98751
0.8	0.5248	0.52468	0.5753	0.57516
1.0	0.4948	0.49479	0.3279	0.32805
1.2	0.4612	0.46114	0.1962	0.19621
1.4	0.4251	0.42507	0.1291	0.12908
1.6	0.3878	0.38783	0.0939	0.09396
1.8	0.3505	0.35053	0.0737	0.07367
2.0	0.3141	0.31414	0.0602	0.06029

[a] Results from Lebedev and Ufliand [B1]
[b] Results from present report

Table B2 — Numerical Value of the Function $H(\tau)$ for a Flat-Ended Cylindrical Indenter on a Film in Smooth Contact with a Rigid Half-Space

τ	$h/a = 2.0$		$h/a = 0.5$	
	LU[a]	YSR[b]	LU	YSR
0.0	1.530	1.5305	4.321	4.3303
0.1	1.529	1.5297	4.303	4.3111
0.2	1.527	1.5274	4.246	4.2584
0.3	1.523	1.5236	4.153	4.1680
0.4	1.518	1.5183	4.022	4.0382
0.5	1.511	1.5116	3.854	3.8693
0.6	1.503	1.5036	3.650	3.6642
0.7	1.494	1.4943	3.416	3.4277
0.8	1.484	1.4839	3.157	3.1671
0.9	1.472	1.4723	2.884	2.8919
1.0	1.460	1.4598	2.608	2.6138

[a] Results from Lebedev and Ufliand [B1].
[b] Results from present report.

Table B3 — Numerical Value of the Kernel $K(u)$ for a Flat-Ended Cylindrical Indenter on a Film Perfectly Bonded to an Elastic Half-Space

$\nu_1 = 0.333$, $\nu_2 = 0.250$					
β	u	$h/a = 3.0$		$h/a = 0.25$	
		Dha[a]	YSR[b]	Dha	YSR
0.00	0.0	−0.150197	−0.150197	−1.802363	−1.80236
	0.2	−0.149575	−0.149575	−1.028806	−1.02881
	0.4	−0.147729	−0.147729	−0.278302	−0.278302
	0.6	−0.144714	−0.144714	−0.085151	−0.085151
	0.8	−0.140617	−0.140617	−0.044783	−0.044783
	1.0	−0.135556	−0.135556	−0.028933	−0.028933
	1.2	−0.129669	−0.129670	−0.020056	−0.020056
	1.4	−0.123110	−0.123110	−0.014720	−0.014720
	1.6	−0.116038	−0.116038	−0.011301	−0.011301
	1.8	−0.108616	−0.108616	−0.008969	−0.008969
	2.0	−0.100997	−0.100997	−0.007297	−0.007298
0.25	0.0	−0.106266	−0.106559	−1.275187	−1.27871
	0.2	−0.105844	−0.106137	−0.746888	−0.749318
	0.4	−0.104594	−0.104885	−0.213979	−0.214720
	0.6	−0.102551	−0.102838	−0.062722	−0.062538
	0.8	−0.099773	−0.100055	−0.029314	−0.028821
	1.0	−0.096338	−0.096613	−0.018148	−0.017619
	1.2	−0.092337	−0.092604	−0.012580	−0.012105
	1.4	−0.087871	−0.088129	−0.009338	−0.008939
	1.6	−0.083047	−0.083296	−0.007270	−0.006942
	1.8	−0.077073	−0.078211	−0.005849	−0.005581
	2.0	−0.072751	−0.072978	−0.004818	−0.004597

[a] Results from Dhaliwal [B2].
[b] Results from present report.

Table B4 — Numerical Value of the Function $H(\tau)$ for a Flat-Ended Cylindrical Indenter on a Film Perfectly Bonded to a Elastic Half-Space.

$\nu_1 = 0.333$, $\nu_2 = 0.250$					
β	τ	$h/a = 3.0$		$h/a = 0.25$	
		Dha[a]	YSR[b]	Dha	YSR
0.00	0.0	1.461578	1.40430	119.6635	10.7832
	0.1	1.461143	1.40392	114.7609	10.7302
	0.2	1.459840	1.40277	103.0672	10.5697
	0.3	1.457678	1.40087	89.7998	10.2972
	0.4	1.454671	1.39823	77.4355	9.90395
	0.5	1.450839	1.39486	67.27787	9.37582
	0.6	1.446208	1.39079	57.93688	8.69071
	0.7	1.440806	1.38604	49.18944	7.81816
	0.8	1.434670	1.38065	40.61215	6.73197
	0.9	1.427838	1.37464	31.97879	5.45602
	1.0	1.420351	1.36806	23.50496	4.12980
0.25	0.0	1.289450	1.25805	4.120174	3.03548
	0.1	1.289188	1.25781	4.025767	3.03001
	0.2	1.288405	1.25711	3.806495	3.01305
	0.3	1.287105	1.25595	3.570212	2.98279
	0.4	1.285298	1.25434	3.368143	2.93574
	0.5	1.282993	1.25228	3.197656	2.86600
	0.6	1.280207	1.24978	3.036678	2.76393
	0.7	1.276957	1.24688	2.860609	2.61524
	0.8	1.273263	1.24358	2.644312	2.40384
	0.9	1.269148	1.23990	2.368507	2.12545
	1.0	1.264636	1.23586	2.039119	1.80981

[a] Results from Dhaliwal [B2].
[b] Results from present report.

Table B5 gives both Chen and Engel's results (Table II in Ref. B3) and our results for the values p^* and d^* for a spherical indenter ($a << R$) on a layer that is in smooth contact with an elastic half-space ($b = 0.1$, $\nu_1 = \nu_2 = 0.3$). The agreement between these two sets of results in excellent only at large h/a values. The reason for the discrepancy at low h/a values is believed to be due to the approximation method used by Chen and Engel. In their analysis, they introduce a "perturbing term" in the expression of the contact pressure. Our comment is that when the elastic properties of the substrate are quite different from that of the layer, or the layer becomes thin enough, then the difference between the contact pressure for the composite and those for the corresponding homogeneous half-space is large enough such that the perturbation approach is no longer appropriate.

It seems to us that the nondimensional quantities p^* and δ^* defined by Chen and Engel [B3] are quite ambiguous. According to their definitions, the p^* and the δ^* can be written as

$$p^* = \frac{p}{p_1}\left(\frac{1}{\gamma_3}\right)^3 , \tag{B1}$$

Table B-5 — Numerical Value of the Parameter p^* and δ^* for a Spherical Indenter on a Film in Smooth Contact with and Elastic Half Space

$\beta = 10.0,\ \nu_1 = \nu_2 = 1/3$				
h/a	p^*		δ^*	
	CE[a]	YSR[b]	CE	YSR
∞	1.0000	1.0000	1.0000	1.0000
16.0	1.0001	1.0001	0.9669	0.9669
8.0	1.0009	1.0009	0.9345	0.9345
4.0	1.0070	1.0070	0.8746	0.8746
2.0	1.0469	1.0469	0.7815	0.7815
1.5	1.0954	1.0954	0.7389	0.7389
1.0	1.2310	1.2309	0.6868	0.6868
0.6	1.5675	1.5680	0.6479	0.6479
0.4	1.9975	1.9971	0.6406	0.6405
0.3	2.3968	2.3960	0.6466	0.6563
0.2	3.0804	3.0846	0.6672	0.6677
0.15	3.6341	3.6485	0.6880	0.6897
0.1	4.4894	4.5130	0.7246	0.7232
0.0	10.0000	10.0000	1.0000	1.0000

[a] Results from Chen and Engel [B3].
[b] Results from present report.
$p^* = p/(p_1\gamma_s^3)$
$\delta^* = a/\gamma_s^2$

and

$$\delta^* = \frac{a}{\gamma_s^2}. \tag{B2}$$

In these expressions, it is clearly seen that p^* is not the load on the indenter for the composite normalized with respect to the corresponding load for the homogeneous half-space, neither it is equal to a_H/a as they claim. The δ^* value presented is not appropriate either because they set a equal to one, which is not correct since, as mentioned previously, the radius of the contact area is not a constant but is a function of the shape of the indenter, the penetration depth, the layer thickness, and the elastic constants of both the layer and the substrate.

REFERENCES

B1. N.N. Lebedev and I.S. Ufliand, *PPM* **22**, 320 (1958).

B2. R. Dhaliwal, *Int. J. Eng. Sci.* **8**, 273 (1970).

B3. W.T. Chen and P.A. Engel, *Int. J. Solids Structures* **8**, 1257 (1972).

APPENDIX VIII

Surface and Coatings Technology, 36 (1988) 61 - 74

VOID FORMATION AND SUPPRESSION DURING HIGH TEMPERATURE OXIDATION OF MCrAlY-TYPE COATINGS*

V. PROVENZANO, K. SADANANDA, N. P. LOUAT** and J. R. REED

Materials Science and Technology Division, Naval Research Laboratory, Washington DC 20375-5000 (U.S.A.)

(Received April 13, 1988)

Summary

Oxidation studies have been conducted on cast Co–22Cr–11Al (CoCrAl) coating alloy in air at temperatures between 700 and 1000 °C. To investigate the role of oxygen-active element additions on the oxidation behavior of the MCrAlY-type coatings, some of the CoCrAl specimens were ion implanted with either yttrium, hafnium or cobalt prior to oxidation. The oxidized specimens were subsequently examined by various electron optical techniques including scanning transmission electron microscopy and electron microprobe analysis.

It was observed that voids formed in the coating alloy at the metal–oxide interface during oxidation. The average size and density of these interfacial voids were dependent on temperature and time. Ion-implanted yttrium or hafnium greatly reduced the rate of void growth for all experimental conditions; cobalt implantation had little effect. This behavior is explained by a vacancy kinetic model which involves the preferential diffusion of either metal or oxygen ions through the growing oxide scale. The results of the present study have significant implications concerning the oxidation kinetics and the adherence of the oxide scale to the coating alloy.

1. Introduction

Small amounts of rare earth metals ("oxygen-active" elements) such as yttrium, hafnium or cerium are known to improve the oxidation resistance of the MCrAlY-type coating alloys (where M ≡ Co, Ni or Fe). In the past, various mechanisms have been proposed to explain the beneficial effect of the oxygen-active element. Whittle and coworkers [1, 2] and Pettit and

*Paper presented at the 15th International Conference on Metallurgical Coatings, San Diego, CA, U.S.A., April 11 - 15, 1988.

**On site contract employee with Geo-Centers, Inc., 10903 Indian Head Highway, Fort Washington, MD 20744, U.S.A.

0257-8972/88/$3.50

© Elsevier Sequoia/Printed in The Netherlands

coworkers [3, 4] proposed a model of mechanical keying due to the formation of oxide pegs rich in active elements, the role of these pegs being to anchor the oxide scale to the coating alloy. Other mechanisms include the prevention of vacancy coalescence at the scale–metal interface by providing alternative sites for vacancy sinks [5], the enhancement of oxide scale plasticity [6], the modification of the oxide scale growth process [7], the formation of graded oxide [8] and, more recently, the segregation of sulfur at the metal–oxide interface [9, 10]. In the latter mechanism it is assumed that the MCrAlY-type coatings contain sulfur as an inherent impurity and that sulfur tends to segregate at the metal–oxide interface during oxidation. This segregation is supposed to weaken the bond between the metal coating and the oxide scale leading to poor oxide adherence and eventual spallation. In this model, the active elements in the coating alloy act as scavengers and trap any sulfur impurity present, preventing its segregation at, and consequent degradation of, the metal–oxide interface.

In considering these models it is noted, in regard to oxide pegging, that several studies have reported very adherent oxide scale in the absence of oxide pegs. In addition, no conclusive evidence has been advanced to show that the presence of an oxygen-active element in the coating alloy increases the plasticity of the oxide scale or that it leads to the formation of a graded oxide. However, the vacancy-sink model remains a postulate.

With reference to the model proposed by Smeggil and coworkers [9, 10], the following observations can be made. Thermodynamic considerations would suggest the formation of yttria rather than yttrium sulfides, because yttria has a much higher negative free energy of formation than the sulfides; -449 kcal mol^{-1} for yttria compared with -29 kcal mol^{-1} for yttrium sulfide at room temperature. Furthermore, it can be expected that, in the circumstances involved in this study, the activity of oxygen will exceed that of sulfur. These expectations are supported by direct microchemical analysis conducted by Ramanaryanan *et al.* [11].

The present research effort is the continuation of a previous oxidation study conducted by Sprague *et al.* [12, 13] using the same cast CoCrAl alloy. The present results show that the formation of voids at the metal–oxide scale interface during high temperature oxidation is greatly inhibited by the presence of rare earth elements. This behavior follows as a natural consequence of the vastly different rates of diffusion of metal (cation) and oxygen (anion) atoms through the rare earth oxides. Thus, by virtue of the large energies of formation of these oxides, it is to be expected that during the first stages of the oxidation process the rare earth ions will tend to migrate and segregate at the surface. This view is supported by the results of Luthra and Briant [14] who found evidence for such segregation from Auger electron spectroscopy and by those of Aprigliano [15]. Here the important consequence of this activity is the formation of an oxide rich in yttria which is expected to act as a barrier to the diffusion of metal ions and the concomitant flux of vacancies. A reduction in this flux implies a reduction in the rate of void formation.

2. Experimental details

2.1. Coating alloy

The composition (wt.%) of the cast alloy used in this study was Co–22Cr–11Al (from now on the alloy will be referred to as CoCrAl alloy). This alloy was prepared by arc melting in a purified argon atmosphere and by drop casting into a chilled copper mold. The ingot was subsequently annealed for 100 h at 1100 °C in argon and furnace cooled. The microstructure of the cast CoCrAl consisted mainly of a β-CoAl matrix phase and an α-Co solid solution phase. Additional details about the alloy microstructure are given elsewhere [12, 13].

2.2. Specimen preparation and ion implantation

After heat treatment, the cast CoCrAl specimens were cut into coupons of approximately 10mm × 10 mm × 2 mm. One surface of each specimen was polished with diamond powder to a 0.5 μm finish. Some of the specimens were ion implanted at the Naval Research Laboratory High Current Ion Implantation Facility with either yttrium, hafnium or cobalt to doses of $(2 - 5) \times 10^{16}$ ions cm^{-2}. These doses correspond to 4 - 5 wt.% of the implanted species. The cobalt ions were used to determine possible effects produced by the physical changes in the near-surface region of the alloys resulting from the ion implantation process.

Ion implantation was used as a tool to obtain a uniform distribution of rare earth elements in the near-surface region of the coating alloy specimens. To allow direct comparison of the oxidation response of implanted and non-implanted CoCrAl, the specimens were masked (approximately 50%) during ion implantation.

2.3. Oxidation exposure and microstructural analysis

Oxidation experiments were performed in dry air at temperatures in the range 700 - 1000 °C for exposure times varying between 3 and 1140 min. To minimize heat-up and cool-down times, the samples were rapidly inserted into and withdrawn from a preheated horizontal tube furnace.

The specimens, both before and after oxidation exposures, were examined by various electron optical techniques which included scanning transmission electron microscopy (STEM) and scanning electron microscopy (SEM) with energy-dispersive X-ray spectroscopy (EDS).

3. Results

3.1. Microstructure of cast CoCrAl alloy

Heat treatment of the cast CoCrAl for 100 h at 1100 °C in vacuum produced a microstructure consisting of an ordered cubic matrix phase of β-CoAl together with an α-Co solid solution phase (Fig. 1). From thin film EDS analysis the compositions in weight percent of the β and α phases are

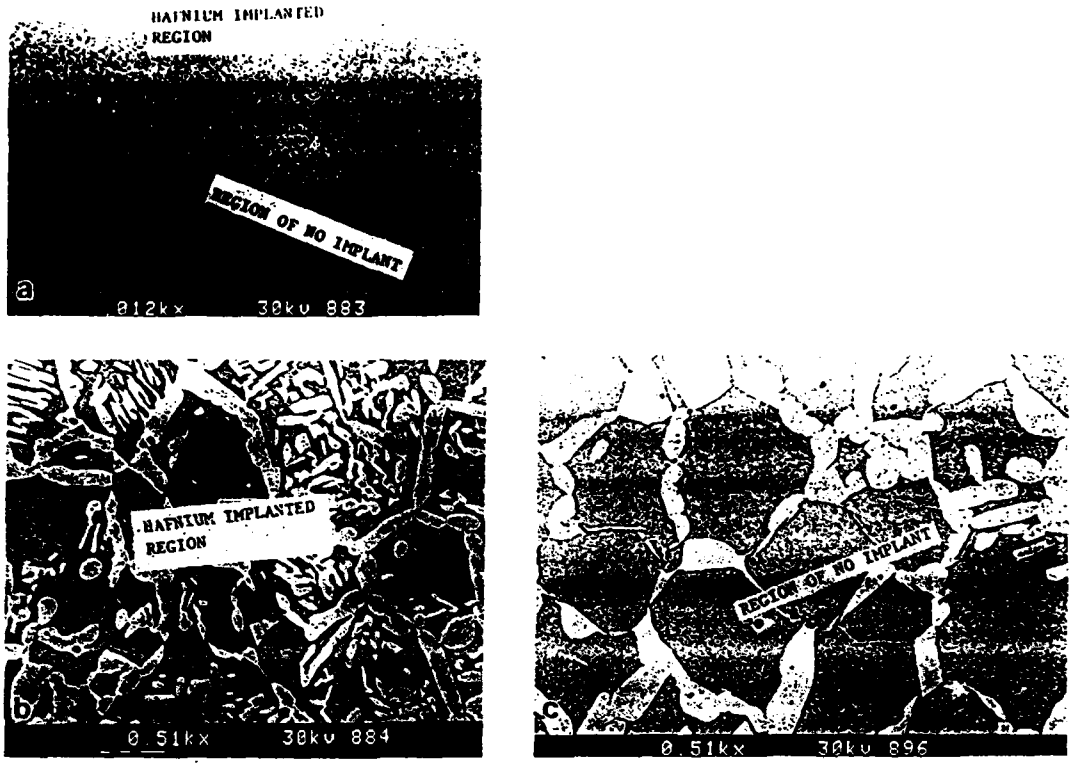


Fig. 1. Scanning electron micrographs of a cast CoCrAl specimen partially implanted with hafnium: (a) low magnification; (b) hafnium-implanted region; (c) unimplanted region.

Co–14Cr–25Al and Co–28Cr–7Al respectively. The α phase forms a network separating the β-phase grains. Figures 1(b) and 1(c) show the effect of ion implantation on the microstructure of cast CoCrAl; Fig. 1(b) corresponds to the region of the specimen surface that had been ion implanted with hafnium and Fig. 1(c) corresponds to the region that had been masked and thus had not been implanted. These two micrographs show that, before oxidation, there is no significant difference between the implanted and non-implanted surfaces.

The scanning electron micrographs presented in Fig. 2 were taken from a non-implanted alloy specimen that had been oxidized in air for 3 min at 700 °C. The micrographs show the presence of voids in the α phase with a greater concentration of voids along the α–β phase boundaries. In addition, no voids are visible in the β-CoAl matrix phase. The same behavior was noted for all oxidation times used in the study. It is known from previous oxidation studies [12, 13] that voids generally form at the metal–oxide scale interface during the oxidation process. In contrast with these results, Sprague *et al.* [12, 13] reported interfacial voids in the β phase and along the α-β phase boundary but not in the α phase. The difference between the two results is probably due to differing oxidation conditions. In accord with



Fig. 2. Secondary electron micrographs of a cast CoCrAl specimen after 3 min of oxidation at 700 °C: (a) low magnification; (b) high magnification. Kirkendall-type voids formed during oxidation in the α phase close to the phase boundary but not in the β-AlCo matrix phase.

this hypothesis it is shown later that void formation is a function of both oxidizing temperature and exposure time.

Figure 3 shows a summary of the oxidation results obtained on the cast CoCrAl alloy oxidized for 3 min at four different temperatures (700, 800, 900 and 1000 °C). From these results the following important observations can be made: (1) raising the temperature from 700 to 800 °C for the same oxidation time results in the formation of interfacial voids both in the α and β phases and at the phase boundary; (2) for the same exposure time, the average void size in both phases increases with increasing temperature (Figs. 4(b) and 4(c)); (3) a further increase in the temperature to 1000 °C causes the spallation of the oxide scale owing to the high density of voids in the α phase (Fig. 4(b)).

The scanning electron micrograph and the corresponding X-ray spectra shown in Fig. 4 provide some important insights into the kinetics of oxide formation on the CoCrAl-type coating alloys. These were taken from the surface of a specimen oxidized for 3 min at 1000 °C. The spectrum given in Fig. 4(b) shows that the oxide scale formed over the α phase is mostly composed of chromium oxide with decreasing amounts of cobalt and aluminum oxides. Conversely, the oxide scale formed over the β phase has less chromium oxide but more cobalt and aluminum oxides (Fig. 4(d)). Also of interest is a comparison of X-ray spectra shown in Figs. 4(b) and 4(c). The spectrum in Fig. 4(c) was taken from a region of the specimen surface where the oxide scale formed over the α phase had partially spalled off. When this spectrum is compared with the spectrum in Fig. 4(b) it can be seen that there is more aluminum and cobalt and less chromium in the unspalled oxide than in the region of the oxide subject to spallation. In addition, in contrast with the findings of Smeggil *et al.* [10], closer examina-

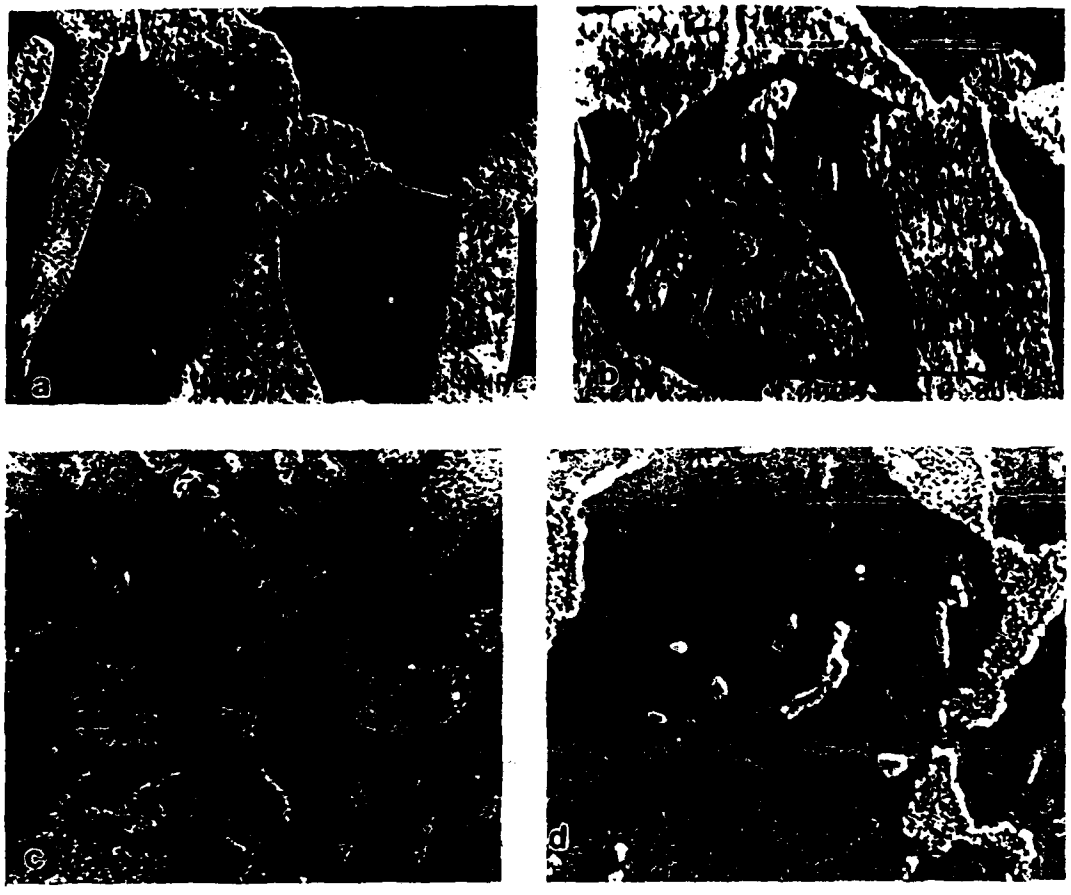


Fig. 3. Secondary electron micrographs of cast CoCrAl specimens after 3 min of oxidation at various temperatures: (a) specimen oxidized at 700 °C; (b) specimen oxidized at 800 °C; (c) specimen oxidized at 900 °C; (d) specimen oxidized at 1000 °C. Kirkendall-type voids formed at the metal–oxide interface during the oxidation exposures; the average size of the voids increased with temperature.

tion of the oxidized surface (Fig. 4(a)) shows that the oxide formed over the α phase is thicker than the oxide formed over the β phase.

Figure 5 illustrates the oxidation behavior of the cast CoCrAl alloy that had been ion implanted with either yttrium or cobalt prior to the exposure to the oxidizing environment; Figs. 6 and 7 illustrate the behavior of the alloy ion implanted with hafnium. For the 50 min exposure at 700 °C, panels shown in Figs. 5(a) and 5(c) clearly demonstrate that the presence of yttrium greatly suppressed the formation and growth of interfacial voids. Ion implantation of cobalt (Fig. 5(d)) did not suppress void growth, but it did affect the average size and the number of voids per unit area when compared with unimplanted CoCrAl (Fig. 5(b)). This latter comparison suggests that void formation and growth is only slightly affected by the physical damage produced on the surface of the alloy by the ion implantation process and/or by the enrichment of cobalt in the near-surface region

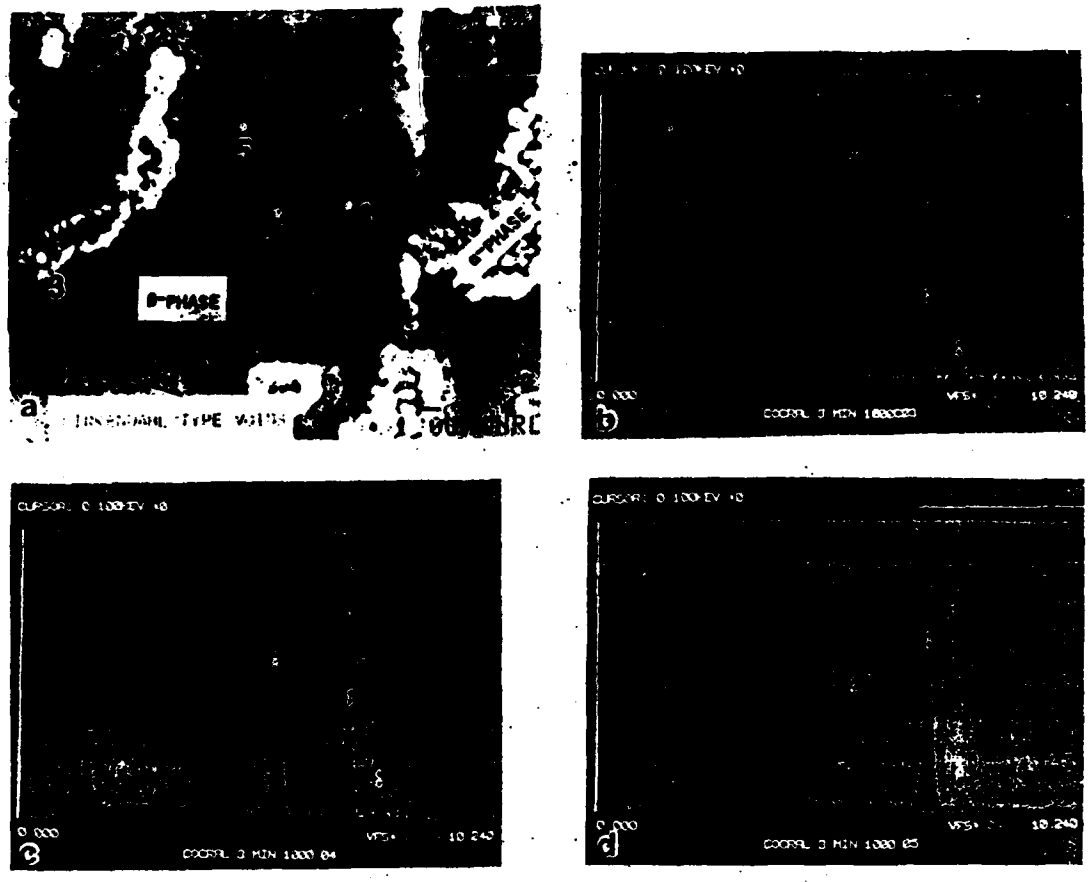


Fig. 4. Secondary electron micrograph and energy-dispersive X-ray spectra of a cast CoCrAl specimen after 3 min of oxidation at 1000 °C. Kirkendall-type voids formed at the metal–oxide interface in both α and β phases; energy-dispersive X-ray spectra show the relative concentrations of cobalt, chromium and aluminum in three different areas.

Ion implanting cast CoCrAl with hafnium and subsequent exposure in air at 700 °C for 1 h resulted in a significant suppression of void formation (Figs. 6(c) and 6(d)). However, the scanning electron micrographs in Fig. 7 show that the presence of hafnium was not as effective in suppressing void formation when the temperature was raised to 900 °C.

3.2. Discussion of results

It is known that the formation and growth of voids at the metal–oxide interface during high temperature oxidation of cast CoCrAl coating is associated with a Kirkendall-type mechanism. This mechanism involves a mass imbalance due to the rapid diffusion of the metal ions from the bulk alloy to the oxide–gas interface. This outward migration of the metal ions occurs first by diffusion through the alloy, followed by diffusion through the growing oxide scale. The removal of the metal ions results in the creation of cation vacancies at the oxide–gas interface. To counterbalance the mass

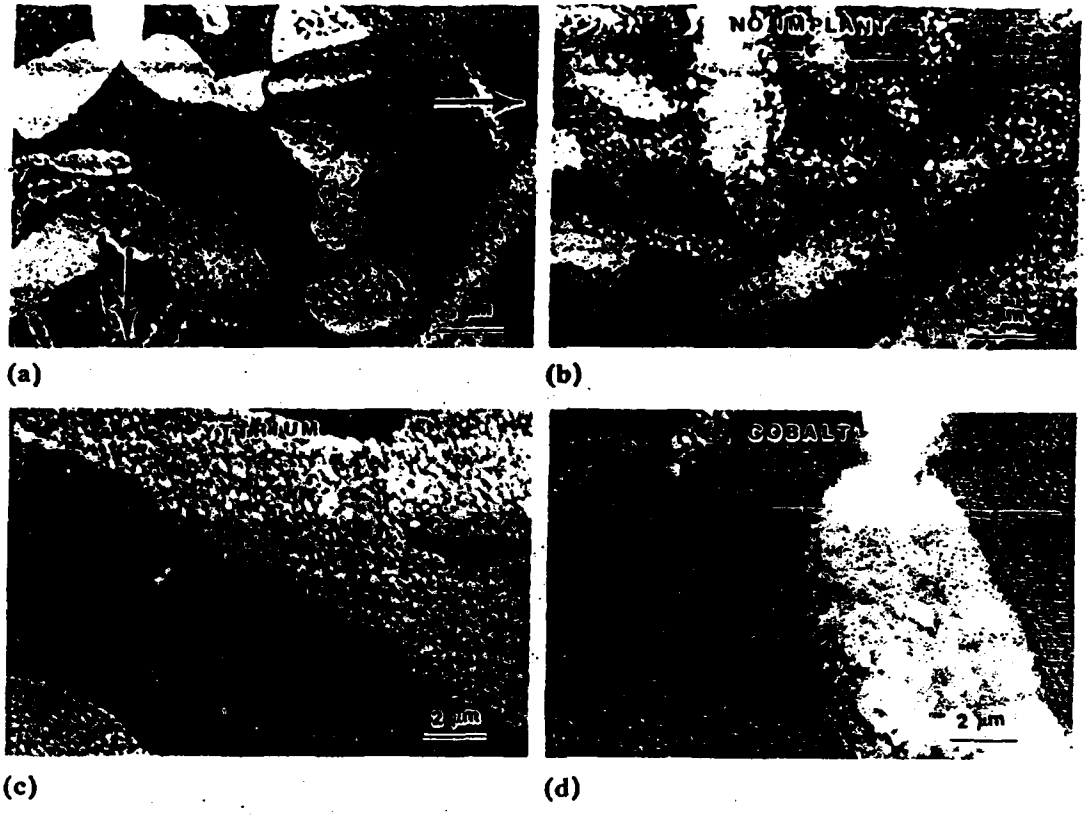


Fig. 5. Secondary electron micrographs of a cast CoCrAl specimen after 1 h of oxidation at 700 °C: (a) low magnification; (b) high magnification of unimplanted region; (c) high magnification of yttrium-implanted region; (d) high magnification of cobalt-implanted region. Micrographs show that Kirkendall-type voids formed on both the unimplanted and cobalt-implanted surfaces but not on the yttrium-implanted surface.

flow outwards, these vacancies diffuse inwards through the oxide scale to its interface with the metal, where, if their concentration exceeds the equilibrium concentration, they deposit. Thus, the interface acts as a vacancy sink, resulting in the formation and growth of interfacial voids. In this model oxide scale growth in the unimplanted alloy mainly proceeds by an outward diffusion of the metal ions rather than the inward diffusion of the oxygen ions through the oxide scale. An important consequence of void formation at the metal–oxide interface is that the adhesion strength of the oxide scale is significantly reduced. In this case the voids not only reduce the contact area between the oxide and metal coating but they also act as stress raisers since they behave somewhat like "penny-shaped" cracks at the interface.

This sequence of events is dependent on the preferential diffusion of the metal ions to the free surface (oxide–gas interface). This requires a faster diffusion of cobalt and chromium in their corresponding oxides than diffusion of oxygen in the same oxides. From the literature values presented in Table 1, it can be seen that the diffusion coefficients of cobalt in cobalt

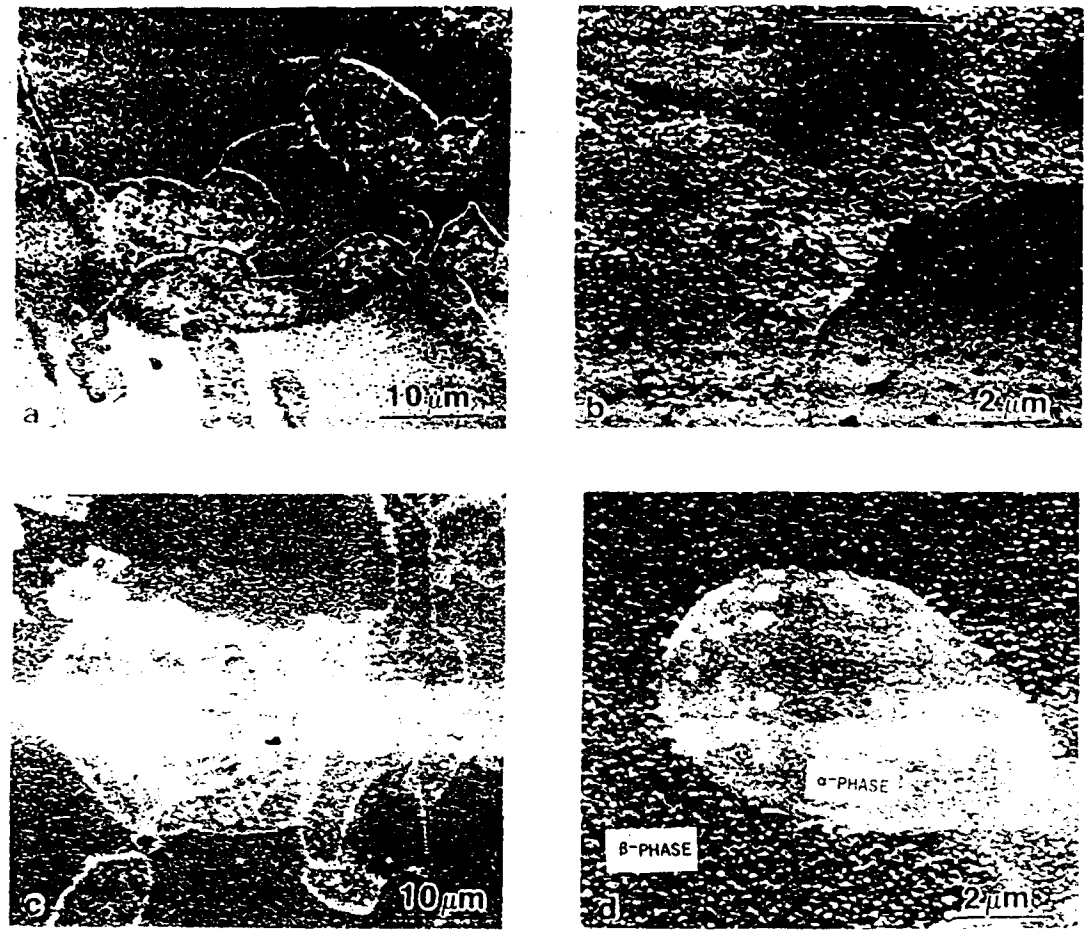


Fig. 6. Secondary electron micrographs of a cast CoCrAl specimen partially implanted with hafnium and then oxidized for 1 h at 700 °C: (a) and (b) unimplanted region, (c) and (d) hafnium-implanted region. Kirkendall-type voids formed on the unimplanted region, but they were largely suppressed on the hafnium-implanted region.

oxide (CoO) and chromium in chromia (Cr_2O_3), at both 1000 and 700 °C, are several orders of magnitude larger than the diffusion coefficient of oxygen in these oxides. In contrast, as reported in Table 1, the diffusion coefficients of aluminum and oxygen in alumina (Al_2O_3) are roughly equal at these two temperatures. As will be shown, these differences in diffusion rates of metal and oxygen ions in these three oxides affect the kinetics of interfacial void formation and growth.

Evidence supporting the hypothesis that interfacial void formation in the CoCrAl alloy is a thermally activated process involving the preferential diffusion of mainly cobalt and chromium at the free oxide surface (oxide-gas interface) is provided by the results presented in Fig. 8. The plot presented in Fig. 8 shows that for a given oxidation time, the void size increases with temperature. A value for the activation energy for void formation cannot simply be deduced from the slope of the line in Fig. 8 because of complexities in the void growth process, such as the [illegible]

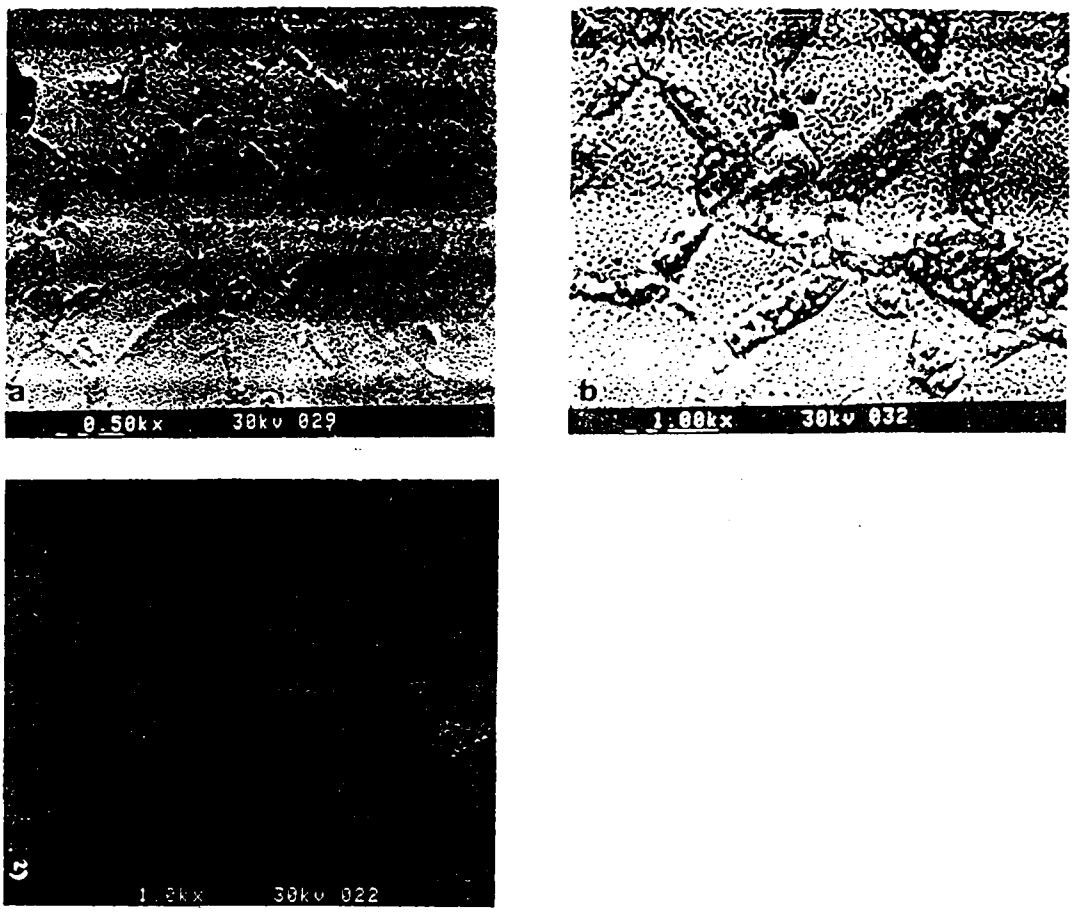


Fig. 7. Backscattered electron micrographs of a cast CoCrAl specimen partially implanted with hafnium and then oxidized for 1 h at 900 °C: (a) low magnification; (b) high magnification of the unimplanted region; (c) high magnification of the hafnium-implanted region. At this higher oxidation, hafnium implantation was not as effective in suppressing the interfacial voids.

creases with both exposure time and temperature, the number of voids per unit area decreases. This implies that smaller voids coalesce into larger voids as either the time or the temperature increase. Consequently, the evolution of void size with either time or temperature is not a simple process. The void formation model proposed above is shown schematically in Fig. 9.

Ion implanting the surface of CoCrAl specimens with either yttrium or hafnium greatly suppressed the formation of interfacial voids for all experimental conditions (Figs. 5 - 7). The following mechanism is proposed to account for these results. From Table 1, it can be observed that the coefficients of oxygen diffusion in yttria (Y_2O_3) at both 700 and 1000 °C are many orders of magnitude higher than yttrium in its oxide. Similarly, the diffusion coefficient of oxygen in hafnia (HfO_2) is much larger than the coefficient of hafnium in HfO_2. The behavior is the reverse of that observed in cobalt and chromium oxides. Owing to the lack of diffusion data in the

TABLE 1

Diffusion coefficients of metal (cation) and oxygen (anion) ions in pertinent oxides

Oxide	*Temperature* (°C)	*Coefficient of cation (metal) diffusion* ($cm^2\ s^{-1}$)	*Coefficient of anion (oxygen) diffusion* ($cm^2\ s^{-1}$)
Cobalt oxide (CoO)	700	4.3×10^{-11}	2.2×10^{-22}
	1000	2.8×10^{-9}	2.4×10^{-16}
Chromia (Cr_2O_3)	700	3.3×10^{-15}	4.6×10^{-22}
	1000	5×10^{-12}	9.4×10^{-17}
Alumina (Al_2O_3)	700	9.4×10^{-18}	1×10^{-17}
	1000		
Yttria (Y_2O_3)	700	6.1×10^{-18}	2.2×10^{-11}
	1000	2×10^{-14}	2.6×10^{-9}
Hafnia (HfO_2)	700	NA	NA
	1000	NA	NA
	1300	NA	5×10^{-7}
Ceria (CeO_2)	700	NA	1.5×10^{-9}
	1000	NA	2.8×10^{-8}

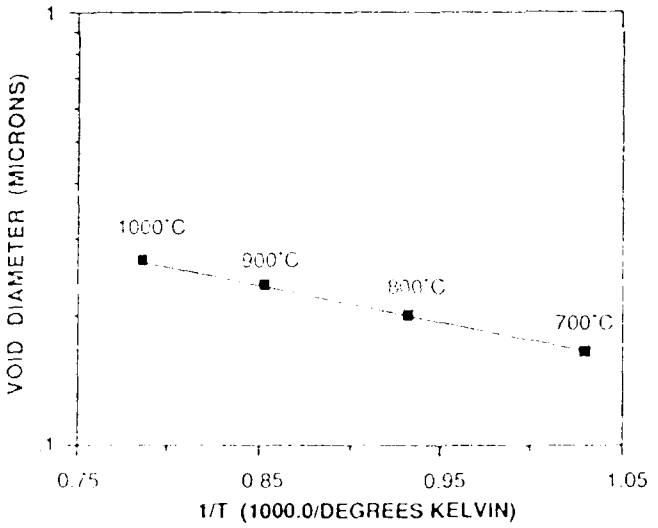


Fig. 8. A plot of the average void size *vs.* the inverse of absolute temperature for the unimplanted CoCrAl alloy for an exposure time of 3 min

multicomponent system, it is assumed that the rates of diffusion of oxygen through either yttria or hafnia are also much faster than those of the metal ions present in cast CoCrAl, namely cobalt, chromium and aluminum.

Now, in view of the high activity of both yttrium and hafnium for oxygen, it is likely that, in the initial stages of oxidation, yttria and hafnia form faster than other oxide species. The presence of the resultant oxide layer on the specimen surface permits the relatively fast inward diffusion

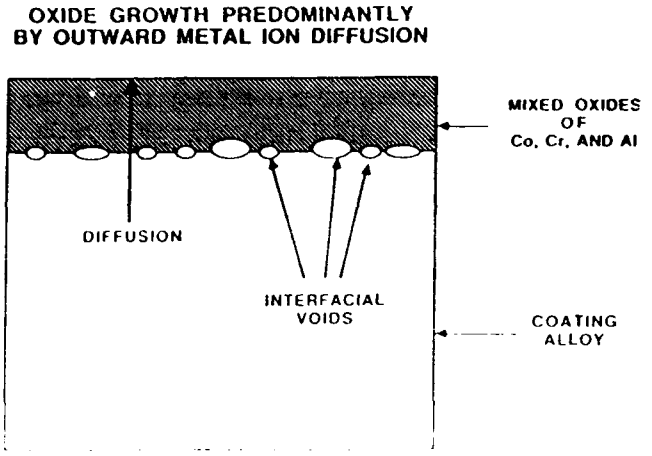


Fig. 9. Schematic diagram of the interfacial void formation model.

of the (oxygen) anions while reducing the outward diffusion of cations (the cobalt, chromium and aluminum metal ions) to the outer surface. Consequently, in contrast with the case of the unimplanted alloy, oxide growth with an oxygen-active element mainly occurs by an inward oxidation process involving the inward diffusion of oxygen ions through the growing oxide scale. The flow of oxygen ions inwards contributes to a reversed flow of vacancies in the oxide which flow outwards to the oxide–gas interface where they are annihilated. However, this process does not lead to the formation of Kirkendall-type voids. A schematic diagram of the void suppression model is presented in Fig. 10. The suppression of void formation at the oxide–metal interface in the presence of an oxygen-active element in the coating alloy significantly improves the adhesion of the oxide scale to metal.

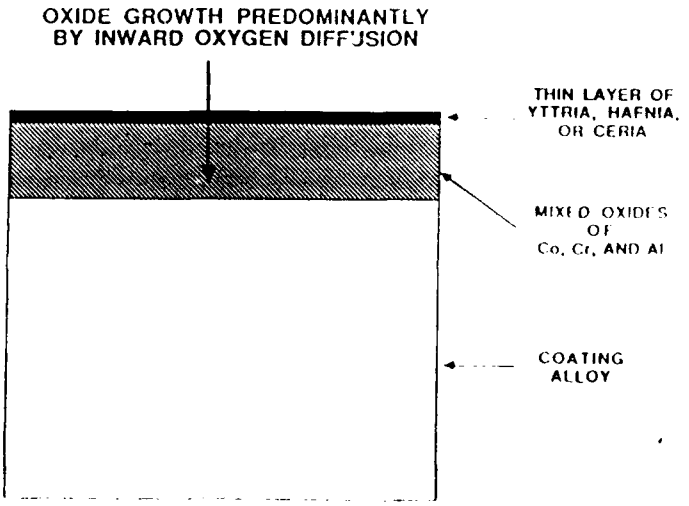


Fig. 10. Schematic diagram of the void suppression model

Two other important results are addressed next, one relating to the effect of cobalt implantation and the other relating to the formation and growth of interfacial voids at the α–β phase boundary. The purpose of cobalt implantation was to determine the effects of physical damage resulting from the ion implantation process. The results (Fig. 5) indicate that effects of such physical damage on interfacial void formation and oxide development are small. In addition, it is noted that for short-time oxidation exposures at 700 °C, the voids in the unimplanted material formed only in the α phase close to the phase boundary. For all other experimental conditions voids in the phase boundary were, on average, larger and more numerous. This may be explained by the fact that boundary diffusion is generally faster than bulk (lattice) diffusion; during oxidation the metal atoms move more easily through the phase boundary than through the bulk of the alloy.

4. Conclusions

Ion implantation was used as a tool to study the effects of oxygen-active elements on the high temperature oxidation behavior of cast CoCrAl coating alloy. During high temperature oxidation of unimplanted CoCrAl specimens, voids formed at the metal–oxide interface. The size and number of these interfacial voids were dependent on the oxidizing temperature and exposure time. Prior ion implantation of CoCrAl specimens with either yttrium or hafnium greatly reduced the nucleation and the growth of these interfacial voids. It was concluded that void formation on the unimplanted coating alloy is the result of a Kirkendall-type porosity mechanism involving the coalesence of vacancies at the metal–oxide interface. These vacancies are produced at the free surface consequent on the diffusion of metal ions to that interface during the oxidation process. The presence of a layer of oxide of an oxygen-active element in the near-surface region of the cast CoCrAl specimens reverses the net mass flow, with the oxygen ions diffusing much faster than the metal ions through the growing oxide. Since the diffusion of oxygen ensues from an interface mechanism that does not produce vacancies, there is no tendency for void formation. It is proposed, therefore, that the improvement in the performance of the coating alloy containing oxygen-active elements is the result of improved adherence of the protective oxide scale owing to the suppression of Kirkendall porosity.

Acknowledgments

The authors gratefully acknowledge the assistance of F. S. Pettit, G. H. Meier, J. R. Caola and S. Y. Hwang of the University of Pittsburgh for providing the cast CoCrAl specimens and the many technical discussions. They also acknowledge the assistance of F. A. Smidt and J. A. Sprague of

the Naval Research Laboratory for the ion implantation experiments. This research was supported by the Office of Naval Research.

References

1 D. P. Whittle and T. Stringer, Improvement in high temperature oxidation resistance by additions of reactive elements or oxide dispersion, *Philos. Trans. R. Soc. London, Ser. A, 295* (1980) 309 - 329.

2 D. P. Whittle and D. H. Boone, Alumina scale adherence to CoCrAl alloys and coatings, *Proc. Int. Conf. on Surfaces and Interfaces in Ceramics and Ceramic–Metal Systems, Berkeley, CA, July 28 - August 1, 1980*, 1981, pp. 487 - 502.

3 C. S. Giggins and F. S. Pettit, Oxide scale adherence mechanisms and effects of yttrium oxide particles and externally applied loads on the oxidation of NiCrAl and CoCrAl alloys, *PWA-5364*, Pratt & Whitney Aircraft, 1975 (ARL-TR-75-0234, AD-A024104).

4 C. S. Giggins, B. H. Kear, F. S. Pettit and T. K. Tien, Factors affecting adhesion of oxide scales on alloys, *Metall. Trans. A, 5* (1974) 1685 - 1688.

5 J. K. Tien and F. S. Pettit, Mechanism of oxide adherence on Fe–25Cr–4Al (Y or Sc) alloys, *Metall. Trans. A, 3* (1972) 1587 - 1599.

6 T. E. Antill and K. A. Peakall, Influence of an alloy addition of yttrium on the oxidation behavior of an austenite and ferritic stainless steel in carbon dioxide, *J. Iron Steel Inst. London, 205* (1967) 1136.

7 F. S. Golightly, F. H. Stott and G. C. Wood, *Oxid. Met., 10* (1976) 163.

8 H. Pfeiffer, *Workst. Korros., 8* (1957) 574 - 579.

9 A. W. Funkenbush, J. G. Smeggil and N. B. Bornstein, Reactive element–sulfur interaction and oxide scale adherence, *Metall. Trans. A, 16* (1985) 1164 - 1166.

10 T. G. Smeggil, A. W. Funkenbush and N. B. Bornstein, A relationship between indigenous impurity elements and protective oxide scale adherence characteristics, *Metall. Trans. A, 17* (1986) 923 - 932.

11 T. A. Ramanaryanan, R. Ayer, R. Petkovic-Luton and D. P. Leta, The influence of yttrium on oxide scale growth and adherence, *Oxid. Met., 29* (5 - 6) (1988) 445 - 472.

12 T. A. Sprague, G. R. Johnston, F. A. Smidt, S. Y. Hwang, G. H. Meier and F. S. Pettit, Oxidation of CoCrAlY and Y-implanted CoCrAl alloys, in S. C. Singhol (ed.), *Proc. Symp. High Temperature Protective Coatings, Metallurgical Society of AIME Annual Meeting, Atlanta, GA, March 6 - 10, 1983*, The Metallurgical Society of AIME, Warrendale, PA, 1983, pp. 93 - 103.

13 J. A. Sprague, V. Provenzano and F. A. Smidt, Initial stages of oxide formation on a CoCrAlY coating at 700 °C, *Thin Solid Films, 95* (1982) 57 - 64.

14 K. L. Luthra and C. L. Briant, *Oxid. Met., 26* (1986) 1587.

15 L. F. Aprigliano, Reaction mechanism of sulfur dioxide with single crystal cobalt and chromium and CoCrAlY coatings, David W. Taylor Naval Ship Research and Development Center, *Rep. DTNSRDC-87/027*, September 1987

METHODS OF PRODUCING HIGH STRENGTH MATERIALS BY ELECTROLESS PLATING, LIQUID INFILTRATION AND COMPACTION OF POWDERS

V. Provenzano, N.P. Louat*, K. Sadanada, M.A. Imam,
C.J. Skowronek, J. Calvert* and B.B. Rath
Naval Research Laboratory
Washington, DC 20375-5000

*Contractor on-site GEO-CENTERS, INC.
10903 Indian Head Highway
Fort Washington, MD 20744

Abstract

A research effort is underway at the Naval Research Laboratory to study and develop superstrength materials for high temperature applications. This effort is mostly based on the theoretical concepts developed by Louat (1).

In this study three different procedures were employed to embed a high volume fraction of submicron-size titanium or tantalum carbide particles in a copper matrix. In the first, carbide particles were coated with copper by an electroless plating technique and then consolidated by hot isostatic pressing (Hipping). In the second procedure, infiltration and consolidation was achieved by first encapsulating the carbide particles in copper followed by two succesive hipping treatments above and below the melting temperature of copper. The third was exactly the same as the second except that the starting powder for this case was a blend of equal volume amounts of carbide and copper powders. For all three cases the room temperature yield strength of the consolidated material was determined by microindentation (impression) tests. The most promising result in terms of mechanical strength was obtained for the tantalum carbide powder encapsulated in copper and hipped. In fact, an average yield strength of 1208 MPa (175 ksi) was measured on this material. This value is nearly six times the strength of copper at room temperature. On the other hand, the average yield strength of the electroless copper-plated titanium carbide particles hipped in copper was only 450 MPa (65 ksi), which is only twice the strength of copper. The consolidated mixture of carbide and copper powders produced an average yield strength of 207 MPa (30 ksi) which is the yield strength of copper.

The above results on the mechanical strength of the consolidated carbides are correlated and discussed in terms of the corresponding microstructural features obtained by high resolution scanning electron microscopy and energy dispersive X-ray analysis.

Proceeding TMS-AIME Symposium on Modification Technology
Second Int Conf.
Surface Modification Technologies
TMS AIME Sept 1988 To be Published

Introduction

It would appear that efforts to attain improved mechanical properties in conventional materials and with conventional methods, has reached a region of diminishing returns and that the achievement of dramatic increases in strength and ductility will require the usage of new and revolutionary approaches.

Here we report some initial results of an investigation of one such approach. Expectations of its effectiveness rest on the prediction that such superior properties can be expected to develop with decreasing particle size in two phase materials, when in a reversal of the normal situation, the major phase is particulate while the minor provides the matrix. Specifically, it is expected that over a wide range of particle size l, the yield strength σ of such materials would follow a Hall-Petch relation,

$$\sigma = \sigma_0 + kl^{-1/2}$$

Since it would appear that the fabrication of such materials necessarily requires and can be acnieved by the agglomenation of preformed powders in a suitable matrix the strengths attainable would be effectively limited only by the (a) particle size attainable and (b) the development of the technology necessary to handle ultra-fine powders. Again, a variant of this approach appears to promise extension of such strength to elevated temperatures. Thus, under circumstances such that the particles form a load bearing skeleton the intervention of the phenomenon of dilatancy is predicted to result in material properties which are virtually independent of the shear strength of the matrix. That is to say, strength should be unaffected when the matrix melts.

An initial experimental confirmation of these expectations has been obtained earlier from the system Fe-Hg(3). There in a particular, a yield strength of 32.4 MPa (4.7 ksi) at 90% of the melting point of mercury was obtained. These numbers as they stand are probably not very informative, it may therefore be helpful to note that this stress represents an elastic strain of ~4%. Such a strain at the same homologous temperature in a material having a nickel matrix would imply a yield of 972 MPa (141 ksi) at 1280°C.

The work reported here represents an extension of this research to materials which are technically more realistic. In large measure we have been concerned to investigate the efficiency of various techniques for material fabrication.

Experimental Details

The carbide particles used in this study were titanium and tantalum carbides in powder form. The purity of the three carbide powders was 99% and the average size of the two types of particles was less than one micron. Three different procedures were used to prepare composite compacts. The compacts were constituted by embedding one type of carbide particle in a ductile copper matrix.

In the first procedure titanium carbide particles were coated with copper using an electroless plating bath. The coated particles were then dried in laboratory air in an electric oven at 120°C. The dried particles were compacted into a pellet through hot pressing. The pellet was subsequently wrapped with a copper foil. The wrapped pellet was placed inside a stainless steel bag and evacuated. The evacuated bag was

hot isostatically pressed (HIP) for 1 hour at 950°C at a pressure of 207 MPa (30 ksi). In the second procedure powder of either tantalum or titanium carbide was placed inside a hollow copper cylinder and then sealed with a copper cap. the sealed cylinder was first wrapped with a copper and then with a tantalum foil. The wrapped cylinder was placed inside a stainless steel bag, evacuated for several hours and given two successive hipping treatments: one for two hours at 1100°C (above the melting temperature of copper) followed by another 2 hours at 950°C (below the melting temperature of copper); the isostatic pressure for the two hipping treatments was 207 MPa (30 ksi). The third procedure was exactly the same as the second one with the exception that the starting powder was a blended mixture of equal volume amounts of carbide and copper powders.

The three different hipped materials were removed from the stainless steel bag and from the wrapping foils, sectioned with a diamond saw and polished by standard metallographic techniques. The yield strength on the polished sections was determined by impression tests using a cylindrically shaped indenter of 1 mm diameter size. Complete details of the experimental apparatus for the impression tests are given elsewhere (2).

The microstructural features of the hipped materials were examined by scanning electron microscopy using a Hitachi Model S-800 high resolution field emission microscopy equipped with a PGT energy dispersive X-ray system for compositional analysis.

Results

The SEM micrographs presented in Fig. 1 show the copper coated titanium carbide particles (panel A) and the microstructure of the coated particles after they had been consolidated and hipped for 2 hours at 950°C. The energy dispersive X-ray spectrum shown at the bottom of Fig. 1 indicates that the electroless process was successful in depositing a copper layer on the carbide particles. The X-ray spectrum displays the presence of some oxygen in the coated particles. Such presence suggests that some oxidation took place during the electroless process. A negligible amount of oxygen was also found on the carbide particles before the copper plating. Figure 1B clearly shows the composite material was porous after hipping. The consequence of this porosity on the mechanical properties of the hipped material will be considered in the Discussion Section of the paper. Here it suffices to say that impression tests on the above material indicated an average yield strength of 450 MPa (65 ksi).

The microstructure of the tantalum carbide powder that was first encapsulated in copper and then hipped for 2 hours at 1100 and another 2 hours at 950 is shown by the SEM micrographs presented in Fig. 2. Panel A in this figure shows a typical indentation mark produced on the hipped material by the impression tests. The higher SEM micrographs (Fig. B and C) provide additional microstructural details. The material at the bottom of the indentation is smooth, fine-grained and dense. By contrast, the material away from the indentation marks is coarser, less dense and somewhat porous. As illustrated by the energy dispersive X-ray spectrum in Fig. 2, the amount of copper in the hipped material was substantial. This indicates that during the hipping process a signficant amount of copper had infiltrated the tantalum carbide powder. Due to the large overlapping between the copper and tantalum peaks in the X-ray spectra we were unable to obtain an average composition of the hipped material. The X-ray spectrum in Fig. 2 also contains a small oxygen peak. A similar oxygen peak was observed in the tantalum carbide powder before hipping. Impression tests conducted at room temperature on the hipped specimen

indicate an average yield strength of 897MPa (130 ksi). The hipping procedure was then repeated. The strength rose to 1208 MPa (175 ksi). This value is nearly six times the yield strength of copper.

The significant microstructural features of the hipped titanium carbide-copper composite specimen are illustrated by the SEM micrographs shown in Fig. 3. As described in the previous section, the composite was obtained by blending equal volume amounts of carbide and copper powders and hipping the blended mixture for 2 hours at 1100°C, followed by another 2 hours hipping at 950°C. Both the SEM micrographs and the corresponding X-ray spectra also presented in Fig. 3 clearly show that the above procedure did not produce a uniform material. In fact, the two powders did not amalgamate well at the microscopic level. The microstructure reveals distinct copper-rich-carbide-poor regions alternating with copper-poor-carbide-rich regions. The carbide-rich regions displayed extensive porosity. Impression tests performed on this sample yielded an average strength value of 207 MPa (30 ksi). Copper yields at 207 MPa (30 ksi).

Discussion

The highest strength measured was 1208 MPa (175 ksi). This was achieved with TaC powder (1 μm diameter) which had been infiltrated with copper by the double hipping process. The thickness of the copper coating was initially unknown. It might be inferred from the variable but definite porosity evident in the micrographs of the hipped materials that the layer is thin, i.e. less than the mean particle radius. However, this conclusion conforms with the observation that there is little if any indication of porosity in the micrographs of the impression pits. This observation together with the fact that a re-hipping procedure give a substantial increase in strength, ~45 ksi suggests rather that the material as tested was poorly compacted. The reason for this is not understood.

The impression that the hipping procedures are not performing as anticipated is reinforced by another set of observations. Thus, the failure to obtain significant infiltration of molten copper into the interstices of the powder compacts under the hipping pressures 207 MPa (30 ksi). For the particle size employed this would be surprising even if the metal did not wet the particles, it is even harder to understand in view of the expectation that wetting does occur. Assuming that the strength is given by

$$\sigma = \sigma_0 + kl^{-1/2}$$

we find ignoring any contribution from σ_0 that when σ = 175 ksi and with l = 1 μm that k is about twice value found for iron.

In conclusion the highest strength 1208 MPa (175 ksi) is encouraging but what could be anticipated on the basis of the Fe-Hg results is mentioned above. The reasons for this discrepancy are likely to be: (a) insufficient thickness of the copper layer to form a continuous matrix, leading to porosity; (b) incomplete wetting between particles and matrix due to oxide formation. It can be expected that much higher strengths will be achieved with better techniques in the preparation of the materials and with the use of finer powders.

Concluding Remarks

Previous theoretical studies by Louat (1) have concluded that superstrength materials for elevated temperature applications can be obtained by embedding a high volume fraction of submicron-size-hard-particles such as carbides in a ductile matrix such as copper. In the present study it has been shown that submicron-size particle of either titanium or tantalum carbide particles can be coated with copper by electroless plating or by an infiltration technique. Consolidation of the electroless plated particles was obtained by hot isostatic pressing. Two successive hot isostatic pressing above and below the melting temperature of copper was also used to infiltrate (coat) and consolidate carbide powders or a mixture of carbide and copper powders. The most promising result in terms of superstrength properties, was obtained for the tantalum carbide particles infiltrated and consolidated by the two successive hipping treatments. In fact, impression tests on this material measured an average yield strength nearly six times the strength of copper. On the other hand, impression tests on the consolidated material obtained from the electroless plated particles indicated a room temperature yield strength about twice that of copper. The lowest yield strength was measured on the material obtained by hipping the blended mixture of carbide and copper powders.

The results of the microstructural and energy dispersive X-ray analysis conducted on the three different materials when correlated to the corresponding mechancial properties showed the following: the infiltrated and consolidated tantalum carbide material was fairly dense and the particles were uniformly mixed with the copper matrix; the particles electroless coated and then hipped displayed extensive porosity and microcracking; it also appeared that deposited copper had been partially oxidized during the plating process. The material obtained from consolidating the mixture of carbide and copper powders showed a network of copper-rich and copper-poor regions. The copper-poor regions were very porous.

References

1. N. Louat, "Alloys, Strong at Room and Elevated Temperatures from Powder Metallurgy," Acta Metall, Vol. 33, No. 1, pp 59-69, 1985.

2. M.A. Imam, R.W. Judy, and B.B. Rath, "Evaluation of Tensile Flow Properties of Weldments in Titanium Alloys," Supplement to the Welding Journal, pp. 210s-214s, July 1987.

3. N.P.Louat and M.A. Imam, "On Strength at High Temperatures," Submitted to Scripta Metall.

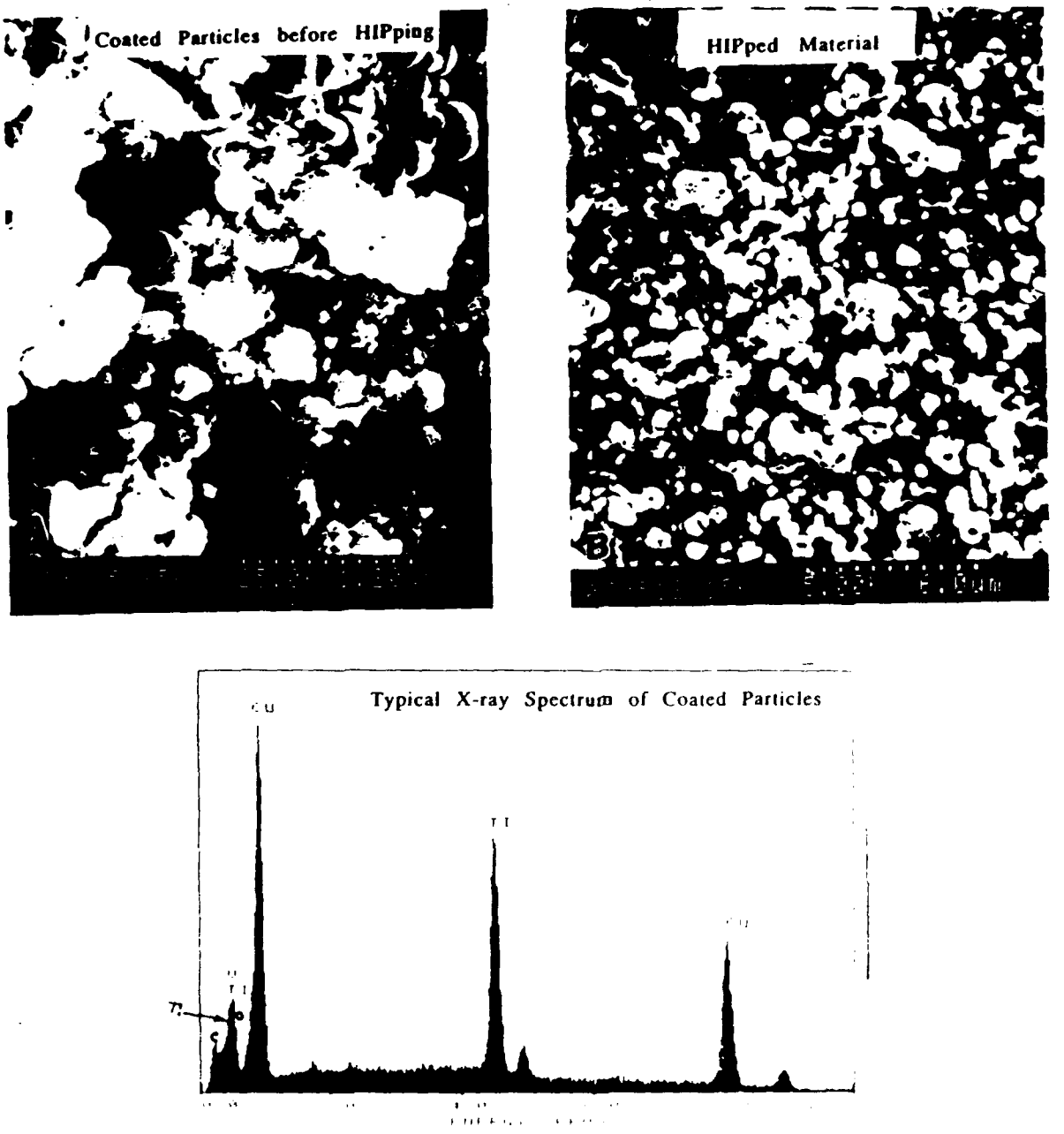


Figure 1 - TiC Particles Coated with Copper (Panel A), Same Material after HIPping (Panel B), and X-ray Spectrum of Coated Particles before HIPping

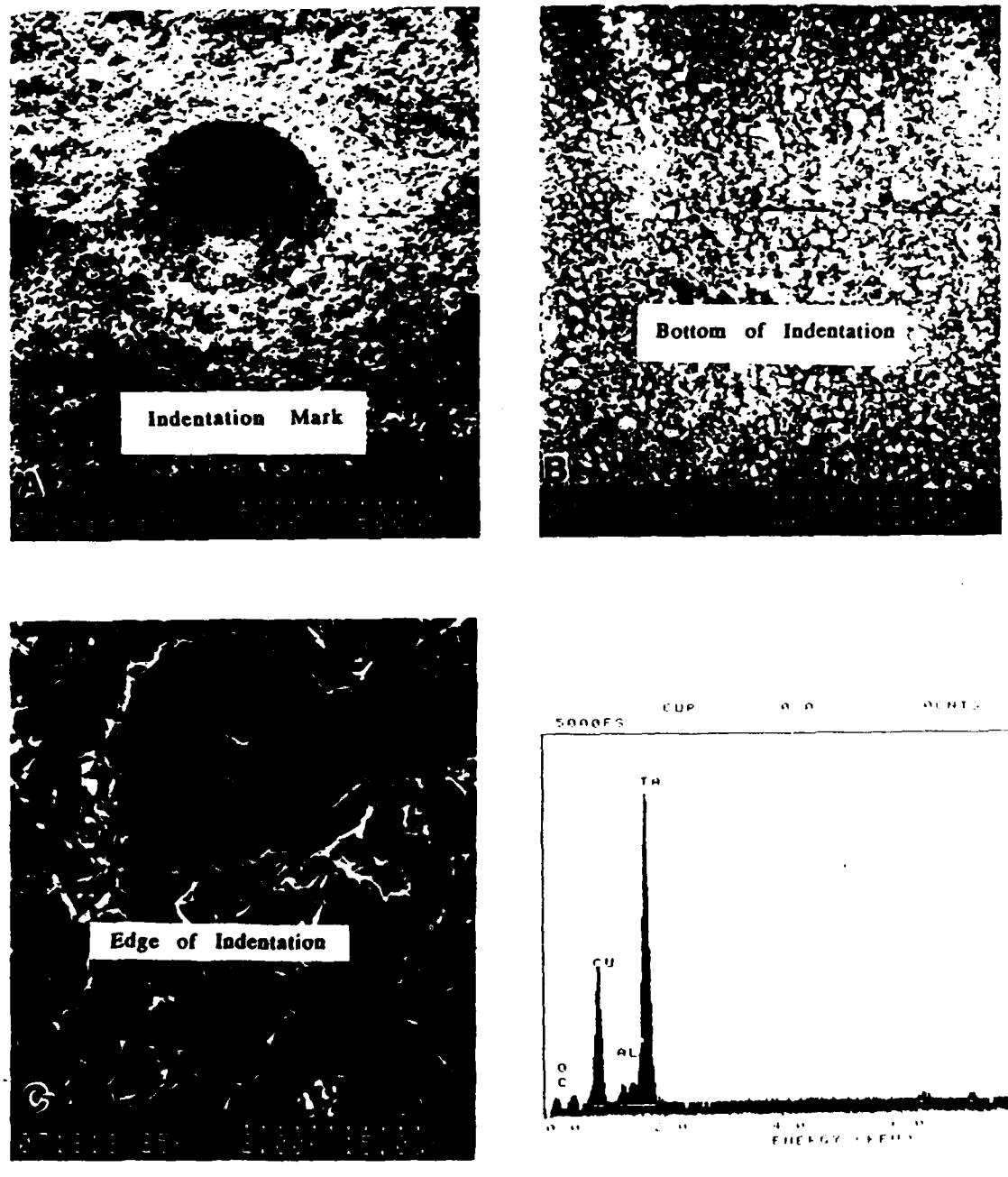


Figure 2 -
Microstructure and X-ray Spectrum of Tantalum Carbide Powder after Encapsulation in Copper and Hot Isostatic Pressing (HIPping) at 950 and 1100°C'

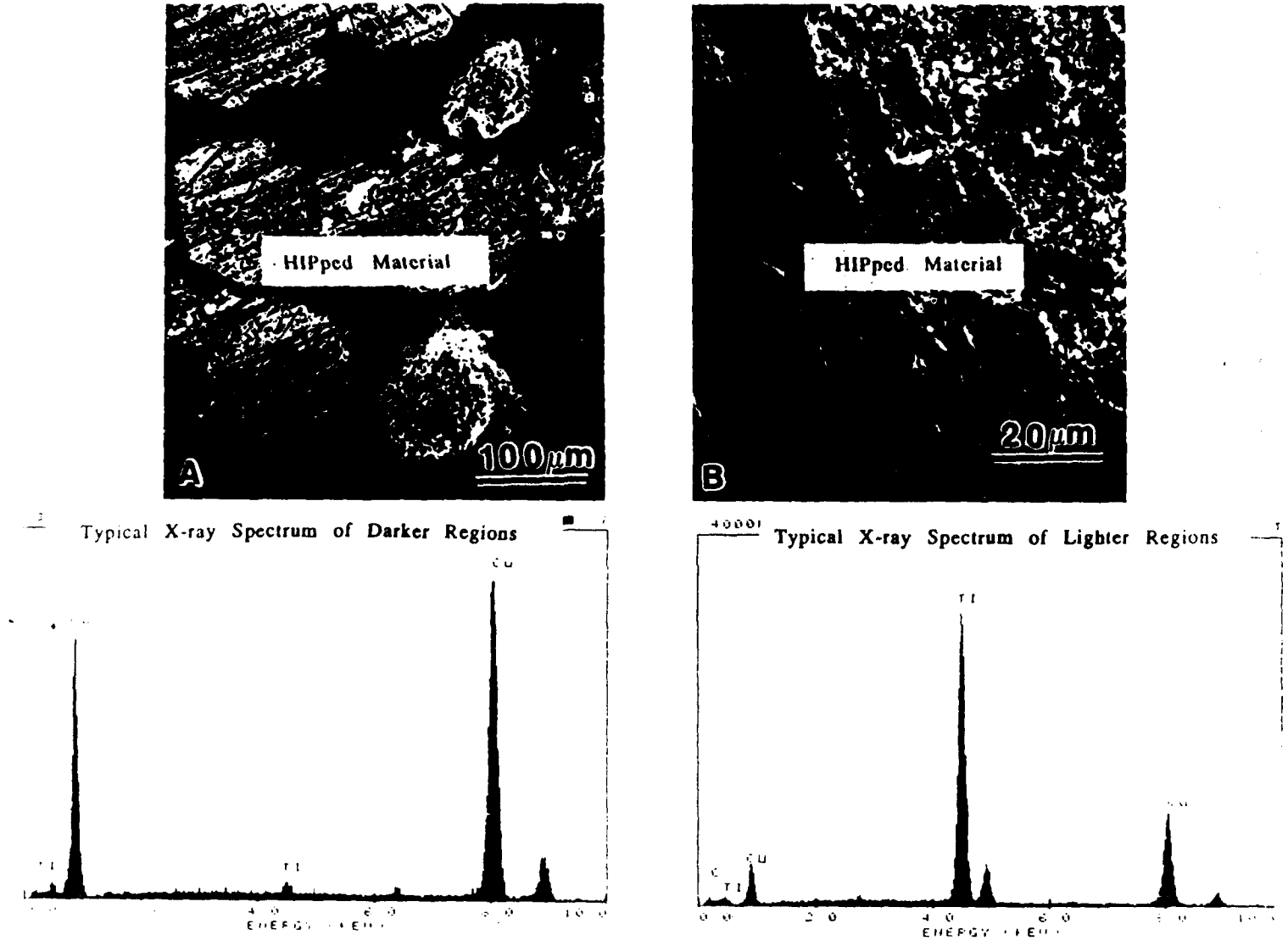


Figure 3 - Microstructure and X-ray Spectra of Blended and Hot Isostatically Pressed (HIPped) Titanium Carbide and Copper Powders (50/50 by volume)

Submitted to Scripta Met

ON THE ACHIEVEMENT OF STRENGTH AT HIGH TEMPERATURE IN BINARY ALLOYS

N. P. Louat* and M. A. Imam
Naval Research Laboratory
Washington, DC 20375-5000

INTRODUCTION

It has recently been pointed out [1] that the strengthening encountered in polycrystals, the Hall-Petch effect, can also be expected in materials which are not necessarily polycrystalline but, insofar as the effect is concerned, are similar to them. Specifically considered were two-phase alloys in which the matrix forms the minor constituent and in which the other, major phase, is particulate. Such alloys are to be considered as equivalent to polycrystals if the matrix is so thin that, at the stress involved, it cannot, independent of the particles, deform plastically. This restriction is also available in circumstances where the particles are replaced by rods or plates, effectively infinite in length.

The operation of the Hall-Petch effect in such materials in which the particle size is now disposable in practice down to diameters conveniently measured in nanometers, allows the possibility of material strengths approaching the theoretical limit.

It has also been noted [1] that the phenomenon of dilatancy which is responsible for the firmness of wet beach sand [2] may have metallurgical applications; a direct analogy being a packed dispersion of particles (each contacts ~ six others) in a metal matrix. If this analogue is to have important consequences at temperatures so high that the matrix approaches its melting point or is actually molten it is necessary that the particles be strong at these temperatures and be very much smaller than ordinary sand grains.

The essential feature of dilatancy is that the total volume of the interstices between particles, which are essentially densely packed and individually rigid, expands upon deformation. When this volume is occupied by a continuous fluid, such expansion must result either: in the formation of voids; a reduction in (compressive) pressure or; in an inward flow from an external surface. When the fluid is liquid, formation of voids is resisted by its cohesion; inward flow by the development at the outer surface of a pressure:

$$p \approx 2\gamma \cos\theta / r_h \qquad (1)$$

where γ is the surface energy of contact between particle and liquid, θ the contact angle and r_h the radius of the hole through which the liquid must flow. Purely elastic behavior of the whole follows from that of the

*On-site contractor for Geo-Centers, Inc.
Ft. Washington, MD 20744

particles at all applied stresses less than p. To examine the magnitude of p, we suppose γ to be of the order of the surface energy of the matrix and thus to be about: $\frac{\mu a}{10}$ where μ is shear modulus and 'a' the lattice parameter distance. Then, from (1) with $\theta \sim 0$: $p \sim \mu/10^4$, $r_h \sim$ 1 micron; $p \sim \mu/10^2$, $r_h \sim .01$ micron. The latter stress is technically large in most cases. The possibility that materials could have such strength near or above a relevant melting point is unique to this approach.

In practice the achievement of packing so close as to satisfy the requirements cited above may be difficult to achieve. This is the first conclusion of an attempt at experimental confirmation of these ideas. The system employed was Fe-Hg. The results obtained are detailed below. Here we note that the largest packing achieved (~66% Fe) was insufficient to achieve a rigid particle skeleton so that deformation of the matrix alone was possible. Deformation under these circumstances is accordingly the concern of the accompanying analysis.

ANALYSIS

For simplicity we separate the discussion into two realms, characterisable by temperature, and deal first with the effects of packing deficiency when the temperature is so low that the effects due to diffusion can be neglected.

In the said circumstances we can suppose that independent plastic deformation of the matrix can occur by bending dislocations into semicircle of radius L/2. This will occur, provided there exists an applied shear stress:

$$\sigma = \frac{\mu b}{L}. \qquad (2)$$

Intuitively, it is clear that L will decrease with decreasing particle radius and with increasing density of packing. The manner of this decrease can be expected to depend on these parameters in a complex way. Rather than undertake a detailed analysis of this question, we recognize that for our present purposes, namely, to recognize trends, a simplified approach dealing only with average values is sufficient. Following Orowan we identify L as the space between particles and assume the particulate phase to be spherical with radius r and to represent a volume fraction f. We then find that the mean density of planar circular intersections having average area $2\pi r^2/3$ is $3f/2\pi r^2$ with average radius $\frac{\pi r}{4}$. Thence, we obtain the mean interparticle spacing:

$$L \approx r\left[\sqrt{\frac{2\pi}{3f}} - \frac{\pi}{2}\right]$$

Numerical values obtained from the use of this formula are to be accepted only with caution, but it would seem to be correct in predicting a linear relation between L and r and in indicating that $L \ll r$ at volume fractions which approach that of close packed spheres: $f=\pi/3\sqrt{2}$. Accepting its validity we find when f=.66 that L/r=0.2 and so we have from (2)

$$\sigma \sim \mu/1400, \quad r = 2 \text{ micron} \qquad (3)$$

However, it is assumed in equation (2) that matrix and particle have the same modulus. Here, where it is to be expected that the moduli are

significantly different, a correction is necessary. Seemingly, an appreciation of its magnitude can be obtained simply from a consideration of the behavior of four straight parallel screw dislocations, the outer pair of separation, $2L-L_1$ represent the near images of the inner pair, separation L_1, in the surfaces having separation L at which the elastic modulus changes from μ_1 to μ_2. We consider the equilibrium of the inner pair under the action of a shear stress τ and write

$$\frac{\mu_1 b}{2\pi}\left[\frac{1}{L_1}+\frac{\alpha(2L-L_1)}{L(L-L_1)}\right]=\tau;\ \alpha=\frac{\mu_1-\mu_2}{\mu_1+\mu_2}\sim 1. \qquad (4)$$

Then, providing the separation of a dislocation and its image is much greater than its core radius, it is easily seen that the stress necessary for passage is given by

$$\bar{\sigma}\approx\frac{\mu_1 b}{2\pi}\left(\frac{1}{L_1}+\frac{\alpha(2L-L_1)}{L(L-L_1)}\right)\approx\frac{\mu_1 b}{L_1} \qquad (5)$$

whence for $\alpha \approx 1$ we find: $L_1 \approx 3L/4$ so that (3) becomes $\sigma \approx \mu/1000$

Apart from misfit stresses which are probably hydrostatic in the main, these considerations appear to exhaust the possibilities of direct inhibition of dislocation motion. There remains the possibility of a special type of work hardening.

The question of the hardening induced by the presence of particles which are essentially unpenetrable to lattice dislocations has been examined previously, e.g. Brown [7], but only for the case of dilute dispersions. In these circumstances cross slip was found to be important in reducing hardening below its potentential. The efficacy of the mechanism invoked may be traced to the fact that the necessary increase in dislocation length involved in by-passing a particle is relatively small. Such should not be so here, where the particle concentration is high. Rather we would expect that plastic deformation of the matrix would by and large, induced by circumscribing dislocation, result in an elastic deformation of the particles of like amount. The accompanying reduction in stress in the matrix may be regarded as a work hardening effect.

For this hypothesis to be valid it is at least necessary that the particles behave in a quasi-impenetrable fashion. To examine this possibility we consider the conditions necessary for the propagation of deformation from the matrix to the particles. This we can estimate using the Hall-Petch relation

$$\sigma = \sigma_o + k\, d^{-1/2}. \qquad (6)$$

To estimate k we refer to the expression given by Louat [1] for the force acting on the head of a pile-up length which terminates at a discontinuity in elastic modulus μ_1 to μ_2.

Thus, $F = \dfrac{16\pi m^2\sigma^2 a}{\mu(1+\cos 2\pi m)} \equiv B\sigma^2 a$, where $m = \dfrac{1}{2\pi}\cos^{-1}\alpha$

Substitution of this expression in the equation given in the same paper for the stresses necessary for activation of slip in the second material (modulus μ_2) namely

$$\sigma_e = \sqrt{\frac{\mu_1\mu_2}{ABa}},\quad \text{where A is a constant results in:}$$

$$\sigma_e = \mu_2\sqrt{\frac{1}{Aa}} \approx \mu_{Fe}\sqrt{\frac{1}{Aa}} \qquad (7)$$

when, as here, $m \approx \frac{1}{\pi}\sqrt{\frac{\mu_1}{\mu_2}} \equiv \frac{1}{\pi}\sqrt{\frac{\mu_{Hg}}{\mu_{Fe}}}$,

is small. A significant feature of (7) is that this critical stress is independent of the modulus of mercury. Accordingly, we may employ (6) with a value for k appropriate to iron. Doing so and setting a in (6) as 2 microns we find that $\sigma_c \approx \frac{\mu_{Fe}}{160}$; a value very much larger than that given in (3).

We now turn to the consequences of important diffusional effects. First, dislocation climb. The rapid work hardening we have invoked cannot be expected when dislocations climb readily. We therefore anticipate substantial decreases in strength as the test temperature progressively exceeds about .50% homologous.

Turning to direct effects of diffusion we remember that diffusional creep rests on the transport of matter between grain boundaries and that this process can be expected [1] to self-terminate by the aggregation of particles into rigid assemblies at boundaries which act as sinks for vacancies. This has been estimated [1] to occur at a strain: $\varepsilon_c = 2\Delta r/G$ where G represents grain diameter and Δ is the change in matrix concentration necessary to achieve close packing. Here, $\Delta \approx \frac{74-66}{100}$.

Metallographic difficulties have prevented a measurement of G in the current experiment. General experience would suggest that G is much larger than 2 microns so that ε_c should not be large. For values which may be thought of as typical: G > 100 microns we have $\varepsilon_c < \approx 0.3\%$.

EXPERIMENTAL

The system Fe-Hg was chosen as the vehicle for a first test of such materials because: Mercury is immiscible with Iron and melts near room temperature. A factor of equal importance is that iron particles can be introduced into mercury with relative ease.

Thus iron particles (4 micron) of 99.5% purity were immersed in a weak acidulated (HCI) solution together with a quantity of mercury. The subsequent addition of mercurous chloride allowed the wetting and absorption of the particles into the mercury. The resultant, essentially solid, material was then compacted by hand and frozen. In this way small specimens ≈ 1c.c. containing roughly equal volume fractions of the two constituents were produced.

The flow characteristics of these Hg-Fe alloys were determined using the so-called impression test method [3] and its associated analysis. Here, stress-strain relations are obtained through simultaneous and precise measurements of applied load and the resultant penetration of a flat-ended circular indentor into a specimen. The (tungsten carbide) indentor is constrained to move in a direction normal to the (flat) surface of the specimen.

Tests were carried out over a range of temperatures derived from the use of dry ice and liquid nitrogen on small specimens in a hydraulic testing machine. The displacement of the punch was found from the output of a LVDT (linear-variable-differential-transformer) attached between the load cell and specimen. This and the corresponding load signal were displayed on an x-y recorder. The indentor speed was chosen to be 8.5×10^{-7} m/sec. This speed is equivalent to a true strain [3] rate of 1.275×10^{-3}/sec.

Theory [4] and experiment [3,5,6] are in accord in providing approximate correlations between true tensile stress, τ, and load, P, on the one hand and true strain, ε, and penetration δ on the other. these are, with error less than 10%: $\tau = P/3$; $\varepsilon = \delta/d$, where d is the diameter of the indentor.

Fig. 1 shows a plot of true stress versus true strain for representative data taken at -110°C and at -62°C using these correlations. From these curves we find a yield stress of σy = 43.5 MPa (6.3 k.s.i.) (-110°C) and 24.13 MPa (3.5 k.s.i.) (-62°C).

DISCUSSION AND CONCLUSIONS

It is apparent from the wide variation in strength between room temperature and -110°C shown by this material that the principle of detailed continuity of deformation previously elaborated [1] does not apply at all temperatures. Thus, when the mercury is molten the restraint afforded by the iron particles is small but large enough for the specimens to stand alone. The process involved here is not clear but it would seem that diffusion would be of dominating importance at temperatures just below the melting point. With progressively lower temperatures the strain rate achievable by diffusion alone will eventually fall below the rate impressed. In this realm the need for detailed continuity of deformation will be increasingly important.

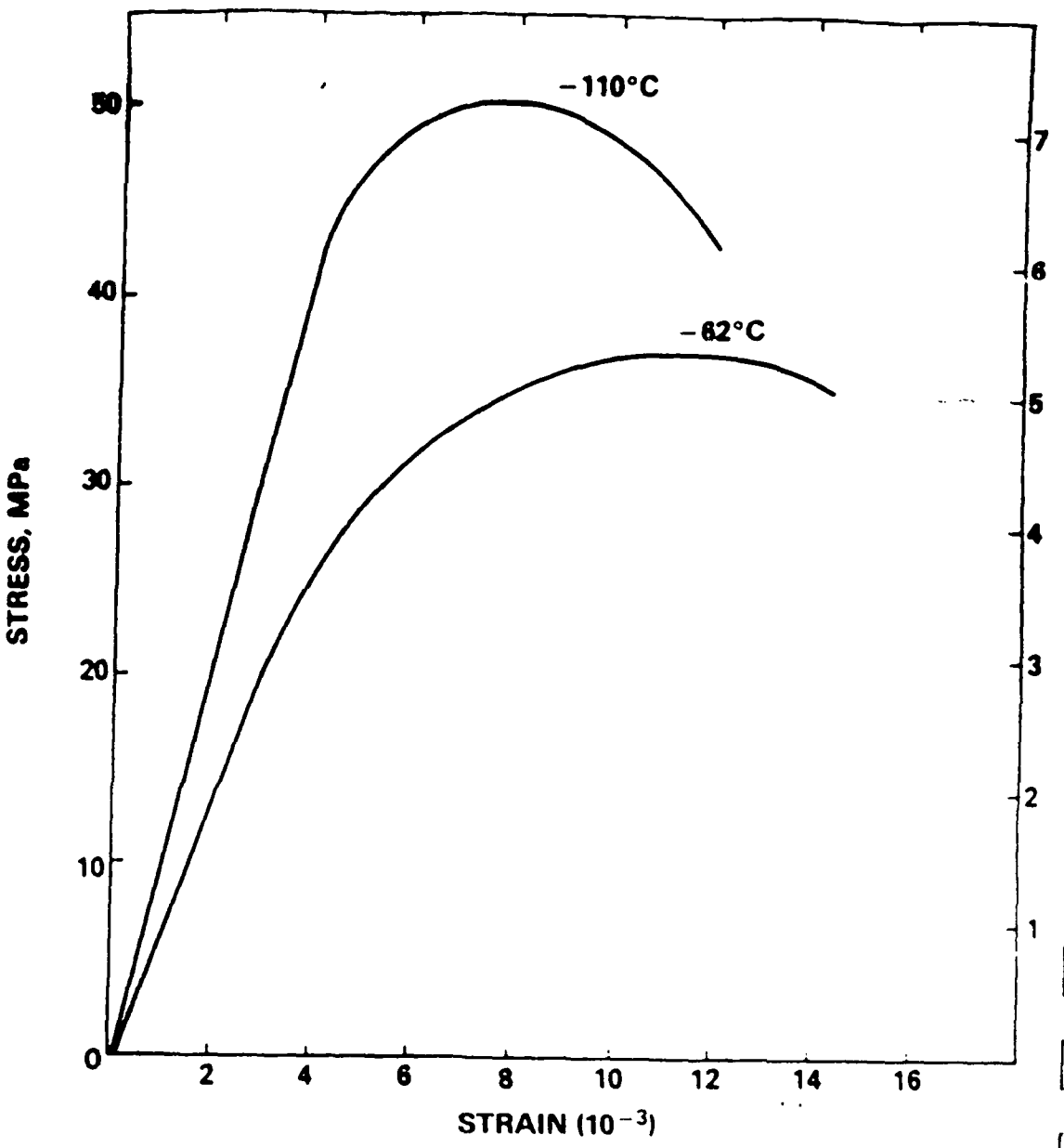
Towards an appreciation of the significance of the results of these measurements we relate them to the elastic moduli of the constituents. Efforts to find data relating to mercury have been unavailing. However, having regard to the generally symbatic correlation between melting point and elastic modulus in metals we expect that, that of mercury will be less than that of Indium since the latter melts at 156.4°C the former at -389°C. The modulus of Indium is 11 x 10^3 MPa (1.6 x 10^3 k.s.i.) that of mercury might well be ~ 6.89 x 10^3 MPa (1 x 10^3 k.s.i.).

Support for the usage of such a value is available from the measured value of the slope of the linear portion of stress-strain relation found at -110°C. thus, this slope is 1.5 x 10^6 p.s.i. accords with a crude formulation using a rule of mixtures.

On this basis the moduli are disparate; the indicated ratio is 30. No such ratio appears to exist between any two materials which might be included as practical. However, for the case of Ni-W, while only 6:1, this ratio is nevertheless significantly larger than unity. The inability to find an exact match in this regard is probably not important. The feature of significance is that plastic deformation lies in the realm of high temperature for mercury and low for iron. This disparity is shared by the combination Ni-W tested at ~ 1300°C. Thus, we suppose that the behavior of alloys constituted respectively of Nickel and Mercury is the same when the homologous temperature and imposed elastic strains are the same. Such an identity of elastic strains indicates the use of a scaling factor of ≈ 30 (μ_{Ni}/μ_{Hg}) in assessing yield stress. Again, at the higher of the two, the homologous temperature was 0.9 (Hg). Applying these factors we find a tensile yield stress of 141 x 10^3 p.s.i. (9.71 x 10^8 Pa.) at 1280°C for a hypothetical Ni-W alloy in which the tungsten is particulate at 4 μm diameter and constitutes ≈ 66% by volume. Such stresses: ≈ $\mu/200$ at 90% of the melting point of the matrix are significantly higher than those previously achieved through more conventional approaches.

REFERENCES

1. N. P. Louat, Acta. Met., 33, 59 (1985).
2. O. Reynolds, Nature, 33, 429 (1986).
3. H. Y. Yu, M. A. Imam, and B. B. Rath, J. Mat. Sc., 20, 636 (1985).
4. D. Tabor, Proc. R. Soc. A192, 247 (1948).
5. H. O'Neill and H. Greenwood, J. Inst. Met., 48, 47 (1932).
6. E. C. Yu and J. C. M. Li, Phil. Mag. 32, 811 (1977).
7. L. M. Brown and w. M. Stobbs, Phil. Mag. (GB) Vol. 23, No. 185, 1201-33, May 1971.



True stress versus true strain curves obtained by impression test

Submitted to Phil. Mag.

SOME CONQUENCES OF THE ELASTIC INTERACTION OF PARTICLES AND FREE SURFACES

N. Louat* and
K. Sadananda
Physical Metallurgy Branch
Materials Science and Technology Division
Naval Research Laboratory
Washington, DC 20375-5000

*On-site Contract Employee from Geo Centers Inc., Fort Washington, MD

ABSTRACT

The stresses developed by misfitting cylinders and spheres proximate to a planar free surface have been calculated.

It is found that the mean normal stresses in the neighborhood of such particles can be so large as to indicate significant increases in the rate of substitutional diffusion.

Again, interactions can be so large that the formation of a crater is energetically favorable.

INTRODUCTION

Almost invariably cracks initiate from a free surface under stress corrosion, corrosion fatigue or high temperature environmental fatigue. Such crack nucleation is accentuated by the presence of inclusions in the proximity of a free surface. These inclusions provide local stress concentrations which accelerate the damage process. In many instances they are produced insitu by the diffusion of oxygen or sulfur through grain boundaries and the resultant internal oxidation or sulphadation of reactive elements or phases below the surface. These processes are inhibited but not eliminated by the use of protective coatings which are sometimes employed in critical conditions as in the hot sections of gas turbines.

Since oxide or sulphide formation normally results in a large increase in volume, the formation of an inclusion near a free surface can induce comparably large mean stresses in the surrounding elastic medium. The object of this paper is to estimate analytically the magnitude of these stresses and their effect on the behavior of the material in a potentially hostile environment. Thus, specific note is taken of the effect of much stresses on the rates of substitutional diffusion and on the energetics of pit formation.

Diffusion in solids, with the possible exception of that involving interstitial atoms, requires the motion of vacancies. In fact the diffusion coefficient, D, can be expressed as

$$D = CF$$

where C is the concentration of vacancies and F is a frequency factor. In general F and C are functions of temperature while C in particular varies with stress. Thus, for a system at equilibrium the local concentration of vacancies at temperature T is:

$$C = C_o e^{\Delta\Omega/kT},$$

where $\Omega(\neq o)$ is the formation volume of a vacancy and D the local mean stress, defined as one third of the sum of the normal stresses k is, as is usual, Boltzmann's constant. We now note, that if D is to reach values corresponding to a few (n) percent elastic strain when T = 900°C that $\Delta\Omega/kT \sim .8n$. This would correspond to an increase in D by a factor of ~10 when n = 3.

Because these numbers indicate the possibility of significant increases in the rates of diffusion consequent on the existence of sufficiently large values of D and because it appears a priori that such values could arise in the neighborhood of oxide particles formed in the proximity of free surfaces, we have here made a formal calculation of them.

To begin we note that to first order in linear elasticity the total dilation introduced in an infinite solid by the presence of a misfitting inclusion is zero. Furthermore, when the inclusion is spherical and the stresses around it have

spherical symmetry, the dilation is zero everywhere, that is to say the sum of the three principal stresses vanishes at every point. This behavior breaks down at a free surface since the stress normal to that surface must vanish.

ANALYSIS

For elastic equilibrium shear stresses in and direct stresses normal to a free surface must vanish. Thus, in the case of a sphere of radius a, which is centered a distance h below a planar surface of an elastically isotropic solid and is under a uniform, say, compressive pressure p (Fig. 1), the stresses at a radial distance r, on the surface, [Timoshenko and Goodier, 1951] are:

$$\sigma_N = - p a^3 \frac{(2h^2 - r^2)}{(r^2 + h^2)^{5/2}} \; ;$$

$$\sigma_S = \frac{3}{2} p a^3 \frac{rh}{(r^2 + h^2)^{5/2}} \; .$$

Of these, the shear stresses σ are annulled by supposing another identical spherical particle to exist at the image point of the first.

We then have

$$\sigma_N = - p a^3 \frac{(2h^2 - r^2)}{(r^2 + h^2)^{5/2}} \qquad (1)$$

The problem can then be expressed as that of finding the normal surface displacements which give surface stresses which are equal and opposite to those of (1) and subsequently using these same displacements to determine the mean stresses at arbitrary points.

These ends can be achieved in a number of ways including the use of the Hankel transform as employed by Sneddon [1951] but we shall follow the method developed by Leibfried [1954] and Louat [1972]. There, one represents the displacements, U, as the aggregate of circular dislocation rings (Fig. 2) and expresses the condition of equilibrium in the form:

$$\frac{\mu\lambda}{2\pi(1-\nu)} \int_0^\infty f(R)\, R\, dR \int_0^{2\pi} \frac{(R - r\cos\alpha)\, d\alpha}{(R^2 + r^2 - 2rR\cos\alpha)^{3/2}} + \sigma_N(r) = 0 \qquad (2)$$

where R and α are used as integration variables. Here, μ is the shear modulus and ν the Poisson's ratio of the material. λ is the unit of displacement which at radius R is U(R). The function f(R) is the dislocation distribution density and is the derivative of U(R). Thus,

$$f(R) = \frac{dU}{dR}.$$

After some manipulation it is found (Louat, 1972) that

$$f(r) = -\frac{1}{\pi^2 A}\frac{d}{dr}\int_r^\infty \frac{s}{(s^2-r^2)^{1/2}}\,ds\,\frac{d}{ds}\int_0^s \frac{dR}{(s^2-R^2)^{1/2}}\left\{\int \sigma(R)\,dR + \frac{b}{R}\right.$$

where b is a constant of integration. Substitution here, for $\sigma(R)$ from (1) gives:

$$f(r) = \frac{3pahr}{\pi A\left(r^2+h^2\right)^{5/2}} \qquad (3)$$

Now Kroupa [1960] has given an integral representation of the stresses at a point (R,y) due to a single circular loop of dislocation of radius r and Burgers' vector b. Thus:

$$\sigma_R = \frac{\mu}{2(1-\nu)}\frac{b}{\pi}\left[I_0^1 - \frac{y}{r}I_0^2 - (1-2\nu)\frac{r}{R}I_1^0 + \frac{y}{r}I_1^1\right]; \qquad (4)$$

$$\sigma_\theta = \frac{\mu}{2(1-\nu)}\frac{b}{\pi}\left[(1-2\nu)\frac{r}{R}I_1^0 - \frac{y}{R}I_1^1 + 2\nu I_0^1\right]; \qquad (5)$$

$$\sigma_y = \frac{\mu}{2(1-\nu)}\frac{b}{\pi}\left[I_0^1 + \frac{y}{r}I_0^2\right]; \qquad (6)$$

$$\tau_{Ry} = \frac{\mu}{2(1-\nu)}\frac{by}{\pi r}I_1^2 - \qquad (7)$$

where

$$I_m^n = \int_0^\infty t^n J_m\left(\frac{tR}{r}\right) J_1(t)\, e^{-\frac{ty}{r}}\, dt$$

and $J_m(x)$ is the Bessel function of order m.

The stresses due to a distribution of such loops are thus expressible in terms of double integrals. For the case of interest here, we consider the sum:

$$\left(\sigma_R + \sigma_\theta + \sigma_y\right)/3 = \frac{\mu(1+\nu)}{3(1-\nu)}\, b\, \frac{I'_0}{r}$$

and thence the expression:

$$\frac{p h a^3}{3\pi A}\,\frac{1+\nu}{} \int_0^\infty \frac{dr}{\left(r^2+h^2\right)^{5/2}} \int_0^\infty t\, J_0\left(\frac{tR}{r}\right) J_1(t)\, e^{-\frac{ty}{r}}\, dt$$

Using the substitution u = tR/r these integrals are resolved in known forms [Gradshteyn and Ryzhik, 1965, pp. 682 and 712] to give a stress*

$$\Delta = (1+\nu)\, p a^3 \left\{ \frac{1}{\left[R^2 + (h+y)^2\right]^{3/2}} - \frac{3(h+y)^2}{\left[R^2 + (h+y)^2\right]^{5/2}} \right\} \qquad (8)$$

This is the actual mean stress present because the contributions from the pressure center and its image both vanish

When particle and matrix have the same value of Poisson's ratio (v=1/3) but different shear moduli we have from (9),

$$p = \frac{8}{3} \frac{\mu_p \mu_m}{\mu_m + 2\mu_p} \tag{10}$$

and for increasing values of the ratio μ_p/μ_m,

$$\frac{8}{3} \mu_p \Delta_o < p < \frac{4}{3} \mu_m \Delta_o$$

It would seem for the case of Ni and NiO that $\mu_p/\mu_m \sim 1/2$. Substitution of these values in (10) gives:

$$p = \frac{2}{3} \mu_m \Delta_o \tag{11}$$

Here, Δ_o is given by

T-1

where T represents the Pilling-Bedworth ratio:

$$\frac{\text{Molecular Volume of Oxide}}{\text{Atomic Volume of Metal}}$$

In the case of Ni, T = 1.52 so that

$\Delta_o = .52$.

The use of this number in (11) give unrealistically large stresses. Such stresses should be obviated through the intervention of localized fracture or through the formation of pairs of prismatic dislocation loops.

In reasonably ductile materials such as nickel-based alloys we anticipate that prismatic loops should form when the shear stresses in regions adjoining the particle are a few, say 4, percent of the elastic modulus [8]. As is readily shown these stresses are comparable to p. Accordingly, we shall suppose $p \sim .04\ \mu_m$.

Effect on Rate of Diffusion

As indicated earlier we suppose that diffusion proceeds through the agency of lattice vacancies and that the local diffusion coefficient is proportional to their local equilibrium concentration. Thus for a complete analysis of diffusion in the neighborhood of a spherical particle we require a solution of the diffusion equation:

$$\frac{\partial}{\partial r} D \frac{\partial C}{\partial r} + \frac{1}{r} \frac{\partial DC}{\partial r} + \frac{\partial}{\partial y} D \frac{\partial C}{\partial y} = 0$$

$$D = D_0 \exp\left(\Delta^S \Omega\ kT\right) \equiv D_0 \exp W(y,r)\ kT$$

with $C = C_1,\ y = 0;\quad C = C_2,\ (y-h)^2 + r^2 = a^2$

solutions for this equation do not seem to be available. Accordingly, we resort to approximation.

Referring to (6) we note that Δ_s and hence W is greatest when y and R are zero and that Δ_s then has a value of $\sim 2pa^3/h^3$. Thence we see, for values of p as stated above ($\sim .04\mu_m$), that unless a/h~1 the quantity:

$$D/D_o = \exp\left(\Delta_s \Omega/kT\right) \sim 1$$

at temperatures T at which diffusion is significant.

Thus, we can expect a significant increase in diffusion anywhere at all in the neighborhood of the particle only if the distance between particle and surface is a small fraction of the particle radius. Furthermore, reference to (6) shows that the region of enhanced diffusion will be confined to the region in which y/h and r/h are small i.e. < say .5. These constraints delineate a small volume lying between the particle and the free surface. Accordingly, we ignore the sphericity of the particle and consider one dimensional diffusion along the length (h-a) of a cylinder of radius ~a.

At steady state the diffusion flux is constant and given by:

$$J \simeq -\frac{\pi a^2}{4} \frac{d}{dy} D(y) C .$$

Solving this equation we find:

$$J \sim \frac{\pi a^2}{4(h-a)} \left(C_1 D_0 \exp\left(W(0)/kT\right) - C_2 D_0 \exp\left(W(h-a)\right)/kT \right)$$

$$\sim \frac{\pi a^2}{4(h-a)} C_1 D_0 \exp\left(W(0)/kT\right)$$

where $W(y) = \Delta_s(y, r) \Omega \quad , r = 0.$

This is to be compared with that which flows when D = constant namely:

$$J_c = \frac{\pi a^2}{4(h-a)} D_0 (C_1 - C_2) .$$

Thus, the ratio of these fluxes is essentially:

$$\exp\left(W(o)/kT \right)$$

We conclude therefore that diffusion of solute to a particle and hence the rate of oxidation can be increased by the presence of hydrostatic stresses developed as a consequence of that oxidation if these stresses are such that $W(o)/kT > 1$. In fact with $p=\mu/25$ as suggested earlier we find this factor to be ~3.0 when T~1000°C.

Surface Pitting

A second particular result of the presence of such stresses is to be noted. The Gibbs free energy G of a system may be reduced if an initially flat free surface is converted to a crater, Fig. 4. The extent to which this process continues can be determined from a consideration of the rate of change of G:

$$\delta G = \delta(\gamma S) - \delta\left(\int_o^v p\, dv \right)$$

Here γ is the surface energy/unit area, S is the surface area of the crater surface and v its volume. To determine such an extent we suppose for simplicity that the crater surface is spherical with radius R_m and represent its area as:

$$S = 2\pi R_m^2 \left(1 - \cos\theta_m \right)$$

where θ_m is the semi-angle subtended by the spherical cap at the center of the sphere. Critically we suppose $R_m \sin\theta_m = h$. Again, since we are interested in the rate of change of energy and since the distance between particle center

and the free surface continually decreases as the crater deepens we shall take:

$$\bar{p} = \frac{(h-t)^2 - r^2}{\left((h-t)^2 + r^2\right)^{5/2}} \cdot \frac{2\rho}{3} a^3 (1+\nu)$$

where t is the depth of the crater. We then write

$$\delta v = 2\pi r\, R\, d\theta \cos\theta\, (\sec\theta_m - \sec\theta)\, dR$$

and get:

$$\int_0^v p\, dv = -2\pi U \int_{\bar{R}}^{\infty} \frac{R^2}{\cos\theta_m} dR \int_0^{\theta_m} \sin\theta\, (\cos\theta - \cos\theta_m) \cdot \frac{\left(h - R(1-\cos\theta)\right)^2 - R^2\sin^2\theta}{\left(\left(h - R(1-\cos\theta)\right)^2 + R^2\sin^2\theta\right)^{5/2}} d\theta ;$$

$$\theta_m = \sin^{-1}\frac{h}{R}, \quad U = \frac{2}{3}\rho a^3 (1+\nu)$$

This formulation is reasonable only provided $h/\bar{R}$ is relatively small i.e. significantly less than unity. Accordingly, we restrict ourselves to circumstances where $h/\bar{R} < \frac{1}{2}$ and so too is θ.

In this case the integral may, with only small error, be written

$$\int_0^v p\, dv = -\pi U \int_{\bar{R}}^{\infty} \frac{R^2\, dR}{\cos\theta_m} \int_0^{\theta_m} \theta\left(\theta_m^2 - \theta^2\right) \frac{h^2 - (hR + R^2)\theta^2}{\left(h^2 + (R^2 - hR)\theta^2\right)^{5/2}} d\theta$$

Using obvious substitutions and the relation h=Rθ the integral in θ gives a result which closely approximates to

$$\frac{h\left(1+.4h/R\right)}{2R^2\left(R-h\right)^2}$$

The integration in R then gives

$$\int_0^V p\,dv \simeq \pi U\left\{1.4\frac{\bar{\theta}}{1-\bar{\theta}} + .4\ln\frac{1}{1-\bar{\theta}}\right\}$$

$$\simeq \pi U\left\{1.4\frac{t}{h-t} + .4\ln\frac{h}{h-t}\right\}; \quad \bar{\theta}=\frac{h}{R}=\frac{t}{h}$$

Whence,

$$q \simeq -\pi U\left(1.4\frac{t}{h-t} + .4\ln\frac{h}{h-t}\right) + \frac{\pi\gamma t^2}{3}$$

where γ is the specific surface energy. The variation of G with the depth of the crater is:

$$\frac{dq}{dt} = -\pi U\left(\frac{1.8}{h-t} + \frac{1.4\,t}{(h-t)^2}\right) + \frac{2}{3}\pi\gamma t \qquad (10)$$

We note, for non-vanishing, positive U, that this quantity is always negative when t is sufficiently small. A crater will therefore commence to

form on flat surfaces adjacent to all particles which are too large for their holes. However, examination of the cubic in t formed from the right hand side of (10) shows that it remains negative only within restricted ranges of t, h, W and γ and necessarily becomes positve at the largest (real) root of associated equation.

Crater growth up to this value is then assured if the quantity $U/\gamma h^2$ can be chosen such that the cubic equation has only one real root. The condition necessary is readily established by writing $t=z+\frac{2}{3}$ so that the cubic becomes

$$z^3 + qz + r = 0$$

where r and q are constants.

and applying the condition

$$\frac{r^2}{4} + \frac{q^3}{27} > 0 .$$

In this way we find:

$$U/\gamma h^2 = \frac{2}{3}(1+\nu)\frac{pa^3}{\gamma h^2} < \sim 1/3 ; \qquad (11)$$

as the necessary condition that the crater will grow until $t=h+\delta;\frac{\delta}{h}<<1$. This value is too large to be physically realistic and we suppose that the satisfaction of (11) corresponds to unlimited growth.

CONCLUSIONS

We have calculated the mean stresses developed when misfitting particle radius a, is centered a distance h below a planar free surface. These stresses can be important in accelerating oxidation and corrosion through increased vacancy concentration and as a direct consequence, increased rates of diffusion. Additionally, their presence can lead to the formation of pits. An example of which behavior can be seen in fig. 5.

A necessary condition for such formation is that $pa^3 > \gamma h^2$ where p is the internal pressure in the particle and γ is the surface energy.

ACKNOWLEDGEMENTS

The authors express their appreciation to Dr. V. Provenzano for many stimulating discussions and for providing the micrograph of fig. 5.

The present research effort is supported by the Office of Naval Research.

REFERENCES

Liebfied, G., Angew, Z., 1954, Phys., 6, 251.

Louat, N., 1962, Nature, 196, 1081.

Louat, N., 1972, Int. J. Eng. Sci., 10, 665.

Love, A. E. H., 1920, A Treatise on the Mathematical Theory of Elasticity, University Press, Cambridge (1920).

Mott, N. F. and Nabarro, F. R. N., 1940, Proc. Phys. Soc. Loud, 52, 87.

Sneddon, I. N., 1951, Fourier Transforms, McGraw-Hill, p. 470-490.

Timoshenko, S. and Goodier, J. N., 1951, Theory of Elasticity, McGraw-Hill, New York, p. 359.

Weatherly, G. E., 1968, Phil. Mag. 17, 791.

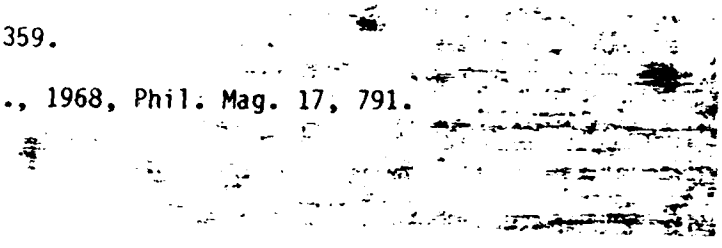




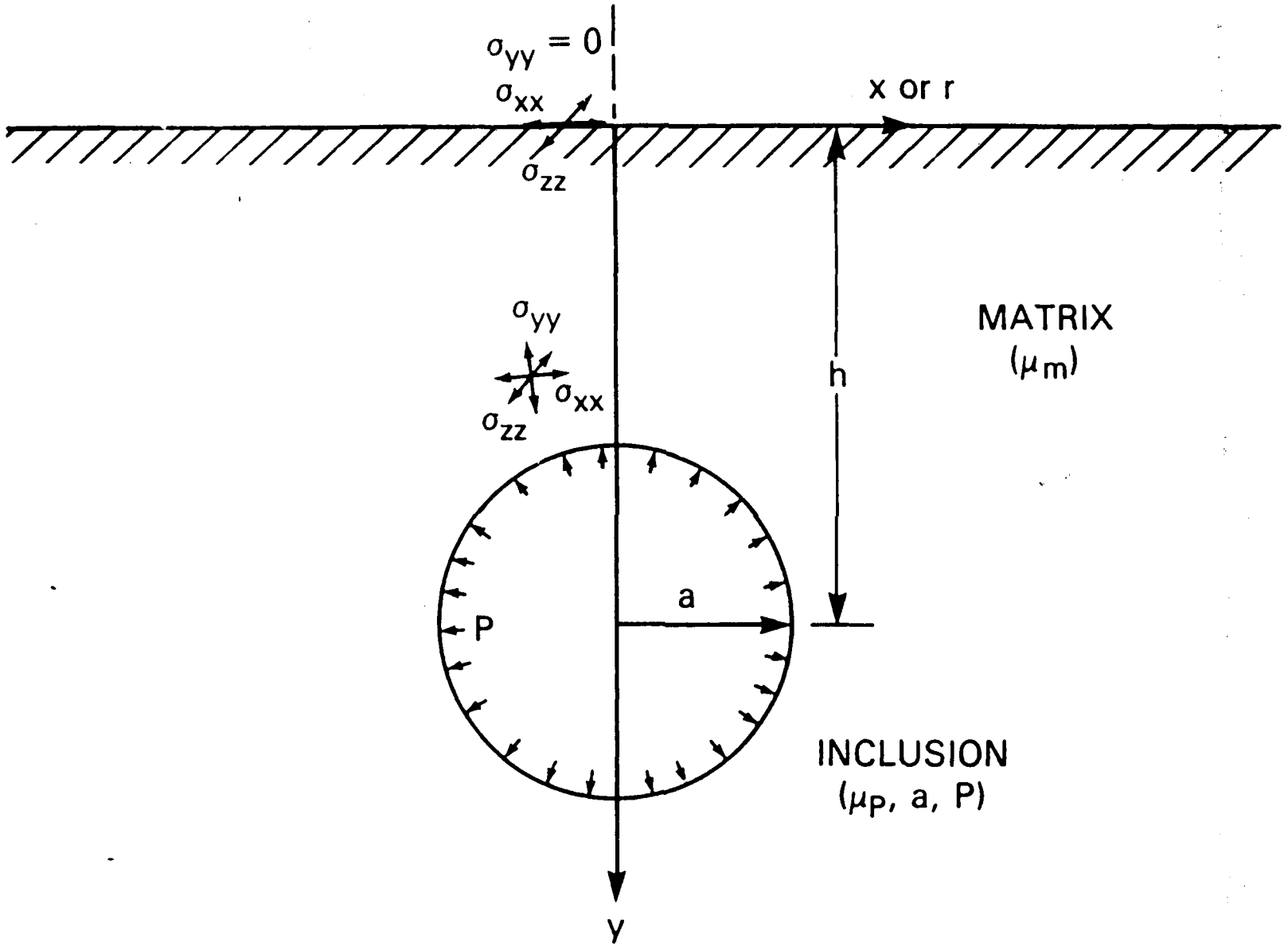
FIGURE CAPTIONS

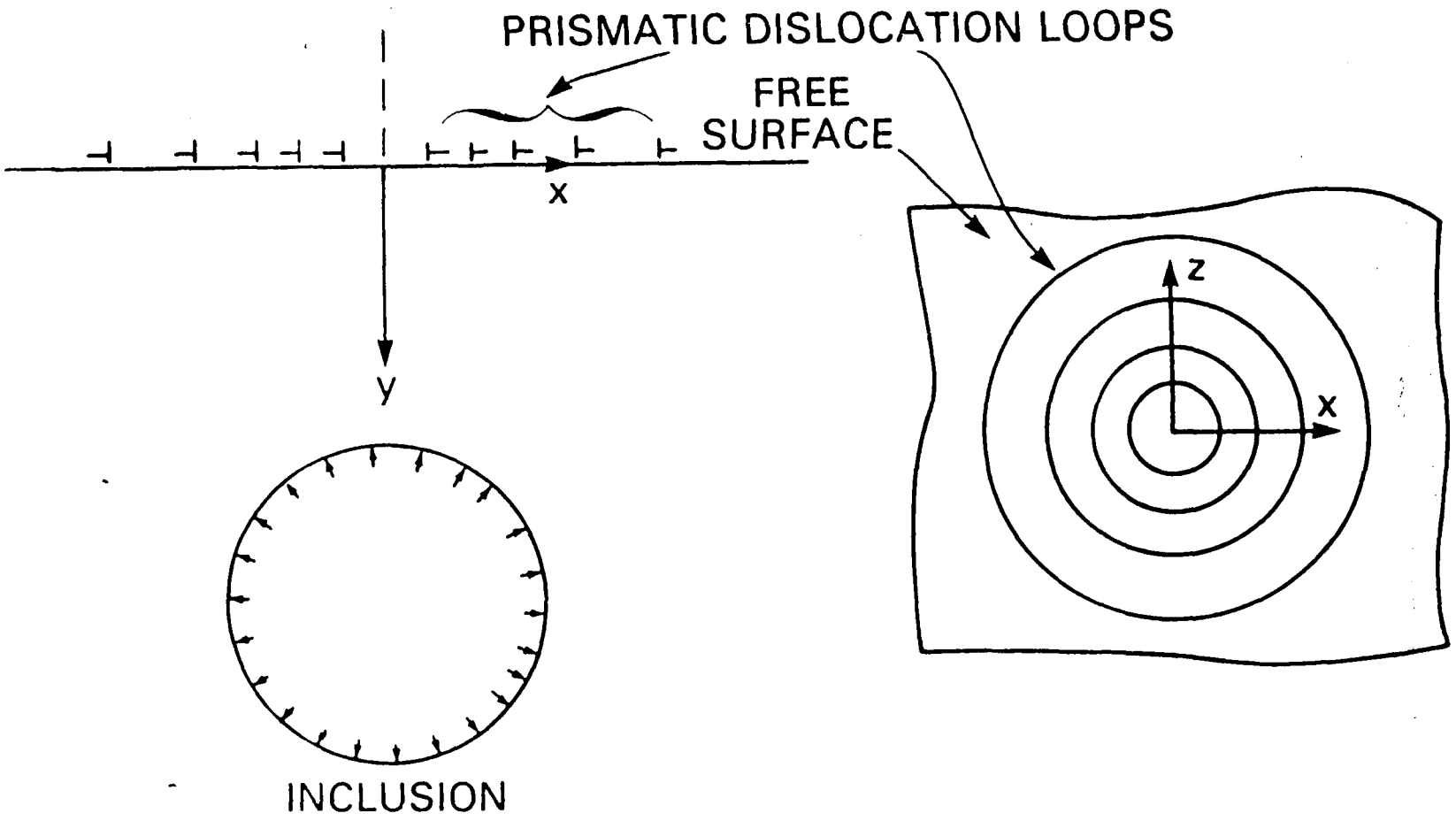
Fig. 1. Formation of an oxide inclusion of radius a at a distance h from a free surface. μ_p and μ_m are the shear moduli of the precipitate and the matrix respectively and P is the internal pressure of the misfitting inclusion.

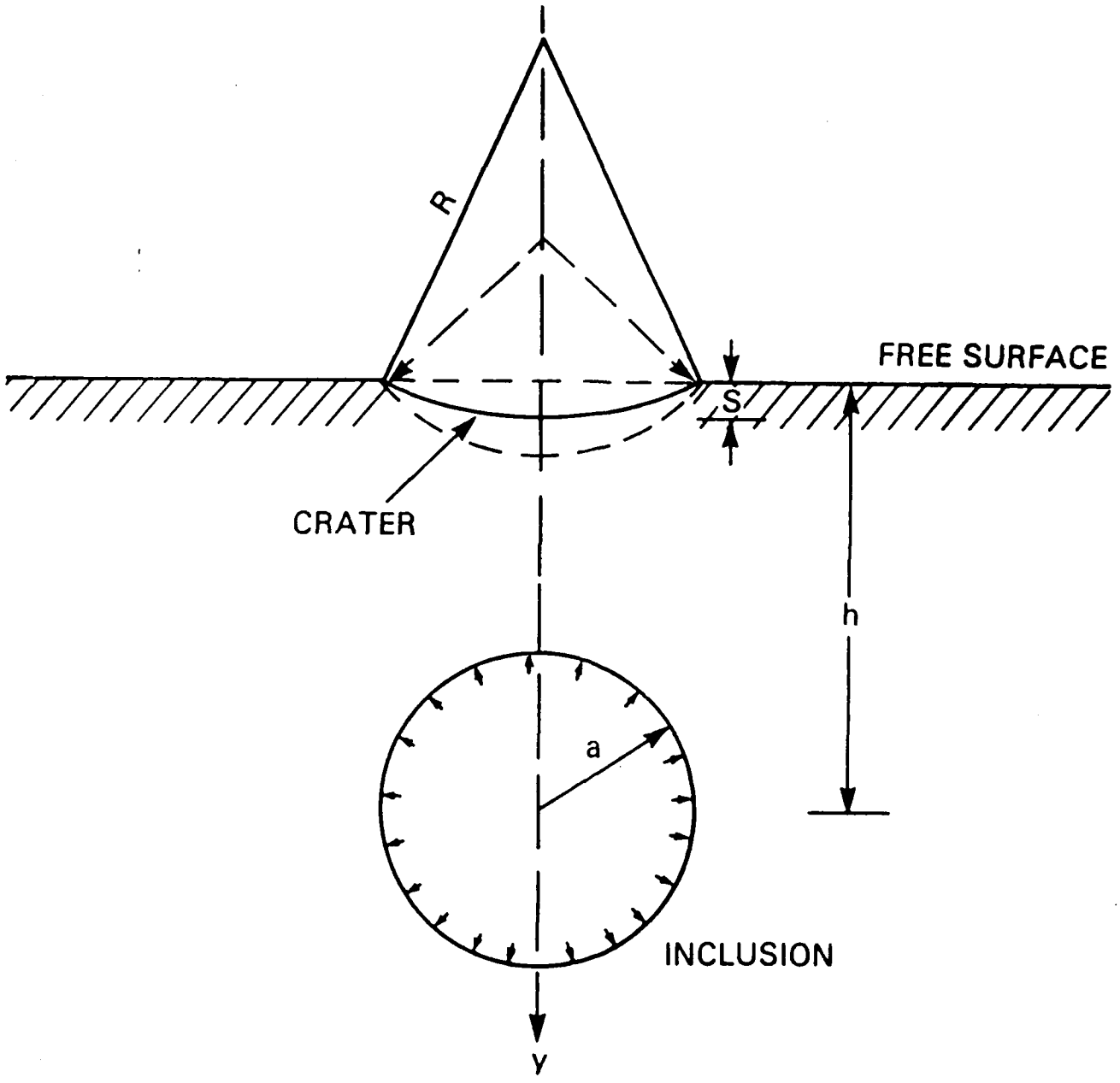
Fig. 2. Schematic illustration showing the distribution of prismatic dislocations on the free surface necessary to balance the normal stresses.

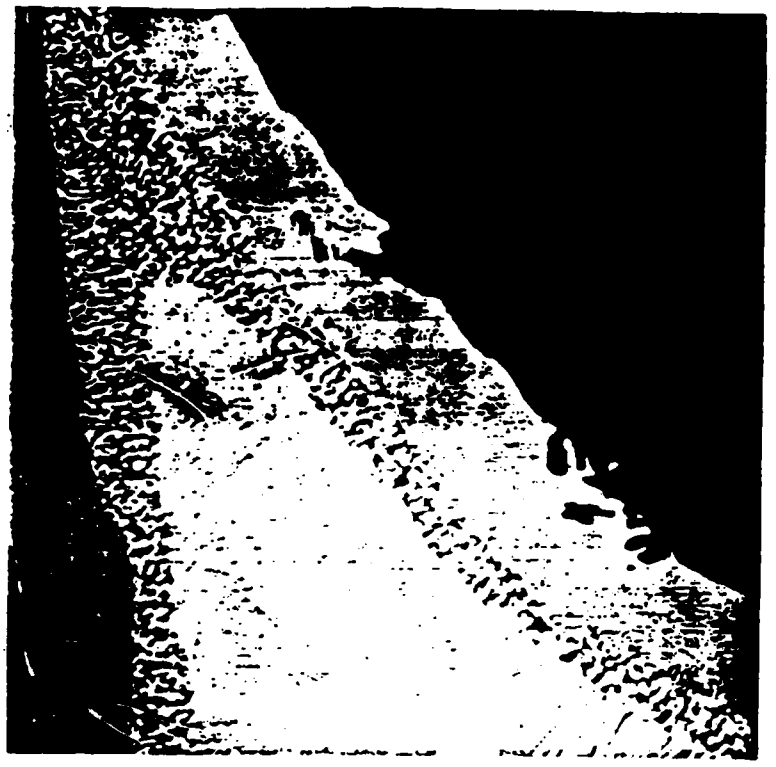
Fig. 3. Formation of a crater of radius R and depth S at the free surface due to the large hydrostatic stresses generated by a misfitting inclusion.

Fig. 4. Micrographs showing the formation of internal oxides in CoCrAlY coating and the resulting pits at the free surface.

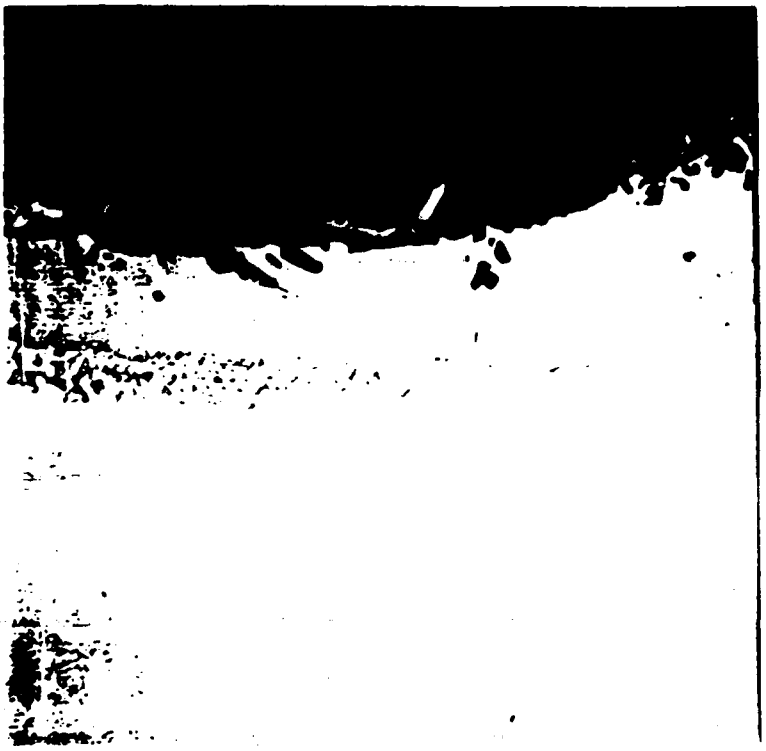

$\sigma_{yy} = 0$
σ_{xx}
σ_{zz}
x or r
σ_{yy}
σ_{xx}
σ_{zz}
h
MATRIX
(μ_m)
a
P
INCLUSION
(μ_P, a, P)
y


PRISMATIC DISLOCATION LOOPS
FREE
SURFACE
x
y
z
x
INCLUSION


R
FREE SURFACE
S
CRATER
h
a
INCLUSION
y



100 μm



To be submitted for publication

PEELING OF EPITAXIAL LAYERS

N. P. Louat* and K. Sadananda

Thermostructural Materials Branch
Materials Science and Technology Division
Naval Research Laboratory
Washington, DC 20375-5000

Analysis

We consider an infinite planar surface of a crystalline material of thickness d and sited thereon a volume of expitaxially deposited second phase having the form of a truncated cylinder of radius a and height h/2, such that $h/2d \ll a/2d \ll 1$. We wish to examine the tendency to spontaneous fracture in the neighborhood of the interface between the phases which may result from the stresses developed in the composite solid.

Such stresses vary with the degree of epitaxiality which can, for our purposes, be characterized by a parameter.

$$\eta = 2\frac{(a_1 - a_2)}{a_1 + a_2}$$

where a_1 and a_2 represent, respectively, the normal lattice spacings for the relevant planes of the materials of substrate and deposit.

*On-site contract employee from Geo-Centers Inc.,
Fort Washington, MD

For simplicity we assume that both materials are elastically isotropic and that they have the same elastic moduli. Again, we shall be concerned with circumstances where $a>>h$ and with the stresses developed at distances $r<<a$ from the edge of cylinder. With these particulars the error involved in ignoring the circularity in the geometry is small. In the interest of simplicity we, accordingly, reduce the problem to one in only two dimensions: one in which the epitaxial layer is a rectangular slab infinite in the z-direction, is of height, $y=\frac{h}{2}$ and of width, $r=2a$, with $h<<2a$. The plane of the interface is $y=o$.

The state of strain consistent with this geometry and with constant y can be imagined to arise as in the following thought experiment. The slab is first isolated from the substate, in a stress free state, tractions are then applied over its interfacial surface so that it expands or contracts so as to conform with the length of the stress free substrate. The surfaces are then rejoined and the surface tractions removed the material deforms to a state of equilibrium.

An alternative description and one in which equilibrium is implicit is to represent the trans-interfacial displacements as a planar dislocation continium. In this representation the isolated slab is supposed to: suffer

uniform elastic strain by the insertion or removal of sheets of matter in planes perpendicular to that of the interface; be returned to its original lateral dimensions by normal forces applied to its lateral surfaces. These forces are removed when the slab is replaced on the substrate. This act engenders the said uniform dislocation continuum. Equilibrium is achieved by the glide of the dislocations. In the special circumstances where there is no restraint to motion the distribution simply vanishes. In the case of interest motion is essentially disallowed by the strong atomic interactions at the interface. Thus, we can suppose the resultant distribution to be constant and equal to that impressed so that the dislocation content in a length δx is

$$\eta \, \delta x = \bar{b}$$

On this basis the final stress may be viewed as being derived from the presence of the fixed interfacial dislocations continuum together with contributions from other such continua induced on the free surface by these fixed stresses.

A first step in the required calculation is to evaluate the stresses arising from a dislocation of magnitude b located in the interface at a point r=t, y=o in the presence of the five free surfaces specified by the coordinates:

$$a \leq |x| < \infty, \; y = 0; \quad |x| < a, \; y = h/2; \quad |x| = a, \; 0 \leq y \leq h/2.$$

Of these we shall neglect the effects of the two vertical boundaries at x=a on the grounds that the dislocation of the interfacial continium are at positions x=t such that, $t \ll a$ nearly always, so that the stresses at these free surfaces are nearly always small. Furthermore, such stresses as do operate on these surfaces have only a relatively small effect because: the displacement induced on a free surface by the operation of a stress is proportional to its length; the stresses induced by such displacements scale with their magnitude; h/2a is small. To deal with the other three surfaces we resort still further to the use of dislocation continua. The use of this approach [1] to represent the results of the interaction of stress fields with planar free surfaces is now well established. Proceeding on this basis we have four equations expressing the conditions that normal and shear stresses must vanish in the free surfaces. We consider the four dislocation distributions: f(x); g(x); h(x) and k(x) developed as a consequence of a dislocation located at a point of the interface (displacement vectors parallel and normal to each surface are necessary). The determination of these functions is the crux of the analysis.

We have:

$$A\left\{\left[\int_{-\infty}^{-a} + \int_{a}^{\infty}\right] f(x)\,\frac{dx}{u-x} + \frac{\bar{A}}{u-t} + P_1(u) = 0\right. \qquad (1)$$

$$A\left\{\left[\int_{-\infty}^{-a} + \int_{a}^{\infty}\right] g(x)\,\frac{dx}{u-x} + P_2(u) = 0\right. \qquad (2)$$

$$A\int_{-a}^{a} h(x)\,\frac{dx}{u-x} + \bar{A}(u-t)\left(\frac{(u-t)^2 - h^2/4}{\left((u-t)^2 + h^2/4\right)^2}\right) + P_3(u) = 0 \quad (3)$$

$$A\int_{-a}^{a} k(x)\,\frac{dx}{u-x} + \frac{\bar{A}h}{2}\left(\frac{(h-t)^2 - h^2/4}{\left((h-t)^2 + h^2/4\right)^2}\right) + P_4(u) = 0 \quad (4)$$

These involve respectively the vanishing of shear stresses (1) and normal stresses (2) on the continuation of the plane of the interface and of shear (3) and normal stresses (4) on the top of the slab. The quantities $P_1(u)P_2(u)$, $P_3(u)$ and $P_4(u)$ represent the stresses developed on one surface by the distributions on the other. Other quantities are: $A=\mu\lambda/2u(1-\nu)$ and $A=\mu b/2u(1-\nu)$, where μ and ν have their usual significance. λ represents the magnitude of the displacement vector of unit dislocation.

Towards a solution of these equations we resort to approximations consistent with the results obtained by using them. These are:

(1) Replace the finite surface forming the free surface of the slab by one of infinite extent;

(2) Ignore the effect of the stresses emanating from the semi-infinite ranges on the finite ranges.

On these bases it remains only to calculate the stresses developed by the arrays formed on the semi-infinite surfaces due to the direct action of the initial dislocation and its "images" in the free surfaces.

The initial justification of these steps are as follows:
(a) calculation shows that provided a~t>h the error involved in treating the upper surfaces as infinite is small, this condition is satisfied for nearly all the epitaxial dislocations.
(b) The stresses from the semi-infinite surfaces are extremely short range, i.e. operative only over distances comparable with h.

To proceed we see that on the basis that $P_1(u)$ and $P_2(u)$ can be neglected we can proceed to the solution of (1) and (2) on the basis that $P_3(u)$ and $P_4(u)$ derive simply from the

imaging effects for edge dislocations at an infinite free surface. We first examine (3).

From a dislocation at t,o we have a stress $A/(x-t)$ at x. Because of the presence of the free surface we have to add an image stress and have a total

$$\bar{A}\left\{\frac{1}{x-t} - (x-t)\frac{(x-t)^2-h^2}{((x-t)^2+h^2)^2} - (x-t)h^2\frac{\left(3h^2-(x-t)^2\right.}{\left(h^2+(x-t)^2\right)^3}\right\}$$

In cases of interest here, when $h/(x-t) \ll 1$ the third term is negligible and this becomes

$$\bar{A}\left\{\frac{1}{x-t} - (x-t)\frac{d}{dh}\frac{h}{(x-t)^2+h^2}\right\}$$

The distribution function is then [2]:

$$h(x) = -\frac{\bar{A}}{\pi^2 A}\frac{1}{(x^2-a^2)^{1/2}}\int_{-a}^{a}(u^2-a^2)^{1/2}\left(\frac{1}{u-t} - (v-t)\frac{d}{dh}\frac{h}{(v-t)^2+h^2}\right)\frac{du}{u-x}$$

$$= -\frac{\bar{A}}{\pi A}\frac{(a^2-t^2)^{1/2}}{(x^2-a^2)^{1/2}}\left(\frac{1}{x-t} - \frac{(x-t)\left((x-t)^2-h^2\right)}{\left((x-t)^2+h^2\right)}\right), \quad |x| < a \quad (s$$

Consideration of this expression shows that h(x) is small when $(x-t) \gg h$.

Now this distribution arises from the presence of just one element of dislocation of magnitude $b=\eta\delta t$. The distribution due to all such elements is

$$H(x) = \eta \int_{-a}^{a} h(x,t)\, dt$$

$$= \frac{A^*}{A} \frac{1}{(x^2-a^2)^{1/2}} \left\{ (x^2-a^2)^{1/2} - \frac{1}{\sqrt{2}} \left(\left(\left(x^2-a^2-h^2+h^2 \right)^2 + 4x^2h^2 \right)^{1/2} + x^2-a^2-h^2 \right) \right.$$

$A^* = \mu\eta$

It is clear from (6) that H(x) is small when $(|x|-a)/h$ is large and in fact detailed examination of this expression shows that H(x)~o when

$|x|-a \sim 3h$.

Because the distribution is short ranged, so too are the stresses developed in the neighborhood of the points (x)=a. For example, the shear stresses developed along the plane y=o by this array can be evaluated approximately in a simple manner by recognizing that the distribution can be approximated by the expression

$$H(x) = \frac{A^*}{A} \frac{1}{B} \left(\frac{C^2-x^2}{x^2-a^2} \right)^{1/2} \qquad -(7)$$

where the constants B and C are chosen to give agreement between the range of the array and its magnitude at x=a. We find $B=\frac{1}{\sqrt{6}}$ and =a+3h.

On this basis the shear at a point t_o near a is

$$\sigma_{xy} = \frac{A^*}{B} \int_D \left(\frac{c^2-x^2}{x^2-a^2}\right)^{1/2} \frac{dx}{x-t} = \frac{\pi A^*}{B} \left(\left(\frac{c^2-t^2}{a^2-t^2}\right)^{\frac{1}{2}} - 1 \right)$$

where D is the union of intervals $a \leq (x) \leq c$.

In the case of the normal stresses there is no direct component of stress from the dislocation at t and we have only the effects of its "image". Thus, we have a stress

$$\sigma_{yy} = \bar{A} \left\{ h \frac{\left(h^2-(x-t)^2\right)}{\left(h^2+(x-t)^2\right)^2} - h \frac{\left(3h^2(x-t)^2+(x-t)^4\right)}{\left(h^2+(x-t)^2\right)^3} \right\}$$

Setting $x-t=nh$ we find that the second term falls like $1/^2$ when $n>2$. Consequently neglect of this term results in error in only a small region. That is to say only in the contribution of those dislocation elements which lie near the ends of the slab. Now somewhat surprisingly, but as concluded by Chou and Louat [3] distributions of dislocations are more sensitive to the stresses where the distribution are sparse than when they are concentrated. This can be simply demonstrated by considering an array developed through the

presence of a stress $\sigma(t)$, who's density is bounded at one end and unbounded at the other. Thus, we have

$$f(x) = -\frac{1}{\pi^2 A}\left(\frac{x}{a-x}\right)^{\frac{1}{2}} \int \left(\frac{a-t}{t}\right)^{\frac{1}{2}} \sigma(t) \frac{dt}{t-x}$$

with a total number of dislocations

$$n = \int_0^a f(x)\, dx$$

$$= \frac{-1}{\pi^2 A} \int_0^a \left(\frac{x}{a-x}\right)^{\frac{1}{2}} dx \int_0^a \left(\frac{a-t}{t}\right)^{\frac{1}{2}} \sigma(t) \frac{dt}{t-x}$$

$$= -\frac{1}{\pi^2 A} \int_0^a \left(\frac{a-t}{t}\right) \sigma(t) \int_0^a \left(\frac{x}{a-x}\right) \frac{dx}{t-x}$$

$$= \frac{1}{\pi A} \int_0^a \left(\frac{a-t}{t}\right) \sigma(t)\, dt$$

Clearly this integral is insensitive to the value of $\sigma(t)$ in the neighborhood of t=a. In the present context we conclude that the number of dislocations in the array is insensitive to approximations involved above. It remains to note that the stresses developed by an array are proportional to n while the force necessary to resist the advance of the array varies with n^2. Thus, the approximation should give comparatively small error in these quantities.

Proceeding from (4) and (7) we have a distribution

$$f_h(x) = -\frac{\bar{A}}{\pi^2 A}\frac{h}{(x^2-a^2)^{\frac{1}{2}}}\frac{d}{dh}\; h\int_D \frac{u^2-a^2}{(u-t)^2+h^2}\;\frac{du}{u-x}$$

$$= \frac{\bar{A}}{\pi A}\frac{h}{(x^2-a^2)^{\frac{1}{2}}}\frac{d}{dh}\;\frac{R\,(t-x)\cos\theta/2 + h\,R\sin\theta/2}{(t-x)^2+h^2}$$

where $\tan\theta = \dfrac{2th}{t^2-a^2-h^2}$, $R = \left\{\left(t^2-a^2-h^2\right)^2 + 4t^2h^2\right\}^{1/4}$

With the approximation

$$R \sim \left(t^2-a^2\right)^{1/2}$$

this becomes

$$h(x) = \frac{\bar{A}}{\pi A}\frac{h}{(x^2-a^2)^{\frac{1}{2}}}\left(t^2-a^2\right)^{\frac{1}{2}}\frac{d}{dh}\left(\frac{(t-x)\cos\theta/2 + h\sin\theta/2}{(t-x)^2+h^2}\right.$$

Adding the effects of all dislocations $\eta\delta t$ we have

$$K(x) = \frac{\bar{A}}{\pi A}\frac{h}{(x^2-a^2)^{\frac{1}{2}}}\int_{-a}^{a}\left(t^2-a^2\right)^{1/2}\frac{d}{dh}\left(\frac{(t-x)\cos\theta/2 + h\sin\theta/2}{(t-x)^2+h^2}\right)dt$$

In the range of interest it may be seen that $\theta \sim o$ so that this reduces to

$$K(x) = \frac{\bar{A}}{\pi A}\frac{h}{(x^2-a^2)^{\frac{1}{2}}}\frac{d}{dh}\int_{-a}^{a}\left(t^2-a^2\right)^{1/2}\frac{t-x}{(t-x)^2+h^2}\,dt \qquad (8)$$

We now remark that these results indicate a square root singularity for both shear and normal stresses at the end of the interface. The detailed form of these stresses are clearly complicated and as we have seen are highly localized at these points. Fortunately, our interest is not in the distribution of these stresses but in the values of the distribution functions at the points n=a. Thus, Bilby and Eshelby [5] have shown that the force acting on the leading element of dislocation arrays (f(x)) such as those found here, is given by the formula

$$F = \frac{\pi^2 A \lambda}{2} \lim_{x \to a} (x-a) f^2(x)$$

In the case of the distribution of (6) we have

$$F_s = \frac{\pi \eta^2 \mu h}{8 (1-\nu)}$$

as the force due to the shear stresses. Integrating (8) we find the same force from the normal stresses.

Now since these forces appear at the termination of free surface they are in effect forces for crack extension. Following Priestner and Louat [4] who showed that these forces are additive in their effect, we have a total crack extension force

$$F_t = \frac{\pi \eta^2 \mu h}{4 (1-\nu)}$$

Features of significance here are the absence of dependence on the length of the slab and the linear dependence on its thickness h/2 and the quadratic dependence on η. In this connection it should be borne in mind that, while the force for crack extension is independent of the sign at η, the crack can propagate only in the case where the logitudinal stresses in the epitaxial layer are compressive.

References

1. N. Louat, Nature, 196, 1081 (1962).

2. A. K. Head and N. Louat, Aust. J. Phys., 8, 1 (1955).

3. Y. T. Chou and N. Louat, J. A. P., 33, 3312 (1962).

4. L. Priestner and N. Louat, ACTA MET., 11, 195 (1963).

5. B. A. Bilby and J. D. Eshelby, Fracture (edited by L. Lubowitz), Vol. 1, p. 1120, Academic Press, New York (1968).

To be submitted for publication

ON THE D.F.Z. AND THE MODIFICATION OF G BY WORK HARDENING

N. Louat* and K. Sadananda+

Abstract

On the basis that a crack may be represented by a dislocation continuum it is shown that a crack extension force (G) cannot occur in the absence of a dislocation free zone (D.F.Z.). Given such a zone it is shown that G is apt to be sensitive to the variation of flow stress in the plastic zone and hence to work hardening.

*On-site employee of Geo-Centers Inc., Fort Washington, MD

+Naval Research Laboratory, Washington, DC 20375

Introduction

It is now widely appreciated that analyses based on elastic-plastic continuous fail to provide any energy for the propagation of a crack [1]. This conclusion is nowhere more evident than in the Dugdale-Bilby, Cottrell, Swinden (B.C.S.) [2,3] models. In these, as intuitively apparent, and as has been demonstrated by detailed calculation [4], the force available for crack extension is zero. This is an obvious defect of the model as it relates to fracture. We shall be concerned to examine the characteristics essential to a distribution in order that an unbalanced force appear. The prime result of this examination is a conclusion that such a force requires a discontinuity in the distribution and that such a discontinuity implies a D.F.Z.

On the basis of the existence of a D.F.Z. a beginning is then make of the determination of the effect of work hardening on the value of the crack extension force G.

ANALYSIS

In the planar two dimensional B.C.S. model the displacements engendered by the operation of an applied shear stress acting on a planar crack on the one hand and a resistance to motion of dislocation which may be supposed to have been emitted from the crack on the other are represented by a continuum of dislocations. The assumptions essential to the associated analysis are that each

element of the dislocation continuum is in equilibrium and that the dislocation density vanishes at the ends of the array.

As stated above these characteristics are apparently and actually at variance with the existence of a force which acts on the crack tip. It is further apparent from a consideration of the behavior of dislocation distributions that equilibrium at a point of the distribution requires continuity at that point. This follows from the equation specifying equilibrium for such distributions:

$$A \int_D f(x) \frac{dx}{x-t} - \sigma(t) = 0$$

where $f(x)$ represents the dislocation density in such a distribution and $\sigma(t)$ an externally supplied stress at a point $x=t$ of the array which occupies a region D of the n-axis. Considering this equation in the neighborhood of the point, we may write when $\delta(x)$ is continuous at $x=t$.

$$A \int_D \left[f(t) + (x-t) f'(t) + \cdots \right] \frac{dx}{x-t} = \sigma(t)$$

$$A \int_D \left[\frac{f(t)}{x-t} + f'(t) + \frac{(x-t)}{2} f''(t) - \cdots \right] dx \qquad (1)$$

This expression is well defined with the understanding that the singularity is treated on the basis of its principal value. If however f(x) is discontinuous at x=t the integral in (1) becomes

$$A \int_{D_1(x<t)} \frac{f_1(t)}{x-t} + f_1'(t) + \cdots \, dx$$

and

$$A \int_{D_2(x>t)} \frac{f_2(t)}{x-t} + f_2'(t) + \cdots \, dx$$

with

$$f_1(t) \neq f_2(t)$$

in which case the singularities persist; the integrals diverge individually and collectively.

Then since equilibrium is achievable only at points where the dislocation distribution is continuous, we anticipate that forces which arise from causes other than interactions between elements of the dislocation distribution must be present when it is discontinuous and conversely that the existence of such a force implies a discontinuity in the distribution.

Allowing then that the existence of a force for crack extension (that is, that G is non-vanishing) requires the presence of a discontinuity in the distribution function, we now inquire as to the physical circumstances in which such discontinuities can arise. Two possibilities exist. The first of these involves the

presence of infinite discontinuities in stress, as are induced by the presence of real lattice dislocation of finite Burgers vector in the place of the array, but these are not of interest here. The second possibility is the abutment of regions in which $f(x)=o$ against regions where $f(x)\neq o$. Such is the case in the familiar circumstances at the tip of a crack. Dislocation is spread within the crack and has non-vanishing density at its tip. External to the crack this density is zero and thus there is a discontinuity in distribution. There is then a net force on the leading element of the array due to all the others and a force for crack extension. In the same way we are lead to conclude that a modified B.C.S. model in which a region or regions of zero dislocation density are introduced in such a way as to result in a discontinuities in this density are accomplished by the appearance of similar forces. Furthermore, we conclude that no such force can arise unless there exists such an arrangement. That is to say we may regard the existence of a discontinuity in dislocation density which borders a region free of dislocation (Dislocation-Free-Zone) as both necessary and sufficient for the existence of a crack propagation force and hence of fracture.

On this basis we now consider the question of how the force G on a crack tip is influenced by the distribution of dislocation within a plastic zone separated from the free crack by a dislocation-free-zone (D.F.Z.). To facilitate an understanding of the analysis we first outline the procedure for the B.C.S. model. We suppose that an infinite body be subjected to a uniform stress σ

and that it contain a planar crack (y=o) which is bounded by the lines at (x)=b. It is further supposed that the motion of dislocations which could have been emitted by this crack is impeded by the action of a lattice resistance, τ, in a plastic zone: $b<|x|<a$, $y=o$.

Invoking the approximation that the displacements in y=o, due to the lattice dislocations of the plastic zone can be expressed in terms of a continuum (f(x)) of elementary dislocation we have for equilibrium [5,6]

$$A \int_{-a}^{a} f(x) \frac{dx}{x-t} = \sigma(t)$$

On the basis that the distribution is bounded when $|x|=a$ the unique solution [7] to this equation is

$$f(x) = -\frac{1}{\pi^2 A}(a^2-x^2)^{1/2}\left\{ \int_{-a}^{-c} \sigma \cdot - \int_{-c}^{c} \tau + \int_{c}^{a} \sigma \right\} \frac{1}{(a^2-t^2)^{1/2}} \frac{dt}{t-x}$$

provided

$$\left\{ \int_{-a}^{-c} \sigma - \int_{-c}^{c} \tau + \int_{c}^{a} \sigma \right\} \frac{dt}{(a^2-t^2)^{1/2}} = 0 \qquad (2)$$

For the stresses specified we have [8]

$$f(x) = \frac{(\tau+\sigma)}{\pi^2 A} \ln \left| \frac{c\,(a^2-x^2)^{1/2} + x\,(a^2-c^2)^{1/2}}{c\,(a^2-x^2)^{1/2} - x\,(a^2-c^2)^{1/2}} \right|$$

provided,

$$\frac{\sigma}{\tau} = \frac{2}{\pi} \cos^{-1} c/a$$

Chang and Ohr modified this model to allow for the existence of a D.F.Z. at the tips of the crack c<| |<b using essentially the same stresses as above. In this case the solution is

$$f(x) = -\frac{1}{\pi^2 A} \left\{ \frac{(b^2-x^2)(a^2-x^2)}{x^2-c^2} \right\}^{1/2} \left\{ \int_{-a}^{-b} (\sigma-\tau) + \int_{-c}^{c} \sigma + \int_{b}^{a} (\sigma-\tau) \right\} \left\{ \frac{(t^2-c^2)}{(a^2-t^2)(b^2-t^2)} \right\}^{\frac{1}{2}} \cdot \frac{dt}{t-x}$$

with a condition

$$\left\{ \int_{-a}^{-b} (\sigma-\tau) + \int_{-c}^{c} \sigma + \int_{b}^{a} (\sigma-\tau) \right\} \left\{ \frac{(t^2-c^2)}{(a^2-t^2)(b^2-\tau^2)} \right\}^{1/2} dt = 0$$

An unfortunate characteristic of the results of the evaluation of the integrals involved is that while they are available in closed form their representation involves elliptic integrals of all three kinds. Appreciation and manipulation of these results is accordingly difficult. To avoid these difficulties Louat [10] introduced an approximate distribution expressed in terms of elementary functions. Thus,

$$f(x) = \frac{Y}{\pi^2 A} \ln \left| \frac{b(a^2-x^2)^{\frac{1}{2}} + x(a^2-b^2)^{\frac{1}{2}}}{b(a^2-x^2)^{1/2} - x(a^2-b^2)^{1/2}} \right| \left(\frac{x^2-b^2}{x^2-c^2} \right)^{\frac{1}{2}} \quad (3)$$

$$\equiv_{\text{def}} \frac{Y}{\pi^2 A} S \ln R \quad ; \quad Y = \sigma + \tau$$

Inspection shows that f(x) is unbounded with the square root singularity characteristic of crack tips at x=c, and vanishes at |x|=b and |x|=a. The total stresses associated with this distribution are:

$$\sigma_1 = 0 \,, \quad |x| < c \,; \quad (4)$$

$$\sigma_2 = Y \leq k_M R, \quad c \leq |x| \leq b; \tag{5}$$

$$\sigma_3 = \frac{Y}{\pi}\left(\frac{x^2 - b^2}{x^2 - c^2}\right)^{1/2} \tag{6}$$

Of these σ_1 is as it should be while σ_3 deviates from the required value $(\sigma+\tau)$ over a length which is small when the D.F.Z. is small in comparison with a-b. Thus, setting the length of the D.F.Z. as

$$\Delta = b - c$$

we find that σ_3 deviates from its required value by less than 10% when

$$\frac{|x| - b}{\Delta} \geq 2$$

The results of (3), (4), (5) and (6) are subject to the same condition as obtains in the case of the B.C.S. crack, here:

$$\frac{\sigma}{Y} = \frac{2}{\pi} \cos^{-1} \frac{b}{a}$$

We now fix the size of Δ by reference to a particular physical basis for its existence. We suppose in conformity with the precepts of the B.C.S. model that a crack length 2c will, under the action of some imposed shear stress $\bar{\sigma}$ emit a dislocation on an otherwise dislocation free plane. This dislocation will glide to a position at which the force of its interaction is just

balanced by the resistance to motion offered by the material. For constant $\bar{\sigma}$ and c, it is apparent that the emission of a second dislocation would be less readily achieved than that of the first and so on. This process would cease when the closest dislocation was at some finite distance from the crack tip. We suppose that this distance is a close approximation to Δ. We fix Δ by requiring that the stress at the crack tip be sufficient to allow the formation of the last dislocation of the sequence. Thus, the stress (6) is to exceed some critical value at a certain distance from the crack tip. We take this distance as one atom spacing (λ) and the critical stress as $\mu/10$ and have the condition:

$$\frac{Y}{\pi}\left(\frac{\Delta}{\lambda}\right)^{\frac{1}{2}} \ln \frac{4(a-b)}{\Delta} \equiv \sigma_c \simeq \frac{\mu}{10}$$

so that

$$\frac{\Delta}{\lambda} \sim \frac{\mu^2}{10\,Y^2} \quad \frac{1}{\ln^2 4(a-b)/\Delta} \qquad (7)$$

Clearly, this ratio increases rapidly with decreasing γ and since the lengths c, b and a are not prescribed it is apparent that situations can occur in which the condition $\Delta/(a-b) \ll 1$ is not satisfied. However, in circumstances typical of fracture: $\gamma \sim \mu/10^3$, a-b~1mm, we find from (7) that

$$\frac{\Delta}{\lambda} \sim 4.5 \times 10^{-3}$$

so that in this case

$$\frac{\Delta}{a-b} \sim 5 \times 10^{-4} \ll 1$$

It is then not surprising that for parameters leading to such values of $\Delta/(a-b)$ as this, the approximate treatment gives results which accord well with the numerical values given by Ohr and Chang [11].

Using Bilby and Eshelby's expression for the crack extension force:

$$G = \pi^2 A \lambda \lim_{x \to c} (x-c) f^2(x)$$

we find

$$G = \frac{Y^2 \lambda}{A} \Delta \ln^2 4 \frac{(a-b)}{(b-c)}$$

And on imposing the condition for dislocation emission (7) we find:

$$G \simeq \mu\lambda/5$$

a value comparable with that for crack extension, namely $2\gamma_s$.

This result is not unexpected in the circumstances of the supposed (col inear) geometry where dislocation emission and crack extension (mode I) are essentially similar. This similarity should not persist to more realistic situations where crack advance and dislocation emission occur on planes inclined at an angle θ ($\theta \sim 70°$) to each other. For this geometry the presence of an edge

dislocation which lies in a glide plane which passes through the crack tip and, when at a distance r from it, provides forces which respectively resist dislocation emission and crack advance and which have magnitudes:

$$\frac{2A'\sin^2\theta}{r} \qquad \text{and} \qquad \frac{A'\sin 2\theta}{r}$$

so that emission is selectively restrained when $\theta > \pi/4$.

Since emission in particular and, plastic deformation in the neighborhood of a crack in general, will tend to result in crack blunting selective restraint of dislocation motion is expected to assist in fracture. Among processes which have such an effect, we distinguish work hardening. Towards an appreciation of the importance of this phenomenon we consider the consequences of the existence of a stress which is largest in regions where dislocation motion is greatest. We suppose in particular that

$$\sigma(x) = \sigma, \quad |x| < b; \qquad \sigma(x) = \sigma - \tau + \alpha\left(|x| - b\right), \quad b \le |x| < a$$

To analyze the consequences of this stress distribution we first require satisfaction of the condition (2):

$$\sigma\int_{-b}^{b}\frac{dx}{(a^2-x^2)^{1/2}} + \left\{\int_{-a}^{b} + \int_{b}^{a}\right\}\frac{\sigma-\tau+\alpha\left(|x|-b\right)}{(a^2-x^2)^{1/2}}\,dx$$

$$= \pi\sigma - 2\tau \cos^{-1}\frac{b}{a} - 2\alpha b \cos^{-1}\frac{b}{a} + 2\alpha (a^2-b^2)^{\frac{1}{2}} = 0 \quad (8)$$

Using the widely valid approximation

$$\cos^{-1}\frac{b}{a} \simeq \left(2\,\frac{(a-b)}{a}\right)^{1/2}$$

and setting

$$\alpha(a-b) = n\tau,$$

the condition (8) becomes

$$\cos^{-1}\frac{b}{a} \simeq \frac{2\pi\sigma}{\tau(4-3n)} .$$

This reduces to the B.C.S. result when n=o.

Corresponding to this arrangement in applied stress we have a dislocation distribution

$$\bar{f}(x) = f(x) + g(x)$$

where

$$f(x) = \frac{(\gamma+\alpha b)}{\pi^2 A} \ln \left| \frac{b(a^2-x^2)^{\frac{1}{2}} + x(a^2-b^2)^{\frac{1}{2}}}{b(a^2-x^2)^{1/2} - x(a^2-b^2)^{1/2}} \right| \left(\frac{b^2-x^2}{x^2-c^2}\right)^{\frac{1}{2}}$$

$$g(x) = -\frac{2}{\pi^2 A}(a^2-x^2)^{1/2} \cos^{-1}\frac{b}{a} \quad , \quad b < |x| < a \; ;$$

$$= 0 \quad ; \quad |x| < b .$$

Thus save a numerical factor

$$\bar{f}(x) = f(x)$$

when $|x|<b$. This is true in particular when $x=c$ so that using the Bilby-Eshelby result as before G the crack extension force is functionally invariant and

$$\frac{G_h}{G} = \frac{16}{(4-3n)^2}$$

where G_h appertains when work hardening is present and G when it is absent; c.f. (1).

The model adopted here for the effects of work hardening as a simple linear decrease in flow stress is most unlikely to be accurate. However, the attainment of a more realistic representation appears to rest on an experimental determination of localized stress and plastic strain in plastic zones. Such measurements are unknown to the author.

REFERENCES

1. A. D. Kfauri and J. R. Rice, Proc. 4th Int. Conf. on Fracture (D.M.R. Taplin, ed.), p. 43, Univ. of Waterloo Press (1977).

2. D. S. Duglekale, J. Mech. Phys. Solids, 8, 100 (1950).

3. B. A. Bilby, A. H. Cottrell and K. H. Swinden, Proc. Roy. Soc. 272(A), 304 (1963).

4. T. Yokobori and M. Ichikawa, Reps. Res. Inst. Tohoku Univ. 2, 21 (1966).

5. Leibfried

6. A. K. Hea d and N. Louat, Aust. J. Phys. 8, 1 (1955).

7. Muskehishvili, Singular Int. Equations, Groningen-Holland P. Noordhoff, N.V., p. 251 (1940).

8. J. Weertman, Proc. 1st Int. Conf. on Fracture, Sendai, p. 153 (1966).

9. S. J. Chang and S. M. Ohr, J. App. Phys.52, 774 (1981).

10. N. Louat, Acta Met. 16, 775 (1982).

11. S. M. Ohr and S. J. Chang, J. App. Phys., 53, 5645 (1982).

To be submitted for publication

COMPUTER SIMULATION OF DISLOCATION MOTION

Principal Investigator: K. Sadananda

Co-investigators: M.S. Duesbery, N. Louat

1. Introduction

It has been known for many years that metals can be hardened significantly by precipitation of a second phase [1-3]. The degree of hardening varies with many factors, including the size and distribution of the precipitates, their elastic strength relative to that of the matrix and the nature of the precipitate-matrix interfaces. Some specific strengthening mechanisms have been identified as follows.

(a) Coherency strengthening [4], caused by the stress field around a particle which does not fit exactly into the cavity in the matrix.

(b) Modulus strengthening [5], caused by a difference in elastic moduli between precipitate and matrix.

(c) Order strengthening [6], caused by the need to create an antiphase domain boundary when a dislocation passes through an ordered precipitate.

(d) Stacking fault strengthening [7], due to a difference in stacking fault energy betweeen precipate and matrix.

(e) Surface Strengthening [8], caused by the creation of new particle-matrix interfaces as the precipitate is sheared.

The principles underlying the hardening effect are understood at a qualitative level. The precipitates act as obstacles to the passage of dislocations, which must bypass the obstacles in order

for plastic flow to proceed. Bypass can occur via any one of a number of processes, depending on the details of the second phase particles and the character of the dispersion. For example, soft precipitates may be easily intersected by dislocations. A harder second phase may require the dislocations to loop around the inclusions, leaving loops and debris which can contribute to the hardening effect; in this case the precipitates can sometimes fail unexpectedly, leading to avalanches of plastic flow and catastrophic failure of the material.

Quantitative understanding, in contrast, is poor, and the development of improved dispersion-hardened materials proceeds in large part by the slow and inefficient avenue of empiricism. This was understandable twenty-five years ago, when the elastic theory of dislocations was insufficiently advanced to treat the self and interaction energies of arbitrarily shaped dislocations, and when the facilities for numerical modelling were severely limited. However, it is now possible to develop formally self-consistent Hamiltonians for the problem and to solve them numerically, making possible a cost-effective alternative to empirical experimentation.

There are two levels to the problem. At the micromechanical level, it is necessary to understand the detailed interaction of dislocations with precipitates of different character, in order to categorize bypass mechanisms as a function of obstacle characteristics and determine the associated critical parameters. These results must then be used at a macroscopic level to model the statistical mechanics of dislocation motion through realistic

distributions of dispersed obstacles.

Our work over the last year has considered the interaction of dislocations with one specific class of precipitate, elastically coherent spherical inclusions.

2. Modelling Methods

The shear stress field at a point P due to an element of length ds at C of a dislocation segment AB (see fig. 1) is given by [9]

$$\sigma = \frac{1}{G} \frac{\sin\beta}{|\underline{r}|^2} \cdot (E + E'') \, ds \qquad (1)$$

where $\underline{r}$ is the vector joining C and P, β is the angle between $\underline{r}$ and the tangent to the dislocation line at C, b is the Burgers vector and E, E'' are the energy of the dislocation per unit length and its second angular derivative, respectively. The stress at P due to the entire segment AB is obtained by integrating (1) along the contour AB. Referring again to fig. 1, it is obvious that the dislocation segment AB will exert a stress on the segment EF by virtue of (1), a stress which remains the same whether EF is part of a physically distinct dislocation or part of the same dislocation as AB (see dashed line in fig. 1). Thus different elements of the same dislocation interact with each other, causing a **self-stress** which influences the shape and flexibility.

The simplest approximation to the self-interaction of the dislocation is the **line tension** model [10], which treats a dislocation as an elastic string with a fixed energy per unit length. The

line tension model is crude, completely ignoring the strong interaction (1), but nonetheless forms the predominant basis for our understanding of dispersion hardening, at both the microscopic and statistical levels.

The self-stress model, introduced as a numerical procedure by Bacon [11] based on Brown's [9,12] self-stress theory, accounts fully for the self-interaction (1). This model has been used [13-16] to investigate dislocation bowing between "impenetrable" obstacles (i.e. infinitely strong obstacles with no local stress field). The most complete treatment was given by Bacon, Kocks and Scattergood [16] (referred to below as BKS), who showed that the predictions of the full self-stress model can be very different from those of the line tension model.

The BKS model, notwithstanding their advanced treatment of the self-stress, treats only impenetrable obstacles and single dislocations in a pre-critical bowed state. We have extended Bacon's ideas to develop a dynamic model which can simulate not only dislocation bowing, but also the full range of bypass processes, including intersection, looping and interaction with debris and other dislocations. This has never been attempted before, and represents a major advance in dispersion hardening theory.

The model treats each dislocation as a set of finite straight segments, each with its own momentum and position, moving in the potential energy field prescribed by the full self-stress Hamiltonian. The segment density varies along the dislocation line, permitting small segment lengths when a high curvature must be

modelled, but large lengths when the curvature is low. The segment density is dynamically reallocated to optimize numerical performance. Obstacles of any kind can be incorporated, provided that an effective stress field can be defined.

3. Results

It is convenient to use the predictions of the line tension model as a baseline, to facilitate comparison and understanding of deviations. For impenetrable obstacles of diameter D and separation L (fig. 2), the line tension model predicts a bypass (Orowan) stress τ_o of [17]

$$\tau_o = Gb/L \qquad (2)$$

where G is the shear modulus and b the magnitude of the Burgers vector. Fig. 2 shows a schematic section of a dislocation line bowed against a linear array of identical obstacles (boundary conditions of translational periodicity in L + D are used), just before the breakthough point. The parameters of interest, the breaking angle ., the maximum bowout Y_m and the closest distance of approach between dislocation and obstacle Y_c are indicated in fig. 2.

The line tension model predicts the breaking angle Θ to be 0° and the bowed shape to be circular with $Y_m/L = 0.5$. BKS showed that this description must be modified in the self-stress model. They found that while the breaking angle remains close to 0°, both

the Orowan stress and the bowout at the critical point can be much less than predicted by the line tension model. This is because the attractive dipolar interaction between the dislocation arms on either side of an obstacle (e.g. X, X' in fig. 2) assists the bypass mechanism. The BKS results were consistent with an Orowan stress given by

$$\sigma/\tau_o = (A/2) \cdot (\ln X + B) \qquad (3)$$

where A is a constant equal to 1 for edge and $1/(1-\nu)$ for screw dislocations (ν is Poisson's ratio), X is the harmonic mean of L and D (i.e. $1/X = 1/L + 1/D$), B is an empirical constant of order unity and τ_o is given by (2). The physical interpretation of (3) is that for large obstacle separations, the logarithmic term is dominated by the obstacle size, reflecting the importance of the dipole interaction between the dislocation arms on either side of the obstacle. This will be termed the obstacle dipole regime. Conversely, for closely spaced large obstacles, it is the interaction of the dislocation arms between obstacles (e.g. X, X'' in fig. 1) which governs the Orowan stress. This will be called the loop dipole regime.

We have taken the self-stress theory one step further by treating coherent spherical precipitates with a lattice constant incommensurate with that of the matrix. For a fractional mismatch of ε, the shear stress field due to each obstacle interacting with an edge dislocation is

$$\sigma_{xz} = -\frac{3G\epsilon D^3}{4} \cdot \frac{zx}{r^5} \qquad (4)$$

referred to the axes defined in fig. 2. We have considered the effect of a range of misfit values from 0.001 to 0.050, for several sets of obstacle size and separation, on the passing stress required for dislocations of initial edge character. The term 'passing' stress rather than Orowan stress is used because for small values of ϵ, bypass takes place by intersection rather than looping.

Typical examples of the intersection and looping processes are illustrated in figs. 3(a) and (b). In both cases the dislocation is moving from bottom to top of the diagrams, through a periodic array of obstacles with diameter D=300b and separation L=400b; horizontal and vertical coordinates are given in units of b. Successive equilibrium positions of the dislocation as the stress is increased in steps to the bypass stress are shown. In fig. 3(a) the obstacle-matrix mismatch is ϵ=0.001 and bypass occurs by intersection. A larger mismatch of ϵ=0.003 in fig. 3(b) forces the dislocation to pass the obstacle array by looping, leaving behind a loop inside the obstacle (A in fig. 3(a)). The passed dislocation is still present in the field of the diagram in fig. 3(b); this dislocation is not in equilibrium, but is straightening out as it moves away from the obstacles. The bypass stress in fig. 3(b) is $0.57\tau_0$, twice that in fig. 3(a); this can be seen from the greater curvature of the dislocations in fig. 3(b).

3.1 The Passing Stress

Consider first the variation of the passing stress with misfit. In all cases bypass occurs by intersection for very low values of the misfit parameter, and in this regime the gradient of the stress/misfit curve is high. For higher misfits, three different types of behavior have been observed, and are shown in fig. 4, illustrated for three different combinations of obstacle sizes and separation. Note that the origins of the vertical (stress) axes in fig. 4 have been offset to separate the graphs. Data points in the intersection and Orowan regimes are denoted by crosses and periods, respectively.

(a) In most cases, the passing stress increases only slightly once the bypass mechanism changes from intersection to Orowan looping. This is illustrated in the curve marked (a) in fig. 4, and is the expected behavior. Once the Orowan mechanism becomes dominant, further increase in the misfit cannot lead to increased strength in the line tension or BKS models. For coherent obstacles, second-order effects can occur because the coherency stress (3) has a finite range which increases with increase in misfit.

(b) When the obstacles are very small, the Orowan mechanism is suppressed even for large misfit parameters. This is because the high curvature of the dislocation when wrapped around a small obstacle generates a large forward stress which aids intersection.

The resulting stress-misfit curve ((b) in fig. 4) shows a decrease in the gradient at the misfit level corresponding to the onset of the wrap-intersection mechanism, but increased misfit leads to further hardening. The continued hardening occurs because increase in misfit enhances the obstacle stress field (3), requiring a larger applied stress to wrap the dislocation to the required curvature.

(c) For closely spaced obstacles, the same transition from intersection to Orowan bypass takes place, but increased misfit produces further, pronounced hardening. This is shown in curve (c) in fig. 4. This type of behavior is observed when the obstacle spacing is sufficiently close for the stress fields (3) from adjacent obstacles to overlap and produce a retarding stress independent of the bypass mechanism.

It is clear from this discussion that the impenetrable obstacle treatments, which would predict a single passing stress for each obstacle size/separation ratio, present only a simplified picture of the problem. In limiting examples, our calculated passing stresses agree with the BKS values. For most cases, however, the strength of the coherent obstacle array is found to be lower than predicted by the BKS treatment, even in the Orowan regime. The physical reason for this is quite clear. The obstacle stress (4) causes an additional attractive force on the dislocation arms X, X' (fig. 2) once the bowed-out loops move past the central

(y = 0) point. Therefore the coherent obstacles are weaker in the obstacle dipole regime. In the loop dipole regime, for large, closely-spaced obstacles, the overlap mechanism (c) above operates to increase the passing stress to a level well above the BKS values.

The BKS expression (3) for the Orowan stress does not allow for different obstacle strengths and therefore is not expected to fit our calculated Orowan stresses, which vary substantially with the mismatch parameter. However, it can be seen from fig. 3(b) that just before Orowan looping occurs, the part of the dislocation which is curved around the particle forms a roughly circular arc with a radius given by the closest distance of approach, Y_c (see fig. 2). This suggests that it may be possible to define an "equivalent impenetrable" obstacle array consisting of obstacles with diameter $D^* = 2Y_c$, separated by distances $L^* = L - 2Y_c$. With these substitutions (3) becomes

$$\sigma/\tau_o = L/L^* \cdot (A/2) \cdot (\ln X^* + B) \qquad (5)$$

where X^* is the harmonic mean of D^* and L^*. Fig. 5 shows our calculated Orowan stresses plotted against $(L/L^*)\ln X^*$; the range of values obtained by BKS is indicated by the line marked 'BKS'. The second straight line in fig. 5 is a line with slope 1/2 drawn so as to pass through the more densely populated region of data points. Although there are deviations, (5) approximates the behaviour quite well. The systematic deviations in fig. 5 for large

values of $(L/L^{\cdot}).\ln X^{*}$ correspond to very small values of L^{*}, of order 10%; for these extreme cases (5) is not expected to give an accurate representation.

3.2 The Flow Stress

In a real system, the arrangement of the dispersoids will in most cases be random, and in this event the breaking angle θ and the maximum bowout Y_m exert an influence on the flow stress of the material. For example, consider fig. 6, which shows a schematic diagram of a dislocation bowed between obstacles A, A', superimposed on a "random" dispersion of obstacles. The semicircular arc between A and A' shows the critical configuration in the line tension approximation. Clearly the dislocation cannot achieve this configuration without contacting other obstacles, thereby decreasing the effective spacing between obstacles. The effective strength of the dispersal will be determined by the maximum obstacle separation for which a semi-circular arc can be described without contacting other obstacles. Obviously, if the breaking angle θ is greater than zero, or if the shape of the loop becomes non-circular with a smaller maximum bowout Y_m (the dashed loop in fig. 6), the critical obstacle separation will be larger, leading to a lower strength. The BKS treatment indicates that for impenetrable obstacles the breaking angle remains close to zero, but the bowout ratio Y_m/L can differ from the line-tension value of 0.5. Specifically, BKS find that the bowout ratio varies principally with the ratio L/D, with a maximum of 1.25 for $L'/D = 3$, dropping steadily

to a value of 0.3 for L/D = 24.

For coherent obstacles, we find that the breaking angle is never lower than 60°, varying from this value to 90° in the Orowan regime, and approaches 180° in the intersection regime. We also find that the bowout ratio reaches a value only of 0.85 at L/D = 3, dropping much more sharply than BKS before levelling out at a similar value for L/D = 24. Both of these dependences indicate a lower strength for coherent obstacle dispersals than predicted by the line tension model or the BKS treatment.

4. Summary

We have modelled the motion of edge dislocations through a periodic array of sperical, coherent precipitates. Bypass was found to occur by intersection for small precipitate-matrix misfit values. For larger misfits Orowan looping acted as the bypass mechanism, except for small precipitates, which continued to fail by intersection, because of the high curvature of the dislocation segments close to the particles.

We have calculated the passing stresses and compared these with analogous values (BKS) for impenetrable obstacles. Our results are generally substantially lower, but for close precipitates can be several times larger, because of the back stress from overlapping precipitate stress fields. Our results can be fitted to the same functional dependence found by BKS for the Orowan stress on the diameter and separation of the particles, provided that we use an "effective" particle radius equal to the closest distance of

approach of the dislocation to the center of the precipitate.

We also find that the critical bypass parameters, the breaking angle and the maximum extent of dislocation bowout, are different from those found for impenetrable obstacles. For coherent precipitates, the breaking angle is larger and the maximum bow-out smaller, both of which would suggest a lower strength for a random obstacle distribution.

5. Future Directions

We have considered only the micromechanics of one possible source of dispersion hardening. The computer program can be used with only minor modifications to examine the other sources of hardening outlined in the introduction. A program must be developed to treat the statistics of dislocation motion through random dispersals of obstacles, using the critical parameters developed from the microscopic models.

So far we have made use only of the end-result static predictions of our model. The dynamical behavior, which is physically realistic, can be used to generate movies or videotapes of the bypass processes, for comparison with in-situ electron microscope observations and for educational purposes.

References

1. M.F. Ashby, First International Conference on the Strength of Metals and Alloys (ICSMA I), Asilomar, California, (1970), vol. II,

p507.

2. L.M. Brown, ICSMA V, (1979), vol. III, p1551.

3. D.J. Lloyd, ICSMA VII, Montreal, Canada, (1985), Pergamon Press, New York, vol. III, p1755.

4. N.F. Mott and F.R.N. Nabarro, Bristol Conference on the Strength of Solids, The Physical Society, London (1948).

5. K.C. Russell and L.M. Brown, Acta Met. 20 (1972) 969.

6. V. Munjal and A.J. Ardel, Acta Met. 23 (1975) 513; ibid. 24 (1976) 827.

7. L.M. Brown and R.K. Ham, "Strengthening Metods in Crystals" edited by A. Kelly and R.B. Nicholson, Wiley, New York (1971).

8. A. Kelly and M.E. Fine, Acta Met. 5 (1957) 365.

9. L.M. Brown, Phil. Mag. 15 (1967) 911.

10. J. Friedel, "Les Dislocations", Gauthier-Villars, Paris (1956).

11. D.J. Bacon, Phys. Stat. Sol. 23 (1967) 527.

12. L.M. Brown, Phil. Mag. 10 (1965) 441.

13. A.J.E. Foreman and M.J. Makin, Phil. Mag. 13 (1966) 911.

14. A.J.E. Foreman, P.B. Hirsch and F.J. Humphreys, NBS publ. #317, (1970) 1083.

15. A.A. Shtolberg, Phys. Stat. Sol. 43 (1971) 523.

16. D.J. Bacon, U.F. Kocks and R.O. Scattergood, Phil. Mag. 1241.

17. E. Orowan, "Symposium on Internal Stresses in Metals and Alloys", (Institute of Metals, London, 1948) 451.

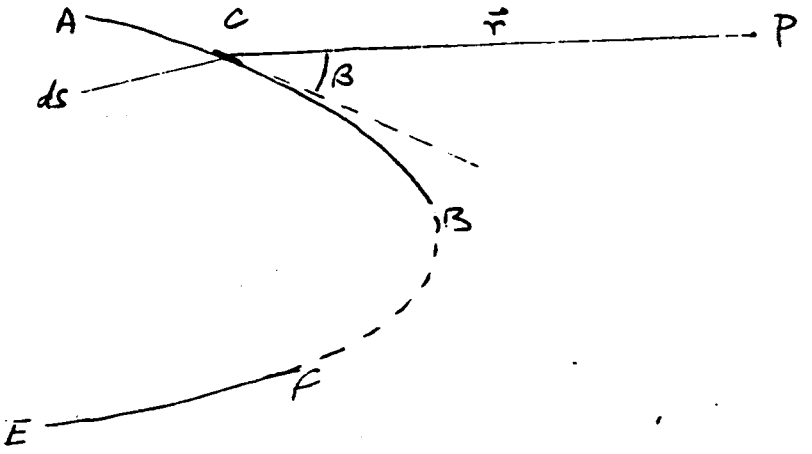


FIG. 1

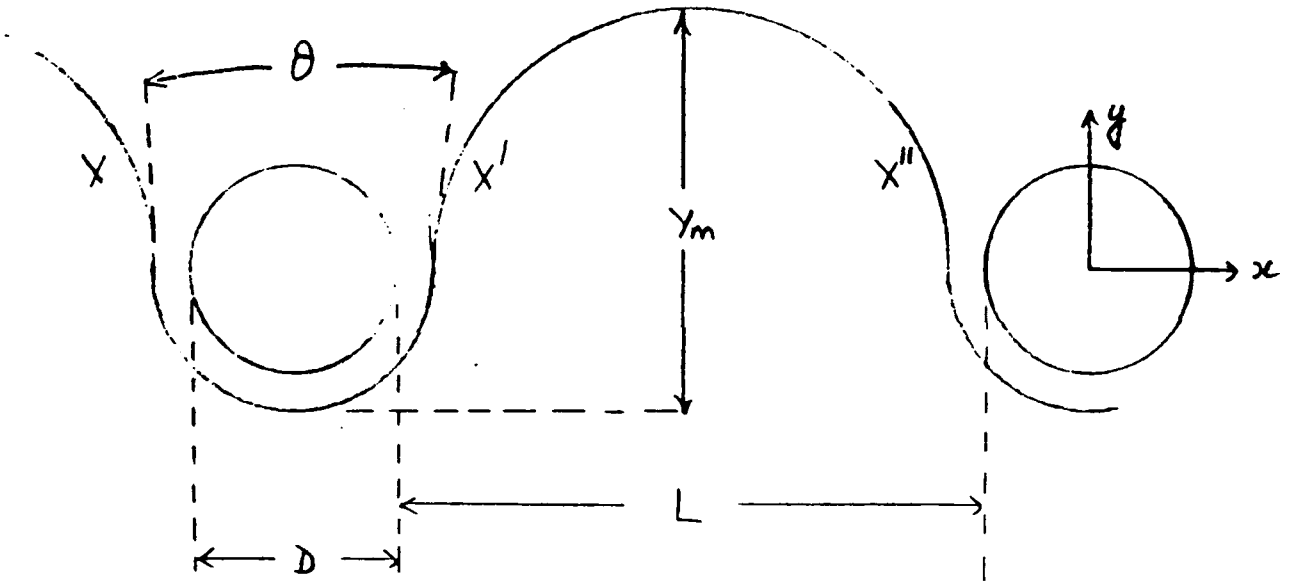
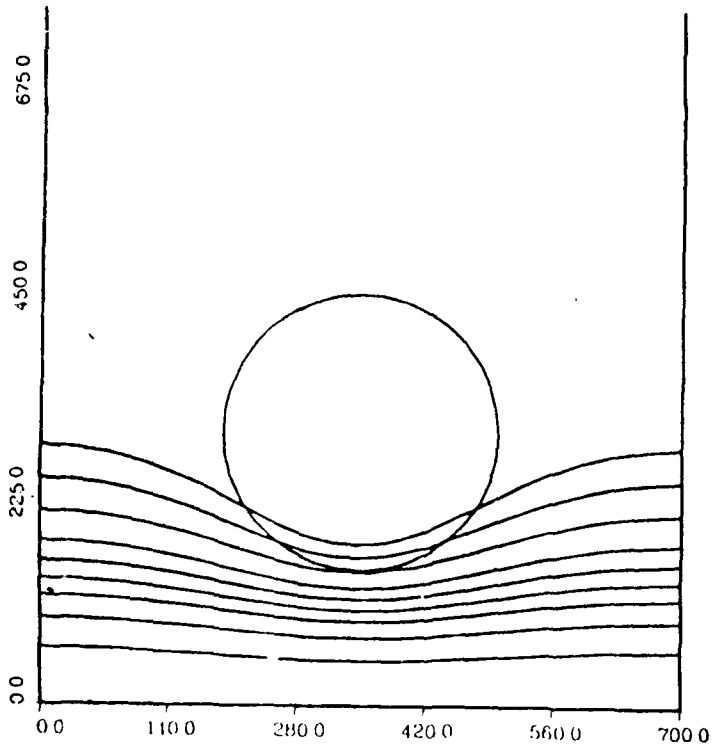
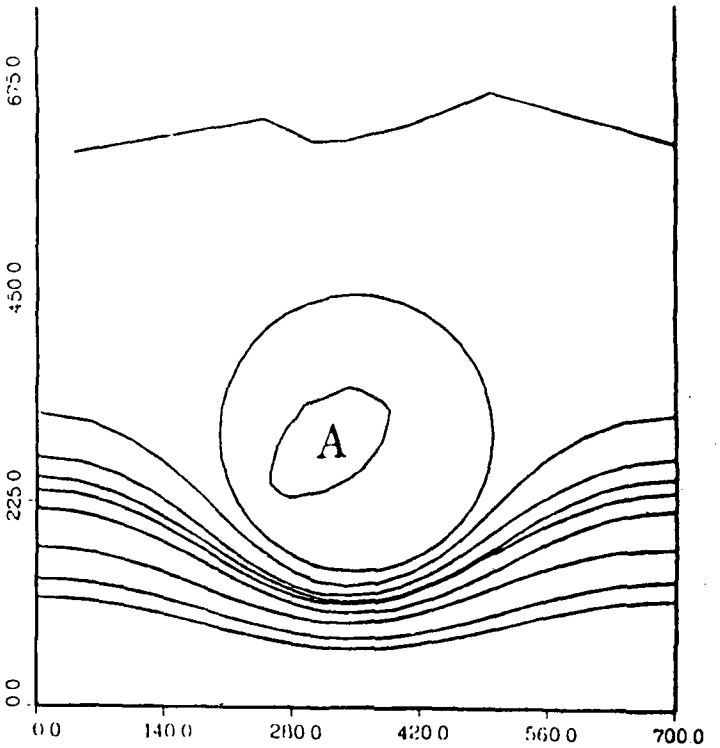


FIG. 2


675 0
450 0
225 0
0 0
0 0
110 0
280 0
420 0
560 0
700 0

a


675 0
450 0
225 0
0 0
A
0 0
140 0
280 0
420 0
560 0
700 0

b

FIG. 3

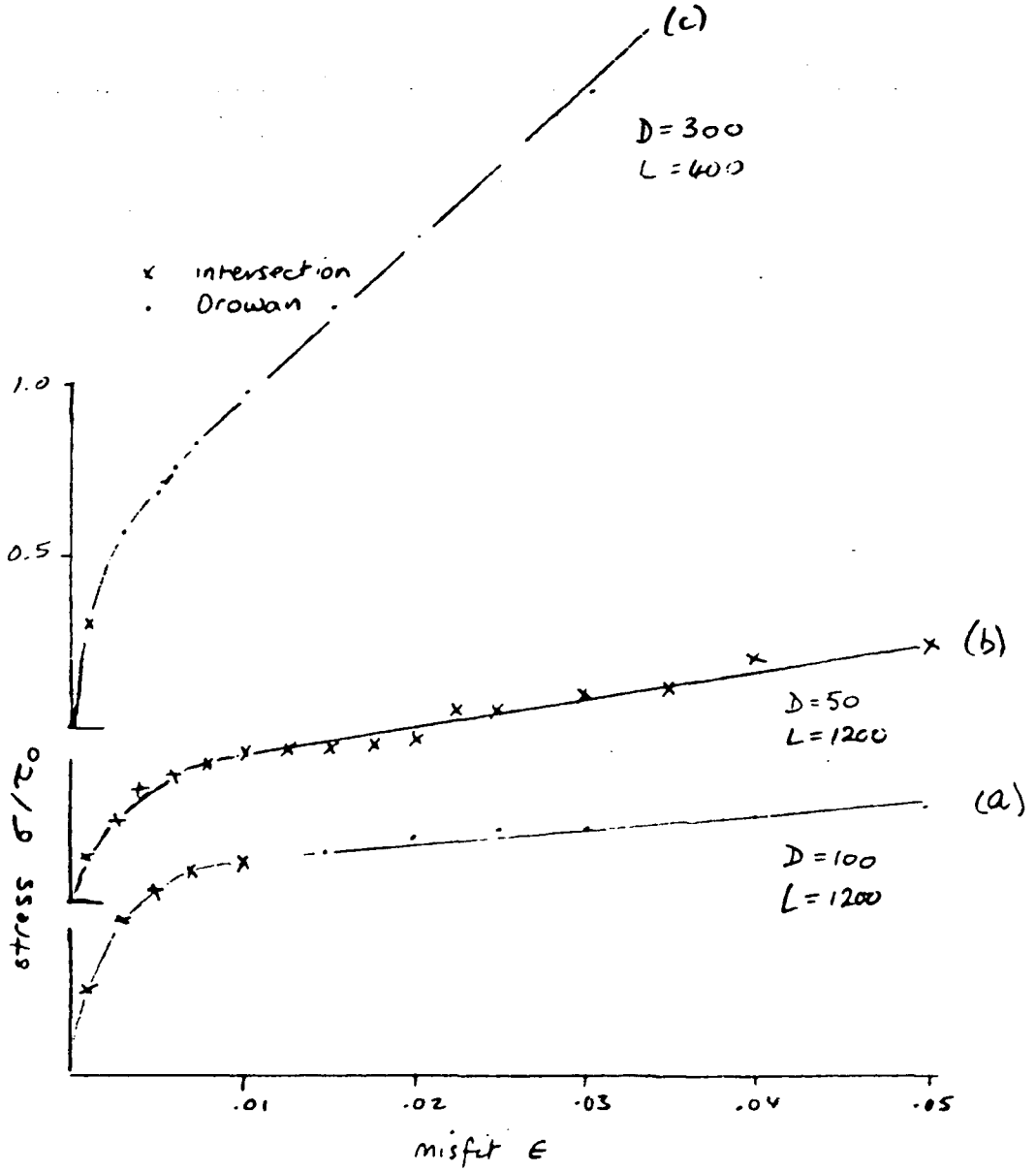

(c)
D = 300
L = 400
× intersection
· Orowan
1.0
0.5
(b)
D = 50
L = 1200
(a)
D = 100
L = 1200
stress σ/τ0
.01
.02
.03
.04
.05
misfit ε

FIG. 4

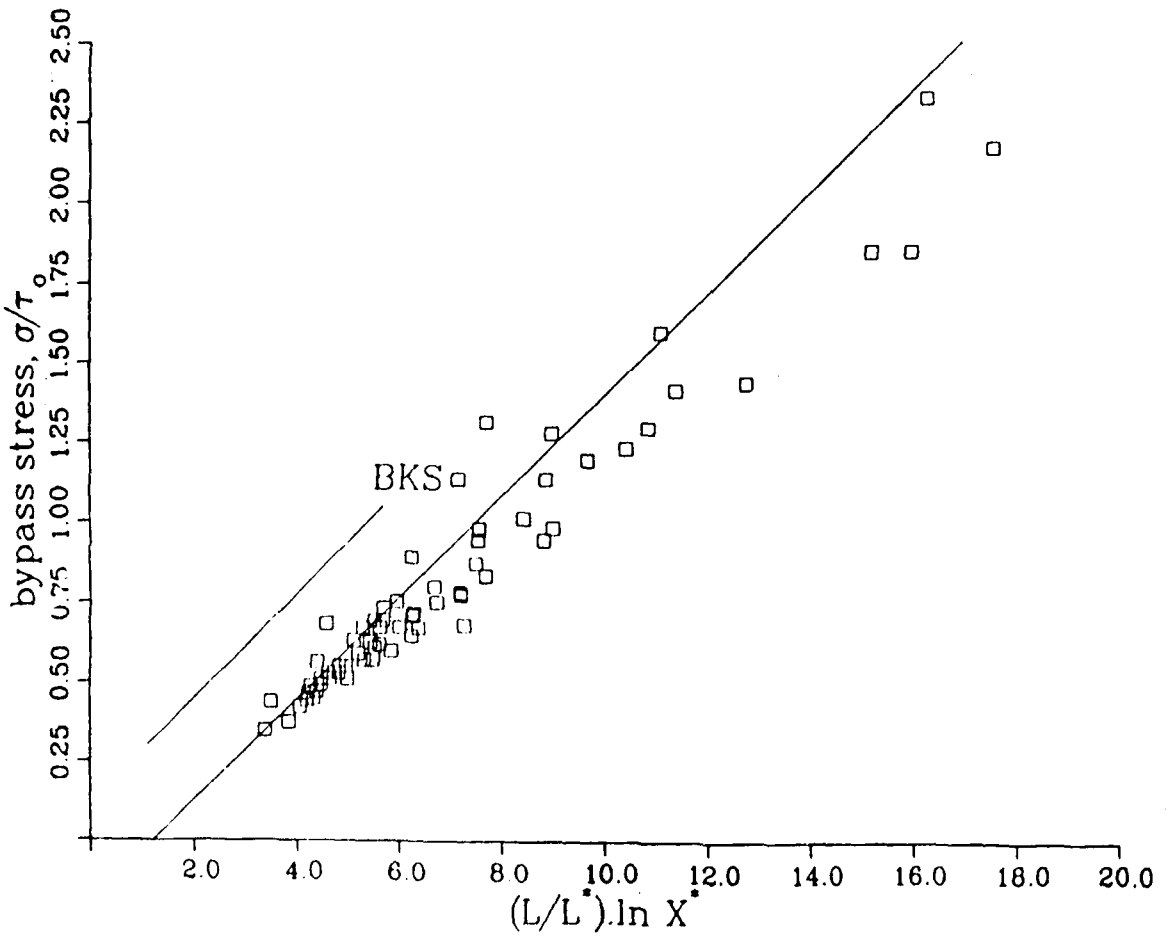

bypass stress, σ/τ_o
0.25 0.50 0.75 1.00 1.25 1.50 1.75 2.00 2.25 2.50
BKS
2.0 4.0 6.0 8.0 10.0 12.0 14.0 16.0 18.0 20.0
$(L/L^*).\ln X^*$

FIG. 5

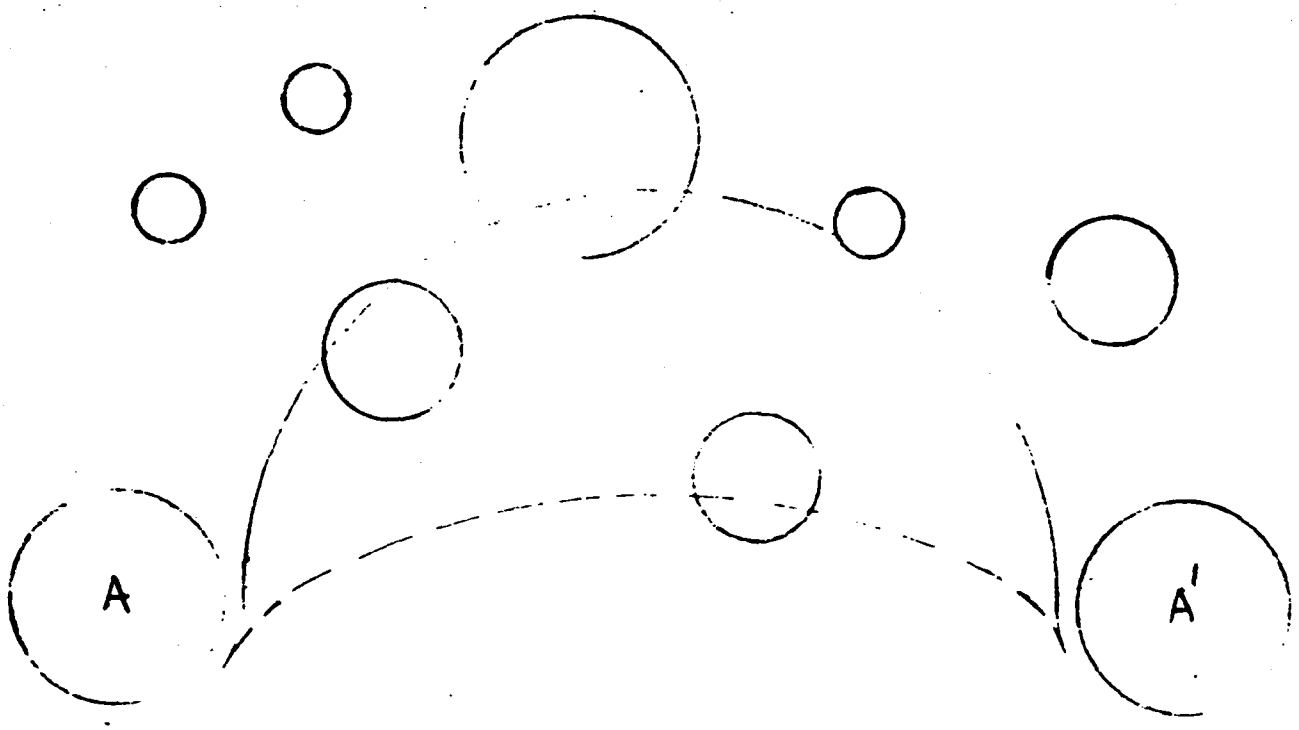


FIG. 8

APPENDIX IX

FATIGUE AND CREEP CRACK GROWTH BEHAVIOR OF INCONEL MA 6000

P. Shahinian* and K. Sadananda

Material Science & Technology Division
Naval Research Laboratory
Washington D.C. 20375

*On-site Contract Employee from Geo-Centers, Inc.

Manuscript submitted for publication to Material Science and Engineering

ABSTRACT

Crack growth in MA 6000 under cyclic load was studied at 24, 760, and 1000°C and under static load at 1000°C in two material orientations. Correlations of fatigue crack growth rate with parameters ΔK and ΔJ were examined. Also comparisons were made of experimental and predicted growth rates.

The rate of growth was influenced by temperature and orientation in addition to the loading mode. Fatigue crack growth rate generally increased with temperature. However in the L-T orientation at 1000°C secondary cracks developed perpendicular to the primary crack and significantly altered its behavior. Creep crack growth at 1000°C was strongly orientation dependent, mainly due to secondary cracking in the L-T oriented specimen in the direction perpendicular to the main crack.

Fracture surfaces were examined by scanning electron microscopy. Also comparisons were made between crack growth behavior of MA 6000, MA 754, and MA 956.

FATIGUE AND CREEP CRACK GROWTH BEHAVIOR OF INCONEL MA 6000

INTRODUCTION

Oxide dispersion strengthened (ODS) superalloys prepared by mechanical alloying have gained interest for higher temperature applications in gas turbine engine applications. Their capability to retain strength to higher temperatures than conventional superalloys would permit higher turbine operating temperatures and in turn improved efficiency and performance.

The Inconel MA 6000 alloy has a microstructure with gamma prime for intermediate temperature strength as well as fine yttrium-aluminum oxide dispersoids for high temperature strength. As a result of the processing, coarse oxides are aligned into stringers and the grains are highly elongated, thus producing anisotropic mechanical properties. Creep and fatigue properties of the alloy have been studied in detail (1-8) and shown to have superior long term strength at high temperatures compared to conventional superalloys. Crack propagation in the alloy has been investigated (6-8) to a limited extent in fatigue and the propagation rate shown to be dependent on temperature and frequency.

The present study examined the characteristics of crack growth in Inconel MA 6000 under cyclic and static loads at

several temperatures and orientations. Salient aspects of the behavior are compared to those of previously studied (9,10) ODS alloys iron-base MA 956 and nickel-base MA 754.

EXPERIMENTAL PROCEDURE

The Inconel alloy MA 6000 employed in this study was received as an extruded plus hot rolled bar, 18-mm thick by 50-mm wide, having the following chemical composition in weight percent: 0.051 C, 1.04 Fe, 14.78 Cr, 2.30 Ti, 4.17 Al, 0.13 Zr, 2.06 Mo, 0.002 S, 1.95 Ta, 3.98 W, 0.53 O, 0.1 N, 90 ppm B and balance Ni. The material which has a grain aspect ratio of approximately 10 was given the following heat treatment by the vendor: 1230°C for 1/2 hr, air cool plus 954°C for 2 hr, air cool plus 845°C for 24 hr, air cool. The alloy is strengthened by both gamma prime precipitation and oxide dispersion.

Compact tension specimens of nominal 3/4 T dimensions except for 7.6 mm thickness and 0.38 mm deep side grooves were prepared with the notch either parallel (T-L orientation) or normal (L-T) to the rolling direction. These were pre-cracked in fatigue at room temperature at relatively low loads prior to creep testing in dead weight machines or fatigue testing in electrohydraulic MTS machines. Static load tests were conducted at constant load using resistance heated furnaces and cyclic tests were conducted in the load control mode with a

triangular waveform cycle at a frequency of 0.17 Hz and R of 0.05 employing induction heating.

Fatigue tests were performed at 24, 760, and 1000°C in air and static load tests were performed only at 1000°C. A cyclic test with a 1-min hold at maximum load was also run as were several static load tests in vacuum of 1×10^{-6} torr or better. To determine crack growth rates the crack length was measured optically at frequent intervals and from plots of crack length versus number of cycles or time, the slope (or growth rate) was measured. Stress intensity factor K was calculated from standard expressions given previously (9).

In several fatigue tests, displacement across the notch mouth was measured using a strain gage extensometer with quartz contact rods, and load-displacement loops were recorded periodically at selected crack lengths. These data were used to determine the non-linear parameter J-integral by a procedure developed previously (11) for load controlled fatigue. It involves measuring the area under the rising part of the load-displacement loop from minimum to maximum load, and calculating ΔJ from the Merkle-Corten equation (12).

$$\Delta J = 2(\alpha_1 A + \alpha_2 P \delta m)/Bb \qquad (1)$$

where A is the area, B the specimen thickness, b the length of uncracked ligament, P the peak load, and δm the displacement

along the load line at maximum load. The constants a_1 and a_2 are functions of a/W and are given in graphical form in reference 12. It was shown previously (11) that values of ΔJ obtained by this estimation procedure are close to those determined by a more accurate but lengthy data reduction procedure. Comparison of fatigue crack growth rate correlations with ΔK and ΔJ are made to see which parameter is more suitable for predictive equations.

Hystersis energy was also determined from the load-displacement loops for different crack lengths and then was used to calculate rate of crack growth according to one of the models in the literature based on critical damage accumulation ahead of the crack tip. Previous analysis of MA 956 data (4) showed that this model gave better agreement with experimental data than several models based on the plastic blunting process. If one assumes that most of the energy is utilized in the crack growth process, the energy required for a unit increment in crack length, U, can be calculated from the area of the loop ΔA as

$$U = \frac{\Delta A}{Bda} \qquad (2)$$

where da represents the crack increment of growth during the cycle and B the thickness. An expression developed by Weertman (13) for fatigue crack growth rate,

$$\frac{da}{dN} = \frac{\Delta K^4}{8\pi^2\mu\sigma^2 U} \qquad (3)$$

where U is the effective surface energy for crack growth, μ the shear modulus, and σ the cyclic yield stress, was used to predict rates from our data.

Fractographic and metallographic examinations also were made to ascertain the nature of cracking and its impact on rate of crack growth.

RESULTS AND DISCUSSION

Fatigue Crack Growth

Crack growth behavior in fatigue was affected by temperature, hold time, environment and particularly material orientation with respect to applied stress. The rate of crack growth generally increased with rise in temperature for both the L-T and T-L orientations, Fig. 1, being particularly pronounced for the latter where the increase is about a factor of 50 in going from 760 to 1000°C. An exception to the trend is the L-T orientation at 1000°C where at high ΔK values the growth rates decreased to values below those for the lower temperatures. This effect is attributed to secondary cracking in the direction normal to that of the main crack, a tendency which increases with rise in temperature because of an increase

in the creep contribution. In a comparison of the two orientations it may be seen that crack growth is faster in the T-L than L-T orientation at both 760° and 1000°C, the difference being particularly large at 1000°C.

Examination of the elastic-plastic parameter ΔJ for suitability in correlation of high temperature fatigue crack growth may be done by comparison with the ΔK parameter. Growth rates were plotted versus the parameter $\sqrt{\Delta J \cdot E}$, where E is Young's Modulus, as well as versus ΔK, Figs. 2-4. Because of the lack of data for MA 6000 the E values used, 160 GPa for 760°C and 143 GPa for 1000°C, were taken from reference 14 and are actually data for an alloy of similar composition, MAR-M 421. For both orientations at 760°C, Figs. 2 and 3, the value of the parameter $\sqrt{\Delta J \cdot E}$ is clearly less than the ΔK value for a given crack growth rate. Since the E values are not accurate and represent only estimates, they could account for much of the observed difference between the two parameters. For example, use of the room-temperature modulus gives very close agreement between the two parameters. On the other hand it one presumes the difference is real then it would indicate that significant plasticity is involved in the crack growth process beyond that accountable by the ΔK parameter. It should be noted that for MA 754 where measured E values were used (10) agreement between the two parameters was reasonably good.

The correspondence between $\sqrt{\Delta J \cdot E}$ and ΔK for MA 6000 at 1000°C is similar to that at 760°C, that is lower values for $\sqrt{\Delta J \cdot E}$ for a given crack growth rate in both orientations. However, the trends of the curves for the two parameters are similar. Comments made regarding the observed differences in parameters at 760°C are equally applicable to the 1000°C data.

Fatigue crack growth rates predicted by equation 3 are also presented in Figs. 3-5. Calculations were made using for 760°C a μ value of 59 GPa, obtained by taking 0.37 of Young's Modulus, and σ values of 734 MPa and 709 MPa for the L-T and T-L orientations, respectively (14). Static yield stress values were employed because of the unavailability of cyclic yield stresses. For 1000°C a μ of 53 GPa and a σ of 320 MPa were used in the calculation. The predicted and experimental crack growth rate curves are quite close for the L-T orientation at 760°C and while for the T-L orientation the data fall in different ranges with only a small overlap the agreement appears to be fair. At 1000°C the agreement between the predicted and experimental curves is also reasonably good except at high crack growth rates where the experimental growth rate decelerates rapidly. As mentioned earlier this decelerating growth effect is most likely related to the development of secondary cracks in a direction normal to that of the main crack. These cracks alter the stress field at the tip of the primary crack and retard the advancement of the crack. This effect of course is not taken into account in the

predicted growth rates. Thus the relationship in equation 3 based on an energy balance model gives fatigue crack growth rates reasonably close to experimental values provided significant secondary cracking does not take place.

Imposing a 1-min hold at the peak load of the cycle altered crack growth behavior in the L-T orientation, Fig. 5. Whereas rate of crack growth increased continuously under cyclic loading without a hold period, application of a 1-min hold caused a continuous decrease in rate after an initial high rate at the start. In this anisotropic material the cause of the decrease most likely is the development of secondary cracks normal to the main crack more readily under periods of static load. Creep promotes void and microcrack formation along the perpendicular grain boundaries and particle stringers and their effect on the main crack stress field becomes significant before the crack advances very far. As a consequence the growth rate decelerates. This suggests that similar behavior may occur in a static load (creep) test.

A comparison of fatigue crack growth behavior of MA 6000 with those of MA 754 (10) and MA 956 (9) is made in Figs. 6-8. At 24°C in the L-T orientation the growth rate is highest for MA 6000 and in decreasing order, MA 754 and MA 956. However at 760°C the growth rates in the L-T orientation are about the same for MA 6000 and MA 754, Fig. 7. In the T-L orientation at this temperature the growth rates are clearly lower in MA 6000

than in MA 754. At 1000°C in the L-T orientation a reversal in the order from that at 24°C is observed with highest rates in MA 956 and the lowest in MA 6000, Fig. 8. Because the ranges of growth rates measured in MA 6000 and MA 754 in the T-L orientation are different and do not overlap a good comparison is difficult but it would appear that any difference would not be large. However the rates in these two alloys are lower than those in MA 956 in the T-L orientation. Thus the resistance to fatigue crack growth of MA 6000 at 1000°C is better than that of MA 754 and MA 956 in the L-T orientation and appears to be as good as or better in the T-L orientation.

Fatigue fracture at 24°C in the L-T orientation was mainly smooth transgranular with sharp perpendicular shear surfaces connecting adjacent smooth fracture planes, Fig. 9. The perpendicular fractures are probably along planes of oxide particle concentration. The zig-zag profile of the perpendicular surfaces conforms to that observed in T-L orientation fracture surfaces. Figure 10 shows that the fatigue fracture in the L-T orientation at 1000°C, a wavy fracture surface with zig-zag profiled perpendicular cracks and surfaces. The main fracture surface is less smooth at 1000°C than at 24°C. In the T-L orientation at 1000°C the fracture surface exhibits furrows running in the crack growth direction, Fig. 11a. As the crack advances, secondary cracks develop along the furrows and tearing occurs in the normal direction to connect cracks on parallel planes, Fig. 11b. These furrowed

surfaces reflect the anisotropic nature of the microstructure and probably occur along particle stringers developed during processing of the material.

Creep Crack Growth

In the analysis of creep crack growth the growth rates are compared on the basis of the stress intensity factor even though it is recognized that a unique relationship might not exist. While the parameter C* would probably be better for correlation of creep crack growth rates, the factor K should be suitable for comparisons to identify effects of orientation and temperature.

Crack growth in the L-T orientation at 1000°C was not normal in that the rate of growth did not increase as the crack lengthened but actually decreased, Fig. 12. The behavior was similar to that observed in the 1-min hold cyclic test. Perpendicular secondary cracks developed rather early because of the nature of the material and retarded the growth of the primary crack. So predominant was the effect that the failure break occurred on the perpendicular plane. Figure 13 is a photograph of the surface of a side grooved L-T oriented specimen and shows many large cracks normal to the direction of the main crack.

In the T-L orientation, crack growth rate increased normally with increase in crack length, Fig. 14. Compared to cyclic growth rates plotted on a time basis the creep crack growth rates appear to be lower although the influence of the vacuum environment was not determined.

A comparison of creep crack growth rate in MA 6000 at 1000°C with that in MA 754, Fig. 15, shows much lower rates in MA 6000 in both L-T and T-L orientations. Although not shown these crack growth rates are significantly lower than those in MA 956 (9). Thus the superior resistance to crack growth under static load of MA 6000 corresponds to its higher creep resistance at 1000°C.

SUMMARY AND CONCLUSIONS

Crack growth behavior in Inconel MA 6000 was influenced by temperature, loading mode, and material-crack orientation. The material was clearly anisotropic with respect to crack growth.

Fatigue crack growth rates generally increased with temperature to 1000°C for both L-T and T-L orientations. Crack growth was faster in the T-L than the L-T orientation. The growth rates predicted by a relationship based on cumulative damage agree reasonably well with experimental rates. An exception to the behavior occurred in the L-T orientation at 1000°C at high ΔK and crack growth rates where the increase in

growth rate began to decelerate. As a result the growth rate became lower than that at lower temperatures and also differed markedly from predicted values. This variation is attributed to secondary cracks developing in the direction normal to the main crack, thus altering the stress field at the tip of the main crack and retarding crack growth. The propensity for the effect increases as the creep contribution increases, for example, with the imposition of hold time.

Correlations of fatigue crack growth rates with parameters ΔK and $\sqrt{\Delta J \cdot E}$ indicate significant plasticity takes place and ΔK might not be an appropriate parameter under these test conditions, although this is not certain because the E values used were only estimates.

The resistance to fatigue crack growth of MA 6000 at 1000°C is better than that of MA 754 and MA 956 in the L-T orientation and appears to be at least as good in the T-L orientation. At 24°C the order of resistance may be reversed.

Crack growth under static load was clearly different in the two orientations at 1000°C. In the T-L orientation, growth rate increased normally as the crack lengthened. However, in the L-T orientation the growth rate decreased as the crack length increased. The rate reduction of the main crack was due to the development of perpendicular cracks along planes of aligned coarse particle stringers.

The resistance to creep crack growth of MA 6000 at 1000°C is greater than that of MA 754 and MA 956.

REFERENCES

1. T. E. Howson, F. Cosandey, and J. K. Tien, "Creep Deformation and Rupture of Oxide Dispersion Strengthened Inconel MA 754 and MA 6000E," Superalloy 1980, Proc., Fourth Int. Symposium on Superalloys, ASM, Metals Park, pp. 563-573.

2. R. F. Singer, R. C. Benn, and S. K. Kang, "Creep-Rupture Properties of Inconel Alloy MA 6000," presented at the "Frontiers of High Temperature Materials II" Conference, Inco MAP book, Inco Alloy Products, Huntington, West Virginia.

3. W. L. Kimmerle, V. C. Nardone, J. K. Tien, "The Effect of the Lower Stress Level on the Cyclic Creep Behavior of an ODS Superalloy," Met. Trans., Vol. 18A, 1987, pp. 1029-1033.

4. J. D. Whittenberger, "Elevated Temperature Compressive Steady State Deformation and Failure in the Oxide Dispersion Strengthened Alloy MA 6000E," Met. Trans., Vol. 15A, 1984, pp. 1753-1762.

5. E. Arzt and R. F. Singer, "The Effect of Grain Shape on Stress Rupture of the Oxide Dispersion Strengthened Superalloy Inconel MA 6000," Superalloys 1984, Proc. Fifth Int. Symposium on Superalloys, Met. Soc. of AIME 1984, pp. 367-376.

6. W. Hoffelner and R. F. Singer, "High-Cycle Fatigue Properties of the ODS-Alloy MA 6000 at 850°C," Met. Trans., Vol. 16A, 1985, pp. 393-399.

7. W. Hoffelner and R. B. Scarlin, "On the Correlation of Microstructure, Fatigue Life and Fatigue Crack Propagation in Nickel Base Superalloys," Fatigue 84, Proc., 2nd Int. Conf. on Fatigue and Fatigue Thresholds, Vol. III, C. J. Beevers, ed., Engineering Materials Advisory Services Ltd, 1984, pp. 1647-1658.

8. A. Tekin and J. W. Martin, "Fatigue Crack Growth Behaviour of MA 6000," Materials Science and Engineering, Vol. 96, 1987, pp. 41-49.

9. K. Sadananda and P. Shahinian, "Fatigue Crack Growth Behavior of an Oxide Dispersion Strengthened MA 956 Alloy," Met. Trans., Vol. 15A, 1984, pp. 527-539.

10. P. Shahinian and K. Sadananda, "Fatigue and Creep Crack Growth in Oxide Dispersion Strengthened MA 754," 1988, to be published.

11. K. Sadananda and P. Shahinian, "A Fracture Mechanics Approach to High Temperature Fatigue Crack Growth in Udimet 700," Engineering Fracture Mechanics, Vol. 11, 1979, pp. 73-86.

12. J. G. Merkle and H. T. Corten, "A J-Integral Analysis for Compact Specimen, Considering Axial Force as Well as Bending Effects," J. of Pressure Vessel Technology, Vol. 96, 1974, pp. 286-292.

13. J. Weertman: in Fatigue and Microstructure, M. Meshii, ed. American Society for Metals, Metals Park, OH, 1978, p. 279.

14. Anon, IncoMAP Data Sheets, Inconel alloy MA [illegible], Inco Products 1981.

FIGURE CAPTIONS

Fig. 1. Effect of temperature and material orientation on fatigue crack growth rate in MA 6000.

Fig. 2. Comparison of fatigue crack growth rates in L-T orientation in MA 6000 at 760°C on the basis of $\sqrt{\Delta J \cdot E}$, ΔK, and predictive formulation.

Fig. 3. Comparison of fatigue crack growth rates in T-L orientation at 760°C on the basis of $\sqrt{\Delta J \cdot E}$, ΔK, and predictive formulation.

Fig. 4. Comparison of fatigue crack growth rates in L-T and T-L orientations at 1000°C on the basis of $\sqrt{\Delta J \cdot E}$, ΔK, and predictive formulation.

Fig. 5. Influence of 1-min hold at peak load on fatigue crack growth rate in L-T orientation at 1000°C.

Fig. 6. Comparison of fatigue crack growth resistance of MA 6000, MA 754, and MA 956 in L-T orientation at 24°C.

Fig. 7. Comparison of fatigue crack growth resistance of MA 6000 and MA 754 in L-T and T-L orientation at 760°C.

Fig. 8. Comparison of fatigue crack growth resistance of MA 6000, MA 754, and MA 956 in L-T and T-L orientations at 1000°C.

Fig. 9. Fatigue fracture surface of MA 6000 in L-T orientation at 24°C.

Fig. 10. Fatigue fracture surface of MA 6000 in L-T orientation at 1000°C.

Fig. 11. Fatigue fracture surface of MA 6000 in T-L orientation at 1000°C showing (a) the beginning of crack growth and (b) a more advanced stage of growth.

Fig. 12. Creep crack growth in MA 6000 in L-T orientation at 1000°C and comparison with crack growth in 1-min hold cyclic test.

Fig. 13. Specimen surface of MA 6000 in L-T orientation at 1000°C (vacuum) under static load showing main crack and perpendicular cracks.

Fig. 14. Creep crack growth rates in MA 6000 in T-L orientation at 1000°C and comparison with fatigue crack growth rate on a time basis.

Fig. 15. Comparison of creep crack growth rates in MA 6000 and MA 754 in L-T and T-L orientations at 1000°C.

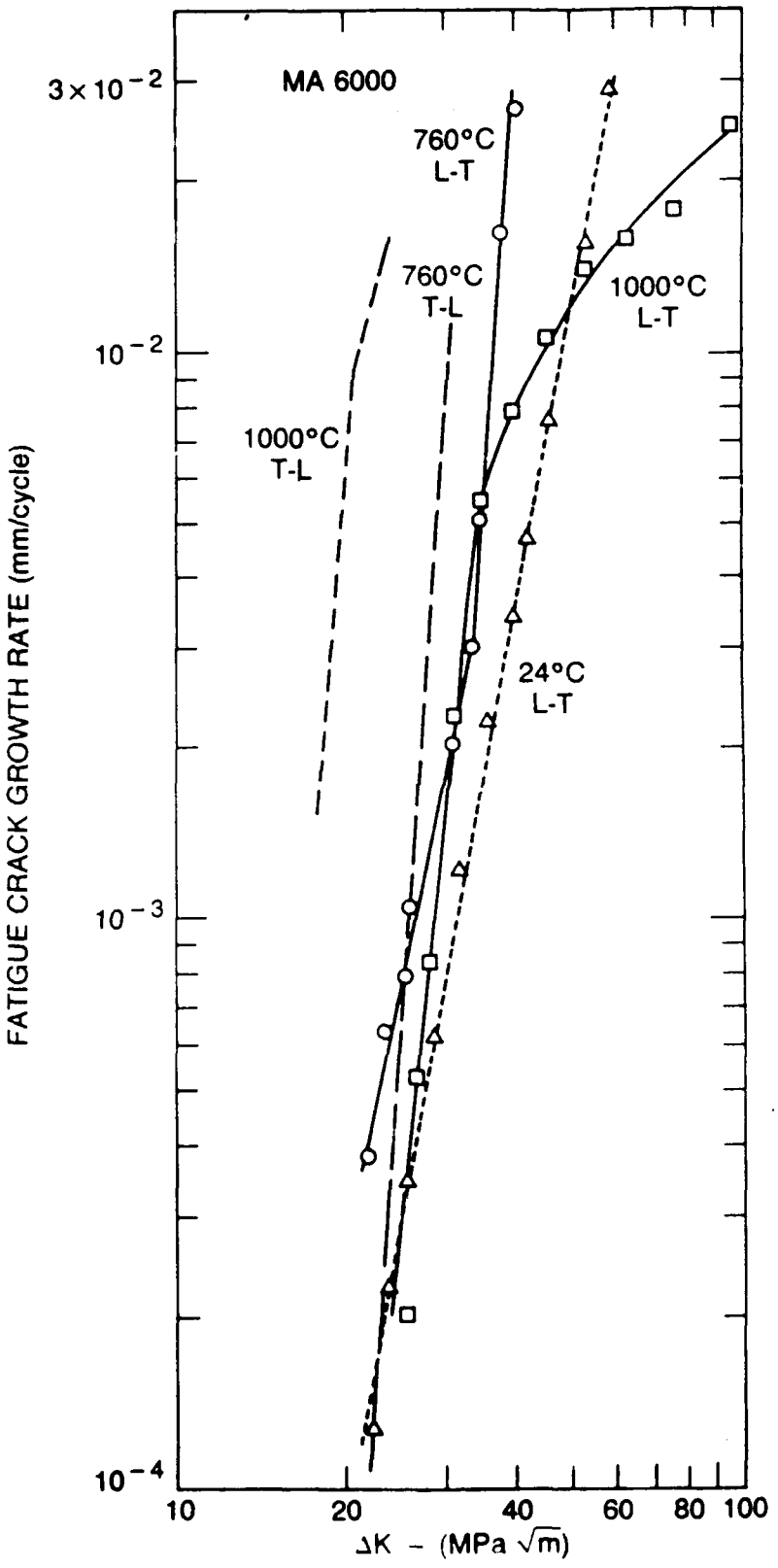


Fig. 1 Effect of temperature and material orientation on fatigue crack growth rate in MA 6000.

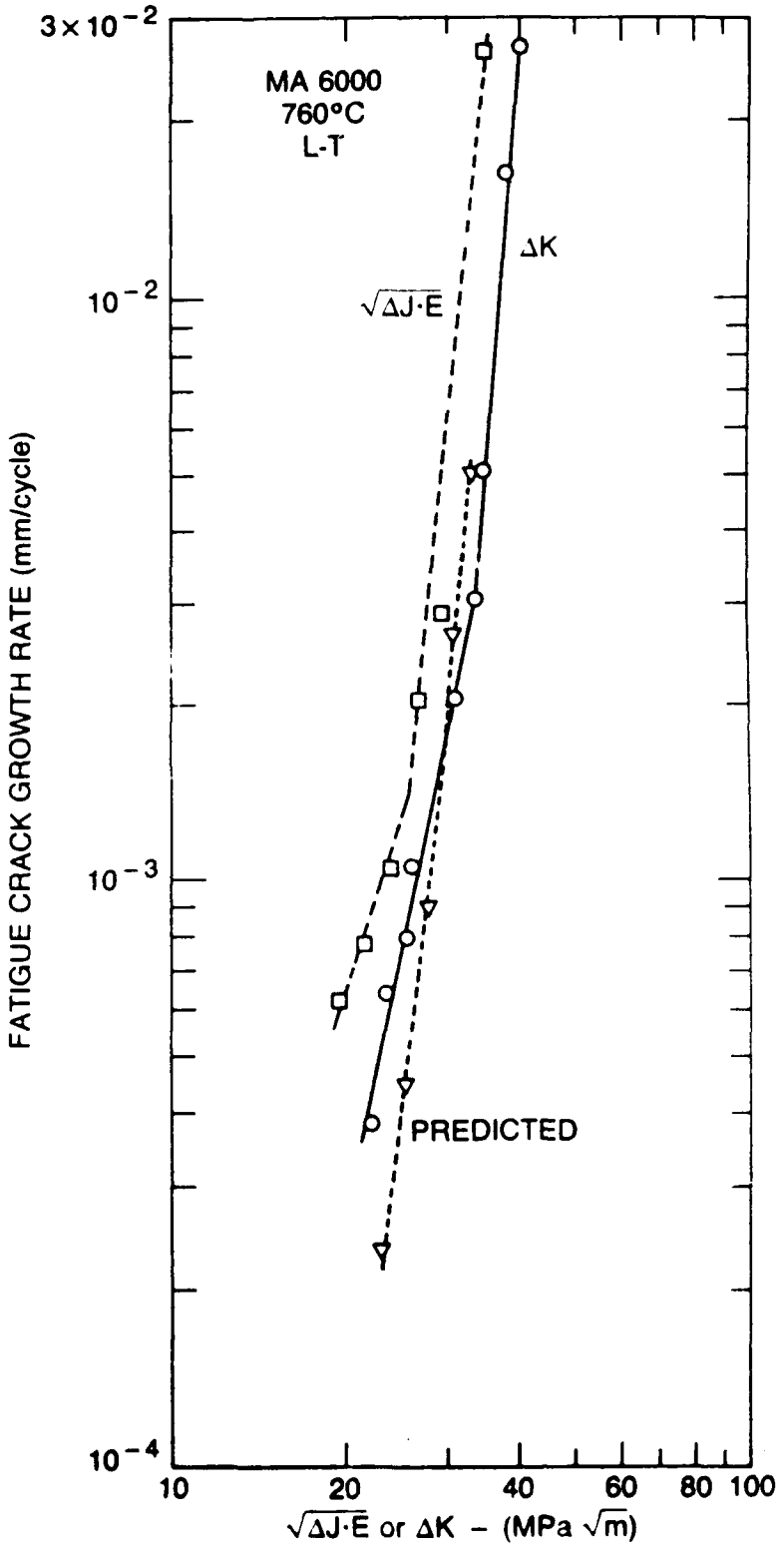


Fig. 2. Comparison of fatigue crack growth rates in L-T orientation in MA 6000 at 760°C on the basis of $\sqrt{\Delta J \cdot E}$, ΔK and predictive formulation

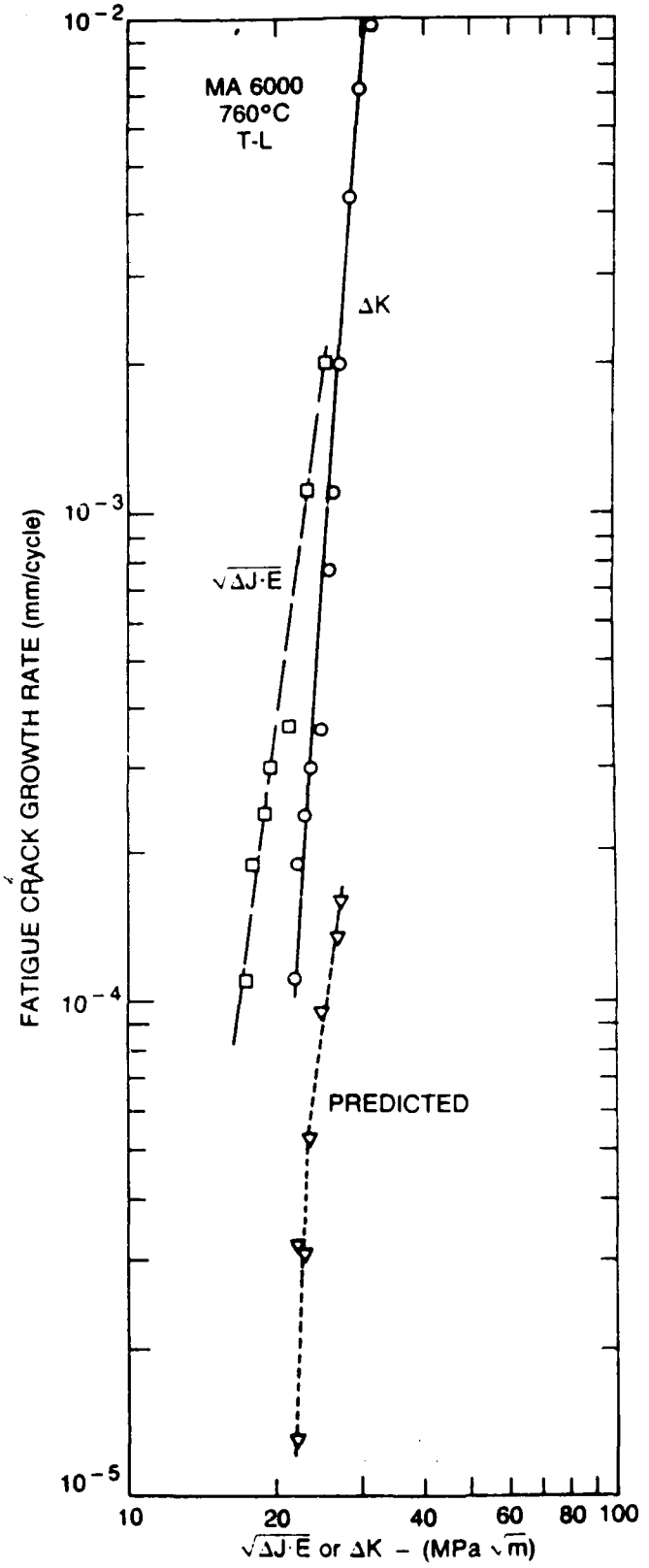


Fig. 3. Comparison of fatigue crack growth rates in T-L orientation at 760°C on the basis of $\sqrt{\Delta J \cdot E}$, ΔK, and predictive formulation

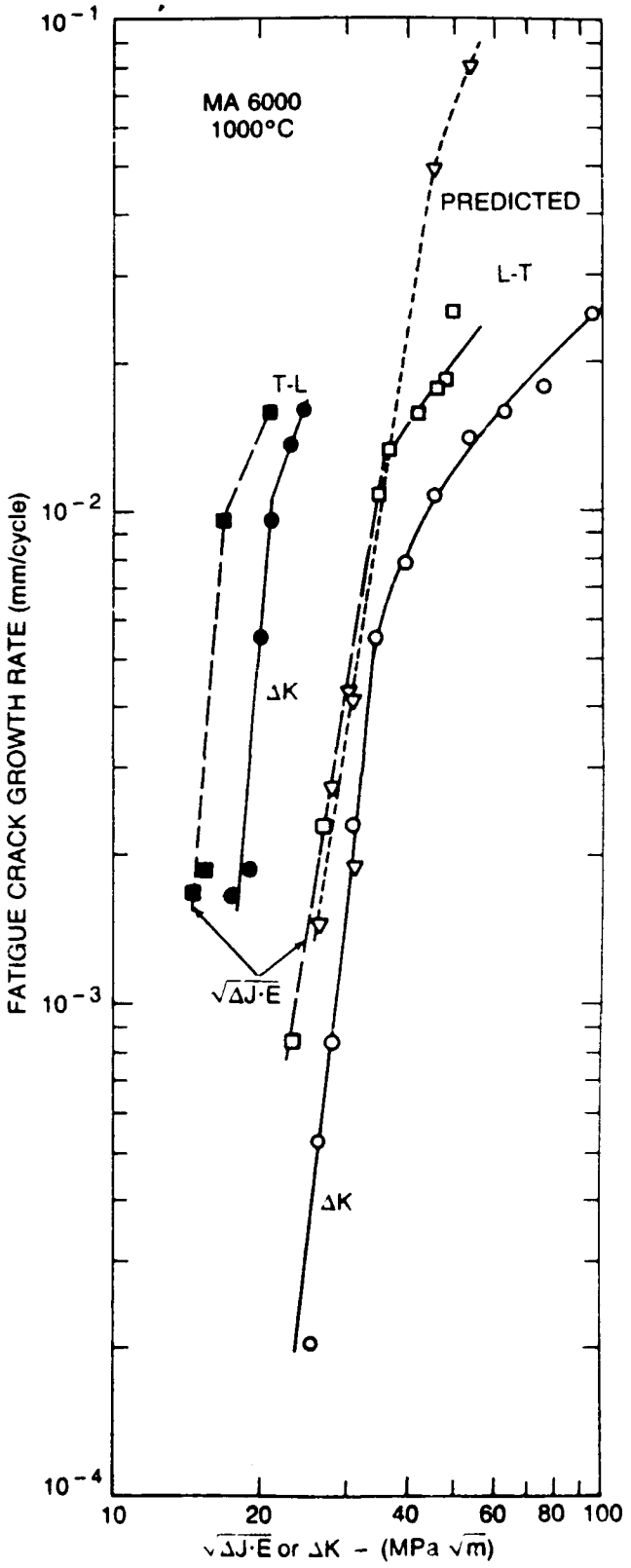


Fig. 4. Comparison of fatigue crack growth rates in L-T and T-L orientations at 1000°C on the basis of $\sqrt{\Delta J \cdot E}$, ΔK,

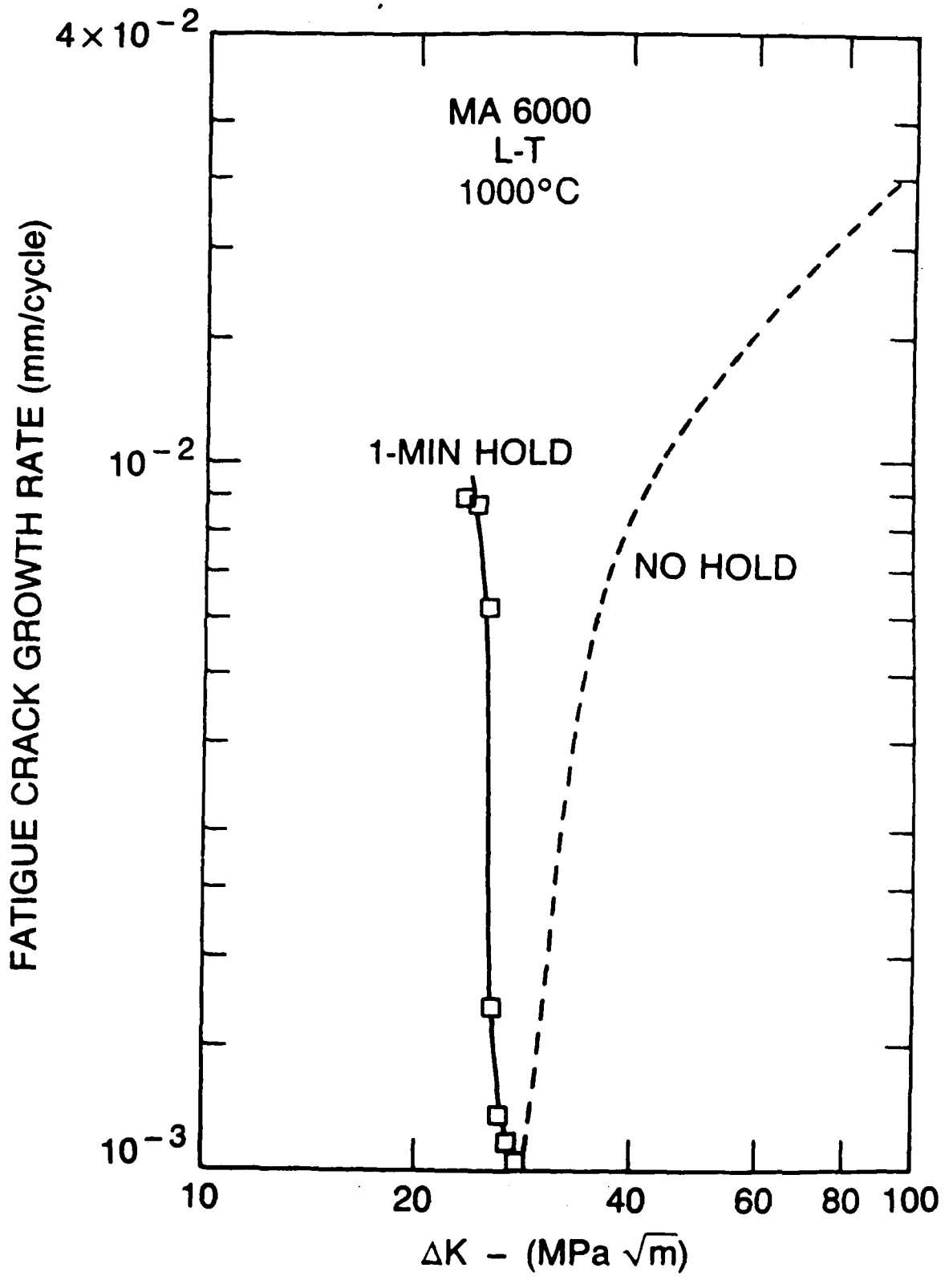


Fig. 5. Influence of 1-min hold at peak load on fatigue crack growth rate in L-T orientation at 1000°C.

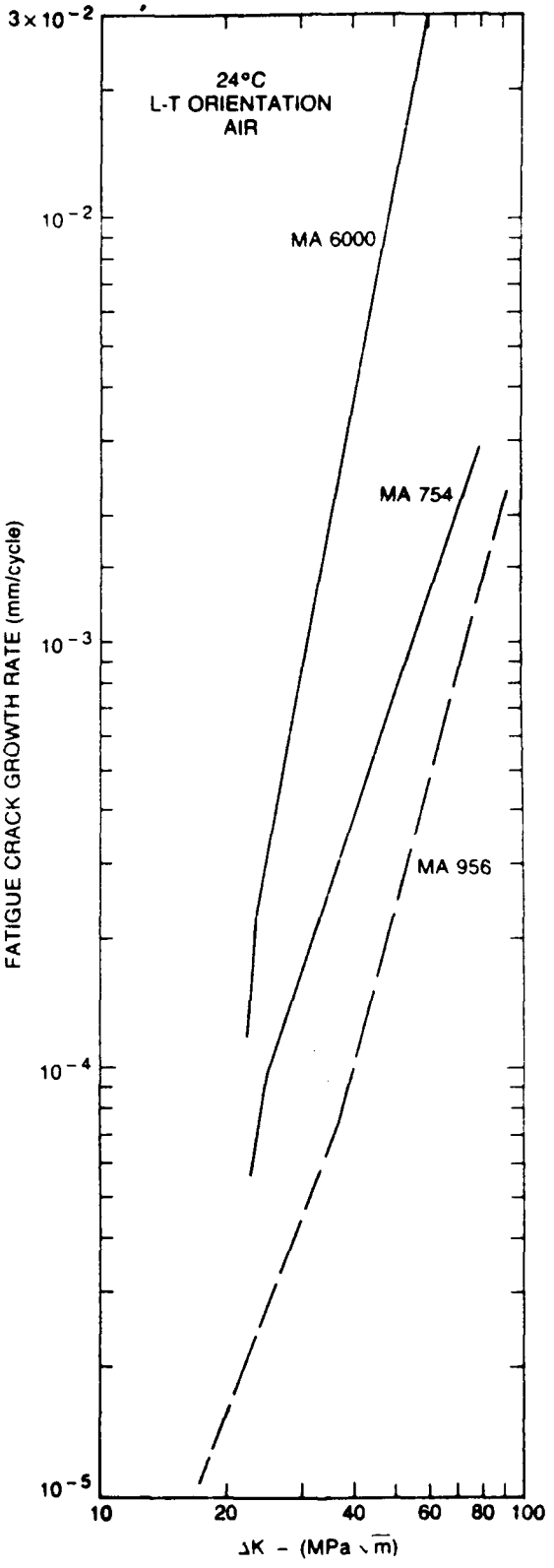


Fig. 6. Comparison of fatigue crack growth resistance of MA 6000, MA 754, and MA 956 in L-T orientation at 24°C.

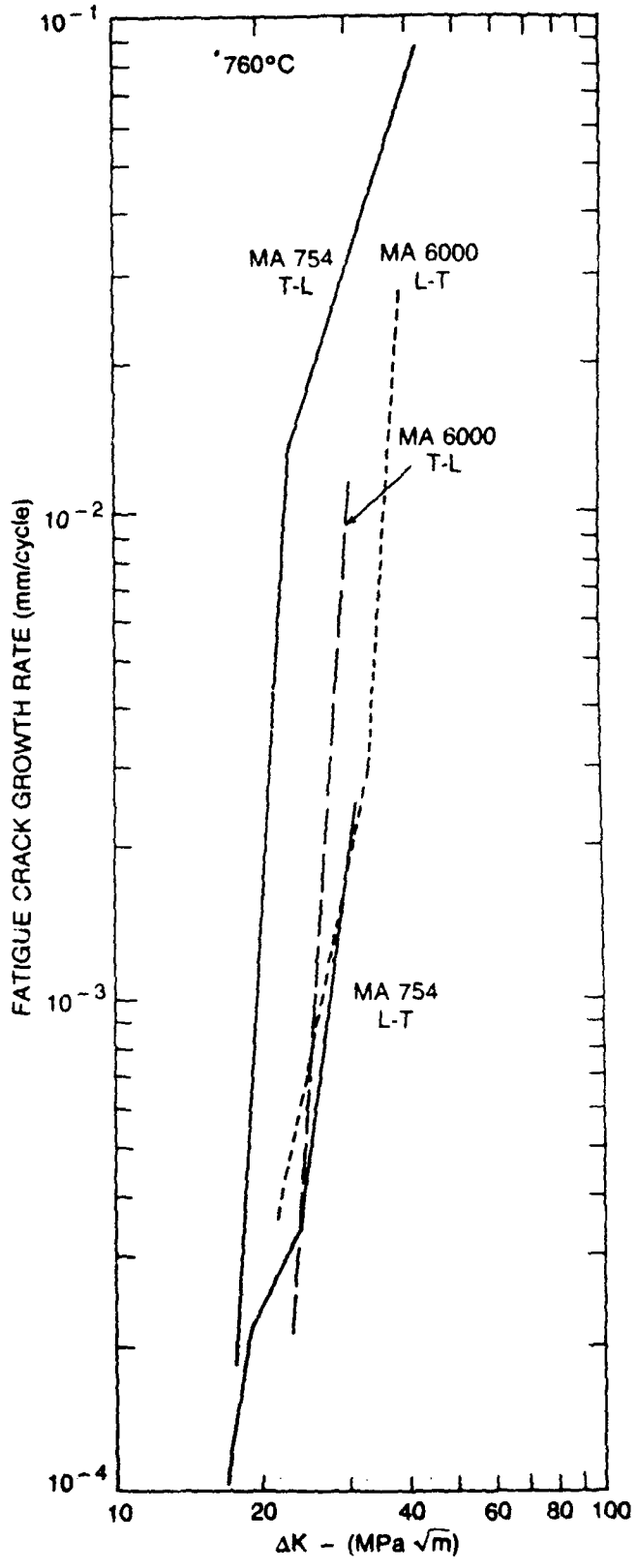


Fig. 7. Comparison of fatigue crack growth resistance of MA 6000 and MA 754 in L-T and T-L orientation at 760°C.

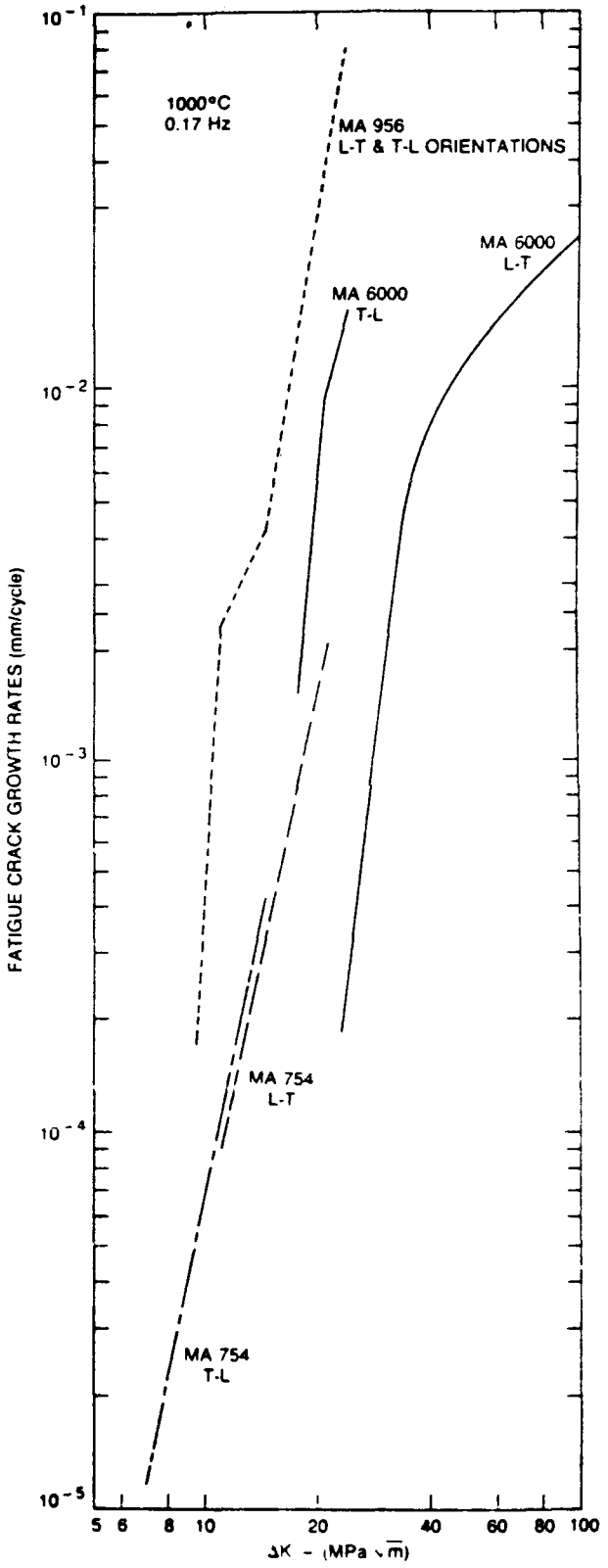


Fig. 8. Comparison of fatigue crack growth resistance of MA 6000, MA 754, and MA 956 in L-T and T-L orientations

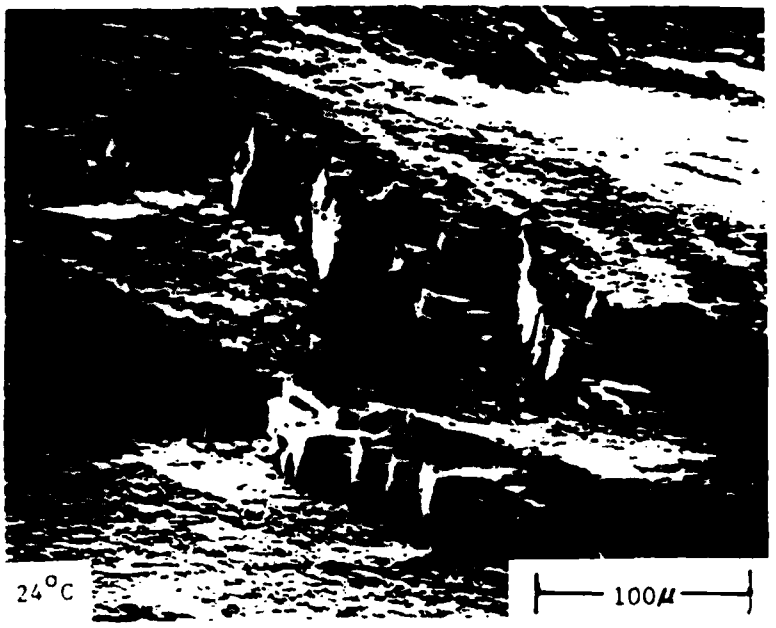


Fig. 9. Fatigue fracture surface of MA 6000 in L-T orientation at 24°C.

crack growth ⟶

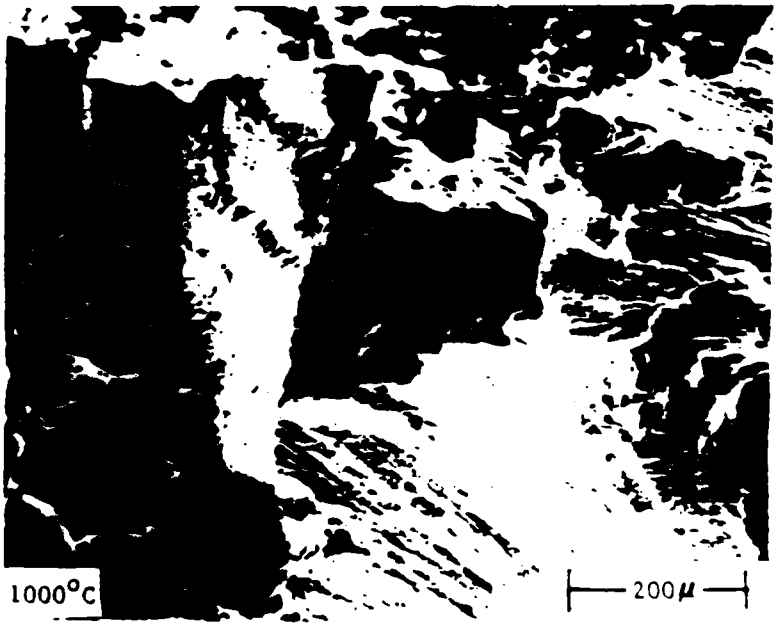
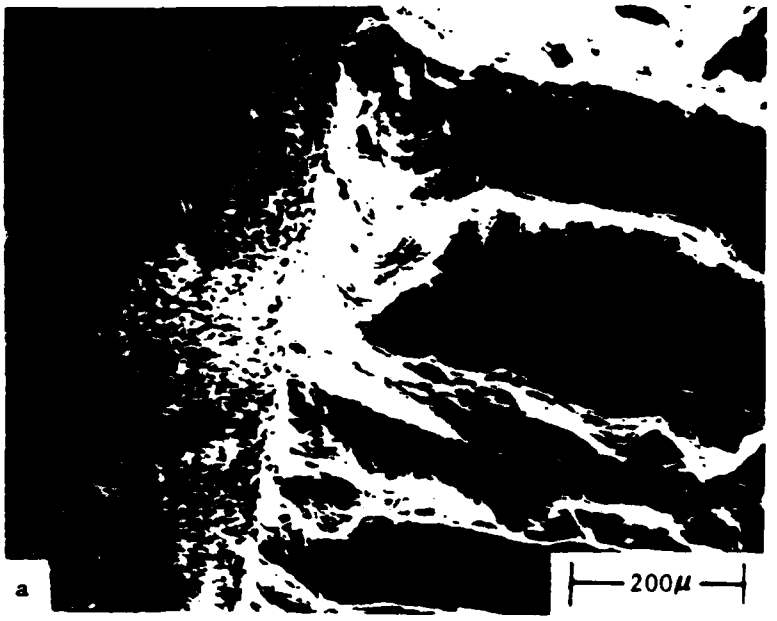


Fig. 10. Fatigue fracture surface of MA 6000 in L-T orientation at 1000°C.



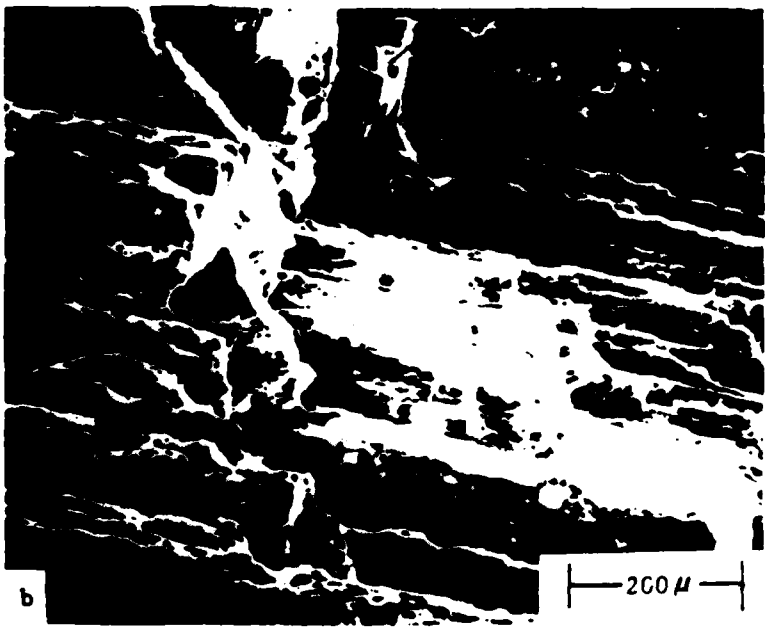


Fig. 11. Fatigue fracture surface of MA 6000 in T-L orientation at 1000°C showing (a) the beginning of crack growth and (b) a more advanced stage of growth.

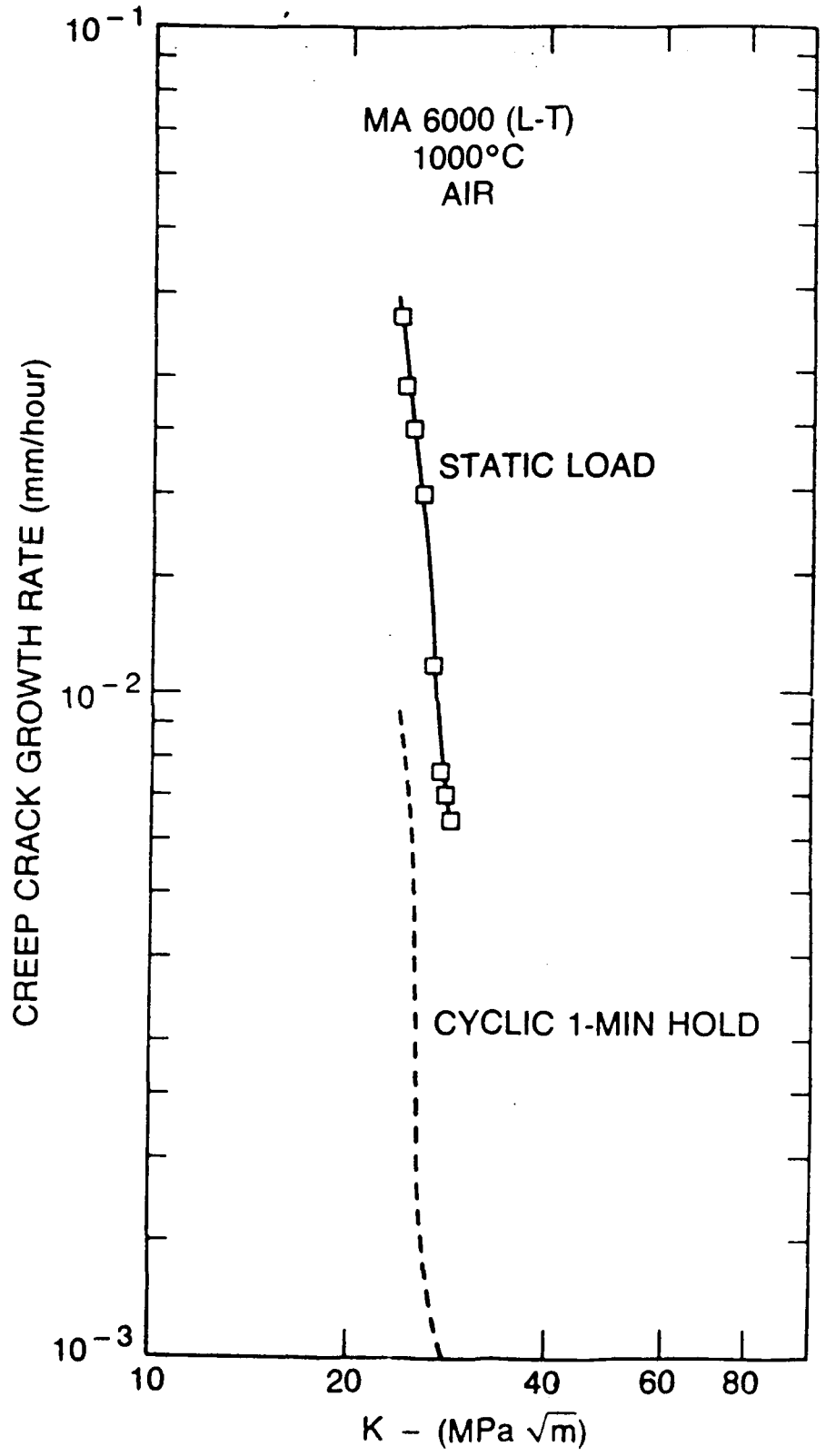


Fig. 12. Creep crack growth in MA 6000 in L-T orientation at 1000°C and comparison with crack growth in 1-min hold cyclic test.

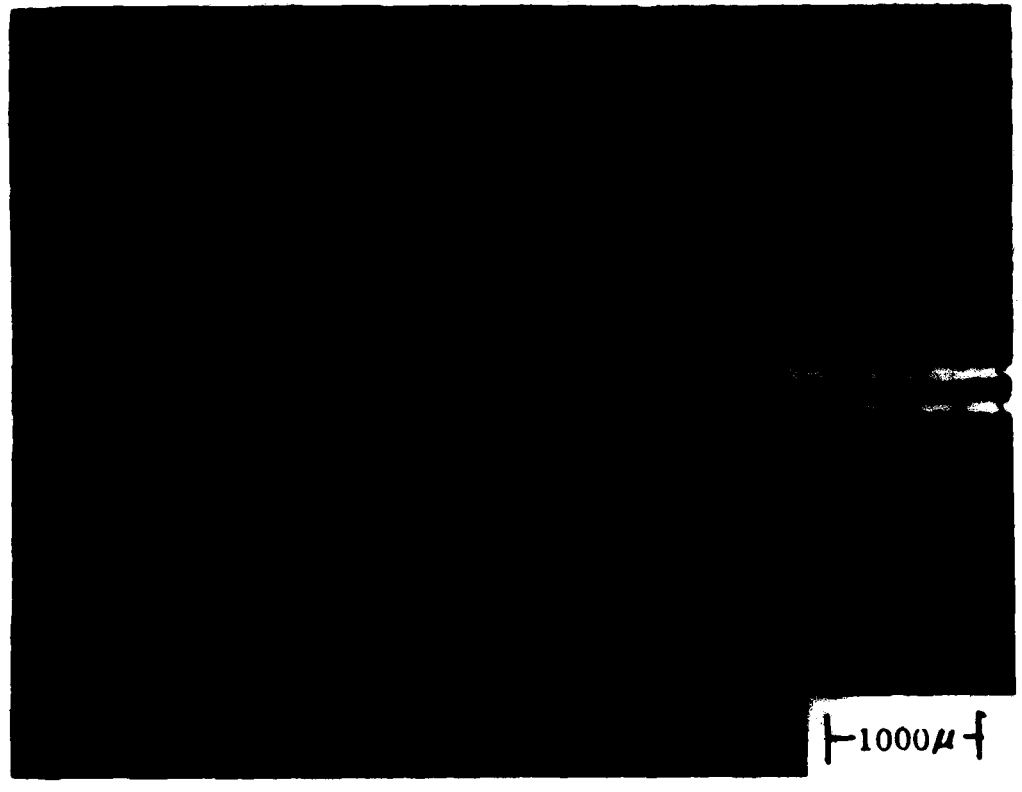


Fig. 13. Specimen surface of MA 6000 in L-T orientation at 1000°C (vacuum) under static load showing main crack and perpendicular cracks.

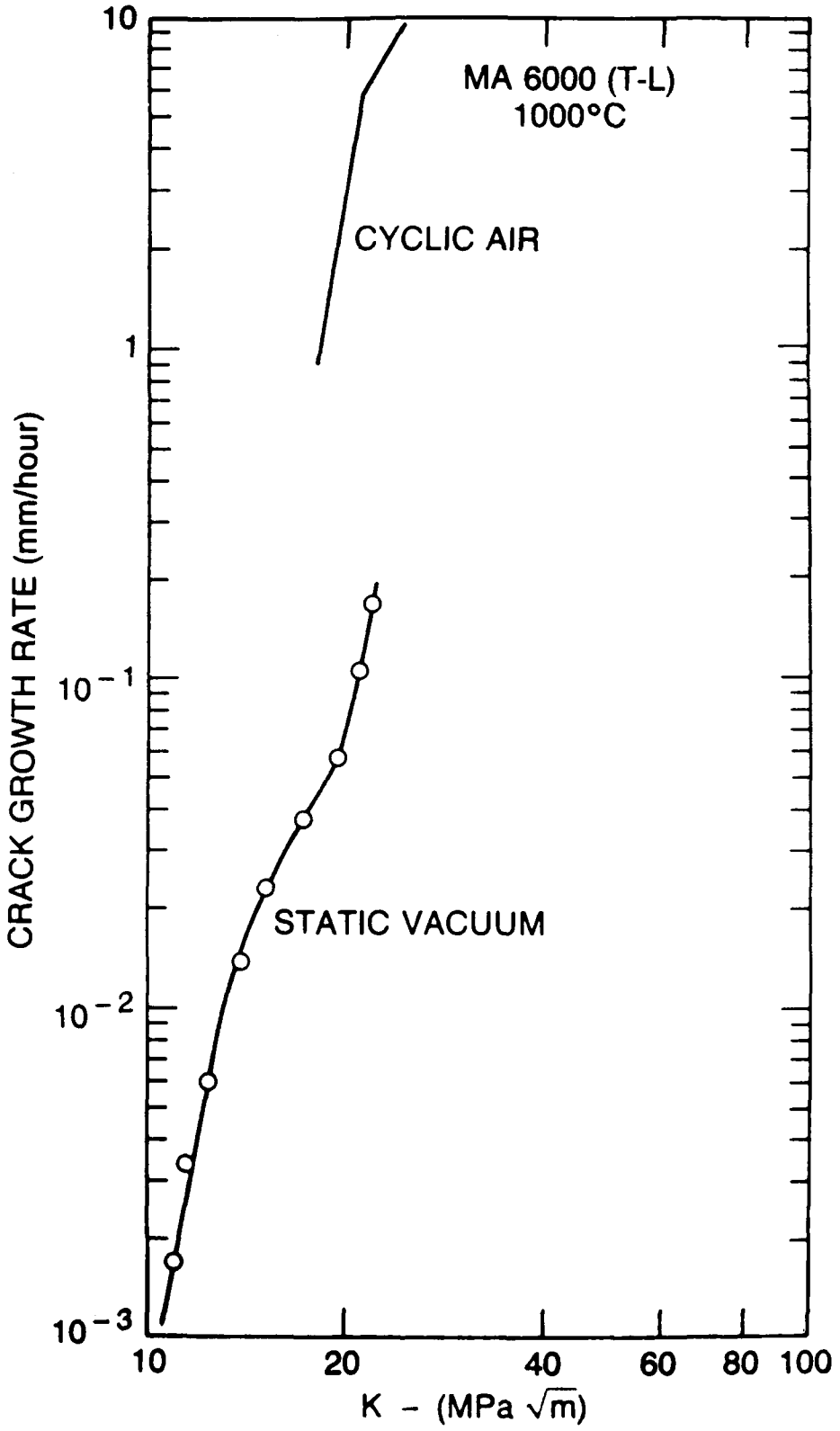


Fig. 14. Creep crack growth rates in MA 6000 in T-L orientation at 1000°C and comparison with fatigue crack growth rate on a time basis.

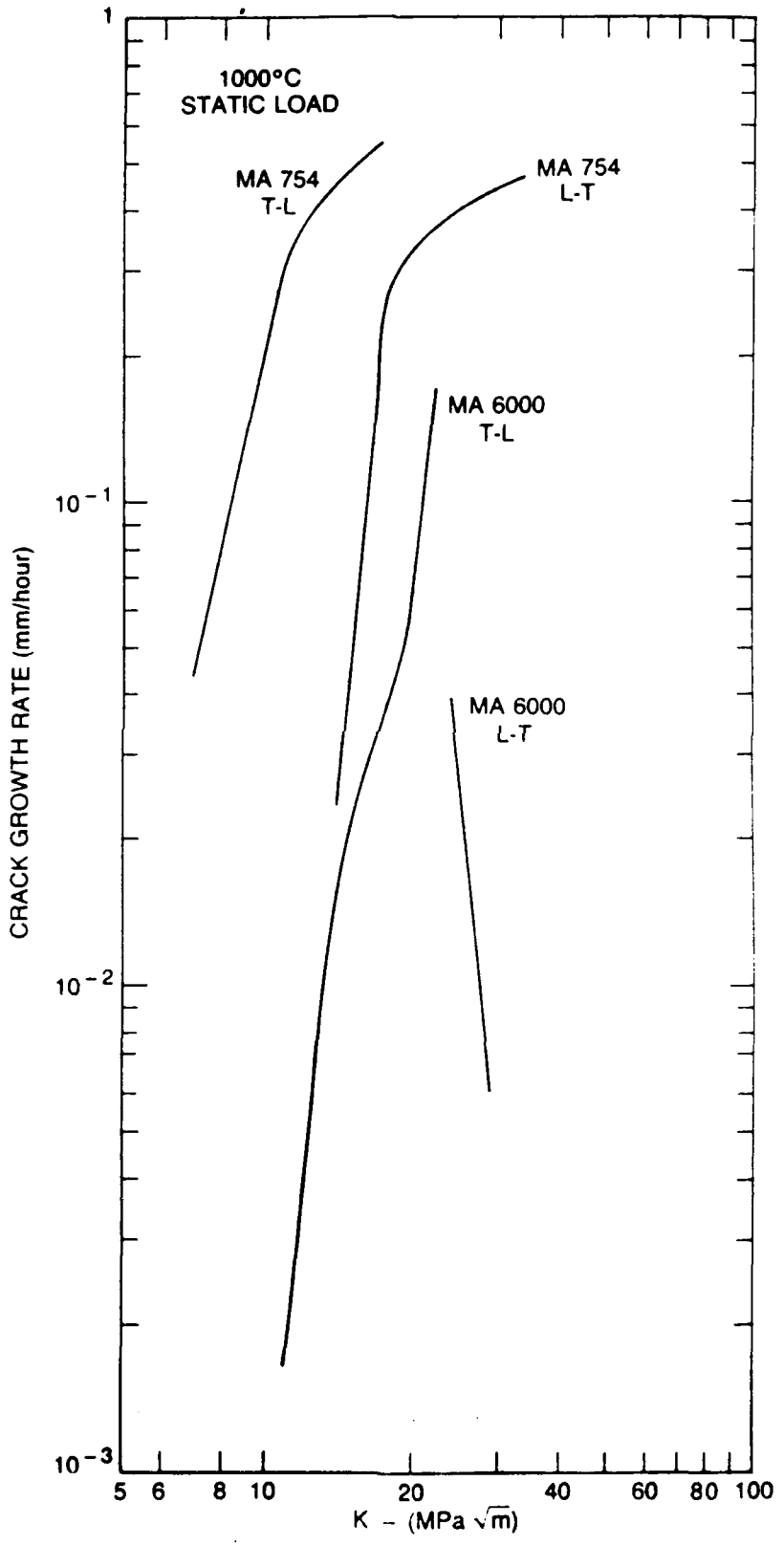


Fig. 15. Comparison of creep crack growth rates in MA 6000 and MA 754 in L-T and T-L orientations at 1000°C.

FATIGUE AND CREEP CRACK GROWTH IN OXIDE DISPERSION STRENGTHENED INCONEL MA 754

P. SHAHINIAN* AND K. SADANANDA
Material Science & Technology Division
Naval Research Laboratory
Washington D.C. 20375

*On-site Contract Employee From
Geo-Centers, Inc.
Newton Centre, MA

Manuscript submitted for publication to Metallurgical Transactions

Fatigue and Creep Growth in Oxide Dispersion Strengthened Inconel MA 754

P. Shahinian[1] and K. Sadananda[2]

ABSTRACT

The influence of temperature, orientation, and environment on fatigue and creep crack growth behavior in oxide dispersion strengthened MA754 was examined. With increase in temperature crack growth rates increase due largely to an increasing creep contribution. Environment also may influence crack growth behavior, the effect depending on orientation. Orientation has a marked effect on crack growth because of the propensity for creep void formation along particle stringers in the microstructure, which form in the processing. Rate of crack growth can be enhanced if the aligned voids are parallel to the main crack or retarded if normal to the direction of the crack. In the T-L orientation crack growth is faster on a time basis in creep than in fatigue, the reverse of that in the L-T orientation.

Predicted fatigue crack growth rates based on a cumulative damage model agree with experimentally determined growth rates.

1. On-site contract employee of Geo-Centers, Inc., Newton Centre, MA
2. Naval Research Laboratory, Washington, DC

INTRODUCTION

Because of their higher temperature advantage over currently used superalloys, oxide dispersion strengthened alloys have received much attention in the pursuit of improved performance and economy in advanced gas turbine engines. More recent efforts have been directed toward the mechanically alloyed materials, specifically iron-base MA-956 and nickel-base MA 754* and MA 6000*. In particular, their tensile, creep, and fatigue strengths (1-5), corrosion resistance, and microstructural details (6,7) have been examined. These alloys exhibit a fine dispersion of yttrium-aluminum oxide particles and, as a result of hot rolling or extrusion, highly elongated grains which impart superior strength at very high temperatures. The crystallographic direction <100> is parallel to the rolling direction. The dispersoids inhibit dislocation motion and the elongated grains minimize boundary sliding. However, these alloys possess a high degree of texture and anisotrophy of mechanical properties.

While the creep and fatigue properties of these alloys have been studied in detail, their crack growth characteristics, particularly in material under static load, have received little attention. Because of the anisotropic nature of the alloys it would be expected that crack growth would be especially sensitive to orientation at high temperatures. Cavitation in grain boundaries and intergranular fracture are known to occur in creep; thus grain morphology could have a marked effect on cracking. Knowledge of crack growth behavior and rates under creep as well as fatigue loads could be used in the application of fracture mechanics principles to predict component failure.

Fatigue crack growth resistance of MA 956 at 1000°C and 0.17 Hz has been found (7) to be essentially independent of grain orientation; the cracking mode was transgranular. However, in the high cycle fatigue of MA 754 at 850°C Nazmy and Singer (8) observed slightly lower crack growth rates in the T-L orientation that in the L-T orientation. As frequency was reduced from 50 to 0.5 Hz the crack growth rate in T-L specimens increased whereas in L-T specimens the rate was unaffected. The mode of crack growth at 50 Hz was transgranular in both orientations. However, at the lower frequency the cracking in the L-T specimen changed to a mixed intergranular-transgranular mode whereas in the T-L specimen it remained transgranular.

* Trademark of the INCO family of companies.

The effect of orientation on crack growth rate could be related to the orientation dependence of the elastic modulus. In high-cycle fatigue of MA 6000 at 850°C (9) crack growth rate was much lower in the T-L than L-T orientation, similar to that observed in MA 754. However, in MA 6000 the lower rate was attributed to crack branching along grain boundaries only in the T-L orientation even though propagation was mainly transgranular in both orientations.

In contrast to the absence of an orientation effect on fatigue in MA 956, crack growth under static load at 1000°C was clearly lower in the L-T direction than in the T-L direction (10). This effect was attributed to the more tortuous cracks path in the L-T orientation compared to the T-L orientation. It is noteworthy that crack growth rate on a time basis was higher under a static load than cyclic load in this alloy, indicating a significant creep contribution.

The data are not entirely consistent on the orientation dependence of fatigue crack growth but this could be related to differences in the test frequencies employed. Variation in frequency could alter the relative fatigue and creep contributions and the data indicate that effect of orientation on crack growth in creep may be different from that in fatigue. In any case the behavior appears to be complex.

In this investigation the crack growth behavior on Inconel MA 754 was examined under cyclic, static, and combined loads in order to provide more information and understanding that when used with conventional data such as creep and tensile strength would permit better prediction of service performance. Characteristics of crack growth as influenced by temperature, environment, and material-stress orientation were studied.

EXPERIMENTAL DETAILS

The mechanically alloyed Inconel MA 754 which has a nominal chemical composition in weight percent of 78 Ni, 20 Cr, 0.05 C, 0.3 Al, 0.5 Ti, 1.0 Fe, and 0.6 Y_2O_3 was obtained from INCO in the form of a hot rolled solution treated 26 mm-thick bar. Figure 1 illustrates the grain structure elongated in the rolled direction with a grain aspect ratio of approximately 10 containing oxide dispersoids, which provide stability of the microstructure and strength at very high temperature.

Compact tension specimens of nominal 1/2 T dimensions except for 7.6 mm thickness and 0.38 mm deep side grooves were prepared with the notch either parallel (T-L orientation) or perpendicular (L-T) to the rolling direction. These were precracked in fatigue at room temperature at relatively low loads prior to creep testing in dead weight machines or fatigue testing in electrohydraulic MTS machines. Creep tests were conducted at constant load and fatigue tests were conducted in the load control mode with a triangular wave form cycle at a frequency of 0.17 Hz and R of 0.05, and for these tests resistance heated furnaces and induction heating were employed, respectively.

Fatigue and creep tests in the L-T and T-L orientations were conducted at 24, 760, and 1000°C in air and in vacuum at $1x10^{-6}$ torr or better, but not all combinations were included . Several cyclic tests with a 1-min hold at peak stress were also run. Crack length was measured optically at frequent intervals with a traveling microscope. Growth rates were then determined from plots of crack length versus numbers of cycles or time using a slope measuring device. Stress intensity factor range (ΔK) was calculated from standard expressions which are given elsewhere (7).

In several fatigue tests, displacement across the notched mouth was measured using a strain gage extensometer with quartz contact rods, and load-displacement loops were recorded periodically at selected crack lengths. These data were used to determine the non-linear parameter J-integral by a procedure developed previously (11) for load controlled fatigue. It involves measuring the area under the rising part of the load-displacement loop from minimum to maximum load, and calculating ΔJ from the Merkle-Corten equation (12).

$$\Delta J = 2 (\alpha_1 A + \alpha_2 P \delta m)/Bb \qquad (1)$$

where A is the area, B the specimen thickness, b the length of uncracked ligament, P the peak load, and δm the displacement along the load line at maximum load. The constants $\alpha 1$ and $\alpha 2$ are functions of a/W and are given in graphical form in reference 12. It was shown previously (11) that values of ΔJ obtained by this estimation procedure are close to those determined by a more accurate but lengthy data reduction procedure. Comparison of fatigue

crack growth rate correlations with ΔK and ΔJ are made to see which parameter is more suitable for predictive equations.

Hystersis energy was also determined from the load-displacement loops for different crack lengths and then was used to calculate rate of crack growth according to one of the models in the literature based on critical damage accumulation ahead of the crack tip. Previous analysis of MA 956 data (7) showed that this model gave better agreement with experimental data than several models based on the plastic blunting process. If one assumes that most of the energy is utilized in the crack growth process, the energy required for a unit increment in crack length, U, can be calculated from the area of the loop ΔA as

$$U = \frac{\Delta A}{B da} \qquad (2)$$

where da represents the crack increment of growth during the cycle and B the thickness. An expression developed by Weertman (13) for fatigue crack growth rate,

$$\frac{da}{dN} = \frac{\Delta K^4}{8\pi^2 \mu \sigma^2 U} \qquad (3)$$

where U is the effective surface energy for crack growth, μ the shear modulus, and σ the cyclic yield stress, was used to predict rates from our data.

Fractographic and metallographic examinations also were made to ascertain the nature of cracking and its impact on rate of crack growth.

RESULTS AND DISCUSSION

Fatigue Crack Growth

Crack growth was generally influenced by temperature, orientation, environment, and hold cycle as well as loading mode. In fatigue, rate of crack growth in both orientations increased by at least a factor of 30 with increase in temperature from 24 to 1000°C, Figures 2 and 3. Crack growth rate with respect to orientation was not the same for the three temperatures. An influence of orientation was not discerned at low growth rates. However at intermediate rates or ΔK, crack growth was faster in the L-T than in the T-L

orientation at 24°C, slower in the L-T orientation at 760°C, and not significantly different between the two orientations at 1000°C. At high ΔK crack growth was slower in the L-T than T-L orientation due possibly to the development of secondary cracks in the L-T oriented specimen, as will be discussed later.

Since the increases in growth rate with temperature are much larger that can be accounted for by the temperature effect on elastic modulus, a change of less than a factor of 2, and thus on the cycle-dependent fatigue process, they could be related to a large extent to time-dependent processes, either/or both creep and environmental effects. It is difficult to ascertain from our data which is largely responsible for the effect. Contrary to expectations for a creep dominated effect the rate increase in going from 760° to 1000°C was much smaller than that in going from 24° to 760°C. However, imposing a 1-min hold at peak load on the fatigue cycle at 1000°C in air, Figure 3, clearly increased the growth rate in the L-T orientation by about a factor of 3, indicating creep may be making a contribution to the growth rate increase. For the T-L orientation although crack growth curves were not obtained, a 1-min hold caused failure in 3 cycles whereas without hold the life was 1260 cycles, employing the same initial stress intensity. These results indicate that crack growth at 1000°C may be at least as sensitive to time as cycles.

That environment is important in the crack growth process may be seen from a comparison of the air and vacuum curves for the L-T orientation in Figures 3 and 4 for 1000° and 760°C, respectively. Whereas crack growth rate in air exhibits a normal increase as the crack lengthens, in vacuum the growth rate after the initial acceleration decreases as the crack length increases until growth of the primary crack virtually ceases. In fact, a secondary crack normal to the main crack may continue to grow and cause complete fracture, as will be illustrated later. This behavior is related to orientation. Secondary cracks normal to the main brack develop due apparently to the anisotropic nature of the material and alter the stress field in the crack tip region. Why this crack growth retardation behavior occurs in vacuum but not in air is not altogether clear but it could be related to the relative growth rates in the two environments. Fatigue crack growth generally is faster in air than in an inert environment. It is possible that in air the main crack extends through the material faster than the secondary cracks develop which except for surface cracks do so in vacuum essentially.

In contrast, in the vacuum environment both the primary and secondary cracks grow in vacuum and the secondary cracks develop to a sufficient size to alter the stress field before the primary crack extends past the particular region. Creep damage ahead of the crack tip occurs predominantly by intergranular sliding. This facilitates secondary cracking for the L-T orientation and even more so when growth of the primary crack is retarded due to the lack of an aggressive environment. One may reason that in T-L oriented specimens crack growth retardation would not occur and none was observed.

The elastic-plastic parameter ΔJ was examined for adequacy in correlation of high temperature fatigue crack growth rates and compared with the linear elastic parameter ΔK. Growth rates were correlated in terms of the parameter $\sqrt{\Delta J \cdot E}$, where E is the elastic modulus, as well as in terms of ΔK, Figures 4 and 5. The E values for 760° and 1000°C were 110 and 92.5 GPa, respectively. Curves representing the two parameters are reasonably close for the 760°C data and for the 1000°C 1-min hold data as well. For the same crack growth rate the value for $\sqrt{\Delta J \cdot E}$ is only slightly lower than that for ΔK if in fact it differs at all. The close agreement between the $\sqrt{\Delta J \cdot E}$ and ΔK curves for the hold-time test would indicate that the microstructural changes due to creep deformation, such as void formation, which cause the higher growth rate compared to the regular cyclic test are not reflected to any significant extent in the stress-strain loop employed for the ΔJ calculation.

Predicted crack growth rates calculated by the energy balance model according to equation 3 was examined for agreement with experimental values. A detailed discussion of this approach is given in reference 14. Calculations were made using for 760°C a μ value of 41 GPa, obtained by taking 0.37 of Young's Modulus, and a σ value of 276 MPa, substituting the static yield stress for the cyclic yield stress, and for 1000°C a μ of 34 GPa and σ of 163 MPa (15). Curves for the predicted and experimental fatigue crack growth rates in MA 754 at 760°C are reasonably close, Figure. 4. The predicted values are about a factor of two higher than the experimental data. However, for fatigue crack growth under a 1-min hold cycle at 1000°C the agreement between predicted and experimental data is not as good, the predicted values being lower by as much as one-fourth of the experimental data. It is of interest to note the predicted curve falls close to the experimental da/dN versus ΔK curve for continuous cycling. Apparently all of the energy in the hysteresis loop

for the hold time test which includes the strain increase (creep) during the hold period does not contribute to crack growth in the same way as in a regular fatigue cycle. Since the energy and crack growth rate are inversely related in equation 3, a higher energy would yield a lower da/dN while in fact the hold period increased crack growth rate. It appears that a cumulative damage model predicts rather well fatigue crack growth rate in MA 754 provided significant contributions of time-dependent crack growth are not present.

The fatigue fracture surfaces at 24°C of both orientations were similar in appearance, being transgranular with secondary cracking, Figure 6. At high magnification the surface of the T-L orientation appears to be smoother that that of the L-T orientation. With increase in temperature to 1000°C the fracture surface characteristics changed as seen from comparison of Figure 7 with Figure 6. While the higher temperature fracture is still mainly transgranular, for the L-T orientation the features are less distinct and show essentially no secondary cracks. Fracture in the T-L orientation at 1000°C, Figure 7b, was substantially different from that at 24°C, Figure 6b and also from that in the L-T orientation, Figure 7a. Fracture occurred along ridges and steps resembling furrows, Figure 7b, which became more pronounced as ΔK increased. Application of a 1-min hold produced more distinct furrows, Figure 8. The room-temperature fatigue precrack surface consisting of a somewhat faceted transgranular fracture is shown in the left half of Figure 8 in contrast.

Specimen surfaces of the L-T orientation showing cracks running perpendicular to the direction of the main crack are shown in Figure 9 for fatigue tests at 760 and 1000°C. The process of development of the perpendicular cracks may be surmised from Figure 10. Cavities form along the aligned particle stringers, interconnect to form microcracks, and these join other crack segments on the same plane or adjacent parallel planes to form large cracks. Some of these cracks may join the main crack tip causing a change in growth direction or deceleration of growth leading to crack retardation, as indicated in Figures 3 and 4. Other cracks may intersect the main crack well behind the crack tip and their effect is not apparent. A 1-min hold fatigue specimen that failed along a perpendicular crack is shown in Figure 11. This behavior of course occurs with the L-T orientation only. In the T-L orientation the formation of cavities and microcracks along the

particle stringers would be expected to assist growth of the main crack. This is indicated by the data for 760°C in Figure 2 but not for 1000°C. It is not clear why this should be but it is possible that if a large number of microcracks form on many parallel planes ahead of the crack tip as may be the case at 1000°C the stress field at the crack tip may be defused to the extent that the growth rate is not enhanced by the cavity and microcracks formation. As mentioned earlier, Nazmy and Singer (8) observed slower crack growth in the T-L orientation in MA 754 at 850°C.

Creep Crack Growth

In the evaluation of creep crack growth the rates under static load are compared on the basis of the stress intensity factor K even though it is recognized that a unique relationship might not exist. While $\dot{J}$ or C^* would be a better parameter for correlation of creep crack growth rates, the factor K should be sufficient for purposes of comparison to identify effects of orientation and environment.

Both orientation and environment had significant influence on creep crack growth at 1000°C, Figure 12. Growth rates were markedly higher in the T-L than in the L-T orientation in vacuum as well as in air. The effect was much greater in vacuum. Furthermore the data indicate the apparent threshold stress intensity for growth is much lower, roughly one-half, for the T-L than the L-T orientation, irrespective of environment. Faster crack growth in the T-L orientation could be related to enhanced development of creep voids on particles aligned parallel to the crack direction making it easier for growth to occur. For the same reason the threshold for growth in the T-L orientation could be lower.

With respect to the environmental effect, the rates in the T-L orientation were lower in air than in vacuum except possibly at very low rates where data are not sufficient to discern an effect. In contrast, in the L-T orientation while the rates at low K values were about equal in air and vacuum, at some point the growth rate of the primary crack in vacuum began to decrease sharply rather than increase normally as in air and eventually the growth appeared to stop.

The crack arrest phenomenon was caused by the development of secondary cracks along the longitudinal structure or rolling direction, perpendicular to the main crack. Cavities are formed along the particle

stringers and coalesce to form microcracks. This retardation of crack growth in the L-T orientation in vacuum was also evident in fatigue. It could be surmised that the development of secondary, perpendicular cracks redistributes stresses and reduces the stress field at the primary crack tip. The perpendicular cracks form in air as well as in vacuum but in air their growth appears to be relatively slower than that of the main crack and consequently is less effective, or at least delayed in influencing rate. It is possible that, at certain conditions of temperature and load, crack retardation could occur in air as well.

In comparison of crack growth in fatigue and creep on a time basis, the rates in the L-T orientation at 1000°C are roughly the same for the creep and 1-min hold fatigue and these are lower than the rates for fatigue, Figure 13. This indicates the growth process even at 1000°C is cycle dependent as well as time dependent. In the hold-time test the cyclic loading comprises only about 10 percent of the total time and therefore does not materially contribute to and alter crack growth rate even though it is more damaging than static loading on a time basis. In the T-L orientation, growth rates are higher in creep than in fatigue. the converse of that in the L-T orientation, Figure 14. This behavior is quite plausible. Cavities tend to form along particle stringers parallel to the crack more readily in creep and thus in the T-L orientation accelerate the crack growth process.

There is a propensity for cavities to form along aligned particles in the microstructure produced by the hot processing of the material and these form more readily under time-dependent creep conditions, high temperature and static load. When the string of cavities is in the direction of the main crack growth, they assist the growth process by joining with the main crack and thereby accelerate the growth rate. However, when the aligned cavities are perpendicular to the main crack they may still join among themselves to form microcracks but now these perpendicular cracks in the vicinity of the main crack tip tend to retard the growth of the main crack by lowering the stress intensity at the tip. Faster creep crack growth in the T-L orientation than the L-T orientation observed here was also reported (7) for MA 956 at 1000°C. Another similarity in behavior with MA 956 is higher crack growth rate on a time basis under static than cyclic load for the T-L orientation.

Creep fracture surfaces have distinct features related to orientation as well as loading mode. This is the result largely of cavity and microcrack

formation along aligned particle stringers which is enhanced by the creep process. Crack growth in the L-T orientation at 1000°C, Figure 15, appeared to be a mixed mode, intergranular and transgranular, the former predominating in the later stages. Figure 15a shows the beginning of creep crack growth. Cavity formation and connection of cavities to produce microcracks in the L-T orientation specimen are shown in Figure 16. Microcracks develop mainly perpendicular to the main crack and divert the direction of the main crack or cause a marked reduction in growth rate.

In the T-L orientation the void formation occurs along the aligned particles parallel to the direction of crack growth. Fracture took place by interconnecting microcracks ahead of the main crack and produced a furrowed surface, shown in Figure 17a. Thus the rate of crack growth in the T-L orientation was enhanced relative to that in the L-T orientation, Figure 12. It is important to note the path of crack growth in this material appears to be influenced more by aligned particles even though particles are present in the boundaries too. Also this effect is more pronounced in creep than in fatigue.

SUMMARY AND CONCLUSIONS

Fatigue crack growth rate in MA 754 for a given ΔK increases with rise in temperature from 24° to 1000°C and may be affected by specimen orientation with respect to rolling direction. The effect of orientation is not the same over the entire temperature range. The growth rate increase due to temperature appears to be related mainly to time-dependent processes, probably creep, and not to an elastic modulus change. A 1-min hold on the fatigue cycle raises the growth rate appreciably, indicating crack growth is as sensitive to time as cycles.

In the L-T orientation significant secondary cracking occurs normal to the direction of the main crack to the extent that final fracture may occur in that direction. Also in vacuum the secondary cracking causes a deceleration in crack growth and virtual cessation.

Comparisons of correlations of fatigue crack growth rates with the elastic-plastic parameter ΔJ and linear elastic parameter ΔK show reasonably good agreement between the two parameters.

Predicted fatigue crack growth rates based on a cumulative damage model agree reasonably well with experimental data but the expression does not seem to take into account hold time effects. It appears the damage model predicts fatigue crack growth rates in MA 754 provided a significant contribution of time-dependent growth is not present.

Creep crack growth rates at 1000°C are higher in the T-L orientation than L-T orientation in both air and vacuum. Furthermore the orientation effect is much larger in creep than in fatigue. Also the apparent threshold stress intensity for creep crack growth is much lower for the T-L than L-T orientation. Faster crack growth in the T-L orientation could be related to creep voids on particles aligned parallel to the growth direction facilitating crack extension, the process occurring more readily in creep than fatigue.

Retardation of crack growth in the L-T orientation in vacuum occurs in creep as it does in fatigue and appears to be related to the development of secondary cracks normal to direction of the main crack. In the T-L orientation retardation was not observed and crack growth is faster on a time basis in creep than fatigue, the reverse of that in the L-T orientation, and appears to be related to the greater tendency for void formation in creep.

ACKNOWLEDGEMENT

The Inconel MA 754 alloy used for this study was provided by INCO Alloy Products.

REFERENCES

1. J. D. Whittenberger, "Tensile and Creep Properties of the Experimental Oxide Dispersion Strengthened Iron-Base Sheet Alloy MA-956E at 1365K," Met. Trans. A, Vol. 9A, 1978, pp. 101-110.

2. J. D. Whittenberger, "Elevated Temperature Mechanical Properties of the Iron Base Oxide Dispersion Strengthened Alloy MA 956 Bar", Met. Trans. A, Vol. 12A, 1981, pp. 845-851.

3. T. E. Howson, F. Cosandey, and J. K. Tien, "Creep Deformation and Rupture of Oxide Dispersion Strengthened Inconel MA 754 and and MA 6000E", Superalloys 1980, Proc., Fourth Int. Symposium on Superalloys, ASM, 1980, pp. 563-573.

4. R. F. Singer, R. C. Benn, and S. K. Kang, "Creep Rupture Properties of Inconel Alloy MA 6000", Frontiers of High Temperature Materials II, INCO Alloy Products Co., 1983.

5. J. J. Stephens and W. D. Nix, "The Effect of Grain Morphology on Logitudinal Creep Properties of Inconel MA 754 at Elevated Temperatures", Met. Trans., Vol. 16A, 1985, pp. 1307-1324.

6. S. K. Kang and R. C. Benn, "Microstructural Development in High Volume Fraction Gamma Prime Ni-Base Oxide-Dispersion Strengthened Superalloys", Met. Trans., Vol. 16A, 1985, pp. 1285-1294.

7. K. Sadananda and P. Shahinian, "Fatigue Crack Growth Behavior of an Oxide Dispersion Strengthened MA 956 Alloys", Met. Trans., Vol 15a, 1984, pp. 527-539.

8. M. Y. Nazmy and R. F. Singer, "High Cycle Fatigue and Fatigue Crack Growth of the Oxide Dispersion Strengthened Alloy MA 754", Met. Trans., Vol. 16A, 1985, pp. 1437-1444.

9. W. Hoffelner and R. F. Singer, "High Cycle Fatigue Properties of the ODS-Alloy MA 6000 at 850°C", Met. Trans, Vol. 16A, 1985, pp. 393-399.

10. K. Sadananda and P. Shahinian, "Crack Growth Behavior in Mechanically Mixed Oxide Dispersion Strengthened Alloys", Proc., MFPG Symposium on "Failure Mechanisms in High Performance Materials", National Bureau of Standards, Gaithersburg, MD May 1, 1984, pp. 87-97.

11. K. Sadananda and P. Shahinian, "A Fracture Mechanics Approach to High Temperature Fatigue Crack Growth in Udimet 700", Engineering Fracture Mechanics, Vol. 11, 1979, pp. 73-86.

12. J. G Merkle and H. T. Corten, "A J-Integral Analysis for Compact Specimen, Considering Axial Force as Well as Bending Effects", J. Of Pressure Vessel Technology, Vol. 96, , 1974, pp. 286-292.

13. J. Weertman: in Fatigue and Microstructure, M. Meshii, ed. American Society for Metals, Metals Park OH, 1978, pp. 279.

14. K. Sadananda, "Fatigue Crack Growth Theory and Experiment: A Comparative Analysis", Scripta Metallurgica, Vol. 17, 1983, pp. 1419-1424

15. Anon, IncoMAP Data Sheets, Inconel alloy MA 754, Inco Products 1981.

Figure Captions

Fig. 1. Microstructure of Inconel MA 754 alloy showing elongated grains.

Fig. 2. Influence of temperature and orientation on fatigue crack growth rate.

Fig. 3. Influence of hold time, environment, and orientation on fatigue crack growth rate at 1000°C.

Fig. 4. Comparison of fatigue crack growth rates at 760°C (L-T orientation) on the basis of $\sqrt{\Delta J \cdot E}$, ΔK, and predictive formulation.

Fig. 5. Comparison of fatigue crack growth rates for 1-min hold cycle at 1000°C (L-T orientation) on the basis of $\sqrt{\Delta J \cdot E}$, ΔK, and predictive formulation.

Fig. 6. Fatigue fracture surfaces at 24°C of (a) L-T orientation and (b) T-L orientation.

Fig. 7. Fatigue fracture surfaces at 1000°C of (a) L-T orientation and (b) T- L orientation.

Fig. 8. Fatigue fracture surface (T-L orientation) of 1-min hold at 1000°C in comparison with fatigue at 24°C.

Fig. 9. Fatigue specimen surfaces (L-T orientation) showing development of perpendicular cracks at (a) 760°C and (b) 1000°C.

Fig. 10. Fatigue specimen surfaces showing crack growth in L-T orientation; (a) cavity formation at 1000°C and (b) microcrack formation at 760°C.

Fig. 11. Fracture in fatigue specimen tested with 1-min hold at 1000°C in air showing final separation in direction normal to main crack.

Fig. 12. Influence of orientation and environment on creep crack growth rate at 1000°C.

Fig. 13. Comparison of crack growth rates (L-T orientation) on a time basis for cyclic, 1-min hold cycle, and static loading at 1000°C.

Fig. 14. Comparison of creep and fatigue crack growth rates at 1000°C on a time basis and dependence on orientation.

Fig. 15. Creep fracture surfaces in L-T orientation at 1000°C in air.

Fig. 16. Creep crack growth specimen surfaces (L-T orientation) showing cavity formation at 1000°C in vacuum.

Fig. 17. Creep crack growth in T-L orientation at 1000°C showing (a) furrowed fracture surface and (b) fracture path along particle stringers.

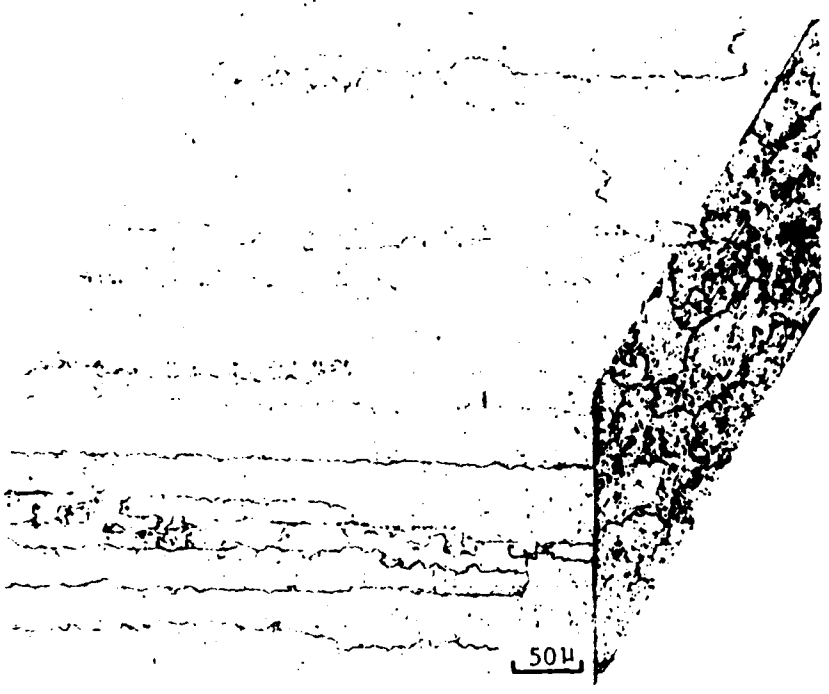


Fig. 1. Microstructure of Inconel MA 754 alloy showing elongated grains.

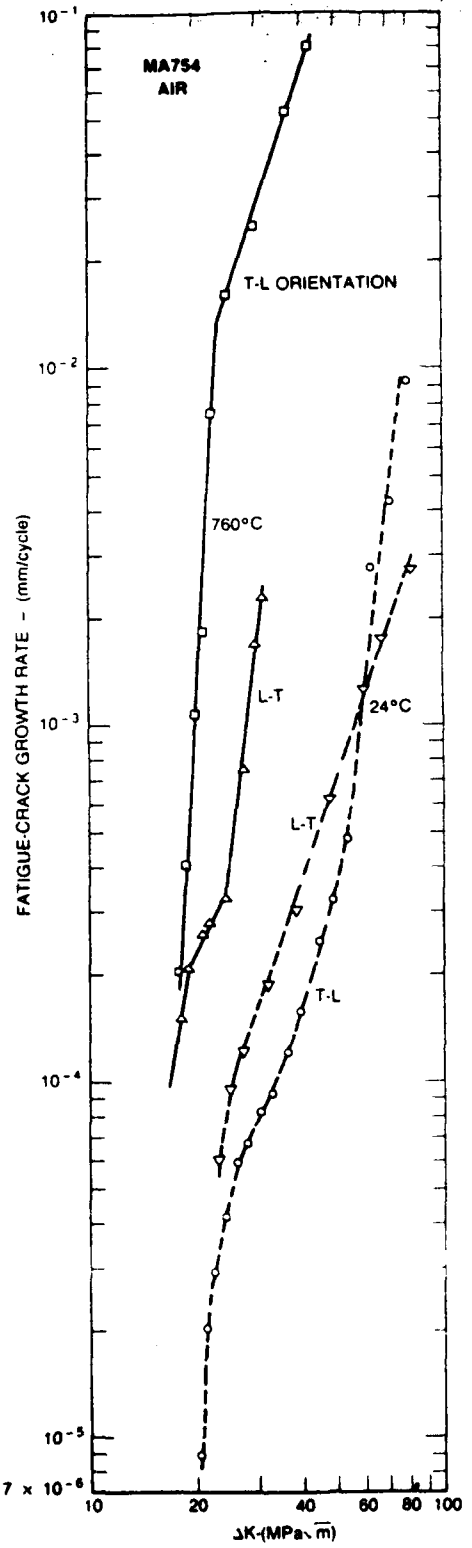


Fig. 2. Influence of temperature and orientation on fatigue crack growth rate.

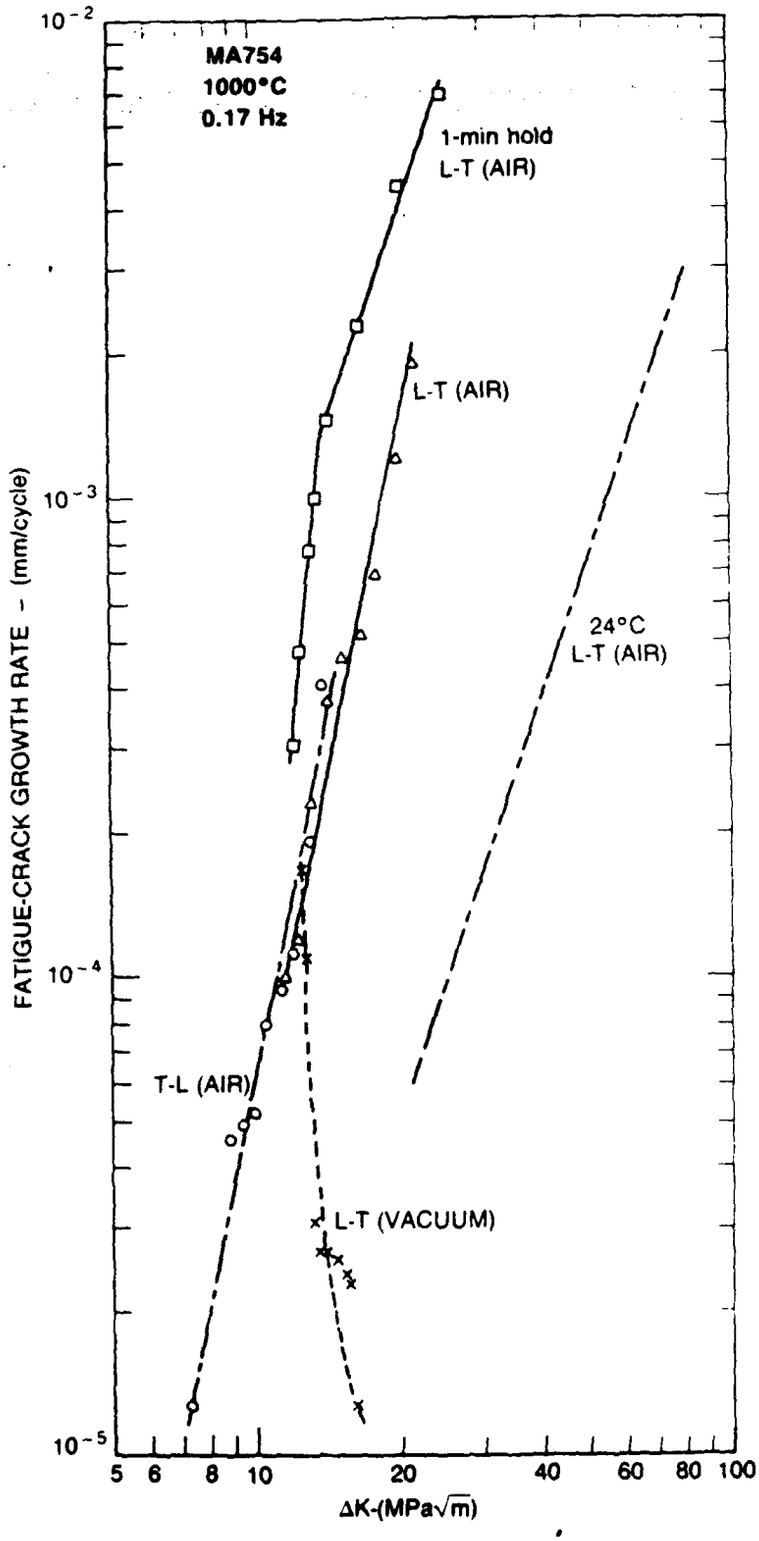


Fig. 3. Influence of hold time, environment, and orientation on fatigue crack growth rate at 1000°C.

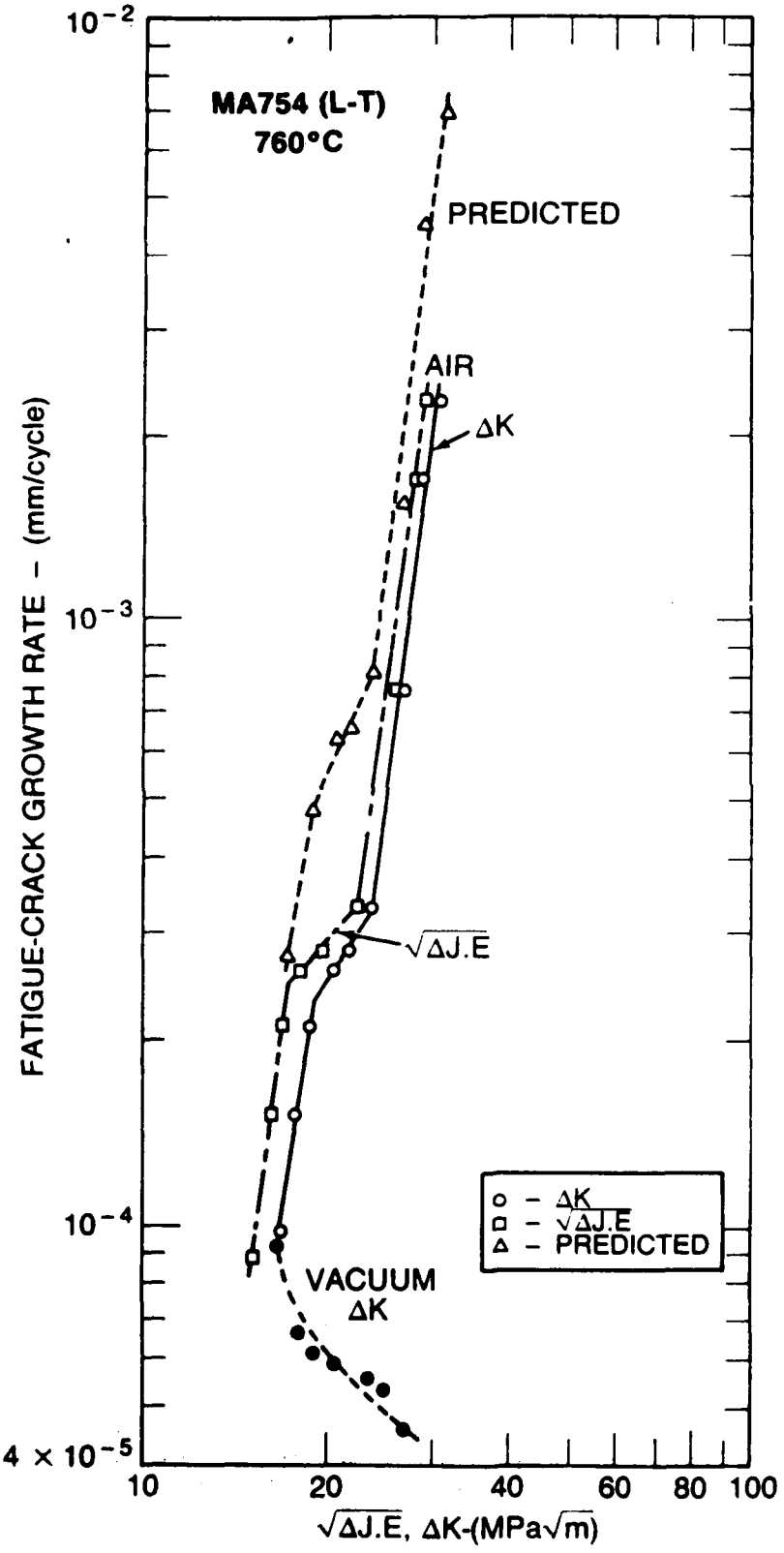


Fig. 4. Comparison of fatigue crack growth rates at 760°C (L-T orientation) on the basis of $\sqrt{\Delta J \cdot E}$, ΔK, and predictive formulation.

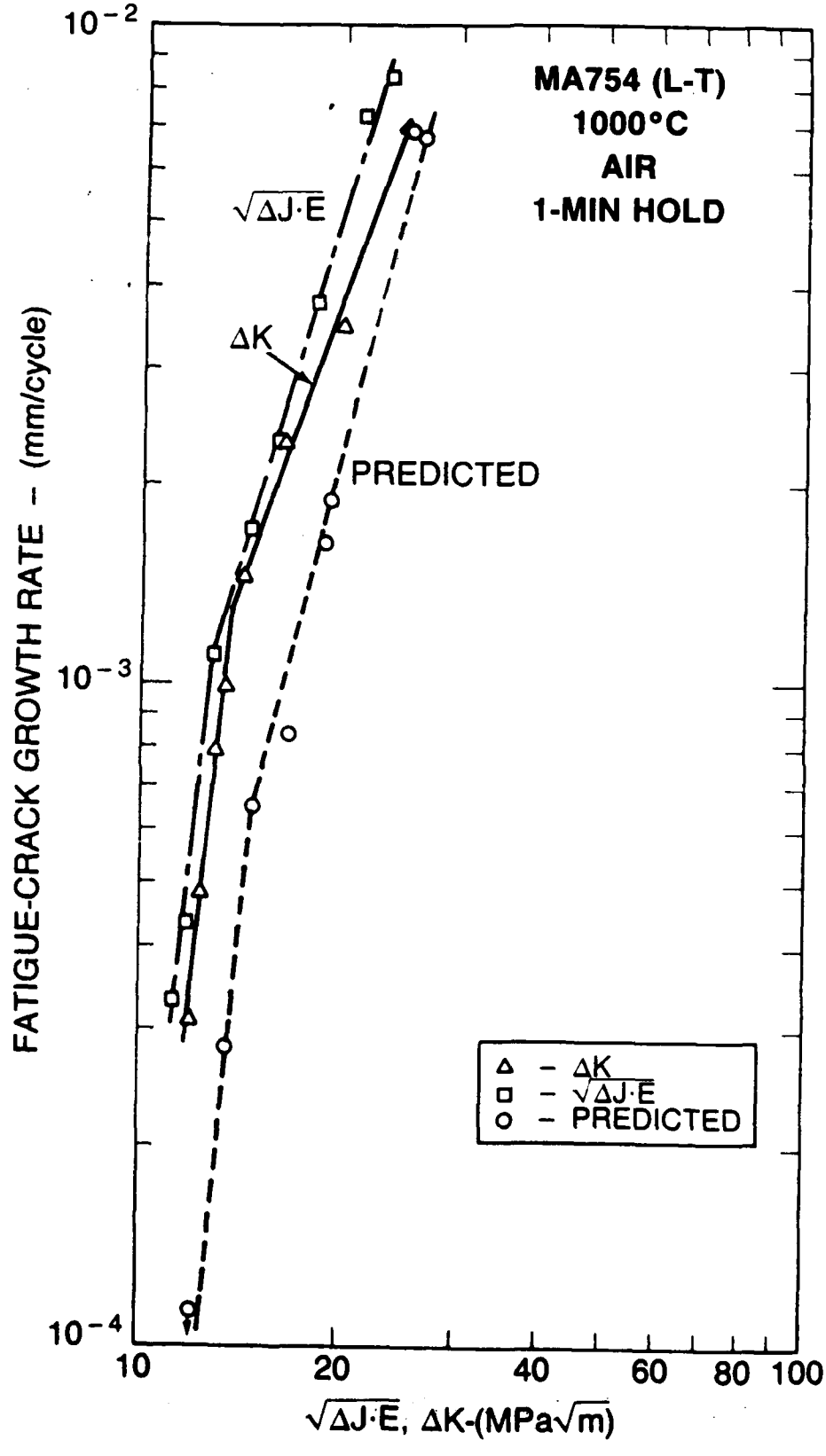
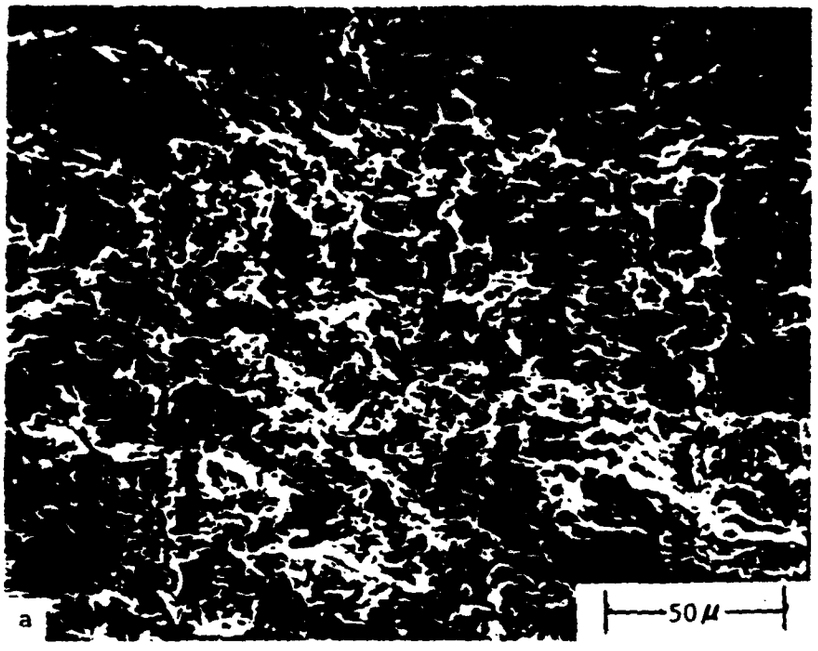


Fig. 5. Comparison of fatigue crack growth rates for 1-min hold cycle at 1000°C (L-T orientation) on the basis of $\sqrt{\Delta J \cdot E}$, ΔK, and predictive formulation.



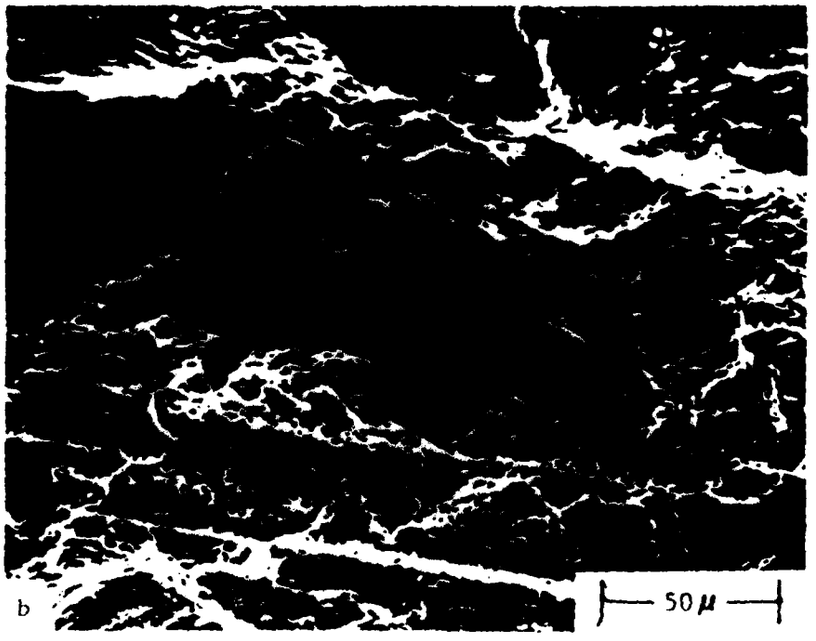
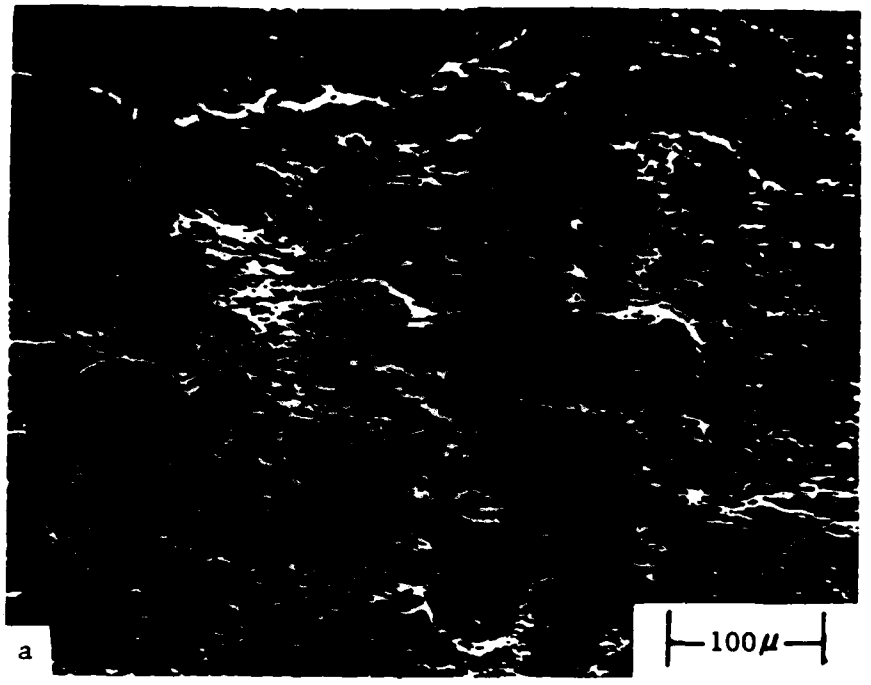


Fig. 6 Fatigue fracture surfaces at 24°C of (a) L-T orientation and (b) T-L orientation.



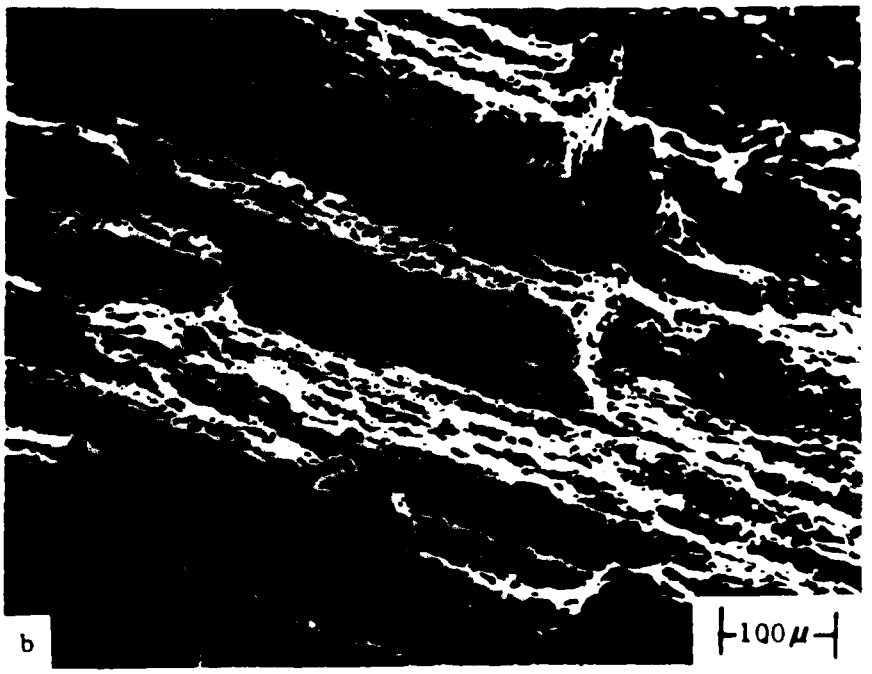


Fig. 7 Fatigue fracture surfaces at 1000°C of (a) L-T orientation and (b) T-L orientation



Fig. 8. Fatigue fracture surface (T-L orientation) of 1-min hold at 1000°C in comparison with fatigue at 24°C

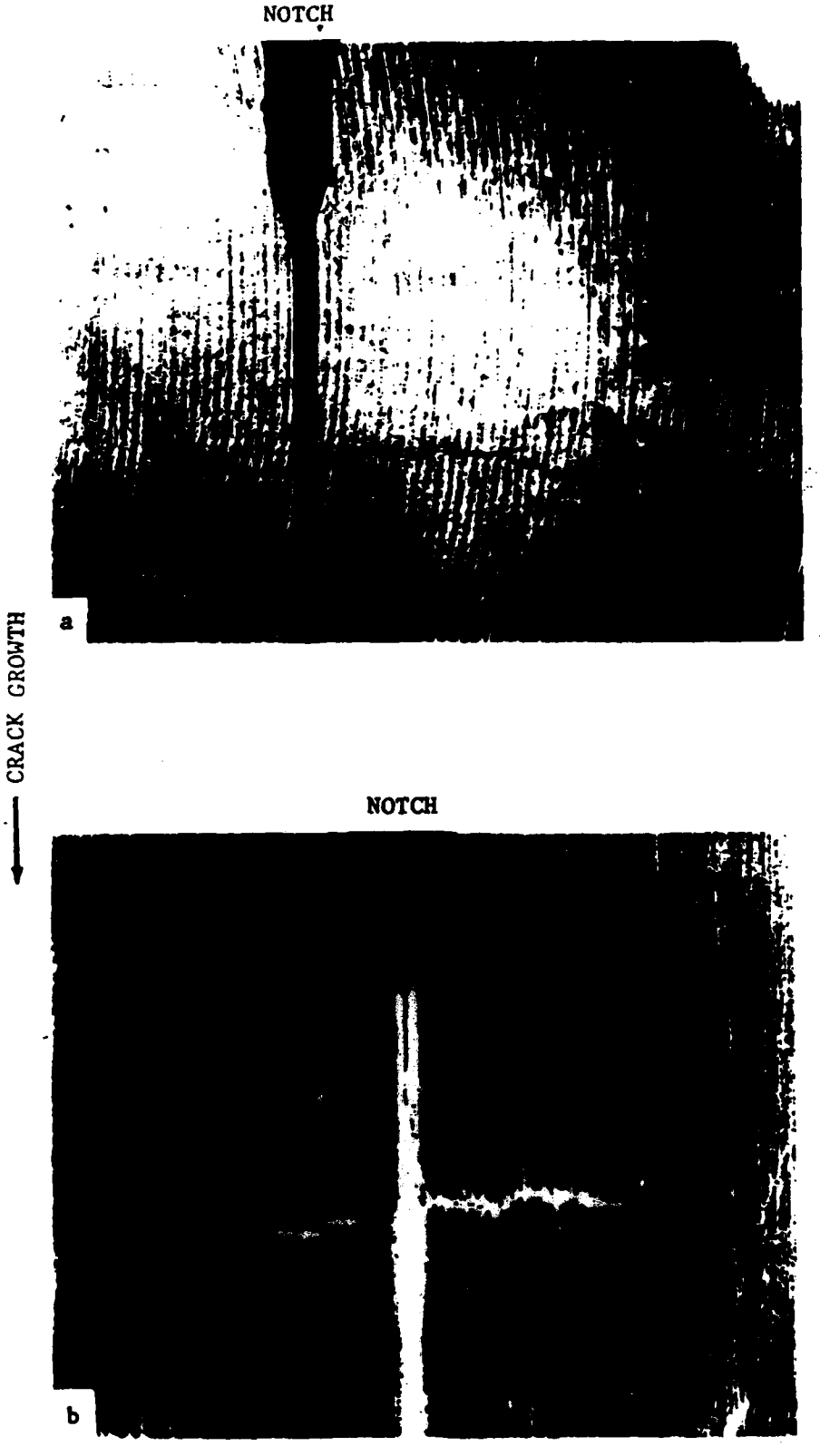
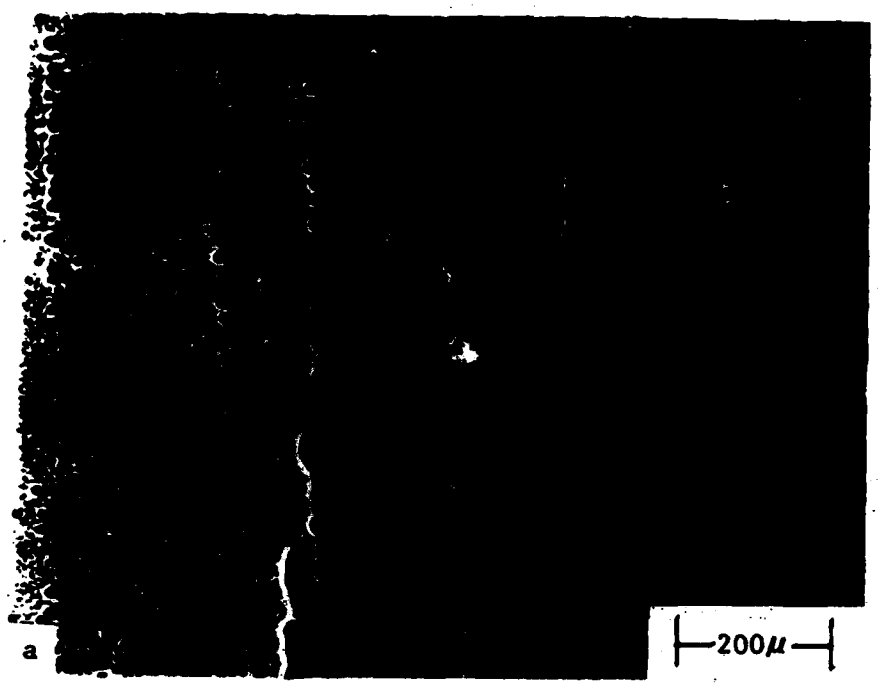


Fig. 9. Fatigue specimen surfaces (L-T orientation) showing development of perpendicular cracks at (a) 760°C and (b) 1000°C.



CRACK GROWTH ⟶



Fig. 10 Fatigue specimen surfaces showing crack growth in L-T orientation, (a) cavity formation at 1000°C and (b) microcrack formation at 760°C.

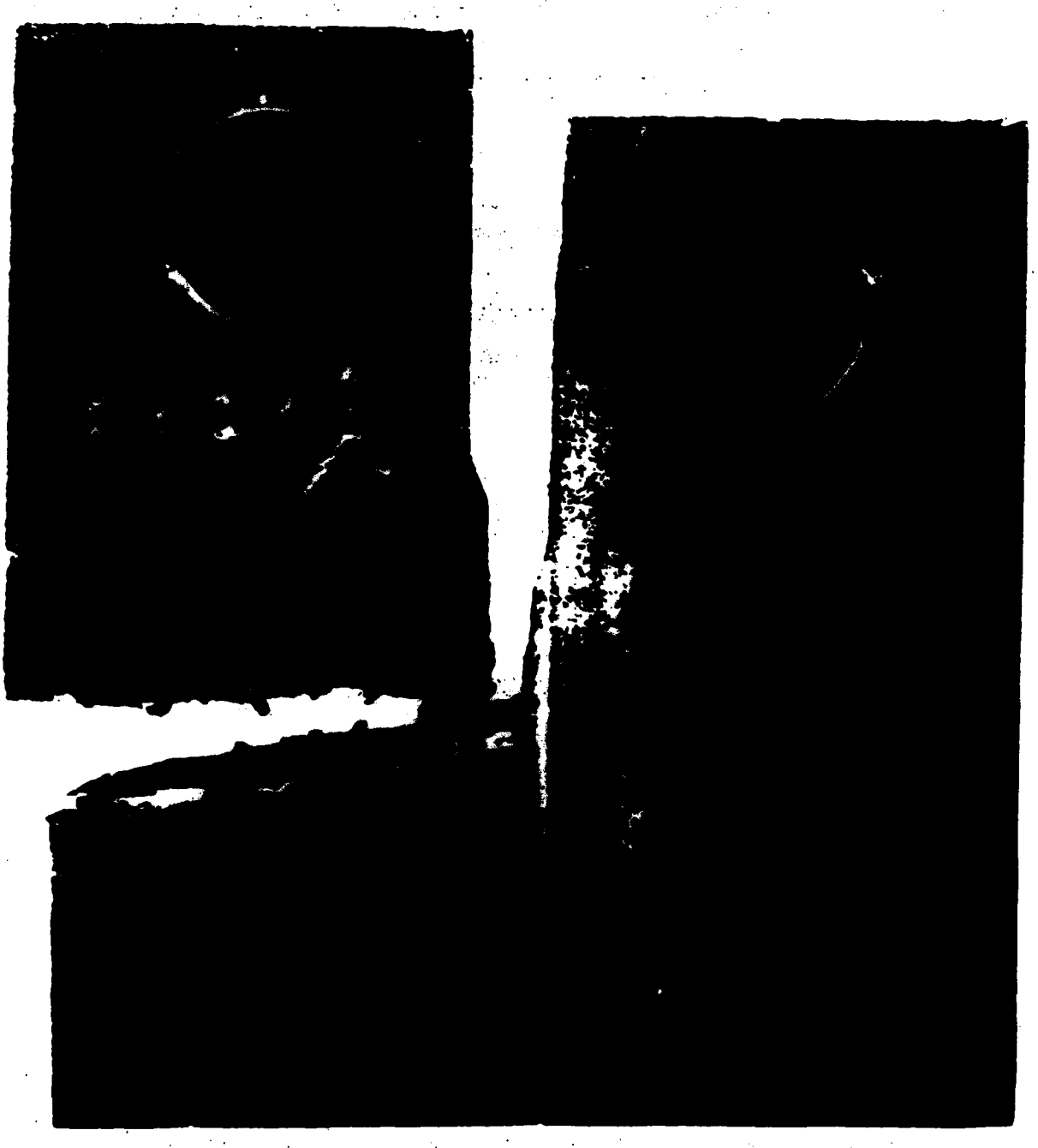


Fig. 11. Fracture in fatigue specimen tested with 1-min hold at 1000°C in air showing final separation in direction normal to main crack.

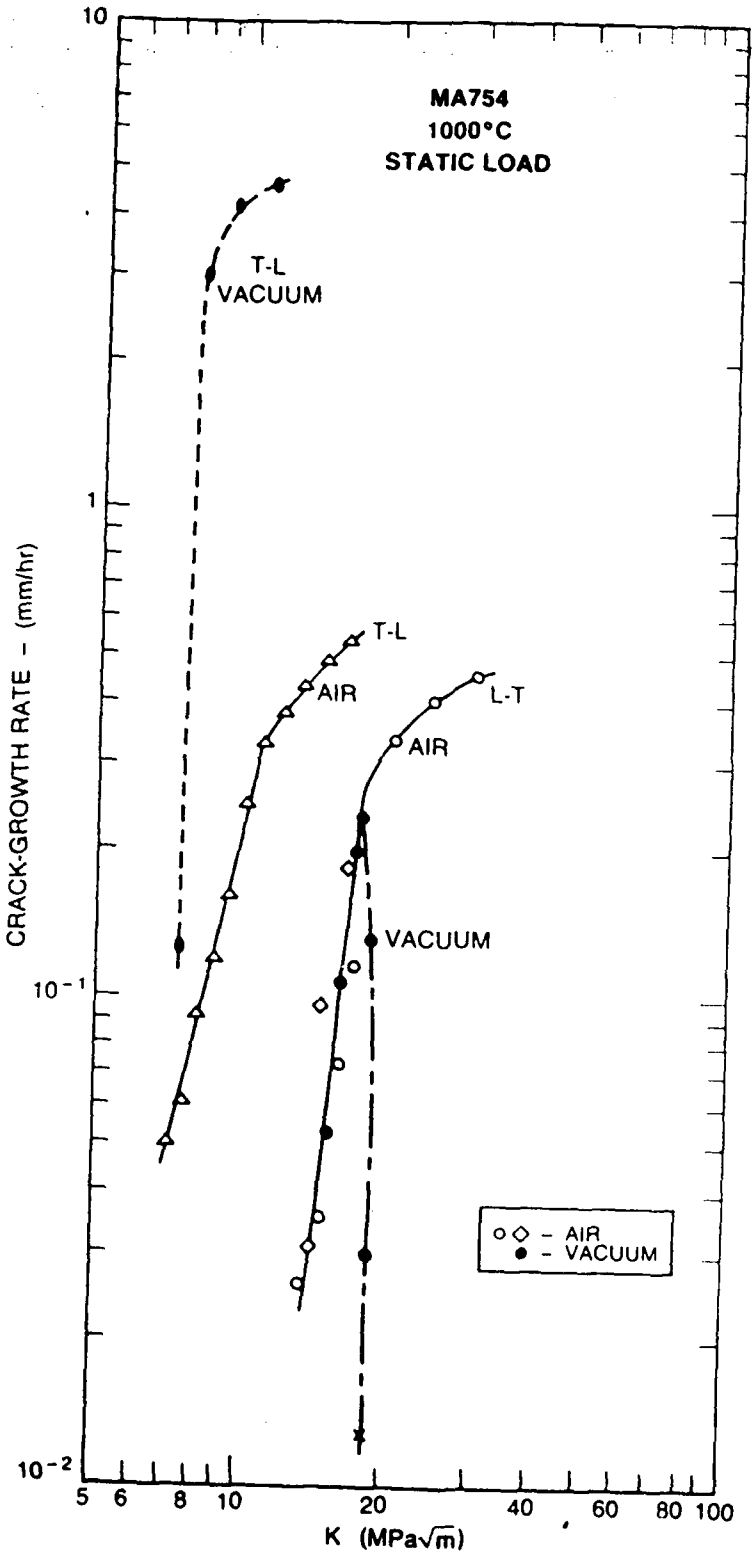


Fig. 12. Influence of orientation and environment on creep crack growth rate at 1000°C.

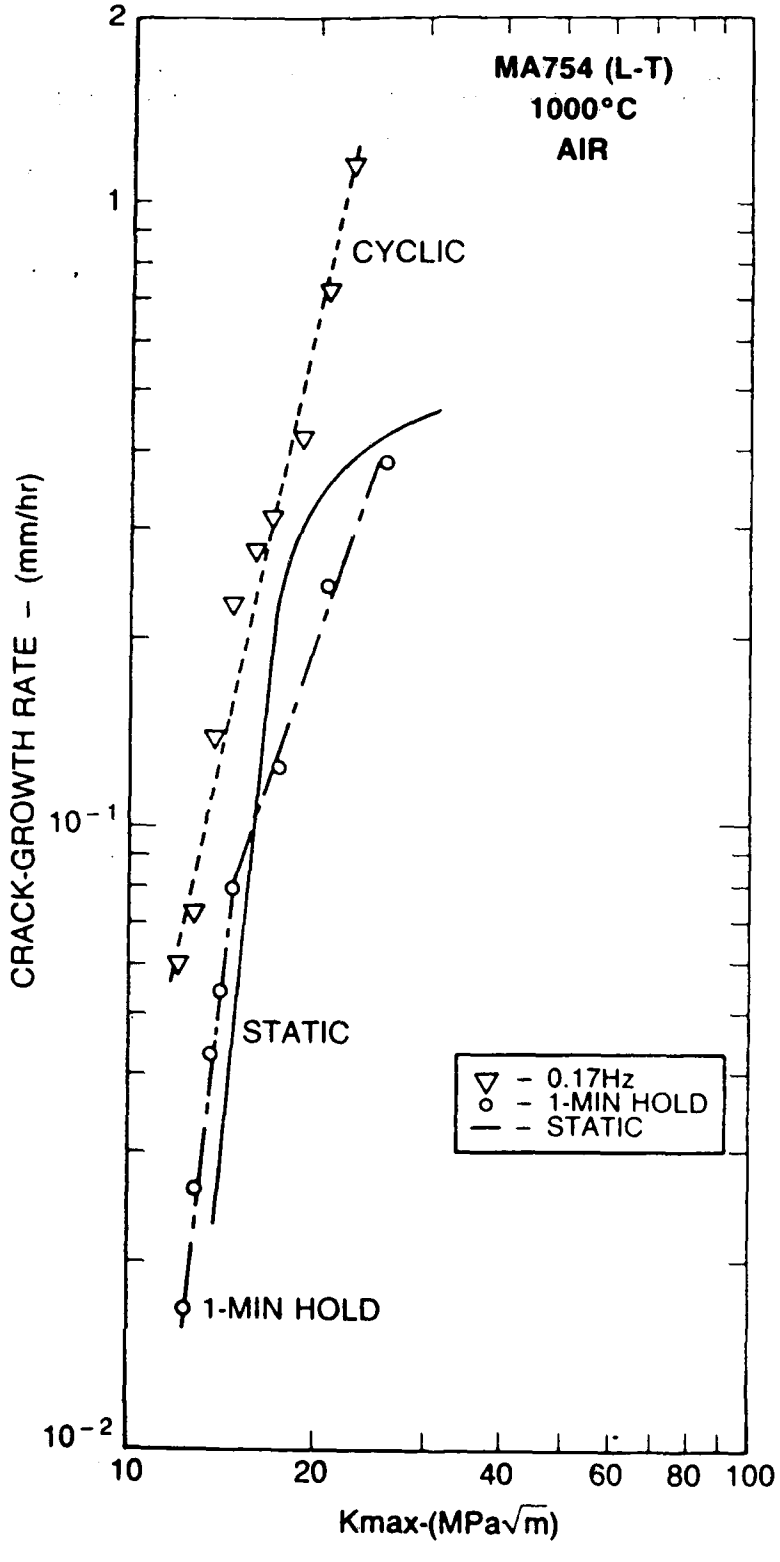


Fig. 13. Comparison of crack growth rates (L-T orientation) on a time basis for cyclic, 1-min hold cycle, and static loading at 1000°C.

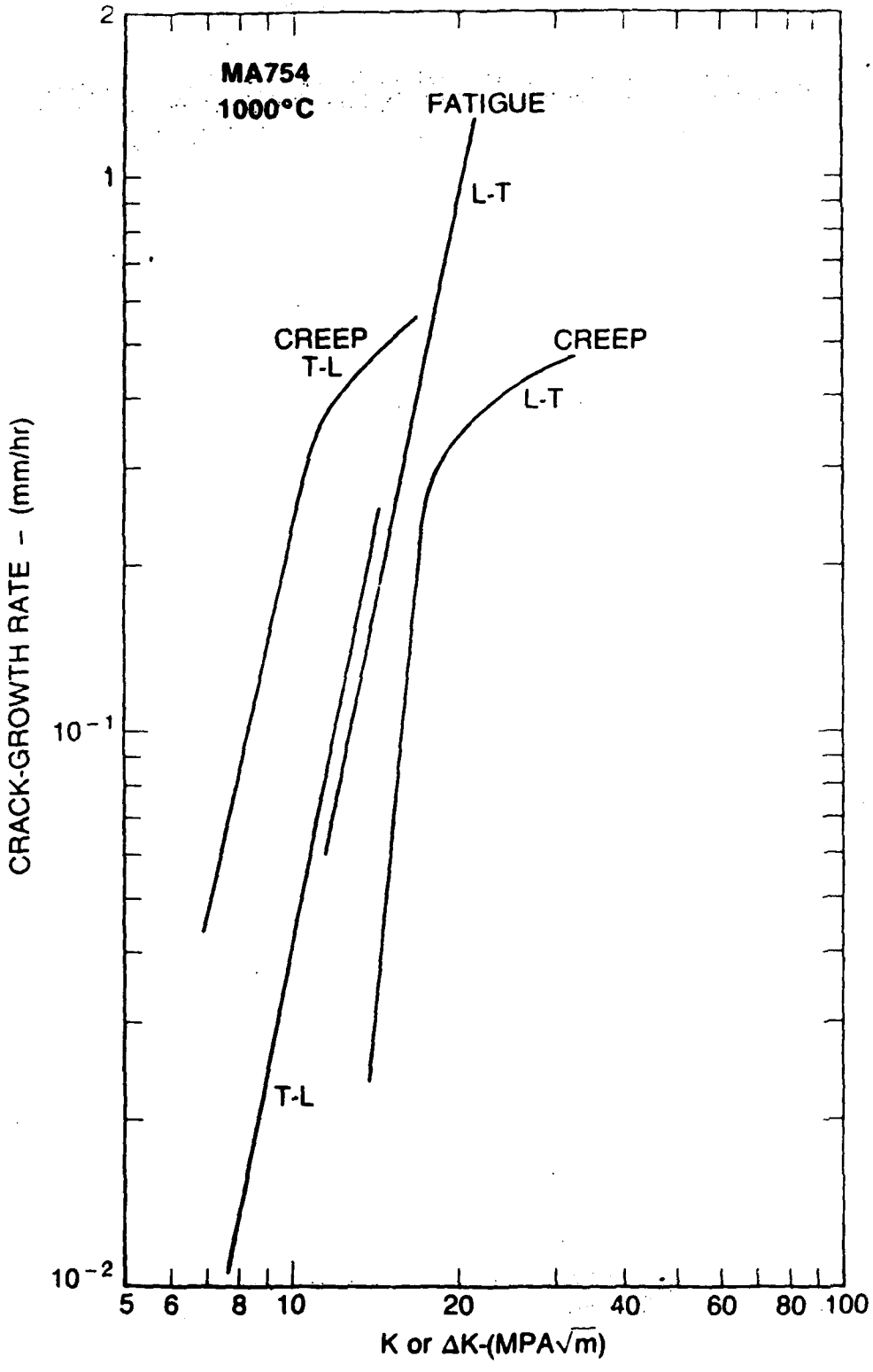
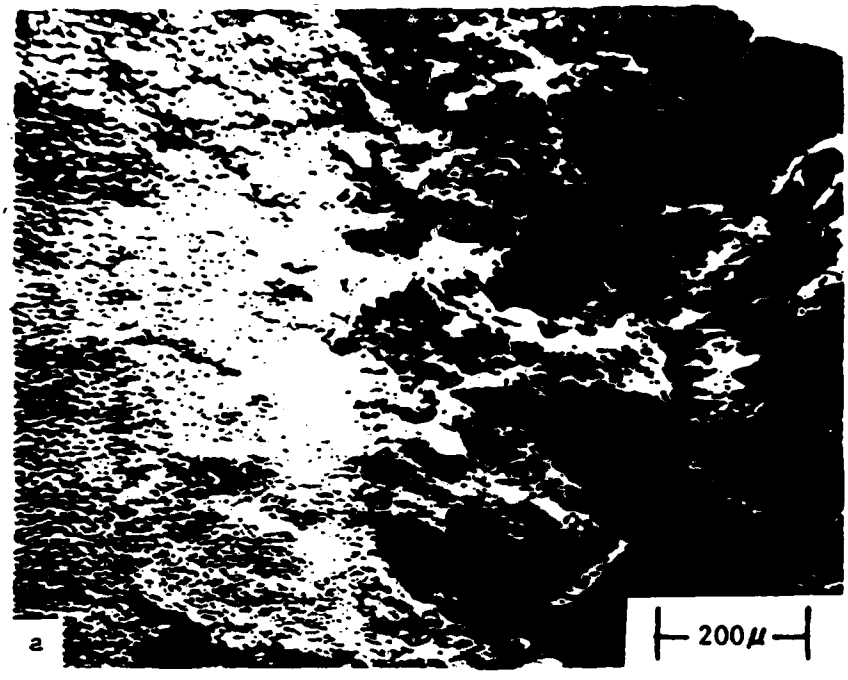


Fig. 14. Comparison of creep and fatigue crack growth rates at 1000°C on a time basis and dependence on orientation.



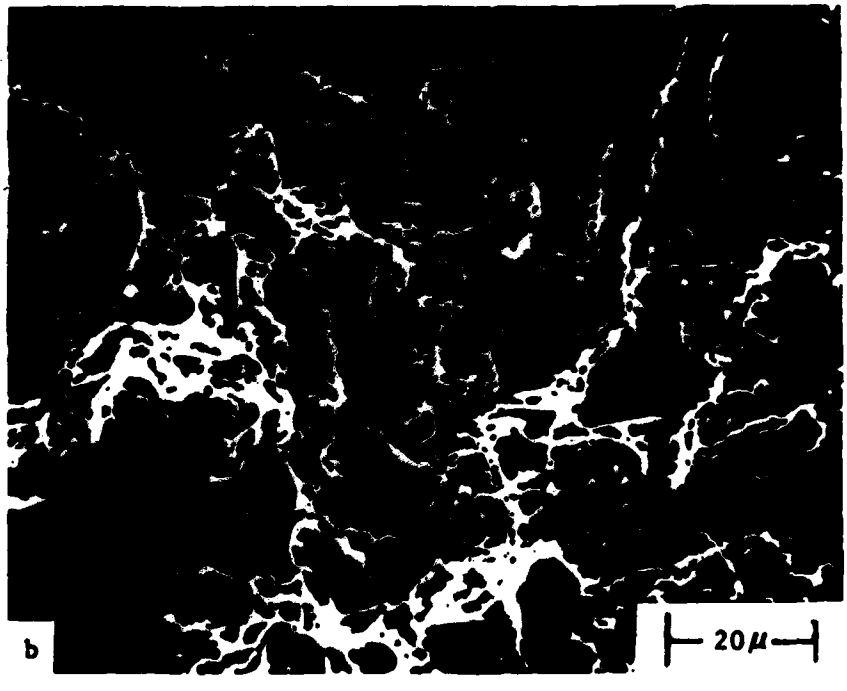


Fig. 15. Creep fracture surfaces in L-T orientation at 1000°C in air.



CREEP CRACK GROWTH ⟶

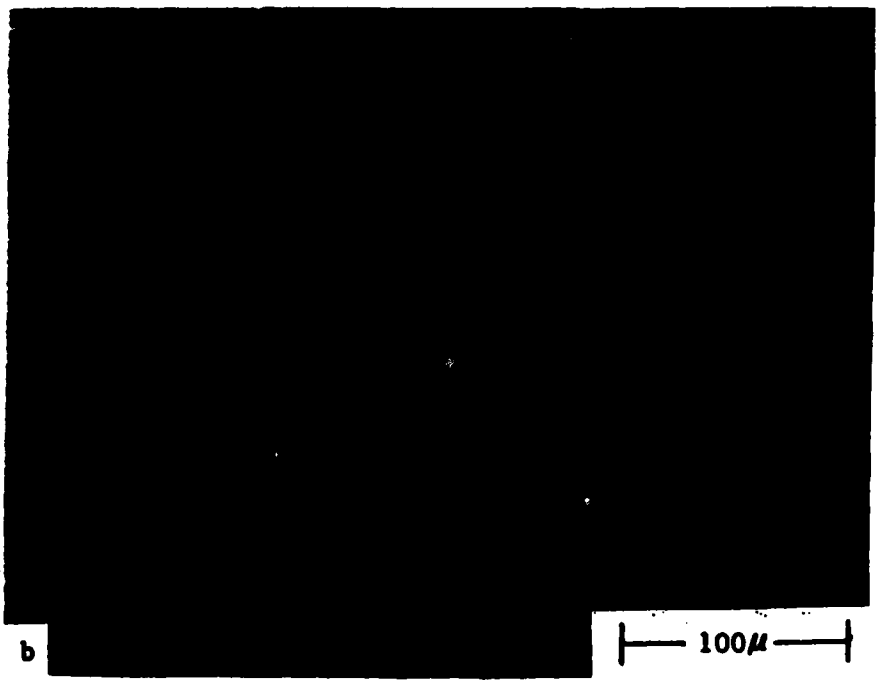


Fig. 16. Creep crack growth specimen surfaces (L-T orientation) showing cavity formation at 1000°C in vacuum.

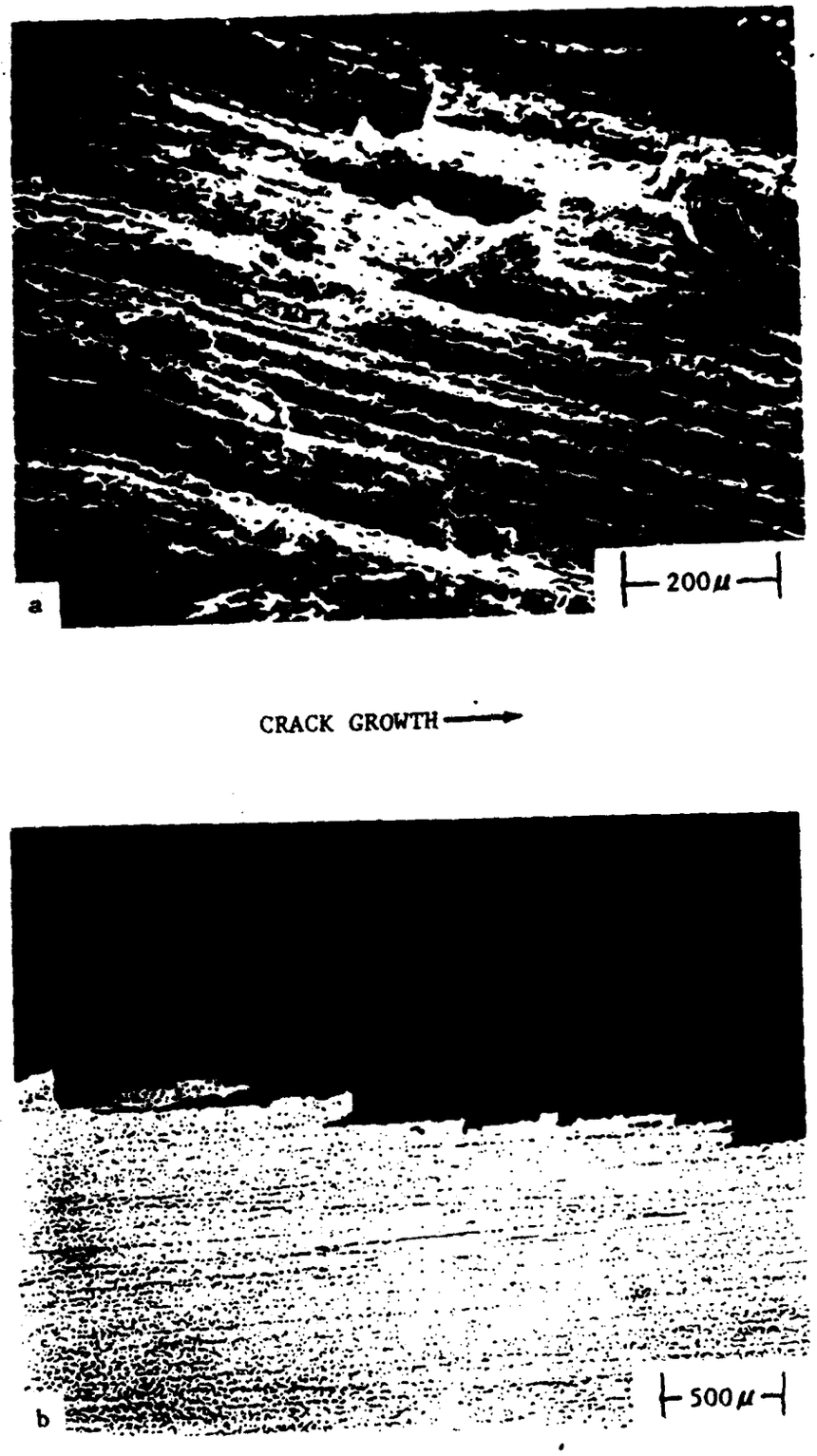


Fig. 17. Creep crack growth in T-L orientation at 1000°C showing (a) furrowed fracture surface and (b) fracture path along particle stringers.

APPENDIX X

RECORD AND DISCLOSURE OF INVENTION

DIRECTIVE ONRINST 5870.1C

DEPARTMENT OF THE NAVY
OFFICE OF NAVAL RESEARCH
ARLINGTON, VA. 22217

INSTRUCTIONS. A Navy inventor or an employee of a Navy contractor should use this form when submitting an invention disclosure to the Department of the Navy. Original and two copies should be printed or typed and forwarded to the Navy Patent representative in the area or directly to the Office of Naval Research at the above address. Where space on form is inadequate, enter "see attached page", identify item by number and use plain pages as needed. When completely executed, this form becomes an important legal document useful in proving priority of invention.

FOR USE BY NAVY PATENT ACTIVITY	
PATENT ACTIVITY *(Name)*	NAVY CASE NO.
DATE DISCLOSURE RECEIVED	LOCAL CASE NO.

PART I. RECORD OF INVENTION

1. INVENTOR(S)	ADDRESS	POSITION TITLE	EMPLOYER *(Activity & Code No., or Company & address)*
J.R. Spann	1944 Kirby Road McLean, VA 22101	Senior Engineer	GEO-CENTERS, INC. 10903 Indian Head Hwy Ft. Washington, MD 20744

2. DESCRIPTIVE TITLE OF INVENTION *(Disclosure details of invention in Part II on reverse)*

Process for Making High Temperature $Ba_2YCu_3O_7$ Superconducting Powder

RECOMMENDED SECURITY CLASSIFICATION AND AUTHORITY ON INVENTION DISCLOSURE

3. CONCEPTION, INITIAL RECORDS AND RESULTS OF FIRST MODEL

a. EARLIEST DATE AND PLACE INVENTION WAS CONCEIVED *(Identify persons and records to support date and place)*

8/3/88 at the Naval Research Laboratory, Code 6370, J.R. Spann - Notebook (Miscel. Exp.) p. 128.

b. DATE AND PRESENT LOCATION OF FIRST SKETCH, DRAWING OR PHOTO AND FIRST WRITTEN DESCRIPTION *(Such as notebook entries, etc.)*

8/4/88 Notebook, p. 128

c. DATE AND PLACE OF COMPLETION OF FIRST OPERATING MODEL OR FULL SIZE DEVICE AND ITS PRESENT LOCATION

8/5/88 NRL, Bldg. 42, Rooms 405, 415

d. DATE AND PLACE OF FIRST TEST OR OPERATION AND THE RESULTS *(Give name and address of witnesses, and pr[illegible]t location of records)*

8/5/88 NRL diffraction x-ray analysis indicated phase pure orthorhombic BYC was produced by a vacuum calcine combined with an oxygen calcine & cooling.

WITNESS: M.T. Chase
13919 Shanon Avenue
Laurel, MD 20707

RECORDS: NRL
Washington, D.C.20375-5000

4. OTHER RECORDS *(Notebook entries, descriptions, reports, drawings, etc.)*

IDENTIFICATION	DATE OF DOCUMENT	PRESENT LOCATION
Philips Diffraction x-ray Computer Storage - S7181C	8/15/88	NRL - Bldg. 42, Rm. 514
S718MGO	8/15/88	
S718BST	8/16/88	
S718ALO	8/16/88	
	8/16/88	

5. OTHER INDIVIDUALS TO WHOM INVENTION WAS DISCLOSED

NAME	ACTIVITY OR COMPANY INDIVIDUAL REPRESENTS	DATE DISCLOSED	TYPE *(Oral or written disclosures)*
M. Khan	Naval Research Laboratory	8/19/88	oral & written
J. Uhm	Potomac Res. Inc. at NRL	8/11/88	oral
S. Lawrence	Naval Research Laboratory	8/6/88	oral
R. Jeffries	GEO-CENTERS, INC.	8/18/88	oral & this document

NAVONR 5870/35 (Rev 5-83)

6 DATE AND PLACE OF OTHER TESTS OR OPERATIONS NAD THE RESULTS (List name and address of witnesses and identify present location of records)

8/15/88 - NRL diffraction x-ray analysis indicsted mixed phase BYC was produced when air calcining alone was used.

WITNESS: J.S. Uhm
13631 S.E. 235th St.
Kent, WA 98042

RECORDS: NRL
Washington, D.C. 20375-5000

7 IDENTIFY ANY PAST, PRESENT OR CONTEMPLATED USE, SALE, OR PUBLICATION OF THE INVENTION

This information was included in a written report to Dr. M. Kahn, Code 6373. It is to be used for publication forthwith.

8. CLOSELY RELATED PATENTS, PATENT APPLICATIONS AND PUBLICATIONS

PATENT OR APPLICATION NO. AND DATE	TITLE OF PUBLISHED ARTICLE	PUBLICATION NAME AND DATE
	Processing & Properties of	Adv. Ceram. Mat. 2,(3B) 1987
	High Tc Superconducting Oxide	
	Ceramics. $YBa_2CO_3O_7$.	
	Processing High Temperature	ACS Symposium Series 351
	Ceramic Superconductors:	AM Chem. Soc. 1987
	Structure & Properties	

PART II. DISCLOSURE OF INVENTION

Describe the invention fully and completely, using the outline given below. Sketches, prints, photos and other illustrations should be attached to this disclosure. Use additional plain pages as needed to complete the disclosure.

1. GENERAL PURPOSE. State in general terms the purpose and objects of the invention.

2. BACKGROUND. Describe the old methods, materiasl or apparatus used to perform the objects of the invention and give their limitations and disadvantages.

3. DESCRIPTION AND OPERATION. Describe clearly and completely the construction of the invention and give a detailed description of its operation and use. In the description, use reference characters to refer to components in attached illustrations.

4. ADVANTAGES AND NEW FEATURES. State the advantages of the invention over the old methods described in paragraph #2 above, and the features believed to be new.

5. ALTERNATIVES. Indicate any alternative methods, materials or constructions of the invention.

6. CONTRIBUTIONS BY INVENTORS. If this is a joint invention, indicate what contribution was made by each inventor.

7. EXECUTION OF DISCLOSURE. The end of the disclosure should be signed and dated by the inventor(s). The disclosure should then be read and understood by two technically qualified witnesses. Under inventor(s) signatures, enter the statement: "Disclosed to and understood by me on (date." The two witnesses should sign under this statement.

See attached

1. General Purpose

This procedure was devised a a method of producing a phase pure superconducting orthorhombic barium yttrium cuprate powder for use in the preparation of thick film coatings on ceramic substrates.

2. Background

Previous experiments with $Ba_2YCuO_{(7-x)}$ (BYC) using the typical air calcining processes produce powders that contain a mixture of orthorhombic and tetragonal phases. Similarly, coating experiments using these powders resulted in thick films that contained a mixture of these two phases. Therefore, experiments were begun to develop a technique for producing single phase orthorhombic BYC powder for use in thick film coatings. Initial experiments indicated that the use of oxygen during calcining inhibited the reaction between $BaCO_3$, Y_2O_3 & CuO by supressing the decomposition of $BaCO_3$ rather than forming BYC.

3. Description and Operation

In this procedure one calcines a stoichiometric mixture of $BaCO_3$, Y_2O_3 and CaO after milling these powders in acetone in an Al_2O_3 ball mill with Al_2O_3 balls. The mixture is dried to 125 °C and subsequently calcined in platinum dishes at 950° C in oxygen. After holding for 1 1/2 hours at 950 °C the powder is cooled slowly (~16 hrs) in flowing O_2 with an intermediate stop at 700 °C. After each cycle the powder is crushed and ground with a mortar and pestle to 45 μm grain size. It is then heated rapidly (~3 hours) to 950 °C, held for 1/2 hr, then oxygen is introduced. The temperature is held at 950 °C for 1 hr and the cooling cycle in oxygen is repeated to obtain the pure phase. Diffraction analysis indicates that an orthorhombic powder is formed.

4. Advantages and New Features

The advantage of this method is that it produces an orthorhombic powder which in turn results in a better orthorhombic superconducting thick film than that obtained from mixed phase powders. The vacuum also aids in removal of CO_2 from the $BaCO_3$, thus enhancing the formation of BYC from the precursor powders.

5. Alternatives

(a) Dry mix the powder with a spex mixer before cycling it through the vacuum-oxygen calcine treatment.
(b) After roller milling in acetone or dry mixing in a spex mixer calcine the powder in air before the vacuum-oxygen calcine cycle.
(c) Substitute an inert gas or air calcine for the vacuum stage of the calcining cycle.
(d) Substitute BaOH for $BaCO_3$.
(e) Use an excess of 0.001 - 0.005 moles of Y_2O_3 to enhance formation of the orthorhombic phase.
(f) Use two vacuum-oxygen cycles without prior treatment.

6. Contribution by Inventors - Single inventor

7. Execution of Disclosure - J.R. Spann 8/26/88
J.R. Spann Date

Disclosed to and understood by me on [illegible]

PAPER NUMBER

TIME

2:20 - 2:40

DATE

April 26, 1989

PAPER TITLE

PREPARATION AND CHARACTERIZATION OF $Bi_4Sr_3Ca_3Cu_4O_{(14-x)}$ and $Bi_4Sr_3Ca_3Cu_5O_{(14-x)}$ FILMS ON CERAMIC SUBSTRATES

AUTHOR(S)

J. R. Spann*, L. Toth, I. K. Lloyd, M. Kahn, M. Chase#, B. Das
Naval Research Lab, Washington D. C. 20375;*GEO-Centers, Ft. Washington, MD;#Potomic Research, Inc., Alexandria, VA

ABSTRACT

A method for producing highly oriented superconducting $Bi_4Sr_3Ca_3Cu_4O_{(14-x)}$ (BSCCO) thick films on polycrystalline and single crystal MgO substrates is described. Highly oriented films are desirable since critical currents at 77K differ by a factor of 1000 between oriented and unoriented films. In the present study a technique similar to that of Akametsu et al [1] was examined in detail and extended to include polycrystalline MgO and Al_2O_3 substrates as well as single crystal substrates.

Thick films (~150 μm) were prepared by briefly melting prereacted, calcined BSCCO powders on the MgO and Al_2O_3 substrates at 1000° C. The powders were prepared in both 4334 and 4336 stoichiometries. After melting, most films were quenched in air and then annealed in air or oxygen for 15 hours from 800-850°C. A few samples were slow cooled in the furnace to the annealing temperature before annealing.

The quenching/annealing procedure produced macroscopically uniform, dense films on the MgO substrates. The BSCCO wets the MgO as evidenced by a partial coating of BSCCO on the back of the substrates. The Al_2O_3 substrates were not totally wetted by the BSCCO and the films on the Al_2O_3 were not as uniform as those on the MgO. X-ray diffraction analysis of the thick films showed that for both the 4334 and 4336 compositions the dominant phase was Bi2Sr2CaCu2Ox (2212) with a~3.82 and c~30.5A (tetragonal pseudocell). This phase was highly oriented with the (001) lines dominating (see figure1). Ca_2CuO_3 was sometimes present, more so in the 4336 compositions than in the 4334 compositions. SEM and Optical Microscopy revealed BSCCO plates with Ca_2CuO_3 needles on the surface. The slow cool/ annealing procedure produced very little 2212 BSCCO. The dominant phases in the slow cooled materials were the Ca-free (2201) BSCCO and Ca(Sr)-Cu-O. Lead BSCCO films are also being examined.

1. Y.Akamatsu, M.Tatsumisago, N. Tohge, S. Tsuboi and T. Minami, Jpn J. Appl. Letters, 27, L1696, 1988.

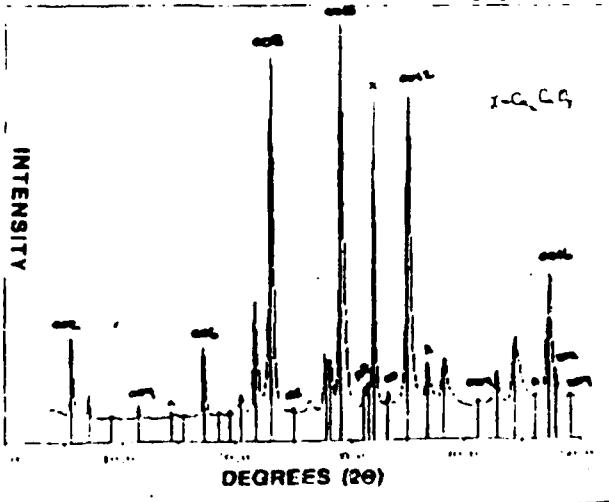


Figure 1: Powder X-ray Diffraction Pattern of a BSCCO Film on Polycrystalline MgO(Initial composition 4336).

PAPER NUMBER

TIME

2:40 - 3:00

DATE

April 26, 1989

PAPER TITLE

PREPARATION AND CHARACTERIZATON OF ORTHORHOMBIC $Ba_2YCu_3O_7$ POWDER FOR THICK FILM COATINGS

AUTHOR(S)

J. R. Spann*, I. K. Lloyd, M. Kahn and M. Chase#
Naval Research Lab, Washington D. C. 20375;*GEO-Centers, Ft. Washington, MD;#Potomac Research, Inc., Alexandria, VA

ABSTRACT

A single calcination step, solid state process to produce single phase orthorhombic (by XRD) $Ba_2YCu_3O_7$ is described. $BaCO_3$,Y_2O_3 and CuO are used as precursor materials, but no residual carbonate is observed after calcination. The use of a vacuum during the initial stages of the calcining process promotes complete decomposition of the carbonate. An oxygen atmosphere during the later stages of calcining ensures proper oxidation to $Ba_2YCu_3O_7$. This single phase powder produces better thick films than multiphase powders. The use of a similar combination vacuum-oxygen calcining schedule should be beneficial in the preparation of chemically derived powders.

$BaCO_3$,Y_2O_3 and fine CuO were mixed and wet milled simultaneously. Calcining for 0.5 hour in a vacuum of 500 mtorr at 950°C, followed by two hours in flowing oxygen at 950°C and a slow cool, including two hours at 700°C in flowing oxygen, produced the best results. Powders calcined under vacuum then oxygen with a two hour hold at 950°C contained fully orthorhombic BYC. Powders which were only held one hour contained tetragonal BYC as well as orthorhombic BYC and small amounts of minor phases. Powders calcined in air or oxygen were multiphase after the initial calcining. They tended to contain $BaCO_3$, $BaCuO_2$ and/or BaY_2CuO_5. The longer hold appeared to serve two functions. First it allowed complete reaction. Second it allowed complete oxidation of the tetragonal BYC formed under vacuum to the orthorhombic phase. While the O=7 stoichiometry can not be formed at such high temperatures, we believe that the longer 950°/c oxidation hold helps to incorporate oxygen into the 0=6 BYC formed under the vacuum. The powders formed by this technique had the blocky morphology typical of solid state powders. After ball milling in acetone they had a typical particle size of about 2-3 μm. The crystallite size was about 0.3 μm.

Thick films were made by painting BYC acetone slurries on polycrystalline MgO, Al_2O_3, Al_3N_4 and $SrTiO_3$ substrates. The films reacted with the Al_3N_4 and $SrTiO_3$ substrates yielding second phases including BaY_2CuO_5. The films on the MgO subtrates were the most adherent and tended to have narrower transitions to zero resistivity than the films on Al_2O_3 substrates.

PREPARATION AND CHARACTERIZATION OF $Bi_4Sr_3Ca_3Cu_4O_{(14-x)}$ and $Bi_4Sr_3Ca_3Cu_6O_{(14-x)}$ FILMS ON CERAMIC SUBSTRATES

J.R. Spann*, L. Toth, I.K. Lloyd, M. Kahn,

M. Chase#, B. Das; Naval Research Laboratory,

*GEO-Centers, #Potomac Research, Inc.

Supported by ONR and DARPA

Acknowledgements to:

- M. Osofsky for R vs T measurements
- T. Francavilla for critical current measurements and
- J. Sponn for assistance in preparation

INTRODUCTION

- Thick, oriented BSCCO films have been produced previously on single crystal MgO.
- Superconducting transport in BSCCO is anisotropic and critical currents are much higher in oriented films.
- Can BSCCO films be aligned on Polycrystalline MgO and Al_2O_3 substrates
- Can the melt/crystallization technique of Akametsu and coworkers be modified and extended to make aligned coatings on polycrystalline substrates?
- Can such coatings be used to prepare devices including devices with complex shapes?

APPLICATIONS:

- magnetic shielding
- thick film devices
  (squids, microstrip transmission lines, etc.)

BSCCO SAMPLE PREPARATION

Raw Materials: Bi_2O_3, $SrCO_3$, $CaCO_3$, CuO

Stoichiometry: 4334, 4336, 2223, and 2234

Substrates: Polycrystalline MgO, polycrystalline Al_2O_3, single crystal MgO

Procedure:

1. Mill raw materials in acetone for 24 hours and flash dry
2. Calcine raw materials in air at ~850°C for 1-4 hours
3. Mill calcined powders and dry
4. Place milled powder as a thin layer on top of the substrate
5. Heat to ~1050°C briefly to insure melting (≤ 20 minutes)

6a. Quench in air to room temperature (≤ 10 minutes)

6b. (Cool slowly in 0_2 to annealing temperature)

7. Anneal in O_2 at 860°C for >15 hours
8. Cool slowly to room temperature in flowing O_2

CHARACTERIZATION

Visual

X-ray diffraction

Optical microscopy

SEM with EDAX

Resistance versus temperature

Critical current

RESULTS

Visual Observations:

On Polycrystalline Al_2O_3:

- substrate not evenly wet by coating
- coating thickness highly nonuniform

On Single crystal or polycrystalline MgO:

- substrate is wet by coating
- uniform dense coating
- film has reflective surface

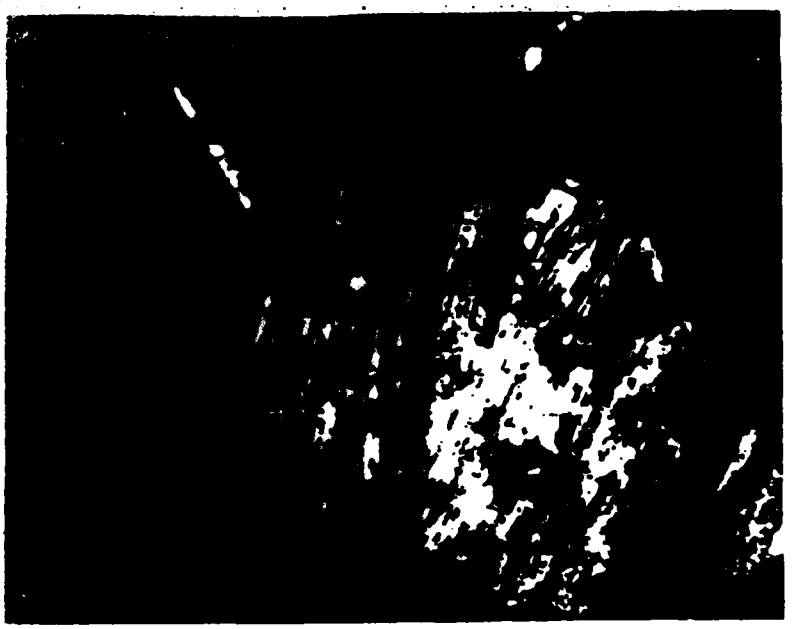
Microscopy (Optical and SEM):

On MgO substrates (with quenched BSCCO coating)

- large flat platelets parallel to the substrate
- needles and fan shaped clusters of needles overlay the platelets
- the needles were richer in Ca than the platelets
- the needles appeared to be oriented with respect to the substrate

1. a. Optical micrograph of 4336 on polycrystalline MgO after initially annealed, showing oriented BSCCO platelets

   b. Ca_2CuO_3 needles as found in certain regions on top of BSCCO film.



(a)



(b)

2. Typical area of well aligned film after mechanical removal of Ca_2CuO_3 and reannealing



XRD RESULTS

- $Bi_2Sr_2CaCu_2O_x$ (2212) was predominant phase for both the 4334 and 4336 powders

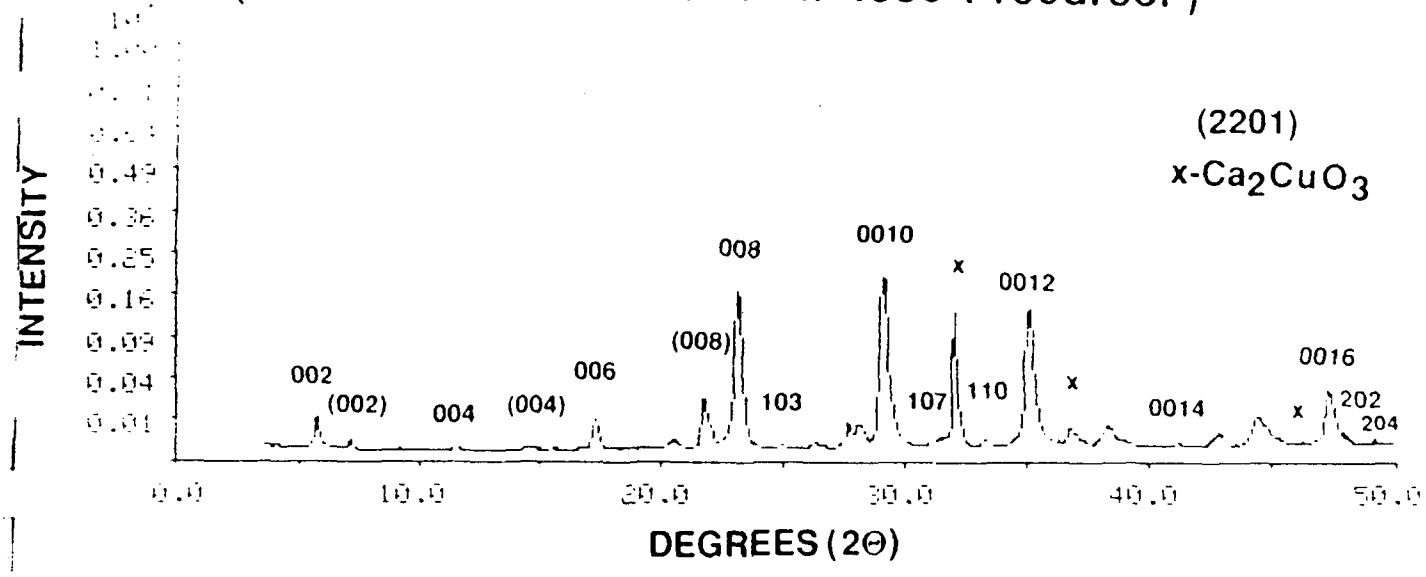
- The 2212 was strongly oriented with (0 0 l) lines having the highest intensities

- The 2212 was analyzed as pseudotetragonal with a=0.382 nm and c=3.05 nm or an othorhombic body

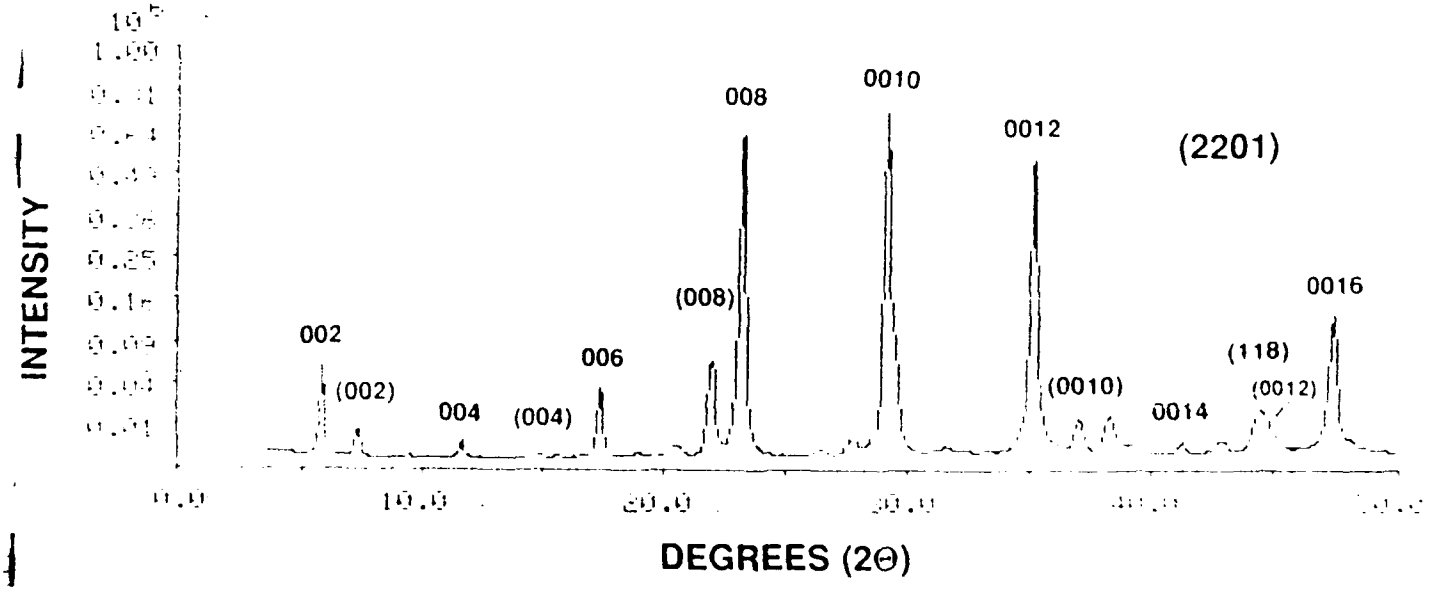
- The needles were Ca_2CuO_3

- Oriented $Bi_2Sr_2CuO_x$ (2201) was generally present as a minor phase (2Θ =7.5 and 21.9°) in some samples

Figure 3
X-ray Diffraction Patterns of a Thick Film on a Polycrystalline MgO Substrate (2212 BSCCO derived from 4336 Precursor)



(a) Film after one anneal, Ca_2CuO_3 peaks present



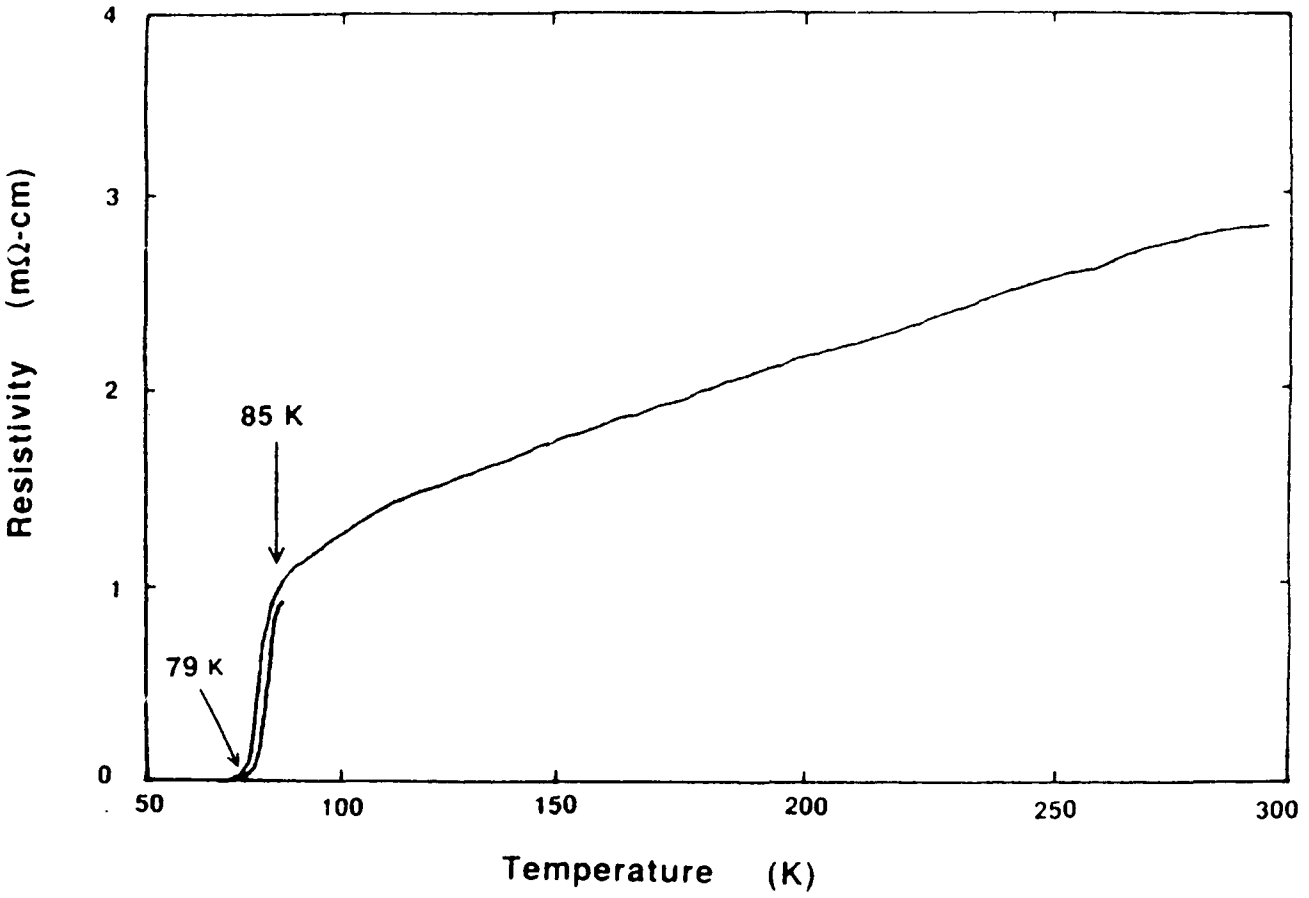
(b) Same Film after surface was mechanically removed then reannealed

Superconducting Behavior:

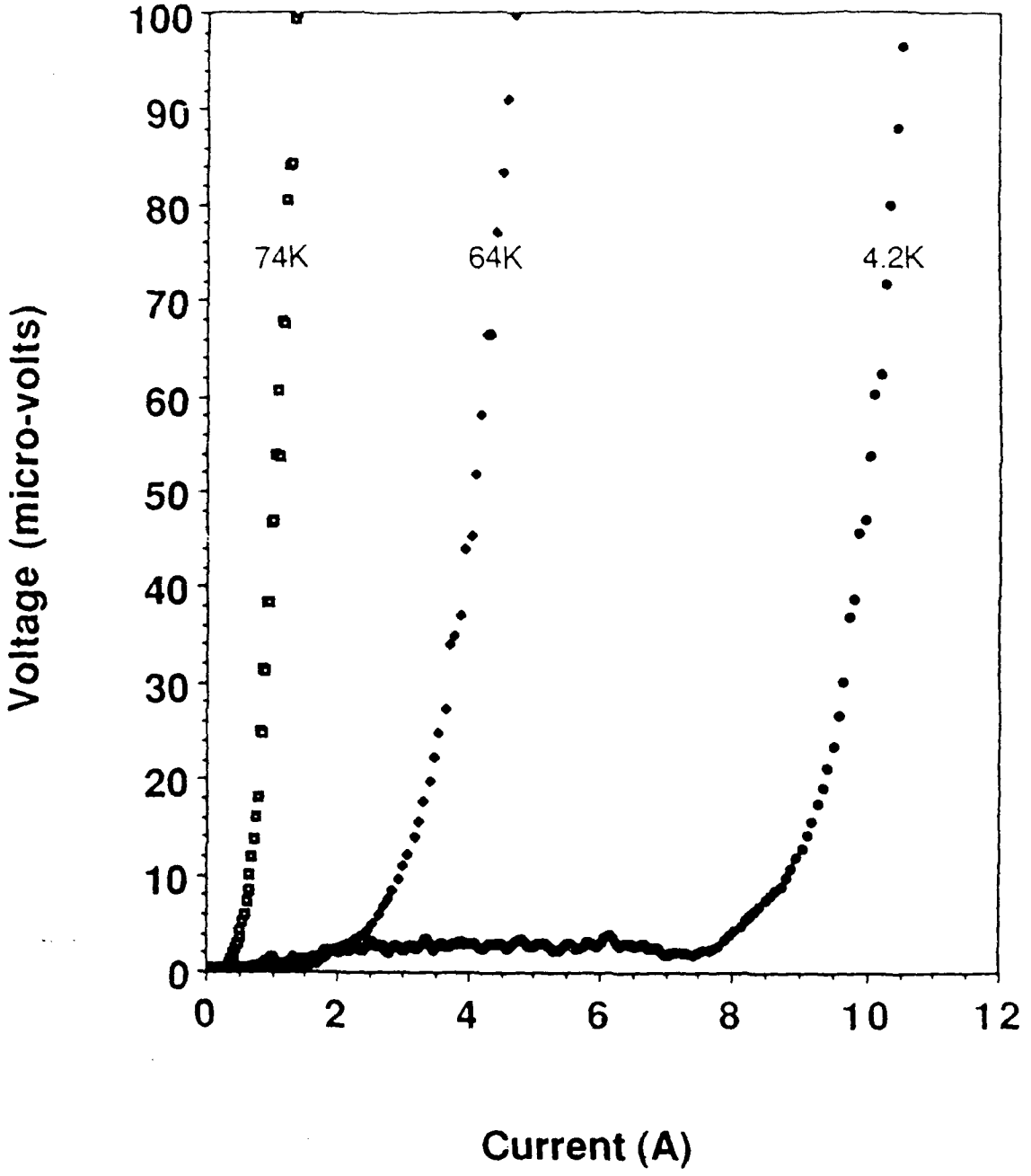
- The samples were superconducting with a T_c between 79K and 85K

- Critical current was a function of microstructure; samples annealed without removal of the overlaying Ca_2CuO_3 needles, showed a relatively low J_c ($\approx$ 100 A/cm^2) at 68K

- After the Ca_2CuO_3 needles were ground off and the sample was reannealed in O_2 a J_c of $\geq$ 2000 A/cm^2 was observed at 68 K and a $J_c \approx$ 7000 A/cm^2 was observed at 4K.



4. Resistivity of a well aligned BSCCO film.
Note that the resistivity values are relatively low,
as compared to those of unoriented films



5. Typical data collected for J_c measurement. The values reported are typically calculated data at 1 microvolt. Sample dimensions are t= 0.1mm, w= 1.3mm, l= 3.4mm

RESULTS (cont)

Melted and Slow Cooled 4336 Not Quenched BSCCO:

- 2201 was the predominant phase
- very little 2212 BSCCO was formed
- Ca(Sr)- Cu-O oxides were also formed
- reannealing did not change the ratio between the amount of 2212 phase and that of the 2201 phase
- phase separation in the melt occurred during the slow cool, yielding Ca-rich and Ca-poor phases
- remelting followed by a quench increased the amount of 2212 phase appreciably

SUMMARY

- Superconducting thick films were prepared that consisted of highly oriented 2212 BSCCO
- Best results were obtained by quenching after melting and annealing the thick film
  - * Tc = 79-85K
  - * Jc = 2000 A/cm^2 at 68 K and 7000 A/cm^2 at 4 K

PREPARATION AND CHARACTERIZATION OF ORTHORHOMBIC $Ba_2YCu_3O_7$ POWDER FOR THICK FILM COATINGS

J.R. Spann*, I.K. Lloyd, M. Kahn, M. Chase#, Naval Research Laboratory, Washington, DC 20375; *GEO-Centers, Ft. Washington, MD; #Potomac Research, Inc., Alexandria, VA

Supported by the Office of Naval Research

Acknowledgements to:

- J. Uhm
- S. Lawrence
- B. Bender
- L. Toth

INTRODUCTION

PHASE PURITY HAS BEEN HARD TO ARCHIEVE IN SOLID STATE REACTED POWDERS

PHASE PURE POWDERS RESULT IN IMPROVED SUPERCONDUCTING THICK FILMS

$BaCO_3$ IS A PROBLEM:

- DIFFICULT DECOMPOSITION
- EASILY FORMS IN THE PRESENCE OF CO_2 OR OF ORGANICS

TETRAGONAL BYC IS NOT SUPERCONDUCTING
AND OFTEN ACCOMPANIES ORTHORHOMBIC BYC

MATERIAL PREPARATION PROCEDURE

MIXING

REAGENT GRADE PRECURSORS:
BARIUM CARBONATE, YTTRIUM OXIDE,
PREGROUND CUPRIC OXIDE

MIXED AND GROUND IN 50g BATCHES:

- MORTAR AND PESTLE
- DRY MILLING
- WET BALL MILLING
  37% ZrO_2 BALLS,
  25% ACETONE AND 37% POWDER,
  FLASH DRIED AT 120°C

CALCINING

TEMPERATURE: 950°C

ATMOSPHERE:
- FLOWING AIR OR OXYGEN
- VACUUM FOLLOWED BY FLOWING OXYGEN

TIME AT PEAK:
1 OR 2 HOURS FOLLOWED BY SLOW COOLING

1 to 3 CYCLES

FINAL SIZING OF POWDERS

BALL MILLING OR ATTRITION MILLING
WITH ZrO_2 BALLS IN ACETONE

CHARACTERIZATION

XRD

PHASE PURITY

RATIO OF ORTHORHOMBIC TO TETRAGONAL PHASE
FROM SPLITTING OF
020-200 (46.7° AND 47.6°)
AND OF 123-213 (58.2° AND 58.8°) DIFFRACTION LINES

SEM

POWDER MORPHOLOGY, CRYSTALLITE SIZE, STATE OF AGGLOMERATION

CENTRIFUGAL SEDIMENTATION

PARTICLE SIZE

MEISSNER LEVITATION

RESULTS AND DISCUSSION

•IMPROVED MIXING

RAISED THE PHASE PURITY OF THE POWDERS

• HAND MIXED AND DRY MILLED POWDERS

TENDED TO CONTAIN GREEN PHASE (BaY_2CaO_5) OR $BaCO_3$

• WET MILLED POWDERS

CONTAINED AT LEAST SOME ORTHORHOMBIC BYC

• IMPROVED MIXING ALONE

COULD NOT PRODUCE SINGLE PHASE POWDERS

IN A SINGLE CALCINING STEP

CALCINING ATMOSPHERE

• AIR OR OXYGEN ALONE
YIELDED POORLY REACTED, MULTIPHASE POWDERS
AFTER A SINGLE CALCINATION STEP

• BOTTLED OXYGEN (<5PPM CO_2/CO)
DID NOT ENHANCE CO_2 DECOMPOSITION:
• $BaCO_3$ WAS PRESENT IN ALL POWDERS CALCINED ONLY IN OXYGEN

• VACUUM DURING INITIAL CALCINING
ENHANCED $BaCO_3$ DECOMPOSITION AND CALCINING REACTION

• SUBSEQUENT 950°C DWELL IN FLOWING OXYGEN
YIELDED PRIMARILY (OFTEN EXCLUSIVELY) ORTHORHOMBIC BYC

RATIONALE

• VACUUM NOT ONLY ENHANCED $BaCO_3$ DECOMPOSITION
IT ALSO ENHANCED THE REACTIVITY
OF Ba, Y, AND Cu PRECURSORS

OXIDATION

• TETRAGONAL BYC

FORMED UNDER VACUUM-TREATMENT

MUST BE ANNEALED IN OXIDIZING ATMOSPHERE

• ONE HOUR HOLD AT 950°C IN OXYGEN

POWDER NOT COMPLETELY CONVERTED

• TWO HOUR HOLD AT 950°C IN OXYGEN

POWDER IS FULLY OXIDIZED, EXCLUSIVELY ORTHORHOMBIC BYC

• BENEFITS OF COMBINING VACUUM AND FLOWING OXYGEN

ARE NOT LIMITED TO SOLID STATE REACTED POWDERS

NOR TO THE BYC COMPOSITION

TABLE I: MIXING TECHNIQUES AND PHASES PRESENT AFTER CALCINING

MIXING TECHNIQUE	CALCINING ATMOSPHERE	RESULTANT POWDER PHASES
hand	air	green phase (BaY_2CuO_5)
dry	air	$BaCuO_2$ and green phase
dry	oxygen	$BaCO_3$, green phase and "other" phases
dry	vacuum then oxygen	orthorhombic and "other" phases
wet	air	$BaCuO_2$, green phase and some orthorhombic
wet	vacuum then oxygen	othorhombic

TABLE II: XRD PEAK SPLITTING AND % ORTHORHOMBIC BYC PHASE IN BYC POWDER

SAMPLE		CALCINING	Δ(200)*	Δ(123)**	%OTHO.***
$Ba_2YCu_3O_7$ (ref. 7)		calcined three times then annealed in O_2 for 27 hrs at 780°C 0.5 hr vacuum then 1 hr in oxygen(1)	0.855°	0.617°	100% (assumed)
NRL	1	1 cycle	0.58°-0.85°	0.4°-0.44°	65-85%
NRL	2	2 cycles 0.5 hr vacuum then 2 hr in oxygen (1)	0.74°	0.42°	75%
NRL	3	1 cycle	0.82°-0.84°	0.59°-0.6°	>95%

* Angular separation between the (002) and (200) reflections
** Angular separation between the (123) and (213) reflections
***% orthorhombic = {[sample Δ(200)/ref Δ(200)] + [sample Δ(123)/ref Δ(123)]} X 100/2

1) heat treatments shown were at 950°C; they were followed by slow cooling in O_2

- VACUUM CALCINED POWDERS CONTAINING ORTHORHOMBIC BYC LEVITATED SMALL MAGNETS AT 77 K

- CALCINED POWDERS HAD BLOCKY MORPHOLOGY TYPICAL OF SOLID STATE REACTED POWDERS

- MILLING BROKE UP AGGLOMERATES AND FRACTURED MANY CRYSTALLITES

ULTIMATE CRYSTALLITE SIZE AFTER 4 HOURS ATTRITION MILLING

~0.3 μm

STOICHIOMETRY EFFECTS IN O_2 ATMOSPHERE CALCINED POWDER

- EXCESS BaO (0.1 MOLE%) INHIBITED FORMATION OF BYC

- EXCESS CuO (0.1 MOLE%) YIELDED TETRAGONAL BYC PLUS SECOND PHASES

- A SMALL EXCESS OF Y_2O_3 (0.1 MOLE%) GAVE PHASE STRUCTURES SIMILAR TO THOSE OF STOICHIOMETRIC POWDERS BUT WITH MUCH MORE REACTIVITY

* 0.1 MOLE% EXCESS Y_2O_3 POWDERS YIELDED ORTHORHOMBIC DISCS AND THICK FILMS WITH NARROW SUPERCONDUCTING TRANSITION

* LARGER ADDITIONS OF Y_2O_3 (0.5 MOLE%) IMPEDED THE FORMATION OF ORTHORHOMBIC BYC

CONCLUSIONS

1. SINGLE PHASE ORTHORHOMBIC BYC CAN BE PREPARED FROM SOLID STATE REACTED POWDERS IN A SINGLE PROCESS, PROVIDED:

- A VACUUM IS USED DURING THE RAMP UP TO CALCINING TEMPERATURE AND DURING THE INITIAL HOLD
- AN OXIDIZING HOLD AND COOL DOWN FOLLOW THE VACUUM TREATMENT

2. SIMILAR CALCINING CONDITIONS WILL BE BENEFICIAL FOR CHEMICALLY DERIVED POWDERS SINCE MANY BARIUM PRECURSORS FORM $BaCO_3$ UPON DECOMPOSITION

3. EXCESS YTTRIA APPEARS BENEFICIAL IN PROMOTING ORTHORHOMBIC BYC FORMATION

APPENDIX XI

MTL TR 89-9

AD

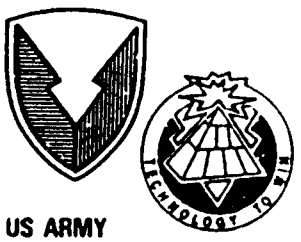
ASSESSMENT OF SOME CORROSION PROTECTION SCHEMES FOR MAGNESIUM ALLOY ZE41A-T5

MILTON LEVY, ROBERT T. BOMBARD, and ROBERT M. HUIE
U.S. ARMY MATERIALS TECHNOLOGY LABORATORY
METALS RESEARCH BRANCH

KUAN LEI
GEO-CENTERS, INC.

February 1989

Approved for public release; distribution unlimited.



US ARMY
LABORATORY COMMAND
MATERIALS TECHNOLOGY LABORATORY

U.S. ARMY MATERIALS TECHNOLOGY LABORATORY
Watertown, Massachusetts 02172-0001

The findings in this report are not to be construed as an official Department of the Army position, unless so designated by other authorized documents.

Mention of any trade names or manufacturers in this report shall not be construed as advertising nor as an official indorsement or approval of such products or companies by the United States Government.

DISPOSITION INSTRUCTIONS

Destroy this report when it is no longer needed.
Do not return it to the originator.

UNCLASSIFIED

SECURITY CLASSIFICATION OF THIS PAGE (When Data Entered)

REPORT DOCUMENTATION PAGE		READ INSTRUCTIONS BEFORE COMPLETING FORM
1. REPORT NUMBER MTL TR 89-9	2. GOVT ACCESSION NO.	3. RECIPIENT'S CATALOG NUMBER
4. TITLE (and Subtitle) ASSESSMENT OF SOME CORROSION PROTECTION SCHEMES FOR MACNESIUM ALLOY ZE41A-T5		5. TYPE OF REPORT & PERIOD COVERED 6. PERFORMING ORG. REPORT NUMBER
7. AUTHOR(s) Milton Levy, Robert T. Bombard, Robert M. Huie, and Kuan Lei*		8. CONTRACT OR GRANT NUMBER(s)
9. PERFORMING ORGANIZATION NAME AND ADDRESS U.S. Army Materials Technology Laboratory Watertown, Massachusetts 02172-0001 ATTN: SLCMT-EMM		10. PROGRAM ELEMENT, PROJECT, TASK AREA & WORK UNIT NUMBERS D/A Project: 1L162105AH84
11. CONTROLLING OFFICE NAME AND ADDRESS U.S. Army Laboratory Command 2800 Powder Mill Road Adelphi, Maryland 20783-1145		12. REPORT DATE February 1989 13. NUMBER OF PAGES 10
14. MONITORING AGENCY NAME & ADDRESS(if different from Controlling Office)		15. SECURITY CLASS. (of this report) Unclassified 15a. DECLASSIFICATION/DOWNGRADING SCHEDULE

16. DISTRIBUTION STATEMENT (of this Report)

Approved for public release; distribution unlimited.

17. DISTRIBUTION STATEMENT (of the abstract entered in Block 20, if different from Report)

18. SUPPLEMENTARY NOTES

*Geo-Centers, Inc., Newton Upper Falls, MA 02164.
Published in Proceedings of Session "Magnesium Developments," World Materials Congress, Chicago, Illinois, September 26, 1988, p. 17-24.

19. KEY WORDS (Continue on reverse side if necessary and identify by block number)

Corrosion inhibition
Corrosion-resistant alloys
Magnesium alloys
Corrosion-resistant coatings

20. ABSTRACT (Continue on reverse side if necessary and identify by block number)

(SEE REVERSE SIDE)

DD FORM 1 JAN 73 1473 EDITION OF 1 NOV 65 IS OBSOLETE

UNCLASSIFIED

SECURITY CLASSIFICATION OF THIS PAGE (When Data Entered)

Block No. 20

ABSTRACT

The U.S. Army has experienced a continuing corrosion problem with magnesium components of aircraft requiring increased maintenance and impacting both cost and readiness. A recent modernization program has replaced a number of magnesium parts with aluminum to reduce the corrosion problem but with a concomitant weight penalty. In order to fully utilize the advantages of magnesium, more corrosion-resistant alloys with improved protective schemes are needed. This paper assesses the corrosion resistance of several protective schemes for magnesium alloy ZE41A incorporating a conversion coating or HAE anodize, with or without a sealer, several primers, and a polyurethane topcoat. The tests employed include 5% salt spray, 100% RH at 100°F followed by tape adhesion, and AC impedance to develop Nyquist and Bode plots. It was concluded that the application of the sealer significantly improved the corrosion resistance of the paint scheme. Best results were obtained when the HAE anodize was used as the initial treatment.

ASSESSMENT OF SOME CORROSION PROTECTION SCHEMES FOR MAGNESIUM ALLOY ZE41A-T5

Milton Levy*, Robert Bombard*, Robert Huie*, and Kuan Lei**

*U.S. Army Materials Technology Laboratory, Watertown, MA 02172-0001

**Geo-Centers, Inc., Newton Upper Falls, MA 02164

Introduction

U.S. Army experience with magnesium alloys as components in aircraft has shown a significant corrosion problem requiring increased maintenance and impacting both cost and readiness. During the Vietnam era there was widespread use of magnesium in Army aircraft to reduce weight and increase performance. But in a recent modernization program, a number of magnesium parts have been replaced with aluminum to reduce the corrosion problem. It is clear that more corrosion resistant magnesium alloys with improved protective schemes are needed before their advantages can be fully utilized.

The best current practice for protecting magnesium in Army aircraft employs an anodize or chromate conversion treatment, an epoxy primer and a polyurethane top coat. This paper assesses a protective scheme for MG alloy ZE41A which has been modified by the British approach of interposing a baked epoxy resin (sealer) between the conversion coating and primer application. For comparison, the current practice described above is also assessed.

Materials

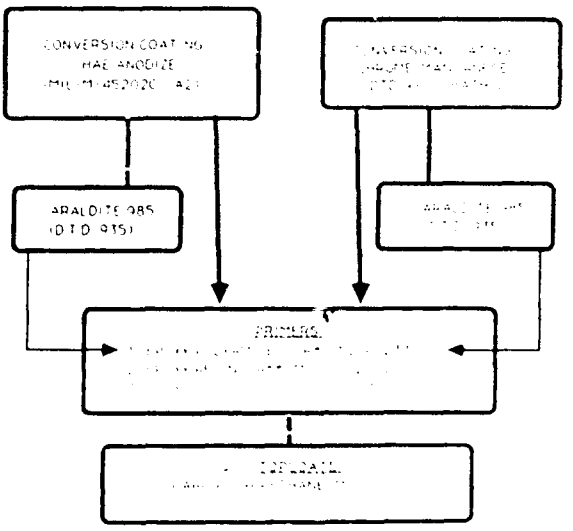
Magnesium alloy ZE41A-T5 was selected because it is presently being used in our newest aircraft. Table 1 contains the nominal composition of this alloy, the heat treatment, and mechanical properties. The corrosion resistance in mpy obtained by both immersion in 3% NaCl solution and electrochemical polarization in both 100 ppm Cl and 3.5% NaCl solutions is also included. Note that the immersion and polarization data in 3.5% NaCl solution are in good agreement, 120 and 115 mpy, respectively.

The protective schemes evaluated are described schematically in Figure 1. The variables include the initial conversion coating, the presence of the sealer, and the primers. The chemical agent resistant polyurethane topcoat was standard for all systems evaluated. The thickness of each coating layer is shown schematically in Figure 2. The procedure for applying the sealer is contained in Table 2. The application of the conversion coatings, the primers and topcoat was carried out in accordance with the specifications and standards shown in Figure 1.

TABLE 1

Mg ZE41A-T5 PROPERTIES

NOMINAL COMPOSITION	Zinc	3.5-5.0 %
	Rare Earths (Ce)	1.2 %
	Zirconium	0.4-1.0 %
	Magnesium	balance
HEAT TREATMENT	525°F (2 hrs.), AIR COOL	
	340°F (10-16 hrs.), AIR COOL	
MECHANICAL PROPERTIES	TENSILE STRENGTH	28.0 ksi
	YS (0.2% offset)	19.5 ksi
	ELONGATION	2.5%
CORROSION RESISTANCE	IMMERSION for 28 days in 3% NaCl	120 mpy
	SALT SPRAY	600 mpy
	POLARIZATION	
	100 ppm Cl NaCl	2 mpy
	3.5% NaCl	115 mpy



* CHEMICAL AND SOLVENT RESISTANT
** CHEMICAL RESISTANT

Fig. 1. Coating Schemes for Mg Alloy ZE41A-T5

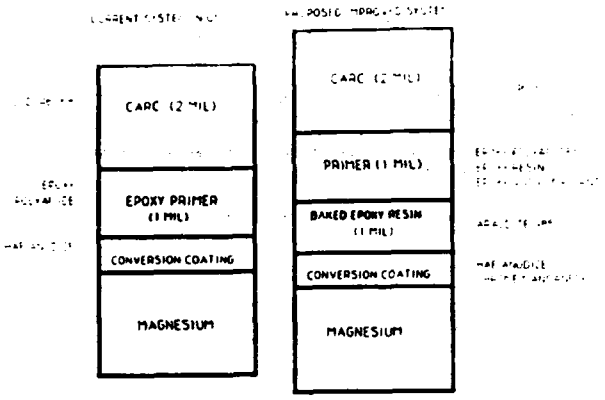


Fig. 2 Schematic Diagram of Current and Improved Coatings Systems

TABLE 2

ARALDITE 985 APPLICATION (D.T.D. 935)

- PRE-HEAT TO 180-200°C
- COOLED TO 60° C
- DIPPED IN RESIN SOLUTION
- DRAINED 15-30 MINUTES
- CURED AT 180° C FOR 15 MINUTES
- COOLED TO 60° C
- REPEAT TWICE
- FINAL CURE AT 180° C FOR 45 MINUTES

TABLE 3

TEST PANELS

- DIMENSIONS: 6"(l) X 4" (w) X 1/8" (t)
- Panels were coated on one side and remaining sides were conversion coated, masked with paraffin wax
- One-half of the panels tested were scribed with an "X"
- Tests in duplicate

TABLE 4

STANDARD TEST METHODS FOR PROCEDURES AND EVALUATION

- Salt Spray (Fog) Testing ASTM B117
  - 5% NaCl, 95° F
- Evaluation of Painted or Coated Specimens subjected to Corrosive Environments ASTM D165H
- Transparent Plastic Grids used to estimate area failed for unscribed panels
- Mean creepage from scribe for scribed panels
- Coated Metal Specimens at 100% RH, 100°F, ASTM F2247 prior to
- Measuring Adhesion By Tape Test ASTM D3359, Method 13
  - Rating on scale 0B to 5B
  - 5B best, 0B worst
  - Based on % of coated area removed from substrate

Experimental

The testing program included exposure to both salt spray (fog) and 100% humidity. Tape adhesion tests were performed after exposure to 100% humidity. The test panel dimensions and preparation are listed in Table 3. The standard test methods for procedures and evaluation are contained in Table 4. In addition to the above, electrochemical AC impedance measurements were carried out to evaluate the performance of the coating/metal systems. The test cell is shown in Figure 3. AC impedance was performed with a PARC273 potentiostat in conjunction with a PARC 5208 Lock-in Amplifier, Apple II computer, and the PARC Softcorr 368 program. Measurements were obtained at the corrosion potential over the frequency range 100K Hz - 0.01 Hz for up to 42 days in 100 ppm Cl solution. The corrosion potential was monitored before each experiment.

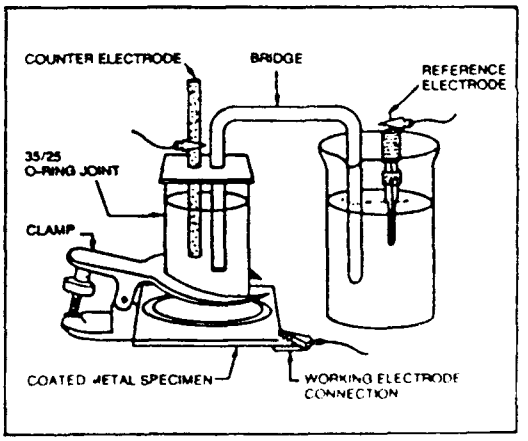


Fig. 3 Test Cell for AC Impedance Measurements

Results and Discussion

Salt Spray (Fog) Test

Conversion Coatings and Sealer and Primers

Results of salt spray testing of the three different primers in conjunction with either the HAE anodize or chrome manganese conversion coating are expressed as % area

failed as a function of exposure time in Table 5 and Figure 4. The data represent an average of two measurements on duplicate panels. It should be noted that the sealer Araldite 985 was applied to only those schemes employing the epoxy polyamide primer (MIL-P-23377). This primer is currently used in Army aircraft in conjunction with the CARC polyurethane topcoat (MIL-C-46186C). The efficacy of the primers applied over the CrMn conversion coating may be ranked in decreasing order of salt spray resistance as MIL-P-52192 > MIL-P-85582 > MIL-P-23377. The application of the sealer Araldite 985 significantly improves the performance of MIL-P-23377 to a level comparable to MIL-P-52192 as also shown in the photographs of Figure 5. Similar data for the HAE anodize as an alternate to the Cr Mn treatment shows the same ranking of primers but the magnitude of the failed area is diminshed in each case.

Conversion Coatings and Sealer and Primers and Topcoat

The salt spray performance of the protective schemes which included the polyurethane topcoat is shown in Table 6 and Figures 6-9. Again, the % area failed represents an average of measurements on duplicate panels. The variables were HAE anodize or CrMn conversion treatment and the three primers. Considering the CrMn treated systems after 42 hours of salt spray exposure, the best performance was exhibited by the scheme employing the sealer, Araldite 985, and the MIL-P-23377 primer. The marked improvement in performance achieved by interposing Araldite 985 between the conversion coating and the primer is shown in Figure 6, and the photographs of exposed scribed panels, Figure 7. Similar results were obtained with the HAE anodized panels as shown in Figures 8 and 9. But the HAE treated systems performed better than the comparably treated CrMn systems. Robinson[1] also has reported the beneficial effect of several sealers in reducing salt spray corrosion when used with chromate conversion coating, primed and finish coated.

TABLE 5

SALT SPRAY PERFORMANCE OF CONVERSION TREATED AND PRIMED PANELS

		%AREA FAILED	
PANEL ID	COAT SYSTEM	DAY 6	DAY 13
A(HAE)	23377	15.38	36.72
B(HAE)	52192	0.00	0.16
C(HAE)	85582	2.73	14.10
D(HAE)	985, 23377	0.12	0.45
M(Cr-Mn)	23377	31.37	63.03
N(Cr-Mn)	52192	0.50	1.30
O(Cr-Mn)	85582	4.05	17.48
P(Cr-Mn)	985, 23377	0.96	3.00

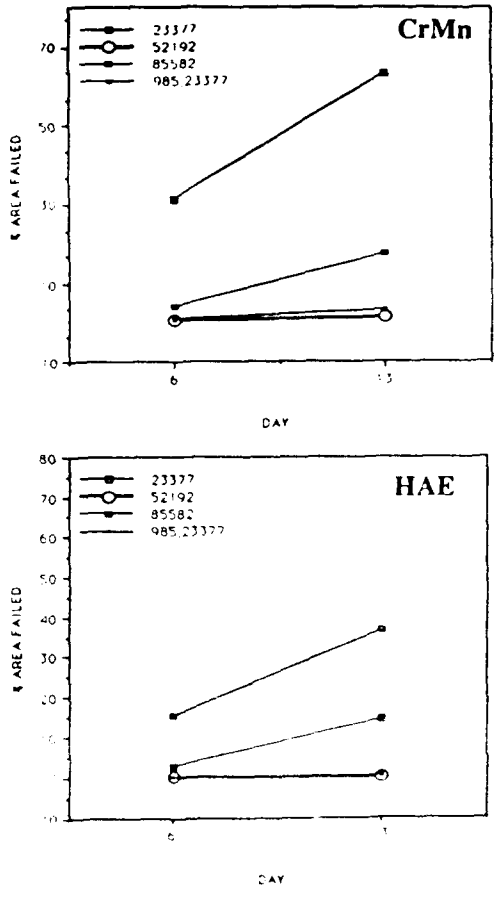


Fig. 4 Comparison of Salt Spray Resistance of Primers on CrMn Coated and HAE Anodized Mg

TABLE 6

SALT SPRAY PERFORMANCE OF CONVERSION TREATED, PRIMED, AND TOPCOATED PANELS

		% AREA FAILED					
PANEL ID	COAT SYSTEM	DAY 7	DAY 14	DAY 21	DAY 28	DAY 35	DAY 42
E(HAE)	23377,46168	0.00	0.46	0.91	5.15	10.44	15.68
F(HAE)	52192,46168	0.00	0.39	1.72	15.01	20.82	26.44
G(HAE)	85582,46168	0.30	0.39	0.42	0.51	0.68	0.89
H(HAE)	985,23377,46168	0.00	0.00	0.00	0.15	0.15	0.48
Q(Cr-Mn)	23377,46168	0.12	1.84	12.62	15.15	20.45	26.20
R(Cr-Mn)	52192,46168	0.12	0.36	0.48	0.69	0.93	5.75
S(Cr-Mn)	85582,46168	0.21	15.06	20.30	25.70	30.90	37.14
T(Cr-Mn)	985,23377,46168	0.01	0.01	0.17	0.24	2.59	3.24

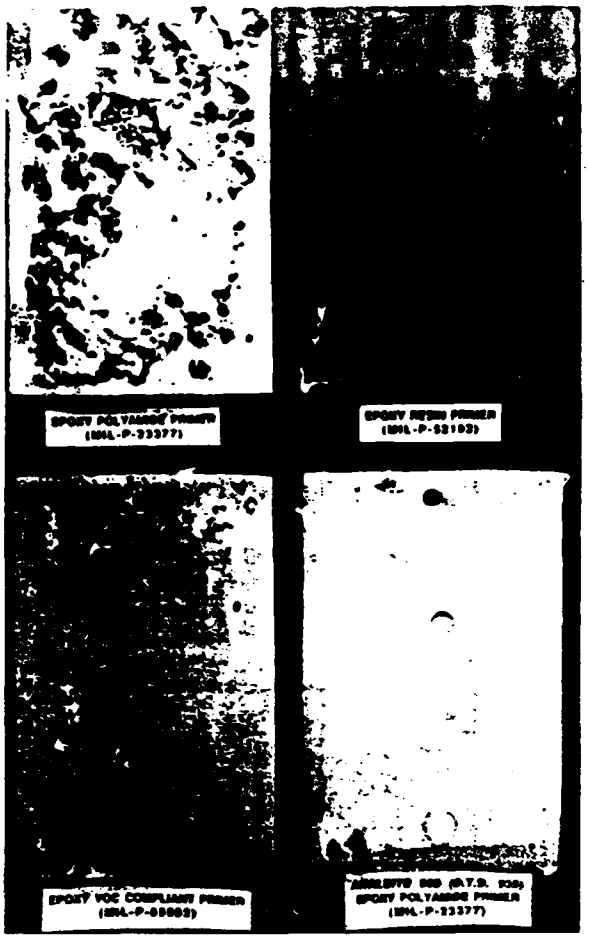


Fig. 5 Comparison of Primers with Chrome Manganese Conversion Coating Exposed to 5% Salt Spray for 14 Days
1. Epoxy Polyamide Primer (MIL-P-23377)
2. Epoxy Resin Primer (MIL-P-52192)
3. Epoxy VOC Compliant Primer (MIL-P-85582)
4. Araldite 985 (D.T.D. 935 Epoxy Polyamide Primer (MIL-P-23377)

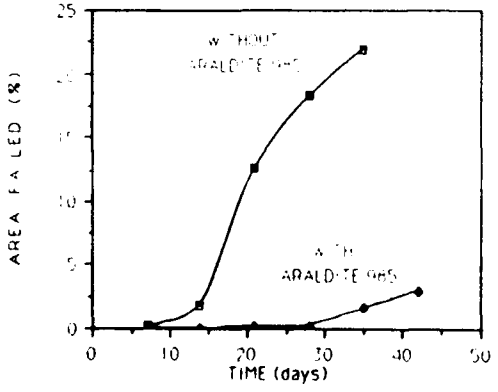


Fig. 6 Area Failed for Coating Systems with Chrome-Manganese Conversion, Epoxy Polyamide Primer and CARC in 5% Salt Spray

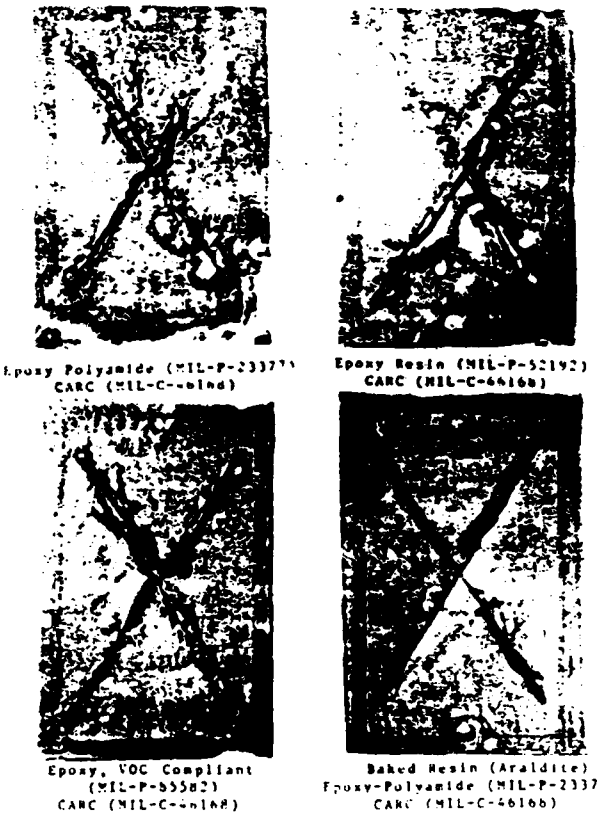


Fig. 7 Comparison of Coating Systems with Chrome-Manganese Conversion Coating Exposed to 5% Salt Fog for 14 Days
1. Epoxy Polyamide (MIL-P-23377) CARC (MIL-C-46168)
2. Epoxy Resin (MIL-P-52192) CARC (MIL-C-46168)
3. Epoxy, VOC Compliant (MIL-P-85582) CARC (MIL-C-46168)
4. Baked Resin (Araldite) Epoxy-Polyamide (MIL-P-23377) CARC (MIL-P-46168)

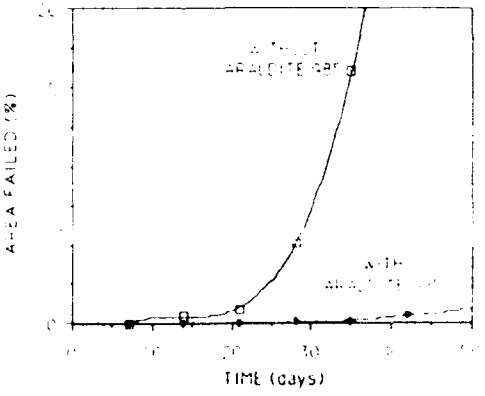


Fig. 8 Area Failed for Coating Systems with HAE Conversion, Epoxy Polyamide Primer and CARC in 5% Salt Spray

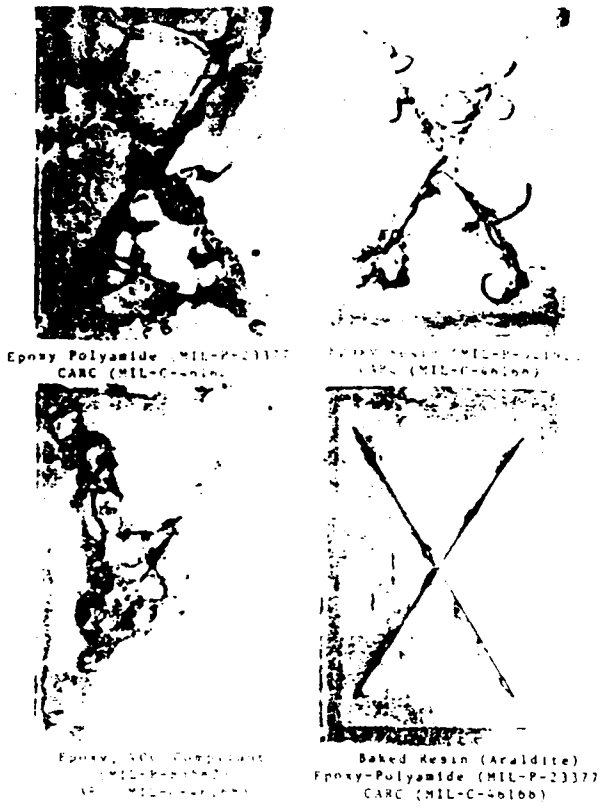


Fig. 9 Comparison of Coating Systems with HAE Conversion Coating Exposed to 5% Salt Fog for 14 Days
1. Epoxy Polyamide (MIL-P-23377) CARC (MIL-C-46168)
2. Epoxy Resin (MIL-P-52192) CARC (MIL-C-46168)
3. Epoxy, VOC Compliant (MIL-P-85582) CARC (MIL-C-46168)
4. Baked Resin (Araldite) Epoxy-Polyamide (MIL-P-23377) CARC (MIL-C-46168)

Tape Adhesion Test

Conversion Coatings and Sealer and Primers

The cross-cut tape adhesion test was performed after the coated test panels were exposed to 100% relative humidity at 100°F with condensation on the specimens at all times during the 5 week exposure. The coating adhesion of the primers that were applied to either CrMn or HAE treated panels was rated on a scale of 0B to 5B as shown in Table 7. These ratings are based on removal of coating from the substrate after application and rapid removal of the tape and inspection of the cross-cut grid area. A rating of 0B represents an affected area of greater than 65%. The best rating 5B represents no flaking and detachment of the coating. All of the primers show very good adhesion except for the case where the sealer, Araldite 985, had been applied between the CrMn or HAE conversion coating and the MIL-P-23377 primer. Failure occurred at the sealant/primer interface since only the primer was removed. Despite the poor adhesion of primer to sealant this coating scheme performed as well as the other primers during the salt spray test. It should be noted that the duration of the 100% humidity exposure was ~3 times as long as the exposure to the 3.5% salt spray.

TABLE 7

RESULTS OF THE TAPE ADHESION TEST

PANEL #	COATING SCHEME	RATING
A	HAE, MIL-P-23377	5B
B	HAE, MIL-P-52192	5B
C	HAE, MIL-P-85582	5B
D	HAE, 985, MIL-P-23377	0B
M	Cr-Mn, MIL-P-23377	4-5B
N	Cr-Mn, MIL-P-52192	5B
O	Cr-Mn, MIL-P-85582	4-5P
P	Cr-Mn, 985, MIL-P-23377	0B

AC Impedance Measurements

Electrochemical impedance techniques are finding increased application in both corrosion research and the evaluation of the performance of organic coating/metal systems. Since corrosion processes occurring on metal substrates under organic coatings are electrochemical in nature, assessment of the corrosion resistance of organic coatings have been made employing electrochemical measurements and much data has been reported showing that various electrical parameters can be important in selecting a corrosion resistant organic coating. Leidheiser[2] has reviewed a number of electrochemical and electrical measurement techniques for predicting corrosion at the metal/organic coating interface. He reported that a coating system resistance measured by both AC and DC resistance techniques degraded with time and a lower limit of about 10^8 ohms/cm^2 existed, below which corrosion occurred underneath the coating. He associated this temporal degradation with ion and water penetration into the coating, transport of ions through the coating, and follow-on electrochemical reactions at the coating/metal interface. Mikhailovskii[3] has reported that in many cases the DC resistance may not be a true measure of the corrosion resistance of paints. Mansfeld[4] has reviewed the current status of polarization resistance measurement and points out the advantages of the AC impedance technique in obtaining the polarization resistance especially for measurements in low conductivity media and for systems with low corrosion rates. Mansfeld has also reviewed methods of analyses of AC impedance data[5,6]. The value of polarization resistance Rp has been obtained from both Nyquist and Bode plots. Scantlebury[7] et al have applied analysis of Nyquist plots (also known as Cole-Cole) to provide an estimate of the film integrity and protective capacity of chlorinated rubber and coal tar epoxy coatings.

Figure 10 contains complex impedance plots of the real impedance Z' versus the imaginary impedance Z'' for each excitation frequency. These plots compare the behavior of the MIL-P-23377 primer which was applied over a HAE treated panel (A) and exposed to a solution containing 100 ppm Cl for 1, 7, 14 and 21 days. Although the behavior after 1 day appears to indicate that the response of the system is solely capacitive over the range shown the response curve beyond the range of the plot is a large semi-circle. The impedance behavior after 7, 14 and 21 days shows that the high frequency intercept of the curves with the Z'-axis is the same, but the reponse curves are smaller semi-circles with the center of the semi-circle lying along the Z'-axis. An estimate of the polarization resistance may be made from the intersection of the low frequency semi-circle with the Z'-axis. Similar impedance behavior for a chlorinated rubber coating has been reported by Scantlebury et al[7]. After 7 and 14 days of exposure the polarization resistance became increasingly smaller as existing pores are permeated or pathways developed, with electrolyte increasing the ionic conductivity in the coating. After 14 days a second semi-circle appeared at low frequencies and at the same time a small area of corrosion was observed under the coating. It appears that Cl ions and water had penetrated into the coating, followed by transport of ions through the coating and substrate ionic/electronic charge transfer reactions at the coating/metal interface. Similar Nyquist plot behavior was observed for the MIL-P-23377 primer which had been applied over the chrome manganese conversion coating (M). Nyquist plots which show the effect of interposing the sealer between the HAE anodize and MIL-P-23377 primer (D) are contained in Figure 11. There is very little effect of exposure time on the response curves even after 42 days of immersion in 100 ppm Cl solution. Thus plots for 7, 14, 21 and 28 days are not shown. Corrosion of the underlying Mg alloy was not observed. This behavior attests to the beneficial effect of the sealer, and correlates well with the data obtained from salt spray tests.

The Bode plot, log |Z| vs. log F (frequency) is an alternative to the Nyquist plot and is more useful because it allows a more effective extrapolation of data from higher frequencies and provides a better estimate of polarization resistance when data scatter precludes adequate fitting of the Nyquist semi-circle.[8] Polarization resistance determinations were made by extrapolation from the linear region of the Bode plot at low frequencies to the log |Z| axis. Figure 12 contains Bode plots for the panel which has been HAE anodized and primed with MIL-P-23377 after immersion in 100 ppm Cl solution for 1, 7, 14 and 21 days. Polarization resistance values extrapolated from these plots are contained in Table 8 and show that polarization resistance decreases with time of exposure as existing pores in the coating are permeated. After 14 days of exposure the coating system resistance degraded to below 10^6 ohms/cm^2 where corrosion of MgZE41A occurred.

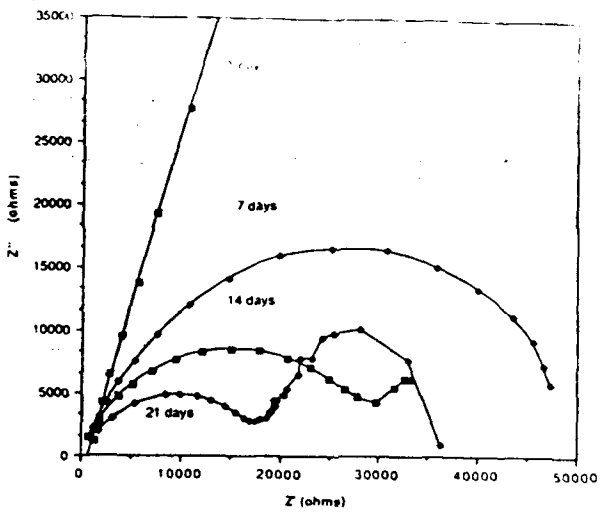


Fig. 10 Nyquist Plot for System A (HAE, MIL-P-23377) in 100ppm Cl Solution

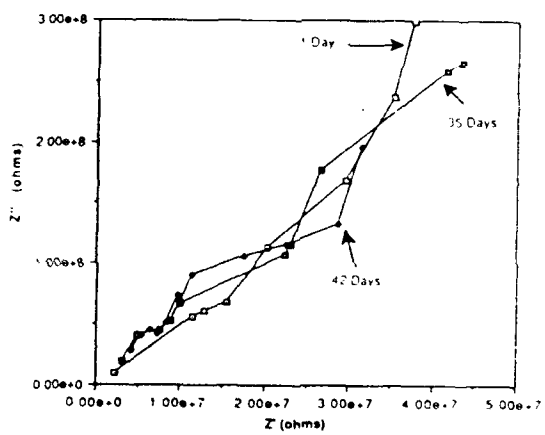


Fig. 11 Nyquist Plot for System D, (HAE, Araldite 985, MIL-P-23377) in 100 ppm Cl solution

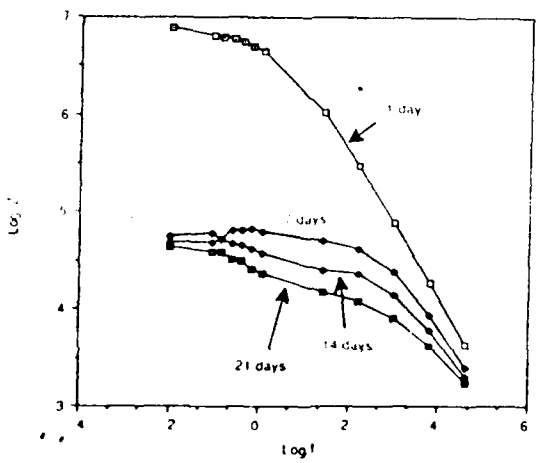


Fig. 12 Bode Plot of System A (HAE, MIL-P-23377) in 100 ppm Cl Solution

The effect of applying the sealer Araldite between the anodize and primer is shown in the Bode plots of Figure 13 and also the polarization resistance values in Table 8. Very little change is apparent even after 42 days of immersion and the lower limit of Rp is well above the critical value of 10^6 ohms/cm^2. The plots for exposure times between 7 and 35 days are not shown becasue they fall in the very narrow region between the 1 and 42 day curves. Again, these data support the results of the salt spray tests.

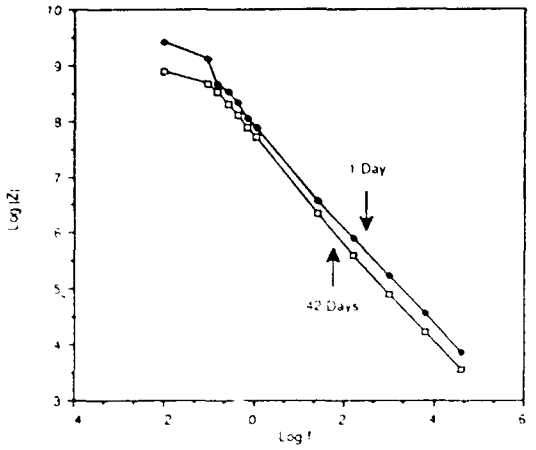


Fig. 13 Bode Plot of System D (HAE, Araldite 985, MIL-P-23377) in 100 ppm Cl Solution

TABLE 8

POLARIZATION RESISTANCE OF PROTECTIVE SCHEMES

DAYS OF IMMERSION	A	D	M	P
1	2.5 X10^7	7.1X10^9	3.0X10^9	2.0X10^7
7	1.6X10^5	2.3X10^9	8.2X10^8	3.0X10^7
14	1.4X10^5	1.7X10^9	4.6X10^6	1.6X10^6
21	1.1X10^5	1.3X10^9	1.1X10^5	1.2X10^4
28		2.0X10^9	7.1X10^4	
35		2.0X10^9	9.1X10^4	
42		6.3X10^8		

Table 8 also contains Rp values for the same coating systems except for the replacement of the HAE anodize with the CrMn conversion coating. Without the sealer, the CrMn treated system performed better than the HAE treated system over a period of 14 days. The application of the sealer provided no beneficial effect with CrMn treated and primed system. The HAE anodize, Araldite 985 sealed and MIL-P-23377 primed system performed the best with no failure after 42 days of exposure. The change in polarization resistance of all of the above described schemes plotted as a function of exposure time is more dramatically shown in Figure 14.

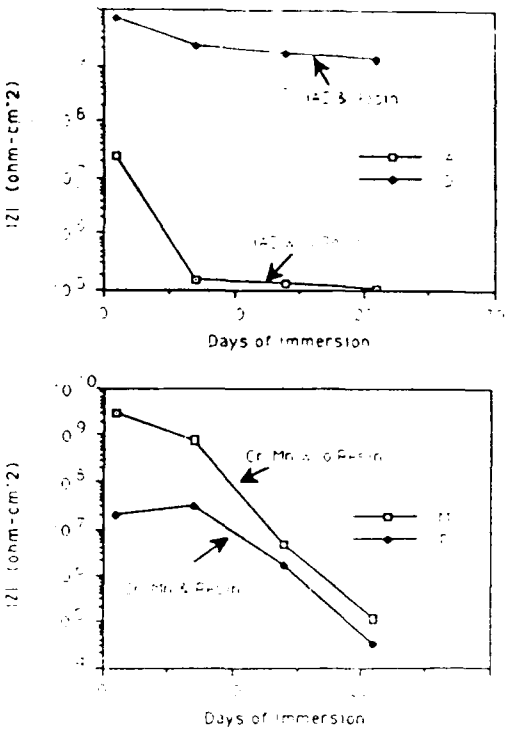


Fig. 14 Effect of Sealer on the Polarization Resistance of HAE or CrMn Treated and Primed System

Conclusions

1. The salt spray resistance of the MIL-P-23377 primer was not as good as either the MIL-P-52192 or MIL-P-85582 primers regardless of the initial treatment (CrMn or HAE anodize).
2. The application of the Araldite 985 sealer significantly improved the performance of the MIL-P-23377 primer particularly when the HAE anodize was used.
3. The AC impedance data also demonstrated the beneficial effect of the sealer in conjunction with the HAE anodize.
4. The Araldite sealer also contributed significantly to improving the salt spray resistance of the polyurethane CARC MIL-C-46186 topcoat regardless of the primer used and the initial treatment.
5. Despite the beneficial effect of the sealer in salt spray resistance of the primers, tape adhesion tests showed that the adhesion of the primer to the sealer was poor after 5 weeks of exposure to 100% relative humidity. As a consequence efforts are now underway to improve the adhesion of sealer to primer by employing a post baking treatment in accordance with a reccommendation by Taylor and Tawil[9]. Also, other sealers are being investigated.
6. The AC impedance data appeared to provide an estimate of the film integrity and protective capability of the primers which correlated with the salt spray test results. Values of polarization resistance below 10^6 ohm-cm^2 indicated significant degradation.

No. of Copies	To
	Chief of Naval Research, Arlington, VA 22217
1	ATTN: Code 471
	Director, Structural Mechanics Research, Office of Naval Research, 800 North Quincy Street, Arlington, VA 22203
1	ATTN: Dr. M. Perrone
1	Edward J. Morrissey, AFWAL/MLTE, Wright Patterson Air Force Base, OH 45433
	Commander, U.S. Air Force Wright Aeronautical Laboratories, Wright-Patterson Air Force Base, OH 45433
1	ATTN: AFWAL/MLC
1	AFWAL/MLLP, D. M. Forney, Jr.
1	AFWAL/MLBC, Mr. Stanley Schulman
1	AFWAL/MLXE, A. Olevitch
	National Aeronautics and Space Administration, Marshall Space Flight Center, Huntsville, AL 35812
1	ATTN: R. J. Schwinghammer, EH01, Dir, M&P Lab
1	Mr. W. A. Wilson, EH41, Bldg. 4612
	Chief of Naval Research, Washington, DC 20350
1	ATTN: OP-987, Director
	Aeronautical Systems Division (AFSC), Wright-Patterson Air Force Base, OH 45433
1	ATTN: ASD/ENFEF, D. C. Wight
1	ASD/ENFTV, D. J. Wallick
1	ASD/XRHD, G. B. Bennett
	Air Force Armament Laboratory, Eglin Air Force Base, FL 32542
1	ATTN: AFATL/DLYA, V. D. Thornton
	Air Force Flight Dynamics Laboratory, Wright-Patterson Air Force Base, OH 45433
1	ATTN: AFFDL/FIES, J. Sparks
1	AFFDL/FIES, J. Hodges
1	AFFDL/TST, Library
	Air Force Test and Evaluation Center, Kirtland Air Force Base, NM 87115
1	ATTN: AFTEC-JT
	NASA - Ames Research Center, Army Air Mobility Research and Development Laboratory, Mail Stop 207-5, Moffett Field, CA 94035
1	ATTN: SAVDL-AS-X, F. H. Immen
	NASA - Johnson Spacecraft Center, Houston, TX 77058
1	ATTN: JM6
1	ES-5
	Naval Air Development Center, Warminster, PA 18974
1	ATTN: Code 063
1	Code 6062
	Naval Air System Command, Department of the Navy, Washington, DC 20360
1	ATTN: AIR-03PAF
1	AIR-5203
1	AIR-5164J
1	AIR-530313
	Naval Post Graduate School, Monterey, CA 93948
1	ATTN: Code 57BP, R. E. Ball
	Naval Surface Weapons Center, Dahlgren Laboratory, Dahlgren, VA 22448
1	ATTN: Code G-54, Mr. J. Hall
1	Code G-54, Dr. B. Smith

No. of Copies	To
	Commander, Rock Island Arsenal, Rock Island, IL 61299
1	ATTN: AMSAR-PPV
	Armament Systems, Inc., 712-F North Valley, Anaheim, CA 92801
1	ATTN: J. Musch
	Beech Aircraft Corporation, 9709 E. Central Avenue, Wichita, KS 67206
1	ATTN: Engineering Library
	Bell Helicopter Company, A Textron Company, P.O. Box 482, Fort Worth, TX 76101
1	ATTN: J. R. Johnson
	Boeing Helicopters, P.O. Box 16858, Philadelphia, PA 19142-0858
1	ATTN: N. Caravasos M/S P30-27
1	Cessna Military, P.O. Box 7704, Wichita, KS 67277-7704
	Fairchild Industries, Inc., Fairchild Republic Company, Conklin Street, Farmingdale, Long Island, NY 11735
1	ATTN: Engineering Library, G. A. Mauter
	FMC Corporation, Central Engineering Labs, 1185 Coleman Avenue, Box 30, Santa Clara, CA 95052
1	ATTN: Gary L. Boerman
	FMC Corporation, Ordnance Division, 1105 Coleman Avenue, Box 1201, San Jose, CA 95108
1	ATTN: William H. Altergott
	General Dynamics Corporation, Convair Division, P.O. Box 80877, San Diego, CA 92138
1	ATTN: Research Library, U. J. Sweeney
	Gruman Aerospace Corporation, South Oyster Bay Road, Bethpage, NY 11714
1	ATTN: Technical Information Center, J. Davis
	McDonnell Douglas Helicopter Co., 5000 East McDowell Road, Mesa, AZ 85205-9797
1	ATTN: Library
	IIT Research Institute, 10 West 35th Street, Chicago, IL 60616
1	ATTN: K. McKee
	Kaman Aerospace Corporation, Old Winsor Road, Bloomfield, CT 06002
1	ATTN: H. E. Showalter
	Lockheed-California Company, A Division of Lockheed Aircraft Corporation, Burbank, CA 91503
1	ATTN: Technological Information Center, 84-40, U-35, A-1
	Vought Corporation, P.O. Box 5907, Dallas, TX 75232
1	ATTN: D. M. Reedy, 2-30110
	Martin Marietta Corporation, Orlando Division, P.O. Box 5837, Orlando, FL 32805
1	ATTN: Library, M. C. Griffith
	McDonnell Douglas Corporation, 3855 Lakewood Boulevard, Long Beach, CA 90846
1	ATTN: Technical Library, C1 290/36-84
	Northrop Corporation, Aircraft Division, 3901 W. Broadway, Hawthorne, CA 90250
1	ATTN: Mgr. Library Services, H. W. Jones
	Parker Hannifin, 14300 Alton Pkwy., Irvine, CA 92718-1814
1	ATTN: C. Beneker